Zaixing Jiang

# Sedimentary Dynamics of Windfield-Source-Basin System

## New Concept for Interpretation and Prediction

**Springer Geology**

The book series Springer Geology comprises a broad portfolio of scientific books, aiming at researchers, students, and everyone interested in geology. The series includes peer-reviewed monographs, edited volumes, textbooks, and conference proceedings. It covers the entire research area of geology including, but not limited to, economic geology, mineral resources, historical geology, quantitative geology, structural geology, geomorphology, paleontology, and sedimentology.

More information about this series at http://www.springer.com/series/10172

Zaixing Jiang

# Sedimentary Dynamics of Windfield-Source-Basin System

New Concept for Interpretation and Prediction

Science Press
Beijing

Springer

Zaixing Jiang
China University of Geosciences
Beijing
China

# Foreword I

A stable energy supply system is the material guarantee to realize the Chinese Dream. Currently, the second venture of the China oil and gas industry is ascending rapidly. In this context, the innovation of theory and method on sedimentology, which is a basic and important discipline, will potentially lead to new discoveries in oil and gas energy industries. In recent years, Prof. Zaixing Jiang has been working on sedimentary dynamics, and focusing on the impact of the windfield on subaqueous depositional environments. As an important supplement and improvement of the existing theories of sedimentology, it is expected to become a hot subject in the future sedimentology study. As a writer of the foreward to this book, I was fortunate to get the manuscript and read it through in advance and found the following innovative progresses:

(1) The research on eolian sedimentology is becoming more and more mature, but the influence of wind on aqueous depositional environments and their responses to the depositional process is not well-understood at present. This book raises the concept of "windfield" from the traditional lakes, oceans and transition depositional environments, and emphasizes its interaction with the source and basin, as well as their dynamical control on most of the sedimentary systems, including the formation and distribution of clastic and carbonate rocks.

(2) Quantitative study on sedimentology is considered as the basic direction during the sedimentology development, however, the quantitative study of paleowindfield, as described in the beginning of this book is rare in the previous research. The quantitative reconstruction methods on paleo-wind also fill the blank of atmospheric circulation in paleoclimatology.

(3) Oil and gas exploration is an important battlefield for sedimentology application, and this book shows examples of windfield-source-basin system and its constraints and influences on the source, reservoir and cap rocks, as well as their combinations in petroliferous basin, providing a new perspective for petroleum geology evaluation.

(4) The book is rich in content, including the results of modern outcrops study, such as the Qinghai Lake, and the deeply buried subsurface deposits, such as the thousands of meters deep deposits in the Shengli Oilfield, the Liaohe Oilfield and the Huabei Oilfield covering different types of sediments in Mesozoic-Cenozoic. Besides, geology, geophysics, hydrology, meteorology and other disciplines are intersected, representing the scientific connotation of "system".

As Prof. Zaixing Jiang's peer researcher, I have been paying attention to his academic achievements over years. He has been leading his team and devoting themselves into the study of sedimentology for decades and published abundant high-quality papers. This book represents the continuous, hard work and innovative results by his team and himself. I would like to recommend this book to every peer researcher on sedimentology and petroleum geology.

May 2016

Yongsheng Ma
Academician of Chinese Academy of Engineering
Sinopec Group

## Foreword II

China is a country of great oil and natural gas production and consumption and has increasing demand for energy recently. Although oil and gas resources are relatively rich, it is still difficult to meet the needs of sustained and rapid development of the national economy, which leads to strong contradiction between the supply and demand of oil and gas. In addition, the major petroliferous basins in China are gradually entered into the high-level explored stage. The onshore oil and gas exploration is mainly targeted on the lithologic oil-gas reservoir, which is subtle and more difficult to explore. Especially for the mature oil and gas exploration area in the eastern basins, the oil and gas reservation and production are not stable and the new areas and new types of oil and gas reservoirs are hard to find. Facing the grim situation and increasingly complex exploration targets, how to expand new field of exploration, broaden new horizons of development of oil and gas, and make new breakthrough for newly discovered oil and gas exploration by further study on petroleum geology and new technical method, are not only major issues to the geologists and petroleum explorationists, but also challenges and opportunities to China's petroleum geology theory and exploration.

The new scientific findings are commonly from the first-hand information from the field work, and the new ideas of exploration are normally from the practice of oil production. It is the new scientific discoveries and new exploring ideas together that promotes the formation of new theories of petroleum geology and exploration, which guides the development of oil and gas exploration. During the long-term research on the sedimentology of petroliferous basins in eastern China, Prof. Zaixing Jiang and his team combine the natural phenomena of "winds spring-up water" with the sand body prediction technique. They proposed the concept of windfield-source-basin system sedimentary dynamics which is original, will guide explanations and distribution prediction of depositional systems.

The book windfield-source-basin sedimentary dynamics points out that the depositional processes is closely related to the wind/climate, source, and basin system, thus involving controlling elements such as paleoclimate, paleo-provenance, palaeogeomorphy, and palaeo-water depth. The windfield and the associated paleoclimate control the internal sedimentary structures and textures of sediments; the provenance is the material basis; and the palaeogeomorphy and paleo-water depth significantly affect the distribution and scale of sedimentary bodies. These factors, with each one being constrained by the other, are changing constantly and interact with its counterparts to influence the depositional system. The windfield-source-basin system sedimentary dynamics research is aimed to explore how these factors control sedimentary processes.

At first, this book introduces the development of depositional system theory in the previous 100 years, focuses on the multi-controlling factors of depositional systems distribution, and suggests that the windfield is an important parameter in the concept of windfield-source-basin system sedimentary dynamics. This book also illustrates the composition elements of windfield-source-basin system sedimentary dynamics, and their influences on the sedimentary processes as well as the research methods. Under the guidance of this theory, authors take the modern depositional systems from Qinghai Lake and the ancient depositional systems from

Paleogene Bohai Bay Basin as cases study and establish modern and ancient models for windfield-source-basin system sedimentary dynamics.

The introduced new concept "windfield" by Prof. Zaixing Jiang promotes the study of sedimentology from traditionally "unitary facies mode" and "binary source-to-sink mode" into a new view of "ternary sedimentary dynamics mode", involving wind, source, and basin elements. This improves the explanation on mechanism of depositional systems (including clastic and carbonate rocks) and the prediction on the distribution of unknown depositional systems (and reservoir). The research ideas windfield-source-basin system sedimentary dynamics not only improves the development of sedimentary facies, depositional system and source-to-sink system theory, but also enriches and expands the lacustrine sedimentology theory and fill the blank in this field. It is of great significance in sedimentology and paleo-climate study, and will provide a new theory and method for further exploration of sand body in mature petroliferous basin.

September 2016

Chengzao Jia
Academician of Chinese Academy of Sciences
Petro-China Company

# Foreword III

Since Charles Lyell inherited and developed "uniformitarianism" after James Hutton, the creed "the present is the key to the past" has influenced the geological science up to now, and also become the core basis of sedimentology. It is not difficult to find out that reports of flume experiments and modern sedimentary simulation is continuing without an end and a large volume of papers have been published on authoritative journal of sedimentology and petroleum geology. By observing the complex depositional processes, these two types of work complete the study of sedimentary dynamics and facies models and exert a far-reaching influence in the academic research. However, "the present is the key to the past" does not apply to every situation due to the lack of geological records and information of some ancient events in the modern deposits such as the Paleocene/Eocene boundary event, Cretaceous oceanic anoxic events and oceanic red beds and other major sedimentary geological. The objective existence of these strata provides a basis for continuously mining the boundary conditions that controls the complicated depositional processes. Hence, "the present is the key to the past" cannot express the ancient geological process completely, and "the combination of ancient and modern" is equally important as well.

Sedimentology was introduced from the west, whereby some concepts or theories, such as facies, facies model, sequence stratigraphy, sedimentary system and source to sink system, were of milestone meanings. They were developed by the western sedimentologists, and our domestic sedimentologists mostly just follow their work and use them as reference without breakthrough. Notably, this book, by taking China's continental basins as the research objective and modern deposition from Qinghai Lake and ancient deposition from the Paleogene Bohai Bay Basin as case studies, combining ancient and modern, emphasizing wind as a control factor for depositional system as well as its interaction with the source and basin dynamic, on the basis of the traditional model and depositional system, proposes the "trinary system of windfield-source-basin system sedimentary dynamics", which is applicable in lacustrine and marine sediments. The theory of this system is originated from China's continental lake system and breaks the shackles of local facies model, depositional system and source to sink system, which is a promotion and innovation of China's continental lake sedimentology. In addition, the paleowindfield is indispensable in paleoclimate study, but it is still weak. The framework of the windfield-source-basin system makes the reconstruction of paleowindfield possible. Using the theory of windfield-source-basin system sedimentary dynamics in petroliferous basin provides a new way to predict oil and gas reservoir.

The windfield- source-basin sedimentary dynamics is the crystallization of Prof. Zaixing Jiang and his team's many years' work. It sets a good example of sedimentology study for adhering to the methodology of "vertically step-down and laterally interactive cross disciplines", which is representative and of potential replication. At the occasion of the book being published, I would extend congrats via this foreword!

October 2016

Chengshan Wang
Academician of Chinese Academy of Sciences
China University of Geosciences (Beijing)

# Preface

Sedimentary processes take place in preferable depositional environments or sedimentary basins and consequently result in the formation of sediments and sedimentary rocks. The formation and distribution of these sediments and sedimentary rocks is controlled by provenances, paleoclimate, and the sedimentary basins.

The concepts of lithofacies, sedimentary facies, facies model, and depositional system have been proposed to understand the distribution and genesis of depositional systems, and eliminate the prediction uncertainty on sand bodies.

The source-to-sink system theory combines sedimentary bodies in the basin with their sediment sources and transportation path in order to better understand the processes of how sedimentary bodies formed. It is well known that climate plays an important role in controlling the sedimentary processes, and there have been a large volume of literature published regarding the influence of temperature and humidity on the weathering of source rock and its production, and physical, chemical and even biological conditions in the basin, and their further influence on the sedimentary characteristics. However, with respect to the important component of climate, the research on how the windfield (including wind direction and wind power), influence the sedimentary processes is still not well-understood. Although the eaolian research has become increasingly mature, the influence of wind on aqueous depositional environment and its sedimentary response is still the weak section in depositional process study. The first reason is that it relates to the cross field of Meteorology and Sedimentology; second, windfield is difficult to be recorded and to be identified in ancient strata resulting in the recovery difficulties in ancient windfield. A series of studies suggest that it is easier to form waves in windward area of shore and shallow sea (or lake) due to the wind blowing in the oceans and lakes. And these waves, affected by the topography during their propagation, are main factors controlling the formation of series of sand bars parallel or oblique to the shoreline. The geometry and size of these sand bars are related to waves and wind power. Therefore, through the identification and measurement of sand bars, paleo-wind direction and paleo-wind power can be quantitatively recovered, which further provides methods for paleowindfield reconstruction. In a sedimentary basin, though both controlled by the internal basin parameters and source condition, sediments distributed in the windward area significantly differs from those of leeward area. Most onshore and shallow water depositional systems themselves are influenced by the wave action, suggesting that the windfield is an important parameter controlling the deposition. These three factors work together and exert full control of the genesis and distribution of depositional systems. The above illustration shows how the windfield-source-basin system sedimentary dynamics is put forward. The core of the theory is to introduce windfield into sedimentation, and emphasizes its interaction with the source and basin dynamic. The "Trinary dimensional attribute" of windfield-source-basin system sedimentary dynamics is improved from traditional "single dimensional attribute" of sedimentary facies and sedimentary model and "binary dimensional attribute" of source to sink system. This makes the genetic explanation on depositional systems (including clastic and carbonate) more reasonable and the prediction of depositional system (or oil reservoir) in unknown areas more comprehensively and accurately. In addition, quantitative recovery

method proposed in this book fills up the blank in the area of quantitative recovery in the atmospheric circulation in deep time. Furthermore, the source, reservoir and cap rocks in the petroliferous basin are also constrained by the windfield-source-basin system sedimentary dynamics, which provides a new view for petroleum geological evaluation.

This book consists of seven chapters. Chapter 1, written by Zaixing Jiang, Junhui Wang and Qing Li, points out the changing of the attention of the sedimentological community in the recent 100 years and the focus of sedimentology gradually shifted from the initial establishment of scientific facies models and explaining depositional environment to explain factors controlling the depositional processes. These control factors include climate, tectonic, source etc, whereby the windfield is considered as an important climate parameters and should be paid more attention as it widely influences the depositional system. Therefore, the genesis and distribution of depositional systems can be summarized as a combined effect of wind, source and basin and the windfield-source-basin system sedimentary dynamics is based on the combination of these factors. Chapter 2 (written by Zaixing Jiang and Junhui Wang) elaborates each element (wind direction, wind power, provenance, topography, water depth etc.) of windfield-source-basin sedimentary dynamic and their effects on the depositional processes. The interaction between various elements and their corresponded deposition are also analyzed. This chapter summarizes and puts forward the recovery method of various elements; improves the trinary sedimentary dynamics system comprehensively considering windfield, source and basin; and sets a classification scheme of depositional systems based on the windfield-source-basin system depositional dynamics. In Chap. 3 (written by Ji Chen and Zaixing Jiang), a modern example of windfield-source-basin system sedimentary dynamics is studied and the related depositional model is established, whereby the modern example is from the Qinghai Lake, by comparison of the leeward with abundant sediment supply and the windward system of relatively less sediment inputs. The leeward system in proximity to source area, consists of alluvial fan, fan delta, rivers and delta. The windward system with weak provenance includes eolian dune, beach barrier, lagoon, littoral and beak-shaped estuary. These modern deposits provide examples for understanding the concept of windfield-source-basin system sedimentary dynamics. Chapter 4 (written by Junhui Wang, Zaixing Jiang and Yuanfu Zhang), conducts the sequence stratigraphy and depositional system study on the fourth Member of Shahejie formation of the Paleogene in Dongying Sag. Based on the core, well log and seismic data, the research ideas and methods apply windfield-source-basin system sedimentary dynamics to recover the paleo-waterdepth, paleogeomorphology, paleoprovenance and paleowindfield. A comprehensive research on the depositional system, their genesis and controlling factors and the model of windfield-source-basin system sedimentary dynamics are presented in this chapter. The middle Eocene evidence of ancient East Asia monsoon is found and its control on sedimentary system is discussed as well for the first time. Chapter 5 (written by Xiabin Wang, Yuanfu Zhang and Zaixing Jiang) illustrates the sedimentary characteristics, genesis types and control factors in the fourth Member of Shahejie Formation of the Paleogene in Liaohe Basin. The beach bar in west Liaohe depression sand body was mainly developed in the early lowstand systems tract and transgressive systems tract. According to the sedimentary genesis, including depositional processes and sediment source, the beach bar can be subdivided into five categories: delta laterally modified, delta front modified, bedrock modified, delta submerg modified and storm modified. The distribution of beach-bar sand body is mainly controlled by the trinary system: wind, source and basin. Chapters 6 and 7 give examples of coarse clastic rocks formed under the background basin of weak wind but large sediment supply. Chapter 6 (written by Hui Liu and Zaixing Jiang) focuses on Daxing conglomerate from Paleogene in Langgu Sag. By detailed core observation and description, reconstruction of palaeoprovenance and paleotopography, three genetic models of the Daxing conglomerate are established, namely fault-trough gravity flow, nearshore subaqueous fan of debris flow and nearshore subaqueous fan of mudslide. The reservoir quality is related to such genesis models. Chapter 7 (written by Lijing Zheng and Zaixing Jiang) elaborates the research on sedimentary characteristics of dense carbonate breccia deposits, tectonic activity, provenance and basin of the

third Member of Shahejie Formation in the Paleogene in Shulu Sag. The conglomerate is divided into two categories: the fan delta conglomerates formed by the interaction of alluvial fan and lakes, and slump fan conglomerates and seismites triggered by earthquake. The reservoir quality of the conglomerate beds with different genesis and different oil-bearing property are discussed in this chapter. The whole manuscript is chiefly edited by Finally Zaixing Jiang.

Beijing, China                                                                                                    Zaixing Jiang
May 2016

# Contents

## 1.1 Depositional System Advances

Sedimentary environment, facies model, depositional system, source-to-sink system and so on have been put forward in the past two centuries, and have become important milestones in the different development stages of sedimentology.

1. Facies. The concept of "facies" was first introduced by the Swiss geologist Gressly into sedimentary rocks research in the late 1930s. He believed that "facies is the sum of sediment changes, the performance of one or other lithological, geological, or paleontological differences." Different sedimentologists have different understandings of this concept. Sedimentary facies in China is defined as "the synthesis of sedimentary environment and sedimentary rocks formed in the environment" (Jiang 2003). By definition, a facies contains both a description attribute (material composition) and an interpretation attribute (depositional environment).

In a geological record, a particular "facies" has similar lithological, physical, and biological features that distinguish it from adjacently overlying, underlying, and lateral "facies" (Fig. 1.1). Because a particular "facies" is formed in a certain environment, we can deduce the sedimentary environment through the analysis of "facies". In fact, after the emergence of the "facies" concept, the purpose of sedimentary facies study focused on the interpretation of the facies parameters or environmental boundary conditions to determine the sedimentary environment. For example, we can determine whether a sedimentary body belongs to a deltaic environment by investigating whether the planar form of a deposition unit is lobate, whether there is a mixture of land and sea organisms, and whether the sedimentary sequence is a coarsening upward sequence. The analysis of the sedimentary facies is controlled by firsthand data, which is usually fragmentary and thus is more frequently used to explain the local sedimentary process and the sedimentary environment. As Fig. 1.1 shows, we can analyze local sedimentary processes and environments of facies A and facies B in an outcrop by studying their lithology, texture, structure, and paleontology, but would be difficult to extend depositional interpretation beyond the outcrop.

2. Sedimentary environment. The sedimentary environment is defined as a surface unit of the Earth's landscape that is physical, chemical, and biologically different from the adjacent area (Selley 1996). The sedimentary environment consists of a series of following environmental conditions, including (1) natural and geographical conditions; (2) climatic conditions; (3) structural conditions; (4) physical conditions of sediment; (5) geochemical conditions of sediment (Jiang 2003, 2010a). The classification of sedimentary environments on Earth's surface is shown in Fig. 1.2.

The sedimentary environment is a place where sedimentation occurs, and the decisive factor for the formation of sedimentary rock. The concept of facies has the interpretation ability to define the sedimentary environment. For example, the deltaic facies are the physical records of the interactions between rivers and marines (or lake) in a land-sea (or lake) transitional sedimentary environment. The ultimate goal of the facies interpretation is to reconstruct the paleo-sedimentary environment (He et al. 1988). However, this process is difficult in practice because, as noted above, there is little or no necessary and sufficient condition to define a sedimentary environment. Some conditions are necessary but not sufficient; Some conditions are sufficient and not necessary (He et al. 1988). Therefore, the sedimentary environment interpretation is a result of a comprehensive interpretation of a variety of boundary conditions, with multiple solutions. In addition, since the recovery of the sedimentary environment is largely dependent on the principle of facies analysis, the sedimentary environment interpretation is also a local scale study, which is highly dependent on the firsthand data.

**Fig. 1.1** Two different lithofacies (Triassic Sanshuihe outcrop in Xunyi county, Xianyang city)
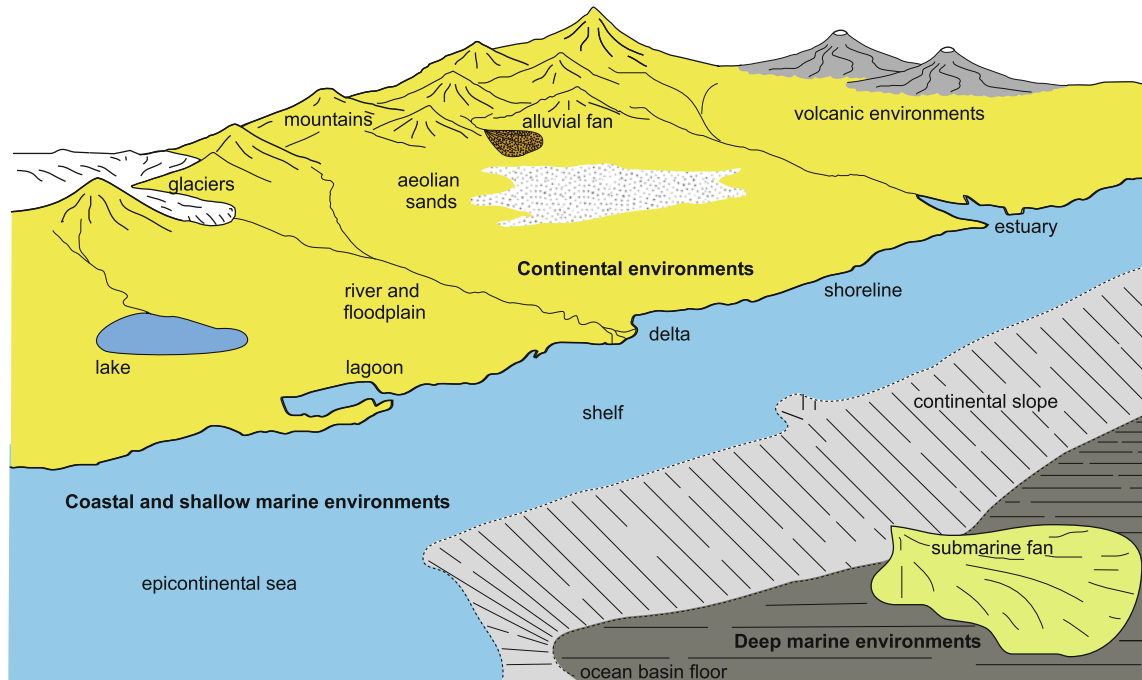




**Fig. 1.2** Summary diagram of principle sedimentary environments (from Nichols, 2009)

3. Facies model. The concept of facies model was proposed by the famous sedimentologist Roger Walker in 1970s. Since "Facies Models" (Walker 1979) was published in 1979, it has been regarded as a monument in the modern history of sedimentology. The facies model is an ideal and general sedimentary facies expressed in terms of diagrammatic, literal, or mathematical methods, and can help to understand complex hydrodynamic mechanisms and sedimentary processes. The facies model is built on a variety of physical records (including sedimentary texture, structures, etc.) that is produced by the variation of the hydrodynamic regime during deposition, and highly summaries the sedimentary environment, sedimentary processes and its products (Walker 1979). The sedimentary environment, with different deposition processes and hydrodynamic mechanisms, forms different physical records and therefore has different facies patterns.

**Fig. 1.3** Bouma sequence and interpretation (modified from Bouma 1962; Feng 1993)

| Lithological description | Grain size | | Features | Interpretation |
|---|---|---|---|---|
| | Sand/Granule | A | Massive, graded | Upper flow regime (?) Rapid depositon (?) |
| | Mud | E | Pelite | Fine-graineds, density turbidity current deposition |
| | | D | Upper parallel laminae | ? |
| | Silt | C | Ripple, wavy or convoluted lamina | Lower part of lower flow regime |
| | | B | Plane parallel laminae | Upper flow regime |
| | Sand (to granule at base) | A | Massive, graded | Upper flow regime (?) Rapid depositon (?) |

Cycle 2 / Cycle 1

Sedimentologists have established a variety of standards or general models of sedimentary facies for the interpretation of sedimentary environments through the observation of geological records, the study of modern sedimentary processes and experimental simulations. For example, the famous Bouma sequence describes the hydrodynamic state for turbidite deposition (Fig. 1.3). The facies model, from the perspective of hydrodynamic interpretation, provides a template and reference for the interpretation of sedimentary facies. Therefore, it can be concluded that the study of facies models is still within the scope of facies and sedimentary environments analysis, and is a local scale study.

4. Depositional system. This concept was first applied by the Texas Bureau of Economic Geology in the late 1960s to the Gulf of Mexico, and was then referred to an assemblage of genetically related sedimentary facies, or an assemblage of three-dimensional lithofacies that is produced by sedimentary process (Davis 1983; Posamentier et al. 1988). The depositional system concept is widely used since it was proposed. Therefore, the genetically related sedimentary facies is the basic unit of the depositional system. Since the concept of "facies" has been used extensively, Galloway (1986) suggested the use of "genetic facies" to represent the basic building blocks of the sedimentary system (Li et al. 2004), which means a particular depositional system is built on specific "genetic facies". Within the depositional system, the different genetic facies are spatially interconnected and regularly arranged (Fig. 1.4). The different genetic facies

within the same depositional system are not isolated but are causally linked to each other by one or several sedimentary processes. In addition, the depositional system incorporates the concept of time, emphasizing the evolution of sedimentary facies assemblages associated with depositional processes and genesis. The physical behavior of a depositional system is a three-dimensional depositional geological body defined by unconformity or depositional hiatus.

The compressive study of the depositional system is a summary process of sedimentary facies distribution, which is also the basis of basin analysis and paleogeographic reconstruction. Therefore, the concept of the depositional system is proposed to further extend the research scale of sedimentology, which previously based on the establishment of local facies model and the interpretation of sedimentary environment (He 2003), and is the continuation and development of sedimentary facies research (Wang and Li 2003). The depositional system analysis method is to study sedimentary process from a higher angle, pointing out the genetic facies exists as a system. Therefore, the study of the sedimentary system is focused on the evolutional process of sedimentary facies assemblage, which is related to sedimentary processes and genesis. Depositional system has gradually become the basic unit of deposition process research.

5. Source-to-sink system. The denuded landforms of the orogenic or uplift areas and the depositional landforms of
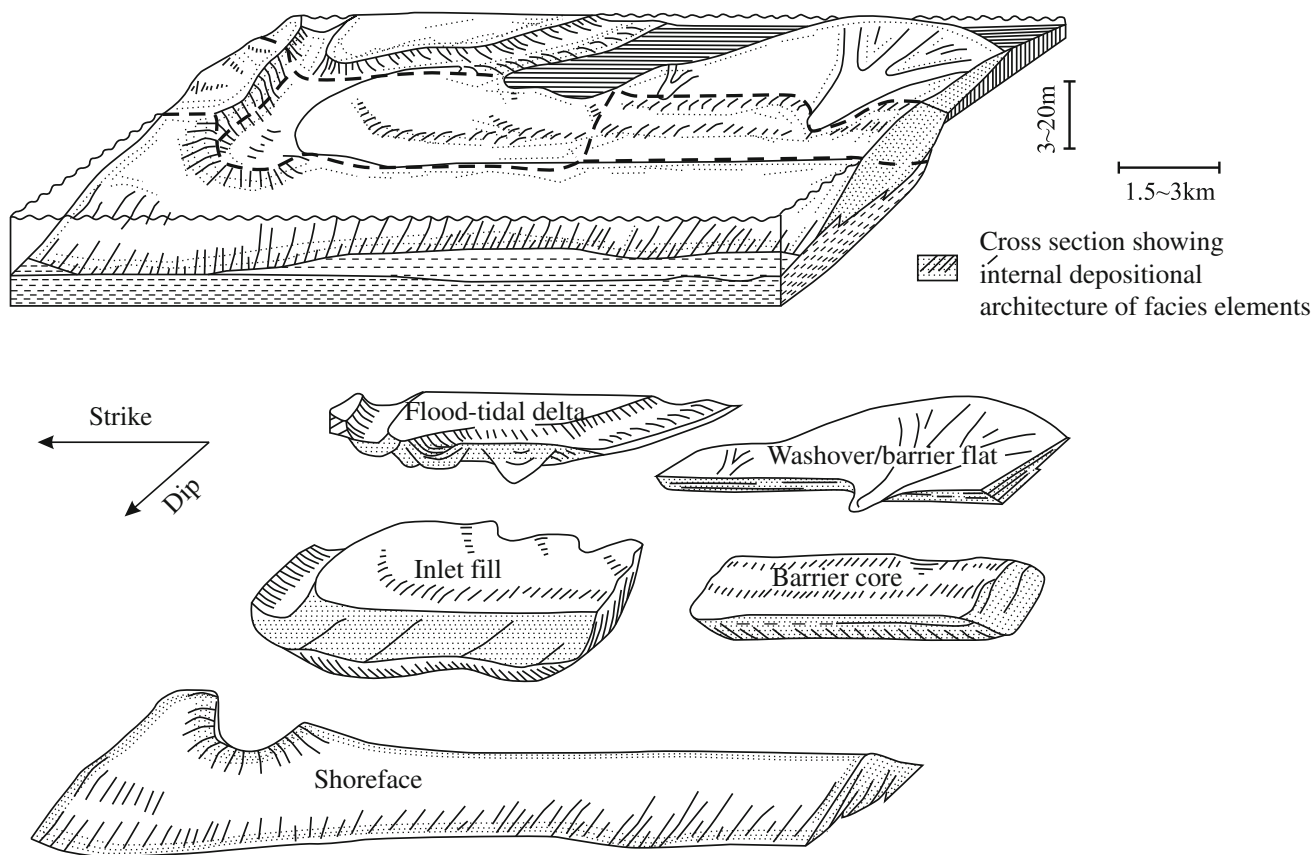
**Fig. 1.4** "Genetic facies" of barrier island in barrier shore system (modified from Galloway 1986)

the basin area are two basic landform units on the Earth's surface (Lin et al. 2015) and are linked by the sedimentary transportation system. The process of sediment eroded from the source area, including physical and chemical weathering, transportation and deposited in the sedimentary basin constitutes the source-to-sink (S2S) system. Source-to-sink system recently is a hot research topic in the field of international geosciences. Sedimentary source-to-sink involves sediment erosion, transportation, and deposition. The source-to-sink system is to study the autogenic, allogenic processes and feedback mechanisms that control sediment delivery from source to sink (Sømme et al. 2009).

In the 1990s, the MARGINS Program, led by the US National Science Foundation (NSF), has extensively studied the source-to-sink system and made significant achievements in the past decades. The core scientific goal of the project is to comprehensively study the dispersion of sediments on terrestrial and in marine environment within a time scale of various depositional processes and to synthesize the elements of the system through observation, experiment, and theory. The key question is focused on how tectonism, climate change, and sea level changes affect the generation, transport, and accumulation of sediments (including particle

and dissolved matter), revealing the processes of erosion and sediment transportation on the Earth's surface, and how the stratigraphic records produced by the interaction of deposition processes. The concept of the source-to-sink system initially emphasizes the quantification of surface processes and combines sediment fluxes with geological processes. At present, the research of source-to-sink system is an important subject in the field of earth sciences.

The geologic information preserved in the source-to-sink system is a record of the whole Earth's surface dynamics from the erosional zone to the deposition area. It is necessary to study the sediment erosion in the source area, transportation in the transfer zone and deposition in the basinal sink as a whole genetically linked system. For example, the current study of the source-to-sink system from land to sea is to reveal how sediments are eroded from uplift region, transported to the continental shelf area, and finally deposited in deep-sea area (e.g., Sømme et al. 2009, 2013; Sømme and Jackson 2013). This source-to-sink system consists of several depositional systems (Fig. 1.5) from the catchment (erosional area), alluvial-coastal plain, shallow continental shelf, continental slope, and deep-sea basins. In this process of surface dynamics, it will be influenced by external forces such as tectonism, climate change, and sea-level rise and fall. Therefore, such research involves a wide range of

Fig. 1.5 Geomorphology and sedimentological features in the source-to-sink system (Sømme et al. 2009)
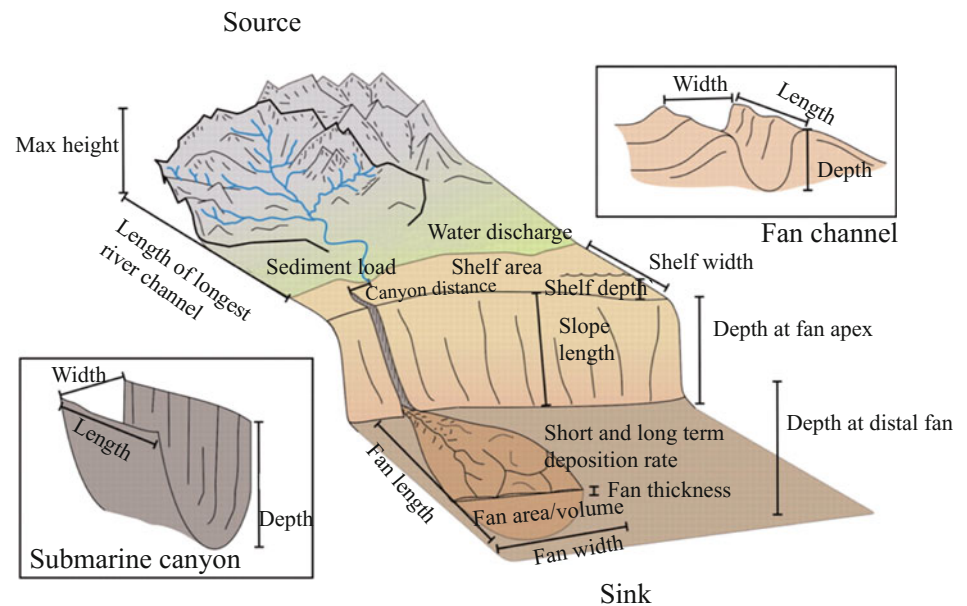
interactions and intersections between solid earth geology, geomorphology, atmospheric science, environmental science, and oceanography, and focuses on the role of external influences on erosion processes and sediment transportation processes (Lin et al. 2015). The proposed source-to-sink concept advances the sedimentary research into a more integrated science and expands the research scope beyond the depositional system. However, the source-to-sink system is still focused on the study of sedimentary characteristics and deposition process interpretation (from the source to sink in the longitudinal direction). The interpretation of the sedimentary system distribution in the region (lateral) is still not fully explored.

## 1.2 The Influence of Windfield on Depositional System

Sedimentary facies research focused on the description of local facies type, mostly for the purpose of depositional environments interpretation, while facies model emphasizes hydrodynamic changes in vertical, is an important supplement of sedimentary facies research. Depositional systems regard the different facies are genetically related and should be treated as a whole system, driving the sedimentary research from basic facies unit to completely depositional system. The source-sink system analyze the whole process of sediment delivery from the source area to basinal sink and reveal how the tectonism, climate change, and sea level rise and fall affect the sediment erosion, transportation, and deposition. It emphasizes the genetic link among depositional systems in one dimension along the depositional pathway. The research scopes mentioned above have

gradually changed from simple to complex, from partial to whole, from the study of the sediment itself to the controlling factors of sediment erosion, transportation, and deposition.

External controlling factors for depositional system include climate, tectonism, sediment source, sea level rise and fall and so on. The fully understanding of these external factors is the key to study the distribution of depositional system and matching relationship between different depositional systems. Among these external controlling factors, the influence of paleoclimate on sediment deposition is less explored so far, especially the influence of the windfield is often neglected. The windfield is an important geological force, not only has affected the sediment erosion, transportation, and deposition, it can also generate waves by blowing water body in the basin to form a broad coastal zone and control of the coastal and shallow water deposition. The effect of the windfield on the sedimentary system is common and usually expressed in the following ways.

### 1.2.1 Influence of Windfield on Clastic Depositional System

#### 1.2.1.1 Wind and Eolian Depositional Systems
The most direct effect of the windfield on the clastic deposition system is the formation of an eolian depositional system or desert system. Because the physical weathering is dominant in arid climate region, the products of weathering are usually rich in sandstone. At the same time, due to limited rainfall, large evaporation, lack of vegetation, long-lasting drought status of earth surface, the wind has a strong influence on earth landforms. The effect of windfield

on earth surface can be expressed in three ways, including erosion, transportation, and deposition. The formation of the alveolar stone, wind-eroded niche, eolian mushroom, wind erosion column, wind erosion depression, wind erosion valley, rock desert, and Gobi desert on earth surface are the result of wind erosion.

Although the transportation capacity of the wind is much smaller than the water, it still can carry a huge amount of sediment. A storm can carry hundreds of thousands of tons to hundreds of millions of tons of material (Chen 2006). As the wind blows a long distance or the wind encounters a variety of obstacles such as mountains and trees, the energy of wind waves and the sediment carried by the wind begin to be deposited. The sandy sediments carried by traction or saltation can result in sand dunes and even deserts, whereas silt and dust transported in suspended form will form eolian loess deposits.

### 1.2.1.2 Influence of Windfield on the Lacustrine System

Wind does not only directly act on the sediment, it can also drive other media to move and affect the distribution of the depositional system. In the lacustrine system, lake waves and lake currents are the most obvious hydrodynamic forces driven by the wind.

There are several important physical interfaces in the lake: the flood surface, the dry (low) surface, the normal wave base, and the storm wave base (Fig. 1.6). Among them, the coastal zone above the normal wave base is the area where the lake waves are significant. The lake waves erode, transport, re-deposit previous lake sediments, and produce various erosional and sedimentary landform, such as beach bar. During periods of storm activity, storm deposits are developed between the storm wave base and normal wave base (Fig. 1.6). These deposits are products of
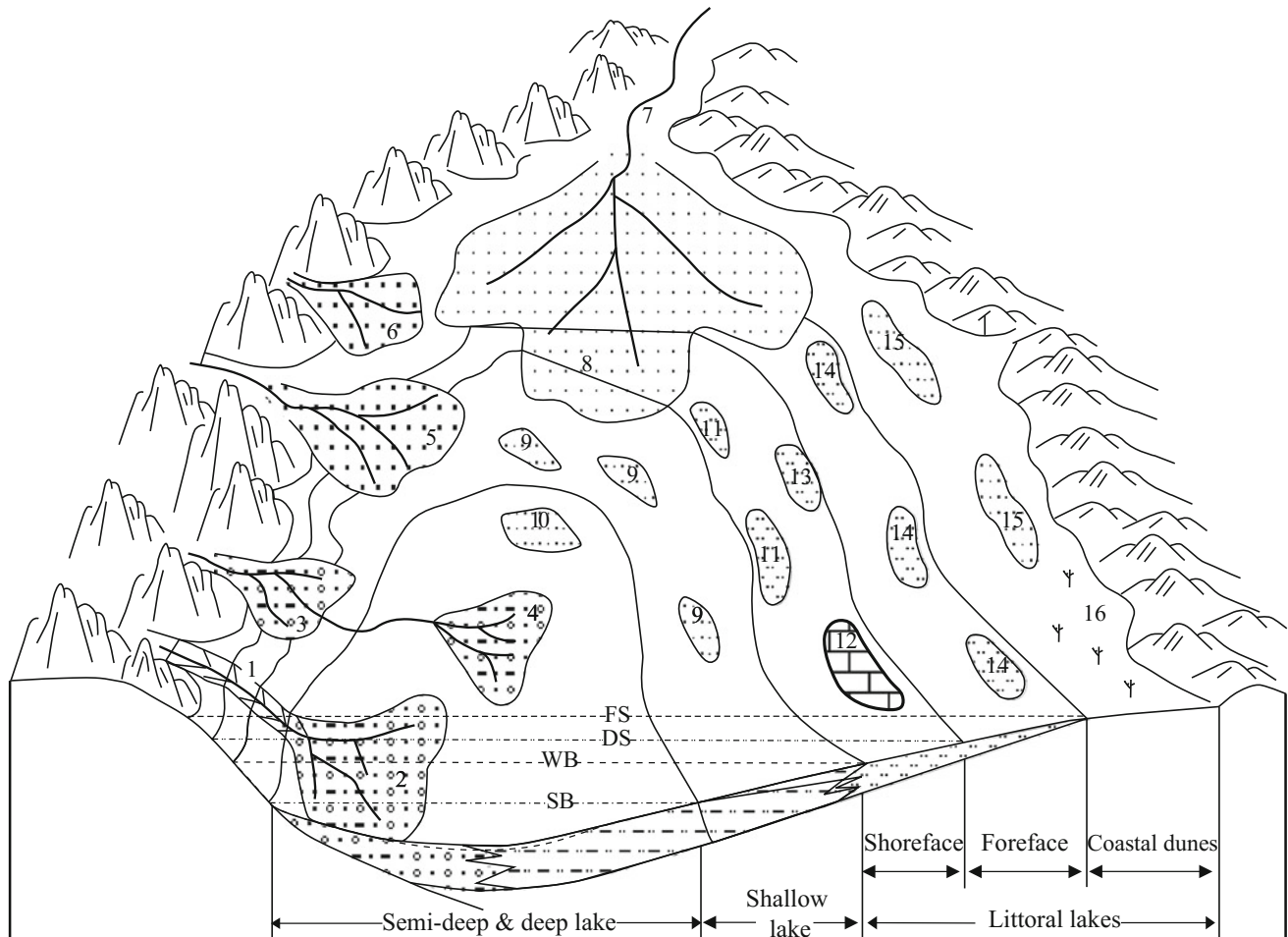


**Fig. 1.6** Schematic diagram showing depositional facies in lacustrine basin (from Jiang 2010a). 1—lake margin canyon; 2—subaqueous fan; 3—fan delta; 4—basin floor fan; 5—braided river delta; 6—alluvial fan; 7—meandering river; 8—meandering river delta; 9—tempestite; 10—turbidite; 11—outer bar; 12—carbonate beach bar; 13—inner bar; 14—coastal bar; 15—aeolian sand dunes; 16—swamp; FS—flood surface; DS—dry water surface; WB—normal wave base surface; SB—storm wave base

windfields that reshape the depositional system in a lacustrine basin. In addition, the delta system developed in the shallow water area, the redistribution of sediments can also occur under the action of wind and waves. For example, the sheet sands and sand beach mouths in the delta front are the results of the redistribution of delta sediment by lake waves and currents. If the waves are strong enough to outweigh the role of the river, the river mouth weill even migrate. In the whole lacustrine depositional system, most of the sediment deposited above normal wave base are more or less affected by wind and waves, excepted the subaqueous fan that deposited below the wave base are nearly unaffected by waves.

In addition to the role of the waves, the friction of wind on the lake surface and the pressure of wind on the wave of the windward surface will make the surface water move forward and generate wind-driven flow. Wind-driven flow is common in a large lake and can cause a large-scale and extensive flow of water in the lake. The latest research indicates that wind-driven flows can be either surface currents or bottom currents, which can act on sediments and modify the lacustrine sedimentary system (Fig. 1.7; Nutz et al. 2015). The circulation of surface currents generally follows the wind direction and rework the sediments near the shoreline, resulting in sand bar and barrier bar deposits. Surface currents will eventually converge in the windward shoreline and generate bottom currents and compensated by the bottom currents. The bottom currents are, in general, opposite to the wind direction and form a "wind-driven

water bodies" (Nutz et al. 2015). The compensated bottom currents generally occur beneath the wave base and carry sediments into the deep water during storm period, forming subaqueous prograding wedges and sediment drifts. The lake dominated by the wind-induced water circulation can be called wind-driven water bodies (Nutz et al. 2015). In fact, the flow dynamics of the wind-driven water circulation could be more complex (Han et al. 2015).

### 1.2.1.3 Influence of the Windfiled on the Land-Sea Transitional Depositional System

There are 80% of the world's coast and shelf areas subject to rework of waves, which are also largely affected by the winds. The land-sea transitional system is one of the depositional systems under an obvious wind-wave influence. The land-sea transitional depositional system includes delta, estuary bay and shore system. These three systems are to some extent unified and interconnected (Fig. 1.8). During the period of sea level regression, the sediment supply is more dominant and it is easy to form a river-dominate delta. Meanwhile, the deltaic system can be divided into river-dominated delta, tide-dominated delta, and wave-dominated delta, according to the relative strength of tide, wave, and river.

One of the major influences of the windfield on the land-sea transitional system is to rework delta system by waves. Because the sediment input from the river will be redistributed under the action of waves, a series of beach
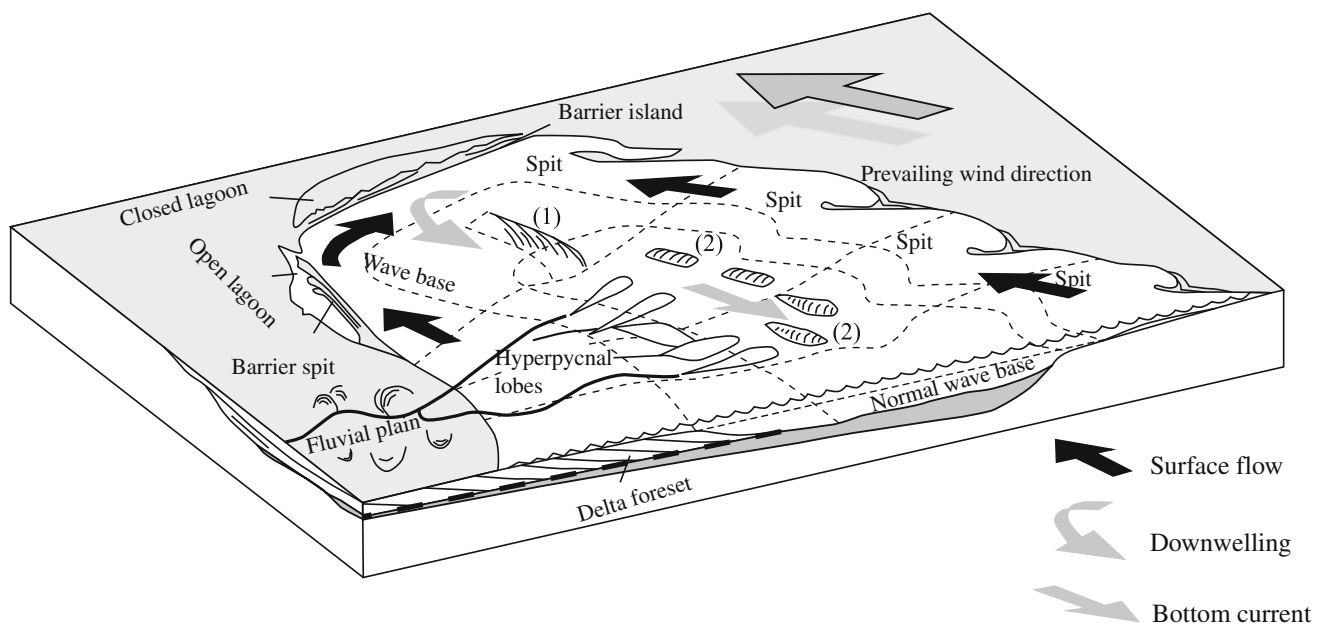


**Fig. 1.7** Sedimentary model under control of wind driven water bodies. The sediment in the vicinity of the shoreline is reworked by wind driven water bodies to form spit and barrier island. Along the wind blowing direction, compensation base flow (downwelling) is

formed near shoreline and backflow (bottom current) is formed above normal wave base, resulting in the development of subaqueous prograding wedge and sediment drift (modified from Nutz et al. 2015)

**Fig. 1.8** Classification of coastal-shallow marine environments (modified from James and Dalrymple 2010) based on the relative strength of tide, wave and river, as well as sea level rise and fall. The upper part is the classification of coastal-shallow marine environments during transgression, while the lower part is the classification of coastal-shallow marine environments during progradation
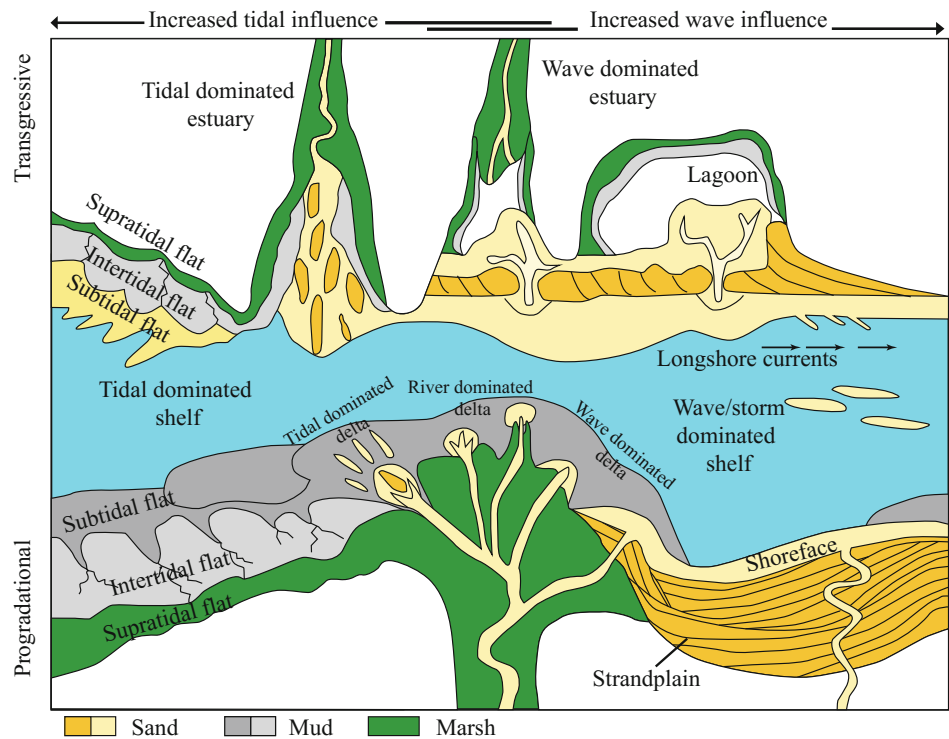
ridge sands that are parallel to the coast will be formed on both sides of the river mouth. Only in the area adjacent to the river mouth, large volumes of sands will be deposited and formed bow-shaped or beaklike delta. The Brazilian San Francisco River Delta or the Rhone Delta is a typical example. If the wave force is strong enough to completely overcome the force of the river, together with a strong one-way longshore flow, it will shift the river mouth to be parallel to the shoreline and significantly redistribute the sands, resulting in barrier island and beaklike delta. African Senegal River Delta is a typical example.

The second effect of the windfield on the land-sea transitional system is to form barrier-free shoreline depositional system. At the same time, the erosion, transportation, and deposition of the sediments are fully controlled by the wave. According to the wave hydrodynamic mechanism, the sedimentary environment can be further divided into nearshore, foreshore, and backshore.

The third effect of the windfield on the land-sea transitional system is reflected by the impact on the estuarine system, making the estuary bay closed. In the process of transgression, the sediment supply is reduced and the tides or waves from sea become more dominant, favoring an estuarine bay system. According to the relative strength of tidal and wave, the estuarine bay system can be further divided into tide-dominated and wave-dominated systems. In the tide-dominated estuarine environment, the flood tide and ebb tides form a scouring ditch and a long and narrow linear tidal

sand ridge following flow direction in the estuarine bay. However, with the enhancement of wave action, the reciprocal motion of the waves and the associated longshore currents dramatically redistribute the tidal sand ridge. The trend of the sand body gradually becomes parallel to the coastline, finally forming barrier island-lagoon-estuarine sedimentary environment.

### 1.2.1.4   Influence of the Windfield on Siliciclastic Shelf Depositional System

The influence of the windfield on the depositional system is also reflected in the siliciclastic shelf depositional system (Fig. 1.9). Seasonal typhoons or hurricanes cause storm waves to penetrate far deeper than normal waves, typically over 40 m and up to 200 m. When the violent storm wave spreads toward the shoreline, the huge energy can form the rising water once the wave encounters coastal area, resulting in storm surge to strongly erode coastal area.

When the wind energy wanes, the storm recirculation (eddy tidal current) carries a large amount of detritus from the eroded nearshore area to the offshore area, forming a density flow to the sea. This kind of fluid has a high flow velocity and can carry detritus up to tens of kilometers or even hundreds of kilometers on the continental shelf. It can significantly erode and modify the sea floor morphology. As the storm energy decays, the flow velocity becomes lower and the clastic material in the density flow becomes to be redeposited to form the shallow marine storm deposition.

**Fig. 1.9** Ideal mechanism of how the storm deposits formed (from Feng 1993)
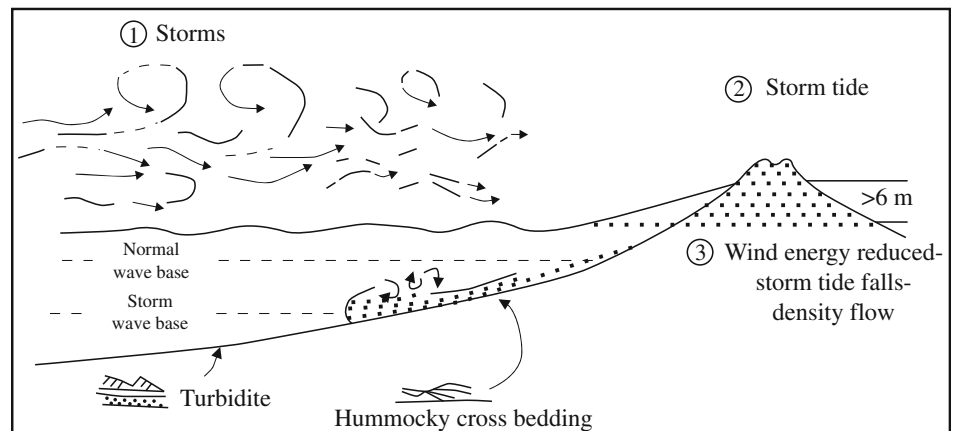


### 1.2.1.5  Influence of the Wind (Wave) on Siliciclastic Depositional System—A Case Study of Beach Bar

The beach bar is a common sand body in the shallow lake (sea) area. It is the general term of beach and bar. Its formation process is mainly controlled by the waves and longshore currents (Komar 1998; Jiang 2010a). Both beach and bar are formed in a very similar environment and overlap each other in vertical and lateral, and thereby sometimes it is difficult to differentiate beach from bar. It is, therefore, to us term beach bar or beach bar complex to describe these types of sand bodies (Wu 1986; Zhu et al. 1994; Deng et al. 2011).

However, they are very different in the formation mechanism and depositional characteristics. The bar is built up by large sediment accumulation, while the formation of the beach is not associated with significant sediment accumulation process. In the plane, the bar is usually in a linear shape and is usually surrounded by sheet-shape beach sands.

(1)  The formation of "bar"

The transportation direction and trajectory of the sediments in the coastal zone are strictly controlled by hydrodynamic conditions, so the formation of beach bar is the result of the combined effect of hydrodynamic conditions. At present, there are several viewpoints on the mechanism of the formation of the sand bar, including subgravity wave, breaker wave (or self-organization model), surfing wave mechanism, and coastal spiral flow. In addition, the longshore current system will also rework the sand bar.

1. Subgravity wave mechanism

The mechanism regards the sand bars are formed under the influence of subgravity waves, including surf beat, bound long wave, edge wave and so on, which are often characterized by standing waves (e.g., Carter et al. 1973). The sand

bar is formed at the node or antinode of the standing wave. If sediments are mainly transported by bedload flow, the sand bars are usually formed at the node of standing wave. On the contrary, the sand bars are formed at the antinode of the standing wave if the sediments are carried as a suspension (Carter et al. 1973; Short 1975). This mechanism well explains the phenomenon of multiple parallel arranged sand bars in the coastal zone and explains the increase in the distance between the bars along with the offshore distance (Carter et al. 1973; Short 1975; Aagaard 1990).

However, the subgravity wave mechanism has some drawbacks. First, the velocity of subgravity wave is much smaller than that of gravitational wave and wave current. In addition, the model requires that the standing wave energy be concentrated in the specific waveband, but the observation of subgravity wave indicate the wave bed is quite broad. Therefore, the subgravity wave may not be the dominant factor for the formation of sand bars. This mechanism has not been well documented in indoor flume experiments (Dally 1987) or modern coastal sedimentary studies (Osborne and Greenwood 1993; Houser and Greenwood 2005), although they have a good explanation of the sand bars formation.

2. Breakpoint or self-organization mechanism

In recent years, the "breakpoint model" or "self-organizational model" that explains the causes of the coastal sand bar has been widely accepted (Dyhr-Nielsen and Sorensen 1970; Coco and Murry 2007). When waves spread toward the coastline and reach the wave base, they begin to touch sea floor and be deformed due to reduced water depth. As the waves continue to spread, when the water depth is reduced to a critical value, the slope value of the wave begins to reach the limit, causing the wave rewind and broken and the formation of breaker waves. On the one hand, the waves transport sediment to the breaker wave zone. On the other hand, the landward broken waves can form the oscillation wave again and

generate a circulation on the shore side of the wave. In addition, when waves propagate to shore, a compensation flow (bottom current) can be formed. Consequently, the breaker wave zone is influenced by both the waves from offshore and coastline. The confluence of landward waves, seaward back circulation, and compensated landward bottom currents caused sediments to be deposited in breaker zone and form sand bars and associated trough (Dyhr-Nielsen and Sorensen 1970; Dally and Dean 1984; Dally 1987) (Fig. 1.10). Therefore, this model believes that the breaker waves control of the offshore location, scale, depth range and formation of the sand bar. The formation of the sand bar, in turn, will interact with the waves. As early as 1948, Keulegan's study found that as the breaker wave bars (shore bar) grows and migrates landward, the position of the breaker waves moves accordingly (Keulegan 1948). The generation and migration and breaker wave sand bars are always corresponding to the movement of breaker waves.

The breakpoint model can be simply expressed as follows. As the wave moves landward and begins to disturb the sea or lake floor, the resulted landward breaker waves and seaward circulation start to accumulate sediments to form sand bars in breaker zone. The formed sand bars, in turn, can interact with the dynamics of waves to reach the new balance and reform sand bars and associated troughs (Houser and Greenwood 2005). In a gentle slope coastal environment, when the waves break at sand bar (shore bar), it can be reformed to a new oscillation wave in the deep troughs. Reformed waves may experience a second or even third

breaker process, forming an internal local breaker zone (Qian and Wan 1991). As a result, multiple sand bars can be formed nearly parallel to the coastal zone. Although the mechanism of the self-organization model of sand bar is based on the marine environment, this model can also be applied to the lacustrine environment under certain conditions. This has been tested and validated by the flume experiment (Keulegan 1948) and the modern lacustrine sedimentary study (Greenwood et al. 2006).

3. Surfing Mechanism

The final destination of waves after breaker is to become surfing waves, forming a "surfing backwash zone". When wave move toward the shore by inertia, the water carried by wave either is infiltrated into sediment or returns directly back down along the slope to become backwash wave. This process will keep repeating until the water disappears, or collides with next surfing waves. In the surfing-backwash zone, the transport capacity of surfing waves is stronger than that of the backwash (Masselink et al. 2005), and thus the surfing waves effectively transport coarse sediments to the shore. The sediment is brought up to the highest position where surfing occurs and accumulates there, forming a sand bar spread along the shoreline, called the nearshore bar (Fig. 1.11). Sediment composition of nearshore bar includes sediments from both the source area and insitu relict sediments after erosion. The relict sediments indicate the height of sediment that can be reached by surfacing.



Fig. 1.10 The genetic model of breaker wave bar
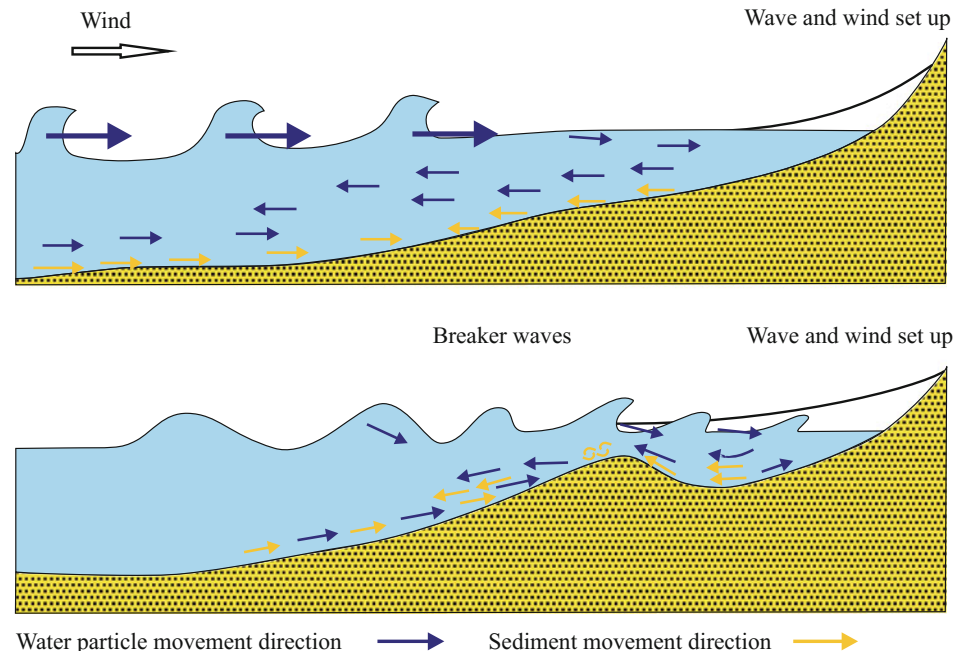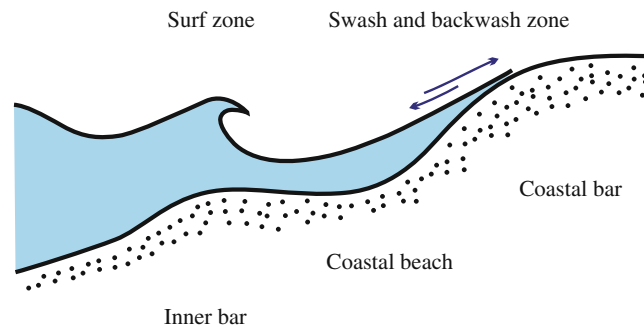
**Fig. 1.11** Schematic diagram showing the topography of surf zone and swash-backwash zone

4. Formation mechanism of longshore spiral flow

The spiral flow mechanism of the bar is proposed by Schwartz (2012). Schwartz (2012), by studying Lake Michigan in North America, proposed a longshore spiral flow can be formed when wind-driven waves flow toward coastline in a low skewed angle (Fig. 1.12). According to the different characters of the wave flow, this spiral flow consists of three parts: the oscillation flow generated by the incident wave, wind-driven longshore current, breaker waves driven longshore current. In this kind of sand bar system, the sediments influenced by spiral flow that is parallel to shoreline, can accumulate to form sand bars and evacuate to form inter-bar troughs. In the micro-topography of the sand bar-trough, the trough is mainly controlled by the longshore current, while the sand bar is mainly controlled by the wave oscillation. From midline of trough to bar crest, the strength of longshore current is reduced and the velocity of the water particle track (oscillatory flow) is enhanced. Under such conditions, the sediments are stripped from the troughs and transport to both sides of slopes and form sand bars. Therefore, the erosion mainly takes place in the troughs,

result in concentration of coarse-grained sediment and lag deposits. The bar is composed of fine-grained sediment after wave sorting. This process leads to the formation of erosion-dominated troughs and deposition-dominated sand bars. In this mechanism, the amount of net sediment transport is toward the coastal direction. Although the bar crest is influenced by the oscillatory flow, it is also affected by the longshore current. This mechanism has been verified in modern shoreline sedimentation (Greenwood and Sherman 1984; Greenwood and Osborne 1991; Schwartz 2012), but the application of this mechanism to ancient sand bars has not been reported.

5. The rework effect of longshore current

The flow generated by nearshore waves is very complex in the plane. In addition to the reciprocating motion directly generated by the waves, there are two additional kinds of wave-generated flow system. They are: (a) a circulation system composed of a fraction and its associated longshore currents, and (b) a longshore current due to oblique incident waves (Komar 1998) (Fig. 1.13a, b). The two systems are



A: Oblique incident wave and wind    B: Hydrodynamics that are composed of longshore current and rotary flow

C: Sedimentary structure suggesting the sediment migrate toward bar crest    D: Sediment movement direction
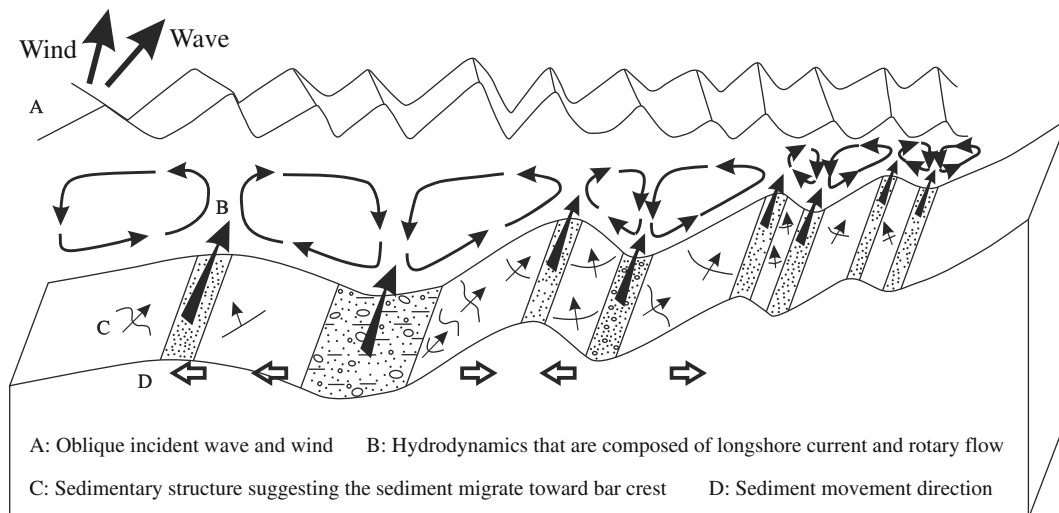
**Fig. 1.12** Schematic diagram showing the sand bars in the coastal area that formed by the mechanism of helical flow (modified from Schwartz 2012)
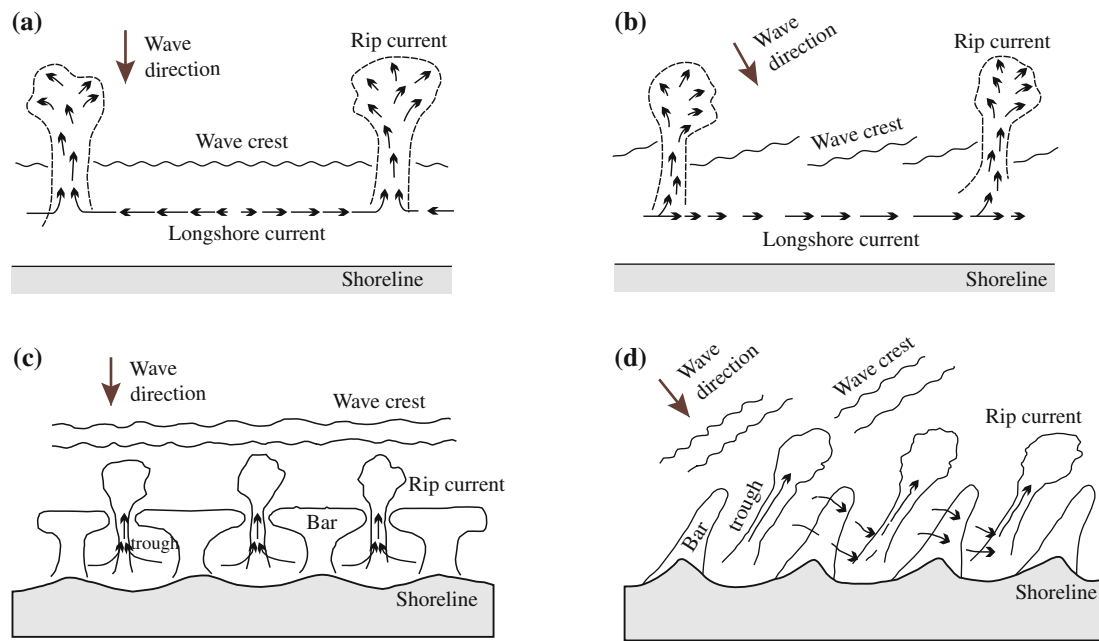
**Fig. 1.13** Nearshore circulation system and oblique wave and its modification to the sand bars (modified from Komar and Inman 1970; Komar 1998). **a** The near shore circulation system caused by forward wave; **b** The nearshore circulation system caused by oblique waves; **c** The reworking of sand bars by the near shore circulation system that is caused by forward wave; **d** The reworking of sand bars by the near shore circulation system that is caused by oblique wave

usually coexistent, and the corresponding erosion, transport, and sedimentation play a significant role in the redistribution of sediments.

After wave broken, due to the complexity of the coastal zone terrain, and inconsistent water level that generated by the different wave height along the coastline will generate wave energy gradient along the coastline, which drives the longshore current to move parallel to the shoreline. The flow will converge to the offshore direction at weaker locations, creating a friction stream that can pass through the breaker zone and dispersed in fan-shaped (Komar 1998) (Fig. 1.13 a). The amount of water lost to the offshore direction is compensated by the mass transport of the water from the breaker zone. The seaward moved flow, compensated longshore flow, and friction flow together constitute the circulation system of the coastal zone (Shepard and Inman 1951). The friction flow and associated longshore currents can redistribute sediment and form multiple sets sand bars that are separated by troughs and corresponding shoreline (Bowen and Inman 1969; Komar 1971) (Fig. 1.13c).

When the incident wave skews shoreline, it will also generate a longshore current nearly parallel to the shoreline, flowing along the bar-trough flow system. The longshore current also has significantly affected the transportation of sands and muds in the coastal area (Fig. 1.13b). When the oblique wave reaches the coastal zone, fractured flow and associated channels and bars would be affected (Fig. 1.13b) and adjusted in the direction that parallel to incident wave

peak, resulting longshore migration and oblique sand (Fig. 1.13d).

(2)   The formation of beach

In contrast to "bar" that is the result of sediment accumulation, "beach" is formed generally with no significant deposits gathering. The beach is mainly sheet-like sand bodies that surround bars, found either between the gaps or outside of bars (Jiang et al. 2015).

Besides the beach sands in the coastal area, during the spreading process, the waves encounter underwater ridge, resulting in reduce of wave energy and unloading the carried sediments. The deposited sediments can be reworked into sand waves under the influences of wave and can be regarded as subaqueous beach sands. Similar sand bodies were found in S4 formation both in the central uplift region of Dongying Depression (Tian and Jiang 2009) or Huiming Depression (Zhang and Zhang 2009). Generally, these ridges are relatively far from the source area, may also form carbonate beach (Zhu et al. 1994; Yang et al. 2010).

### 1.2.2   Effect of the Wind on Carbonate Depositional System

The factors affecting carbonate sedimentation is very complex, including tectonism, biological, hydrological, and

physical process. Among them, the wind and wave are important factors in controlling carbonate deposition.

### 1.2.2.1  The Influence of Wind and Waves on Carbonate Platform and Associated Sediment Types

(1)  Influence of wind on carbonate platform type

During the development of carbonate platform, hydrodynamic changes can shape the slope and morphology of carbonate platform. In the case of increasing hydrodynamic power, the original low and flat platform slope become steep due to erosion and the grain size of sediment increases corresponding. On the contrary, as the water energy weakened, the steep slope of the original area becomes to accumulate finer grained sediments and then reduce the angle of slope.

Thus, original platform slope that created by tectonism can be modified by hydrodynamics and correspondingly the sediments deposited there can be also changed (Gu et al. 2009).

High-energy environment induced by strong wind and wave favor growth and development of reef organisms. The framework of the reef and rapid cementation of seawater can be resistant to waves and formed a high-energy coastal fringing reef. This kind of reef can be usually found at the turning point of the continental shelf and slope, forming a rimmed carbonates shelf. Compared with rimmed carbonate platform, rim-free platform or open platform often developed on the leeward side of the wave. When wave energy is relatively weak, the shelf margin lacks the grain beach facies or reef zone to form rims (Jiang 2010a).

(2)  Influence of wind on sedimentary facies of carbonate platform

Water energy is the main factor controlling carbonate sedimentation. Shaw (1964) for the first time discussed the water energy of epicontinental sea environment and proposed the sedimentary differentiation of epicontinental sea carbonates depends mainly on the energy of the seawater. Waves, currents, and tides in the epicontinental sea are the main factors controlling the carbonate zonation. Irwin (1965) further proposed epicontinental sea depositional model and idea sequence of energy zones. From offshore to coastal area, the epicontinental sea can be divided into three zones, X, Y, and Z, according to the energy level (Fig. 1.14) (Liu and Zeng 1985).

X zone is characterized by low energy, below wave base and hundreds of kilometers wide. This zone is rarely disturbed, except bottom currents can affect sea floor. The sediments are mainly fine-grained with materials are delivered from the high-energy Y zone. The depositional rate is generally slow with thinner sediment thickness in this zone. Sediments are general in dark color and are characterized by typical parallel bedding.

Y zone is characterized by high-energy, tens of kilometers wide, active waves and tides are, sunny, rich in oxygen, and flourish of benthic algae. It often forms reefs or reef beaches. In the shore side of Y zone, due to the strong hydrodynamic various coarse-grained allochthonous carbonate particles are deposited, such as oolitic, and bioclastic and other autochthonous debris. Grains are mainly composed of sandy and gravel clastic with very few muds. Since bioclastic or oolitic are reworked and sorted by waves and currents in Y zone, the limestone formed there are characterized by cross-bedding and well-sorted particles.

Z zone is characterized by low-energy, hundreds of kilometers wide, shallow sea level that no more than a few meters and restricted water circulation. Z zone is mainly influenced by the tide and only slightly affected by the wave. Only storm can induce large waves to affect Z zone. Carbonate sediments of this zone are mainly low-energy marls, some of which are transported from the high-energy zone, and the others are the physical and chemical precipitation directly from seawater. Micritic limestone or laminar limestone and dolomite are major types of carbonate developed in this zone.

Wilson (1975) integrated a number of modern and ancient carbonate depositional models and the energy zone classification that based on the water energy with various parameters, including sea floor topography, tidal, wave, oxide interface, salinity, depth, water circulation, and climate conditions to establish a comprehensively standard carbonate depositional facies model. The marine carbonate can be divided into three facies zone and ten standard facies zone (Fig. 1.15). The basic framework is still composed of the low-energy, high-energy, low-energy zones. In the distal basinal facies zone, major facies zones are basinal facies, deepwater shelf facies, slope toe of platform facies and are located below wave base, which is characterized by low energy and corresponds to the low-energy X zone defined by Irwin (1965). In platform-margin facies zone, major facies zones are the slope of platform facies, platform-margin reef facies, platform-margin beach facies and are located above the wave base, which is characterized by high wave energy and corresponds to high energy Y zone defined by Irwin (1965). In platform facies zone, the open shelf platform facies, restricted platform, evaporate platform facies are major facies zones. The platform facies zone is located in the landside of platform margin and is commonly influenced by tide with little effect from the wave. This facies zone has relatively low water energy and corresponds to the low-energy Y zone defined by Irwin (1965). In some cases, part of open platform area may also have a higher hydrodynamic energy.
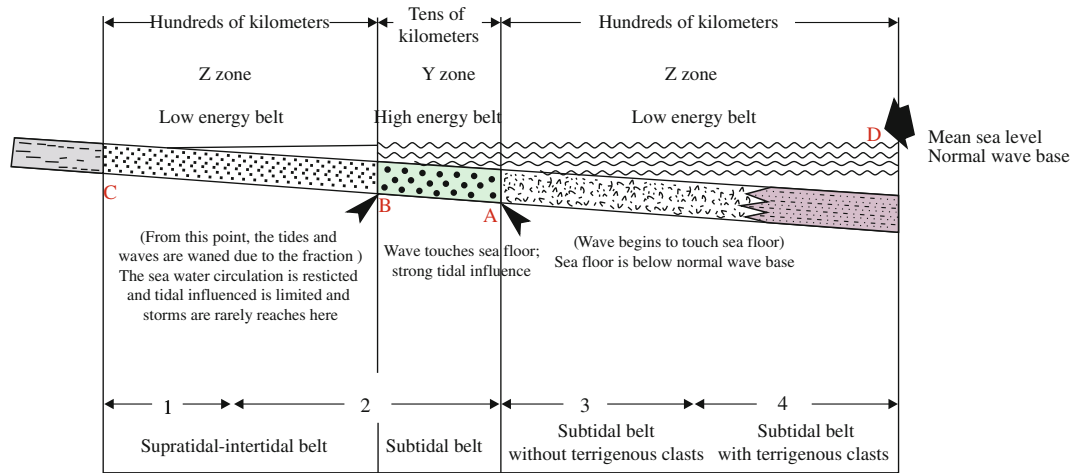
**Fig. 1.14** Carbonate depositional patterns in epicontinental sea platform and ramp (modified from Liu and Zeng 1985; Flügel 2004). A-Wave base surface; B-Average low tide level; C-Mean sea level; D-Average high tidal level
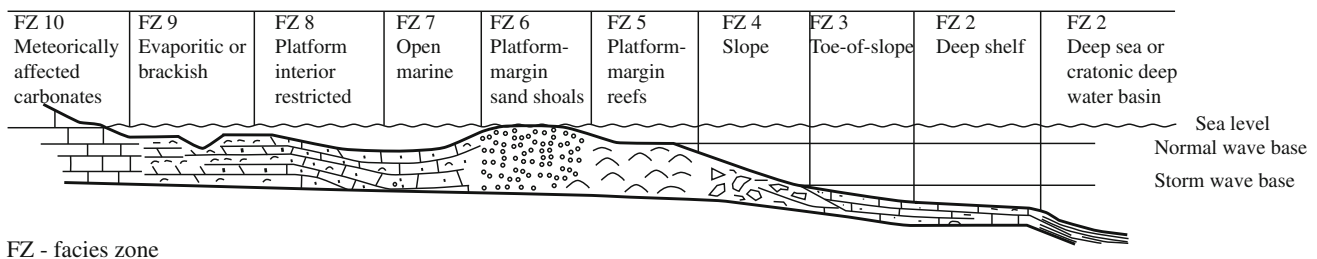


**Fig. 1.15** Rimmed carbonate platform: modified from Wilson facies model (from Flügel 2004)

(3) Influence of wind on in situ growth of reef

Biological process is one of the important causes of carbonate deposition. Some organisms have ability to live in the high-energy water environment and build reef under high-energy waves and currents. In the high-energy zone, due to landward winds and tides, the waves begins to stir and cause seawater pressure changes. This make the raised seawater from bottom to be warm up and pressure released, leading to release of $CO_2$ and deposition of $CaCO_3$. Meanwhile this process also bring a lot of nutrients to shallow surface to enhance the growth and development reef. Therefore, fringing reef can be formed in the high-energy zone near shoreline, while the barrier reef is usually formed in shelf-margin (Chen et al. 2004). Because of the rapid cementation of biological framework and seawater, the reef can be resistant to waves and formed rimmed carbonate platform.

In addition, hydrodynamic conditions have a significant influence on the reef facies. Based on paleogeography and its corresponding hydrodynamic conditions and reef facies compositional characteristics, reef facies can be divided into three basic types (Fig. 1.16).

Type I is slope marl mound, located on the front edge of the continental shelf platform slope and composed of bioclastic marls. It has a linear shape in plane and has gentle slope angle, ranging from 2 to 25°.

Type II is ramp knoll reef, formed by linear reefs that build on the platform margin. It has a seaward gentle slope, ranging from a few degrees to 15 degrees. Due to the lack of strong wave action, it has lack organism that builds a massive framework, but the surface of the reef can be attached with other organisms.

Type III is steep slope skeleton reef, located in steep slopes fringe with a slope angle of 45° or even upright. This reef can grow to sea surface or wave stirring zone and mainly is composed of the biological framework.

(4) Influence of wind on sedimentary texture

Different water energy conditions will produce different sedimentary texture. Carbonate platform margin shoal depositional environment is a high-energy environment in platform-margin facies zone. It is located in the open shallow shelf with no barrier islands and vast algal mat, and thus the carbonate deposition is directly controlled by the marine and

**Fig. 1.16** The influence of wave energy and sedimentation rate on reef type, shape and growth (from Flügel 2004)



Low water energy

Tidal flat   Lagoon sedimentary cycle   Tidal flat sand island-calcareous sandstone

Foreslope mudlump   Foreslope debris

Type I

Low-medium water energy

Lagoon sedimentary cycle   Tidal flat sand island-calcareous sandstone   Platform reef mound

Type II

High water energy

Tidal flat   Lagoon mud   Patch reef-sand bar   Autochthonous atoll   Foreslope debris or blocks

Type III

tidal waves. The wave (including tide) and its associated longshore currents, bottom currents have winnowed the carbonate deposits to form clean carbonate grain deposits. In this winnowing process, the fine-grained materials are sorted out from carbonate deposits and thus it forms coarse-grained sandy or gravel beach, shell beach or longshore sand bars. The lithofacies generated in this environment is rich in sparite limestone, oolitic limestone, other grainstone and rounded bioclastic limestone and is characterized by good sorting, roundness and light color. The sorted out fine-grained clasts (e.g., marls) are deposited on the shelf-margin or deep water basin in front of barrier island or lagoon and tidal flat behind barriers.

Flügel (2004) studied the relationship between winnowing strength of the coquina, sorting, roundness and strength

of waves or currents (Fig. 1.17). The marls formed in low energy environment has experienced little sorting (A), while in moderate to the high-energy environment it has medium (B) to good sorting (C and D) respectively. The increase of wave and current energy can increase the sorting grade of sediments from C to D and generate grading beds. The increase of roundness (E) may also reflect the increase in the water energy. In abnormal environments, such as storm, the sorting and roundness of carbonate grains are reduced (F and G).

(5) Storm-induced shallow marine carbonate deposits

Big storms can reach tens of meters below the storm wave base and interact with the sea floor, generating waves and

**Fig. 1.17** The relationship between winnowing, sorting and roundness and hydrodynamics (from Flügel 2004)



| Angular | | Well-rounded | Break up again |
| Poor-sorted | | Well-sorted | Mixed grain size, poor-sorted |
| Marl matrix | | Sparry calcite cement or porosity | |

Degree of development

Winnowing   Sorting   Rounding

Wave or current strength

?

A Biomicrite   B Weakly flushed biosparite   C Poor-sorted sparite bioclast limestone   D Well-sorted sparite bioclast limestone   E Well-rounded sparite bioclast limestone   F   G Turnover structure

**Fig. 1.18** The influence of storm on slope and ramp sedimentation (from Tucker and Wright 1990)
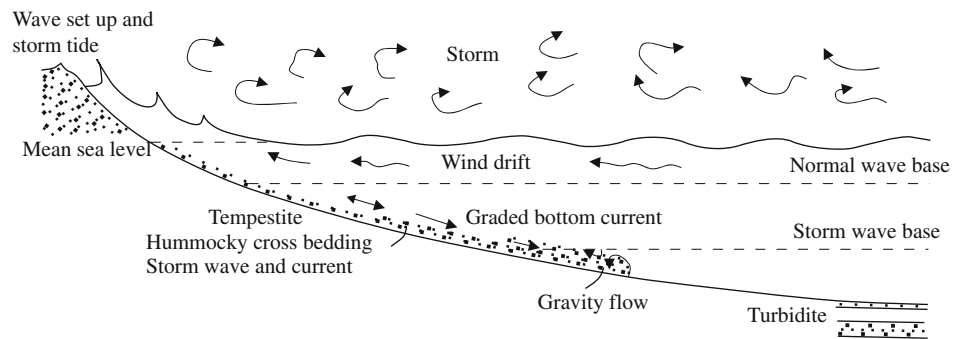


currents to stir sediments and to produce specific sedimentary structures (e.g., hummocky cross stratification) and deposits (e.g., Tempestite). Violent storm can erode shoreline, destroy tropical islands and reefs, redistribute the sediment in nearshore and offshore, and create large-scale tidal deposits. The strong storm is characterized by (1) transportation of sediments on the shelf and even to slope and deep water basin, and (2) destruction of the reef.

Landward storm can cause upwelling of water and when it attenuates, it can form seaward backwash currents that can carry the sediments from nearshore to offshore by the high-density flow. The sediments can enter below storm wave base and generate storm-induced turbidite. This kind of deposits is more commonly in the windward continental shelf and slope, due to sediment-laden storm churning through the opposite direction returning carried sediment from the coast to the deep water offshore in outer slopes. As the storm waned, these sediments redistributed along the slopes, forming sheet-like deposits (Fig. 1.18) in the low-energy environment below storm wave base. These deposits show a clear trend in proximal sources and distal source, such as Arabian Strait. Tempestite in the rimmed platform (e.g., Florida) has high internal compositional varieties. In the isolated platform, the storm only affects the platform margin.

Under the influence of storm-driven macro waves, the sediments deposited in nearshore, shoal and subtidal zone can be washed and crushed to form various types of Tempestite, such as calcirudite, redeposited oolitic limestone, wackestone with hummocky cross bedding, and turbidity limestone (Chen et al. 2004). In addition, storm can affect reef to form breccia and isolated reef blocks on the slope of reef complex.

(6)	Eolian carbonates

Eolian carbonate mainly refers to coastal dunes limestone that is originated from carbonate rock fragments in the shallow marine and modified by the wind (Brooke 2001; Zhao et al. 2014). Eolian carbonate usually consists of multi-phases sand dunes and each phase is divided by the unconformity surfaces, which are marked by paleo-soils,

shallow marine deposits, interbedded lagoon deposits and cave deposits. Eolian carbonates are usually in linear shape and parallel to the coastline. These parallel-linear carbonate ridges can be merged to be a carbonate complex and formed oblique or parabola-shape or crescent-shaped dunes. These dunes are major features for Quaternary coastal landscape and record the depositional history of shallow marine carbonate and history of coastal environmental changes (Fairbridge 1995; Vacher and Rowe 1997).

Eolian carbonate rocks can be divided into terrestrial eolian carbonate and islands eolian carbonates, and are widely distributed in the world (Fig. 1.19). Eolian carbonate rocks are not evenly distributed in latitude, with more than 80% of the eolian carbonate located between 20 and 40° in north and south. There are much less eolian carbonates developed within the lower latitude or higher latitude. Most of the eolian carbonates are found in South Australia, southwest coast of Australia and the Mediterranean area.

The development of eolian carbonates requires warm climatic conditions and steady landward wind, allowing the beach deposits continuing to accumulate and build sand dunes (McKee and Ward 1983). In addition, the development of eolian carbonates also requires favorable topographical, climatic, and oceanic conditions (Brooke 2001; Zhao et al. 2014). The strength of the wind and wave energy will also affect the accumulation rate of carbonate rocks, as well as the thickness of eolian calcarenite. High wind strength can increase the wave energy and thus increase the transport capacity of sediment to shore. Therefore, in the low energy Mediterranean West Bank the thickness of eolian calcarenite is only up to several tens of meters (Fumanal 1995), while in the relatively high energy Australia's southern coast (in the late Pleistocene period), the thickness of eolian calcarenite sequences can be up to 150 m (Belperio 1995).

### 1.2.2.2 Case Study from the Bahamas and the Great Barrier Reef

The Bahamas platform is an isolated platform, surrounded by deep water, with no apparent supply of terrigenous clasts. Great barrier of Australia is rimmed ramp carbonate platform. The Great Barrier Reef is roughly parallel to the coast but some distance from the coast. The inside of Great Barrier Reef is a
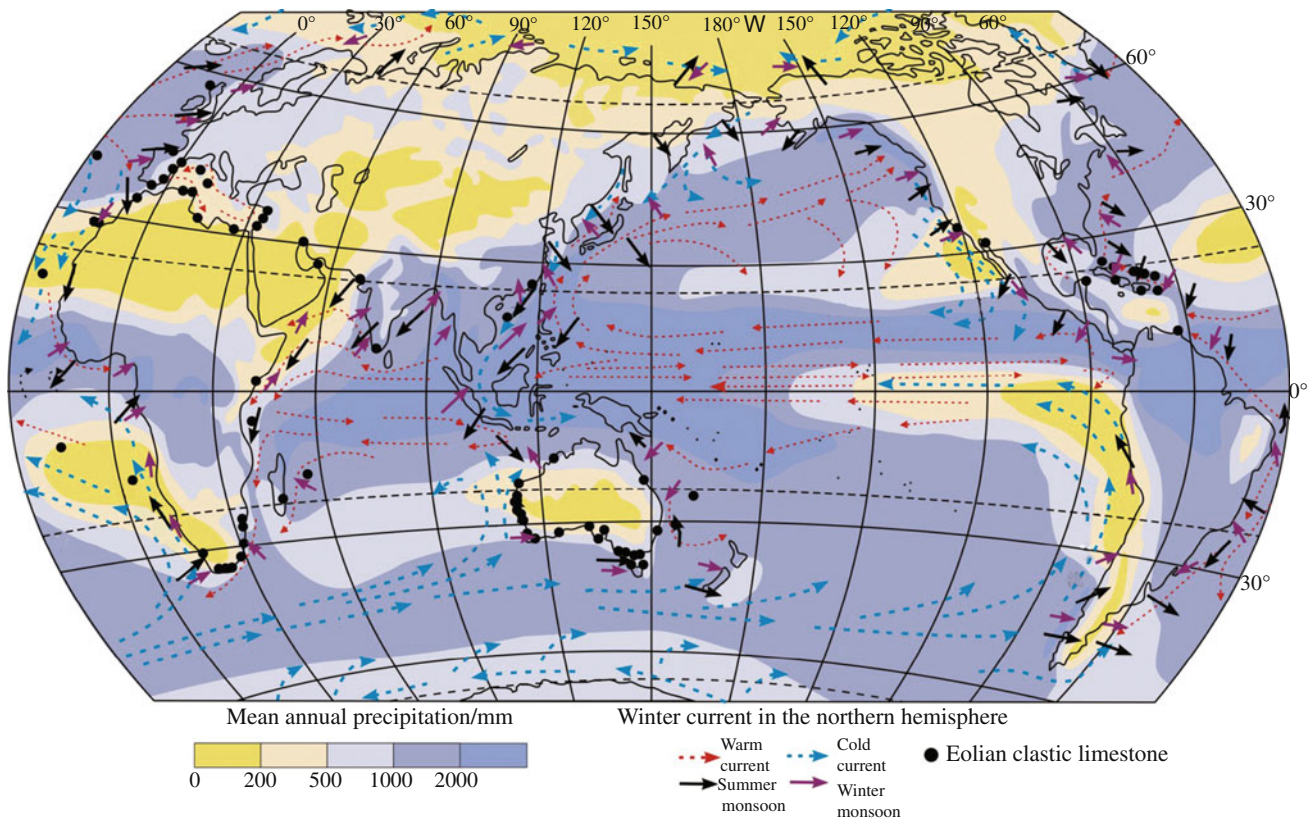
**Fig. 1.19** Distribution map of global aeolian arenaceous limestone, annual average rainfall, oceanic currents and wind direction (modified from Brooke 2001; Zhao et al. 2014)

restricted platform, whereas the outside is an open platform with an obvious supply of terrigenous clasts (Flügel 2004).

**(1) Bahamas platform**

The Bahamas Islands are located between the Grand Bahama Island on Florida's southeast coast and Great Inagua Island of Haiti and extend as far as 1200 km. Bahamas Islands consist of a series of islands and sandbars that are built on the carbonate platform. One of the biggest platforms is the Grand Bahama Bank with a water depth of ~20 m. The Bahamas is in a subtropical climatic zone with the average temperature of 24–32 °C.

The Bahamas is a typically isolated platform, covering an area of 700 km × 300 km. It is bounded by Straits of Florida in the east and bounded by Providence strait in the west with a water depth of ~200 m. The platform is mainly composed of Pleistocene limestone, which overlays the Cretaceous and Paleogene and Neogene limestone and is overlain by Holocene limestone. However, as the Bahamas is bounded by two subtropical arid area, the climate is very sensitive to changes in ocean currents. If the currents weakened, this area could be easily influenced by arid climate.

The sediments of the Bahamas are related to the sedimentary environment, wind direction, and hydrodynamic energy. The controlling factors for the sediment distribution in the Bahamian platform include the direction of the windward direction and leeward direction, the open or restricted water cycle, the conditions prevailing by waves or storms. The Coral reefs are located on the windward side, east of Andros Island (Newell et al. 1959). Skeleton particle (Coral algae), oolites and reefs are developed in platform margin. The oolites are formed in the strong hydrodynamic areas, such as the southern tip of the tidal bar area and the northwest margin of the platform. Skeleton grains are deposited at the margin of the platform with a width of thousands of meters (Flügel 2004). The interior area of the Bahamas platform is a restricted platform, with weak hydrodynamic forces and fine-grained sediments, and higher salinity than normal sea (Figs. 1.20 and 1.21) (Gu et al. 2009).

Holocene eolian carbonate sediments are common in the Bahamas. According to the Rao Carbonate classification (Rao 1996), the Bahamian eolian carbonate is an example of the development of carbonate in the tropical zone. The structure of the Bahamas is relatively stable, and the eolian carbonate rocks are generally developed into lateral, vertical, and superimposed complexes (Hearty et al. 1998). The
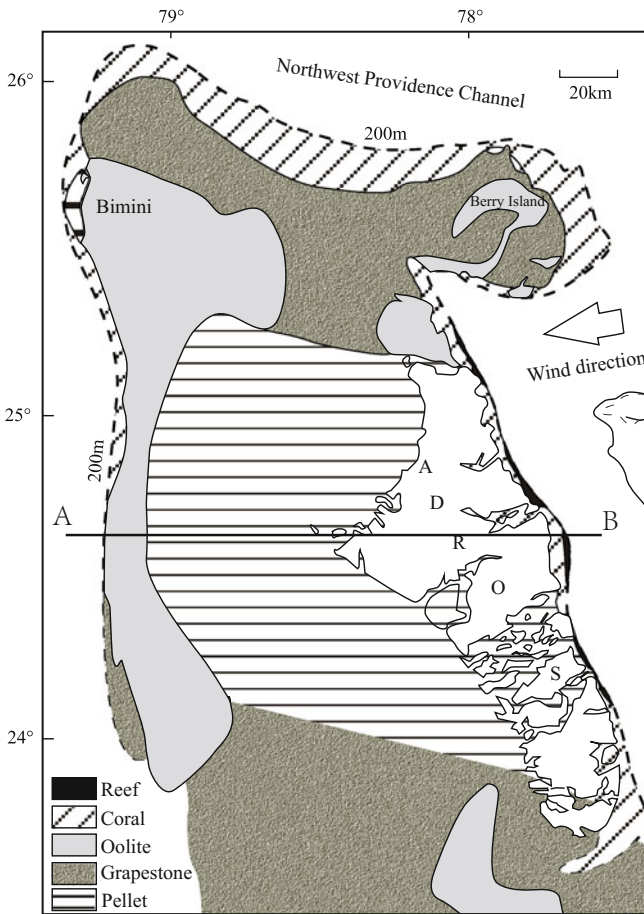
**Fig. 1.20** Sediment plane distribution map of Bahamas (modified from Newell et al. 1959). Cross section of A-B is displayed in Fig. 1.21

eolian carbonates in the Bahamas often develop a continuous extension of the coastal ridge, which is usually developed in the sea cape during the early formation of carbonate rocks or stacked by dunes under high-energy environment. The gentle and large-scale beach facies sediments in the Bahamas region provide sufficient debris for the development of the beach-dune complex. Warm seawater and strong shore
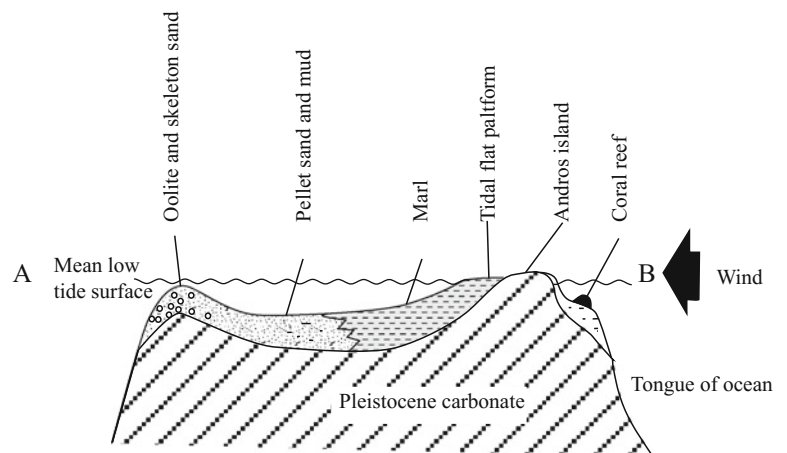
currents create the favorable conditions for the development of oolites on the beach and increase sediment supply.

Crescent-shaped dunes are mainly formed in unidirectional wind-dominated areas, and dune ridges point to the direction of the wind (McKee 1979). Kinkler and Strasser (2000) suggested that the dune ridge was tilted in the direction of N 245°. This direction is consistent with the constant North-East trade wind in the Bahamas region, indicating that the accumulation of dunes is mainly controlled by the northeastern and eastern winds.

(2) Great Barrier Reef platform

The Great Barrier Reef is located in the east of Queensland, Australia. It is a northwest-southeast-oriented reef complex located on the northeastern Australia shelf, stretching about 2000 km in length and 20–240 km in width (Fig. 1.22). It is the longest and largest coral reef area in the world and consists of about 2500 reefs (Orpin and Ridd 2012). The continental shelf occupied by the Great Barrier Reef is generally narrowed to the north and widened southward. The study of the carbonate platform of the Great Barrier Reef indicates that from the north to south the thickness of the reef is becoming obviously thinner and the initial growth age of the reef is becoming younger.

The Great Barrier Reef is located in the tropical waters of Papua Bay and the Tropic of Capricorn and the western Pacific Coral Sea. It is influenced by southern hemisphere climate and the prevailing wind is east and southeast wind (Puga-Bernabeu et al. 2013).

The edge of the Great Barrier Reef platform has strong winds and waves, which is conducive to the development of reef organism growth and formation of large-scale wave resistant reefs to build rimmed carbonate platform. The Great Barrier Reef is not a single big reef but consists of thousands of small reefs. The reefs are not connected but isolated by trenches, with restricted water circulation and weak hydrodynamic power between reefs. Therefore, behind

**Fig. 1.21** Cross section profile of sediment distribution in the Bahamas beach (modified from Flügel 2004). Please see location in Fig. 1.20
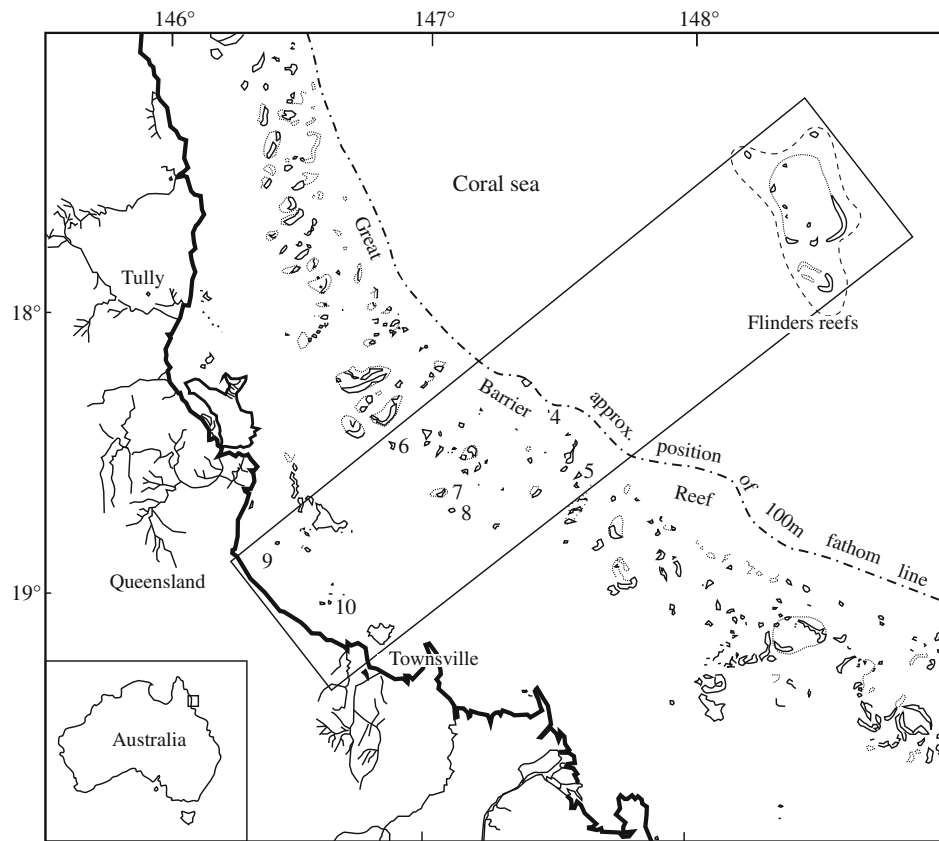
**Fig. 1.22** Location and characteristics of Great Barrier Reef in northeast Australia (from Done 1982)
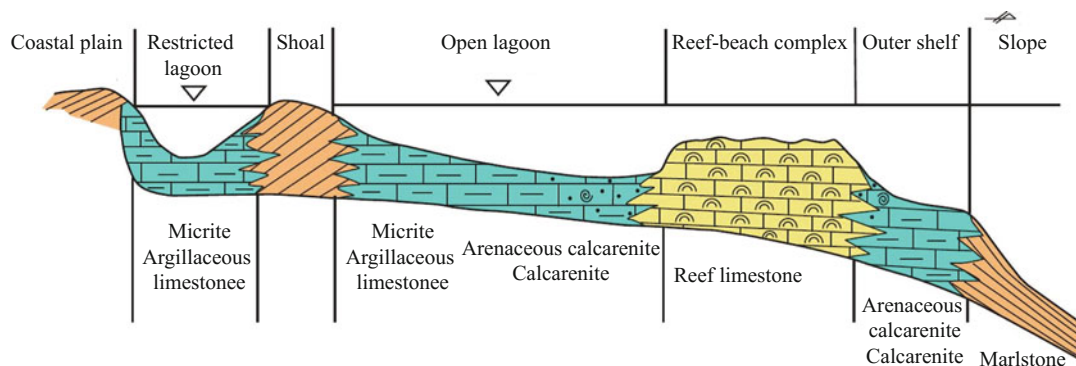


**Fig. 1.23** Modern carbonate sedimentary model in Cairns region of the eastern coast of Australia (from Gu et al. 2009)

the reef, the vast area of the platform is deposited fine-grained biological muds and biological debris in the water depth of 10–20 m. In the coastal area, due to the flat terrain and the rework of the waves, the majority of areas are covered by tidal flat deposits, with major lithology of micritic limestone and argillaceous limestone. Fine-grained arenite limestone and bioclast limestone are the main deposits in the subtidal zone (Fig. 1.23).

Done (1982) divides the Great Barrier Reef into four areas from the offshore to the near-shore direction (Fig. 1.24). Area 1 is a windward reef in the coral sea area,

with strong waves and development of partial underwater atolls, which is adjacent to the sea depth of about 200 m. The reef edge slope is steep to vertical with lagoon depth of about 60 m. Area 2 is the outer shelf reef influenced by a strong wave and is adjacent to the sea depth of 80–100 m. The reef has a steep slope in the northeast and leeward. The lagoon in area 2 has a water depth of 15–20 m and shallowed to the direction of the wind. Area 3 is a mid-shelf reef influenced by a medium wave and is adjacent to the sea depth of about 50 m. The reef has a steep slope in the northeast and leeward. The lagoon in area 2 has a water
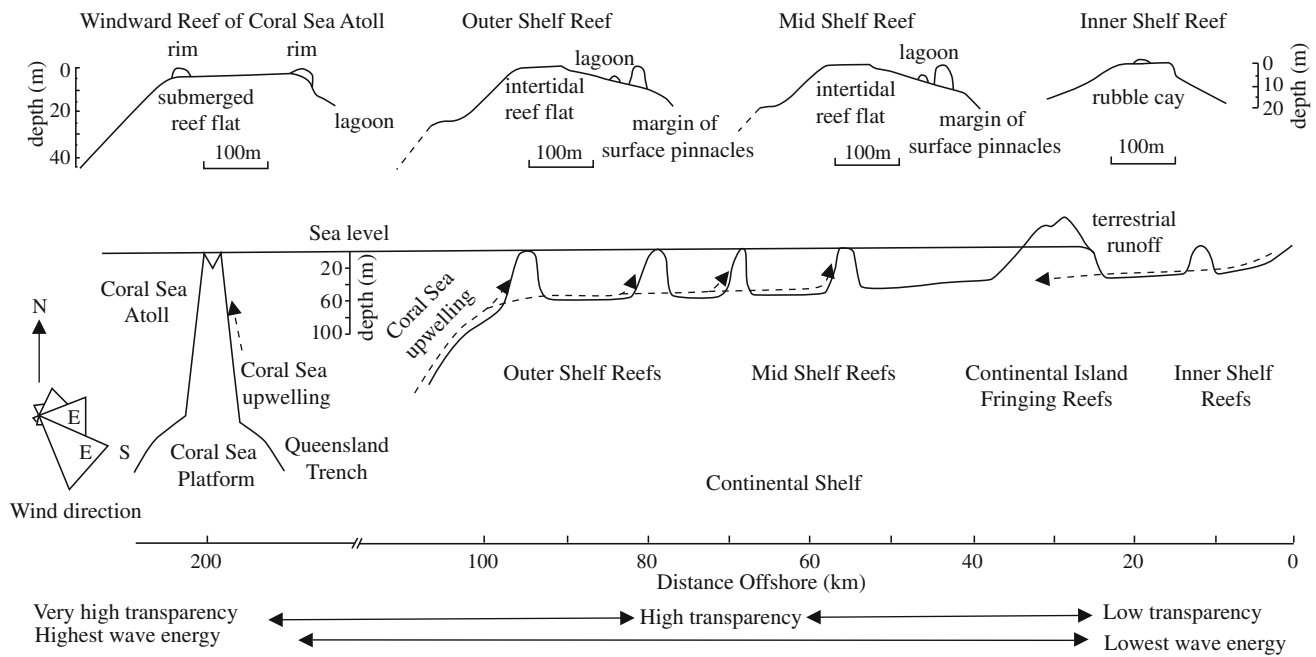
**Fig. 1.24** Composite profile of the Great Barrier Reef from broad sea to coast direction showing winds and waves (from Done 1982)

depth of 15–20 m. Area 4 is mainly inner shelf reef influenced by weak waves and is adjacent sea depth of about 20 m. The reef margin has a gentle gradient and deposits carbonate rocks and terrigenous clastic rocks. It can be seen that the windfield and the waves affect the form of the platform as well as the shape and sedimentation characteristics of each reef. In each of the reefs, the windward slope is developed with a strong vertical growth barrier and a small lagoon after the vertical reef.

## 1.3 Multiple Control of the Genesis and Distribution of Depositional Systems

The development of sedimentology makes the research object from single to diversity, from simple to complex, from fragment to integration, which advances sedimentology to a new high level. The purpose of sedimentary research has graduated shift from facies classification, model establishes, and sedimentary environment interpretation to understand the mechanisms to explain the occurrence of sedimentation, that is, external conditions (e.g., tectonic, sea level change, provenance, climate, etc.) affect the depositional environment and deposition process. However, most of the previous studies are focused on the provenance, geomorphic features and sequence evolution of the basin, and interpret depositional system based on the local studies. Therefore, the ability to predict the depositional system in unknown areas is inadequate. The distributions of the depositional system are controlled by factors such as climate (including windfield),

sediment sources, tectonics, and sea-level fluctuation. Through the study of these controlling factors, the distributions of the depositional system can be reasonably predicted.

In the previous study of sedimentology, with the integrated study of sequence stratigraphy, sea-level rise and fall, tectonic movement, provenance have greatly increased our understanding of the controlling factors that influence the depositional system. However, the study of climate change on the deposition process is still relatively weak, although climate change has significantly affected the formation of sediments (weathering), transportation, and deposition. Therefore, the relationship between climate and land surface has always been the focus of attention (e.g., Clift et al. 2008; Wang et al. 2008).

Paleoclimatic recovery and its coupling with sedimentary products have also made great progress in recent years. However, previous studies focused on the depositional record of climate change, that is, through the sediment properties (such as particle size, etc.), paleontological data, geochemical data to determine the sediment source and paleoclimatic evolutions and restore paleo-environment. In recent years, many scholars have noticed the impact of climate change on the deposition process and sedimentary products, and have made significant progress, such as the influence of monsoon climate on the lacustrine paleogeography and sediment deposition (e.g., Wang et al. 2013a, b; Chamberlain et al. 2013), river (Plink-Björklund 2015) and delta system (Ventra et al. 2015).

Sedimentary facies, depositional systems, and source-to-sinks are the most commonly used concepts in sedimentology. Sedimentary facies emphasizes the characteristics of

sedimentary records and the sedimentary environment of the basin itself and lacks consideration of provenance and climate. The depositional system emphasizes the sediment supply, depositional process, and product, with less focus on analyzing climatic factors. The source-to-sink study analyzes the process involves sediment erosion, transportation, and deposition and integrate climate as an important influence on sediment transfer from the source area to basinal sink. However, the source-to-sink mainly consider the temperate and humidity of climate with less focus on the wind circulation and its effect on sediment deposition. However, one of the advances in the concept of source sinks is that the formation and distribution of sediments are not isolated in sedimentary basins, but rather products of the whole systems. We believe that the depositional process occurs in the wind (climate)-source (sediment supply)-basin (water) system (referred to as "wind-source-basin" system), involving the study of paleoclimate, provenance, paleogeography, paleowater depth and other controlling factors (Jiang 2010b, 2015). The authors propose the research ideas and research methods of the "wind-source-basin" system dynamics, and semi-quantitatively and quantitatively study the above-mentioned controlling factors to understand the characteristics and distribution of sediments in the basin.

This section briefly demonstrates how the wind-source-basin system affects the depositional system, using a case study from the Es in the Dongying Depression, Bohai Bay Basin (Fig. 1.25). The case study is also detailed described in Chap. 4.

(1) The influence of windfield on depositional system

The East Asian monsoon has been already formed during the late period of 4th member of Eocene Shahejie Formation (Es$_4$) in Dongying Depression. The winter monsoon (northerly wind) intensity is stronger than the summer monsoon (southerly wind). Under the influence of the winter monsoon, the waves travel from the northern part of the Dongying depression to the south, forming a wide range of wave influenced zones in the southern gentle slope zone (upwind side). Due to the relatively gentle terrain and shallow water depth in the southern part of the Dongying depression, the waves and backwash flow have a high energy to develop large-scale beach bar deposits in the northern part of Luxi Uplift. This continuous wave effect can also redistribute the sediments of the delta front developed in the southeast of the sag, forming beach bars deposits in front or on side of delta front.

The summer monsoon is generally weaker than the winter monsoon. Driven by summer moon the waves propagated northward and rework the fan delta deposits to form beach bars in front of fan delta on the southern slope of Binxian Uplift. Due to the weak windfield and the steep terrain, the beach bars in the north of Dongying depression is less developed compared to the southern part. In the process of wave propagation, the wave energy will reduce when it encounters positive topography and begins to erode sediments from lake floor, transport and unload them to form beach bars in the Central Uplift region.

(2) The influence of sediment supply on the depositional system

Sediment source is one of the fundamental factors controlling the type and distribution of sediments. During the late period of Es$_4$ in west of Dongying Depression, the sediments were characterized by the nearshore subaqueous fan (the southern slope of Chenjiazhuang), the fan delta (the southern slope of Chenjiazhuang), the delta (between the Qingtuozi Uplift and Guangrao Uplift) and lake erosion (northern slope of Luxi Uplift) and other mechanism into the basin. Because of the source supply of these deposits, the waves continually rework these sediment and finally form a large area beach bar deposits on steep slope in the north, the



**Fig. 1.25** Depositional model of beach bar in the upper part of 4th member of Shahejie Formation in Dongying Depression (modified from Li 2009)
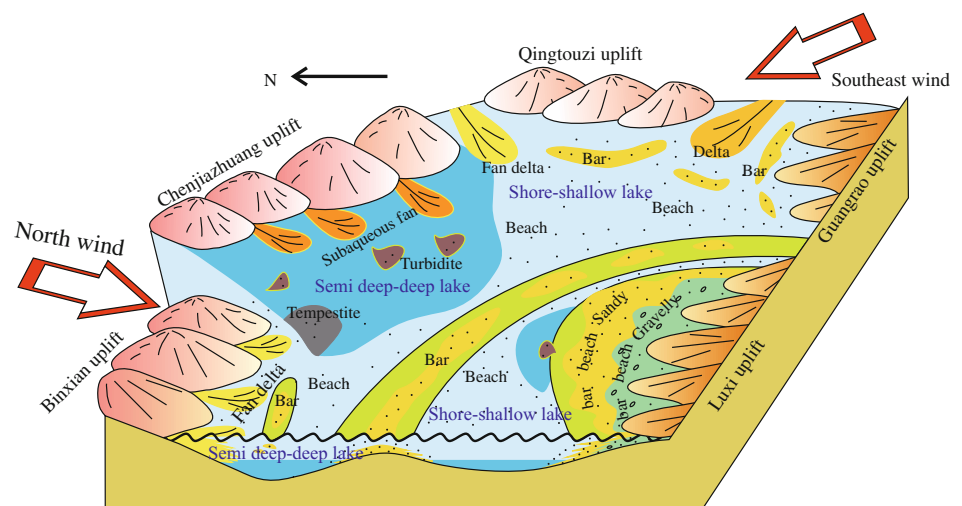
Central Uplift region and gentle slope in the south. The sandy beach bars are especially well developed in the low-stand system tract, which has limited accommodation space and high sediment supply. During the period of transgressive system tract and highstand system tract, the increase of accommodation space outweighs the sediment supply, causing deposits of carbonate-rich beach bar and lacking terrigenous beach bars.

(3) The influence of basinal characteristics on depositional system

Dongying depression is a typical half-graben rift lacustrine basin, oriented in northeast-southwest direction. The basin is characterized by high topography in the north, low relief gentle slope in the south, central uplift in the middle, and west-east orientated axial zone. It has high diversities of sediment source, supply, and depositional environment. (1) The topography of northern steep slope is controlled by basin marginal fault systems. It has a high lake water-depth gradient. Because the northern steep slope is adjacent to mountain uplifts, the sediment provided by the Chenji-azhuang uplift entered deep basin directly by gravity flow, forming nearshore subaqueous fans and basinal fans. The amplitude offset of northern boundary fault in Dongying depression decreases from east to west and correspondingly the northern slop also become more gent in the west. In the southern slope of Binxian Uplift, the slope gradient is further reduced as well as lake water-depth gradient, resulting in the development of fan delta. (2) In the southern gentle slope area, the line-sourced alluvial fan provided large volumes of terrigenous sediments from toe of Luxi Uplift to the basin. These coarse-grained clasts are carried and reword by winter monsoon to form sandy and gravelly beach bars. (3) In the east-west axial zone, because the gentle slope gradient and small water-depth gradient, the rivers carry sediment into basin to form delta deposits. In the middle of basin is the Central Uplift region, which is a favorable place for beach bar development. In the deep water area of the depression (below the wave base), the effect of the sediment source and windfield on the sedimentation can be neglected. The sedimentary activities here are mainly dominated by autogenic process, including the suspended sedimentation of the sediments, biological, chemical deposition of fine particles. In deep water area only fine-grained and chemical rocks are preserved.

The depositional system is controlled by a variety of parameters in the "windfield-source-basin" system. The paleo-windfield has provided driven force for sediment erosion, transportation, and deposition, whereas the sediment source provided the physical material for deposition. The paleogeography and paleowater depth together determine the location and scale of sediments. In fact, each

dynamics of the Earth's surface not only works alone but also interacts with other dynamics constantly (Wang and Xiang 2001).

In terms of the ubiquitous existence of the "windfield-source-basin" system, we can study the sediments from a more broad perspective using "windfield-source-basin" principle to analyze the controlling factors that influence the depositional system. This new concept and approach can be used to predict the type of depositional systems in the unknown area and to guide the exploration and development of hydrocarbon resources.

## 1.4 Research Significance

### 1.4.1 Significance in Sedimentology

The sedimentary processes in the "windfield-source-basin" system involve paleoclimate, sediment source, paleogeography, and paleowater depth. The paleo-winds and the associated paleoclimate have controlled the structure and texture of sedimentary rocks. The sediment source provided the physical material for deposition, whereas the paleogeography and paleowater depth together determined the location and scale of sediments. The study of the "windfield-source-basin" system is aimed to figure out the controlling factors that influence sediment transportation and deposition (see Chap. 2 of this book). By introducing the concept of "windfield", the sedimentology research is advanced from the "one-dimensional" traditional facies model and the "two-dimensional" source-to-sink system to the "three-dimension" sedimentary dynamics system. The sedimentary dynamics of the "windfield-source-basin" system expands the theory of lacustrine deposits.

The sedimentary dynamics of the "windfield-source-basin" system provides a new research idea and research method for carrying out sedimentology research in the sedimentary basin. The study is divided into two independent main lines, depositional system analysis and controlling factors study. Depositional system analysis is based on the theory of sedimentology and sequence stratigraphy theory and requires a large number of cores and logging data to build sequence stratigraphic framework, interpret sedimentary facies, and build facies model. The controlling factors of depositional system analysis use core, paleontology, well, seismic, and other data to semi-quantitatively and quantitatively study the parameters within "windfield-source-basin" system, including reconstruction of paleowindfield, paleo sediment sources, paleogeography, and paleowater depth. The reconstructed parameters are used to compare with the evolution of the depositional system to reveal the interactive relationship between these external forces and internal depositional process changes.

## 1.4.2   Significance in Paleoclimate

The study of paleoclimate mainly includes paleo-temperature, paleo-humidity, paleo-wind strength, and direction (Pang and Yun 2013). However, in current paleoclimate study, most researchers are focused on the recovery of temperature and humidity, while the paleo-windfield, which is just as important as the temperature and precipitation, is less studied (Liu and Jiang 2011). Therefore, the paleo-wind analysis has been in a subordinate position of paleoclimate studies for a long time (Allen 1993). The paleo-windfield is a direct result of atmospheric circulation, which provides information for atmospheric pressure gradients, storm paths, and atmospheric circulation patterns (Thompson et al. 1993). Paleo-wind analysis plays an important role in understanding climatic change and the formation of modern climate.

The study of the paleo-windfield includes two aspects: the paleo-wind strength and paleo-wind direction. In the restoration process of the paleo-windfield, the alternative indicators for the reconstruction of the paleo-wind direction are relatively easy to obtain (Liu et al. 2007; Scherer and Goldberg 2007; Wang et al. 2007; Zhang et al. 2009; Liu and Jiang 2011; Jiang et al. 2013), but the study of paleo-wind strength is relatively weak. There are very few studies carried out on the restoration of paleo-wind strength reported in China. It is easy to get modern windfield parameters by measurement of wind using certain equipment. However, such measurement is only limited to the time scale range of the past few decades. To reconstruct paleo-windfield in geological history, we need to obtain alternative indicators to interpret paleo-wind strength.

However, due to the low viscosity of the air, there is little information left to record ancient atmospheric flow field activities, and thus it is difficult to interpret paleowindfield from the geological record. The current reported paleo-wind reconstruction work is a qualitative research. For example, the strength of the wind can be reflected through its ability to carry sediment. Therefore, we can study the geological records of eolian deposits to understand paleo-wind strength approximately.

The idea of "windfield-source-basin" system dynamics can provide a new method for quantitative restoration of paleowind field. The approach is based on following principles. (1) The wind can generate waves in the basin and thus the there is a quantitative relationship between waves and winds. (2) beach bars can be used to restore paleo-waves, and then we can use the quantitative relationship between waves and winds to restore the paleo-wind strength. Based on this, this paper proposed a method to recover the paleowind field by using the beach bar deposits in the basin, which fills the gap of the paleo-wind field in the paleoclimatic study. This approach uses the orientation and lateral asymmetry and thickness of sand bars in breaker zone as well as the thickness of sandy or gravelly nearshore beach bars to reconstruct paleo-wind field quantitatively.

The method proposed in this paper opens up a new way for the restoration of the paleowind field and the paleoclimate. This is a comprehensive method, which needs to integrate paleogeographic restoration, paleowater depth restoration, and sedimentary facies analysis. This approach could apply to the large-scale lacustrine system. For example, apply this approach to the upper part of $Es_4$ in the Dongying depression indicates that northeast wind with speed of 6.4–21.9 m/s and the southeast wind with speed of 6.3–14.6 m/s are co-existed about 45 Ma. The strength of winds are inversely correlated and are interpreted to be Paleo-Asian Monsoon. This work also found the strength of paleo-north wind has experience two phases of enhancement in lowstand system tract, one phase decrease in transgressive system tract and one phase of enhancement in highstand system tract. The changes of paleo-wind strength have controlled the evolution of the temperature and humidity in the study area, and future affects the types and distribution of sedimentary rocks.

## 1.4.3   Significance in Hydrocarbon

### 1.4.3.1   "Windfield-Source-Basin" System and Reservoir Parameters

The "windfield-source-basin" system can be further divided into seven sub-systems, each of which can control the distribution of the depositional system by alone or interaction, thereby restraining element that composes petroleum system, such as source, reservoir and seal rocks.

(1)  Influence of basin-dominated system on source rock

The formation of source rocks is mainly controlled by the internal elements of the basin, and influence from terrestrial debris is relatively weak. The major basinal elements include: (1) the formation of medium-high organic matter content of fine-grained source rocks by natural suspended sedimentation, biological, and chemical deposition; (2) the favorable anoxic preservation condition that formed during transgressive and highstand system tract. It should be noted that the "basin-dominated system" only emphasizes the importance of the basin's autogenic role to the formation of hydrocarbon source rocks and does not preclude the effects of sediment source and climate effects on the formation process of hydrocarbon source rocks.

At the same time, these source rocks can also act as seal rock. For example, the source rock in the lithologic trap can be either source rock and seal rock.

(2) Influence of windfield-source-basin system on reservoir and hydrocarbon migration

① Influence of "windfield-source-basin" system on reservoir quality

First, the wind-induced dunes in "windfield-source-basin" system have good sorting and compositional maturity and are usually able to form high-quality reservoirs. Then the tectonic background has determined the direction of the sediment source, and then further determined the distribution of sediments. Large oil and gas fields are often rooted on the main sand bodies, where sandstones are often thick and high-quality reservoirs. Therefore, the exploration process of oil and gas basins always focus on the major area of sediment input.

In addition to the main sand body that developed in the direction of strong sediment supply, the beach bar sand bodies formed in the coastal area could also be high-quality reservoirs (Li 2009). The formation of these sand bodies is closely related to the elements of "windfield-source-basin". The beach bar sand body has also become a new area for oil and gas exploration and production. For example, in the eastern part of China huge amount of hydrocarbon are produced from these beach bar deposits.

In addition, the physical properties of the reservoir are also controlled by provenance and basin geomorphology. For example, differences in sediment sources can affect reservoir lithology, maturity, cementation types, and diagenesis, which are important controlling factors of reservoir properties (He et al. 2011; Liu et al. 2012, 2014).

② Influence of "windfield-source-basin" system on hydrocarbon migration

The skeleton sand body is not only the main place of oil and gas accumulation but also as a pathway for oil and gas migration. The skeleton sand body in the plane is widely distributed and in vertical is multi-layer stacked, and thus has relatively good physical properties for hydrocarbon migration. The hydrocarbon generated from source rock has entered into the skeleton sand bodies and migrated from high-pressure areas to low-pressure areas.

The oil and gas migration system is also closely related to the development of the fault zone that created by the tectonic movement. The fracture and the fissure can increase the connectivity of poor quality sandstone in the vertical direction.

③ Influence of basin-dominated system on the driven force of petroleum system

The overpressure is usually the driving force for oil and gas migration and is partially controlled by the property of sediment sources. For example, after the deposition of the $Es_4$ in the Dongying depression, the rapid progradation of Dongying delta has quickly buried the pro-delta muds of $Es_3$ and $Es_4$ formation, leaving the deep lake mud in an uncompacted status. In addition, the overburden delta sandstone and underlying thick mudstone have been fully compacted to form a relatively closed space for pressure to accumulate. Finally, this process induces overpressure zone in the subsurface, e.g., Dongying depression began to appear abnormal high pressure from the depth of 2200 m (Feng et al. 2006; Wang et al. 2012). These anomalous-pressure zones usually appear in deep locations (such as depressions) in the secondary tectonic zone. The fluid pressure can be increased during the process of hydrocarbon generation and clay mineral conversion. When the fluid pressure approaches or exceeds the fracture pressure of its boundary rock, the pressure will release from the high potential area (source rocks) to the low potential area (reservoir rocks).

### 1.4.3.2 "Windfield-Source-Basin" System and the Prediction of Sand Bodies in Weak Source Areas

Most of our oil fields have entered the middle and late stage of exploration, with the proven degree of more than 70%. The traditional exploration method of "locating the main structure and major sediment sources" is less applicable. However, exploration practice has also confirmed that in the areas where the main sources fail to reach at, high-quality sandstones still can be formed and their potentials are underestimated. The beach bar sandstone is one of the major thin-bedded reservoirs not directly influenced by major sediment supply from source areas. These reservoirs have now become an important oil and gas exploration target and have huge hydrocarbon potential. However, due to these reservoirs are thin and fine-grained, they are difficult to identify. The study of these sand bodies is still in an infant status and lacks an effective theoretical model to understand their distribution.

Current research indicates the formation of the beach bars is mainly controlled by wind, waves, sediment sources, landform (including macro-topography and micro-topography), water depth and other factors (Li et al. 2008; Li 2009; Jiang et al. 2015). Beach bar sandstones are the result of the combined effect of "windfield-source-basin" system.

First, the winds and waves are the major forces to form beach bars. The wave and its associated longshore flow are the major hydrodynamic mechanism for the formation of beach bars deposited in the shallow lake area (Cao et al. 2009). The energy of the waves changes constantly in different environments and water depths and thus has different effects on sediment transportation and deposition. Grains with similar properties can be distributed to different locations by different wave energy and form beach and bar deposited (Komar 1998). The beach bars that are not located on the main source area, are the products of reworking of previous deposits by winds and waves.

Second, the sediment source is the control of the type of sediments and is the physical basis for sedimentation. The sediment sources for the beach bar sandstones are reworked from previous nearby deposits. In the case of adequate sediment supply, sandy or gravelly beach bars are well developed, while in the case of low sediment supply, the carbonate beach bars are more commonly developed (Jiang et al. 2009; Wang et al. 2011; Yang et al. 2011).

Finally, the structural patterns, micro-topography, water depth, and sequence evolution of basin have all controls the location of beach bar development and distribution. Beach bars are well developed on the gentle slope of the lacustrine basin, while they are not commonly developed in the steep slope area (Soreghan and Cohen 1996). The micro-topography of the basin has also significantly controlled the formation of beach bars. In general, the positive topography, convex bank and the windward side of the slope are the zone where wave energy decreases rapidly and beach bar forms (Wang et al. 2011). In contrast, the concave bank and negative topography have a relatively weak wave energy and less likely develop beach bar. The water depth that defines wave energy, together with shoreline and wave base determines the distribution of beach bars (Jiang 2010b). The position of shoreline and wave base is also influenced by sequence stratigraphy and the sedimentary environment. The evolution of beach bar deposits in the lacustrine basin are the result of the dynamic interaction of sediment supply and accommodation space (A/S). Beach bar system developed in littoral areas is sensitive to the accommodation space changes that are induced by lake level changes (Lin et al. 2010). Different stages of sequence evolution, as well as sediment source changes, have significantly affect beach bar deposits. For example, during the transitional phase of sea level fall to rise, the wave energy starts to get stronger and to rework the previous deposits that are supplied during lowstand sea level.

Each of the above factors does not work alone, but jointly control the development of the beach bar. Among them, waves are the hydrodynamics forces to control beach bar evolution and distribution. The sediment sources are the physical basis for the formation of beach bars. The sediment supply rate and the direction of sediment source all affect the beach bar distribution in the basin. In addition, the evolution of paleogeography and water depth of the basin has determined the beach bar location and distribution. On the plane, macro-paleogeography determined the favorable location of beach bar areas, while micro-paleogeography affected the local hydrodynamic energy and thus control the local distribution of sand body. In general, the windward side, ramp, and positive topography are locations favorable for large-scale of beach bar deposits, which can be also affected by sediment supply and lake level changes from falling stage to rising stage. In the case of low sediment supply and low wave energy, the carbonate beach bars are more commonly developed.

Therefore, the beach bar deposits are a typical product of "windfield-source-basin" system. The "windfield-source-basin" system offers a good explanation for the formation of this kind of deposits and provides new ways to predict the distribution of such thin interbedded reservoir. It establishes a new beach bar predictive model, using paleo-wind direction and strength, sediment sources, paleogeography, and paleowater depth to predict the distribution and evolution of beach bar deposits. The geophysical method would also help predict the beach bar distribution. Combined the "wind-power-basin" system dynamic modeling with the geophysical method, we are able to make a great breakthrough to predict the thin interbedded sandbody of beach bar.

## References

Aagaard T (1990) Infragravity waves and nearshore bars in protected, storm-dominated coastal environments. Mar Geol 94 (3):181–203

Allen JRL (1993) Palaeowind: geological criteria for direction and strength. Philos Trans R Soc London Series B 341: 235–242

Belperio AP (1995) The quaternary. Geological Survey of South Australia, vol 2, pp 218–281

Bouma AH (1962) Sedimentology of some Flysch deposits: a graphic approach to facies interpretation. Elsevier, Amsterdam

Bowen AJ, Inman DL (1969) Rip currents, 2: laboratory and field observations. J Geophys Res 74(23):5479–5490

Brooke B (2001) The distribution of carbonate eolianite. Earth Sci Rev 55:135–164

Cao YC, Wan J, Liu HM et al (2009) Sedimentary characteristics and models of beach bar sandbodies in the upper part of the fourth member of Paleogene in the south slope of Dongying depression. J China Univ Pet (Natural Science Edition) 33(6):5–10

Carter TG, Liu PLF, Mei CC (1973) Mass transport by waves and offshore sand bedforms. J Waterways Harbors Coast Eng Div 99 (2):165–184

Chamberlain CP, Wan X, Graham SA et al (2013) Stable isotopic evidence for climate and basin evolution of the Late Cretaceous Songliao basin, China. Palaeogeogr Palaeoclimatol Palaeoecol 385:106–124

Chen XQ (2006) Physical geography. Peking University Press, Beijing

Chen JQ, Zhou HR, Wang XL (2004) Sedimentology and paleogeography. Geological Publishing House

Clift PD, Hodges KV, Heslop D et al (2008) Correlation of Himalayan exhumation rates and Asian monsoon intensity. Nat Geosci 1:875–880

Coco G, Murray AB (2007) Patterns in the sand: from forcing templates to self-organization. Geomorphology 91(3–4):271–290

Dally WR (1987) Longshore bar formation-surf beat or undertow? In: Advances in understanding of coastal sediment processes, Coastal sediments. American society of civil engineering (ASCE), New York, pp 71–86

Dally WR, Dean RG (1984) Suspended sediment transport and beach profile evolution. J Waterway Port Coast Ocean Eng 110(1):15–33

Davis RA (1983) Depositional systems: a genetic approach to sedimentary geology. Prentice-Hall, Englewood Cliffs, NJ

Deng HW, Xiao Y, Ma LX et al (2011) Genetic type, distribution patterns and controlling factors of beach and bars in the second member of the Shahejie Formation in the Dawangbei Sag, Bohai Bay, China. Geol J 46:380–389

Done TJ (1982) Patterns in the distribution of coral communities across the central Great Barrier Reef. Coral Reefs 1(2):95–107

Dyhr-Nielsen M, Sorensen T (1970) Sand transport phenomena on coast with bars. In: Proceedings of the 12th international conference on coastal engineering. American Society of Civil Engineering (ASCE), New York

Fairbridge RW (1995) Eolianites and eustasy: early concepts on Darwin's voyage of HMS Beagle. Carbonates Evaporites 10(1):92–101

Feng ZZ (1993) Sedimentary petrology. Petroleum Industry Press, Beijing

Feng YL, Li ST, Zou CN (2006) The study of sequence stratigraphy in the continental faulted basin: a case study of Dongying depression in the Bohai Bay basin. Science Press, Beijing

Flügel E (2004) Microfacies of carbonate rocks: analysis, interpretation and application. Springer

Fumanal MP (1995) Pleistocene dune systems in the Valencian Betic cliffs (Spain). INQUA Subcommision on Mediterranean and Black Sea Shorelines Newsletter 17:32–38

Galloway WE (1986) Reservoir facies architecture of microtidal barrier systems. AAPG Bull 70(7):787–808

Greenwood B, Osborne PD (1991) Equilibrium slopes and cross-shore velocity asymmetries in a storm-dominated, barred nearshore system. Mar Geol 96(3):211–235

Greenwood B, Sherman DJ (1984) Waves, currents, sediment flux and morphological response in a barred nearshore system. Mar Geol 60(1–4):31–61

Greenwood B, Permanand-Schwartz A, Houser CA (2006) Emergence and migration of a nearshore bar: sediment flux and morphological change on a multi-barred beach in the Great Lakes. Géog Phys Quatern 60(1):31–47

Gu JY, Ma F, Ji LD (2009) Types, characteristics and main controlling factors of carbonate platform. J Palaeogeogr 11(1):21–27

Han YH, Li XY, Wang Q et al (2015) Hydrodynamic control of sedimentary systems in shore zone of Qinghai Lake. Acta Sedimentol Sin 33(1):97–104

He QX (2003) Sedimentary Earth sciences: Yesterday, Today And Tomorrow. Acta Sedimentol Sin 21(1):10–18

He QX, Ye ZZ, Zhang MS (1988) Comparative sedimentology theory and practice. Mar Geol Quat Geol 8(1):1–8

He J, Feng SB, Huang J et al (2011) Effects of Provenance on porosity development of chang 6 sandstone of the Yanchang formation in the center of ordos basin. Acta Sedimentol Sin 29(1):80–87

Hearty PJ, Neuman AC, Kaufman DS (1998) Chevron ridges and run up deposits in the Bahamas from storms late in oxygen isotope substage 5e. Quatern Res 50:309–322

Houser C, Greenwood B (2005) Hydrodynamics and sediment transport within the inner surf zone of a lacustrine multiple-barred nearshore. Mar Geol 218:37–63

Irwin ML (1965) General theory of epeiric clear water sedimentation. AAPG Bulletin 49:445–459

James NP, Dalrymple RW (2010) Facies models, 4th edn. St. John's, Geological Association of Canada

Jiang ZX (2003) Sedimentology. Petroleum Industry Press, Beijing

Jiang ZX (2010a) Sedimentology. Petroleum Industry Press, Beijing

Jiang ZX (2010b) Studies of depositional systems and sequence stratigraphy: the present and the future. Oil Gas Geol 31(5):535–541

Jiang ZL, Deng HW, Lin HX et al (2009) Methods and application of paleo-geomorphologies rebuilding: an example of the second member of Shahejie Formation, Zhuangxi Area, Jiyang Depression. Geoscience 23(5):865–871

Jiang ZF, Wu H, Cui XZ et al (2013) The reconstruction of Paleogene wind direction and general atmospheric circulation style in Sichuan Basin, Southwestern China. Geol Bull China 32(5):734–741

Jiang ZX, Wang JH, Zhang YF (2015) Advances in beach-bar research: a review. J Palaeogeogr 17(4):427–440

Keulegan GH (1948) An experimental study of submarine sand bars. U.S. Army Corps of Engineers, Beach Erosion Board Tech Report (3), p 40

Kinkler P, Strasser A (2000) Palaeoclimatic significance of co-occurring wind-and water induced sedimentary structures in the last-interglacial coastal deposits from Bermuda and the Bahamas. Sed Geol 131:1–7

Komar PD (1971) Nearshore cell circulation and the formation of giant cusps. GSA Bull 82(9):2643–2650

Komar PD (1998) Beach processes and sedimentation. Prentice Hall, Upper Saddle River, NJ, p 543

Komar PD, Inman DL (1970) Longshore sand transport on beaches. J Geophys Res 75(30):5914–5927

Li GB (2009) Study on the sedimentary system of Beach and Bar in the upper Fourth Member of Shahejie formation of the Paleogene in the Western Dongying Sag. China University of Geosciences (Beijing), Beijing

Li ST, Xie XN, Wang H et al (2004) Sedimentary basin analysis principle and application. Higher education Press, Beijing

Li GB, Jiang ZX, Chen SW et al (2008) Sedimentary characteristics and controlling factors of beach bars in the Upper Submember of the Fourth Member of the Shahejie Formation in the Lijin subbasin. Geol China 35(5):911–921

Lin HX, Deng HW, Qin YQ et al (2010) Control of sequence stratigraphic evolution on the distribution and hydrocarbon accumulation of beach and bar reservoirs. Petrol Explor Dev 37(6):680–689

Lin CS, Xia QL, Shi HS et al (2015) Geomorphological evolution, source to sink system and basin analysis. Earth Sci Front 22(1):9–20

Liu LA, Jiang ZX (2011) Advances in the indicator of Palaeowind direction reconstruction. Prog Geogr 30(9):1099–1106

Liu BJ, Zeng YF (1985) Lithofacies Paleogeography foundation and research method. Geological Publishing House, Beijing

Liu P, Jin CS, Zhang S et al (2007) Early quaternary loess-paleo soil sequence magnetic fabric characteristics and paleo wind field recovery in Longdan area of Gansu province. Chin Sci Bull 52(24):2922–2924

Liu H, Jiang Z, Zhang R et al (2012) Gravels in the Daxing conglomerate and their effect on reservoirs in the Oligocene Langgu Depression of the Bohai Bay Basin, North China. Mar Pet Geol 29:192–203

Liu J, Cao YC, Fan TL et al (2014) An analysis of the source system and its effect on the reservoir of the middle-lower submember of 3rd Member of Shahejie Formation in Minfeng area, Dongying depression. Geol China 41(4):1399–1410

Masselink G, Evans D, Hughes MG et al (2005) Suspended sediment transport in the swash zone of a dissipative beach. Mar Geol 216 (3):169–189

McKee ED (1979) Sedimentary structures in dunes. In: McKee, ED (ed) A study of global sand seas. Geol Surv Prof Pap 1052, pp 83–113

McKee ED, Ward WC (1983) Eolian environment. American Association of Petroleum Geologists, Tulas, OK, pp 132–169

Newell ND, Imbrie J, Purdy EG et al (1959) Organism communities and bottom facies, Great Bahama Bank. Bulletin of the AMNH, 117

Nichols G (2009) Sedimentology and Stratigraphy, 2nd edn. Wiley-Blackwell, Chichester, West Sussex, p 83

Nutz A, Schuster M, Ghienne JF et al (2015) Wind-driven bottom currents and related sedimentary bodies in Lake Saint-Jean (Québec, Canada). GSA Bull 127(9/10):1194–1208

Orpin AR, Ridd PV (2012) Exposure of inshore corals to suspended sediments due to wave-resuspension and river plumes in the central Great Barrier Reef: a reappraisal. Cont Shelf Res 47:55–67

Osborne PD, Greenwood B (1993) Sediment suspension under waves and currents—time scales and vertical structure. Sedimentology 40:599–622

Pang JG, Yun ZW (2013) Research advances in the Paleo climate recovery of Lacustrine Basin. J Yangtze Univ (Natural Science Edition) 10(20):54–56

Plink-Björklund P (2015) Morphodynamics of rivers strongly affected by monsoon precipitation: review of depositional style and forcing factors. Sed Geol 323:110–147

Posamentier HW, Jervey MT, Vail PR (1988) Eustatic controls on clastic deposition I—conceptual framework. In: Wilgus CK, Hastings BS, Kendall CGSC et al (eds) Sea level changes—an integrated approach, vol 42. SEPM, Special Publication, pp 109–124

Puga-Bernabeu A, Webster JM, Beaman RJ et al (2013) Variation in canyon morphology on the Great Barrier Reef margin, north-eastern Australia: the influence of slope and barrier reefs. Geomorphology 191:35–50

Qian N, Wan ZH (1991) Mechanics of sediment transport. Science Press, Beijing

Rao CP (1996) Modern carbonates tropical, temperate, polar: introduction to sedimentology and geochemistry. University of Tasmania, Hobart

Scherer CMS, Goldberg K (2007) Palaeowind patterns during the latest Jurassic–earliest Cretaceous in Gondwana: evidence from aeolian cross-strata of the Botucatu Formation, Brazil. Palaeogeogr Palaeoclimatol Palaeoecol 250(1):89–100

Schwartz RK (2012) Bedform, texture, and longshore bar development in response to combined storm wave and current dynamics in a nearshore helical flow system. J Coast Res 28(6):1512–1535

Selley RC (1996) Ancient sedimentary environments and their sub-surface diagnosis, 4th edn. Routledge, New York

Shaw AB (1964) Time in stratigraphy. McGraw-Hill Inc, New York, p 365p

Shepard FP, Inman DL (1951) Nearshore circulation. In: Johnson JW (eds) Proceedings of first conference on coastal engineering, California. Council on Wave Research, San Francisco, pp 50–59

Short AD (1975) Multiple offshore bars and standing waves. Coastal Studies Institute, Louisiana State University, Baton Rouge, USA

Sømme TO, Jackson CA-L (2013) Source-to-sink analysis of ancient sedimentary systems using a subsurface case study from the Møre-Trøndelag area of southern Norway: Part2—sediment dispersal and forcing mechanisms. Basin Res 25:512–531

Sømme TO, Helland-Hansen W, Martinsen OJ et al (2009) Relationships between morphological and sedimentological parameters in source-to-sink systems: a basis for predicting semi-

quantitative characteristics in subsurface systems. Basin Res 21 (4):361–387

Sømme TO, Jackson CA-L, Vaksdal M (2013) Source-to-sink analysis of ancient sedimentary systems using a subsurface case study from the Møre-Trøndelag area of southern Norway: Part1—depositional setting and fan evolution. Basin Res 25:489–511

Soreghan MJ, Cohen AS (1996) Textural and compositional variability across littoral segments of Lake Tanganyika: the effect of asymmetric basin structure on sedimentation in large rift lakes. AAPG Bull 80(3):382–409

Thompson RS, Whitlock C, Bartlein PJ, et al (1993) Climatic changes in the Western United States since 18,000 yr B.P. In: Wright HE, et al (eds) Global climates since the last glacial maximum. University of Minnesota Press, Minneapolis, MN, pp 468–513

Tian JJ, Jiang ZX (2009) Sequence stratigraphy characteristics and sedimentary system evolution of upper Es4 in the Dongying depression. Acta Geol Sin 83(6):836–846

Tucker ME, Wright VP (1990) Carbonate sedimentology. Blackwell Scientific Publications, London, p 482

Vacher HL, Rowe MP (1997) Geology and hydrogeology of Bermuda, vol 54. Elsevier, Amsterdam, pp 35–90

Ventra D, Cartigny MJB, Bijkerk JF et al (2015) Supercritical-flow structures on a Late Carboniferous delta front: sedimentologic and paleoclimatic significance. Geology 43(8):731–734

Walker RG (ed) (1979) Facies models: geoscience Canada reprint series, 1, 1st edn. Geological Association of Canada

Wang CS, Li XH (2003) Sedimentary basin: from principles to analysis. Higher education press

Wang CS, Xiang F (2001) Global climate change as result of Tectonic uplift in Cenozoic. J Miner Petrol 21(3):173–178

Wang Y, Pan BT, Gao HS (2007) Magnetic fabric based reconstruction of the paleowind direction from a loess sequence in the northeastern Qilian Mountain. Chinese J Geophys 50(4):1161–1166

Wang C, Zhao X, Liu Z et al (2008) Constraints on the early uplift history of the Tibetan Plateau. PNAS 105(13):4987–4992

Wang YZ, Song GQ, Wang XZ et al (2011) The controlling effect of paleogeomorphology on different types of beach bar: a case study from south slop of eastern Dongying depression. Petrol Geol Recovery Effi 18(4):13–16

Wang YS, Liu HM, Gao YJ et al (2012) Sandbody genesis and hydrocarbon accumulation mechanism of beach-bar reservoir in faulted-lacustrine-basins: a case study from the upper of the fourth member of Shahejie Formation, Dongying Sag. Earth Sci Front 19 (1):100–107

Wang C, Feng Z, Zhang L et al (2013a) Cretaceous paleogeography and paleoclimate and the setting of SKI borehole sites in Songliao Basin, northeast China. Palaeogeogr Palaeoclimatol Palaeoecol 385:17–30

Wang C, Scott RW, Wan X et al (2013b) Late Cretaceous climate changes recorded in Eastern Asian lacustrine deposits and North American Epieric sea strata. Earth Sci Rev 126:275–299

Wilson JL (1975) Carbonate facies in Geologic history. Springer-Verlag, New York

Wu CJ (1986) Sandbodies in Lake Basin. Acta Sedimentol Sin 4 (4):1–27

Yang JP, Yang J, Deng AJ et al (2010) Carbonate rock facies model of the upper third member of Shahejie formation of Paleogene in the central uplift belt of Raoyang depression, Heibei Province. Acta Sedimentol Sin 28(4):682–687

Yang YQ, Qiu LW, Jiang ZX et al (2011) A depositional pattern of beach bar in continental rift lake basins: a case study on the upper part of the fourth member of the Shahejie Formation in the Dongying Sag. Acta Petrolei Sinica 32(3):417–423

Zhang X, Zhang JL (2009) Composite deposits of Beach Bar and Tempestite in the upper fourth member of Shahejie formation in the central uplift belt of Huimin depression. Acta Sedimentol Sin 27 (2):246–253

Zhang YF, Li CA, Chen L et al (2009) Magnetic fabric characters of sand-dune sediments and its paleowind field in the middle reaches of Yangtze River 52(1):150–156

Zhao Q, Xu H, Hua QF et al (2014) Global distribution of carbonate eolianite in the word and implication for Xisha Islands. Mar Geol Quatern Geol 34(1):153–163

Zhu XM, Xin QL, Zhang JR (1994) Sedimentary characteristics and models of the Beach-bar reservoirs in faulted down Lacustrine Basins. Acta Sedimentol Sin 12(2):20–27

# Elements and Research Methods of Sedimentary Dynamics of Windfield-Source-Basin System

The depositional process occurs in the windfield (climate)-source (provenance)-basin (basin evolution) system (referred to as "windfield-source-basin" system), involving the paleoclimate, ancient provenance, paleogeomorphology, paleo-water depth, and other factors (Jiang 2010b). The aim of the "windfield-source-basin" system is to clarify the control effect of each factor on the depositional process. The focus and difficulty of the study are the quantitative recoveries of the single factor.

For the elements of the "windfield-source-basin" system, the study on provenance analysis is relatively mature, while the study of basin-related paleogeomorphology, paleo-water depth and paleotectonic movement (such as earthquakes) and others are relative difficult and in an infant status, especially the recovery of the paleowindfield is a long time unsolved problem (Jiang 2010b). This chapter mainly reviews the control effect of the single factor on the depositional process, especially the beach bar deposition, and summarizes and enriches the recovery methods of single factor. The semi-quantitative and quantitative studies of the above factors are aimed to reflect the depositional processes more accurately.

## 2.1 Windfield

### 2.1.1 The Generation of Wind and Three Kinds of Windfield

Simply speaking, the horizontal movement of the atmosphere forms winds. Solar radiant energy is the basic source of movement in the Earth's atmosphere. As the surface of the uneven heating, in the same level will form a difference in pressure, and then form a horizontal pressure gradient. The force generated by the horizontal pressure gradient will promote the movement of the atmosphere in the horizontal direction from high pressure to low pressure. In this process, the wind force will be influenced by the Coriolis force and

be deflected, which is the direct cause of wind. Windfield can be influenced by different scales of forces and have different scales of strength.

(1) The influence of atmospheric circulation and planetary wind system on sediment deposition

Atmospheric circulation and planetary winds refer to the global state of atmospheric motion, which reflect the basic state and changing characteristics of atmospheric movement, nurture and constrain small-scale air movement.

The formation mechanism of atmospheric circulation can be explained by the different absorption rates of total amount of solar radiation for high- and low-latitude areas. First, in low-latitude area, as the air absorbs the net solar radiation energy it rises to high altitude and tends to move toward to the high-latitude area. On the one hand, on the way the air flows from low latitude to the poles, the air motion is affected by the geometric force (Coriolis force) and will be deflected in latitude direction. When the deflection of air motion increases, it will block the air movement in longitudinal direction. Meanwhile, when the air is cooled and sinking, it will move toward the north and south in the low altitude, and thus forms trade wind zone and westerly zone under the influence of the geostrophic force. Second, in the poles, when the air is cool and sinking, it moves to a low-latitude area in the low altitude. It will become east wind quickly under the influence of geostrophic force and forms polar easterlies. When the cold polar easterly wind encounters the warm westerly wind from low latitude, it lifts the wind motion upward, and consequently, forms the ideal model for atmospheric circulation and three circulation loops (Fig. 2.1). It is not only the fundamental mechanism for the formation and development of climate systems of all sizes but also the driving forces of weather, climate formation, and evolution (Zhao 1992).

As indicated by the three-cycle circulation model of atmospheric circulation (Fig. 2.1), an equatorial low-pressure

**Fig. 2.1** The three-loop model
of atmospheric circulation and the
distribution of air pressure belt
and wind belt on the earth surface
(modified from Wu et al. 2008)
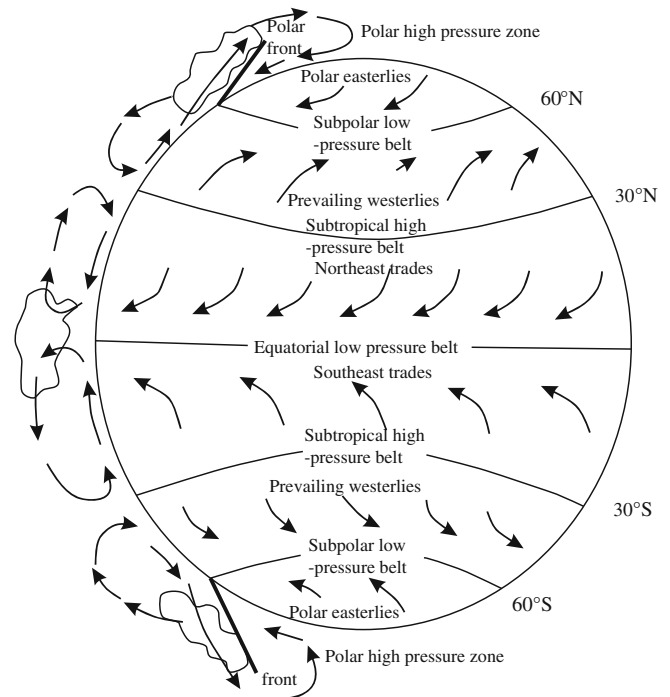


zone forms due to the heating of the air in the equator, while
subtropical high-pressure forms due to the air subsidence
near 30° north and south in latitude. Near the latitude 60°
north and south, as the warm air is uplifted by the cold air, the
airflow outflows and forms the subpolar low-pressure zone,
whereas, in the area of poles, the air becomes dense and sinks
downward, which causes high ground air pressure and forms
a polar high-pressure zone. At the same time, the northern
and southern hemispheres are symmetrically distributed from
the low latitudes to the high latitudes with three wind bands:
the trade wind zone, the prevailing westerly zone, and the
polar easterlies wind zone. This is a zonal distribution of the
pressure zone and wind zone in the global range called as the
planetary wind system.

The atmospheric circulation largely controls the global
climate. For example, there are two peaks in the distribution
of precipitation in the world. One is located in the equatorial
low-pressure zone, where there is a convergent upflow
producing a large amount of convective rain. Another one is
located in a mid-latitude westerly zone with heavy rainfall
too. While the subtropical high-pressure zone between the
two prevails with subsided airflow, which results in very low
precipitation and the formation of the largest arid zone on the
Earth. Sedimentologist has long noted the effects of climatic
conditions on sediment accumulation and sedimentary
environments. In turn, sediments also contain a large number
of paleoclimate records, such as Eolian deposits, paleosols,
fauna and flora signatures, salt deposits (potash, rock salt,
and gypsum), and coal seams, which have clear paleoenvi-
ronmental implications (Liu et al. 1998), and can be used to

help reconstruct the paleoclimate. In addition to analyzing
the influences of temperature and humidity on the sediment
deposition, the study of the paleoclimate should also utilize
the dynamic theory of the atmospheric circulation to restore
the characteristics of the ancient atmosphere flow field in the
geological history.

(2) Cyclone and anticyclone and their controls of
    sedimentation

Cyclone and anticyclone are components of atmospheric
circulation, and their formation, movement, and intensity
changes are closely related to the background of atmospheric
circulation. The cyclone is the horizontal air vortex produced
by the rotation of the horizontal airflow in the atmosphere
with the center air pressure lower than the surroundings.
Since the cyclone has been systematically and comprehen-
sively studied in the field of meteorology, this chapter will
only briefly describe the formation mechanism of the
cyclone and will not present other aspects.

In tropical or subtropical oceans, due to the high tem-
perature of the oceanic surface, a large amount of air gets
heated and rise, lowering the air pressure near oceanic sur-
face and forming a low-pressure zone. Consequently, the
surrounding airs start to fill the low-pressure space due to the
horizontal pressure gradient force and will spin up under the
influence of Coriolis force. On the other hand, the air in
low-pressure center gets cooled and starts to lose the mois-
ture when rises up, and then the air continuously releases
heat and accelerate the air in the low altitude to rise up. As a

result, both the pressure in the low-pressure zone and the pressure gradient increase rapidly, inducing a more intensive air flow spins and finally may form a typhoon (called typhoon in the Pacific Northwest, hurricane in the Atlantic or the eastern part of the Pacific, and cyclone in the southern hemisphere).

In contrast to cyclones, anticyclones are generated by the rotation of the horizontal airflow in the atmosphere, and the central air pressure is higher than the surrounding horizontal air vortex. As the central part has higher pressure, anticyclone is characterized by horizontal pressure gradient from the center point to the surrounding. Anticyclone is generally active in the high latitudes, which mostly occurrs in winter and blows toward the low-latitude area. Large-scale mobile anticyclones can affect the lower latitude area to form strong wind and reduce the temperature.

Strong tropical cyclones or anticyclones have enough energy to stir the sediments beneath the normal waves in the lake or the ocean. It is reported that the bottom-flow velocity induced by a cyclone can reach 1–3 and 2–70 m/s on the continental shelf and continental slope, respectively, enough to erode and move gravel-grade sediments to form tempestite. Previous research indicates that the range of modern tropical cyclones is limited to the range of 5°–45° on both sides of the equator, while the winter anticyclone generally occurs in the range of >25° latitude. Therefore, the latitude region of 25°–45° is the interactive region of cyclone and anticyclone (Marsaglia and Klein 1983; Duke 1987). According to statistics, about 70% of the ancient tempestite occurred in this range (Marsaglia and Klein 1983). Assuming that the conditions for tempestite to be formed is similar to the modern conditions and the astronomical conditions do not change much over time, Marsaglia and Klein (1983) summarize the palaeogeographic distribution of the Paleozoic and Mesozoic tempestite deposits and reconstruct the global nature of the tempestite deposits in that period of geological history.

(3) Monsoon and its control of sedimentation

Monsoon, an important part of the atmospheric circulation, is defined as a wide range of prevailing winds or air pressure systems with significant changes seasonally (Gao and Lu 1988). The monsoon can be divided into two categories, namely sea-continental monsoon and the planetary monsoon (Jiang et al. 2000). The sea-continental monsoon is formed by the heat difference between sea and land, whereas the planetary monsoon is formed by the seasonal movement of the planetary wind zone. In this work, we focus on sea-continental monsoon.

In the summer, the continent has a lower ratio of specific heat and thus the temperature will raise up rapidly when heated by solar radiation, whereas the adjacent ocean, which has a higher ratio of specific heat, has temperature raise much slower. Therefore, the heated air in the continental side raises up and induces low pressure in high altitude, forming horizontal pressure gradient from ocean to continent. As a result, the relatively cold air in the surrounding sea surface starts to flow to the continent and forms summer monsoon, driven by this horizontal pressure gradient force. In the winter, the continent cools faster than the ocean, forming a horizontal pressure gradient from the continent to the sea. Since the end of the twentieth century, with the continuous workis on regional monsoon research, the monsoon has been studied as a global phenomenon both in China and abroad. The concept of global monsoon has been widely recognized, and the definition of monsoon has changed accordingly. The study of global monsoon has also achieved many progresses, however, this is not the focus of this chapter and is not discussed here. This chapter is still based on the definition of the traditional sea-continental monsoon.

The most prominent areas of the monsoon on the planet are mostly distributed in the tropics and subtropics. In these areas where this monsoon prevails, the monsoon climate can have a decisive influence on the sedimentation and dispersion system in the region. For example, in the Ganges basin of northern India, the source–sink system is strongly controlled by the Indian monsoon. Within a short period of 4 months under the influence of monsoon, the Ganges flow accounts for 80% of the year, whereas the total amount of sediment transported from the Ganges basin to the Bengal Bay accounted for 95% of the year. According to the study, the local atmospheric circulation caused by Indian monsoon has a stronger influence on sediment deposition than that of provenance, shoreline, and so on (Goodbred 2003).

### 2.1.2 The Influence of the Wind

The wind, as an important geological force, has influenced the earth surface in three ways.

(1) Wind erosion

Wind erosion includes both erosion and abrasion. When the wind blows over the ground, the wind pressure and wind turbulence induce sands to blow up. This effect is called erosion. Not all winds can produce erosion, and only when the wind reaches the critical speed enough to move the sand, the wind is called the sand-moving wind. The strength of the sand-moving wind is not static and varies with the surface roughness, the moisture of debris particles, and the size of the particle size. The undulating rough ground has higher friction resistance and thus requires a high wind strength to

move sand. The flat smooth surface has a lower friction resistance, which requires a lower wind strength to move sand. The sands with higher moisture require strong wind to be moved, whereas dry sands require much less wind strength to be moved. Taking the grain size of 0.25–0.5 mm as an example, the wind needs to be 4.8 m/s to move sand in a dry condition, while in a wet condition the wind speed needs to be up to 12 m/s to move the sand grains. The size of the sand-moving wind also depends on the size of the particles (Fig. 2.2). Sand grains in most of the desert in China is characterized by the particle size of 0.1–0.25 mm, which requires sand-moving wind speed of 4 m/s. For the grain size of 0.25–0.5 mm, the sand-moving wind speed is 5.6 m/s, while for the grain size of >1 mm the sand-moving wind speed is 7.1 m/s. The blowing of wind-induced sands of medium–fine grain size should be concentrated in the downwind direction and the formation of eolian deposits. The gravel, pebbles, and coarse-grained sands are left behind and form "rock desert" or "Gobi".

Sand-moving wind carrying sand, not only erodes the ground but also abrades the ground. This process can reshape gravel surface to form ventifact. When wind cuts into rocks deeply, it can form some special geomorphological phenomenon, such as wind erosion recess and wind niche, or abrades the base of the stone pillars to become mushroom like.

(2)   Influence of wind on sediment transportation

Air is a very important media for transporting sediment. The movement of the wind is mainly through the wind-sand flow to move sands. Although air and water have similar mechanisms for sediment transportation and deposition, they have important differences. First, the air can only carry debris material, and cannot carry dissolved substances. Second, the air density and viscosity are much lower than the water, resulting in the air can only carry fine particles. Under the same flow speed, the carrying capacity of air is only 1/300 of the water. Third, the scope of air transportation is not limited by the solid boundary. For example, water is obviously subject to gravity control, but the wind can transport particles from the low terrain to the height.
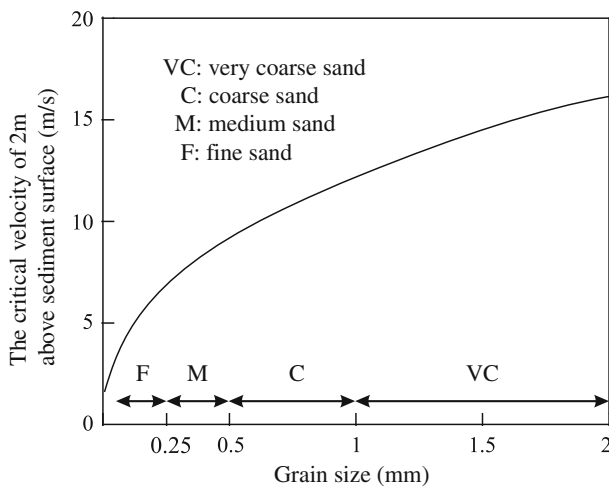
The major transportation way of clasts in wind is saltation and secondary ways are suspension and rolling (often referred to in the wind peristaltic transport). Most of the sand is within 30 cm from the ground, especially within 10 m. The observation indicates that the particle size of the sand grains is generally less than 0.5 mm, especially the fine sand (0.1–0.3 mm) is the most active grains, accounts for about three-fourths of the grains carried by the wind. The peristaltic transported sand particles are in the range of 0.5 to 2–3 mm and account for about one-fourth of the grains carried by the wind. The larger sand particles generally remain in place. Sand particles less than 0.1–0.2 mm are transported by suspension and only accounts for 1–5% of the grains carried by the wind. For the grains even less than 0.1 mm, they can also reach the suspension status. Particles with a grain size of less than 0.05 mm can be transported to a long distance as dust, and in the event of a storm, the transportation is more intense. If the dust is only transported by a short distance and deposited locally in the desert, it can be remobilized and carried by the wind in the next event. When the dust is carried out of the desert area, it can be deposited and preserved, such as the loess in the northern China. Dust material can be transported to the shelf and deep sea and deposited in the deep-sea basin.

As the wind speed changes, these three transportation ways can be transformed into each other. However, modern observation of desert deposits indicates there is a constant relationship between particle size and transport mechanism. The magnitude of the wind-sand flow is proportional to the third order of the threshold velocity for transportation of sand. This means that the wind speed is significantly higher than the threshold velocity for transportation of sand, the amount of sands carried by the wind will increase dramatically.

(3)   Eoposition

When the wind is weakened or trapped, or two winds meet the wind load decreases, and the sand particles in the wind are settled down to the ground. This phenomenon is the eoposition. The carrying capacity of the wind determines that the range of particle size is narrower, mainly fine sand and loess. Particle is characterized by well sorting, good roundness, frosting, and faceted pebble and deposited into different kinds of sand dunes.



**Fig. 2.2** The relationship between the critical wind speed (2 m from sediment surface) and sediment particle size (modified from Bagnold 1941)

### 2.1.3 Wind Waves

#### 2.1.3.1 Formation and Characteristics of Wind-Generated Waves

Wind, as a geological force, can not only erode, transport and deposit sediments but also generate waves by blowing water bodies. For the lake, the waves are only generated by wind. Modern observation suggests the lake surface is as smooth as mirror unless the wind blows on the water body to generate waves. Once the winds stop, the waves immediately disappear. This is the so-called "no wind no waves". Under the direct influence of wind, the friction generated between wind and water surface can transform energy and generate waves.

In the process of wave formation, the water particles are disturbed, leaving the original equilibrium position for periodic upward, downward, forward, and backward movement, and will spread to the surrounding. The description of the size and shape of the waves is illustrated by the wave elements (Fig. 2.3). The basic elements of the waves are crests, troughs, wave height, amplitude, wavelength, wave steep, period, frequency, wave velocity, and so on.

(1) Wave crest—The highest point of wave
(2) Wave trough—The lowest point of wave
(3) Wave height (H)—The vertical distance between the adjacent peaks and the trough
(4) Wave amplitude (a)–Half of wave height, a = H/2
(5) Wave length (L)—The horizontal distance between two adjacent peaks or two adjacent waves
(6) Wave steep ($\delta$)—Ratio of wave height and wave length, $\delta$ = H/L
(7) Period (T)—During the process of propagation, the time required to pass a fixed point for adjacent two peaks or two troughs successively
(8) Frequency (f)—The reciprocal of the period, f = 1/T
(9) Wave speed (C)—The horizontal displacement of a crest or trough in a unit time (the speed of waveform propagation), C = L/T.
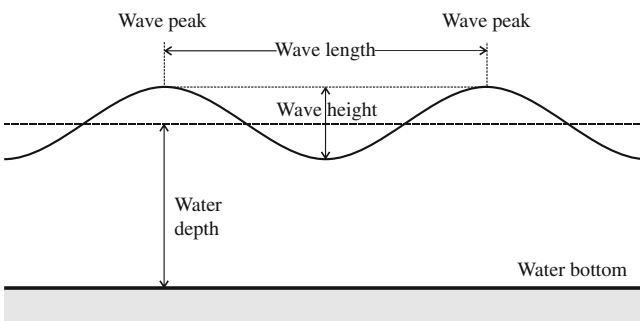


**Fig. 2.3** Schematic diagram showing elements of wave

The occurrence, rest, intensity, and range of winds are mainly controlled by three factors: (1) Wind speed; (2) Fetch length—also known as wind blowing distance, refers to the scope of the wind speed and wind direction acting on water bodies, namely the distance between the wind and the surface friction; (3) Wind blowing time—the time of wind speed and direction acting on water bodies. In addition, the wind and wave size are also affected by factors such as water depth and lake basin conditions, wind speed, fetch length, and wind blowing time. The wind and wave size of shallow water area is much smaller than that of deep water. Most lakes have lake area less than the fetch length, so the fetch length is limited by the length of the lake. Generally, the big wave is associated with high wind speed, long fetch length, long wind duration, and deep water depth. However, wind waves size will not increase indefinitely even if the wind blowing time keeps on increasing. The wind has a critical value, and when it is above this critical value, the size of the wind is no longer increasing. The wind and waves have reached a steady state at this time, which are known as stationary waves.

The form of the stationary waves will not be curve shaped because the wave will not be infinitely steeper, but there will be a critical value of steepness, and the wave is broken when steepness exceeds this value. Stokes (1849) pointed out that there is a critical value for wave steepness, called $\delta_{lim}$. If the steepness exceeds this value, the angle at the top of the crest is 120°. In 1893, Mitchell calculated the limit wave stiffness proposed by Stokes as $\delta_{lim}$ = 0.142, or $(H/gT^2)$ = 0.027 (T-wave period).

#### 2.1.3.2 Evolution of Waves

As the wave spreads from the deep water to the shallow water and gradually approaches the shoreline, a series of changes will occur. When the water depth reduces, the wave velocity will slow down accordingly and wave shape will be deformed too, such as the wave peaks rise steeply and the wave heights increase until they break. The wave will also be refracted due to the changes of topography on the shore.

1. Deformation of waves when shoaling

According to the movement pattern of water particles, the surface wave can be divided into two categories: (1) in a wave cycle, water particles occur only in a circular or elliptic trajectory oscillation and there is no significant net displacement of the wave, that is called oscillation wave; (2) at the peak of moving wave, the water particles move along the direction of the wave, which is called a propulsion wave or an isolated wave.

Oscillatory waves occur mainly in deepwater areas. When an ideal wave passes through the water, the wave profile is a series of symmetrical crests and troughs, similar to sinusoidal

curves. When the crest passes, the water rises, and all the water particles below the crests move forward with the waves. After the wave crest passes, the water surface gradually decreases and water particle also moves downward. When the wave trough arrives, it drives the water particle to move in the direction of the reverse wave. After the trough passes, the water particle continues to move upward. In each wave period, the water particle will draw a circular orbit in the vertical plane perpendicular to the wave and will keep repeating this process.

It can be seen that the diameter of the circular orbit of the water surface is the wave height of deepwater wave. However, the diameter of this circular orbit decreases exponentially with the increase in the depth of the water. According to the calculation, when the water depth reaches the depth of $1/2$ deep water wave ($L_0$), the orbital diameter becomes $1/23$ of the value on the water surface, and the water body is almost stationary. So we usually regard the depth of $L_0/2$ as the wave base level. From the wave base to the offshore direction, the wave has no longer influenced the water bottom. However, from the wave base to the shore, the wave begins to interact with the water bottom.

In the field of geology, waves are generally believed to be propagated to the base of waves. When waves reach the bottom and deformation occurs in shallow water depth and deepwater waves become shallow water waves (Fig. 2.4). When the wave is propagating to shallow water, the phenomenon of wave elements changes due to the decline of water depth called shoaling deformation. The shoaling deformation of waves is a gradual process. After the occurence of the wave in shoaling deformation, the motion of the particle of water changes from circular to an elliptical shape. Elliptical radius decreases with the increase of the water depth. Meanwhile, the vertical radius of the ellipse is becoming smaller and smaller than the horizontal radius of ellipse, until the vertical radius of ellipse reaches 0. In this process, water is reciprocating along the bottom. In addition, the elliptical orbit of the water particles gradually shifts from closed to non-closed as the shoaling deformation process deepens. In the same wave period, the landward velocity of the water particle is greater than that of the seaward movement and the oscillation wave starts to change into the propulsion wave. The closer the wave reaches the shoreline, the more obvious the asymmetry, the more serious the wave deformation, until the waves are broken.

Under ideal conditions, in the process of the waves moving toward the shoreline, almost all the wave elements change as the water depth decreases, but the waves are always constant. In addition, wave height experienced a brief decrease in the propagation of waves in shallow water areas (Qian and Wan 1991). When h (water depth)/$L_0$ (deep wave wavelength) <0.15, the wave height begins to increase

(Fig. 2.4). Since the wave period is constant, the velocity of the water point will increase with the increase of the wave height and the decreases of wavelength, until the waves are broken.

Therefore, after the waves into the shallow water area, the wave velocity is decreasing but the movement speed of water particle accelerates. In this way, there is always a moment of water point movement, speed at wave peak will catch up and exceed the speed of the wave propagation, and at this time the waves will be broken and consume a lot of energy, resulting in the formation of waves.

Regarding the critical condition of the breaking of the wave, there are complex calculations in the field of coastal engineering. Different scholars have different views on this, and there has been great debates and discussion on the wave breaking index. In 1970, Goda, a Japanese scholar who is famous for the theory of irregular wave, proposed an empirical formula (Eq. 2.1), to calculate the critical depth of the broken waves , according to several beach slope data:

$$\frac{H_b}{d_b} = \frac{A\left\{1 - \exp[-1.5\pi d_b/L_0(1 + 15\tan^{4/3}\alpha)]\right\}}{d_b/L_0} \quad (2.1)$$

In Eq. (2.1), $d_b$ is the depth of the waves; $H_b$ is the wave height; A is the coefficient, Goda thinks it should be 0.17; $L_0$ is the deepwater wavelength; $\alpha$ is the slope.

The equation is transformed into a curve and is shown in Fig. 2.5.

Equation (2.1) and Fig. 2.5 have been cited by Harbor Hydrological Norms. The following scholars, such as Li and Dong (1993) amended the above equation according to the experiment. They suggested the coefficient A should be 0.15 and, therefore, the "Harbor Hydrological Norms 98" regulates that the $H_b/d_b$ read from Fig. 2.5 should be a multiple of 0.88.

According to the different topographies of the shore, different water flows can be obtained after the wave is broken. If the shoreline slope is steep, a shock flow will be formed due to the breaker wave, which will flow back at a certain height on the beach. During the upwelling and falling, the wave energy gets dissipated completely.

If the shoreline slope is gentle, the waves will be broken again after the formation and will continue to spread (Fig. 2.6). If the water depth is deep enough nearshore, the water in the breaker may reform into a smaller oscillation wave. This kind of reborn oscillating wave can be broken again in a shallow area. In special cases, the regeneration process may even be repeated several times, eventually turning into surfing backflow. The water in the breaker may also be turned into an isolated wave, propagating in the direction of the wave until it forms a surfing backflow. The flushing water moves toward beach and the energy gradually gets reduced and dissipated.

Fig. 2.4 Waveform changes in wave propagation
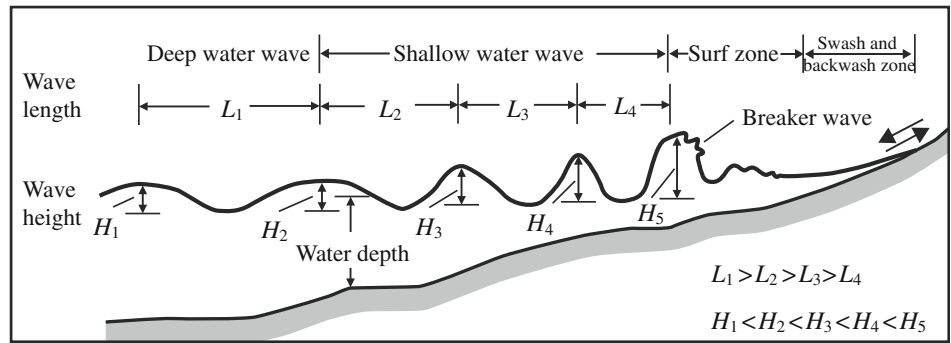
Fig. 2.5 The relationship between the ratio of the wave height and breaker wave depth ($H_b/d_b$), the ratio of the breaker wave depth and deepwater wave length ($H_b/L_0$) and slope (modified from Goda 1970)
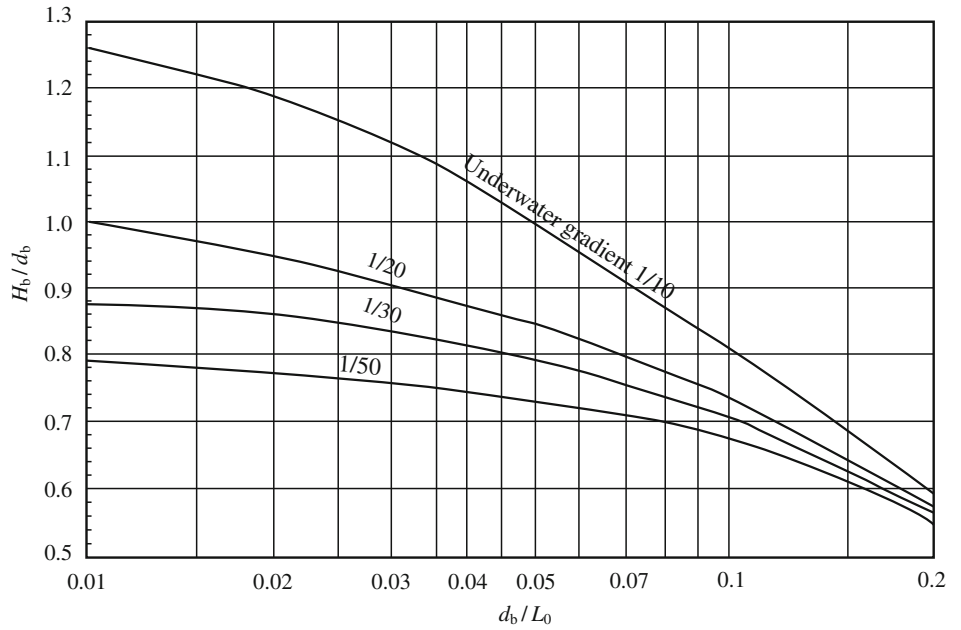
Fig. 2.6 Schematic diagram showing flow situation in the breaker wave area (from Qian and Wan 1991)
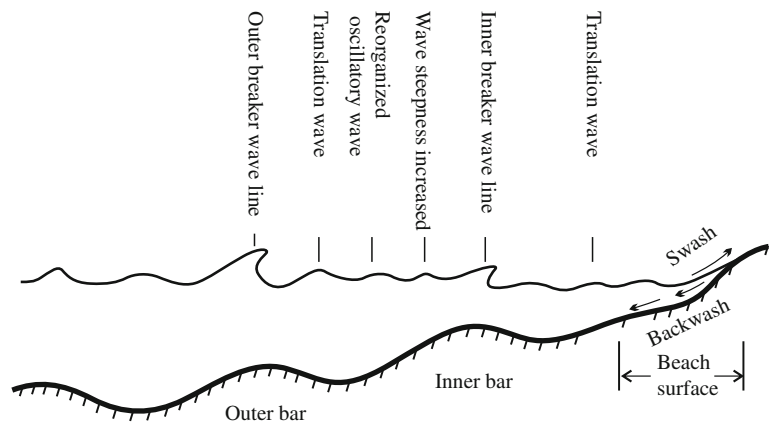
2. Wave refraction

The wave refraction refers to when wave propagates from offshore to onshore, the wave lines and peaks are curved.

The wave crest line is in the deep water area is perpendicular to the direction of the wave-driving force which is also the direction of way propagation. However, in the shallow water area, the direction of the wave propagation is often oblique

with the shoreline. At this point, the depth of the water at both ends of the same wave can be significantly different.

For example, when the deepwater wave enters the shallow water zone, the crest line and the bottom terrain are often not parallel and deflected to a certain angle $\alpha_0$ (or wave direction line and isobath line is not perpendicular to $90° - \alpha_0$; wave direction line refers to the line that is perpendicular to the wave peak and pointing the wave propagation and energy propagation direction; Komar 1998). The water depth of each point on the same wave line is different. Because the wave velocity decreases with the depth of the water, the velocity of each point on the same wave peak is also different. As the first waves arrived in the shallow water it begins to slow down, while the wave crest of the deeper waves moves faster than the lower ones, resulting in the transition of the wave crest and the wave direction. The direction of the transition is to make the crest line gradually parallel to the parallel lines, and finally tend to be consistent with the shoreline. While the wave direction line tends to be perpendicular to the contour line ($\alpha_0$ gradually decreases), which finally become perpendicular to the shoreline.

Wave refraction can cause dispersion or concentration of wave energy. Once the change of the wave direction line is studied, we can investigate the effect very well. Because the energy flux between the two waves is constant, the expansion of wave direction line induced by refraction can spread the same energy to a much higher wave peaks. If the wave direction line is converted, it has opposite situation (Fig. 2.7).

Due to the irregular shape of the shoreline and the complex topography of the underwater terrain, the distortion of the wave direction and the wave crest line in the shallow water area will be present in its various shapes and is characterized by complex refraction. In addition, the wave height and energy will change along the coast. Figure 2.7a, b shows the different influences of the underwater topography on wave refraction. In the case of smooth shoreline, the canyon-like bottom surface can spread the wave direction line to two sides, resulting in lower wave height and waned energy (Fig. 2.7a). While the ridge-shaped underwater topography can cause wave direction line converge to the middle (ridge) and increase the wave energy and wave height (Fig. 2.7b). Figure 2.7c, d shows the situation for the wave refraction in an irregular shoreline, which indicates that the wave direction lines converge at the headland (Fig. 2.7c) and scattered around bay of sea or lake. Therefore, the actual type of wave refraction depends on the characteristics of the offshore terrain.

### 2.1.4  Distribution of Beach Bar Sand Bodies Under the Influence of Wind Force

The deformation or broken occurrs when the waves enter the shallow water area could erode, transport, and redeposit the sediment in the water bottom.

After the waves are deformed, the movement of the water particles gradually becomes a non-closed ellipse, and there is



Fig. 2.7 Influence of micro-paleogeomorphology on wave refraction (modified from Komar 1998)
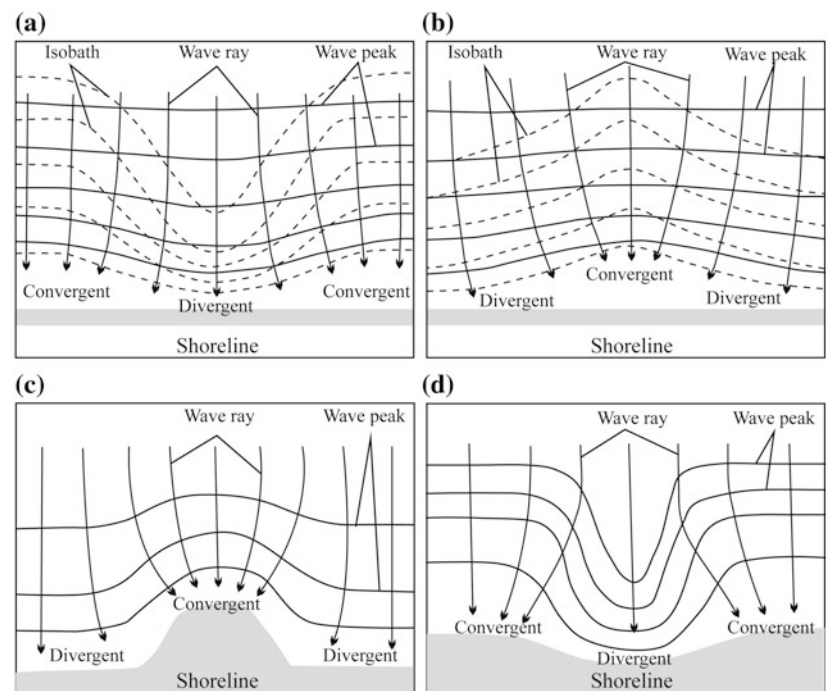
a net displacement toward the shore. This effect acts on the bottom sediments, because the interstitial water between the loose particles on the surface of the seabed sediments is also involved in this non-closed elliptical orbit (for a shoreline consisting mainly of non-cohesive sediments). This will have four effects on the bottom sediments: (1) upward lift; (2) cut to the shore bank; (3) downward pressure; (4) seaward shear. With the passage of each waveform, these four effects are repeated in turn (Friedman and Sanders 1978). When the crest approaches, the bottom water mass moves upward. Under each shallow water peak, the bottom water exerts a shear stress toward the shoreline. When the crest passes, the bottom water swings down quickly, resulting in the additional seaward shear forces to the underwater sediments under each shallow trough. When the stress applied to the sediment reaches the critical starting shear force, the deposited particles begin to move and form a wave mark.

Besides the formation of wave marks, the movement of the bottom sediments is systematically classified. The intensity of the reciprocating motion of water varies with wavelength and depth, and the movement pattern of the deposited particles will be different. The movement of sediment particles under wave action can be divided into five groups according to the interaction between the sediment and the water (Table 2.1).

In different environments and different water depths, waves have different energy and different influences on sediment transport and deposition. The grains with similar shape and specific gravity are accumulated together to form sand bars. The morphology of sand bars in the shallow water area will be adjusted accordingly under the influence of following waves. The accumulation of this kind of sand bar has obvious zonality due to different hydrodynamic forces.

### 2.1.4.1 Storm Energy Zone

The storm induced by the seasonal cyclone and anticyclone has a great amount of energy, which can influence a much greater water depth than the normal wave base. The maximum depth that storm can influence is called storm wave base.

In the marine environment, in the process of storm traveling toward the coastal zone, the barometric effect generated by storm and associated horizontal pressure gradient can make the coastal zone water rise. Meanwhile, at the same time, the storm will generate wind drift wave and storm wave to the shore, or banked-up water along the coast. As a result, the water level will be greatly raised to form a storm surge, which is proportional to the square of the wind speed. The storm surge has strong erosions of the coastal zone and disturbs the sediments deposited along the coast and nearshore or offshore. In the marine environment, the water surface tilted by the barometric effect, wind drift, and storm surge are compensated by the storm backflow at the bottom, also known as the gradient flow (Aigner 1985). In the contrast to the marine environment, in the event of a storm occurrence in the lake, there are not only large waves generated in the lake, but the lake will also have seiche activity that is caused by the shake of lake water body. The formation of the seiche activity is caused by the continuous influence of the storm from a certain direction, which forms the backwater on the windward side of the lake and induces the lake-level rises. On the contrary, the lake-level falls on the leeward side of the wind. As the storm wanes, the lake waters will move in the opposite direction, forming a water oscillation until the level is restored.

Gradient current or lake oscillation (seiche activity) can carry a lot of the detrital material from the shore. The eroded sediment can be delivered to deep water and form gravity flow, which can strongly erode and flush the bottom sediments. The gravity flow can flow below the normal wave base and forms tempestite deposit. The tempestite is strongly controlled by storm activity and is characterized by gravity flow and traction current.

### 2.1.4.2 Wave Shoaling Zone

In normal weather, it is generally believed that the waves are exposed to shoaling deformation when they start to contact with the bottom of the wave base and can start to move particles. This is the low-energy belt that waves begun to influence the sea floor. The sediment particles in this area have a tendency to move toward the shore due to the effect

**Table 2.1** The movement of sediment particles under wave action (modified from Friedman and Sanders 1978)

| | Movement of sediment particles |
|---|---|
| 5 | Suspension, move landward or seaward under the influence of onshore or offshore flow and gravity |
| 4 | The particles swing, but the net displacement is seaward |
| 3 | The particles swings, but do not move toward shore or leave the shore particles. The amount of movement toward shore under the wave peak is equal to the amount of seaward activity in the wave trough |
| 2 | The particles swing, but the net displacement is landward (Particles only moves ashore under the crest of the wave; Particles will not move to the shore in the wave trough, and will end up on the beach) |
| 1 | No movement of particles |

of the wave, and on the other hand, there is the trend of offshore movement under the gravity. The direction of the sediment movement is determined by the balance between the two forces. If the wave and gravity forces are offset, the sediment particle oscillates back and forth, resulting in a net displacement of zero. The particles that are on the seaward side of the equilibrium point gradually move offshore, and with decreasing of wave energy the particles finally enter into a deeper water area and deposit there. The particles on the landward side of the equilibrium point are subjected to increasing the shear force and moving towards the shore at a faster rate. In this process, the particles are subjected to the shear force. The shear force also generates ripples. The characteristics of the ripples are related to the relative strength of the shear force on the shore or offshore. In general, the ripple changes gradually from the symmetric to asymmetric shape and from small to large, reflecting the increased asymmetry and influence the bottom sediment. Sediment moving from the balance point to the shoreline moves to breaker zone. The wave entering the shallow water is not only experience orbital motion but also experience the whole motion to form water flow, which results in landward flow at the bottom and seaward flow on the surface (Fig. 2.8). The sediment of the belt is mainly fine grained and silty sand and interbeds with muddy layers, which is characterized by wave mark and ripple cross lamination. The sands form wide-flat beach and are named as outer beach.

### 2.1.4.3 Breaker Zone

The waves that are prorogated from the shoaling zone is associated with increased wave height when continuously moving toward the shoreline. As the water depth keeps decreasing, the slope steepness will reach critical value or water particles movement speed exceed the wave propagation velocity, forming the breaker zone. Breaker zone, as a strong wave energy zone, is associated with strong wave deformation and disturbance of water bodies, which strongly wash and sort the clasts to form coarse-grained sand bars. These bars are called outer bar or breaker bar.

The waves from shoaling zone have bottom currents flowing toward the shoreline (pulse flow, each arriving wave peak will produce a pulse) and deliver sediments to breaker zone. After the wave breaks, it likely forms an oscillating wave and a circular flow on the landward side of the breaker zone. As a result, in the breaker zone water flow from two directions to the breaker line, resulting in sediments getting accumulated around the breaker line and forming outer bar and trough (Fig. 1.10). Evans (1940) suggested that stronger waves will generate deeper water depth for the outer bars and associated troughs. This is because the bigger the wave is, the deeper water depth of waves begins to be broken. The formed outer bars will reversely affect the breaker zone, which consists of the self-organizing genetic model for outer bars. Keulegan (1948) found that when outer bars migrates landward, the position of the breaker zone moves landward accordingly. The position of outer bar is always related to the location of breakers. Therefore, breaker zone has control on the location and scale of outer bars.

### 2.1.4.4 Zone of Reorganized Waves

In the low slope of the shoreline, the wave is often recovered in the troughs after waves are broken in the breaker zone. Reorganized wave could be experienced when it is second or third time broken and form inner breaker zone, bars, and troughs, before reaching the surf zone (Figs. 2.6 and 2.9). The number of bars or the number of waves broken/reborn times highly depend on the total slope of the bank, in which a gentler slope is usually associated with a large number of sand bars and more times of waves broken. Each bar reflects the average breaking position of the wave on a certain scale. The deepest sandbars correspond to the biggest waves. The scale of the bar increases with the increase of distance away from onshore (Evans 1940), which is related to the size of the breakers. As the outer bars and newly formed bars efficiently consume the wave energy, the reorganized wave has a much less energy.

Due to the decreased size of the reorganized wave, the formed sand bars and troughs are also smaller. In addition, the wave reorganized-surf zone is located in the shallow depth, bar-trough will be eroded or remobilized by the waves with the changing of wave size, which evolves into the underwater beach. For example, during the storm, the waves



**Fig. 2.8** Schematic diagram showing the hydrodynamics of wave shoaling zone (modified from Friedman and Sanders 1978)

**(a)** **(b)**

Breaker wave line    Outer breaker wave line    Inner breaker wave line

Outer bar    Outer bar    Inner bar

Inter-bar beach
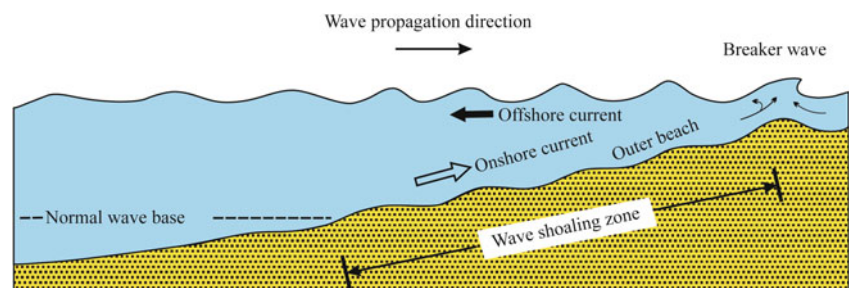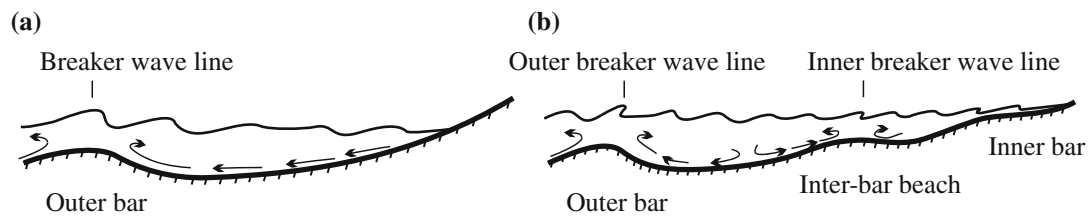
**Fig. 2.9** Hydrodynamic conditions of wave-reorganized zone (modified from Chan and Wan 1991)

will be broken on all the bars, with the biggest waves broken on the deepest bars, medium-scale waves broken on the inner side of sand bars, and small-scale waves broken on the shoreline. During the period of the small waves, the waves will have no influence over the deeper outer bar (the outer bars) and will not be broken before reaching the relatively shallow waters of the inner sand bar. As a result, the inner bars have a relatively high mobility than the outer bars and thus flat sand sheet can be formed in wave reorganized-surf zone, called inter-bar beach deposit in this work (Fig. 2.9b).

### 2.1.4.5 Surf Zone

When the wave moves further to the shoreline, the waves can be completely inverted and broken, and the wave is always in a broken state. The wave height, which is completely broken, is in direct proportion to the local water depth, known as the "Surf wave", which is also known as the "Surf Zone". The ratio of the wave height to the depth of the Surf zone can be written as

$$H/h = \gamma \tag{2.2}$$

In Eq. (2.2), $\gamma$ is the ratio of the wave height to the depth of water in the surf wave zone. It is usually recommended to be 0.7–1.

Surf zone, located between the breaker zone and uprush–backwash zone, is the main dissipation of wave energy area and associated with strong wave motion. It is also the most vigorous coastal zone for sediment movement. The existence of the surf wave zone and its width are mainly controlled by the slope of the topography (Jiang 2010a). If the slope of the terrain is gentle, a wider band of surf zone can be formed. As the water depth becomes shallow and the wave energy dissipates, the sediment carried by the waves can be unloaded. The inflow flows down the slope under the force of gravity to form a backflow (bottom flow), and the sediments that have been eroded from the shoreline are also deposited in the surf zone. The linear bars that are formed by inflow and backflow is called inner bar in this work.

### 2.1.4.6 Swash and Backwash Zone

The ultimate destination of the breaker waves is to become surfing and form a "swash and backwash zone". When the surf wave enters the coastal zone, it can continue moving toward shoreline under the effect of inertia force, called uprush. If the water does not infiltrate the sediments, the remaining water body will move backward to form backwash. This backwash flow will not stop until the water disappears, or a collide with another coming surf waves (Fig. 1.11). In addition, if the waves are affected by long-lasting winds, the lake surface would be uplifted by wind and form backwater.

As a result, this zone has both swash–backwash flows that are formed by the inertial force of surfing and reduced backflow, and the backwater that is uplifted by winds. Therefore, the hydrodynamic condition is complex and strong in this region and keep reworking the sediment. On the one hand, under the action of surfing, the sediment will move upward by overcoming the friction and gravity. On the other hand, under the influence of backwash flow, the sediment will overcome the friction and move downward. Therefore, beaches are commonly developed in this region. Especially in a gentle slope coast, a wide beach can be formed. This kind of beach is named as coastal beach in this work.

In the swash–backwash zone, the swash capacity is stronger than the backwash (Masselink et al. 2005). In the process of water carrying sediment into the highest point, gravity, friction, and water loss due to leakage and infiltration together will reduce the wave propagate velocity and induce the sediment unloaded in the highest point, forming beach shoulder that is parallel to the shoreline. The sediment composition of the beach shoulder includes both the sediments from the basin and residual sediment in situ. The beach shoulder marks the ultimate height of the flushing sediment, known as the coastal bars in this work (Fig. 1.11). If the bars are closed to the sediment source area, gravel beach bars can develop.

### 2.1.4.7 Nearshore Circulation System and Longshore Current

Nearshore zone refers to the coast (shoreline) extend in the direction of the offshore to just outside of the realm of the breaker zone area (Komar 1998). It includes the previously discussed breaker zone, waves reorganized-broken zone, the surf zone, and the backwash zone. In the nearshore zone, the distribution of the flows produced by a wave on the plane is very complex. In addition to the direct reciprocating motion

produced by the waves, there are at least two water flow systems that are influenced by waves. They are aforementioned (1) coastal circulation system composed of the rip flow and its associated longshore currents, and (2) the longshore currents (Komar 1998) generated by the oblique wave on the shore. These two wave systems usually exist simultaneously (Fig. 1.13).

As mentioned above, the nearshore circulation system can redistribute the sediment in the shore zone and form the nearshore sand bars and the corresponding edged shoreline (Bowen and Inman 1969; Komar 1971) (Fig. 1.13). Bowen and Inman (1969) also pointed out that the flow of rip in the offshore direction would break out of a watercourse, and, consequently form divided inner bars and shorelines. The rip current can also carry sediment to the offshore direction, sometimes more than seven or eight hundred meters (Qian and Wan 1991).

Longshore current is also important for sediment transport onshore. The component of wave movement along the coast line can form a separated force, which can adjust the beach bars parallelly to the direction of incident wave peaks. This force can drive the beach bars to migrate along the shoreline and form sand bars that are oblique to the shoreline (Fig. 1.13). In addition, the longshore current also forms an important part of the spiral flow along the coast, and can well explain the mechanism of the coastal spiral flow to form beach bars (Fig. 1.12).

The moving direction and trajectory of sediment along the shoreline are governed by hydrodynamic conditions, which are the result of the comprehensive effect of hydrodynamic conditions. In general, the different hydrodynamic zones in the coastal zone can form many columns of sand bars that are almost parallel to the coastline. According to their development position, the relationship between different wave action zones and beach bar distribution can be established (Fig. 2.10). In this chapter, the sand bars that develops in the breaker zone is called the outer bar. The sand bars developed in the surf wave zone is called the inner bar, whereas the sand bars developed in the swash zone is called the coastal bars. The beaches formed in the area of shoaling waves, reorganized waves, and backwash are called outer beach, the inter-bar beach, and the coastal beach, respectively. On the plane, the beach is mainly in the form of a sheet that surrounds the sand bar, namely inter-bar or outside bar beaches. In addition, when subjected to intense atmospheric disturbances (such as strong typhoons, cold waves, etc.), a storm deposit can be formed between the normal wave base and the storm wave base. Under ideal conditions, the above hydrodynamic action zone and the beach bar micro-geomorphological units can all be developed, but this depends on the slope of the shore and the direction of the wave relative to the shoreline. Therefore, in reality, there may be a lack of a hydrodynamic zone. For example, in the shoreline of a steeper slope, the surf waves tend not to develop, and the waves break up and erode directly onto the shoreline. Therefore, when applying the model, it should be suitable for local conditions. In different hydrodynamic zones, the formed beach bars have different morphologies, particle sizes, the sedimentary structures, and biological combinations. In turn, the beach bars on the shoreline can also provide a basis for the classification of shoaling waves zone, breaker zone, reorganized waves zone, surf zone, swash and backwash zone, and storm zone.

**Fig. 2.10** The classification of hydrodynamics in coastal zone and their corresponding beach bar distribution pattern
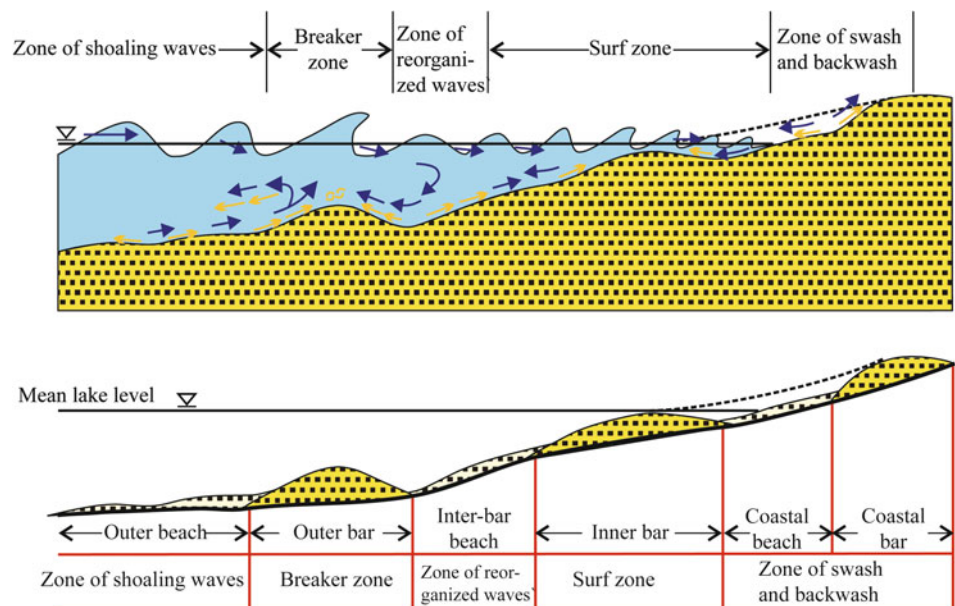
### 2.1.5 Research Methodology of Paleo-Windfield—The Recovery of Paleo-Wind Direction

Paleoclimate studies have significant implication as paleoclimate has influenced various geological processes, sediments accumulation, and the formation of sedimentary mines (Pang and Yun 2013). The research contents of palaeoclimate mainly include paleo-temperature, humidity, paleo-wind and paleowind direction (Quan et al. 2011, 2012a, b; Pang and Yun 2013; Wang et al. 2013; Licht et al. 2014). In previous work, paleoclimate researches are mainly focused on using alternative indicators to interpret paleo-temperature and precipitation, with less emphasis on paleo-windfield (Liu and Jiang 2011). This is because the low viscosity and low density of the air limit the ability of the wind to move sediment so that there are few alternative indicators of the paleo-windfield preserved in the geological record. Therefore, for a long time, studies on paleo-windfield have been neglected (Allen 1993; Liu and Jiang 2011). However, paleo-windfield study is important, because it is a direct result of the atmospheric circulation, which could provide information for atmospheric pressure gradient, the path of the storm, and atmospheric circulation patterns (Thompson et al. 1993).

The study of paleo-windfield should contain two aspects: paleowind direction and paleowind force. For the recovery of the paleowind direction, the alternative indicators to reconstruct paleowind direction are relatively easy to obtain (Liu et al. 2007; Scherer and Goldberg 2007; Wang et al. 2007a, b; Zhang et al. 2009; Liu and Jiang 2011; Jiang et al. 2013). The most intuitive way to recover the paleowind is to analyze the Eolian geomorphology.

1. Restore paleowind direction sing Eolian sandstone

Eolian deposits are formed under the action of wind. The compositional characteristics, sedimentary structures, and stacking sequence of the Eolian deposits contain a large amount of palaeoclimate information.

The Eolian sandstone with high-angle cross-bedding can be used as a proxy to reconstruct paleowind direction. The cross-bedding within Eolian sand dunes, which can be observed in the outcrop and drilling cores, can be used to indicate the morphology of dunes and the direction of migration, and thus become a widely used paleowind direction indicator (Allen 1993). The cross-bedding of a transverse dune is characterized by plane shape and long and flat foreset lamination and the dip of bedding points to the downwind direction. It has become a very common method to reconstruct the paleowind direction by identifying transverse dune and the dip of foreset lamination. This type of Eolian sandstone can be preserved for a long time in the geological history and is widely distributed in arid and semi-arid regions as well as in the strong sediment supplied coastlines (sea or lake). By far, the dip of lamination in Eolian sandstone is one of the most widely used methods to restore paleowind direction, especially to reconstruct the paleowind direction of the Holocene Epoch.

2. Restore the paleowind direction using the magnetic rate of clay

The magnetic fabric analysis of clay deposition can be used to reconstruct the paleowind direction. The long axis of the magnetizability in Eolian sediments has good correlation with wind direction with a deviation of no more than 20° (Wu et al. 1998). The inherited magnetic direction of Eolian sediments is closely related to the depositional process and neglectfully influenced by the post-depositional process. Maximum magnetic susceptibility in anisotropy of magnetic susceptibility is parallel to the airflow direction, which can be used to reconstruct the paleowind (Wu and Yue 1997).

The method has been widely used to reconstruct paleowind direction. However, the magnetic fabric of Eolian sediments is still affected by many factors, which could strongly influence the outcome of the reconstructed paleowind. Therefore, Eolian sandstones from arid and semi-arid areas that are less disturbed are best samples to reconstruct paleowind direction. It is difficult to obtain satisfactory results from samples influenced by biological disturbances or weathering in wet climate regions.

3. Restore paleowind direction from aqueous deposit

In addition to directly acting on sediment, the wind can also drive movements of other media and leave traces of the paleowind in the sediments. The wide and flat surface of water bodies is a common medium to link the wind and sediments (Liu and Jiang 2011). In various groundwater bodies, the movement of lake water is relatively simple, which is mainly controlled by windfield. Detailed analyses of the aqueous deposit can be used to restore paleowind direction. The strike of wave mark ridge is generally perpendicular to the wind direction, while the dip of the steep side of asymmetrical wave mark is often consistent with the downwind direction (Pochat et al. 2005). In a wind-influenced wide lake water bodies, the direction of the sand spit can also reflect the paleowind direction (Nutz et al. 2015). The strike of the sand bars formed in breaker zone is usually perpendicular to the wave propagation direction or wind blowing direction. The transect of sand bars in breaker zone usually displays asymmetric shape, with windward side characterized by a gentle slope and long extension, and leeward side characterized by a steep slope and short

extension (Fig. 1.10). Therefore, the sand bars in the breaker zone is also a good alternative indicator for reconstructing the paleowind direction.

## 2.1.6 Paleo-Windfield Research Method—Paleo-Wind Strength Recovery

Compared with the recovery of paleowind direction, the study of paleowind strength is relatively weak. There are very few reports of paleowind recovery study both in China or abroad. It is easy to obtain the windfield features by using equipment to measure the modern wind. However, this methodology only records the wind strength in the past few decades. To recover the paleowind strength for a period of the geologic history, we can only use the proxy to indirectly reflect the strength of windfield. On the one hand, wind as an important sediment transport media and force, the strength of wind can be reflected by its ability to transport sediment. Therefore, we can restore the strength of the paleowind by analyzing the grain size of Eolian deposits (Rea 1994; Xiao et al. 1995). On the other hand, in addition to being a direct geological force, the wind can also act on the water bodies to form waves. There is a quantitative relationship between the size of the wind and the wave features. Many scholars have long since found that sediment deposited in the coastal zone can provide clues to the recovery of the paleowave (Jewell 2007; Forsyth et al. 2010). Based on the relationship between wind strength and wave scale, we can further recover the paleowind strength. This section will summarize and explore the recovery methods of paleowind strength through above-mentioned two approaches.

### 2.1.6.1 Qualitative Recovery of Paleowind Strength

The current works of literature on paleowind recovery are mostly in the qualitative stage. The particle size and composition of the sediments are reflective of the media carrying capacity, which is a good proxy to interpret the natural geographical environment and the dynamic conditions of the deposition. (Jiang 2010a). Eolian deposits are widely preserved in the geological record and their size and composition record the paleowind strength. For example, the more coarse-grained composition and specific gravity preserved in the Eolian deposits, the greater wind strength is required. This study has been widely applied in the study of loess, polar ice cores, and deep-sea sediments (Xiao et al. 1995; Lu et al. 1999; Wang et al. 1999; Ding et al. 2001).

The tempestite deposited between the normal wave base and the storm wave base is relatively easy to preserve because of the distance from the shoreline. The thickness of the tempestite in the geological record often indicates the storm energy during its deposition. A thick tempestite is usually associated with strong storm activity. Therefore, the thickness of tempestite sometimes can have implication for restoring paleowind strength (Brandt and Elias 1989).

The above-mentioned method can only obtain the relative strength of ancient wind force but has not been applied to the quantitative restoration of ancient wind.

### 2.1.6.2 Quantitative Recovery of Paleo-Wind Strength

(1) Recovery of paleowind strength by the grain size of lake gravelly beach

Many scholars have long since discovered that sediment deposited in coastal–shore zone can provide clues to the recovery of paleowaves (Tanner 1971; Allen 1981, 1984; Dupré 1984; Diem 1985; Jewell 2007; Forsyth et al. 2010). The wind speed, wind blowing time, and fetch length determine the size of the wind and waves (Komar 1998) and there is quantitative relationship between the winds and waves (CERC set 1977, 1984), Therefore, the size of paleowaves can provide a clue for quantitative reconstruction of paleowind. Adams (2003, 2004) studied the Gravelly Beach in the Salt Lake in U.S. and proposed a BPT technique, which is based on the analysis of the grain size of gravel, to obtain the maximum waves capacity for carrying the largest grain. Based on this correlation, we can restore the paleo-waves by analyzing the coastal–shore sediments and further interpret the size of paleowind.

The BPT technique (beach particle technique) is proposed by Adams in 2003. The method is based on the theory of isolated wave and utilizes the relationship between unidirectional flow maximum capacity and the carrying grain size to obtain the critical wave conditions for transporting gravel particles. This approach can be described as follows: (1) analysis of the characteristics of gravel size distribution in the gravel flats near the coastline of the lake could provide clues to interpret the critical shear force to move the gravel; (2) the critical shear force can be converted to the critical wave velocity; (3) the wave velocity can be converted to height of breaker wave; (4) the height of breaker wave can be converted to wave height in deepwater region; (5) the wind pressure coefficient can be calculated according to the parameters of effective wave height and wind fetch length in deepwater area; (6) the wind speed can be obtained by analyzing the wind pressure coefficient.

The specific application of this method is shown in Adams (2003, 2004). Using the above methods, Adams (2003, 2004) first conducted the research on the modern gravel beach in the Great Salt Lake of the U.S. and obtained the wind speed range of 6.5–17.4 m/s between 1986 and 1987, which was consistent with the record of the

anemometer. Adams also applied this BPT method to the Late Pleistocene Gravelly Beach in the western region of the Great Basin in U.S. and obtain the paleowind velocity ranging from 9.7 to 27.1 m/s, which is faster than the modern wind speed. Knott et al. (2012) also used the BPT method to study the Holocene Gravelly Beach in Manly Lake of U.S. and got the wind speed in the range of 14–27 m/s, which is consistent with today's wind speed records. Their research also confirmed that it is a modern windfield formed with the characteristic of Manly Lake today.

However, due to the size of the sediment near lake coast distribution not only affected by the original waves, but also influenced by backwash flow and reflection waves, and, therefore, the critical condition of waves obtained from the size of sediments deposited on the coastal zone might not reflect the original paleo-wind and waves. Gravelly Beach near the lake shoreline is largely controlled by source, which means the size of gravel depends largely on the composition, weathering, and transportation process in the source area, and thus it is not reasonable to associate the grain size with paleo-winds and waves without considering these conditions. In addition, the sediment deposited near the shoreline of the lake is easy to be eroded, resulting in incomplete depositional records, so that the continuous process of paleowind change cannot be obtained. Finally, since the shape, sorting, and particle size distribution of gravel is more easily obtained on outcrop, and therefore these two methods are usually applicable to outcrop research and not commonly applied to drilling core.

(2)  Restore paleowind strength by using the thickness of breaker bars

Based on the "breakpoint model" or "self-organizational model" of breaker sand bars, this work puts forward a method of restoring paleowind force by using the thickness of breaker bar. As mentioned above, the "breakpoint model" or "self-organizational model", which explains genesis of the bars, has been widely accepted. Breaker model can be simply expressed as: sediment starts to disturb the bottom bed with waves (Fig. 2.11a) and are accumulated in the breaker line area due to the effect of both the onshore current and offshore current (Fig. 2.11b). When the hydrodynamics in breaker line reach a balance between the onshore current and offshore current, the breaker bars start to grow in situ and form trough. The location and scale of the bars theoretically have a strict corresponding relation with the size of the breaker wave (Fig. 2.11c) (Davidson-Arnott 2013; Houser and Greenwood 2005; Price and Ruessink 2011). It is assumed that the wave model based on marine environment is also applicable to the lake environment, and the quantitative relationship between the size of the breaker

wave and the size of the bar can also be used to restore the paleo-wave and wind.

Previous studies indicate that the larger the wave, the larger the water depth of the breaker bars and troughs (Keulegan 1948; King and Williams 1949; Shepard 1950). This is because larger breaker waves correspond to greater water depth, which may explain why the breaker bars migrate to deeper water during the storm activity. The migration of breaker bar will finally reach a balance with wave height (Davidson-Arnott 2013; King and Williams 1949; Houser and Greenwood 2005; Price and Russeink 2011). This balance is the result of combined effects from onshore current, offshore current, and water depth of bar top, which are all related to the size of breaker wave. Therefore, the breaker wave size is the most important factor for the formation of the bars by controlling the size, water depth, and location of breaker bars.

Although the breaker bar is controlled by the breaker waves, the shape of the bar is not related to the size of the waves (Keulegan 1948). It is because the transportation and accumulation of nearshore zone sediments can always establish a balance with the features of waves, especially for breaker waves (Davidson-Arnott 2013). No matter how big the wind and wave, the sand bars are formed in a similar shape but the scale of the sand bars will be different.

A large number of observations show that the cross section of breaker bar has an obvious asymmetry, characterized by steeper slope angle in landward side and gentler slope in seaward side and the slope angle of landward side can reach even angle of repose (Gallagher et al. 1998; Thornton et al. 1996). In addition, Keulegan (1948) found the ratio of trough depth and bar depth ($d_t/d_b$) reaches around 1.69 by flume experiment, while Otto (1912) and other German scientists observed a mean ratio of 1.66 in the Baltic Sea, which basically agrees with the experimental values measured by Keulegan in 1948. However, Evans (1940) described in detail the naturally formed sand bars are relatively flat and broad, which is characterized by a $d_t/d_b$ ratio of 1.42 and 1.55. In this work, we used a compromised ratio value, 1.60.

Based on the relationship between the sand bar size and the breaker wave size, we can estimate the wave characteristics of the sand bar from the thickness of bar, which can be further used to restore the windfield conditions according to the relationship between the winds and waves. In particular, according to the geometry of the breaker wave sand bars, the following relations (Eq. 2.3) can be obtained:

$$t_b = d_t - d_b + \frac{(d_t - d_b)\tan\alpha}{\tan\theta} \qquad (2.3)$$

The meanings of each parameter in the above equation are shown in Fig. 2.11c, where $t_b$, $d_t$, and $d_b$ are recommended for m. According to literature from Gallagher et al.

**Fig. 2.11** Breaker wave model for the formation of sand bars in coastal area (modified from Dolan and Dean 1985; Davidson-Arnott 2013). **a** Sediments are by landward and seaward current; **b** Sediments are concentrated in the vicinity of the breaking wave line to form a wave bar. The shape and scale of breaker wave sand bars can be finally determined by reaching their balance with the breaker wave. **c** Diagram showing the parameters of waves and bars. t is the original thickness (m) of breaker wave bar; $d_b$ is the breaker wave depth (m), which is also water depth at the top of breaker wave bar; dt is the depth (m) of the groove on the landward side bank of the breaker wave bars; $\alpha$ is the basal slope of breaker bar; $\theta$ is the slope angle of the landward breaker bars
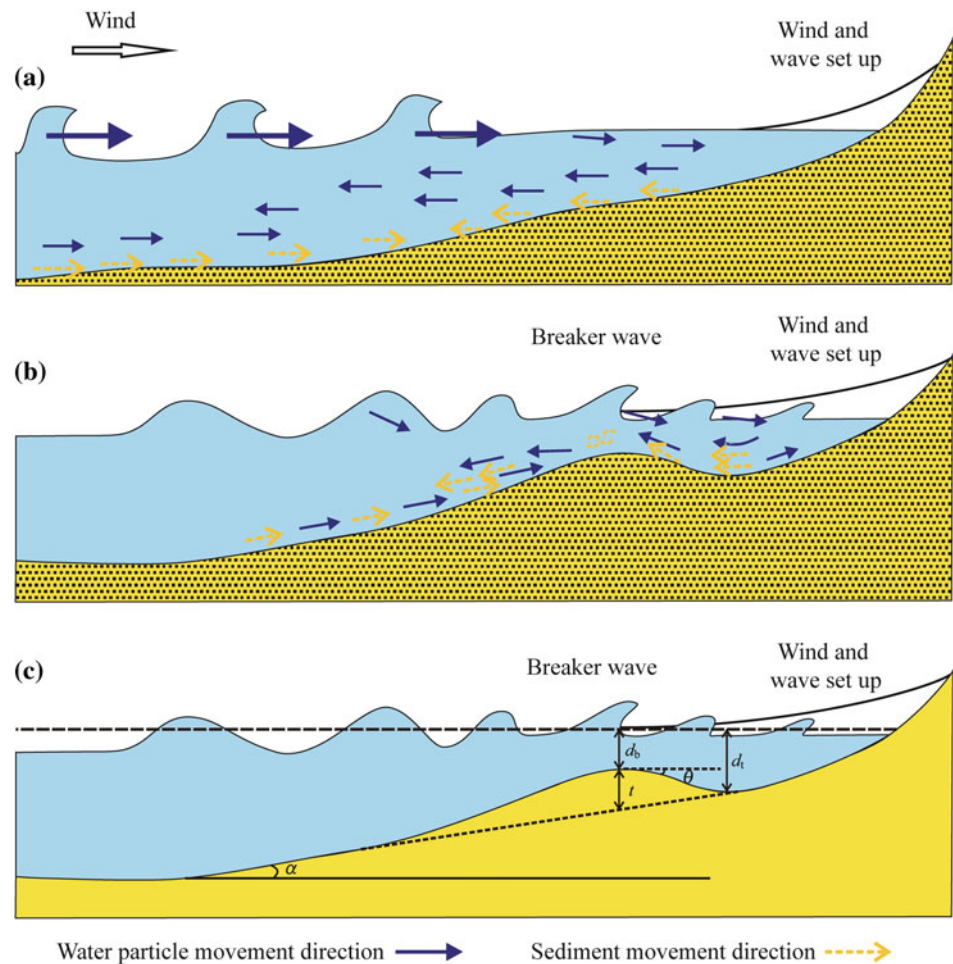


(1998) and Thornton et al. (1996), the ideal value of $\tan\theta$ is 0.63. As mentioned above, $d_t/d_b$ is approximately 1.60, thus the equation (2.3) can be simplified to

$$t_b = (0.6 + 0.95 \tan \alpha)d_b \qquad (2.4)$$

Therefore, according to the equation (2.4), if we obtain the thickness of breaker bar ($t_b$) and slope of bar ($\alpha$), we can calculate the water depth of breaker wave ($d_b$).

Goda (1970) has drawn an empirical curve based on the experimental data of several beach slopes—called the Goda curve (Fig. 2.5), which can convert the parameters of the wave depth ($d_b$) to the wave height ($H_b$). In the process of waves moving toward the onshore, wave height increases gradually and reaches the maximum wave height in breaker zone and then decreases gradually due to wave energy consumption. Therefore, the wave height of breaker zone determined by Goda curve can be approximately equal to the maximum wave height, $H_b \approx H_{max}$. According to the statistical characteristics of the wave, the maximum theoretical wave height $H_{max}$ is twice as high as the effective wave height in the deep water area, i.e., $H_{max}$ is approximately $2H_s$

(Sawaragi 1995). Therefore, the wave height $H_b$ in the breaker zone can be approximately converted to $H_s$, that is, $H_b$ is approximately equal to $2H_s$.

According to a relatively simple wave prediction equation from the coastal engineering research center (CERC), the wind pressure coefficient $U_A$ can be obtained as follows:

$$U_A = \frac{H_s}{(5.112 \times 10^{-4})F^{0.5}} \qquad (2.5)$$

In Eq. (2.5), F is the length of wind zone (m); $H_s$ is effective wave height (m) in deepwater area.

The wind pressure coefficient UA is associated with wind speed (CERC 1984):

$$U_A = 0.71U^{1.23} \qquad (2.6)$$

In Eq. (2.6), U is the wind velocity (m/s) at 10 m above the water surface.

Accordingly, the parameters required to restore the paleo-wind using thickness of breaker wave include: (1) original thickness of breaker bars, which can be accurately identified and measured and restored by compaction

correction; (2) paleo-slope of coastal area and wind fetch by studying the paleo-shoreline and palaeogeomorphology of lake (see Sect. 2.3.2.2); (3) the breaker wave height, which is converted from breaker wave bar thickness based on the breaker bar morphology and paleo-slope parameters as well as the critical condition for breaker waves; (4) the high wave height is converted to the effective wave height in the deepwater region; (5) the wind pressure coefficient that is calculated from the effective wave height and the fetch length in the deepwater area (Eq. 2.5); (6) calculate the wind speed according to the wind pressure coefficient (Eq. 2.6).

**(3) Recovery of paleowind strength by gravelly coastal bars**

Based on the relationship between swash–backwash zone and coastal Gravelly Beach bar, this work also proposes a method to restore the paleowind strength by the thickness of the sandy–gravelly coastal bars.

The thickness ($t_r$) of the sandy–gravelly bars is approximately the limit height of the wave swash and backwash, which is the limiting position of the lake (sea) water entering the land. This limit height is the sum of storm backwater height ($h_s$), wave set up height ($h_{su}$), and wave run up height ($h_{ru}$) (Fig. 2.12) (Dupré 1984; Nott 2003) which can be expressed in Eq. (2.7).

$$t_r = h_s + h_{su} + h_{ru} \qquad (2.7)$$

In this way, the thickness of sandy–gravelly ($t_r$) coastal bars can also be associated with the paleowave conditions, which can also be used to calculate the paleowind size through the correlation between wind and wave. The specific operational methods are as follows:

According to the design specification of embankment engineering in China (GB 50286-2013), storm surge can be expressed through windfield parameters and basin parameters, as shown in Eq. (2.8):

$$h_s = \frac{KU^2F}{2gd}\cos\gamma \qquad (2.8)$$

K is the comprehensive friction coefficient, which can be $3.6 \times 10^{-6}$. D is the average depth of water; $\gamma$ is the angle between the wind direction and the normal line perpendicular to the shoreline; Other parameters are the same as above.

According to a previous study example (Nott 2003), the wave set up height ($h_{su}$) can be approximately 10% of the effective wave height ($h_s$) in the deepwater area (Eq. 2.9). Wave run up height ($h_{ru}$) can be approximately 30% of $H_s$ (Eq. 2.10).

$$h_{su} = 0.1H_s \qquad (2.9)$$

$$h_{ru} = 0.3H_s \qquad (2.10)$$

Substitute Eqs. 2.8–2.10 into Eq. 2.7, Eq. 2.7 can be expressed as Eq. 2.11 as follows:

$$t_r = \frac{KU^2F}{2gd}\cos\gamma + 0.1H_s + 0.3H_s \qquad (2.11)$$

Then, according to Eqs. 2.5 and 2.6, Eq. 2.11 can be converted to 2.12.

$$t_r = \frac{KU^2F}{2gd}\cos\gamma + \left(1.452 \times 10^{-4}\right)U^{1.23}\sqrt{F} \qquad (2.12)$$

According to Eq. 2.12, if the paleowind fetch length (F), paleowater depth of the lake basin (d), and paleowind angle relative to the shoreline ($\gamma$) is known, we can calculate the paleowind speed (U) by the thickness of sandy–gravelly coastal bars ($t_r$).

In summary, the detailed approach to restore paleowind by using thickness of sandy–gravelly coastal bars can be simply expressed as: (1) identify single phase formation of the sandy–gravelly coastal bars and measure its thickness accurately from sedimentary records, such as outcrops, drilling cores, etc.; (2) if the sandy–gravelly bar is subjected to a significant compaction process, it should be corrected to obtain its original thickness; (3) the paleowater depth of the basin can be restored by depositional records (see Sect. 2.3.3 for specific methods); (4) the paleowind direction can be interpreted by depositional record (see Sect. 2.1.5 for specific methods); (5) based on the interpretation of paleowind direction, identifying the paleo-shoreline (see Sect. 2.3.2.3 for specific method, or refer Jiang and Liu 2010) and its strike direction to obtain paleowind fetch length and the angle between paleowind direction and the normal line perpendicular to the coastline; (6) based on the above-mentioned parameters, the paleowind strength can be calculated by Eq. 2.12.

**Fig. 2.12** Influence of waves on sorting of sediment in coastal zone (from Wu et al. 2008)
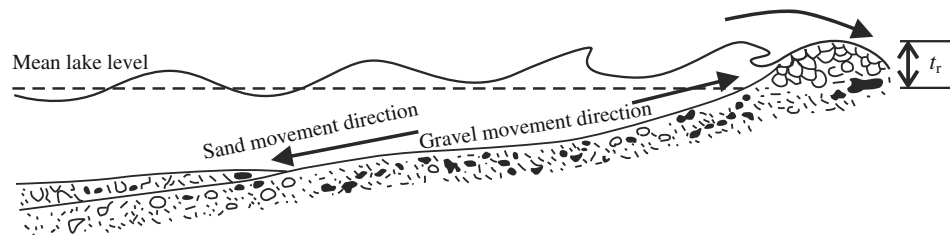
## 2.2  Source

### 2.2.1  Formation of Sediment Source

In a broad sense, the entire surface of the earth can be divided into two basic topographic units: the denudated orogenic belt or uplift area and the sedimentary basin. Sedimentary topography can also be called the sedimentary region, which is the occurrence of sedimentation. Denudated topography can provide material sources for sedimentary areas, called the source area. Therefore, provenance refers to the source area of sediments. The exposed or had been exposed magmatic rocks, metamorphic rocks, or sedimentary rocks on the earth's crust have experienced weathering and disintegration in the source area and transportation to the sedimentary area, under the influence of tectonics, weathering, and various geologic forces.

The denudation of the source area is determined by the process of tectonic movement and climate-driven denudation kinetics. The tectonic activity in orogenic belts has a great destructive power and the tectonic compressive or plate collision can result in deformation and morphological changes of large surface areas. The destruction of high mountains and rocks formed by plate collision or tectonics is the driving force that causes the sediment to collapse, peel off, and flow on the surface. Weathering and erosion depend largely on climatic factors, and the erosion of the tectonic uplift can be carved into a crisscross valley landscape, providing a large supply of materials to the sedimentary areas. Therefore, tectonic movement and climate are important factors for the formation of the source area.

### 2.2.2  Control of Source on Sedimentation

The sediment source is one of the basic factors controlling the types and distribution of sediments, which is the material basis for forming various sedimentary bodies.

First, the location of the sediment source determines the type of depositional system. Sediment derived from different source areas can form different sedimentary systems under different sedimentary hydrodynamic conditions. Especially for continental faulted basins, the area of the depression is small but with multiple directional sources feeding the faulted basins. In general, in the steep slope of the faulted basin, although the basin is located close to the source area, the sediment supply from source is relatively small and often forms small subaqueous fans or fan delta system. Compared with the steep slope belt, the gentle slope can form different types of sedimentary systems, such as delta, fan delta, and coastal depositional systems. The long axis entrance area of

the basin is often the largest source area, often forming a large delta system (Fig. 1.6).

Second, the direction and position of the source area determine the distribution pattern of the sedimentary system and the fabric of the skeleton sand body. The long axis of the faulted basin is the main sediment entrance pathway from source and often forms large delta system or fan delta system. The gentle slope or steep slope in depression is the secondary place influenced by source area and usually develops an isolated or plane composite system of alluvial fan, delta, fan delta system, and subaqueous fan system, depending on point source or linear source. According to the distribution pattern of sand body, the region where the received sediment supply from source has mostly the developed sand bodies and is characterized by thick sandstone and high sand/mud ratio. This region is also the focus of oil and gas exploration.

Third, the sediment supply strength also has an important influence on depositional patterns, especially for the reworked sedimentary bodies (such as the beach bar depositional system). In general, for a multiple source system, the intensity of sediment supply from different sources tend to be different, while for single-source system, the sediment supply intensity is also varied in the different locations of the basin or in the different periods of geological history. For the beach bar system, its formation is mainly caused by the waves reworking on the nearby sand bodies. Therefore, the sediment sources near the beach bars have played an important role in the formation and scale of beach bars. In the case of adequate supply of siliciclastic materials, sandy beach bars are very well developed, while in the case of limited the supply of terrestrial debris carbonate beach bars are often formed. Yang et al. (2011) established the beach bar classification scheme based on the relationship between the source area and the beach bar. In their classification, there are two main types of beach bar developed in the Dongying Sag: rich source type and poor source type. The rich source type can be divided into bedrock-beach bar depositional system, normal delta-beach bar depositional system, and fan delta-beach bar depositional system. The poor source is mainly carbonate rock beach depositional system.

In addition, from the point of view of sequence stratigraphy, the relative change in the level of the sea (lake) can change the balance between sediment source supply and depositional system. In lowstand systems tract, the sedimentary basin is characterized by a drop of base level and expansion of source area. Besides the long-lasting sediment source area, the exposed local highs in the margin of a sedimentary basin in Lowstand Systems Tract can also experience erosion and contribute sediments to the basin. In

addition, in the lowstand systems tract, the river carves deeply into underlying strata and the depositional center begins to migrate to basin center, forming shelf margin delta, lowstand fan, etc. In the transgressive and highstand systems tract, due to the expansion of water bodies and a rise of sea/lake level, only the long-lasting source area can keep dumping sediments into the basin.

Sediment source, in addition to the control of sedimentary facies, the plane distribution pattern and scale of sand body, has also influenced the reservoir properties of sand bodies. The difference of source conditions can affect the stratigraphic thickness, reservoir lithology, maturity, matrix type and composition, and even diagenesis, which are important for properties of reservoir rock. For example, He et al. (2011) evaluated the reservoir quality of Chang 6 sandstone of Yanchang Formation in the middle of Ordos Basin, northern China, by identifying different types of sediment sources, and concluded the reservoir properties are mainly controlled by main sediment sources. Liu et al. (2012) also evaluated the reservoir properties of Daxing conglomerate and suggested the reservoir quality of dolomite conglomerate reservoir is better than that of limestone breccia reservoir (see more detail in Chap. 6).

## 2.2.3 Source Analytical Method

Source analysis (mainly terrigenous sedimentary rocks provenance analysis) is using the end product of sedimentary process to infer the petrology characteristics of parent rocks, tectonic setting, and climatic conditions of the source areas (Pettijohn et al. 1987). Sediment source analysis, as an important part of basin analysis, is helpful for the identification of the paleo-erosional area, reconstruction of paleo-geomorphology characteristic, reappearance of paleo-river system, a track of parent rock, and restore the climate and tectonic background of sedimentary basins (Wang and Li 2003). Provenance analysis based on two premises: first, there is a genetic relationship between the parent rocks and siliciclastic rocks; second, the sedimentary rocks formed under different tectonic background have different compositions and texture (Weltje and von Eynatten 2004).

Provenance analysis is aimed to reconstruct depositional environment and paleogeography, by studying the position of the sediment sources, the property and the compositional characteristics of the parent rock, climate conditions and tectonic setting in the source area, sediment transport process, etc. Therefore, the provenance analysis plays an important role in the study of sedimentary facies and depositional systems.

The integration of geological methods, including sedimentology, tectonics, well logging, seismic and others, with the disciplines of chemistry, physics, mathematics, as well as

the application of advanced technology such as electron probe, cathode luminescence to the field of geology, have enriched the methodology to analyze sediment provenance and promote the provenance analysis from the qualitative description to semi-quantitative and quantitative analysis, making provenance analysis results more reliable. The commonly used provenance analysis method is shown in Table 2.2. Due to the data availability the provenance analysis can be carried out accordingly.

### 2.2.3.1 Qualitative Description of the Sediment Source

The source supply system of a clastic sedimentary body includes erosional area, depositional area, transportation pathway, and manner (Zhang et al. 2002). Fully recovering the paleo-provenance is difficult, however, combining the known distribution of depositional systems and the change of sediment characteristics can largely restore the paleo-sediment provenance system.

1. Sedimentary methods

The sedimentary method is mainly based on the sedimentary principle and the source analysis of clastic rocks. The analysis of the distribution pattern of sandstone can provide certain evidences for the provenance analysis. The spatial structure of sandstone can not only reveal paleocurrent direction and numbers of sediment sources but can also effectively reveal the influence of sediment source and its stability over time. For the same depositional system, the closer the source area, the higher sand ratio and sand thickness can be observed (Jiao et al. 1998). Therefore, the distribution pattern of the sand dispersion system can indicate the direction of the paleocurrent and thus further reveal the direction of the sediment source (Wang et al. 2007a, b).

Based on the drilling, well logging, and seismic data, as well as detailed correlation and division of stratigraphy, the strata isopachous map, sand ratio contour map, and the sedimentary facies for a certain geological period can be drawn and used to infer the relative location of sediment source. When the above work is combined with the changes of lithology, grain size and its proportion, sedimentary structure, rose diagram, paleocurrent data, and paleogeographic analysis, a more accurate sediment provenance can be concluded. The application of the sedimentary method to the sediment source analysis should be based on a large number of field observations and (or) data statistics, which require analyzing as many data points as possible to ensure the reliability of the conclusions. This method can determine the general direction of the source, however, it is not sufficient to reveal the specific information of the source area and the properties of the parent rock (Yang et al. 2013).

**Table 2.2** Common provenance analytical methods

| Identification of provenance | Sedimentological methods | Stratigraphic thickness and sand content analysis | Qualitative description |
|---|---|---|---|
| | | Palaeogeomorphologic analysis | |
| | | Sedimentary facies analysis | |
| | | Palaeoflow analysis | |
| | Petrographic methods | Grain-size analysis of clastic rocks | |
| | | Sandstone compositional analysis | |
| | | Clastic particle structure analysis | |
| | | Compositional analysis of conglomerate | |
| | | Rock fragment analysis | |
| | | The luminescence analysis of rock-forming mineral | |
| | | Heavy mineral compositional analysis | |
| | Geochemistry | Constant element | |
| | | Trace elements | |
| | | Rare-earth elements | |
| | | Isotopic analysis | |
| | Geophysics | Well logging | |
| | | Seismic stratigraphy | |
| | | Bouguer gravity anomaly | |
| Calculation of erosional rate | Geological methods | Volumetric balance method | Quantitative analysis |
| | | Sedimentation rate method | |
| | | Undenuded formation trend extension method | |
| | | Wave process analysis | |
| | Geochemistry | Vitrinite reflectance method | |
| | | Apatite fission track method | |
| | | The cosmogenic nuclide analysis | |
| | | Fluid inclusion method | |
| | | Sporopollen method | |
| | | Geothermal method | |
| | Geophysics method | Sonic time difference | |

2. Petrological Methods

Traditional petrological methods can play an important role in sediment source analysis. The siliciclastic rocks from the basin are derived from the parent rock in the source area, so the compositional analysis of rocks in the basin can infer the source rock type. In particular, the gravel composition of conglomerate can not only directly reflect the composition of the basement rock and the composition of parent rock but also reflect the degree of abrasion, climatic conditions, and tectonic setting. Therefore, the various characteristics of gravel are the direct markers of the source area and the sedimentary environment (Yang et al. 2013). The lithic fragment in the clastic rock is also a direct sign of the source. The type and content of the lithic fragment can accurately reflect the lithology, mechanism of weathering, the degree of weathering, and the transport distance. The type and proportion of lithic fragment in the source area should be consistent to that of parent rocks.

Dickinson et al. (1983) based on the statistics of a large number of sandstone detrital components, established the relationship between mineral composition and provenance system and drew the multiple triangular diagrams for provenance analysis. This approach is still widely used for the tectonic setting analysis of the source area, however, this method did not consider mixture source and the effect of

weathering, transportation, diagenesis etc., Therefore, in some cases, this petrological method fails to accurately predict sediment source (Wang 2002; Yang et al. 2013).

The luminance analysis of major main rock-forming minerals helps to identify the sedimentary environment and the cause of sedimentary rock. The luminance of quartz, feldspar, and lithic fragment in the clastic rock is associated with the characteristics of source rocks, and therefore, the color of clastic particles observed under cathode light can be used to interpret the sediment source (Götze et al. 2001; Augustsson and Bahlburg 2003). However, the judgment of the cathode luminescence on the provenance interpretation was influenced by experience and many random factors (Yang et al. 2013).

Heavy minerals are generally resistant to abrasion and stability and can retain the characteristics of their parent rocks, which plays an important role in the source analysis (Zhao and Liu 2003). The overall characteristics of heavy minerals in the clastic sediments are determined by the nature of the parent rock, the dynamic conditions of the water, and the distance of the transport. The combination of heavy minerals in clastic rocks is similar to the same provenance and drainage system, while the rocks from different parent rocks are characterized by different heavy mineral composition.

In the transportation process of siliciclastic minerals, the unstable heavy mineral experienced mechanical abrasion or chemical decomposition, resulting in a reduction of unstable heavy mineral and increase of stable heavy mineral content (Xu et al. 2009). Provenance analysis can use the heavy mineral combination of sandstone, ATi (apatite/tourmaline)—Rzi ($TiO_2$ mineral/zircon)—MTi (monazite/zircon)—CTj (chromium spinel/zircon) index, as well as the heavy minerals such as zircon–tourmaline–rutile index (ZTR index) to indicate the sediment source (Morton et al. 2005). For the older aged rocks, the heavy mineral would experience burial, diagenesis, and other effects, which result in losing provenance information and making provenance interpretation more ambiguous. Therefore, the younger the sediments, the higher the accuracy of using heavy mineral for interpreting sediment sources (Yang et al. 2013). In addition, the hydrodynamic can affect the heavy mineral properties. Because there are some drawbacks of using the heavy mineral combination for provenance interpretation, it is important to also analyze the composition of the unstable heavy mineral. To some extent, the unstable mineral is more important to determine the sediment source (Shi et al. 2009). With the application of electronic probe, some scholars use the geochemical differentiation of the single mineral (such as pyroxene, hornblende, tourmaline, zircon, garnet, etc.) to distinguish the sediment source (Sabeen et al. 2002; Morton et al. 2004). For example, the electron probe analysis of garnet has its unique superiority for provenance

interpretation, which can minimize the influence of hydrodynamics or diagenesis (Yang and Zhao 1996).

3. Element geochemical methods

Element geochemistry has been an effective approach for studying areas of complex tectonic setting (He et al. 2005), and has been widely used by scholars both in China and abroad (Yang et al. 2013), including constant elements, characteristic element and their ratio method, trace elements (including rare-earth elements) method. Some elements of the parent rock are not easily removed during the process of weathering, erosion, transportation, deposition, and diagenesis. As a result, these elements can entirely be transferred to the siliciclastic sedimentary rocks and can be used to trace sediment source, such as Th, Sc, Al, Co, Zr and Hf, Ga, Nb, Ti, rare-earth elements (REE), etc. Especially, the REE is widely used in tracing sediment sources because of its special geochemical properties (Yang et al. 1999).

The environmental and source information preserved in the sediments (rock) can be extracted by many kinds of element geochemical method to trace sediment source, such as through the study of element composition, combination, relative content, distribution rule, the relationship between the ratio, and the multiple parameter diagrams, distribution patterns, as well as the relationship between the element and isotope (Yang et al. 2013).

Some certain characteristic elements in the sediments are relatively chemically stable and are mainly influenced by the source and are relatively independent of the depositional environment and diagenesis. In the process of weathering denudation, transportation, deposition, and diagenesis, the composition of these characteristic elements remains the same and can be used to correlate between rocks in the basin and in the source area (Bhatia 1983). By means of characteristic element method, the sediment source can be discriminated, which can effectively avoid the influence of hydrodynamics sorting, mineral composition, and other factors, and highlight the source information (Yang et al. 1999; Jiang and Li 2002). Such research has achieved a considerable effect in the past two decades. However, most characteristic elements are affected by diagenesis, resulting in ambiguous provenance interpretation. Some characteristic elements are characterized by the same chemical properties, a strong correlation between each other, and enrichment in the sedimentary rock. The ratio between these characteristic elements can thus be used to trace sediment source and effectively avoid the influence of diagenesis, making a more accurate judgment of sediment provenance direction (Cao et al. 2007). Cao et al. (2007) utilize ten characteristic elements, including Ni/Co, V/Co, Mg, Mn, Mn/Sr, Ba/Mn, Fe, K, Mg/Ca, Ba/Sr, Mg/Al, Al/Na element ratios to analyze the sediment sources of the Well 58 in the Dongying depression.

In recent years, some scholars have also used electronic probe, laser ablation, and other instruments to measure the constant elements in heavy minerals and quartz particles. According to mineral composition and relative content of trace element, element combination, a multivariate diagram, and distribution patterns can be established to discriminate tectonic background, sediment source, and depositional environment (Bhatia and Crook 1986; Čopjaková et al. 2005). In addition, under the condition of the non-recrystallization, the oxygen isotope ratio ($\delta^{18}$O) in quartz would not change in the process of transportation, deposition, and diagenesis and preserve the rock formation environment (Clayton et al. 1978). Therefore, the $\delta^{18}$O in the quartz can be used to explore the formation environment of quartz, tracking provenance, and the characteristics of the parent rock (Aléon et al. 2002).

4. Geophysical methods

The application of geophysics in the analysis of sediment sources mainly includes well logging and seismic stratigraphy (Yang et al. 2013).

The well logging method mainly utilizes the fractal dimension of natural gamma curve, and the diplog to determine the direction of the sediment source (Li and Wang 1995; Li et al. 2009a, b). Seismic stratigraphy can be also used to determine the provenance and paleocurrent direction in the case study (Jiang et al. 2005). For example, Huang et al. (2009) use the seismic reflection feature to draw the direction of progradation and recover the sediment source system for the Paleogene Sha-3 Formation in the Beitang Depression.

### 2.2.3.2 Calculation of Denudation

The sediment supply area of the sedimentary system can be inferred from the region beyond the distribution range of a certain stratum, and generally, the denudation area is the sediment source area (Zhang et al. 2002). In order to achieve quantitative reservoir prediction, it is necessary to calculate the denudation amount of the source area in a certain geological period (Xu 2013).

1. Geological method

(1) Mass balance method

Hay et al. (1989) believed that in a certain time interval, the amount of eroded sediments caused by tectonics and erosion should be equal to the total amount of deposition. Considering isostatic correction, decompaction correction, sea-level correction, thermal subsidence correction, the sediment eroded from source area can be recalculated from the

sediment deposited in the basin and thus can reconstruct the paleogeography. Based on this theory, Métivier et al. (1999) also considered the influence of tectonic uplift on sediment erosion and suggested there is a balance between the sediment accumulation and sediment erosion caused by tectonic uplift and built a more reasonable paleogeography reconstruction method.

Métivier et al. (1999) believed that the material eroded away from the mountains can be entirely transported and deposited in the corresponding basin when the whole source to sink system is closed. The sediment accumulated in the basin has a much higher preservation potential than that of orogenic belt. Therefore, the study of total sediment amount and average depositional rate in the sedimentary basin can help to recover the evolution of orogenic belt (Xiang and Wang 2001).

(2) Sedimentation rate method

If time interval of the erosional or unconformity surface (including the depositional time of the eroded interval and time for this interval eroded), the interval eroded, as well as the sedimentation rate of eroded interval, and the absolute age of the strata bounded the unconformity surface can be obtained, then the thickness of eroded sedimentary strata can be calculated. To calculate the eroded strata, it is necessary to make a judgment that whether the rate of denudation is equal to the rate of deposition of the strata below the unconformity, or the depositional rate of the strata above the unconformity. When making this judgment, the tectonic movement of the study area should be taken into account (Liu et al. 1995; Zhang et al. 2000).

(3) Formation correlation method

We can use the principle of diminishing thickness or other extrapolation to compare the eroded strata of an area with the uneroded layer in the adjacent area and obtain the thickness of the eroded strata. The method is applicable to the region with a high degree of research, and the uneroded area mentioned here is only a relative concept. Therefore, the calculated thickness of eroded strata is usually less than the truly eroded thickness (Liu et al. 1995; Zhang et al. 2000).

(4) Thickness trend method

According to the detailed interpretation of the seismic section, the unconformity surface and the residual top surface of the eroded strata can be determined. The strata below the erosional surface are eroded away. When the residual top surface of the eroded strata can be determined, the eroded strata can be recovered (Yang et al. 2006; Liang et al. 2009).

(5) Wave analysis method

The sedimentary cycle or sedimentary rhythm we observed, which is closed to a period but not behave exactly periodical, is actually a stacking of several cyclic strata (Liu et al. 1995). Wave analysis method is mainly based on the depositional–erosional process and using the paleontology and isotopic age to determine the sedimentation rate. Then, the mathematical method is used to build the wave equation of depositional rate to obtain the amount of eroded strata and predict the depositional–erosional process of the missed strata (Liu et al. 1995; Jin et al. 1996; Zhang et al. 2000).

As shown by the depositional–erosional process balance analysis (Fig. 2.13), the histogram of the diagonal line in the graph is the deposition rate of a measured section. Because the depositional thickness is the integral of time and sedimentation rate (the area of histogram in Fig. 2.13), the entire area of the curve X is equal to the thickness of the sedimentary strata.

In geologic time 1 and 2, sedimentary rocks are deposited more than the modern observation, but some parts of sedimentary rocks have been eroded during the geological time 3. At the time of geological time 4, new layers of rock were deposited, which were all eroded at the time of geological time 5. In geological time 6, the strata deposited were entirely eroded during geologic time 7. The remaining lower strata were eroded at geological time 8 (Zhang et al. 2001).

The detailed procedure is first to collect geological data of various groups and formation of the study area after obtaining accurate stratigraphic division data. The sedimentary rate of each group and formation can be obtained by dividing the original thickness of each group or formation by the depositional time of each group or formation, and then the deposition rate histogram of each group and formation can be drawn. The mathematical treatment of the histogram of depositional rate can generate a periodic curve. Based on the method of moving average, the depositional–erosional processes in the basin can be described and the erosional rate of different geological periods can be also calculated (Liu et al. 1995; Jin et al. 1996; Zhang et al. 2000, 2001).

2. Geochemical methods

(1) Vitrinite reflectance method

According to the intermittent or jump of the organic matter thermal evolution curve that is determined by the reflectivity of the vitrinite, the existence of unconformity can be determined and the erosional thickness of the strata can be calculated (Wang et al. 2005). Under normal circumstances, vitrinite reflectance $R_o$ is a function of depth x. For continuous sedimentary strata, the vitrinite reflectance has a logarithmic relationship with depth, while in the semi-log rectangular coordinate system, the vitrinite reflectance has a linear relationship with depth. Based on the vitrinite maturity trend line of the residual strata under the unconformity surface, the trend line can be extended to minimum $R_o$ near paleo-surface (currently it is generally accepted that the $R_o$ minimum value is 0.18–0.20% near the surface), which is around 0.20%. The difference between the current unconformity depth and the depth represented by Ro is the thickness of strata eroded (Wang et al. 2005) (Fig. 2.14).



**Fig. 2.13** Equilibrium profile of depositional–erosional process (from Zhang et al. 2001)
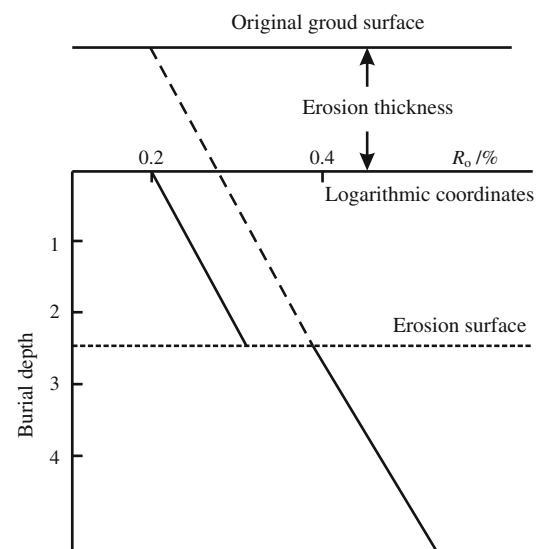


**Fig. 2.14** Principle diagram showing how to use vitrinite reflectance to restore erosion thickness (from Wang et al. 2005)

(2)   Apatite fission track analysis method

Apatite fission track analysis is a new method to recover the heat history of sedimentary basins in recent decades. Apatite fission track analysis of the sedimentary rocks provides not only a formation through maximum paleo-geothermal, but also gives the change of temperature in the geological history, which can give the amount and timing of tectonic uplift. Therefore, through the apatite fission track analysis, in addition to getting information about the thermal history of sedimentary basins, some scholars have also used to determine the formation of the uplift time, denudation rate, and denudation amount in recent years (Wang and Jin 1999).

The application of apatite fission track for restoring paleo-temperature and the amount of strata denudation caused by tectonic uplift is based on the path of spontaneous fission induced by $^{238}U$, which is subjected to heating and annealing behavior based on the principle of chemical dynamics (Wang and Jin 1999).

Basically, according to the fission track age, average fission track length, and fission track length distribution pattern, we can determine the thermal history evolution of the sampled interval and calculate maximum buried depth and paleo-geothermal of the minimum depth and finally calculate eroded thickness (Wang and Jin 1999).

In the process of practical calculation, the most effective method is to combine burial history, geothermal evolution history of strata with the fission track annealing simulation to reveal the amount of strata denudation caused by tectonic uplift, as well as the starting and ending time of the tectonic uplift and erosional processes (Wang and Jin 1999).

(3)   The cosmogenic nuclide analysis

The method of geochronology of cosmogenic nuclide refers to the method of isotopic dating based on the accumulation of certain nuclides and the generation rate of nuclides in the cosmic rays. The cosmogenic nuclide is the radionuclide (Lal and Peters 1967) produced by the nucleus of minerals in the rocks of the earth's surface and its nearby rocks receiving cosmic ray bombardment. When cosmic rays penetrate through the earth's surface into the inside of rock, the nuclear reaction, and ionization loss will occur. Meanwhile, the energy of cosmic rays decreases with the increase of the depth to the surface, which leads to the decrease of nuclide production rate with the increase of depth (Li et al. 2004a, b). Long time exposure or slow erosion rate leads to the cosmic radiation of earth surface for a long time, causing the mineral particles containing a high accumulation of cosmogenic nuclides (Wang and Jin 1999).

In the case of stable denudation rate, the erosional rate of E (cm/a) is inversely proportional to the concentration of N (atomic/g) of the stable cosmogenic nuclide in the rock surface.

$$E = P_0 \Lambda / N \qquad (2.13)$$

$P_0$ is the production rate of surface nuclides (atomic/g a.), $\Lambda$ refers to the free path length of nuclear reaction particles in the rock. The E obtained from Eq. 2.13 represents the average erosional rate for the presently exposed outcrop rock to be elevated to the earth surface. N must be the sum of the cosmogenic nuclide caused by this process of the erosion.

This method is generally used to recover and determine the erosional rate and the amount of eroded strata in the recent geological period (Wang and Jin 1999).

(4)   Fluid inclusion method

Applying fluid inclusion method to calculate the thickness of eroded strata is based on the principle that fluid inclusions can record the geothermal and pressure condition in the different geological periods. In the continuous strata, the temperature (or pressure) of the trapped inclusions are generally in good linear relationship with the corresponding values of burial depth. However, in the strata bounded the erosional unconformity surface the temperature or pressure systems are very different and show an obvious jump across the unconformity surface (Liu 2002) (Fig. 2.15a).

When using fluid inclusion method to calculate the thickness of eroded strata, the key points are: (1) select the fluid inclusions that are formed at the same stage; (2) it is necessary to do decompaction correction to obtain true burial depth; (3) obtain the paleo-surface temperature, which is generally believed that for surface temperature of the strata younger than the Eocene can be replaced with modern temperature.

Therefore, in the depth–temperature coordinate diagram, connect the values of depth and temperate (or pressure) below the unconformity surface into a straight line using regression method and extend the line to the earth surface to get paleo-surface temperature. The elevation corresponding to this temperature is the paleo-earth surface and the distance from the erosional unconformity surface to the paleo-surface is the thickness of eroded strata (Liu 2002; Fig. 2.15b).

(5)   Spore method

The thermal index, transmittance, fluorescence color, and strength data can be used to analyze the thermal history of strata. Due to the optical characteristics of the spore in the

**Fig. 2.15** Correlation between temperature recovered from fluid inclusion and burial depth (from Liu 2002)
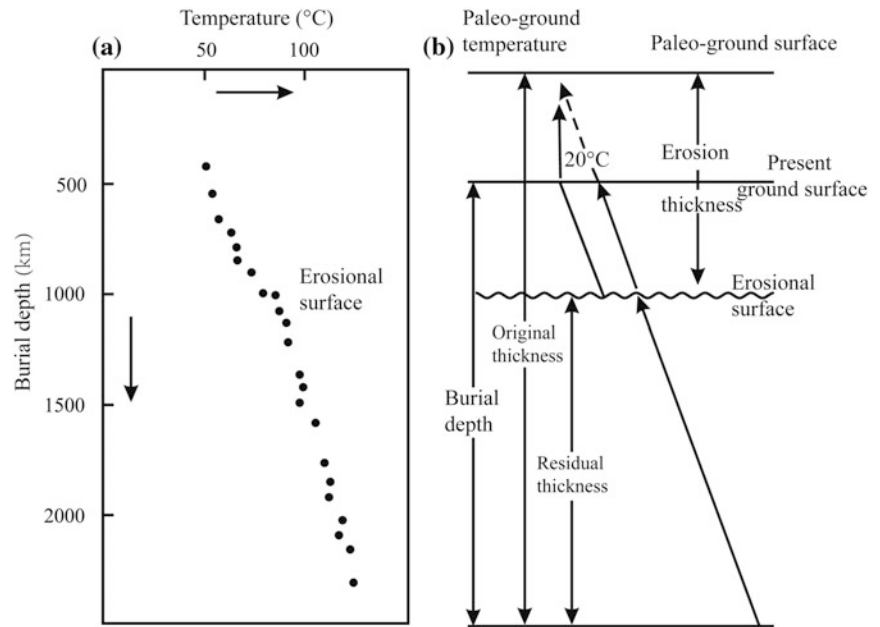
process of thermal change, such as thermal alteration index, light transmittance, fluorescent color, intensity etc., spore can be used to determine the maturity of organic matter. The principle is very similar to the vitrinite reflectance $R_o$ (Li et al. 2004a, b).

(6) Geothermal method

Estimation of the eroded strata thickness can also be obtained from the relationship between time and continuous temperature curve, oil-tested temperature data, fluid inclusion recorded temperature, and vitreous reflectance $R_o$. Under normal conditions, the same region has the same trend of temperature change in the geological history, which the temperature increases with the increase of burial depth. The sedimentary layers formed in different tectonic periods shows a different trend of temperature change, due to the influences of paleoclimate environment, crust thickness, basement burial depth, and basin tectonic evolution. The tectonic activity causes the sedimentary strata to be uplifted and eroded, making it the most significant factor causing either different regions have different temperature trends during the same geological period or the same region has different temperature trends during the different geological periods, while the difference between the measured paleo-geothermal and measured well temperature reflects the different correlation between depth and temperature in different areas.

If the measured temperature of the fluid inclusions gradually increases from the core of quartz to the rim, it records the increase in temperature during the growth of fluid inclusion and the order of the quartz overgrowth. Therefore, according to the abrupt change of geothermal temperature,

the uplifted or eroded elevation of corresponding strata can be estimated, or according to the geothermal change trend, the thickness of eroded strata can be calculated. The gas–liquid inclusions homogenization temperature of the quartz overgrowth and the evolution of vitrinite reflectance $R_o$ analysis can be used to analyze the geothermal temperature, while continuous temperature curve, oil-tested temperature data, high-pressure material temperature data can be used to confirm the measured well temperature. In order to calculate eroded strata thickness, it is necessary to have sufficient geothermal temperature analysis data, which should be accurate and reliable to represent the condition of the main activity period of the tectonic movement (Li et al. 2004a, b).

3. Geophysical methods

In geophysics, acoustic logging data is the main approach to calculate the thickness of erosion (Liu et al. 1999).

When the thickness of eroded strata is large and the burial depth is shallow, acoustic logging data is usually used to estimate the compaction trend of the shale and calculate the size of the eroded strata. (Liu et al. 2000). The basic principle is based on that under the condition of the normal compaction, mud porosity decreases exponentially with the increase of buried depth (Liu et al. 1995). In the consolidated strata that are characterized by small pores distributed uniformly, there is a linear correlation between acoustic interval travel time and porosity (Wyllie et al. 1956) and a linear correlation between acoustic transit time and buried depth in a semi-log coordinate system (Wu et al. 2001). If an area has experienced uplift and erosion, the trend line between acoustic interval travel time and buried depth would shift to
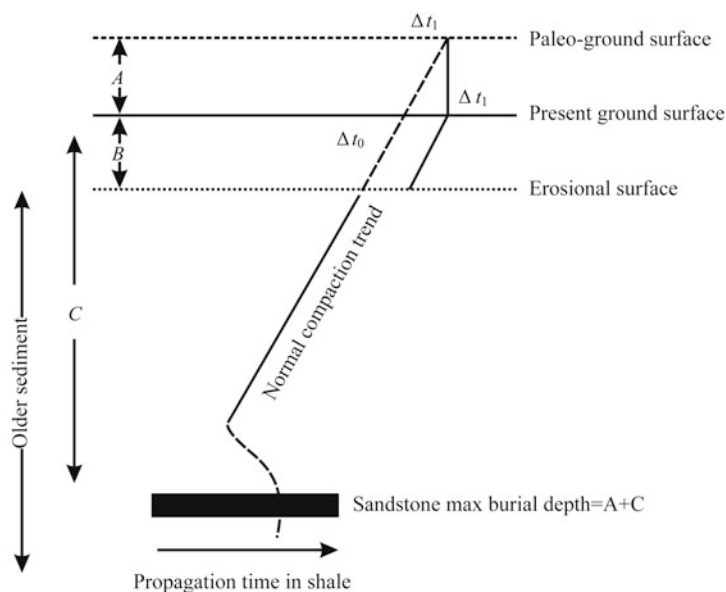
higher compaction degree direction when compared to the strata without erosion. According to the trend of shift, one can extend the compaction trend line to uncompacted point $\Delta t_0$. The height difference between the depth obtained from $\Delta t_0$ point and erosional surface is the thickness of eroded strata (Wu et al. 2001; Wang et al. 2005; Fig. 2.16).

First, carry logarithmic regression on the curve of the acoustic transit time-buried depth of the shale below and above unconformity surface. Two regression equations can be obtained in this step. Then assume the burial depth equal to 0, according to the regression equation for the acoustic transit time-buried depth of the shale above the unconformity surface, the acoustic transit time on the surface $\Delta t_0$ can be calculated. Second, substitute $\Delta t_0$ into the regression equation for the acoustic transit time-buried depth of the shale below the unconformity surface to obtain the depth or height of paleo-ground surface before erosion occurred. Finally, the difference between calculated paleo-ground surface before erosion and the unconformity surface is the thickness of eroded strata (Wu et al. 2001).

Using acoustic logging data to calculate erosional thickness requires the eroded strata to be thicker than the overlying redeposited strata because when the overlying strata are far thicker than the eroded strata thickness, the overlying strata would modify the preestablished compaction trend (Liu et al. 2000).

Recovery of eroded strata thickness, although many methods have been proposed, is not yet mature. When dealing with actual problems, a variety of methods should be used to complement each other to obtain credible erosional thickness.

## 2.3 Basin

This section discusses the influences of sedimentary basin on the sedimentary process in the lacustrine basin. The lacustrine basin is the prerequisite topography for forming a lake, while water is the essential material for lake formation. Generally speaking, lakes are relatively smaller and shallower relative to the ocean, and lake water flow circulation is more restricted. Therefore, the regional climatic conditions have a more influential effect on the lake than the ocean. For example, the changes in climate (e.g., dry or wet; cool or hot) could cause the changes in weathering rate of parent rock, weather product, water flow rate, sediment concentration, evaporation of the lake, and the change of the lake level. Consequently, the above-mentioned changes also cause the change of lake hydrodynamic and geochemical conditions, which result in different distribution patterns, thickness, lithology, and facies of lacustrine sediment, and the types of organic matter. In addition, global sea-level changes will also affect the nature of lakes when there is a link between nearshore lakes and oceans. To sum up, regional tectonic, terrain, climate, and provenance have more influential control on lacustrine sedimentary environment and sediment than the ocean. Among these factors, tectonism and climate are the dominant factors controlling the shape of lake and the geochemical conditions of water bodies. The tectonics usually controls the size, shape, and topography of the lake, while the climate controls the water level and geochemical conditions of the lake. In different geotectonic regions, climatic zones, geographical and source regions, lacustrine deposits are quite different.

### 2.3.1 Basic Characteristics of the Basin

#### 2.3.1.1 Physical Characteristics

The lake is usually pale blue, blue, yellow, or tan colored. The color of the lake is affected by the amount of sediment, the size of sediment particles, the types of plankton, and the number of them. Generally speaking, the lake is usually pale blue or blue under the condition of a small concentration of sand, fine sediment grain size, and less plankton. Otherwise, the lake shows yellow or tan color.

The hydrodynamic conditions of the lake are similar to that of the sea. There are also waves and currents in the lake. From the lakeshore to the lake, the hydrodynamic strength gradually decreases, and the sediment is accordingly distributed from the coarse-grained to fine-grained lithologic lithofacies. The larger the lacustrine basin, the greater the similarity to the marine basin, especially the shallow sea, which does not have significant tidal activity. However, generally speaking, the water bodies of lakes are much smaller than oceans and the lakes are characterized by no tidal activity and much weaker waves and currents strength. The lakes are greatly influenced by external factors such as climate, rivers, etc. Therefore, the water movement of lakes is very complicated. Wind, water, atmospheric heating, differential pressure, and gravity can all induce different reactions and movements in the lake. The waves and currents are the most dominant hydrodynamic factors affecting lacustrine deposits.

In a lake, the siliciclastic materials carried by river bed-loading or suspension are controlled by the hydrodynamic characteristics of the lake. From the perspective of sedimentary hydrodynamics, in the areas of above normal wave base and away from the estuary, the sediments are affected by wave transportation and erosion, especially in large lakes. While in the areas below the normal wave base are dominated by sediment deposition. When the slope angle is higher enough (greater than 5°), the soft sediments begin to move along the slope and transforms into gravity flow. Similar to the sediment gravity flow from the sediment collapse of the delta front, they are deposited in the bottom or plain areas of the deep lakes.

The stratification of water is an important feature of the lake system. The water (freshwater) density reach its highest point at a temperature of 4 °C. The surface water temperature changes with the change of season, which results in the stratified density in the lake. In the summer, the upper lake water body is called epilimnion, whereas the lower cooler and denser lake water body is called hypolimnion. These two parts of water bodies are separated by thermocline (or middle level of the lake). This temperature distribution is called a positive temperature distribution. In the winter, when the lake temperature is below 4 °C, the water temperature increases with the increase in depth, then this temperature distribution is called inversed temperature distribution.

These two opposite stratifications of water bodies in vertical alternate in spring and autumn, which cause exchange of waters in epilimnion and hypolimnion and form backwater phenomenon. Such phenomenon usually occurs in cold-temperate zone lakes, which is also known as dual cycle lake. In addition, according to the temperature stratification conditions, there is noncircular lake (amictic lake), cold single-cycle lake (lake water temperature is always less than 4 °C; lake water only circulates during summer season; usually found in cold- and high-altitude area), warm single-cycle lake (lake temperature never falls below 4 °C and such lake is usually found the temperate and subtropical zone, which is affected by the oceanic climate region), multi-cycle lake (lake water circulates frequently and such lake is usually found in areas of wind changes rapidly, big daily temperature differences and the small seasonal temperature differences, less circulation lake (temperature is much higher than 4 °C, generally appear in the tropics area with irregular and rare water circulation). Temperature stratification is evident in deeper lakes, but not in shallow lakes. In a large lake, the surface epilimnion in the lake is full of oxygen due to continuous water circulation, while the lower layer is the anoxic hypolimnion layer. Rivers bring nutrients like phosphate and nitrates into lakes and accelerate the growth of life in the upper water layers in the lake. The precipitation of these suspended organics leads to hypoxia of the lower layer and forms a nutrient environment that most organisms cannot live in, which is most evident in the tropics.

The stratification of the lake can influence the depositional process. When rivers flow into the stratified lakes, according to the relative scale of river water density and lake water density, there are three situations which can happen: (1) When the river water density is lighter than the density of upper part of lake water, in this case, the rivers are displayed as plume flow on the lake water surface to disperse sediment into the basin; (2) When the river water density is between the lower and upper lake water, the coarse-grained clasts are deposited in the wide areas of lake bottom, while the fine-grained clasts are suspended in the thermocline zone and form seasonal lamination when the lake water exchanges with the changes of season; (3) When the salty or cold water bring sediments into basin, it usually generates bottom flow, which can carry mixed sediment into deepwater basin as a semi-continuous turbidity; (4) When the density of injected water is equal to lake water density, the rapid mixing of two water media in three dimensions cause bed-loading sediment to be deposited quickly in local and suspended sediment deposited not away from shoreline, which is beneficial to the growth of the delta.

Regional tectonism, terrain, climate, and provenance have more influential control on lacustrine sedimentary environment and sediment accumulation than the ocean. Among these factors, tectonic and climate are the dominant factors controlling the shape of the lake and the geochemical conditions of water bodies. The tectonics usually controls the size, shape, and topography of the lake, while the climate controls the water level and geochemical conditions of the lake. In different geotectonic regions, climatic zones, geographical and source regions, lacustrine deposits are quite different.

### 2.3.1.2  Chemical Characteristics and Effects

The chemical composition of the lake is roughly the same, but the contents of the chemical elements can vary greatly from time to time or from areas to areas. The salinity of lake water varies greatly, from less than 1‰ to more than 25‰, which is significantly different from seawater, which is generally 35‰. The changes of salinity of the lake can directly reflect the chemical type of the lake, and can indirectly reflect the environmental conditions of the accumulation or dilution of the lake's salts. The main factors that determine the salinity of the lake are climate and watershed geochemical characteristics. The salinity of the lake in an arid climate is generally higher than that in a humid climate. At the same time, the hydrodynamic conditions and biological process have greatly influenced the plane distribution of lake salinity. The lake currents, wave hydrodynamic prompted the lake salinity uniformly distributed, especially when the lake is shallow and broad, the salinity of lake is distributed more evenly. In addition, lakes receive waters from different source regions, and thus the chemical composition of the lake has varied greatly. The geochemical characteristics of the lake partly reflect the changes in the climatic conditions in the basin and changes in source materials properties in the source area.

The salinity in the profile of the lake water is usually unevenly distributed and displayed in stratification. Due to evaporation and increased salinity brine supply, a density difference is induced to form a halocline to separate the surface water of low salinity and bottom water of high salinity, which is called chemical stratification of lake water.

The chemical stratification of lake water can promote the stratification of salinity.

The stable isotopes and rare elements of lake sediments are different from the sea. The ratio of $^{18}O/^{16}O$ and $^{13}C/^{12}C$ in the lake are lower than that in the marine environment. The ratio of sulfur isotope of marine-generated hydrocarbon is stable, while this ratio in lacustrine-generated hydrocarbon varies greatly. Trace elements in freshwater lake, including B, Li, F, and Sr, are less than that of ocean. The Sr/Ba ratio is less than 1 in a freshwater lake.

The dissolved substance may be displayed in forms of colloidal solution or true solution. Therefore, the chemical sedimentation in the lake basin can be divided into colloidal condensation and chemical sedimentation of the true solution (Table 2.3). The oxide of aluminum, iron, manganese, and silicon is difficult to dissolve in water and is often carried in colloidal solution. Colloidal solution will lose stability under certain conditions, which will promote the colloidal particles condensed into larger particles and further condensed into floc. These flocs will gradually deposit under the influence of neutrality. This process is called coagulation or flocculation. Colloidal condensation can form clay minerals, phosphate minerals, bauxite, iron ore, and manganese ore. Chlorine, sulfur, calcium, sodium, magnesium, and potassium are dissolved in water and are carried in a true solution state. Their transportation and deposition are affected by solubility, pH, redox potential (Eh), temperature, pressure, and other factors. The precipitation sequence is generally followed by carbonate, sulfate, and chloride.

### 2.3.1.3  Biological Characteristics and Effects

The seemingly placid surface of the lake contains complex biological effects. Rivers can feed large amounts of nutrients into lakes, which are consumed by a variety of biological communities. Sunlight provides an opportunity for the creatures at the bottom of the food chain (mainly algae) to perform photosynthesis. Therefore, lake water and sediment provide biotic community a suitable living environment and rich inorganic and organic matter. According to different water salinities, the lake can either develop freshwater biota or develop brackish water and salty water biota (Benthos such as Gastropod and Lambranchia) as well as Ostracoda,

**Table 2.3** Chemical deposition and biodeposition

| Chemical sedimentation | Biological sedimentation |
| --- | --- |
| Product: | Product: |
| Polymerization-induced colloid aggregation: | Kerogen |
| Iron–manganese–aluminum and other sedimentary deposits | Stromatolite |
| True solution chemical deposits: | Bioclastic limestone |
| Sinter | Biophosphorus nodal limestone |
| Gypsum rock | Diatomite |
| Carbonate | Chalk |
| … | … |

Conchostraca, fish, and other plankton and swimming creatures. In addition, lower plant (e.g., algae) and aquatic higher plant are commonly found.

Bacteria in the lake also plays an important role in biological effects. For example, when bacteria decompose the organic materials of plankton and advanced organisms, they consume a considerable amount of dissolved oxygen, which in turn affects the biochemical cycle in the lake. Oil production depends primarily on the massive production of organic matter from all kinds of organisms. For the lacustrine basin, apart from the organic matter in the sediments derived from the residual body of terrestrial plants, the majority of organic matters are produced and enriched by the aquatic organisms in the basin.

Organisms can participate in sedimentation (Table 2.3), which is shown as follows: (1) direct deposition of biological remains. In the course of life, on the one hand, creatures can form organic matter by photosynthesis or absorption of nutrients. On the other hand, creatures can absorb calcium, phosphorus, silicon, and other inorganic minerals to form shells and bones by biological secretion. Bioclastic sand, bioclastic limestone, biophosphorous nodal limestone, diatomite, chalk, and reef limestone are the products of the direct deposition of biological remnant or remains. (2) Biochemical sedimentation. The process of biological life or the decomposition of a biological body will produce large amounts of gases such as $H_2S$, $NH_3$, $CH_4$, $CO_2$ or absorb a large number of $O_2$ gas, which can cause the change of physical and chemical conditions and prompt some dissolved substances precipitated. For example, the photosynthesis of algae is by absorbing $CO_2$ to causes the lake's pH to rise, which in turn leads to the precipitation of $CaCO_3$. The biochemical sedimentation can be also displayed by the adsorption of organic matter to precipitate certain elements. For example, in coal and black shale, the accumulation of various metal elements is related to adsorption of organic matter during sedimentation. (3) Biophysical sedimentation. This process is displayed by that the materials are captured, bonded, and cemented by the biophysical activity. The stromatolite in the lake is a typical representative of biophysical sedimentation.

## 2.3.2  The Influence of Paleogeomorphology on Sedimentation and Its Research Method

### 2.3.2.1  The Influence of Paleogeomorphology on Development of Sand Bodies

The research contents of the lacustrine basin include the geomorphological features of the basin (including the macroscopic and microscopic geomorphologies), the basin water depth and the tectonic movement of the basin. These characteristics of the basin play an important role in the development of sand body.

Paleogeomorphology refers to the fluctuations and changes of the original topography of the basement, including the macroscopic paleogeomorphology and the microscopic paleogeomorphology (Shuai 2010). Macroscopic paleogeomorphology refers to the original terrain's ups and downs and changes in basin scale (Wang et al. 2012), which controls the sediment erosion, transportation, deposition, and the development of provenance system and depositional system. Microscopic paleogeomorphology refers to the fluctuations and changes of local topography, mainly in the form of shoreline and topographic relief of local topography (Wang et al. 2012). The influence of microscopic paleogeomorphology on sediment deposition is mainly reflected by that it can control the specific geographic location for sediment unloading and accumulation. The transition zone between the paleogeomorphology highs and lows are usually the areas of reduced hydrodynamic energy and sediment unloading. The influence of macroscopic and microscopic paleogeomorphology on the sediment deposition is mainly reflected in the following:

(1) Macroscopic paleogeomorphology determines the distribution and development of the provenance and depositional system. Taking the lacustrine lake basin as an example, the lacustrine basin can be divided into the rift lacustrine basin and depression lacustrine basin. The basin margin of the rift basin can be classified into the steep slope and gentle slope, which has different genetic types and distribution range of the sand body.

Steep slope belt near mountain cliffs is controlled by the development of basin margin fault systems and is characterized by large lake water depth gradient. The major types of sedimentary facies developed in steep slope are coarse-grained fan delta, nearshore subaqueous fan, and its associated deepwater gravity flow, which are distributed near shoreline and on a steep slope and characterized by quick facies changes and narrow facies belt. While in gentle slope belt, due to the wide and shallow environment, small short axis delta or linearly distributed alluvial fan are the major sedimentary facies and are subjected to the rework of currents and waves to finally form beach bars. Soreghan and Cohen (1996) studied the Tanganyika Rift basin in East Africa and divided basin margin into four different facies belts, according to the macroscopic paleogeomorphology of the basin, with each of them characterized by different sedimentary processes.

Generally, depression basin is developed in the later stage of rifting and thus has a relatively weak tectonic activity and

is characterized by disk shape. The central part of depression is relatively flat and the topography raised gradually toward basin margin, which is very similar to the gentle slope of rift basin. In the long axis of depression, the basin is usually developed in large constructive deltas, while in the short axis of depression the basin is usually associated with small-scale fan delta and delta (Jiang and Liu 2010).

(2) The microscopic paleogeomorphology can be displayed by the local topographic relief. Wang et al. (2011) divided the microscopic paleogeomorphology into three categories based on previous research, as follows:

Positive unit: further divided into high point, paleo-ridge, and fault nose;
Negative units: further divided into syncline, trench, and sag;
Slope units: further divided into gentle slope, terrace and steep slope.

Different microscopic paleogeomorphology has different controlling effects on the formation of beach bars.

Similar to the convex bank, the paleo-terrain high in the shallow water area also has the ability to converge wave energy and reduce it rapidly, favoring sediment sorting and accumulation. When the terrigenous detrital material carried by waves and longshore currents spread towards positive topographic unit, the energy of waves and longshore currents are consumed gradually, which causes sediments easily unloading in the transition zone between high and low topography. For example, beach bars are usually developed around positive topographic high, such as paleo-subaqueous high. Therefore, microscopic geomorphology in shallow lake area is an important controlling factor on the beach bar distribution in plane. In the broad and flat topography, thin beds of beach sands are widely distributed and surround the bar sands (Fig. 2.10), while in the areas of relief changes and rising slope angle, thick beds of bar sands are restrictedly distributed around the topographic highs.

(3) The microscopic paleogeomorphology can also determine the location and shape of shoreline, which in turn can influence the distribution of various sand bodies on the shore (Fig. 2.17). For example, the locations of beach bars and delta front sand bodies were controlled by the paleo-shoreline and would migrate with the changes of paleo-shoreline. The sand bodies distribution is followed the lake shoreline trajectory and surround the lake as a ring (Li et al. 2009a, b).

Different shoreline morphologies play different roles in controlling sediment deposition and distribution on shore. In a relatively flat shoreline of the coastal-shallow lake, the wind is nearly perpendicular to the shoreline, and the thus the hydrodynamics of the wave is also parallel to the shoreline. The sand body of beach bars formed under such hydrodynamic control is basically parallel to the coastline. For example, the beach bar system in Zhoushan Putuo island is typically parallel to the coastline (Zhu et al. 1988).

For the basins with the curved shoreline, some areas of the basin margin are characterized by concave bay, while some areas are characterized by cape. The water depth of the concave lake bay is larger than the bounded convex bank and waves are easily deflected when spreading toward the concave shoreline. As mentioned before, the deflected waves can cause the dispersion or concentration of waves. This phenomenon can lead to gather of waves energy around the convex bank, resulting in convex bank to be high-energy area to rework sediments into coarse-grained beach bar deposits, while this deflection can lead to reduced wave energy in lake bay, resulting fine-grained sediments deposited there.

In addition, the changes of geomorphology and shoreline can induce waves to be deflected (Fig. 2.7), which generates the longshore currents that are nearly parallel to the shoreline. When the sediments are eroded and carried by longshore currents pass through the above-mentioned concave lake bays (Zhu et al. 1994) or delta front area (Cao et al. 2009), due to the topography changes from convex to concave, the energy of waves and longshore currents are consumed. Consequently, the carried sediments are unloaded in these areas and form linear sand spit by longshore currents in the downstream direction of convex bank.

### 2.3.2.2  Recovery of Paleogeomorphology

Paleogeomorphology is one of the key factors to control the development of depositional systems. The study of paleogeomorphology helps to reveal the characteristics of the source system, depositional system, and its spatial
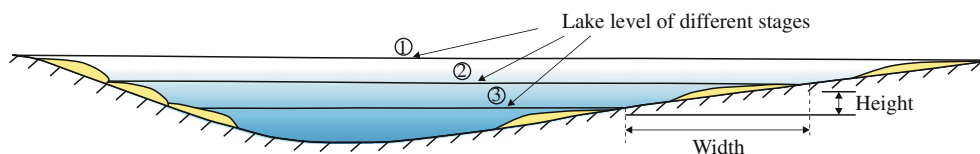


**Fig. 2.17** Schematic diagram of the relationship between the migration of shoreline and the distribution of sand body in the depression lake basin (from Li et al. 2009a, b)

configuration. The recovery of paleogeomorphology is a comprehensive subject, which is also a hot topic but difficult problem in the field of oil and gas exploration. The current research is mostly in the qualitative stage. The residual thickness and compensating thickness impression method and the back stripping and filling methods are the common methods and theoretical basis for recovery of paleogeomorphology. However, because these methods do not take into account many geological factors (e.g., different rocks have different degrees of compaction, etc.), many problems existed in these methods resulting in big errors in recovery of paleogeomorphology.

Currently, the paleogeomorphology recovery method is gradually developing in the comprehensive and quantitative direction and the accuracy of recovery also keeps improving. Jiang et al. (2009) based on previous research and proposed a combined tectonics-sedimentary method to recover paleogeomorphology. This method is based on various data, including: (1) seismic data that can be traced throughout the entire study area and thus not be limited by the density of the drilling, which makes it easy to carry structural correction; (2) drilling data that record sedimentary history, which can be used to carry decompaction and paleo-water depth recovery; (3) basic geological map, such as paleogeography map before deposition, tectonic map, sedimentary strata isopach map, sandstone isopach map, and so on. All these data are then combined with genetic facies analysis, paleo-currents analysis, and erosion thickness calculation to comprehensively recover the paleogeomorphology, based on residual thickness and compensating thickness impression method and the back stripping and filling method.

The detailed procedures can be explained as followings. First, seismic, logging and drilling data can be used to study the sequence stratigraphy, and establish the isochronism of the stratigraphic framework for the purpose of ensuring the stratigraphic interval are isochronous. These data are then used to draw residue thickness map and calibrate the apparent thickness. Second, utilize the basin simulation software to simulate the basin burial history and carry strata decompaction. Third, combined with seismic data to make the equilibrium profile (if the study area has experienced erosion, erosion thickness recovery should be also performed) and comprehensively analyze characteristics of paleogeomorphology (Gui 2008; Jiang et al. 2009; Jiang 2010a). Finally, the paleo-water depth data obtained by the analysis of the sedimentary facies and paleontology should be used to correct the result to make the recovery of paleogeomorphology more accurate (Fig. 2.18). This process can be realized by basin mode software.

The key techniques used here are erosion thickness recovery, true thickness correction, decompaction, paleodepth correction, and equilibrium profile drawing. In this section, the recovery of erosion thickness is described before and the paleo-water depth recovery will be introduced in the next section. This section focuses on introducing true thickness correction, decompaction, and balanced profile drawing.

(1)  True thickness correction

The sedimentary strata are not always horizontal and could be tilted due to the tectonic movements. In some cases, the drilling well intersects the strata at oblique angles rather than vertically penetrate through the strata. Therefore, the strata thickness read from drilling data (apparent thickness) cannot truly reflect the true strata thickness, which is actually thicker than the true thickness. It is necessary to do true thickness correction before decompaction correction.

The principle and method of the true thickness correction can be found in the references from Gui (2008), Hu (2008) and Jiang et al. (2009) and explained in Figs. 2.19 and 2.20, which can be described briefly as follows:

In Fig. 2.19, t is the true thickness of inclined strata, whereas t′ is the thickness of the strata that is read through drilling data. Apparently, t′ is thicker than t. Assume the angle between t′ and t is α. According to the Pythagorean theorem, the equation can be formatted as

$$t = t' \cos \alpha \qquad (2.14)$$

As indicated by Eq. 2.14 and Fig. 2.19, the true thickness of the strata can be calculated from the apparent thickness of the strata, as long as the angle between t and t′ is obtained.

The way to obtain α is shown in Fig. 2.20. First, choose a fixed point, O, from targeted strata. Second, draw a square with the point, O, as a central point, and select endpoint and middle point of line (8 in total) to represent eight different directions (Fig. 2.20a). Take point A in Fig. 2.20 as an example, assume the angle between line OA and the horizontal line is α′. Then α′ = α (Fig. 2.20b).

Set s is the horizontal distance between point A and O, and Zo and Za are burial depth of point O and A. Then the equation can be described as

$$\alpha = \alpha' = \arctan[(Zo - Za/s)] \qquad (2.15)$$

In this approach, the dip angle of strata in OA direction can be obtained. Similarly, the same calculation can be performed on the other seven points of Fig. 2.20a and in total eight α′ can be obtained. Then choosing the biggest angle α′ to represent the true dip angle of strata at point O. The cos α can be further calculated and substituted into Eq. 2.15. Finally, the true strata thickness of strata can be calculated from the apparent strata thickness t′.

**Fig. 2.18** The technological route to recover paleogeography by using a combined tectonics-sedimentary method (from Jiang et al. 2009)
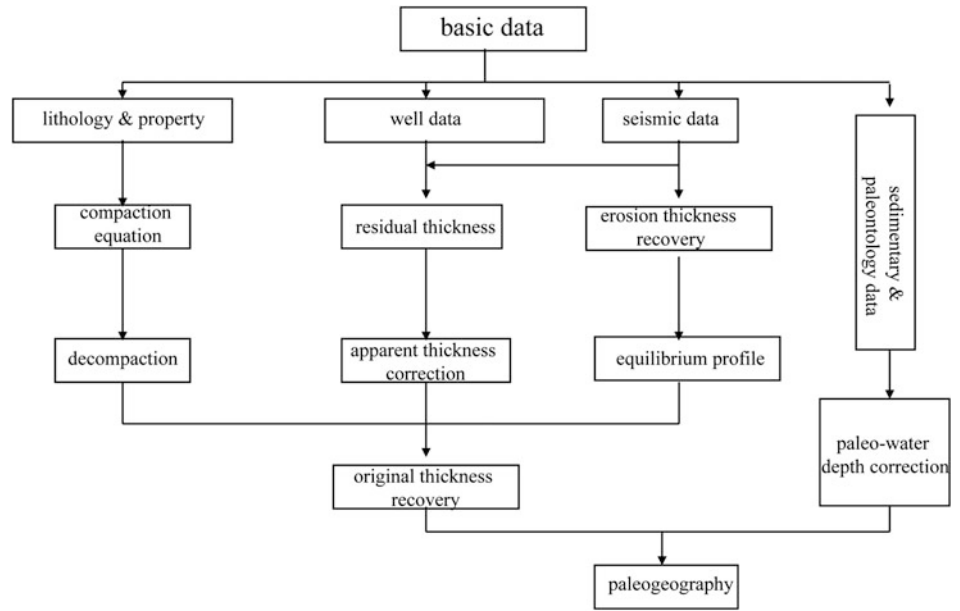


**Fig. 2.19** Principle diagram of true thickness correction (from Hu 2008; Gui 2008)



$$t = t'\cos\alpha$$
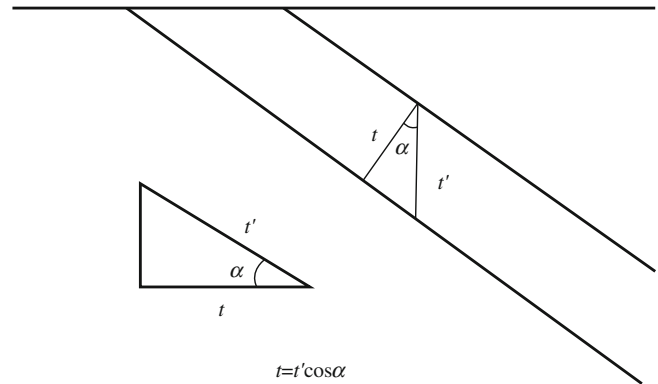
**Fig. 2.20** Schematic diagram showing point distribution of strata in plane view (A) and the approach to obtain α (from Hu 2008; Gui 2008)



$$\alpha = \arctan[(Z_a - Z_o)/d]$$
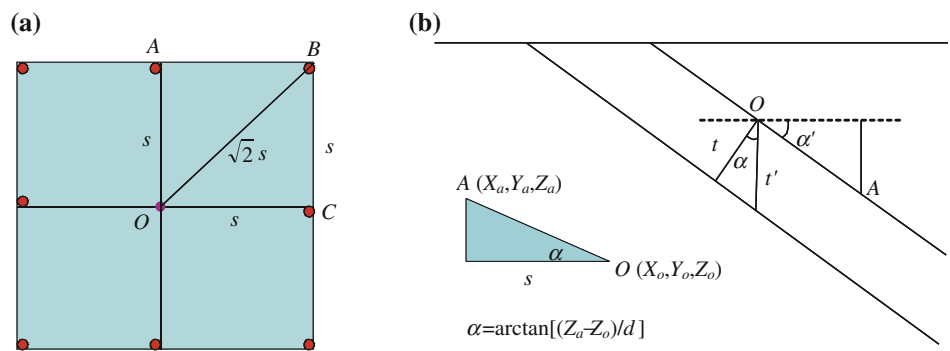
(2)   Decompaction

In the process of sediment burial, under the combined action of gravity and overburden sediment, the porosity of sediments and the thickness of the strata decrease. In the process

of compaction, different lithologies have a different reaction to compaction. The initial porosity of mudstone and siltstone is about 52 and 52%, respectively. Under the impact of compaction, the porosity can be rapidly reduced to below 10%, whereas the strata thickness can be reduced about 40%

in relative to the original thickness of strata. Therefore, it is of great significance to carry decompaction before studying the paleogeomorphology.

Decompaction is built on the several premises. (1) During the process of strata compaction, rock skeleton has always remained the same size. The only change is the reduction of porosity, which is irreversibile. (2) The strata remain the same on the horizontal side, but the thickness of the strata varies with the strata volume, i.e., the change of formation volume is mainly due to the change of strata thickness. (3) The compaction of strata is not reversible, which means the strata thickness is controlled by the maximum buried depth. (4) The depositional rate of the same strata should be same. (5) If there was an erosional event occurred, the missed strata should be eroded in a single event and the erosional rate should be same across the strata. The procedure of decompaction mainly includes two aspects: establishment of compaction equation and the recovery of compaction thickness.

**(1) The establishment of compaction equation**

The porosity of rock decreases with depth and porosity and depth have the following relations:

$$\Phi = \Phi_0 e^{(-C*D)} \qquad (2.16)$$

The $\Phi$ is the modern rock porosity, whereas $\Phi_0$ is the initial porosity of strata during deposition. E is the Napierian base. C is the compacting factor and D is the burial depth.

The compacting factor, C, and initial porosity $\Phi_0$ are both related to lithology (Shi et al. 1998). As long as the porosity of strata in different depth is obtained, the $\Phi - D$ curve can be drawn. The initial porosity $\Phi_0$, compacting factor C, and $\Phi$ for strata of any depth can be obtained by the correlation.

The compacting factor, C, and initial porosity $\Phi_0$ are both related to lithology. Different lithologies have different initial porosities and compaction coefficients. The experiment shows that the compaction coefficient of mudstone is the largest and the sandstone is secondary, and the compaction coefficient of carbonate rock is between the above two. If the strata have more clay content, the strata perform like mudstone, otherwise, the strata perform more like sandstone. Evaporite can be considered as uncompacted (Shi et al. 1998).

**(2) Compaction thickness recovery**

Based on above approaches, basin simulation software can recover the compaction rate and original thickness. To simplify the model and for the convenience of program design, the compaction thickness recovery method has the following premises. First, strata rock skeleton volume remains the same after compaction and thickness loss due to compaction is only derived from the reduction of porosity in rocks. Second, secondary changes occurred in the process of diagenesis are not considered. Third, compaction process is irreversible (Jiang et al. 2009).

On the basis of the above assumptions, according to the model of Jiang et al. (2009), The approach can be described as follows. First, we can assume $D_1$, $D_2$ to represent the depth of the top and bottom of modern strata, respectively. Then we strip the overlying strata, the depth of the top and bottom are $D_1'$ and $D_2'$. The relationship can be displayed in the following equation:

$$\int_{D_1}^{D_2} (1 - \phi(D))dD = \int_{D_1'}^{D_2'} (1 - \phi(D))dD \qquad (2.17)$$

The left and right sides of the equation represent the skeleton height of the unit area before and after the recovery of the strata. The $D_1'$ and $D_2'$ can be obtained by solving this equation. This process can be realized by basin simulation software (Jiang et al. 2009).

**(3) Equilibrium profile drawing**

The balance of profile is a basic geological law. The profile is balanced when the length or area of the strata remain the same before and after deformation. If they are not equal and cannot fully be explained, then the profile is unbalanced. The geological interpretation of an unbalanced profile must be wrong and meaningless, which is the key idea of the equilibrium profile (Liu and Jiang 1995).

There are three main methods to generate profile balance, including forwarding method, restoration method, and inversion method. The detailed explanation of these methods is not discussed here. To ensure the correctness of the equilibrium profile, four principles should be followed:

(1) The principle of area (volume) invariance. the area (two-dimensional space) or volume (three-dimensional space) of the strata is invariable before and after the deformation. Since most tectonic compressions occurred after deposition, strata have been subjected to diagenetic compaction before deformation, so the area (volume) loss caused by tectonic compaction should not be considered. If the density (or porosity) of the same type of rock in the deformed and the undeformed region are the same, the compaction can be neglected.

(2) The principle of rock thickness invariable. When the strata are folded, there is only bedding shear between

different strata. Therefore, in the form of concentric circular fold, the thickness of the rock is the same before and after deformation.

(3) The length of each marker in the profile is consistent. If there is no discontinuity between the strata, the restored original length of strata should be consistent in the same profile. Otherwise, there will be a discontinuity between the long and short layers.

(4) The displacements of bilateral strata along the same fault should be consistent. Otherwise, the inconsistency may be caused by the several reasons. First, the inconsistency might be due to the folding caused by fault propagation. The displacement of fault can be transformed into fold. Because of the conservation of length, the shortening of each layer is inconsistent. Second, when the fault bifurcates, displacement is dispersed to each small fault. Third, the inconsistency can also be caused by slip fold function, of which the mechanism is very similar to folding caused by fault propagation (Liu and Jiang 1995).

An accurate balanced profile can determine the deformation history of a region, which is important to understand the paleogeomorphology of the region in a certain geological period.

(4) Paleowater depth correction

When sediment is deposited, its depositional interface is in a certain depth under water. Thus, the sediment thickness is not representative of its subsidence depth and needs to be calibrated with paleo-water depth data. The paleowater depth can be estimated by comprehensive analysis of sedimentary facies and paleontology assemblage. In recent years, a number of scholars have worked on improving the recovery method of paleowater depth and increased the accuracy of restoration constantly (please see more in Sect. 2.3.3.2). Then, the depth of sediment being deposited can be calculated by adding the obtained paleowater depth to the sediment thickness.

The specific procedures of paleogeomorphological restoration can be also found in the literature of Hu (2008), Gui (2008) and Jiang et al. (2009).

In addition, geomorphological features can be analyzed by the data of Bouguer gravity anomaly. A gravity anomaly is a difference between the observed gravity on a planet's surface and the corresponding value predicted from a model of the planet's gravity field, which can be used to reflect the geological structure and materials of strata (Zeng 2005). A larger gravity anomaly indicates a higher topography, while a smaller gravity anomaly indicates a lower topography. Meanwhile, a dense contour line represents a steep terrain, whereas a sparse contour line terrain shows a gentle terrain.

### 2.3.2.3 Identification of the Paleo-shoreline

The shoreline is the intersection between the lake and the land, which is the dividing line between subaerial and subaqueous deposits (Jiang and Liu 2010). The identification of the paleo-shoreline mainly includes the following methods (please see more details in Jiang and Liu 2010).

1. Sedimentary methods

(1) Special types of rock. The special types rocks developed near the shoreline, including peat, coal seam, evaporite, lake beach rock, and well sorted and rounded sandy-gravelly layers that are oriented along the longshore currents, can all be used to identify paleo-shoreline. For example, there are many lake beach rocks developed near the current shoreline of Qinghai lake, which can be used as an alternative indicator for shoreline position in the evolution of Qinghai Lake (Li et al. 1995).

(2) Sedimentary structures. Sedimentary structures can record the hydrodynamic conditions and sedimentary environment during deposition. The sedimentary structure formed near the shoreline, in turn, records the general position of the paleo-coastline. The swash cross-bedding, wave marker, oxidation strip in mudstone, plant root tracing, mud cracks, exposed structure such as the rain mark, and carbonate karst erosion belt, etc., can all be used as a marker to identify paleo-shorelines.

(3) Sand body type. Various types of sand bodies are developed near the shoreline and can be used to interpret the position of paleo-shoreline. The foreset of delta (or fan delta), linearly distributed gravelly beach, and sand dunes developed near shoreline are good indicators of paleo-shoreline. For example, the boundary between delta plain and front is the location of the shoreline, which can be determined by comprehensive analysis of single well data, well log, and seismic data.

2. Paleontological method

Fossilized remains of the organism and trace fossil that records the activities of organism are markers for identification of paleo-shoreline. (1) Shell beaches are composed of fossils of bivalves and gastropods and are well developed in the beach environment and thus are good markers for recognition of paleo-shoreline. (2) Trace fossils including *Scoyenia* and *Psilonichnus* record the living environment of the organism and can be used to identify shoreline. In addition, the margin of the lake is often enriched of the spore particles of aquatic plants, and thereby it is possible to identify the shoreline of paleo-lake according to the relative enrichment of spore.

Fig. 2.21 Paleo-lake shoreline indicated by the progradation of sedimentary strata (modified from Zhong 2002)
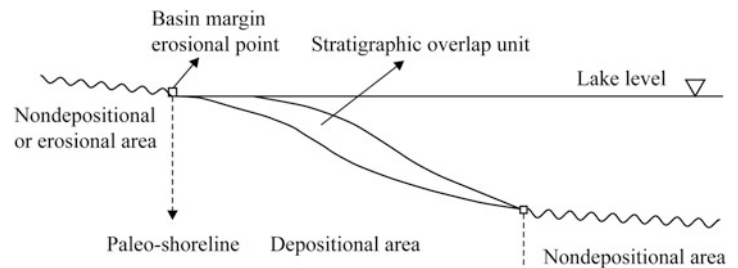


3. Geophysical methods

Seismic is an important data for oil and gas exploration. Paleo-shoreline positions can be interpreted by the seismic line that is in oblique or perpendicular to the shoreline (Fig. 2.21). On seismic reflection data, the onlap termination or lateral termination usually indicates the range of sediment deposition in the lateral direction, which can determine the location of paleo-shoreline. It is important to note that due to the strata near the coast may suffer from erosion or by compaction, it is necessary to correct the slope angle and strata thickness to their original status.

4. Geochemical methods

The special sedimentary environment near shoreline, such as oxidation, reduction, water medium properties, water depth change trend, etc., can be reflected by geochemical information and can be used to indicate the position of paleo-shoreline (Jiang 2003; Jiang and Liu 2010). In addition, in salt-lake sedimentary environment, the trace element content (such as B, Sr, Rb, etc.) or its ratio (such as Sr/Ba, Rb/K) can be used to recover the paleo-salinity and further confirm the position of paleo-shoreline (Han et al. 2007; Zheng et al. 2008).

### 2.3.3 Influence of Paleo-water Depth on Sediment Deposition and Its Research Method

#### 2.3.3.1 Paleo-water Depth and Sand Body Distribution

The depth of water determines the hydrodynamic zone. For example, a lake has four important interfaces, including flood water level, low water level, normal wave base, and storm wave base, which are used to divide lake into nearshore, shallow lake, and deep lake subfacies (Jiang 2010a) (Fig. 1.6). Above the normal wave base, based on the characteristics of wave and their influences on the transportation and deposition of sediments, the littoral subfacies is further divided into the coastal dunes, foreshore, and shoreface. Different water depth ranges correspond to

different sedimentary subenvironments and different depositional processes (Fig. 1.6). For example, the beach bars are mainly developed above the normal wave base, where the hydrodynamics are strong and complicated. Accurately identify the position of normal wave base helps determine the potential development range of the beach bars.

In addition, paleo-water depth is an important controlling factor for the development of carbonate beach bars. If the water depth is too shallow, the accommodation space would be too small to preserve carbonate. While if the water depth is too deep, then due to the relatively weak evaporation of lake water, the production rate of carbonate rock also decreases obviously. Wang (2011) studies the carbonate beach bars in the lower part of fourth member of Eocene Shahejie Formation ($Es_4$) in Dongying Depression and suggested the favorite water depth for development of carbonate is between 3 and 32 m, with the maximum production rate of carbonate occurred in a water depth of 24.5 m.

#### 2.3.3.2 Recovery of Paleo-water Depth

1. Qualitative recovery of paleo-water depth

(1) Paleontological method

Organism lives in a certain environment. Similarly, different water depths are associated with different types of organism. Paleontological method is a commonly used method to recover the paleo-water depth. Some organisms are good water depth markers, such as calcium algae, benthos, planktonic foraminifera, and benthic foraminifera ratio (P/B), coral community, diamoeba, and kelp (marine phase). On the basis of paleontology identification, different depth zones can be divided according to different fossil abundance and their combinations (such as algae) (Zou and Ge 2000).

The diversity of fossil group has a good correspondence with the water depth. According to the modern ecological research, modern Ostracoda is most prosperous near the normal wave base. The diversity of Ostracoda decreases toward both shallow water and deepwater zone. (Li et al. 2005) (Fig. 2.22). Using the information function to quantify the dominance differentiation degree of the Ostracoda group

**Fig. 2.22** The corresponding relationship between the dominance diversity of Ostracoda in Paleogene of Dongying Depression (from Li et al. 2005)
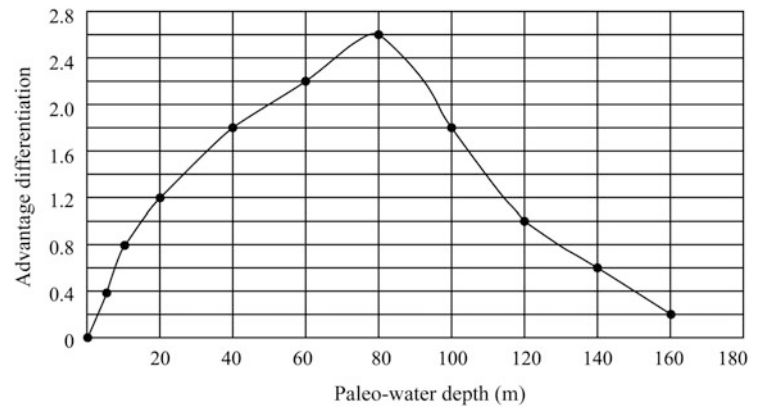


**Table 2.4** The relationship between different ichnofacies and water depth (from Zhang and Ren 2003)

| Ichnofacies | Water depth/m |
|---|---|
| *Skolithos* | 1–2 |
| *Intortusichnus* | 2–10 |
| *Aductusichnus* | 10–17 |
| *Protopaleodictyon* | 17–25 |
| *Paleodictyon* | >30 |

and building its corresponding relationship with depth are effective to confirm the paleo-water depth. Li et al. (2005) used this method to recover the water depth for Es$_3$ in Dongying Depression.

In addition, when the fossilized remains are missed, the trace fossil can be used to determine the relative paleo-water depth. Paleontologists suggested *skolithos* ichnofacies occurred in water depth of 1–2 m, *intortusichnus* occurred in water depth of 2–10 m, *aductusichnus* occurred in water depth of 10–17 m, *protopaleodictyon* occurred in water depth of 17–25 m, and *paleodictyon* occurred in water depth of >30 m (Frey and Howard 1990) (Table 2.4).

(2)  Sedimentary method

The distribution of sediment can determine the relative water depth. In general, from shallow to deepwater the sandy-gravelly content in sediment decreases and the muddy content increases and in deepwater the sediments are nearly all mudstone (except gravity flow deposits) (Zhang and Ren 2003; Kang et al. 2000). Therefore, the distribution of lithofacies in the basin can help qualitatively determine the paleo-water depth (Table 2.5). In addition, the color of mudstone is also a good indicator of the relative depth of the water. For example, the mudstone color of coastal lake is mainly light green, indicating that the paleo-water depth is about 0–5 m, whereas the color of mudstone in a shallow lake is mainly gray and light gray, indicating paleo-water depth is about 5–30 m. The mudstone in a semi-deep lake is dominated by dark gray, suggesting a water depth greater than 30 m (Wang 2011). Some scholars have divided lakes into three zones based on the water depth, including coastal lake (water depth is <5 m), shallow lake (water depth of 5–20 m), and deep lake (water depth >20 m) (Cai 2011). The criteria for dividing lake by water depth should be combined with the actual situation of the basin (Kang et al. 2000). For

**Table 2.5** Correlation between different lithologies and their corresponding water depths (from Zhang and Ren 2003)

| Lithology | Water depth/m |
|---|---|
| Evaporite | 0–5 |
| Conglomerate | 1–10 |
| Oolitic limestone | 1–15 |
| Argillaceous siltstone | 5–20 |
| Reef limestone | 5–25 |
| Dark mudstone | >20 |
| Oil shale | >50 |

wells without a lithological profile, the lithology interpreted by well logging can be used to analyze the paleo-water depth (Kang et al. 2000).

The formation of various types of sedimentary structures depends on the depth and hydrodynamic conditions of the water (Ji and Zhang 1996). For example, in a normal condition shore-shallow lake is characterized by low-angle cross-bedding, ripple cros- bedding, and wavy bedding, while in arid condition, a coastal-shallow lake is likely exposed and characterized by mud crack, rain print, and rill mark. The semi-deep or deep lake is mainly composed of horizontal bedding, but it may also develop structures that formed by gravity flow. The correlation between lithology and water depth is shown in Table 2.6.

In addition, the formation of autogenic minerals such as aluminum, iron, and manganese is not only determined by specific environment, but is also related to the water depth. Iron-containing autogenous minerals, such as hematite, limonite, siderite, and pyrite, indicate the water depth changes from shallow to deep and from an oxidizing environment to a reducing environment (water depth changes from 0–1 to 1–3 m, 3–15 to >15 m) (Zhang and Ren 2003). Different kinds of iron-containing autogenous minerals are displayed in different colors in different rocks. The mineral colors in claystone are particularly powerful to determine the water depth.

(3) Geochemical method

Using the geochemical characteristics that can represent the depositional environment (e.g., U/Th, K/Th) could qualitatively recover the paleo-water depth.

For example, U/Th, K/Th can reflect the water environment. U belong to the family of actinide elements and is very susceptible to oxidation. The U can be enriched during the process of sedimentation through two ways, by either reducing and preserving in the sediments, or absorbing by organic matter or clay minerals. Therefore, the level of U content indicates the degree of reduction. K element is abundant in sediments. In sandstone, the abundance of K tends to be inversely proportional to the granularity of the detrital particles and inversely proportional to the hydrodynamic strength. Th is a relatively stable element in the family

of natural radioactive elements and is generally not affected by the later diagenesis.

Therefore, U/Th can indicate the oxidation or reduction of water body, and K/Th can indicate the dynamic environment of water. There are close relationships among the water depth, oxidation, or reduction degree of water body and hydrodynamics condition. High ratios of U/Th and K/Th usually indicate a more reducing environment and deep water depth. Otherwise, low ratios of U/Th and K/Th suggests shallow water depth.

In addition, $Fe_2O_3$ and MnO content can clearly indicate the water depth. As the water depth becomes deepening, MnO content increases gradually and $Fe_2O_3$ content decreases gradually. Comparing the relative content of these two kinds of minerals in sediments can help determine the trend of water depth change (Jiang and Liu 2010).

2. Quantitative recovery of paleo-water depth

(1) Facies-order method

According to the beach bar development mode discussed earlier, the coastal bar is developed in the upper limit zone of swash and backwash and its bottom surface can be considered as the mean lake level. The inner bar is developed in the breaker wave zone. If assuming that the inner bar is fully developed and reaches the average lake level, then the thickness of the inner bar records the depth of the breaker waves before it forms. The outer bar is developed in the breaker zone. If assume the outer bar is fully developed, which the top surface of outer bar can reach the level of the basal surface of inner bar, then the water depth for the formation of outer bar can be calculated by adding the thickness of inner bar and outer bar. Similar principle can be applied to the storm zone and to restore the depth of the storm influenced area. As shown in Fig. 2.23, the water depth of inner bar formed can be expressed as $H_1$, while the water depth of outer bar formed can be calculated as $H_1 + H_2$. Similarly, the depth of storm-generated beach bars can be expressed as $H_1 + H_2 + H_3$ (Fig. 2.23).

To quantitatively restore paleo-water depth in a specific study area, first, it is necessary to recognize the beach bars deposits from cores, well logging, and mud logging data.

**Table 2.6** Correlation between different sedimentary structures and water depth (Ji and Zhang 1996)

| Sedimentary structure | Water depth/m |
| --- | --- |
| Rain print, mud crack, salt crystal, bird eye structure | 0–1 |
| Large cross-bedding | 0.5–5 |
| Wavy bedding and parallel bedding | 5–20 |
| Horizontal bedding | >17 |
| The Bouma sequence, groove mode, and hummocky cross-bedding | >30 |
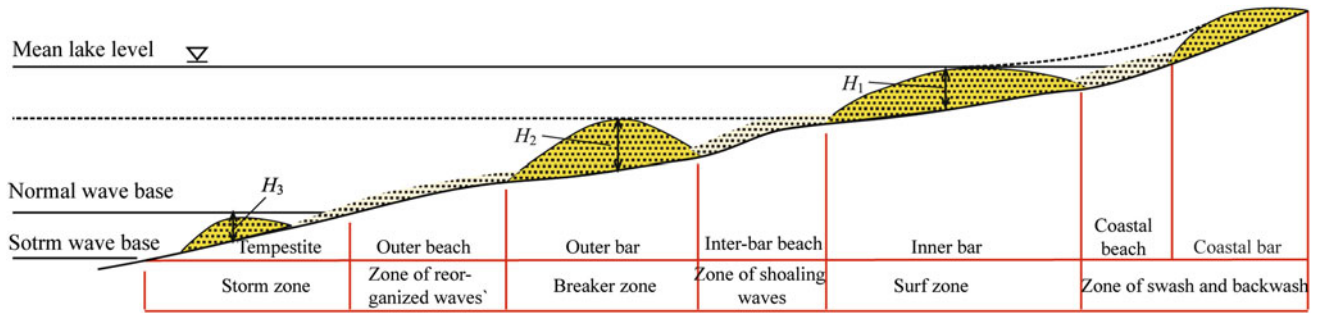
**Fig. 2.23** Calculation of the paleo-water depth by sand bar thickness (modified from Jiang et al. 2014)

Then, a well-tie cross-section, that is, perpendicular to the shoreline is required to correlate the beach bar facies and calculate the thickness of bars. The compaction correction should be performed to obtain final water depth. Finally, a paleo-water depth contour map can be drawn in the plane.

(2) Wave mark method

The wave mark preserved in the geological record, which is generated by oscillation flow, provides a good foundation for the reconstruction of paleo-depth. According to the study of paleo-ripples, mathematical expressions can be applied to estimate the paleo-water depth and the formation conditions of paleo-ripples.

First of all, in order to accurately estimate the water depth of the ripple formed, selected ripple should meet certain conditions: the symmetry index of biggest ripple is limited within 1.5 and the vertical form index cannot exceed 9.

The nomenclature that describes the relationship between a wave mark and moving water body is shown in Fig. 2.24.

Miller and Komar (1980) pointed out that, for symmetric wave, if the wavelength of wave mark, $\lambda$ (cm), has the following relationship with particle diameter, D ($\mu$m):



**Fig. 2.24** Schematic diagram showing the terminology of wave markers and water particles. u is the velocity of the water particle motion; $\eta$ is the height of wave mark; $\lambda$ is the wavelength of the wave mark; $d_0$ is track diameter of water particle near lake bottom

$$\lambda < 0.0028\,D^{1.68} \tag{2.18}$$

Then, the movement track diameter of water particle bottom, $d_0$, can be expressed by the following equation:

$$d_0 = \lambda/0.65 \tag{2.19}$$

The critical velocity $U_t$ to move the sediment particles can be displayed in the following equation:

$$U_t^2 = 0.21(d_0/D)^{1/2}(\rho_S - \rho)gD/\rho, \quad D < 0.5mm \tag{2.20}$$

$$U_t^2 = 0.46\pi(d_0/D)^{1/4}(\rho_S - \rho)gD/\rho, \quad D < 0.5mm \tag{2.21}$$

In Eqs. 2.12 and 2.20, $\rho$ is the density of water and $\rho_s$ is the density of sediment. G is the acceleration of gravity.

For the critical velocity $U_t$ and the corresponding wave length is $L_t$, which has the following relation:

$$Lt = \frac{\pi g d_0^2}{2U_t^2} \tag{2.22}$$

Assuming a ripple is formed by a breaker wave, when the wave breaks (also see Sect. 2.1.3.1) the height of wave and wave length can be expressed as

$$H_{max} = 0.142 \times L_t \tag{2.23}$$

whereas $H_{max}$ is the maximum possible wave height for breaker waves.

In the shallow water, an empirical equation was proposed by Diem (1985):

$$h = H/0.89 \tag{2.24}$$

whereas H is the height of wave (refer to $H_{max}$) and h is the depositional depth.

In the process of calculation, the wavelength of the ripple marks can be directly measured, and the diameter D of sediment particles can be obtained from the grain-size analysis of sedimentary rocks. Since the water depth recorded by wave marker is in a depth range, D should be the average particle diameter. The density of water medium, $\rho$, can be estimated

by the different rational selections of salinity, such as freshwater density should be assumed to be 1 g/cm$^3$. The density of sediment $\rho_s$ can be directly measured by the density log or sample. Similarly, due to the water depth recorded by wave marker is in a depth range, the sediment density, $\rho_s$, represents the average density. Finally, the paleo-water depth can be calculated by using the wave mark.

It is important to note that the wave marked perseveres in the sedimentary rocks was affected by compaction and the wave mark parameters should be different from that of original status. Therefore, when using the wave mark to restore paleo-water depth, the compaction should be taken into account and be corrected.

(3) Multifamily micropaleontological method

Multifamily micropaleontological method is mainly based on the ecological principle that the water depth can influence the aquatic organisms. For aquatic organisms, their living environment is result of the interaction of comprehensive ecological factor, such as physical, chemical, and biological factors. Therefore, different types of paleontology have their suitable survival depth, which can indicate the depth of water (Su et al. 2012). The knowledge of how water depth influence on an organism has mainly based the principle of "Uniformitarianism" and derived from studies on the preservation environment and its corresponding organism. Using paleontology data to restore absolute paleo-water depth, not only the correlation between modern certain species of organis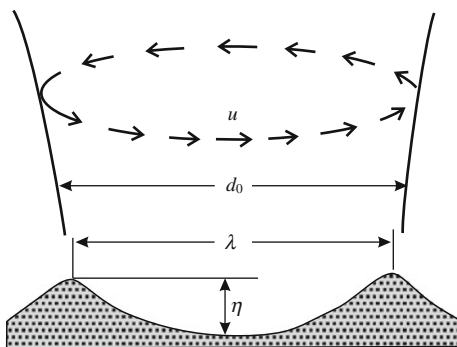m and water depth should be obtained, but also the previous research on certain species living habit should be taken into account. For example, studies on the correlation between modern ostracod and lake depth point out that the ostracod can indicate the absolute water depth, which can be used to restore paleo-water depth of lacustrine basin in China. Benthic algae are organisms living at the bottom of the lake and controlled by the sunlight penetrated into the water. Different species live in the different water levels and sensitively reflect the water depth. In addition, benthic algae are attached to the lake bottom and are resistant to be moved, which are more representative of the original environment (Su et al. 2012) (Fig. 2.25). By conducting the analysis of benthic living macroalgae and combining with other living organisms or preserved environments, the depth of the original environment can be obtained. In order to restore paleo-water depth as accurate as possible, Su et al. (2012) put forward methods called of "Multi-class creatures stacked depth" and "Weighted comprehensive method for determining water depth". The methods are based on the existing paleo-water depth indicator to estimate paleo-water depth of each paleo-data and then combine these interpretations together to obtain a stacked water depth (Fig. 2.26). The interpretation is then combined with lithology of the overlying and underlying strata, other water depth indicator, as well as sequence stratigraphy and sedimentary research, to give an absolute water depth and draw absolute water depth contour map.

To restore absolute water depth for a specific study area, the detailed procedures of the multifamily micropaleontological method can be expressed as follows: (1) investigation and establishment of the criteria to determine paleo-water depth; (2) samples and paleontological data collection; (3) analysis and appraisal of the paleontological data and samples; (4) interpretation of the ecological and water depth of different species of palaeobios; (5) overlay analysis of the depth that is indicated by multifamily micropaleontological analysis; (6) multifactor weighted comprehensive analysis (Su et al. 2012).

## 2.3.4 Influence of Tectonic Activity on Sedimentation

The tectonic activity of the basin is mainly displayed as the activity of the fault, especially the episodic activity of the control basin boundary fault. The combination of the controlling fault system and its associated second-order faults determines the basin configuration. Especially the controlling boundary fault system has directly influenced the formation of sequence boundary, order of boundary, and the property of the boundary. In addition, the faulting distribution style and pattern has controlled the lacustrine basin sequence stratigraphy geometry and depositional filling type and size.

Tectonic activity plays an important role in the sedimentation of basins, especially in a rift basin, where faults and sedimentation occur simultaneously. Fault activities are sometimes performed as earthquakes. In the event of an earthquake, it can affect and modify the soft sediments contained in consolidated strata, loose layer without water and layers rich in water. The catalytic events deposits that are produced by seismic and are characterized by seismic-depositional structures and seismic-depositional sequence can be called seismites. The formation of seismites rocks is very complicated and caused by server mechanisms, including plastic deformation, brittle deformation, extrusion, shear, liquefaction, and water escape, and sometimes with the injection of sediments.

There are various types of seismites rocks and can be divided into three categories according to the deformation mechanism (Montenat et al. 2007; Qiao and Li 2009). The first category of seismites is formed in soft sediments, which can be future divided into two types. A type of category 1 seismites is formed by strong shear force, such as liquefied hydraulic structure, liquefied vein, liquefied curled
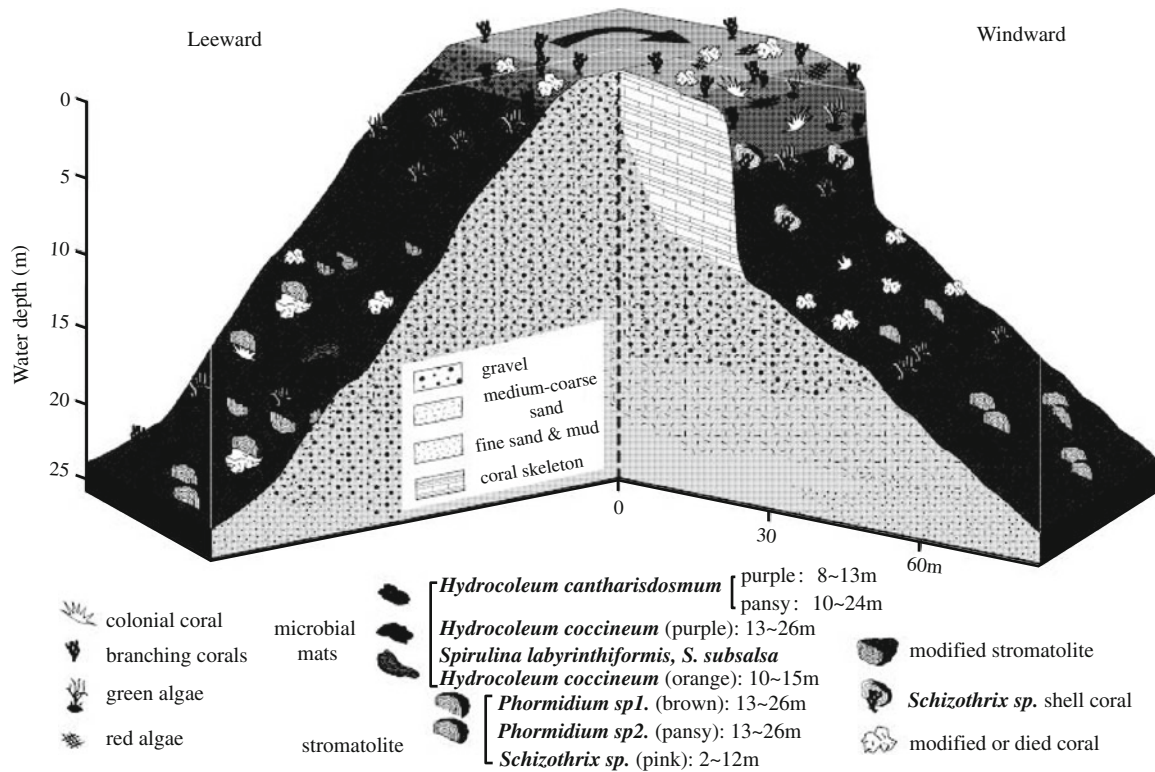
**Fig. 2.25** The relationship between algae and absolute water depth (from Sprachta et al. 2001)



**Fig. 2.26** Diagram showing the method of multi-class creatures stacked depth and multifactor weighted comprehensive analysis
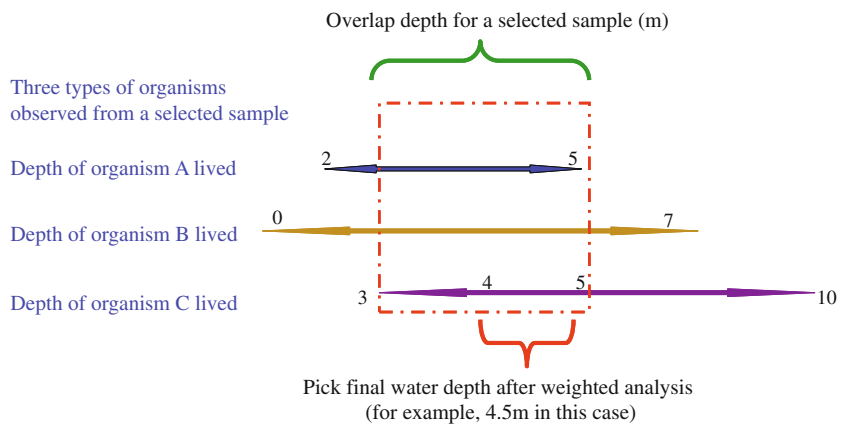
deformation, diapirs, load-flame structure, and pillow structure and so on are all products of strong shear force. Another type of category 1 seismites are caused by the extrusion or tensile stress without sediment liquefied, such as continuous layers. Category 2 is dominated by brittle deformation, such as syndepositional fault and fractures. Category 3 refers to the slumping sediments caused by a seismic event, such as debris flow and turbidity current (Fig. 2.27).

Evidence of seismites have been found in the Es$_3$ in Sulu sag. The early stage of Es$_3$ was dominated by strong faulting and extensional activities and the topography of basin was characterized by great slope falls and narrow slope. In this stage, the sediment supply was strong. When earthquake event occurred, it would affect and modify the preexisted sediments to form diapir structures, liquefied vein, and other in situ seismites. The earthquake could also cause the exposed basement rock to be broken up in the source area, or remobilize the loose sediment of the fan delta system in the proximal source region to form allochthonous deposits by debris flow. In the process of transportation, the seismites could erode the underlying soft sediments and carry them forward. As the energy of flow decreased, the sediments carried were released and deposited quickly and abruptly
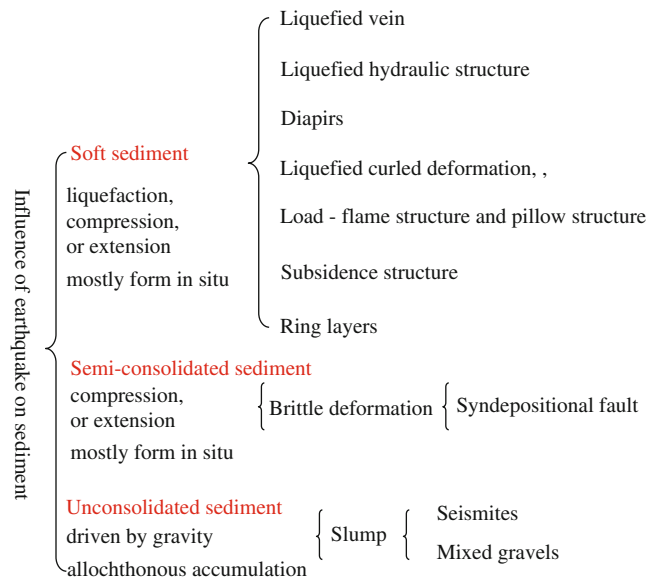
Fig. 2.27 Main types of seismites (modified from Montenat et al. 2007; Qiao and Li 2009)

contact underlying strata (please see more details in Chap. 7).

## 2.4 Windfield-Source-Basin Dynamics

### 2.4.1 Interactions Between the Elements of the Windfield-Source-Basin System

Taking the beach bar system as an example, the development of beach bar deposits is sensitive to controlling factors included in the windfield-source-basin system. In a plan view, beach bars usually develop in locations where waves are stable and sustaining, and with sufficient sediment supply. In general, the development and distribution of beach bars are controlled by hydrodynamics, sediment supply and tectonic features, and bathymetry of the basin, which can be summarized that the beach bar system is controlled by the windfield-source-basin system. Controlling factors included in the windfield-source-basin system are seldom functioning independently but usually interact with each other to control the development of the depositional system.

(1) Interactions between wind and topography

As mentioned before, the slope and topographic relief of the nearshore zone not only directly influence the width of hydrodynamic zones, but also the position of breakers and hydrodynamic of the coastal circulation (Zhu et al. 1988). In basins where a large extent of coastal zone are rimmed, waves would touch the bottom sediments to a large extent.

The refraction of waves is dominated by the coastal topographic relief. The shoreline curvature and local topographic relief result in distortion of wave crests or wave rays, and finally, the wave crests tend to be parallel with isobaths, which further determines the energy distribution of waves. For example, the convex bank and positive relief would concentrate wave rays and thus cause energy concentration, while the concave bank and negative relief would diffuse wave rays and cause energy dispersion. Therefore, convex bank and positive relief in the windward would be more responsible for energy consumption and thus sediment depositing, while in the concave bank and negative relief regions the wave energy is usually low. Such an energy distribution of waves would cause a different depositional process in different topographic reliefs. In a monoclinic relief where isobaths are straight and parallel to each other, depositional processes are also usually parallel to the isobaths as well as the shoreline.

Reversely, waves also shape the coastal topographic reliefs to some extent. The transportation and deposition of coastal sediments are strictly controlled by hydrodynamics. Therefore, different hydrodynamics would cause various topographic reliefs. Take a gently planar and monoclinic coast as an example, the outer bar developed in the breaker zone and inner bar developed in the surf zone are usually parallel to each other, spaced by inter-bar troughs. Sometimes, the scale of the bar-trough relief is significant (Zhu et al. 1988). Particularly, in coast which are suffered from storms, the reshape of coastal relief by waves is more remarkable (Zhang et al. 1998). In addition, if waves propagate to the shoreline obliquely, spits would form near concave shorelines, which might gradually grow into barrier islands and result in the barrier island–lagoon system.

(2) Interactions between sediment supply and topography

Macroscopic geomorphologic pattern strictly dominates the sediment supply from the provenance. Geomorphic features control the position of sediment source, drainage network, and depositional center. Strata above the base level would suffer from erosion and act as provenance. Gullies or valleys determine the transportation route of sediments, serving as conduits for sediment transportation, while lowlands or basins and slope-break zones are locations where the hydrodynamic energy sharply reduced, are positions where sediments get deposited.

Sediment supply and allocation are also varied in different locations according to the topography. Based on paleo-geomorphologic reconstruction combined with provenance analysis of the southern slope of Dongying Depression, Wang et al. (2011) suggested that geomorphology and sediment supply coupling would control the formation of beach

Fig. 2.28 Lacustrine depositional system controlled by paleogeomorphology and sediment supply (modified from Wang et al. 2011)
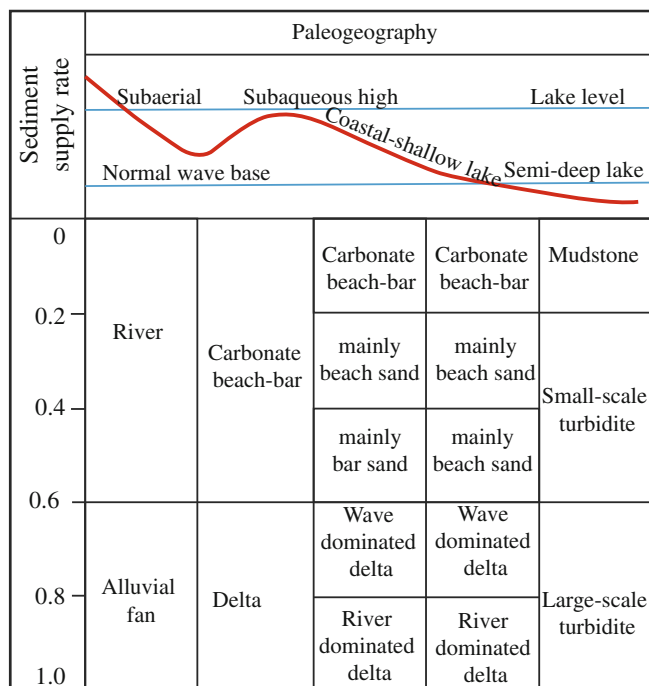
bar system (Fig. 2.28). For example, the development of alluvial rivers and alluvial fans are dependent on sediment supply rate, while the former one usually has a sediment supply rate less than 0.6 and the later one usually has a sediment supply rate larger than 0.6. In subaqueous uplifts, while the sediment supply rate is less than 0.6, calciclastic beaches usually form and when the sediment supply rate is larger than 0.6, there usually develops a delta. In subaqueous slopes or low-lying lands, it would develop deltas, siliciclastic beach bars and calciclastic beaches when the sediment supply rate is larger than 0.6, 0.2–0.6, and less than 0.2, respectively. In the settings of semi-deep or deep lakes, there usually develop muddy suspended sediment (sediment supply rate less than 0.2), and smaller scale to larger scale turbidite fans (sediment supply rate is ranging at 0.2–0.6 for the former and 0.6–1 for the later).

(3)　Interactions between water depth and sediment supply

Even at stable geological periods, the area of provenance is not constant but influenced by relative water-level changes. To some extent, the expanding and shrinking of provenance is in pace with relative water level falls and rises, respectively. This relationship would be more significant in gentle slope of rifted basins or intracratonic basins. In these regions, several meters of water level oscillation would induce several kilometers or tens of kilometers fluctuation of shoreline (Jiang and Liu 2010).

In different periods of stratigraphic evolution, the variation of provenance would influence the depositional process

(Fig. 2.29). During LST, the effect from provenance (and the sediment supply index) would be stronger compared to the lower water level, which would result in progradational stacking patterns of the depositional system. In TST or HST, however, the effect (or the sediment supply index) from local provenance would weaken and even retreated due to an increase of water area, and as a result, the increasing potential energy of the water body would cause erosion or redistribution of depositional systems. For the beach bar depositional systems, during the transformation from relative lower water level to relative higher water level, or relative increase of the water level during LST periods, beach bar deposits are more likely to develop (Wang et al. 2012). In these periods, the sediment supply remains sufficient, while the potential energy of the water body is increasing.

(4)　Interactions between wind and sediment supply

For siliciclastic beach bars, redistribution of sediments by waves might be the most important mechanism, therefore, waves and sufficient sediment supply are the two prerequisites (Jiang et al. 2011): waves provide the power for beach bar formation and the sediment supply provides the material base. Under conditions of poor sediment supply, however, calciclastic deposits might accumulate.

In spite of beach bar systems, effects form interactions between wind and sediment supply are also reflected in other systems. For example, in hinterland regions, the transportation capacity of winds and the intensity of sediment supply determines the erosion–deposition process: If the sediment

**Fig. 2.29** Relationship between source area and relative water-level fluctuation (modified from Lai et al. 2010)
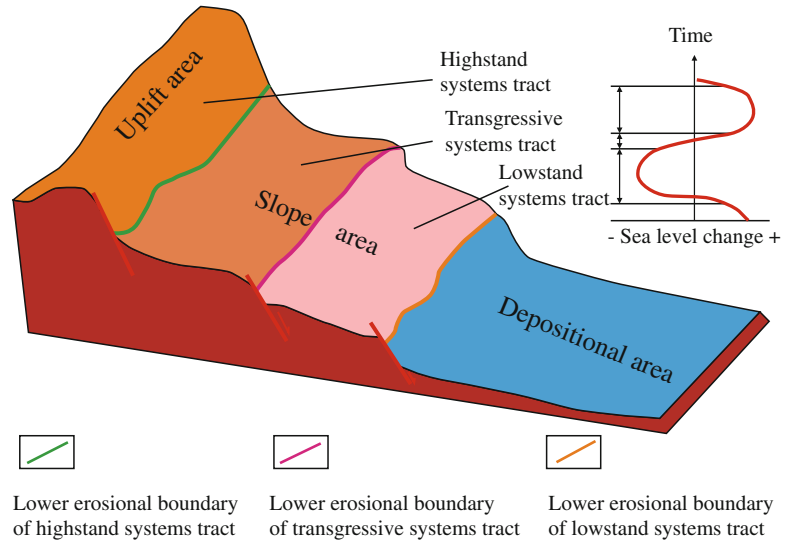
supply overcomes the transportation capacity of winds, deposition is then dominant, and forming eolian deposits; while the transportation capacity of winds overcomes sediment supply, erosion is more significant to form wind-erosion landforms such as Gobi Desert.

## 2.4.2 Classification of the Windfield-Source-Basin System

In spite of the coastal beach bar depositional system, the influence of the windfield-source-basin system can be seen in many other systems. The windfield-source-basin system could be further divided into seven subsystems (Fig. 2.30), discussed as follows:

The windfield-source-basin system includes 3 end members, which are: (1) Wind-dominated system, characterized by wind forces which induce erosion such as forming wind-eroded landforms. Wind-dominated system also includes influences from climate factors such as temperature and humidity controlled by windfield, but seldom consider forces from sediment supply and basin dynamics. (2) Source-dominated system, which is mainly controlled by external forces provided by sediment supply and seldom takes wind power and basin dynamics into consideration. Source-dominated system mainly includes provenance area



**Fig. 2.30** Subclassification of the windfield-source-basin system
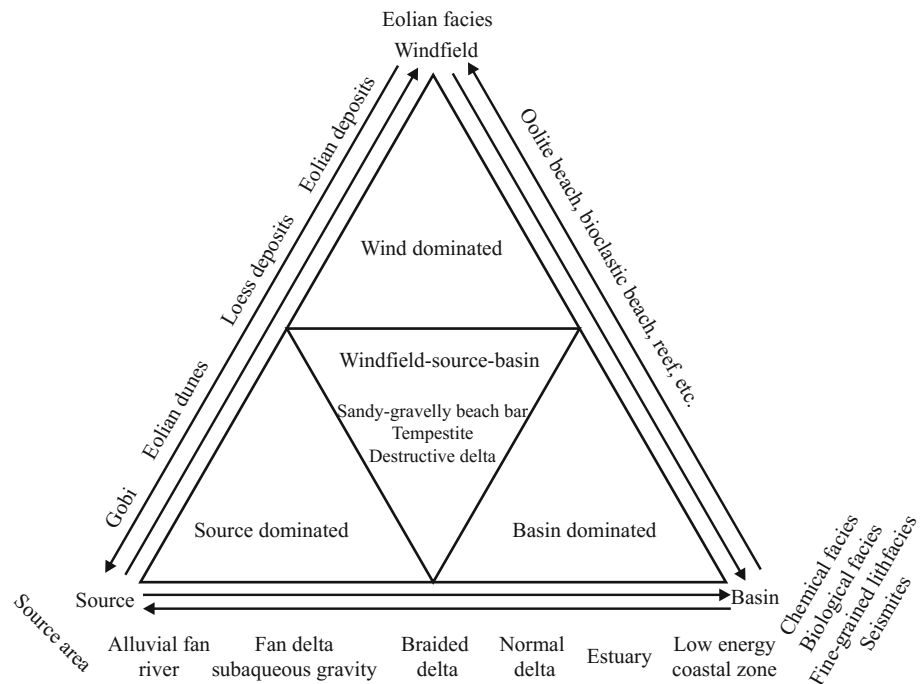
or erosion region. (3) Basin system, by comparison, is mainly dominated by intra-basin dynamics such as tectonic activity and intra-basin physicochemical effects, while wind power (including climate) and sediment supply are seldom taken into consideration. Examples from pure basin system include bioclastic accumulations, chemical precipitations, and seismites.

The 3 end members of the windfield-source-basin system could also be interacted in pairs, which results in: (1) Windfield-source system, in which the depositional system is mainly controlled by wind power (including the related climatic conditions) and sediment supply, whereas the basin is dispensable. Examples of the Windfield-source system include eolian deposits (e.g., eolian dunes, eolian loess), and also include deposits such as silts, clays, and pollens that are transported by the wind and finally deposited in a receiving basin. (2) Windfield-basin system, in which sediment supply is excluded but wind power (including the related climatic conditions) and basin dynamic is mainly considered. In a wind-basin system, terrigenous clastics are seldom injected, and therefore, the system is represented by oolitic beaches, bioclastic beaches, gypsum-salt bed, and so on. (3) Source-basin system, in which terrigenous sediment supply, as well as basin dynamic and evolution such as tectonic activities and sequence evolution, are mainly considered, independent from wind and climate conditions. Common depositional systems such as alluvial fan, delta, subaqueous sediment flow related system, and terrigenous clastic-dominated grained stones should be classified into the source-basin system.

In addition, the wind power, sediment supply, and basin dynamic is sometimes a trinity and can combine together to influence a depositional system. A representative example resulting from the trinity influence is the coastal beach bar system. First, as illustrated previously, waves provide the power to redistribute sediments provided from provenance. Hydrodynamic zones of wind waves controlled the distribution patterns of beach bar deposits. In the existence of prevailing winds, the windward side of the basin is favorable for beach bar development. Second, the provenance provides the material base for beach bar system. The intensity and position of sediment sources controlled the scale and general position of the beach bar system. Third, the topography and bathymetry formed during the basin evolution controlled the exact basinward extent and position of the beach bar system. In plane view, paleogeomorphology in macroscopic scale controls the general extent of beach bar system, which means that beach bar deposits are more likely to develop in gentle slope. Since paleogeomorphology is relatively microscopic usually controls the distribution of hydrodynamic energy, it is supposed that local positive reliefs, such as subaqueous highlands and edges of nose structures, on the

windward side of the basin, are most responsible for reduction of wind-wave powers, and thus, these positive reliefs are more likely to develop beach bar complexes. In addition, the sequence evolution of the basin also influences the development of beach bar deposits. In general, beach bar systems develop in shallower water zones, where the accommodation is relatively limited and is more susceptible to basement subsidence and water-level fluctuations. It is easy to infer that during the transition from relative lower water level to relative higher water level, beach bar deposits are more likely developed. Therefore, favorable conditions for large-scale beach bar development includes: (1) facing prevailing winds, (2) gentler basement slope, (3) positive reliefs, (4) sufficient sediment supply, and (5) the water level is experiencing an increase from a relatively low level. By contrast, in regions where the sediment supply is poor and hydrodynamic energy is low, beaches would be more likely composed of calciclastics if they develop.

Another example reflecting the integrality of windfield-source-basin system is the deposits of tempestites. Wang et al. (2015) reported lacustrine storm seiche deposits preserved in the Lijin Sag of the Dongying Depression. Based on the discussion of paleo-environmental conditions such as paleogeography, paleoclimate, paleogeomorphology, provenance, and paleo-water depth, these authors stated that steep depositional slope, bathymetry, and sufficient sediment supply may be favorable for the formation of storm deposits under influence of typhoon blown from western pacific ocean. Specifically, these favorable conditions are: (1) The Dongying Depression was exposed to typhoon belts. During stormy weather conditions, not only do large waves form in a lake environment, but the storm may also induce seiche activity which might cause sloshing and oscillatory movement: seiche lifts up the water level considerably in the windward side of the lake, and then the water moves back in the other direction when the storm moves away and winds relax. (2) The contemporary proximal fan delta system was keeping progradation, which would provide sufficient sediment materials. Under the influence of storm waves and seiches, these sediments might be eroded and resuspended, and then transported by seiche movement into a deeper environment. (3) From a stratigraphic viewpoint, these storm-related deposits were developed during the late LST period, when the water area of the lake was expanding and the potential energy of the water body was increasing, which would contribute to the formation of storm deposits. (4) During the deposition of the storm deposits, the locally topographic slope reached 2°–3°, which is another favorable factor for these storm deposits. Therefore, storm events, sufficient supply, deeper water environment, and steeper slope constituted the four main favorable conditions for the formation of storm deposits, reflecting the trinity of windfield-source-basin system.

# References

Adams KD (2003) Estimating palaeowind strength from beach deposits. Sedimentology 50(3):565–577

Adams KD (2004) Estimating palaeowind strength from beach deposits–Reply. Sedimentology 51(3):671–673

Aigner T (1985) Storm depositional systems. In: Friedman GM, Neugebauer HJ, Seilacher A (eds) Lecture notes in earth sciences 3. Springer, Berlin, pp 1–5

Aléon J, Chaussidon M, Marty B et al (2002) Oxygen isotopes in single micrometer-sized quartz grains: tracing the source of Saharan dust over long-distance atmospheric transport. Geochim Cosmochim Acta 66:3351–3365

Allen PA (1981) Wave-generated structures in the Devonian lacustrine sediments of south-east Shetland and ancient wave conditions. Sedimentology 28:369–379

Allen PA (1984) Reconstruction of ancient sea conditions with an example from the Swiss Molasse. Mar Geol 60:455–473

Allen JRL (1993) Palaeowind: geological criteria for direction and strength. Philos Trans R Soc Lond, Ser B 341: 235–242

Augustsson C, Bahlburg H (2003) Cathodoluminescence spectra of detrital quartz as provenance indicators for Paleozoic metasediments in southern Andean Patagonia. J S Am Earth Sci 16:15–26

Bagnold RA (1941) The physics of wind blown sand and desert dunes. Methuen, London

Bhatia MR (1983) Plate tectonics and geochemical composition of sandstones. J Geol 91:611–627

Bhatia MR, Crook KAW (1986) Trace element characteristics of graywackes and tectonic setting discrimination of sedimentary basins. Contrib Miner Petrol 92:181–193

Bowen AJ, Inman DL (1969) Rip currents, 2: laboratory and field observations. J Geophys Res 74(23):5479–5490

Brandt DS, Elias RJ (1989) Temporal variations in tempestite thickness may be a geologic record of atmospheric $CO_2$. Geology 17:951–952

Cai J (2011) Reconstruction and evolution of Paleogene geomorphology in the overlap fault belt in the south of Nanyang sag. Spec Oil Gas Reservoirs 18(6):57–60 (In Chinese with English abstract)

Cao YC, Wang YZ, Xu TY et al (2007) Application of the ratio of characteristic elements in provenance Analysis: a case study from the upper part of the fourth member of the Shahejie Fm. in theW58 area, Dongying Depression. Acta Sedimentol Sin 25(2):230–238 (In Chinese with English abstract)

Cao YC, Wang J, Liu HM et al (2009) Sedimentary characteristics and models of beach bar sandbodies in the upper part of the fourth member of Paleogene in the south slope of Dongying depression. J China Univ Pet 33(6):5–10 (In Chinese with English abstract)

CERC (1977) Shore protection manual, 3 vols. U.S. Army Coastal Engineering Research Center, Fort Belvoir

CERC (1984) Shore protection manual. U.S. Army Corps of Engineers, US Govt. Printing Office, Washington, DC, p 607

Clayton RN, Jackson ML, Sridhar K (1978) Resistance of quartz silt to isotopic exchange under burial and intense weathering conditions. Geochim Cosmochim Acta 42:1517–1522

Čopjaková R, Sulovský P, Paterson BA (2005) Major and trace elements in pyrope–almandine garnets as sediment provenance indicators of the Lower Carboniferous Culm sediments, Drahany Uplands, Bohemian Massif. Lithos 82:51–70

Davidson-Arnott RGD (2013) Nearshore bars. In: Shroder J, Sherman DJ (eds) Treatise on geomorphology, vol 10. Academic Press, San Diego, pp 130–148

Dickinson WR, Beard LS, Brakenridge GR et al (1983) Provenance of North American Phanerozoic sandstones in relation to tectonic setting. Geol Soc Am Bull 94:222–235

Diem B (1985) Analytical method for estimating palaeowave climate and water depth from wave ripple marks. Sedimentology 32 (5):705–720

Ding Z, Yu Z, Yang S et al (2001) Coeval changes in grain size and sedimentation rate of eolian loess, the Chinese Loess Plateau. Geophys Res Lett 28(10):2097–2100

Dolan TJ, Dean RG (1985) Multiple longshore sand bars in the upper Chesapeake Bay. Estuar Coast Shelf Sci 21:727–743

Duke WL (1987) Hummocky cross-stratification, tropical hurricanes, and intense winter storms. Sedimentology 34(2):344–359

Dupré WR (1984) Reconstruction of paleo-wave conditions during the late Pleistocene from marine terrace deposits, Monterey Bay, California. Mar Geol 60:435–454

Evans OF (1940) The low and ball of the eastern shore of Lake Michigan. J Geol 476–511

Forsyth AJ, Nott J, Bateman MD (2010) Beach ridge plain evidence of a variable late-Holocene tropical cyclone climate, North Queensland, Australia. Palaeogeogr Palaeoclimatol Palaeoecol 297:707–716

Frey RW, Howard JD (1990) Trace fossils and depositional sequences in a clastic shelf setting, Upper Cretaceous of Utah. J Paleontol 64 (5):803–820

Friedman GM, Sanders JE (1978) Principles of sedimentology. Wiley

Gallagher EL, Elgar S, Guza RT (1998) Observations of sand bar evolution on a natural beach. J Geophys Res: Oceans 103 (C2):3203–3215

Gao GD, Lu YR (1988) Climatology. China Meteorological Press, Beijing (In Chinese)

Goda Y (1970) A synthesis of breaker indices. Proc JSCE, 39–49. (In Japanese)

Goodbred SL (2003) Response of the Ganges dispersal system to climate change: a source-to-sink view since the last interstade. Sed Geol 162(1):83–104

Götze J, Plötze M, Habermann D (2001) Origin, spectral characteristics and practical applications of the cathodoluminescence (CL) of quartz—a review. Mineral Petrol 71:225–250

Gui BL (2008) The palaeogeomorphologic reconstruction of Es2 in Zhuangxi area, Bohai Bay Basin. China University of Geosciences, Beijing (In Chinese with English abstract)

Han YL, Wang HH, Chen ZH et al (2007) Paleosalinity analysis and trace element geochemistry of Chang 6 member in Gengwan-Shijiawan area, Ordos Basin. Lithol Reservoirs 19 (4):20–26 (In Chinese with English abstract)

Hay WW, Shaw CA, Wold CN (1989) Mass-balanced paleogeographic reconstructions. Geol Rundsch 78(1):207–242

He Z, Li J, Mo S et al (2005) Geochemical discriminations of sandstones from the Mohe Foreland basin, northeastern China: tectonic setting and provenance. Sci China, Ser D Earth Sci 48 (5):613–621

He J, Feng SB, Huang J et al (2011) Effects of provenance on porosity development of Chang 6 sandstone of the Yanchang Formation in the center of Ordos Basin. Acta Sedimentol Sin 29(1):80–87 (In Chinese with English abstract)

Houser C, Greenwood B (2005) Hydrodynamics and sediment transport within the inner surf zone of a lacustrine multiple-barred nearshore. Mar Geol 218:37–63

Hu XY (2008) The palaeogeomorphologic reconstruction of $Es_4^S$ in Zhuangxi area Bohai Bay Basin. China University of Geosciences, Beijing (In Chinese with English abstract)

Huang CY, Wang H, Zhou LH et al (2009) Provenance system characters of the third member of Shahejie Formation in the Paleogene in Beitang Sag. Earth Sci - J China Univ Geosci 34 (6):975–984 (In Chinese with English abstract)

Jewell PW (2007) Morphology and paleoclimatic significance of pleistocene lake bonneville spits. Quatern Res 68:421–430

Ji YL, Zhang SQ (1996) Sequence stratigraphy in terrestrial rift lake basins. Petroleum Industry Press, Beijing (In Chinese)

Jiang ZX (2003) Sedimentology. Petroleum Industry Press, Beijing (In Chinese)

Jiang ZX (2010a) Sedimentology. Petroleum Industry Press, Beijing. (In Chinese)

Jiang ZX (2010b) Studies of depositional systems and sequence stratigraphy the present and the future. Oil Gas Geol 31(5):535–541. (In Chinese with English abstract)

Jiang FQ, Li AC (2002) Geochemical characteristics and their implications to provenance and environment of surface sediments from the south Okinawa Trough. Acta Sedimentol Sin 20(4):680–686 (In Chinese with English abstract)

Jiang ZX, Liu H (2010) Lacustrine palaeoshore line and its controls on sandbodies and hydrocarbon. J Palaeogeogr 12(5):589–598 (In Chinese with English abstract)

Jiang XS, Pan ZX, Fu QP (2000) Primary study on pattern of general circulation of atmosphere before uplift to the Tibetan Plateau in eastern Asia. Sci China, Ser D 30(5):526–532 (In Chinese with English abstract)

Jiang ZX, Xing HQ, Li RW et al (2005) Research on provenance and paleocurrents in the Meso-Cenozoic Hefei basin. Geocsience 19(2):247–252 (In Chinese with English abstract)

Jiang ZL, Deng HW, Lin HX et al (2009) Methods and application of paleo-geomorphologies rebuilding an example of the second member of Shahejie Formation, Zhuangxi area, Jiyang depression. Geocsience 23(5):865–871 (In Chinese with English abstract)

Jiang ZX, Liu H, Zhang SW et al (2011) Sedimentary characteristics of large-scale lacustrine beach bars and their formation in the Eocene Boxing Sag of Bohai Bay Basin, East China. Sedimentology 58:1087–1112

Jiang ZF, Wu H, Cui XZ et al (2013) The reconstruction of Paleogene wind direction and general atmospheric circulation style in Sichuan Basin, Southwestern China. Geol Bull China 32(5):734–741 (In Chinese with English abstract)

Jiang ZX, Liang SY, Zhang YF et al (2014) Sedimentary hydrodynamic study of sand bodies in the upper subsection of the 4th Member of the Paleogene Shahejie Formation in the eastern Dongying Depression, China. Pet Sci 11:189–199

Jiao YQ, Li Z, Zhou HM (1998) The integrated study of sediment sources in sedimentary basins: an example from the Eogene Nanpu rift subbasin. Sediment Facies Palaeogeogr 18(5):16–20 (In Chinese with English abstract)

Jin ZJ, Zhang YW, Liu GC et al (1996) Physical analysis method for sedimentary basin—wave analysis. Geol Rev 2(SI):170–180. (In Chinese with English abstract)

Kang A, Zhu XM, Wang GW et al (2000) Application of paleobathymetric curve in the sequence stratigraphy of well-logging data. Acta Sedimentol Sin 18(1):63–67 (In Chinese with English abstract)

Keulegan GH (1948) An experimental study of submarine sand bars. U.S. Army Corps of Engineers, Beach Erosion Board Tech. Report (3), p 40

King CAM, Williams WW (1949) The formation and movement of sand bars by wave action. Geogr J 113:70–85

Knott JR, Fantozzi JM, Ferguson KM et al (2012) Paleowind velocity and paleocurrents of pluvial Lake Manly, Death Valley, USA. Quatern Res 78(2):363–372

Komar PD (1971) Nearshore cell circulation and the formation of giant cusps. GSA Bull 82(9):2643–2650

Komar PD (1998) Beach processes and sedimentation. Prentice Hall, Upper Saddle River, p 543

Lai WC, Song ZQ, Zhou XH et al (2010) Model of dynamic source controlling sand. Pet Explor Dev 37(6):763–768 (In Chinese with English abstract)

Lal D, Peters B (1967) Cosmic ray produced radioactivity on the earth. In: Kosmische Strahlung II/Cosmic Rays II. Springer, Berlin, pp 551–612

Li YC, Dong GH (1993) Breaker indices of irregular waves on gentle beach. J Hydrodyn, Ser A 8(1):21–27 (In Chinese with English abstract)

Li J, Wang GW (1995) Applieations of high resolution dip log to the study of sand reservoir. Well Logging Technol 5:352–357 (In Chinese with English abstract)

Li YC, Zhang LY, Zhou SZ (1995) Study evolution of Holocene Lake-Level on Ka time scale in Qinghai Lake. J Qinghai Norm Univ (Nat Sci) 3:39–45 (In Chinese with English abstract)

Li CH, Ji YL, Zhang SQ et al (2004a) Estimation of exposure time and erosion rate as well as thickness of erosion surface using cosmogenic nuclides 10Be and 26Al. J Univ Pet, China 28(1):1–4 (In Chinese with English abstract)

Li ZK, Huang FX, Zhang YJ et al (2004b) Application of denudation thickness restoration in the denudation volume study of Shanshan Arcuate Belt. Tuha Oil Gas 9(2):130–134 (In Chinese with English abstract)

Li SJ, Zheng DS, Jiang ZX et al (2005) Water depth of palaeo-lacustrine basin recovered by dominance diversity of Ostracoda: an example from sedimentary period of the Member 3 of Shahejie Formation of Paleogene in Dongying sag, Shandong Province. J Palaeogeogr 7(3):399–404 (In Chinese with English abstract)

Li C, Cao QB, Shou JF et al (2009a) Application of fractal dimension of natural gamma logging curve in provenance analysis—a case in lower member of Ganchaigou Formation, Qigequan-Shibei area, Qaidam Basin. Nat Gas Geosci 20(1):148–152 (In Chinese with English abstract)

Li YH, Liu CY, Du YG et al (2009b) Sedimentary characteristics of shallow water delta and lake shoreline control on sandbodies of Chang 8 oil-bearing interval of the Upper Triassic Yanchang Formation in northwestern Ordos Basin. J Palaeogeogr 11(3):265–274 (In Chinese with English abstract)

Liang QS, Liu Z, He XH et al (2009) Study of stratigraphic denudation recovery by seismic data in new exploration area. Xinjiang Pet Geol 30(1):103–105 (In Chinese with English abstract)

Licht A, van Cappelle M, Abels HA et al (2014) Asian monsoons in a late Eocene greenhouse world. Nature 513:501–506

Liu B (2002) Calculation of denuded strata thickness by fluid inclusion data—a case study of three depressions in the East China Sea Basin. Pet Geol Exp 24(2):172–180 (In Chinese with English abstract)

Liu GY, Jiang LQ (1995) Balanced section technique and seismic data inter-Pretatio. Oil Geophys Prospect 30(6):833–844 (In Chinese with English abstract)

Liu LA, Jiang ZX (2011) Advances in the indicator of palaeowind direction reconstruction. Prog Geogr 30(9):1099–1106 (In Chinese with English abstract)

Liu GC, Jin ZJ, Li JC (1995) A new method on the quantitative study of depositional and erosional processes of sedimentary basins—an application of wave process analysis during basin evolution. Acta Sedimentol Sin 13(3):23–31 (In Chinese with English abstract)

Liu DS, Zheng MP, Guo ZT (1998) Initiation and evolution of the Asian monsoon system timely coupled with the ice-sheet growth and the tectonic movements in Asia. Quat Sci 3:194–204 (In Chinese with English abstract)

Liu JY, Lin CS, Xiao JX et al (1999) Characteristics and erosions of the major tertiary unconformities and their significance to petroleum exploration in the Xihu Trough, the east China sea. Geoscience 13 (4):432–438 (In Chinese with English abstract)

Liu JY, Lin CS, Yu YM et al (2000) An improved method to calculate denuded amount by sonic well logs. Exp Pet Geol 22(4):302–306 (In Chinese with English abstract)

Liu P, Jin CS, Zhang S et al (2007) The early Quaternary loess paleosol sequence characteristics of magnetic fabrics and the ancient field recovery, Longdan, Gansu. Chin Sci Bull 52(24):2922–2924 (In Chinese with English abstract)

Liu H, Jiang Z, Zhang R et al (2012) Gravels in the Daxing conglomerate and their effect on reservoirs in the Oligocene Langgu Depression of the Bohai Bay Basin, North China. Mar Pet Geol 29:192–203

Lu H, Huissteden K, An Z et al (1999) East Asia winter monsoon variations on a millennial time-scale before the last glacial–interglacial cycle. J Quat Sci 14(2):101–110

Marsaglia KM, Klein GDV (1983) The paleogeography of Paleozoic and Mesozoic storm depositional systems. J Geol 117–142

Masselink G, Evans D, Hughes MG et al (2005) Suspended sediment transport in the swash zone of a dissipative beach. Mar Geol 216 (3):169–189

Métivier F, Gaudemer Y, Tapponnier P et al (1999) Mass accumulation rates in Asia during the Cenozoic. Geophys J Int 137:280–318

Miller MC, Komar PD (1980) A field investigation of the relationship between oscillation ripple spacing and the near-bottom water orbital motions. J Sediment Petrol 50(1):183–191

Montenat C, Barrier P, d'Estevou PO et al (2007) Seismites: an attempt at critical analysis and classification. Sed Geol 196(1):5–30

Morton A, Hallsworth C, Chalton B (2004) Garnet compositions in Scottish and Norwegian basement terrains: a framework for interpretation of North Sea sandstone provenance. Mar Pet Geol 21:393–410

Morton AC, Whitham AG, Fanning CM (2005) Provenance of Late Cretaceous to Paleocene submarine fan sandstones in the Norwegian Sea: integration of heavy mineral, mineral chemical and zircon age data. Sed Geol 182:3–28

Nott JF (2003) Intensity of prehistoric tropical cyclones. J Geophys Res: Atmos 108(D7)

Nutz A, Schuster M, Ghienne JF et al (2015) Wind-driven bottom currents and related sedimentary bodies in Lake Saint-Jean (Québec, Canada). GSA Bull 127(9/10):1194–1208

Otto T (1912) Der Darss und Zingst. Jahrb. d. Geo. Gesell. zu Greifswald 13:393–403

Pang JG, Yun ZW (2013) Progress of paleoclimate reconstructions in continental facies deposition. J Yangtze Univ (Nat Sci Ed) 10 (20):54–56 (In Chinese with English abstract)

Pettijohn FJ, Potter PE, Siever R (1987) Sand and sandstone. Springer, New York

Pochat S, Van Den Driessche J, Mouton V et al (2005) Identification of Permian palaeowind direction from wave-dominated lacustrine sediments (Lodève Basin, France). Sedimentology 52:809–825

Price TD, Russeink BG (2011) State dynamics of a double sandbar system. Cont Shelf Res 31:659–674

Qian N, Wan ZH (1991) Mechanics of sediment transport. Science Press, Beijing (In Chinese)

Qiao XF, Li HB (2009) Effect of earthquake and ancient earthquake on sediment. J Palaeogeogr 11(6):593–610 (In Chinese with English abstract)

Quan C, Liu C, Utescher T (2011) Paleogene evolution of precipitation in northeastern China supporting the middle Eocene intensification of the east Asian monsoon. Palaios 26:743–753

Quan C, Liu Y, Utescher T (2012a) Eocene monsoon prevalence over China: a paleobotanical perspective. Palaeogeogr Palaeoclimatol Palaeoecol 365–366:302–311

Quan C, Liu YSC, Utescher T (2012b) Paleogene temperature gradient, seasonal variation and climate evolution of northeast China. Palaeogeogr Palaeoclimatol Palaeoecol 313:150–161

Rea DK (1994) The paleoclimatic record provided by eolian deposition in the deep sea: the geologic history of wind. Rev Geophys 32 (2):159–195

Sabeen HM, Ramanujam N, Morton AC (2002) The provenance of garnet: constraints provided by studies of coastal sediments from southern India. Sed Geol 152:279–287

Sawaragi T (1995) Coastal engineering-waves, beaches, wave-structure interactions. Elsevier

Scherer CMS, Goldberg K (2007) Palaeowind patterns during the latest Jurassic–earliest Cretaceous in Gondwana: evidence from eolian cross-strata of the Botucatu Formation, Brazil. Palaeogeogr Palaeoclimatol Palaeoecol 250(1):89–100

Shepard FP (1950) Longshore bars and longshore troughs. U.S. Army Corps of Engineers, Washington DC Beach Erosion Board (20), p 26

Shi GR, Mi SY, Zhang QC et al (1998) Principles and method of basin modelling. Petroleum Industry Press, Beijing, pp 129–132

Shi YH, Li Z, Bu XP et al (2009) Detrital garnets from Cenozoic sandstones across Boxing Sag for provenace indicator and its implication for the Luxi Uplift. Acta Sedimentol Sin 27(5):967–975 (In Chinese with English abstract)

Shuai P (2010) Palaeotopographic features and their depositional control in Palaeogene Jiyang depression. Pet Geol Recovery Effi 17 (3):24–27 (In Chinese with English abstract)

Soreghan MJ, Cohen AS (1996) Textural and compositional variability across littoral segments of Lake Tanganyika: the effect of asymmetric basin structure on sedimentation in large rift lakes. AAPG Bull 80(3):382–409

Sprachta S, Camoin G, Golubic S et al (2001) Microbialites in a modern lagoonal environment: nature and distribution, Tikehau atoll (French Polynesia). Palaeogeogr Palaeoclimatol Palaeoecol 175(1–4):103–124

Stokes GG (1849) Notes on hydrodynamics. VI On waves. Camb. Dublin Math. J. 4: 219–240

Su X, Ding X, Jiang ZX et al (2012) Using of multi-microfossil proxies for reconstructing quantitative paleo-water depth during the deposit period of LST of $Es_4^s$ in Dongying Depression. Earth Sci Front 19 (1):188–199 (China University of Geosciences (Beijing); Peking University). (In Chinese with English abstract)

Tanner WF (1971) Numerical estimates of ancient waves, water depth and fetch. Sedimentology 16(1–2):71–88

Thompson RS, Whitlock C, Bartlein PJ et al (1993) Climatic changes in the western United States since 18,000 yr B.P. Wright HE et al (eds) Global climates since the last glacial maximum. University of Minnesota Press, Minneapolis, pp 468–513

Thornton EB, Humiston RT, Birkemeier W (1996) Bar/trough generation on a natural beach. J Geophys Res: Oceans 101(C5):12097–12110

Wang GC (2002) A new approach to determine the exhumation history of the sediment provenance: detrital zircon and apatite fission-track thermochronology. Geol Sci Technol Inf 21(4):35–40 (In Chinese with English abstract)

Wang YZ (2011) Controlling action of palaeo-water depth on the development of carbonate beach and bar. Pet Geol Oilfield Dev Daqing 30(6):27–31 (In Chinese with English abstract)

Wang Y, Jin ZJ (1999) Progress of the methods on the recovery of the thickness of eroded strata in basin. Adv Earth Sci 14(5):482–486 (In Chinese with English abstract)

Wang CS, Li XH (2003) Principles and methods for sedimentary basin analyses. Higher Education Press, Beijing (In Chinese)

Wang L, Sarnthein M, Erlenkeuser H et al (1999) East Asian monsoon climate during the Late Pleistocene: high-resolution sediment records from the South China Sea. Mar Geol 156:245–284

Wang Z, Zhang ML, Wang ZY et al (2005) Erosion thickness restoration of unconformities in the Xihu Sag, the Shelf Basin of East China Sea. Pet Geol Exp 27(1):90–93 (In Chinese with English abstract)

Wang SH, Jiao YQ, Wu LQ et al (2007a) Spatial combination of paleoprovenance and depositional lobe of Mid-Lower Yanchang Formation in the northwest of Ordos Basin [J]. Earth Sci - J China Univ Geosci 32(2):201–208 (In Chinese with English abstract)

Wang Y, Pan BT, Gao HS et al (2007b) Magnetic fabric-based reconstruction of the paleowind direction from a loess sequence in the northeastern flank of the Qilian Mountains. Chin J Geophys 50 (4):1161–1166 (In Chinese with English abstract)

Wang YZ, Song GQ, Wang XZ et al (2011) Controlling effect of paleogeomorphology on deposition of beach and bar san reservoir —case study of south slope, east Dongying depression. Pet Geol Recovery Effi 18(4):13–16 (In Chinese with English abstract)

Wang YS, Liu HM, Gao YJ et al (2012) Sandbody genesis and hydrocarbon accumulation mechanism of beach bar reservoir in faulted-lacustrine-basins: a case study from the upper of the fourth member of Shahejie Formation, Dongying Sag. Earth Sci Front 19 (1):100–107 (China University of Geosciences (Beijing); Peking University). (In Chinese with English abstract)

Wang D, Lu S, Han S et al (2013) Eocene prevalence of monsoon-like climate over eastern China reflected by hydrological dynamics. J Asian Earth Sci 62:776–787

Wang J, Jiang Z, Zhang Y (2015) Subsurface lacustrine storm-seiche depositional model in the Eocene Lijin Sag of the Bohai Bay Basin, East China. Sed Geol 328:55–72

Weltje GJ, von Eynatten H (2004) Quantitative provenance analysis of sediments: review and outlook. Sed Geol 171(1):1–11

Wu HN, Yue LP (1997) The anisotropy of magnetic susceptibility of eolian dust sediment: the paleowindfield in Chinese Loess Plateau. Acta Geophys Sin 40(4):487–494 (In Chinese with English abstract)

Wu HB, Chen FH, Wang JM et al (1998) A study on the relationship between magnetic anisotropy of modern eolian sediments and wind direction. Acta Geophys Sin 41(6):811–817 (In Chinese with English abstract)

Wu ZP, Liu JG, Zhang WH et al (2001) Study on the erosion amount of hiatus surface between neogene and eugene in north part of east Depression, Liaohe Basin. Geol J China Univ 7(1):99–105 (In Chinese with English abstract)

Wu GH, Wang NA, Hu SX et al (2008) Physical geography. Higher Education Press, Beijing (In Chinese)

Wyllie MRJ, Gregory AR, Gardner LW (1956) Elastic wave velocities in heterogeneous and porous media. Geophysics 21:41–70

Xiang F, Wang CS (2001) Mass balance: a quantitative method for orogeny reconstructing of Qinghai–Tibet plateau. Adv Earth Sci 16 (2):279–283 (In Chinese with English abstract)

Xiao J, Porter S, An Z et al (1995) Grain-size of quartz as an indicator of winter monsoon strength on the Loess Plateau of central China during the last 130,000-yr. Quatern Res 43(1):22–29

Xu CG (2013) Controlling sand principle of source-sink coupling in time and space in continental rift basins: basic idea, conceptual systems and controlling sand models. China Offshore Oil Gas 25 (4):1–11 (In Chinese with English abstract)

Xu TW, Song HQ, Kuang H et al (2009) Synthetic application of the provenance analysis technique: a case study of Member 1 of

Taizhou Formation in Gaoyou sag, Subei Basin. Acta Geosci Sin 30 (1):111–118 (In Chinese with English abstract)

Yang CX, Zhao CL (1996) Application of electron microprobe analysis of detrital garnet to provenance studies. Acta Sedimentol Sin 14 (1):162–166 (In Chinese with English abstract)

Yang SY, Li CX, Zhang JQ (1999) Provenance study of Holocene sediments in Subei coastal plain—comparison between elemental geochemistry and heavy mineral methods. Acta Sedimentol Sin 17 (3):458–463. (In Chinese with English abstract)

Yang JF, Hong TY, Xu JQ et al (2006) Application of trend analysis method in denudation recovery in the inner Junggar basin. West China Petroleum Geocsiences 2(1):83–86 (In Chinese with English abstract)

Yang YQ, Qiu LW, Jiang ZX et al (2011) A depositional pattern of beach bar in continental rift lake basins: a case study on the upper part of the fourth member of the Shahejie Formation in the Dongying Sag. Acta Petrolei Sin 32(3):417–423 (In Chinese with English abstract)

Yang RC, Li JB, Fan AP et al (2013) Research progress and development tendency of provenance analysis on terrigenous sedimentary rocks. Acta Sedimentol Sin 31(1):99–107 (In Chinese with English abstract)

Zeng HL (2005) Gravitational field and gravity exploration. Geological Publishing House, Beijing (In Chinese)

Zhang SQ, Ren YG (2003) The study of base level changes of the Songliao Basin in Mesozoic. J Chang'an Univ (Earth Sci Ed) 25 (2):1–5 (In Chinese with English abstract)

Zhang DS, Zhang JL, Zhang CK et al (1998) Tidalcurrent work—surge destruction—tidal current restoration: a preliminary study on the dynamic mechanism of the development of the radical submarine sand ridges of the South Yellow Sea. Sci China, Ser D 28(5):394–402 (In Chinese with English abstract)

Zhang YW, Li JC, Jin ZJ et al (2000) A new calculating method of denuded amount for prototype basin—wave analysis. Oil Gas Geol 21(1):88–91 (In Chinese with English abstract)

Zhang QS, Zhang J, Zhang QC (2001) Study on the sedimentary degradation history of Sanzhao area with wave analysis. Pet Geol Oilfield Dev Daqing 20(6):23–24 (In Chinese with English abstract)

Zhang JL, Lin CS, Zheng HR (2002) Controlling action of fractures, palaeogeomorphology and material sources of rift lake basin on sedimentary system—taking Es3 Gubei subsag as example. Pet Geol Recovery Effi 9(4):24–27 (In Chinese with English abstract)

Zhang YF, Li CA, Chen L et al (2009) Magnetic fabric characters of sand-dune sediments and its paleowindfield in the middle reaches of Yangtze River. Chin J Geophys 52(1):150–156 (In Chinese with English abstract)

Zhao XW (1992) Introduction to paleoclimatology. Geological Publishing House, Beijing, pp 7–40. (In Chinese)

Zhao HG, Liu CY (2003) Approaches and prospects of provenance analysis. Acta Sedimentol Sin 21(3):409–416 (In Chinese with English abstract)

Zheng RC, Wang HH, Han YL et al (2008) Sedimentary facies characteristics and sandbody distribution of Chang 6 member in Jiyuan area of Ordos Basin. Lithol Reservoirs 20(3):21–26 (In Chinese with English abstract)

Zhong GF (2002) Late Cenozoic seismic onlap-offlap sequences and sea level changes on the northern Sunda Shelf, South China Sea. Ph. D. Thesis, Tongji University, Shanghai. (In Chinese with English abstract)

Zhu JC, Zhang GD, Wang YY et al (1988) Migration of ridge (bar) runnel systems and the resultant sedimentary characteristics on modern coast, Zhoushan archipelago. Oceanol Limnol Sin 19 (1):35–43 (In Chinese with English abstract)

Zhu XM, Xin QL, Zhang JR (1994) Sedimentary characteristics and models of the beach–bar reservoirs in faulted down lacustrine basins. Acta Sedimentol Sin 12(2):20–27 (In Chinese with English abstract)

Zou XQ, Ge CD (2000) Coccolith method for the quantitative study of former water depth–submarine sand ridges of the Yellow Sea as an example. Geoscience 14(3):263–266 (In Chinese with English abstract)

Geologists have generally agreed that "the present is the key to the past." Comparative sedimentology and the methodology of "Uniformitarianism" are widely applied in modern sedimentology. In 1960s to 1970s, in order to understand the sedimentary characteristics and oil generation capacity of lacustrine sediments, the Chinese Academy of Sciences founded the Qinghai Lake Comprehensive Research Team, which was constituted by scientists from the Lanzhou Institute of Geology, Institute of Microbiology, Institute of Hydrobiology and Nanjing Institute of Geology and Paleontology. The research team has carried out comprehensive and multidisciplinary research on Qinghai Lake, including geology, evolutionary process, the physical and chemical characteristics of the water body, hydrodynamic zonation, the relationship between microbes and organic matter, and the geochemical characteristics and early diagenetic processes of lake sediments (Lanzhou Institute of Geology, Chinese Academy of Sciences et al. 1979).

In 1989–1991, the Lanzhou Branch of Chinese Academy of Sciences and Research Center of Resources and Environment of Western China gathered scientists from the Lanzhou Institute of Geology, Lanzhou Institute of Plateau Atmospheric Physics, Institute of Glaciology and Permafrost, Northwest Plateau Institute of Biology, Qinghai Salt Lake Research Institute and other related research institute. They conducted detailed research on the meteorology, hydrology, sedimentology, hydrochemistry, and biogeochemistry of Qinghai Lake and its surrounding areas, studied the environmental evolution of Qinghai Lake since the late ice age,and predicted its future development (Lanzhou Branch of Chinese Academy of Sciences et al. 1994). Since then, the study of modern sediments in Qinghai Lake mostly focused on single sedimentary facies (Shi et al. 1996, 2008; Song et al. 1999, 2000, 2001; Han et al. 2015).

Tertiary continental rift basin in eastern China (e.g., Bohai Bay Basin) are similar to Qinghai Lake in turns of geological structure (rift lacustrine basins) and water environment (brackish-salt water). The study of the modern sedimentary system in Qinghai Lake can provide an analogy for the study of sedimentary systems in ancient continental-rift lacustrine basins, which is helpful to study the distribution of sand bodies in continental-rift lacustrine basins in eastern China, and thus helps guiding oil and gas exploration.

In recent years, many geologists have proposed applying source-sink analysis to studying the dynamic process of surface sedimentation. At present, most foreign scholars use this method in researches of modern and ancient marine strata (Moore et al. 1969; Moreno and Romero Segura 1997; Anthony and Julian 1999; Somme et al. 2009, 2013). Domestic scholars also use this idea in researches of ancient continental-rift lacustrine basins (Xu 2013; Lin et al. 2015; Wu et al. 2015). However, few scholars have carried out detailed analysis and research on modern rift lakes as an analog. Qinghai Lake is surrounded by orogenic belts, with a number of source-sink deposition systems. The analysis of its peripheral water system, topography and sedimentary facies can help fully understand the modern surface sedimentation dynamics in this area and can be regarded as a modern example of the dynamics of windfield-source-basin system.

## 3.1 Geographical and Geological Background

### 3.1.1 Geographical Location

Qinghai Lake is the largest inland plateau brackish lake in China. It is located in the northeastern part of the Qinghai-Tibet Plateau, and about 200 km southeast of the provincial capital of Qinghai Province, Xining City. The longitude of Qinghai Lake is between 99° 36′E to 100° 16′E and the latitude is between 36° 32′N to 37° 15′N.

The lake is surrounded by high mountains. To the north of the lake is the nearly E-W going Datong Mountain, whose

main peak's elevation is above 4200 m. To the east of the lake are mountain groups with N-NW strike, including Tuanbao Mountain (4025 m), Daban Mountain (4389 m), Riyue Mountain (4800 m) and Bison Mountain (4500 m). To the south of the lake is the NW-W extending South Qinghai Mountain. The South Qinghai Mountain can be divided into three sections from west to east. The western section consists of three parallel mountains, which are Cut-cross Daban (3500 m), Central Wunong Mountain (3800–4300 m) and North Chaka Mountain (4300–4700 m). These mountains extend westward, and become the watershed between the Qinghai Lake Basin and the Qaidam Basin. The middle section includes the Tawen Mountain, Hada Moutain and Longbaoqian Mountain (4200–4500 m), which is the watershed between the Qinghai Lake Basin and the Republic Basin to the south. The eastern section is the Gala Mountain (3800–4000 m), which forms the watershed between the Qinghai Lake Basin and the Guiyang Basin with the Bison Mountains (Fig. 3.1).

Qinghai Lake is about 106 km in the long-axis direction (near E-W), about 63 km in the short-axis direction (near S-N), and 3193–3198 m in elevation. The area of the lack is 4264–4473 km$^2$, and the circumference is about 360 km. The lake is nearly oval, with long axis ∼315° NWW. The average depth of the lake is 21 m, with maximum depth of 32 m, and water storage capacity of ∼100 billion m$^3$.

Qinghai Lake peripheral region has nearly 40 inland closed rivers, most of which are intermittent rivers (Lanzhou Institute of Geology, Chinese Academy of Sciences et al. 1979). The water systems are significantly asymmetric. The larger rivers are distributed in the west and north, such as the Buha River, Salix River, Quanji River, and Haergai River. The smaller rivers are distributed in the east and south, such as the Ganzi River, Daotang River, and Dark Horse River.

Buha River, which is originated from the Amu Niniku Mountain of the Qilian Mountains, is the largest river flowing into the Qinghai Lake. The total length of the river is about 300 km, with downstream width of 22 m and drainage area of 16,570 km$^2$. The Buha River flows into the Qinghai Lake from northwest to southeast, with annual runoff of nearly 1.1 billion m$^3$, accounting for more than 67% of the total runoff into the lake (Li et al. 2010). The Shaliu River, which is originated from the Sang Sizha Hill in Gangcha County, has a total length of about 106 km and drainage area of 1442 km$^2$. It flows from northwest to southeast into the Qinghai Lake (Li et al. 2010). The Haergai River lies on the northeast of the short axis of Qinghai Lake and is the third largest river in the region. The length of the river is about 100 km, the drainage area is about 1420 km$^2$, and the average flow is 7.67 m$^3$/s from northeast to southwest (Song et al. 2000; Li et al. 2010). Daotang River is located at the southeast edge of the Qinghai
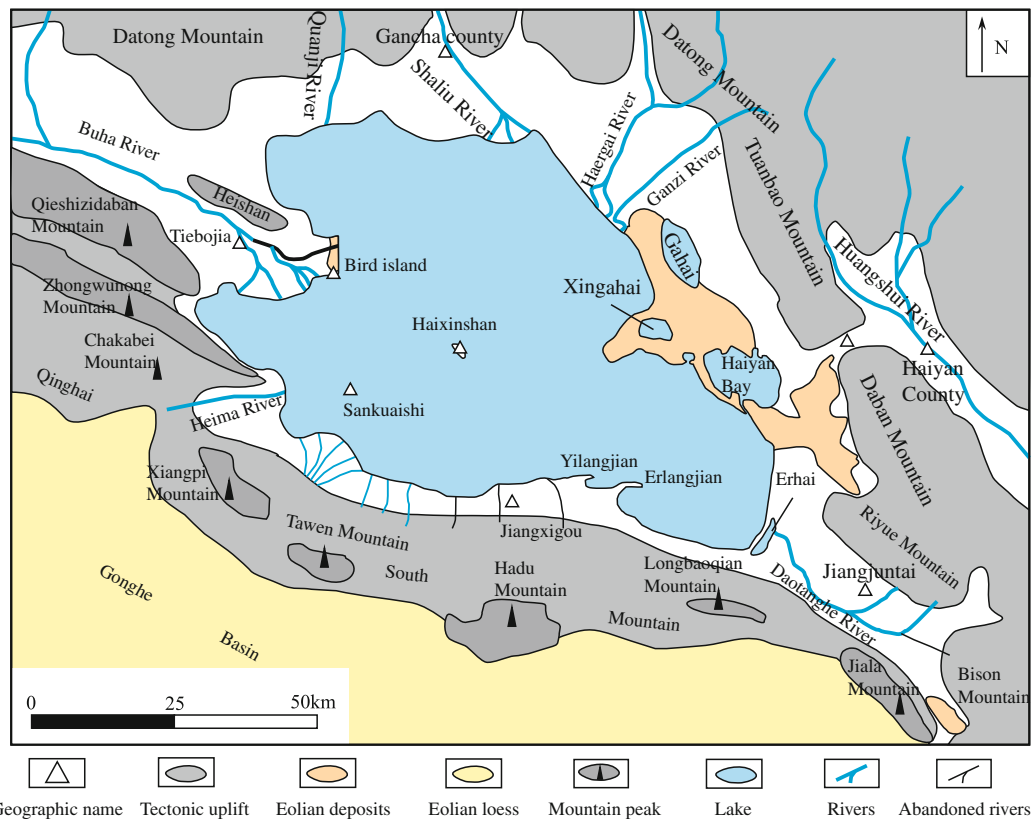


**Fig. 3.1** Geographical overview of Qinghai Lake

Lake's long axis and is the only river flowing from southeast to northwest in this area. Its source is snowmelt water from the Riyue Mountain and Bison Mountain. Therefore, this river is small and often seasonally dry.

There are three sub-lakes in the east of Qinghai Lake, which are Gahai, New Gahai, and Erhai. Gahai ($\sim$47.5 km$^2$) is located at the northeast of Qinghai Lake, in front of the Tuanbao Mountain area. Its long axis is near NW, about 12 km long, and its short axis is about 6 km wide. Gahai has water depth of 8–9.5 m. Its water is weak alkaline (PH $\sim$ 9.25), with relative density of 1.0229, and salt content of 31.734 g/l (Lanzhou Institute of Geology, Chinese Academy of Sciences et al. 1979). The Erhai is located in the southeastern margin of Qinghai Lake, with an area of about 8 km$^2$ and depth of 2–5 m. Its water has PH value of 9.52, relative density of 0.9983, and salt content of 1.393–0.896 g/l (Lanzhou Institute of Geology, Chinese Academy of Sciences et al. 1979). The New Gahai was formed by the closure of sand islands in the recent 20 years and has an area of $\sim$ 4 km$^2$.

## 3.1.2 Climate of Qinghai Lake

Qinghai Lake has a typical arctic continental climate. Although the lake body has a role in regulating the temperature, the Qinghai Lake area is characterized by large seasonal temperature differences, low precipitation, hot rainy season, and clear wet and dry seasons (Lanzhou Institute of Geology, Chinese Academy of Sciences et al. 1979; Li et al. 2008). The average temperature increases in the Qinghai Lake area are greatest in the south, and become less significant successively from the east, west to north. The average temperature increase in autumn and winter is greater than that in spring and summer (Yan et al. 2011). Since the 1970s, the humidity of Qinghai Lake has been declining obviously (Xu et al. 2007; Wang et al. 2003). The climate warming has led to increased evaporation and decreased water level (Shi et al. 2005; Liu et al. 2008; Chen et al. 2011). The climate warming also led to severe desertification in the Qinghai Lake area, with obvious grassland degradation, reduced river flow and decreased lake water level (Li et al. 2002).

The Qinghai Meteorological Bureau collected meteorological data (monthly average temperature, average relative humidity, most common wind direction, average wind speed, precipitation and evaporation) from two adjacent representative stations (the Gangcha station to the north and the Jiangxigou station to the south). Meteorological data were collected by the Gangcha station from 1961 to 2015, and collected by the Jiangxigou station from 1956 to 1962 and 1974 to 1997. In addition, wind direction frequency data of relevant years were collected by the Tiebaijia and Haiyan stations (Shen and Yu 2007). The specific locations of the four meteorological stations are shown in Fig. 3.1.

According to the 1961–2013 meteorological data from the Gangcha station, the average temperature of Qinghai Lake is −11.5 °C in winter, 10 °C in summer, and around 0 °C in spring and autumn. Based on the overall trend, the temperature in the Qinghai Lake area has gradually increased over time. The rise in temperature is most obvious in winter. The seasonal precipitation in this area is uneven, which is lowest in winter (only 1 mm on average) and highest in summer (84 mm on average). In the past 50 years, the precipitation gradually increased in summer, and tended to be stable in winter. The wind speed in this area is relatively uniform, with slightly higher wind speed in spring. The wind speed in this area has decreased gradually from $\sim$4 to 3.5 m/s in the past 50 years.

According to the wind direction data from the four stations around the lake, the annual wind frequency is calculated and the wind speed rosette is plotted (Fig. 3.2). The Gangcha station is dominated by north wind, mainly due to the influence of planetary wind system (north wind). The Jiangxigou station is dominated by south wind, mainly due to the influence of Qinghai Lake and South Qinghai Mountain. The Tiebojia station is prevailed by NWW wind, which is largely constrained by the narrow vally of the Buha River. The Haiyan station is located in a valley, and is dominated by NW and SE wind (valley wind) as the result of terrain constraints.

In turns of annual climate, during 1974–1997, the monthly mean humidity of the Jiangxi station was 57%, the
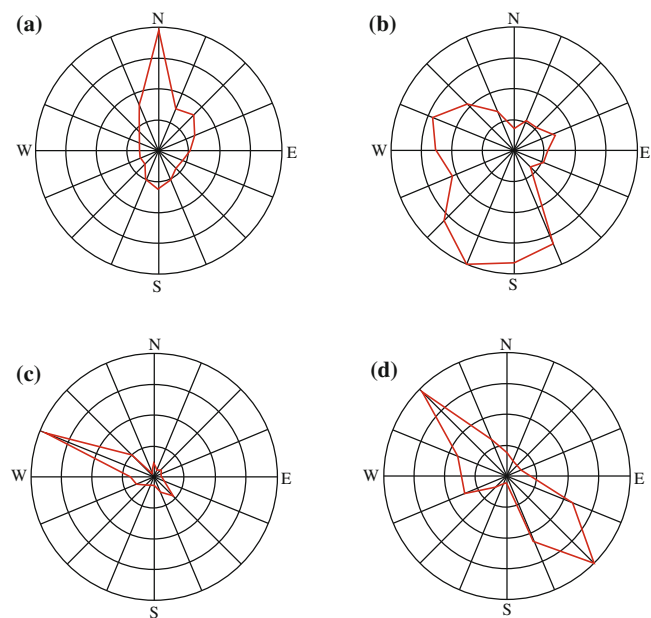


**Fig. 3.2** Annual wind direction frequency rosettes of four meteorological stations around Qinghai Lake. **a** Gangcha station; **b** Jiangxigou station; **c** Tiebaijia station; **d** Haiyan station; the locations of the stations are shown in Fig. 2.1

**Fig. 3.3** Comparison of monthly
mean meteorological data of
Gangcha and Jiangxigou stations.
**a** Monthly mean temperature;
**b** monthly mean humidity;
**c** monthly precipitation;
**d** monthly evaporation
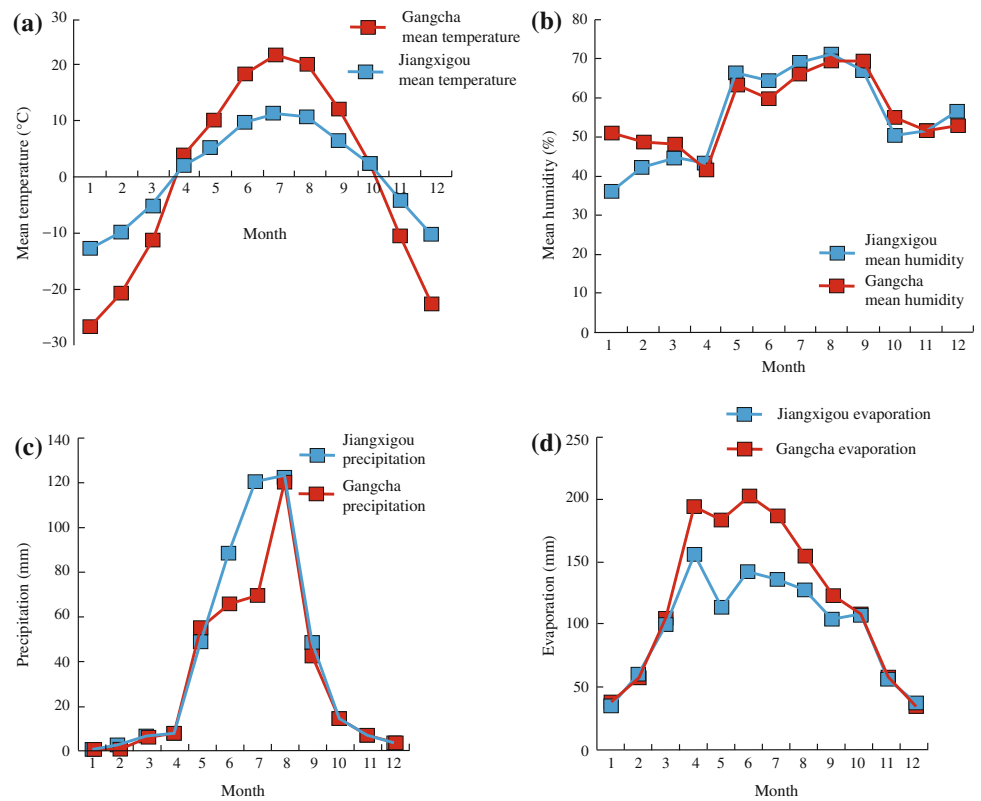


monthly mean precipitation was 34.87 mm, and the monthly mean evaporation was 113.4 mm. The monthly mean humidity of the Gangcha station was 54%, the monthly mean precipitation was 31.81 mm, and the monthly mean evaporation was 120.4 mm. The results show that Gangcha has less precipitation, more evaporation, and lower humidity, reflecting the south coast is more humid than the north shore.

In order to compare the climate of Gangcha and Jiangxigou in the same time period, we compare monthly meteorological data from January through December, in order to find the correlation between the two. From April through October, the monthly mean temperature of Gangcha is higher than that of Jiangxigou. From October through April, the monthly mean temperature of Gangcha is lower than that of Jiangxigou. Overall, the annual temperature variation at Gangcha is greater than that at Jiangxigou (Fig. 3.3a). From April through December, the monthly mean humidity of Gangcha is slightly higher than that of Jiangxigou. From April through December, the monthly mean humidity of Gangcha is not much different from Jiangxigou. Both Gangcha and Jiangxigou have an abrupt change in monthly mean humidity, mainly due to the whole Qinghai Lake entering rainy season (Fig. 3.3b). From August through May, the monthly precipitation of Gangcha and Jiangxi are basically the same. From May through August, the monthly precipitation of Jiangxigou is significantly higher than that of

Gangcha (Fig. 3.3c). These features indicate more precipitation in the southern part of Qinghai Lake than in the northern part during summer time (rainy season). From October through March, the monthly evaporation of Gangcha was basically the same as that of Jiangxigou. From March through October, the monthly evaporation of Gangcha was significantly higher than that of Jiangxigou (Fig. 3.3d). Due to the different topography of the north and south coast, Jiangxigou is closer to Qinghai Lake than Gangcha. Therefore, the lake effect is more significant at Jiangxigou, reflected in a smaller temperature difference and more precipitation.

### 3.1.3  Hydrology of Qinghai Lake

The main hydrological characteristics of Qinghai Lake lie in the change of the lake level. Looking for the changes of lake level in recent decades is favorable to the study of modern sediments. We collected the annual mean absolute elevation of the lake surface from 1959 to 2013 at the Hydrometric Station of Qinghai Lake, which belongs to the Water Authority of Qinghai (Fig. 3.4). From 1959 to 2004, the water level of Qinghai Lake decreased from 1959 to 2004, and increased from 2005 to 2013. The water level was 3196.57 m above sea level in 1959, and 3193.61 m above sea level in 1988. There was a 2.96 m decrease in water

**Fig. 3.4** Variation of the water level of Qinghai Lake (1959–2013)
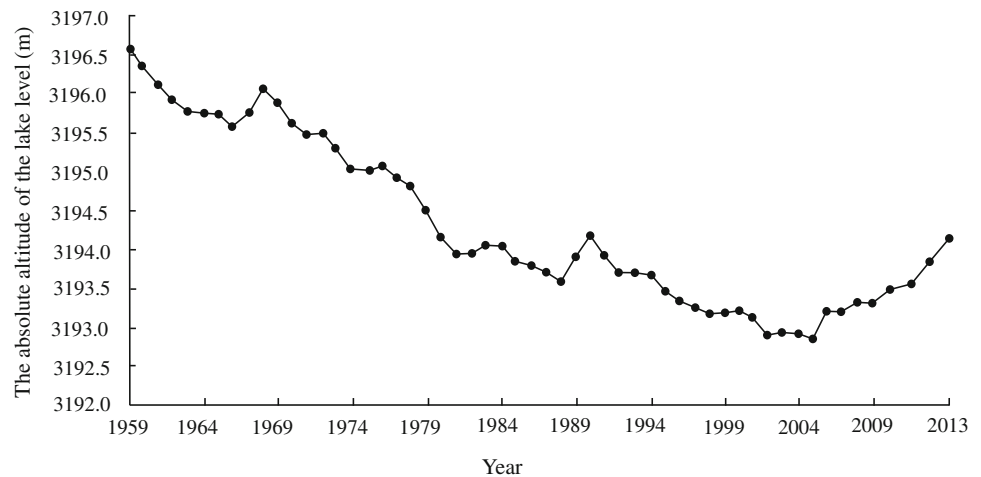
level from 1959 to 1989. The water level was 3194.3 m in 1990, increased by 0.69 from 1988 to 1990 (0.345 m/a). The water level in 2005 was 3192.79 m, and the water level decreased by 1.51 m in 15 years from 1990 to 2005, with an average decrease of 0.1 m/a. In 2013, the water level was 3194.26 m, and the water level rose by 1.47 m in 7 years from 2005 to 2013, with an average increase of 0.21 m/a.

From 1959 to 2013, the main features of the lake water level change can be divided into two major stages: the stage of water level decline from 1959 to 2005 and the stage of lake water level rise from 2005 to 2013. In the 46 years from 1959 to 2005, the lake water level declined in 35 years, accounting for 76% of the total number of years. The lake water level rose in 11 years, accounting for 23.9% of the total number of years. The water level remained unchanged for only 3 years. Meanwhile, there have been two periods of relatively significant rise in water level: 1966–1968 and 1988–1990. The greatest rise in water level was 0.43 m/a during 2005–2013. By 2013, the water level has been restored to the same level as in 1990. Therefore, the water level of Qinghai Lake is not always a downward trend, but the overall trend is decreasing, with small increases in between.

### 3.1.4 Stratigraphy of Qinghai Lake Basin

The main lithology of mountains surrounding Qinghai Lake is volcanic and metamorphic rocks (Fig. 3.5). The Lower Paleozoic low-grade metamorphic rocks and granites are exposed in the northern part of Datong Mountain (north of the Buha Valley). The strata west of Gangcha are mainly composed of Mesozoic sandstone and shale, whereas the strata exposed on the eastern side are pre-Sinian and Sinian metamorphic rocks (Lanzhou Institute of Geology, CAS 1979). Riyue Mountain on the eastern side of the lake is primarily composed of pre-Sinian geniss, granite and

granodiorite. South Qinghai Mountain on the southern side is mainly composed of Permain and Triassic limestone, metamorphic sandstone, slate, granite and diorite (Lanzhou Institute of Geology, CAS 1979).

Quaternary sediments are well developed in the Qinghai Lake Basin, mostly lacustrine (Fig. 3.5). Middle-lower Pleistocene Hadatan Formation, Upper Pleistocene Erlangjian Formation and Holocene Buhahe Formation are developed from the bottom up (Qinghai Geology and Mineral Resources Bureau 1991).

(1) Hadatan Formation: Based on the 16-hole profile of Qinghai Lake in Gonghe County, the Hadatan Formation can be divided into five layers. The bottom layer is khaki-colored clay breccia (up to 25 m thick), which is overlaid by a layer of brown, light gray, yellowish green silty clay with median-coarse grained lenticular sand body and manganese nodules (24 m). Then there is a layer of light gray, yellowish green, brownish yellow muddy sand loam with clay (53 m), overlaid by a layer of slightly-red loess sand loam with loess silt and gravel (up to 130 m thick). On the top is a layer of khaki loess silt with silt containing gravel (less than 10 m thick). Because the Hadatan formation contains loess, it was also known as the Leigonghe Loess Formation (Qinghai Geology and Mineral Resources Bureau 1991). The underlying strata are the strata of Lower Silurian, and the contact relationship is angle unconformity. Gastropods, ostracods, sporopollen and other fossils are abundant in this formation. The most abundant gastropods are *Valvata aff. Pulchellula*, *Pupilla cf. muscorum*, and *Succinea* sp. Ostracods are mainly *Limnocythere dubiosa*, *Candona neglecta*, *Eucypris inflata*, *Ilyocypris bradyi*, and *Candoniella* sp. Pollen accounted for 74.4%, Liliaceae accounted for 15.6%, Allium accounted for 24.6%, Leguminosae accounted for 33.6%; woody plant pollen accounted for

**Fig. 3.5** Stratigraphy of Qinghai Lake. Modified from the Lanzhou Institute of Geology, CAS 1979



| System | Series | Stage | Lithology | Palaeontology description | Age (Ma) |
|---|---|---|---|---|---|
| Quaternary | Holocene | Buhahe Formation | | Transition from the forest period to the grassland period. The forest only contain Pinus, Pieea Dietr and Populus. The herbage is composed of Chenopodiaceae, Leguminous and Artemis, indicating climate changes from warm and wet to cold and dray. Then herbages are dominant plants, which are composed of Gramineae, Chenopodiaceae, Asteraceae, Leguminosae and Salix, indicate a dry climate | |
| | | Erlangjian Formation | | Forest type vegetation. The vegetation is dominated by woody plants, which is composed of Pinus, Cupressaceae, Juglans, Betula. The understory herbaceous plants are dominated by Allium, Chenopodiaceae, and Compositae, reflecting a warm and humid climate. The flora in the Upper part of ErlangJian Formation is dominated by Pinus, indicating a cool and humid climate. | 0.0117 |
| | Pleistocene | Hadatan Formation | | Forest and grassland are mainly composed of Lily Branch, Leguminosae, Walnut, Quercus etc., reflecting a humid climate at that time. The Upper part of Hadatan Formaiton is dominated by Pieea Dietr, Quercus and Artemisia, suggesting climate had changed to cold, but humid climate remained. | ? |

Sandy gravel | Gravelly sandstone | Sandstone | Siltstone | Silty mudstone | Muddy siltstone | Transition layer | Mudsonte | Reddish loess layer | Loess layer

17.3%, of which Populus (*Populus davidii*), Polypodiaceae Accounting for 5.2%, Salix 6%, Juglans 1.5%, Quercus accounted for 3.7%. In the top of this group, there were pollen assemblages dominated by Pinaceae pollen, and nearly Picea accounted for 78.8%. Herbaceous pollen accounted for only 6.1%, composed of leguminous pollen and Artemisia (Yang and Jiang 1965). The Hadashan flora was dominated by forest herbaceous plants, which reflected the temperate climatic conditions at that time. The upper flora was dominated by spruce, indicating that the climate was once cool and overall still humid.

(2) Erlangjian Formation: Erlangjian Formation deposits (74–102 m thick), including slit, muddy slit, sandy mud and gravel layers, are widely distributed in the lake area. Based on the Qing 5-hole drilling profile, the Erlangjian Formation can be divided into 3 layers. The bottom layer contains grey-yellow sandy layer with gravel, fine gravel layer with loess, silt and muddy silt (22 m). The middle layer is blue-gray silty mud with silt (40 m). The top layer is light gray-green muddy siltstone with mud and conglomerate (12 m) (Qinghai

Geology and Mineral Resources Bureau 1991). The underlying strata are Hadashan Formation, with unconformity contact. The Erlangjian Formation is rich in sporopollen, of which woody plant pollens account for 53.8% (17.1% are *Populus*, the rest are *Picea*, *Pinus*, *Alnus*, *Pinaceae*, *Cupressaceae*, etc.), herb pollens account for 40.2% (18% are *Potamogeton*, the rest are *Artemisia*, *Ephedra*, *Lathyrus*. *Chenopodiaceae*, *Urticaceae*, *Compositae*, etc.), and Fern spores account for 6% (mainly *Pteris* and *Polypodiaceae*). The presence of *Potamogeton* and *Sophora Japonica* indicates that the lake water is fresh. The vegetation of the Erlangjian Formation is primarily forest based, dominated by woody plants and followed by herbs, indicating cool and humid climate conditions (Yang and Jiang 1965).

(3) Buhahe Formation: The Buhahe Formation is dominated by lacustrine sediments followed by alluvial sediments, and is distributed in the modern Qinghai Lake and the Buhe River estuary. Alluvial sediments are mainly distributed along the Buhahe River valley ($\sim 4$ m), with gravel layer in river bed, and floodplain dominated by

grayish yellow fine sand with silty clay. The lacustrine sediments are mainly gray-black silt and mud silt with a small amount of silty mud or fine sand, with coarser particles farther away from the lake center (thickness varying from 2 to 24 m). Drilling program reveal the presence of aorta loess in Holocene strata at the lake bottom. The aorta loess is mostly grayish yellow medium-fine grain sand, with good sorting and unknown thickness (Qinghai Geology and Mineral Resources Bureau 1991). The sporopollen content in the Buhahe Formation is significantly lower than that in the Erlangjian Formation. Pollens of woody plants account for 48% of the sporopollens in the lower formation (predominately *Populus*, *Salix*, *Pinus*, *Picea*), herb pollens account for 28% (predominately *Artemisia*, *Leguminosae*, *Chenopodiaceae*), and spores of ferns increase to 24% (predominately *Polypodiaceae*). Herb pollens is up to 95% in the upper formation (predominately *Chenopodiaceae*, *Compositae*, *Ephedra*, *Asparagus*), with a small amount of pollens of woody plants (predominately *Salix*). Unfossilized ostracoda, including *Limnocythere dubiosa*, *Eucypris inflata*, *Ilyocyris bradyi* etc., is present in the lacustrine sediments in this formation (Yang and Jiang 1965). The vegetation of the Buhahe Formation has changed from forest vegetation to grassland vegetation. In the early days, the amount of woody plants deceased significantly, whereas the amount of herbaceous plants increased slightly, indicating the climate changed from warm and humid to dry and cold. Subsequently, herbaceous plants predominated, with a very small amount of shrubs, but lack arbor species, consistent with dry weather conditions.

### 3.1.5 Structural Features and Evolution of Qinghai Lake Basin

Qinghai Lake is surrounded by mountains, with three levels of flattening (Chen et al. 1964), indicating several large intermittent uplift in the new tectonic period of the lake. Previous studies suggest there are 3 uplifts (Datong Mountain, Tuanbao-Riyue Mountain and Qinghai Nanshan), 3 grabens (Ganzihe-Huangshi, Buhahe and Daotanghe), and Qinghai Lake fault basin (Fig. 3.6a; e.g., Lanzhou Institute of Geology, CAS 1979; Bian et al. 2000). The Qinghai Lake fault basin can be divided into Heishan-Haixinshan horst, Shankuaishi horst, Erlangjian horst, north slope, south depression, and southeast depression, which are affected by the fault zone at the southern margin of the Middle Qilian Mountains, Zonglongshan-Qinghai Nanshan fault zone and Heimahe-Dari fault (Fig. 3.6b). The stratigraphic structure of

the lake basin is formed by the normal fault. Deep water area (>20 m) in lake center accounts for 56.5% of the total lake area (Lanzhou Institute of Geology, CAS 1979). The main axis of the lake is parallel to the main fracture structures in the region (NNW-NW-NWW), and the edge is controlled by the secondary fault of "X", with diamond-shaped outline.

The formation and development of the Qinghai Lake Basin has undergone the following three periods:

(1) Late Tertiary (Miocene): The second orogeny of the Himalayas during late Tertiary has caused strong block differential uplift and subsidence movements in this area, resulting in mountain uplift and basin decline, and formation of the prototype of the lake basin (Chen et al. 1964).

(2) Early to middle Quaternary: The third orogeny of the Himalayas during late Pliocene to early Quaternary caused another block strong differential uplift and subsidence movements in this area. The Qinghai Lake Basin further subsides, and the Qinghai Lake became a "crossing lake" in ancient Buhahe-Daotanghe River (ancient Buhahe River passed through ancient Daotanghe River and then emerged into ancient Yellow River), where thick fluvial-lacustrine sediments were deposited (Wang and Shi 1992).

(3) Late Quaternary: During middle-late Pleistocene, the Qinghai Lake was fully developed. In late mid-Pleistocene, the flow direction of Daotanghe River reversed, due to the rapid rise of Riyue Mountain and Bison Mountain, cutting off the channel of Buhahe River flowing into Yellow River. Qinghai Lake continue to sink, and ultimately formed a closed inland lake (An et al. 2006). The block differential uplift and subsidence movement intensified during Late Pleistocene. Heishan Mountain, which was an underwater hill, was lifted out of the water and became an island. Bird Island, Haixin Mountain, and Jiangjuntai on the southeast extension of the Heishan Mountain were also raised during this period (Lanzhou Institute of Geology, CAS 1979). Meanwhile, the horst zone in the middle of the lake basin also began to form, and the deepest fault zone of the lake basin appeared on the north and south sides of the horst zone. Since Holocene, as the mountains further uplifted and the climate became increasingly dry, the area of the lake reduced and water level decreased (Zhang et al. 1988). At this time, the lakeside terraces continue to rise, and lake islands increased in numbers and became connected with the land. For example, Heishan Mountain and Jiangjuntai became lakeside mountains, Bird Island and Buha Delta connected to be a peninsula, Sand Island connected with sand dunes on the east coast.

**Fig. 3.6** **a** Tectonic map of Qinghai Lake. **b** N-S cross section of Qinghai Lake. Modified from the Lanzhou Institute of Geology, CAS 1979
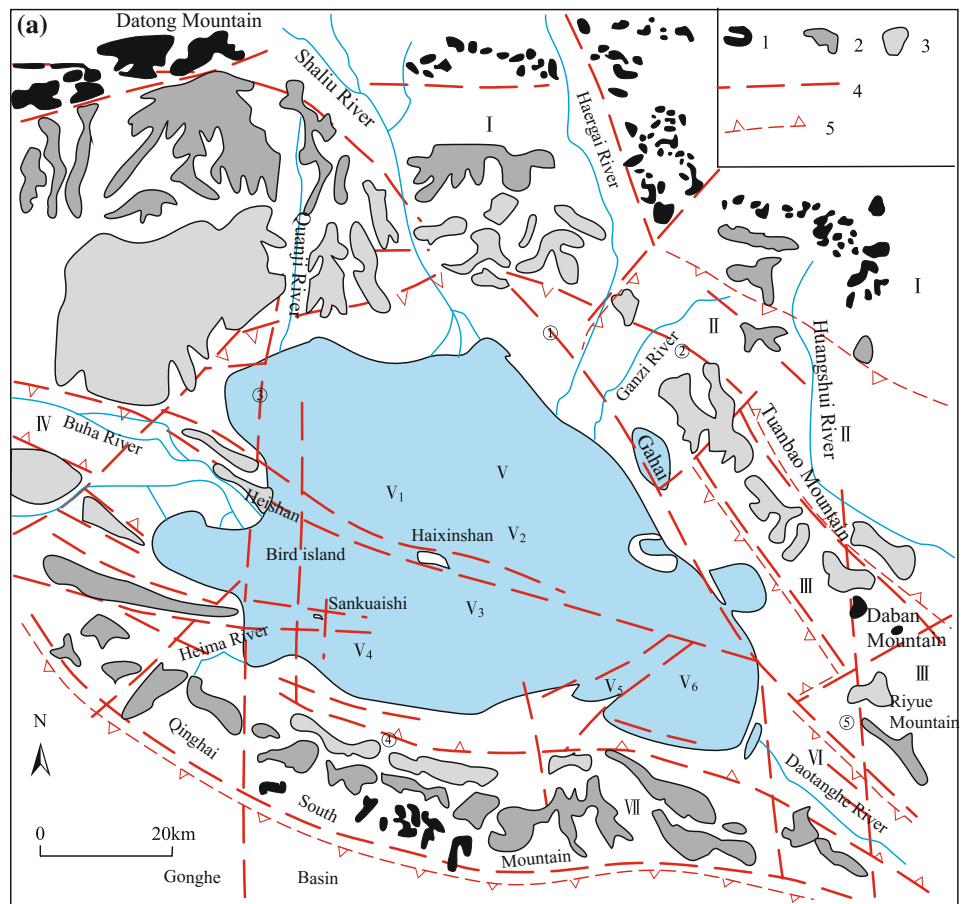


1- Level I planation surface      2- Level II planation surface      3- Piedmont denudation surface      4- Fault

5- Boundary of uplift            I - Datongshan Mountain uplift        II- Ganzi River–Huangshui graben

III- Tuanbao Mountain–Riyue Mountain uplift    IV- Buha River granben      V- Qinghai Lake rift basin

V1- Northern secondary rift basin       V2- Heishan –Haixinshan horst       V3- Southern secondary rift basin

V4- Sankuaishi horst       V5- Erlangjian horst       V6- Southeastern secondary rift basin       VI- Daotang River graben

VII-Qinghai South Mountain uplift    ① Fault system in southern margin of middle Qilian block

② Laji Mountain fault system       ③ Heima River–Dari fault belt       ⑤ Haiyan–Nianbaoyuze fault belt

④ Zongwulong Mountain–Qinghai South Mountain fault belt
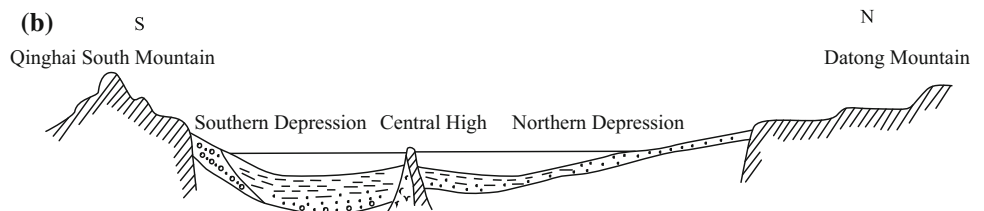


## 3.2  Modern Sedimentary System of Qinghai Lake

The core of the "source-sink" sedimentary system is to establish a sedimentary system from the source region to the sedimentary area. "Source-sink" system is to reveal the processes of sediment formation, transportation, and deposition. According to the topographic features, lithology characteristics, water features and sedimentary characteristics of Qinghai Lake and its surrounding areas, six different sedimentary dynamic processes from the source area to the sedimentary area are identified, so there are six "source-sink" sedimentary systems and one lake sedimentary system. The

**Fig. 3.7** The observation points of Qinghai Lake and the distribution of "source to sink" systems
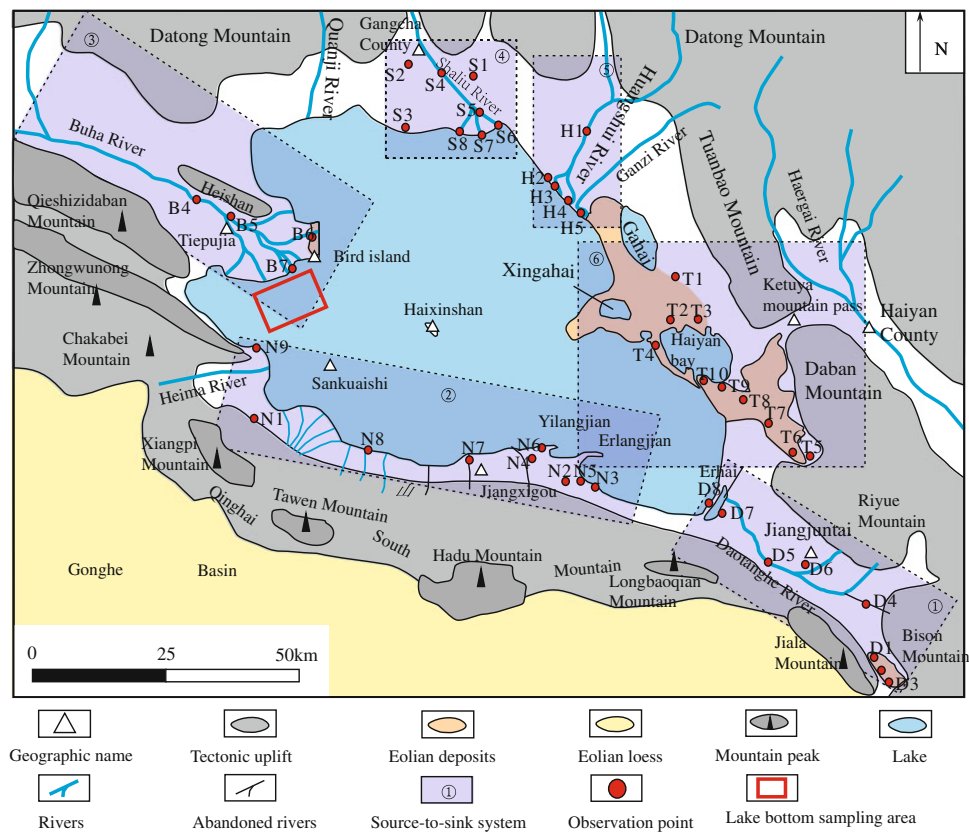


six "source-sink" sedimentary systems are the Riyue/Bison Mountain–Daotanghe River–barrier island depositional system (① in Fig. 3.7), the Qinghai Nanshan–alluvial fan–fan delta/coast depositional system (② in Fig. 3.7), the Buha River–delta depositional system (③ in Fig. 3.7), the Datongshan–alluvial fan–fan delta/braided river-meandering river delta depositional system (④ in Fig. 3.7), the Haergai/Ganzi River–barrier island depositional system (⑤ in Fig. 3.7), and the Tuanbao/Daban Mountain–alluvial fan/coast–wind depositional system (⑥ in Fig. 3.7). Through the field investigation of the observation points shown in Fig. 3.7, it was found that the six "source-sink" depositional systems all have their own source and sedimentary facies features. We will take the first two depositional systems as examples and discuss them in detail below.

### 3.2.1 The Riyue/Bison Mountain–Daotanghe River–Barrier Island Depositional System

The Daotanghe River is located at the southeastern margin of the Qinghai Lake Basin. Back to 1938, Sun Jianchu proposed that Daotanghe River changed flow direction and Qinghai Lake became an inland lake as the results of eastern terrain rise and western subsidence (Sun 1938). Many later studies also agree with this interpretation, and further

suggested that the ancient Daotanghe changed to its present form due to the uplift of Qinghai Nanshan Mountain, Riyue Mountain and Bison Mountain during late mid-Pleistocene or early late-Pleistocene, which blocked the eastern outlet of ancient Qinghai Lake (Chen et al. 1964; Yuan et al. 1990; Pan et al. 2004; An et al. 2006). As the regional climate became warmer and drier, the last shrinking of lake area during late Holocene has led to the formation of an ancient bank which separated the Qinghai Lake and Erhai (∼2600 years ago; Lanzhou Institute of Geology, CAS 1994). Recently, Zhang et al. (2010) applied satellite remote sensing data to study the ancient channel and lake facies distribution, and proposed that strong tectonism (∼0.1 Ma) led to the uplift of Riyue Mountain. This process, combine with the arid climate during the last glaciation, makes the ancient river cannot further cut into the uplift, and Qinghai Lake was gradually separated from the ancient Yellow River.

#### 3.2.1.1 The Source Characteristics of Eastern Riyue Mountain, Bison Mountain, and Easter Qinghai Nanshan

Eastern Riyue Mountain and Bison Mountain are source area of the present Daotanghe River. The ancient W-E Daotanghe River valley is located between Qinghai Nanshan and Riyue-Bison Mountain.

The rock mass in eastern Riyue Mountain is mainly granite formed in the late stage of Hualixi. The rock assemblages are granite, biotite granite and two-mica granite, which are exposed as irregular oval batholith. The long axis direction of the rock mass is NW-SE, which is basically the same as the regional tectonic lineament (Qinghai Geology and Mineral Resources Bureau 1991). The rock mass of the Bison Mountain is mainly gray to grayish green calcareous siltstone and silty slate, with limestone and a small amount of conglomerate of Middle Triassic ages (Qinghai Geology and Mineral Resources Bureau 1991).

The lithology of the rock mass in eastern Qinghai Nanshan is more complicated. The rock mass in the Longbao Mountain area on the northern side of the eastern Qinghai Nanshan is mainly Lower Silurian clastic rock, whereas the western side is granite formed during late Indosinian. Lower Triassic strata are exposed to the east of Jiala Mountain at the southern side of the eastern Qinghai Nanshan Mountains. The lower part is dominated by dacite and rhyo-dacite, with some slate and phyllite. The middle part is dominated by conglomerate, sandstone, intermediate-basic igneous rock, breccia, and volcanic tuff. The upper part is dominated by conglomerate, sandstone, tuffaceous sandstone, slate and crystalline limestone (Qinghai Geology and Mineral Resources Bureau 1991) (Fig. 3.8). Now there is no surface water at eastern Qinghai Nanshan, where many riverside terraces of ancient Daotanghe River are observed (Zhang et al. 2010).

The eastern Riyue Mountain located on the north side of the Daotanghe River valley is arc shaped (convex facing the valley). The Bison Mountain is located at the southeastern end of the river valley, and separated from the Riyue mountain by a mountain pass and from the eastern Qinghai Nanshan by Langma Shegang sand area. The arc-shaped eastern Qinghai Nanshan is located on the south side of the river valley, which is symmetrical with the Riyue Mountain (convex facing the valley). Based on remote sensing images, the highest peak of Riyue Mountain is up to 4800 m, the highest peak of Bison Mountain is up to 4500 m, and the highest peak of eastern Qinghai Nanshan is up to 3500 m. The area above the snow line is much larger at the Riyue Mountain than the latter two, which is the main reason why the present water source of the Daotanghe River is mainly Riyue Mountain. The entire river valley is higher to the northeast and lower to the northwest, which causes the present river locating on the west side of the valley (Fig. 3.8).

The average annual precipitation in the study area is 300–350 mm, and the average annual evaporation is 900–1000 mm. The average annual evapotranspiration is higher than the average annual precipitation, consistent with arid climate condition.

Nowadays, Daotanghe River is mainly sourced from Riyue Mountain and Bison Mountain. However, due to the dry climate and the decrease of rainfall, water from Bison Mountain is almost dried up, leaving only water supply from Riyue Mountain. This climate change has not only resulted in a reduction in the runoff of the present Daotanghe River, but also caused a significant reduction in vegetation coverage. The lack of vegetation on the surface has caused the revival of many ancient sand dunes at the valley plain, making this area one of the major desertification areas around the Qinghai Lake (Yao et al. 2015).



**Fig. 3.8** The location of Riyue/Bison Mountain–Daotanghe River–barrier island depositional system. D1, D2, D3, and D6 are the preserved ancient Daotanghe River deposition
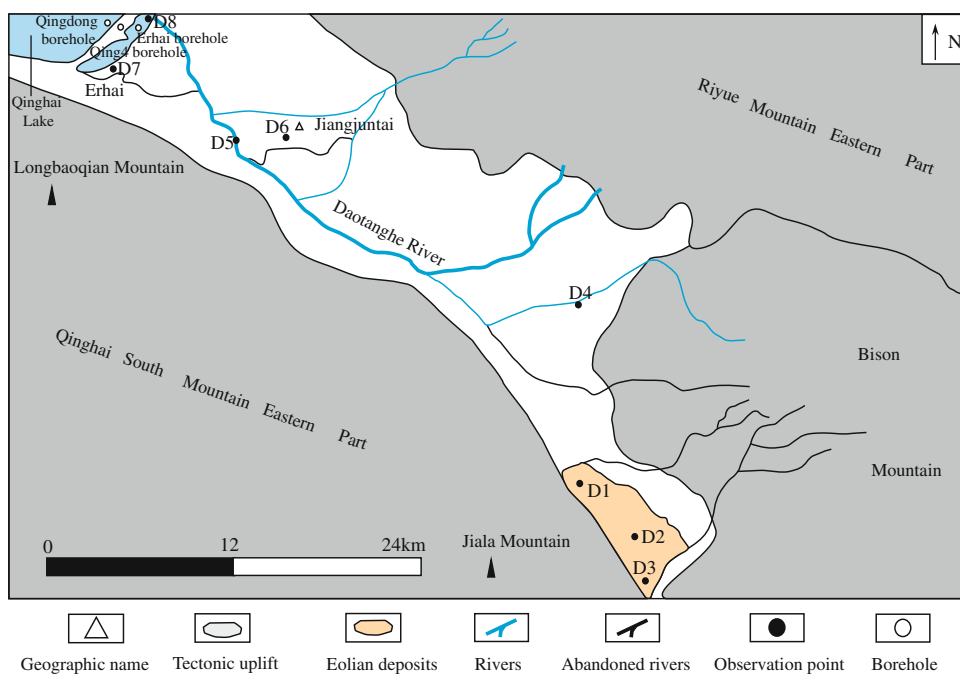
### 3.2.1.2  Ancient Daotanghe River

As mentioned earlier, the late Pleistocene period was the main uplift period of the Riyue Mountain, Bison Mountain and Jiangjuntai, and also the most important evolution period of the Daotanghe River valley. In this study, two residual deposits of ancient Daotanghe River were found at the watershed of Daotanghe and the foot of Jiangjuntai. The flow direction of the ancient river is from northwest to southeast. Field work suggests that the residual deposition of the ancient river is only present in the southeastern margin of the ancient river valley (observation points D1, D2 and D3).

The lower part of the section of the observation point D1 is sediments from the ancient Daotanghe River. Low angle cross bedding suggests the flow direction was from northwest to southeast (Fig. 3.9a), and the upper part is Holocene eolian sand deposits. The observation point D2 section is Holocene eolian loess deposits, rich with sub-angular to angular gravels (Fig. 3.9b). It is speculated that after the backflow of the ancient Daotanghe River, the increasingly warm and dry climate led to the accumulation of a large amount of eolian sand and loess on top of the ancient river deposits.

From bottom to top of the section at observation point D3, the gravel layer is gradually thinned, the lenticular sand layer gradually thickens, and grain size decreases (Fig. 3.10). The lithology of fluvial sediments is dominated by gravel and medium-coarse sand. The gravel layer has imbricate structure, with gravel diameter varying from 4 to 50 cm. By measuring the maximum flat surface of the gravels, the dip angle of the gravels is mostly 280°–310°, with dip angle of 30°–40°. Most gravels are granite. The lithology of the Bison Mountain and southern Qinghai Nanshan is Triassic clastic rock, which is inconsistent with the fluvial gravel deposits. Granite is exposed in middle (Erlangjian–Jiangxigou) and northern (Buha River valley) Qinghai Nanshan and Riyue Mountain. Therefore, the fluvial gravel deposit most likely derive from ancient Buhahe River valley or the northern bank of ancient Daotanghe River. At the top of the fluvial sediments there is a gravel layer of about 50 cm thick, which is in abrupt contact with the overlying eolian loess.

Jiangjuntai is located at the bottom of the ancient Daotanghe River valley. The local cinerous and brown strata was interpreted as late Pleistocene lacustrine gravel and gravel-bearing sand layers (Zhang et al. 2010). However, this study suggests this area is actually a set of late Pleistocene alluvial fan deposits formed due to the uplift of the Jiangjuntai block.

Accompanied by the differential uplift of the Jiangjuntai and Riyue Mountain, a series of alluvial fans were formed along the mountains. Observation point D6 is at Daotanghe sand mining field to the northwest of Jiangjuntai. The section examined in this study is 800 m away from Jinagjuntai. The top of Jiangjuntai is about 3354 m above sea level and the bottom is about 3274 m above sea level. The elevation of examined section is about 3264 m. Based on the vertical profile elevation map of the alluvial fan, the alluvial fan can be divided into two parts: the upper part is close to the foothills of the Jiangjuntai, with huge slope; the lower part has gentle slope (Fig. 3.11). The can be divided into three parts section from bottom to top.

Lower section: This section is dominated by frequent interbed of fine sand and silty mud (Fig. 3.12a). The thickness of fine sand layers is generally about 8–10 cm, with brown color. Silty clay layers are generally about 2–4 cm thick, with reddish brown color generated by surface oxidation.

Middle section: According to the roundness and composition analyses of middle section sediments, the alluvial fan contains about 74% gravel and 25% sand. The gravels are mainly sub-round (41%) and sub-angular (32%), with some angular (19%) and round ones (8%). This indicates that these sediments is formed by temporary water flow. The gravels are mostly metamorphic rocks ($\sim 87\%$). The most significant sedimentary structures is foreset cross bedding in single bedset, and the foreset cross bedding has an obvious tendency of upward convergence (Fig. 3.12b). The gravels are clearly oriented with dip angle varying between 30° and 40°, which decreases towards southeast (Fig. 3.12c). These features suggest that under the influence of intermittent rivers, gravel deposits spreaded rapidly after entering the topographic low area.

**Fig. 3.9**  **a** Field picture of observation point D1. **b** Field picture of observation point D2
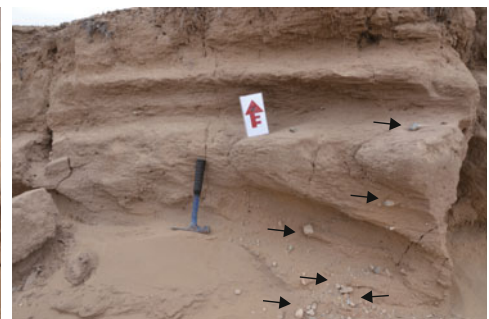


(a) Observation point D1                         (b) Observation point D2
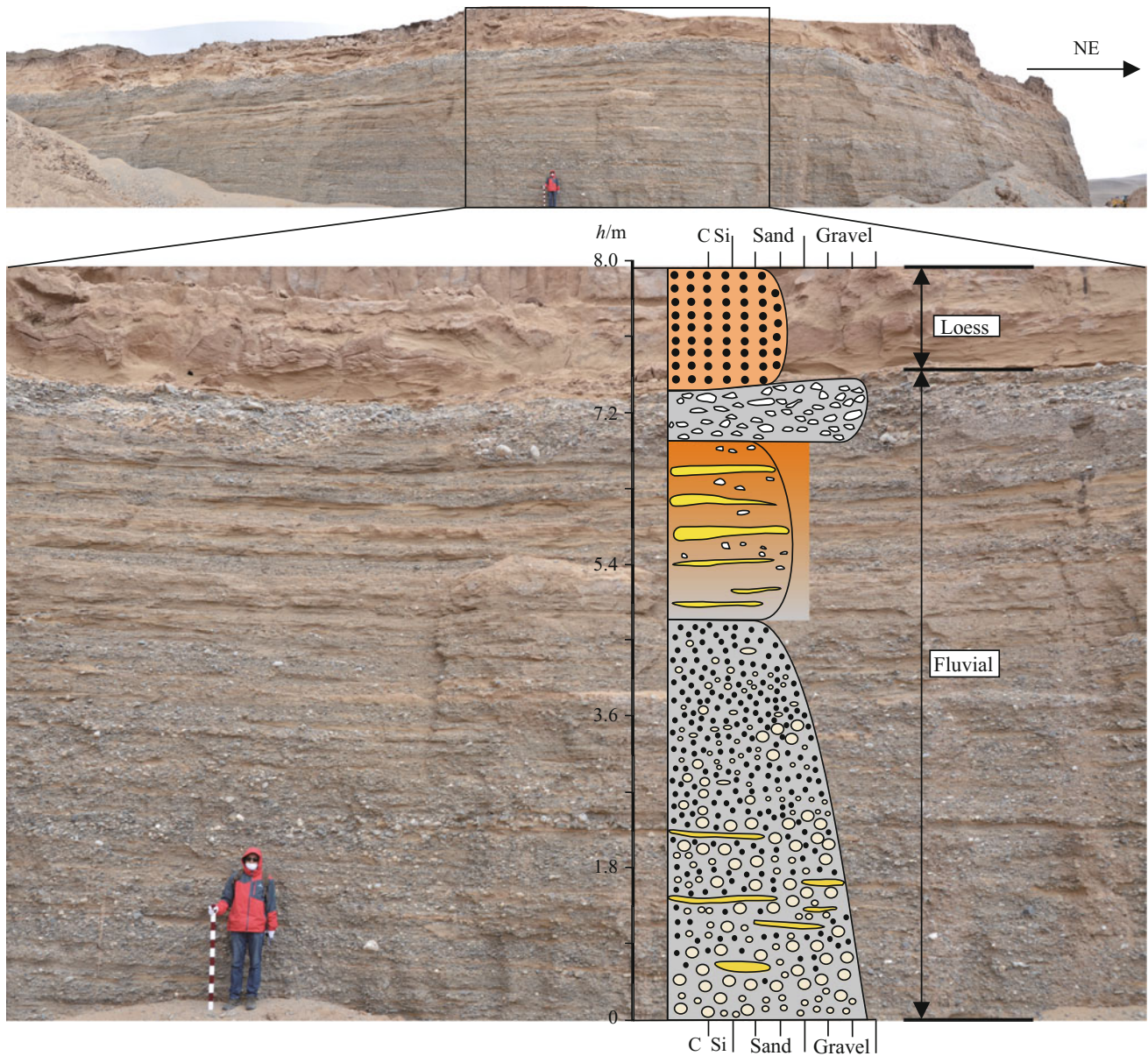
**Fig. 3.10** The cross section of ancient Daotanghe River deposition at observation point D3

Top section: The type and composition of gravels are more complicated. Gravels are mostly parallelly aligned, with medium sorting (Fig. 3.12d). The gravel layer appears alternately in the vertical direction, with varying thickness is unstable, and no obvious bedding surface. This set of sediments is interpreted as diluvium deposits formed by one or multiple lamellar flow.

There are usually two types of transportation and deposition processes on alluvial fans: one is traction flow deposition induced by temporal water flow (lamellar flow), the other is terrestrial gravity flow deposition such as mudslide. These two types of deposition processes depend on the characteristics of water and sand mixture on alluvial fans.

The lithology at Jiangjuntai is relatively homogeneous, lacking mud deposits. The depositional features of the section and the roundness of gravels both suggest that the formation of the alluvial fan mostly depends on water transportation and deposition. Since the late Pleistocene, the uplift of Jiangjuntai has generated the height difference of the drainage basin. Earlier strata were washed out by the temporary river to form the alluvial fan.

**Fig. 3.11** The location, elevation cross-section and piedmont picture of Daotanghe sandpit (observation point 6)
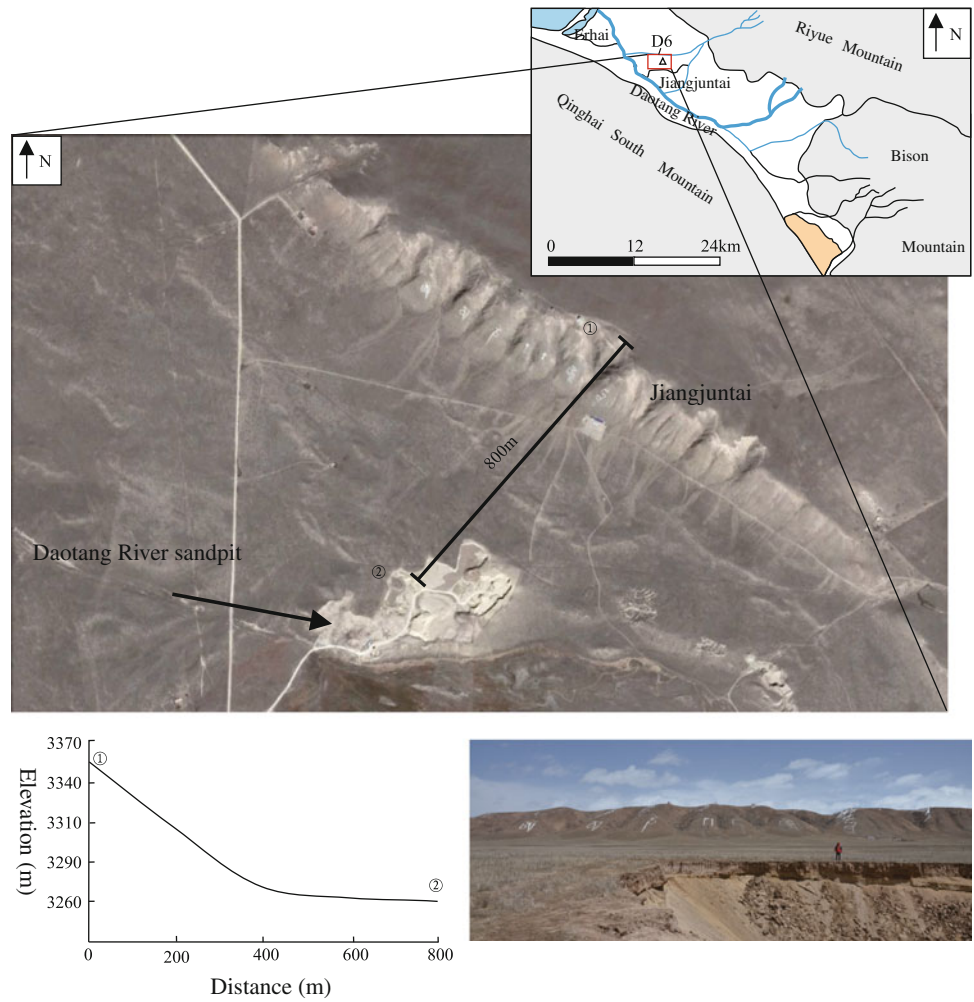


**Fig. 3.12** Field picture of alluvial fan. **a** Interbedding of fine sand and reddish brown mud. **b** Foreset bedding that diverges downward in the middle layer. **c** Closeup of the red box in (**b**). The gravels are clearly oriented. **d** Parallel bedding of the top layer
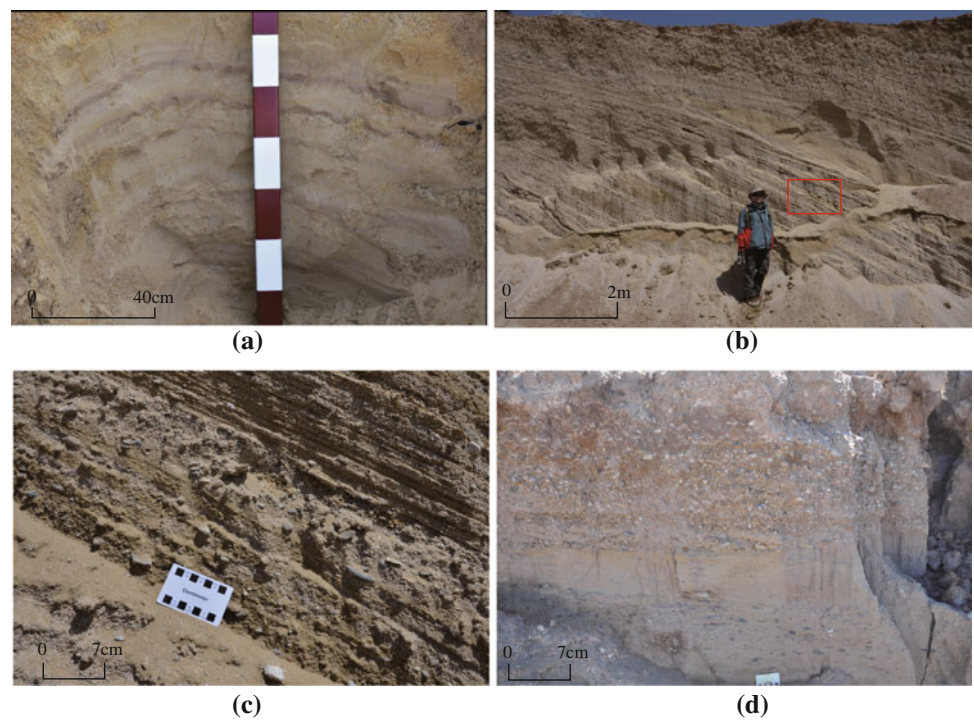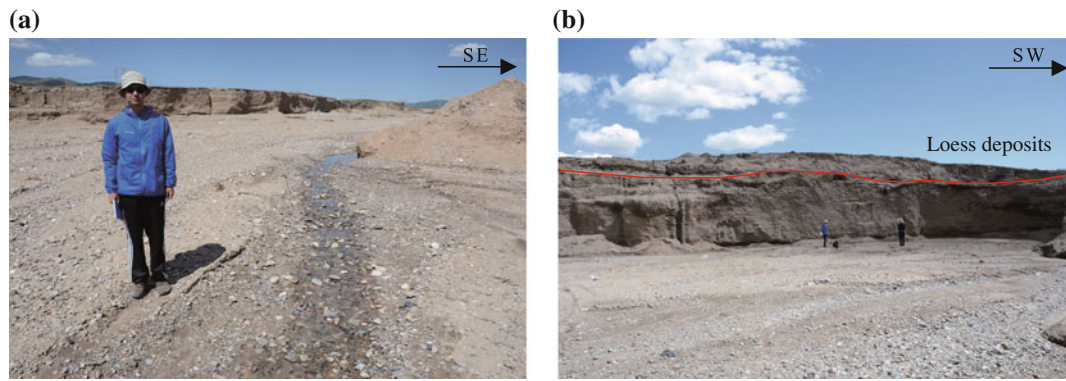
**Fig. 3.13** **a** The modern Daotanghe River derived from the Bison Mountain is almost dried up. **b** The abandoned river terrace is covered by eolian loess

### 3.2.1.3 Modern Daotanghe River

The flow direction of the modern Daotanghe River is from southeast to northwest. Upstream tributaries derived from the Bison Mountain is mostly dried up (Fig. 3.13a), which provides favorable conditions for us to study the upstream sedimentary characteristics of the modern Daotanghe River.

The observation point D4 is a section on the modern river terrace, which is covered by Holocene eolian loess (Fig. 3.13b). The whole section is mainly composed of gravel, with minor mud (Fig. 3.14a). Gravel diameter varies between 3 and 10 cm. Medium size gravels are mostly angular to sub-angular. Fine gravels are sub-angular to sub-rounded. The gravels in the lower part of the section are mostly medium-coarse grained, whereas the gravels in the upper part is mostly medium-fine grained (Fig. 3.14b, c). The dip direction of the maximum flat surface of the gravels are mostly 30°–50°, with dip angle of 30°–40°. The poor roundness and sorting of the gravels suggest that the upstream tributaries from the Bison Mountain were not subjected to long-term hydrodynamic process. In other words, the tributaries dried up in a relatively short period of time.

At present, the downstream water of Daotanghe River is mainly from tributaries on one side of the Riyue Mountain. According to the Qinghai Provincial Bureau of Geology and
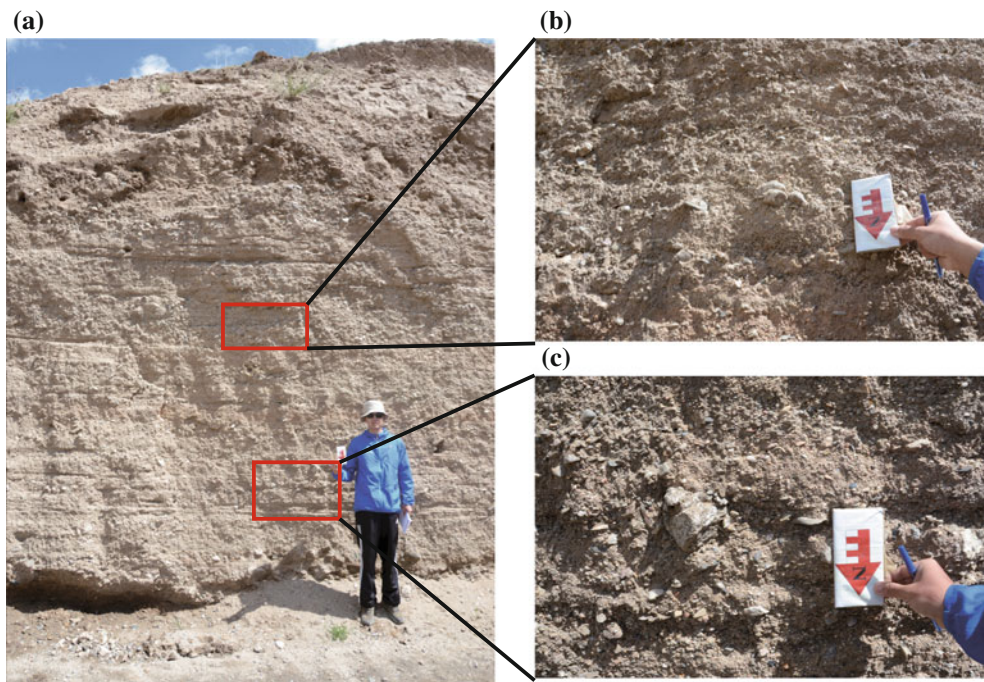


**Fig. 3.14** **a** Cross section of the modern Daotanghe terrace. **b** Gravels on the top are mainly fine-medium grained. **c** Gravels at the bottom are mostly medium-coarse grained

Mineral Resources, the piedmont diluvial and alluvial oblique plains are infiltration zones of runoff water, where water depths are 5–25 m and aquifer thickness ranges from 20 to 75 m. Therefore, a large proportion of the downstream water of the river is supplied from underground water.

The downstream of the Daotanghe River is dominated by meandering river deposits. The width of the river is generally 8–10 m, and the curvature is generally greater than 1.5. Four subfacies, including riverbed, coastal, flood plain and oxbow lake were identified.

The riverbed subfacies of the Daotanghe river can be divided into fluvial lag microfacies and point bar microfacies (Fig. 3.15a). Water in riverbed takes away suspended small particles, and leaves coarse particles, such as the gravel, at the bottom of riverbed, eventually forming riverbed sediments (Fig. 3.15a). Point-bar is the product of the lateral migration of riverbed and lateral aggradation of sediments. It is located on the convex bank and gently dips toward the river. The width of point bar here is similar to the width of the river. The point bar is usually covered by helophytes (Fig. 3.15a).

The coastal subfacies is developed on the side of the riverbed, parallel to the river extension direction (Fig. 3.15a). Coastal sediments are significantly finer than riverbed sediments. The coastal subfacies can be divided into natural levee and crevasse fan microfacies. Natural levee is asymmetric, with steep slope on the river side and gentle slope on the floodplain side. The particle size of natural levee sediments is smaller than that of point bar, yet is bigger than that of floodplain. The crevasse fan is formed when natural levees are flooded during flood season (Fig. 3.15b). The crevasse fan is developed on the concave side of the riverbed, has fan shape planform, and covers earlier river floodplain.

River floodplain is located outside of natural levee, at relatively low and flat terrain. The width of the floodplain is generally narrower than 260 m (Fig. 3.15b) due to the relatively small amount of water flowing. The curvature of the Daotanghe River is high, easy to be cut off, resulting in the development of many oxbow lakes (Fig. 3.15b). Oxbow lake sediments cover earlier river floodplain. There are two different types of oxbow lake. As the narrowest neck of meandering river is suddenly cut off, one type of oxbow lake is formed when the entrance and exit of truncated meandering ring are quickly blocked by sediments after new river channel is formed. The other type of oxbow lake is formed when the meandering belt is blocked, as the meandering river channel is repeatedly cut off, discarded and filled by fine particles to a certain stage. During flooding season, avulsion can be caused by a single levee failure. The second type of oxbow lake usually coexists with crevasse fan.

### 3.2.1.4 Daotanghe Delta

When the modern Daotanghe River enters plain area, it gradually migrates downstream. Close to the Erhai inlet, the distributary river channel does not keep the same width or gradually widen before entering the lake. Instead, it forms a narrow water puddle before entering the lake in the form of a mini meandering river with negligible width. The reason for the formation of this narrow water puddle is the barrier of the first and second lake embankments (Fig. 3.16a). These embankments prevent the direct inlet of the river, and lead to massive water accumulation on the east side of the embankments. As a result, the river can only cut a small incision on the embankments, and enter the Erhai with relatively small water discharge.

After entering Erhai, the modern Daotanghe formed a mouth bar, which is about 80 m wide. By comparing the remote sensing images of 2002 and 2014, it is found that the water level of the Erhai is rising. This is consistent with rising water level of the Qinghai Lake in the past decade, indicating that the water level of these two lakes is positively correlated. The front of the Erhai delta partially overlaps the Erhai delta plain in 2014. The underwater distributary channel in front of the Erhai delta in 2014 is actually the on land distributary channel of the Erhai delta plain in 2002.
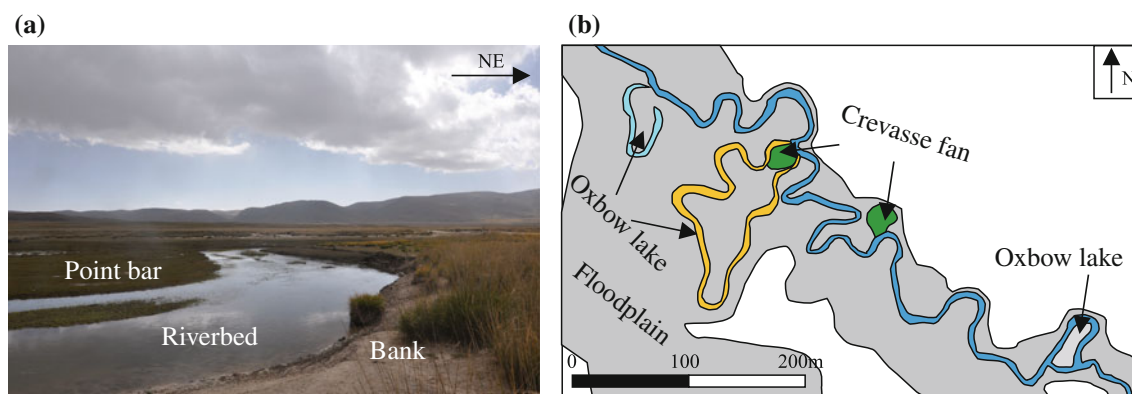


**Fig. 3.15** **a** Field picture of the downstream of modern Daotanghe River. **b** Crevasse fan and oxbow lake of modern Daotanghe River
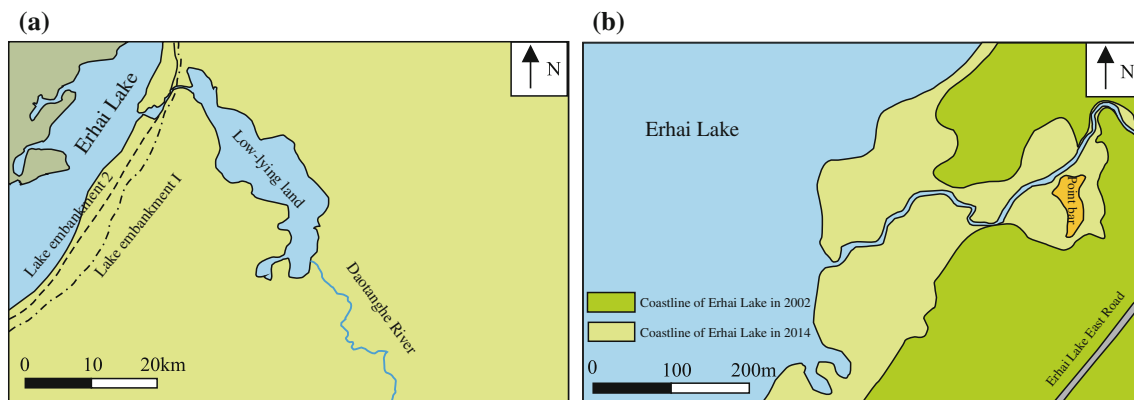
**Fig. 3.16** **a** The location of the low-land area before Daotanghe entering the Erhai. **b** The migration map of Daotanghe delta

This indicates that the front of the Daotanghe River delta is controlled by the lake's elevation (Fig. 3.16b).

### 3.2.1.5  Erhai Lake

From the view of east and west lake embankment, Erhai has been separated from the Qinghai Lake for a long time. Erhai is a small narrow lake that proximately extends north to south. Its east shore is smooth, whereas the west shore is uneven. The Erhai is separated from the Qinghai Lake by an ancient lake embankment that is 0.25–1.25 km wide and smooth on the Qinghai Lake side. The first lake embankment on the east side is about 150 m from the Erhai, and about 10 m above the lake. Flushing cross bedding is clearly observed at the observation point D7 (Fig. 3.17a), indicating that the lake water level reached the first embankment during late Holocene. The second embankment closer to the lake is near the East Lake Road, and about 3 m above the lake. According to field measurements and remote sensing images, the surface of Erhai is 3 m higher than that of Qinghai Lake.

The third embankment on the west side of the lake is the largest one, and the highest point of the embankment is about 5 m higher than the Qinghai Lake. The embankment separates the Erhai from the Qinghai Lake. Two holes have been drilled on this embankment: one is the Qing East Hole located on the west side of the embankment; the other is the Qing 4 Hole, located on top of the embankment (Fig. 3.18a). The depth of the Qing East Hole is about 1 m, and is dominated by muddy silt and fine sand. This is consistent with the fine sand coastal bar observed in the field close to the Qinghai Lake shoreline (Fig. 3.17b).

Qing 4 Holes is located on top of the embankment, with total depth of 180 m (Fig. 3.18b). The top 0–2.6 m is gravel layer of the Buhahe Formation. According to the sporopollen assemblage (semi-desertification), the climate was semi-arid, and the lake area was shrinking. The underlying 12.6–121 m is interbedding of fine sand and silt, with occasional gravel layers (Erlangjian Formation). The thickness of gravel layers decreases from bottom to top. The sporopollen assemblage evolved from *Pinus koraiensis-Pine* forest to *Populus davidiana-Picea schisophila* forest, indicating transition from the coexistence of rivers and lakes to the closure of lakes. There is a significant unconformity between the Erlangjian Formation and the underlying Leigonghe Loess



**Fig. 3.17** **a** Swash cross bedding at observation point D7. **b** New silt coastal bar developed to the west side of the third embankment

**(a)**

Qing4 Borehole

Erhai

Southeast Bay

Qingdong Borehole

III

II I

Elevation (m)

3200

3190

3180

12.6m

1.5km

**(b)**

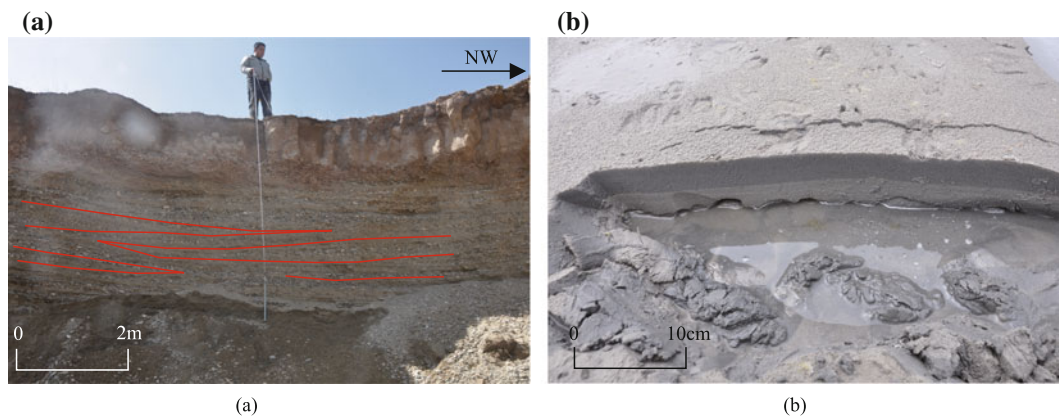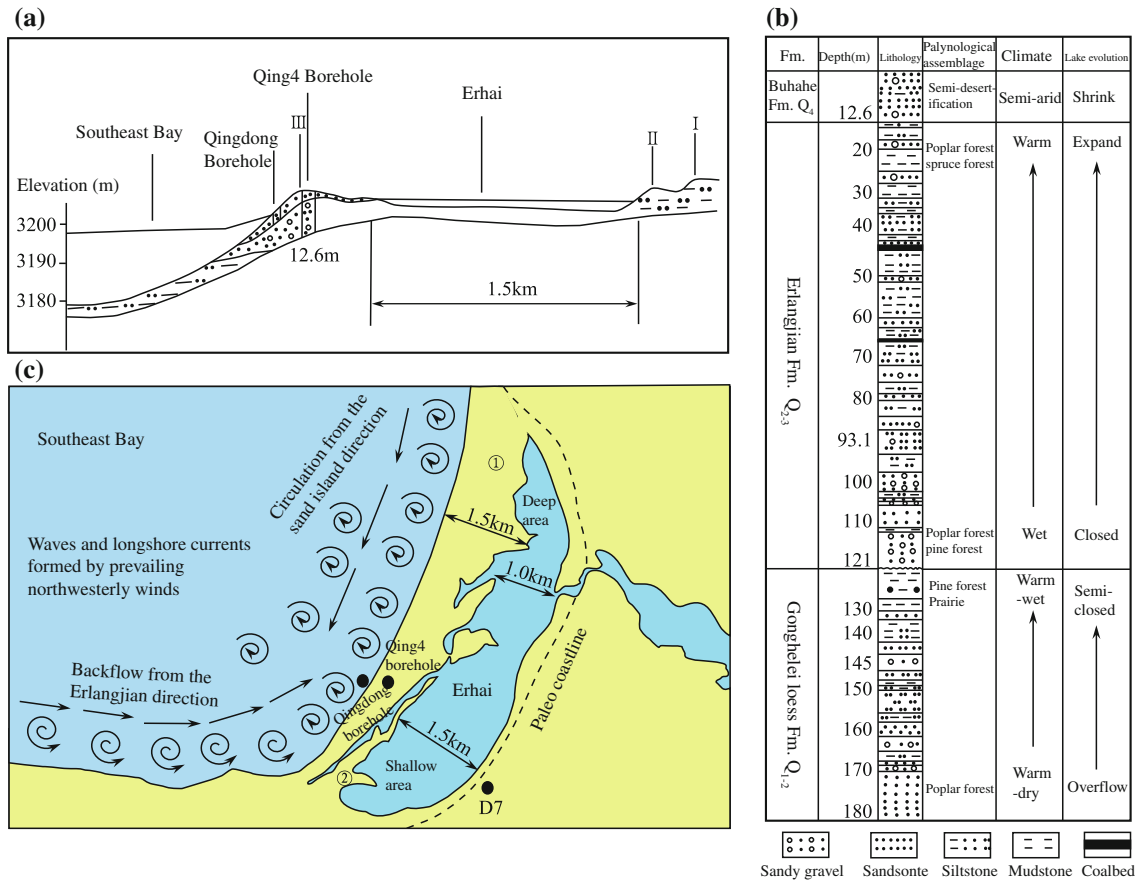| Fm. | Depth(m) | Lithology | Palynological assemblage | Climate | Lake evolution |
|---|---|---|---|---|---|
| Buhahe Fm. Q$_4$ | 12.6 | | Semi-desert-ification | Semi-arid | Shrink |
| Erlangjian Fm. Q$_{2,3}$ | 20 | | Poplar forest spruce forest | Warm | Expand |
| | 30 | | | | |
| | 40 | | | | |
| | 50 | | | | |
| | 60 | | | | |
| | 70 | | | | |
| | 80 | | | | |
| | 93.1 | | | | |
| | 100 | | | | |
| | 110 | | Poplar forest pine forest | Wet | Closed |
| | 121 | | | | |
| Gonghelei loess Fm. Q$_{1,2}$ | 130 | | Pine forest Prairie | Warm-wet | Semi-closed |
| | 140 | | | | |
| | 145 | | | | |
| | 150 | | | | |
| | 160 | | | | |
| | 170 | | Poplar forest | Warm-dry | Overflow |
| | 180 | | | | |

Sandy gravel  Sandsonte  Siltstone  Mudstone  Coalbed

**(c)**

Southeast Bay

Circulation from the sand island direction

Waves and longshore currents formed by prevailing northwesterly winds

Backflow from the Erlangjian direction

Qing4 borehole

Qingdong borehole

Erhai

Deep area

Shallow area

Paleo coastline

1.5km  1.0km  1.5km

① ② D7

**Fig. 3.18** **a** Cross section of the sedimentary facies of southeast bay and Erhai. **b** Lithologic log of Qing 4 Hole. **c** The formation model of the third embankment. **a** and **b** are both modified from Lanzhou Branch of Chinese Academy of Sciences (1994)

Formation, suggesting a sudden climate change (from humid to moist). Qinghai Lake changed from a semi-closed lake to a completely closed lake during this period of time. The Buha Formation at the top 12.6 m is the main constituent part of the present third embankment (Fig. 3.18a). The muddy silt and fine sand in the Qing East Hole is the product of lake shrinking.

A very special phenomenon is observed by remote sensing. The northern part of the Erhai is deeper than the southern part. The norther part is about 1.0 km wide, whereas the southern part is about 1.5 km wide (Fig. 3.18c). The northern part is supposed to be shallower, as the Daotanghe River continues to bring sediments into the Erhai. From map view, the third embankment can be divided into two parts. Bank ① is relatively large, with width up to 1.5 km, and gradually narrowed from north to south. Bank ② is smaller, with width up to 200 m, and gradually narrowed from south to north. Under the effects of coastal flow generated by the prevalent northwest wind and waves and lake current from the Sand Island, bank ① was formed by transportation and deposition of massive sand and gravel. Bank ② was formed by southeast lake bay circulation from the Erlangjian Formation.

Bank ① is significantly larger than bank ② because of the stronger transportation and deposition ability of coastal flow and lake current relative to bay circulation. Before the two dams were completely closed, large amount of sediments entered the southern part of the Erhai through the narrow channel between the two dams, causing a large amount of sediment to accumulate on the southern side, resulting in relatively shallow southern Erhai.

### 3.2.1.6 Summary

At the end of the late Pleistocene, the Riyue Mounatin and Bison Mountain area uplifted, the ancient Daotanghe River outlet was blocked, and the modern Daotanghe River began to form. At the same time, the uplift of Riyue Mountain and Jiangjuntai horsts lead to formation of alluvial fans in front of the mountains. Water supply was sufficient for the modern Daotanghe River in early days. However, as the climate became warmer and drier during the late Holocene, the tributary from the Bison Mountain was basically dry and the vegetation coverage was reduced. The river terraces were covered with thick eolian sand and loess, and many ancient sand dunes on valley plains remobilized.

After entering valley bottom, the modern Daotanghe River migrates towards the Erhai in the form of meandering river. Refined by the first and second lake embankments, the meandering river forms a narrow water puddle before entering the lake. The meandering river forms a small delta after entering the lake through a small channel. The sediment distribution in front of the delta is obviously controlled by lake water level. The embankment that separates the Erhai and Qinghai Lake is composed of bank ① on the north side and bank ② on the south side. Combined with the water depth and climate change of the Erhai, we can see that the third embankment is formed by the closure of bank ① and ②, under the combined effects of decreased water level, strong wave and coastal flow.

### 3.2.2 Qinghai Nanshan–Alluvial Fan–Fan Delta/Coast Depositional System

The Erlangjian-Jiangxigou-Heimahe area in front of the Qinghai Nanshan is the steep slope zone of the entire lake basin. The distance from the piedmont to the present lake shoreline is very short. There are a variety of sedimentary facies present (alluvial fan, fan delta, sand spit, lake bar, etc.). Song et al. (1999) divided the coastal facies here into 3 categories: coastal gravel bar, gravel beach, and mudflat. Wang et al. (1997) mentioned that a variety of alluvial fans and fan delta deposits are developed here. Shi et al. (2008) the fan delta here as underwater fan. The following discussion will focus on the source-sink analyses of Qinghai Nanshan.

#### 3.2.2.1 The Source Characteristics of the Western and Middle Qinghai Nanshan

The rock mass of Qinghai Nanshan is mainly composed of Lower Triassic and Upper Carboniferous strata and intrusive rocks. The Upper Carboniferous Middle Wunongshan Group in the Zongwulong Mountain area is typical trough-type Carboniferous sediments. The lower part is mainly clastic rocks, whereas the upper part is mainly carbonate. The Middle Wunongshan Group outcropped at the western Qinghai Nanshan is the main upper subgroup of this group. It is mainly composed of dark and light gray crystalline limestone, with a small amount of phyllite and meta-sandstone (Wang and Wang 1980). The Lower Triassic strata outcropped at Chaka Beishan Mountain, Heima River and Jiala Mountain area is dominated by dacite and rhyo-dacite in the lower part and conglomerate and sandstone in the middle-upper part (Qinghai Geology and Mineral Resources Bureau 1991). The mafic and ultramafic rock intrude into the middle-lower Triassic strata of Zongwulong Mountain and the Lower Triassic strata of Qinghai Nana during the Indosinian period. The diorite bodies distributed

in the Chaka Beishan area are formed during late Indosinian, and contains abundant gabbro and a small amount of pyroxenite xenoliths. Quartz diorite formed during late Indosinian is distributed in the Hadu Mountain Area. The Longbaoqian Mountain is mostly covered by plagiogranite formed during late Indosinian, while Lower Silurian clastic rocks are exposed in some area.

From the geomorphologic point of view, Qinghai Nanshan, which is part of the Zongwulong Mountain-South Qinghai Lake Mountain rock belt, is a bow-shape mountain range (the concave side embraces the Qinghai Lake). The peaks of Qinghai Nanshan are generally high and continuous, with many small mountain pass. There is a stable intermountain river at the mountain pass close to Hema River, where a fan delta is developed. The river at the mountain pass close to Erliangjian-Jiangxigou is intermittent, and alluvial fan is developed. The coastal zone in front of mountains gradually narrows from Erlangjian to Jiangxigou (Fig. 3.19).

According to the meteorological data of Jiangxigou from 1974 to 1997, the monthly average humidity of Jiangxigou Station is 57%, the monthly average rainfall is 34.87 mm, and the monthly average evaporation is 113.4 mm. Precipitation shows distinct seasonal variations (rainfall is mainly concentrated in summer). Compared to Gangcha Station and Haiyan Station, Jiangxigou Station has higher monthly average precipitation and lower monthly average evaporation. Therefore, the monthly average humidity of Jiangxigou is also the highest around the lake. In addition, the average annual precipitation is also different between Heima River and Jiangxigou, which both located on the west coast. The average annual precipitation of Heima River can reach more than 400 mm, whereas the average annual precipitation of Jiangxigou is about 350 mm (Lanzhou Institute of Geology, CAS 1994).

Differences in natural conditions lead to different types of soils in different lots. Alpine desert soil is mostly distributed in the rock flowing slope below the snow line and the gentle slope below. Qinghai Nanshan is a shady slope. Alpine meadow soil is distributed on its upper part and top. Alpine shrub meadow soil is distributed on the lower part of the Qinghai Nanshan. Chestnut soil is widely distributed on the plain area.

Restricted by natural conditions, the vegetation type in the study area is also diverse (Table 3.1). Vegetation coverage is usually studied by coverage degree (the ratio of the projected area of plants on ground). Coverage degree can be divided into the total coverage (coverage of plant community) and sub coverage (coverage of species).

By comparing vegetation type and coverage, it is found that there are obvious regional differences of plant communities in Qinghai Nanshan. Previous study compared the relationship between vegetation coverage and elevation of
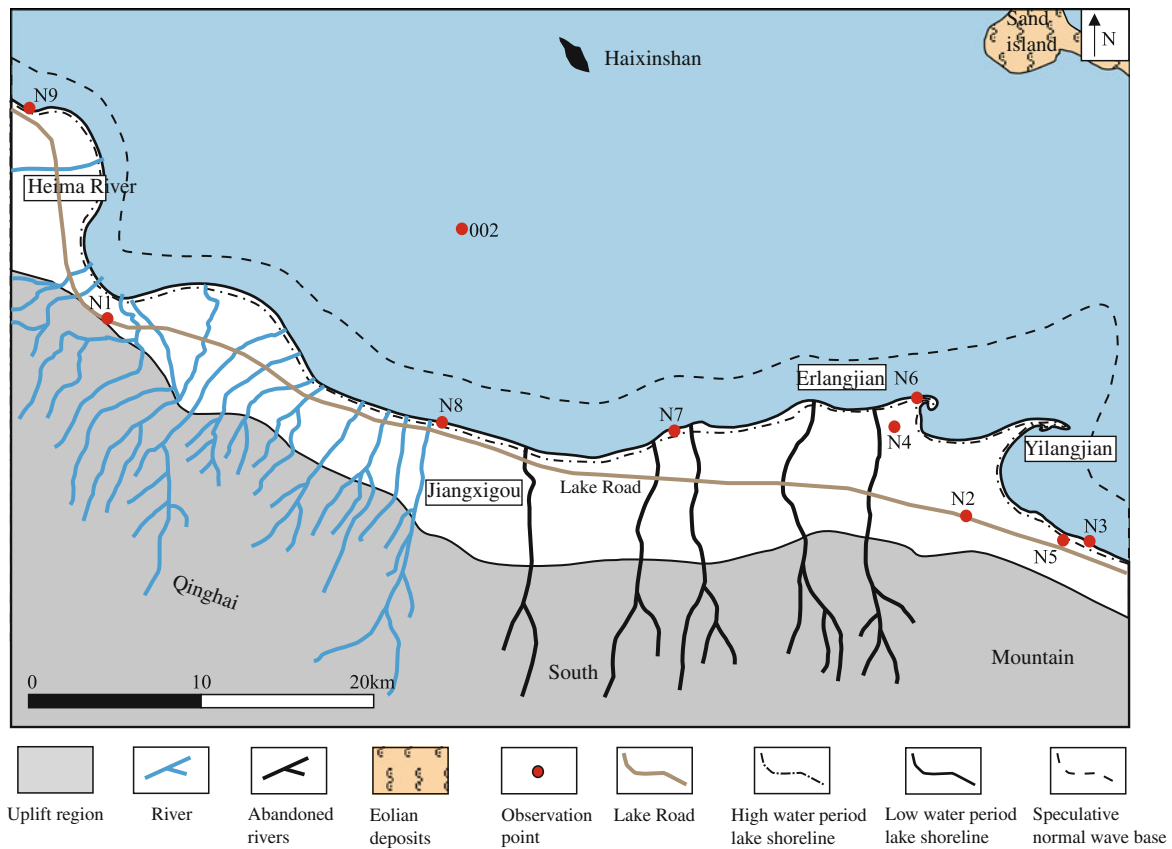
**Fig. 3.19** The location of the Qinghai Nanshan–alluvial fan–fan delta/coast depositional system

**Table 3.1** Vegetation types and coverage in Nanshan study area, Qinghai Province

| Location | Elevation (m) | Vegetation type | Total coverage (%) | Sub coverage |
|---|---|---|---|---|
| E Qinghai Nanshan | 3500–3650 | *Salix Oritrepha* shrub | 85–95 | 35–55%, up to 65% locally |
| E Qinghai Nanshan | 3500–4200 | *Kobresia Pygmaea* meadow | 65–90 | 25–50% |
| W Qinghai Nanshan | 3400–3900 | *Salix Oritrepha* shrub, *Potentilla Fruticose*, and *Caragana Jubata* shrub | 75–95 | Up to 80% for dominated species, 60% for herb layer |
| Shady, semi-shady, and semi-sunny slope of W Qinghai Nanshan | 3500–4000 | *Potentilla Fruticose* shrub | 70–90 | 30–60% |
| W Qinghai Nanshan | <3400 | *Kobresia Humilis* meadow | 65–80 | |
| W Qinghai Nanshan | >3400 | *Kobresia Pygmaea* and *Kobresia Humilis* meadow | 55–95 | 40–85% |
| Qinghai Nanshan | 3230–3300 | *Stipa Breviflora* steppe | 70–85 | 40–65% |
| Coastal plain of Qinghai Nanshan | 3200–3300 | *Achnatherum Splendens* steppe | 40–60 | 30–40% |
| Erlangjian sand area | 3200 | *Golden Clematis* dessert | 25–50 | 20–45% |
| Periphery of Erlangjian sand area | 3200 | *Ephadra Intermedia* dessert | 50–60 | |
| Farms south of Qinghai Lake | 3200–3400 | Planted vegetation | | |

Revised from Lanzhou Branch of Chinese Academy of Sciences and Western Resources and Environment Research Center (1994)

the Erlangjian-Longbaoqian Mountain profile and the Heima River-Tawen Mountain profile, and found significant differences (Lanzhou Branch of the Chinese Academy of Sciences 1994). For the Erlangjian-Longbaoqian Mountain profile: between 3200 and 3300 m, as the temperature change is relatively small at low elevation and the water content of soil increases with elevation, the vegetation coverage increases with elevation. Between 3300 and 3900 m, the water content of soil is constant, thus the total vegetation coverage is also constant. Between 3900 and 4200 m, although the water content of soil increases with increasing elevation, total vegetation coverage decreases significantly as the result of decreasing temperature. The vegetation coverage of the Heima River-Tawen Mountain profile is significantly better than the previous one. This is because this area is dominated by alpine meadows. Precipitation in this area is relatively good as it is located on windward slope. The change of soil water content and temperature in this area is small as this terrain has gentle slope. Therefore, the plant community coverage in the study area depends on elevation, temperature and soil water content, etc.

### 3.2.2.2 Alluvial Fan

A variety of alluvial fans is distributed on the piedmont inclined plain. The southern slope of the lake basin is narrow, generally only 1–6 km. From the Daotanghe town to Heima River, alluvial fans fluctuate along the road around the lake (Fig. 3.20a). These alluvial fans have steep gradient and are poorly preserved, with area generally less than 30 km². Granite boulders with diameter >1 m are found at the mountain pass near the Heimahe toll station (observation point N1; Fig. 3.20b). Therefore, the sediment source should be the Xiangpi Mountain in middle Qinghai Nanshan. Gravel size decreases towards the lake, and gravels on the lake coast are only 3–5 cm.

The section at observation point N2 (located in front of the Longbaoqian Mountain) is covered by late Holocene eolian loess. The sediment is dominated by mixed accumulation of gravel, sand and muddy sediments (Fig. 3.21a). Gravels have complex composition, are poorly sorted and angular, and are mainly matrix supported. Gravels are suspended in dark muddy sediments (Fig. 3.21b). The muddy sediments are rich in debris and plant roots, indicating that this location is the root of the alluvial fan. Middle fan and fan margin are vast alluvial plains, and gradually transit to lake shore facies.

### 3.2.2.3 Fan Delta

Fan delta is formed as alluvial fan directly enters the lake. According to the relationship between different facies, fan delta can be divided into near-mountain fan delta and near-fan delta (Chen et al. 2007).

The lobe fan on the southeast side of Heima River has the following characteristics: (1) close to Qinghai Nanshan, and located in the steep slope area controlled by the Zongwulong Mountain-Qinghai Nanshan fault; (2) several small rivers carrying sediments exit mountains and enter the Qinghai Lake directly, and form lobe fan body adjacent to fan root; (3) the radius of the fan is about 8 km and the slope angle is about 1° 10′ (Lanzhou Institute of Geology, CAS 1979); (4) the elevation difference between the lake surface to mountain pass is about 300 m, according to the contour map based on DEM elevation data (Fig. 3.22); and (5) several stable braided distributary channels are developed on the fan body.

The fan delta plain is the on-land part of fan delta, and can be divided into braided distributary channel and floodplain swamp. The sedimentary characteristics of braided distributary channel is similar to braided river, with a large amount gravels distributed in the middle of river channel (Fig. 3.23a). The diameter of gravels is mostly between 3
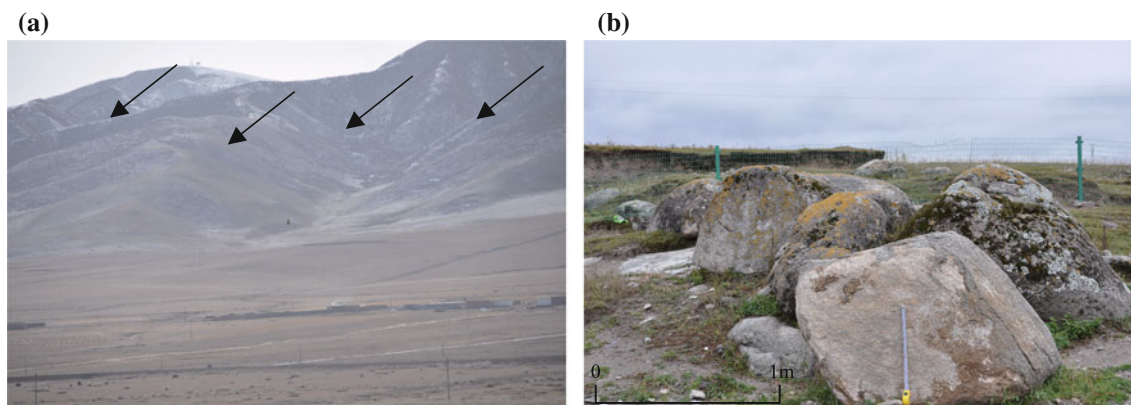


**Fig. 3.20** **a** Alluvial fan skirt. **b** Boulders near the Heimahe Toll station
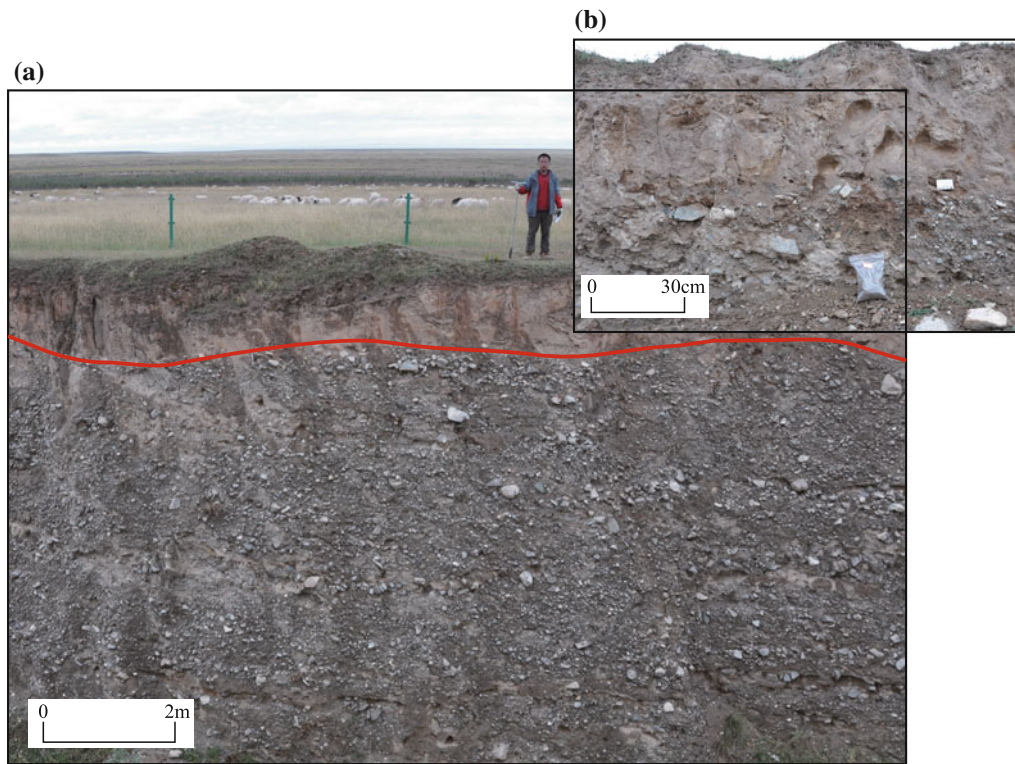
**Fig. 3.21** **a** Cross section of the root of the alluvial fan. **b** The gravels are mostly angular, and mud sediment is rich
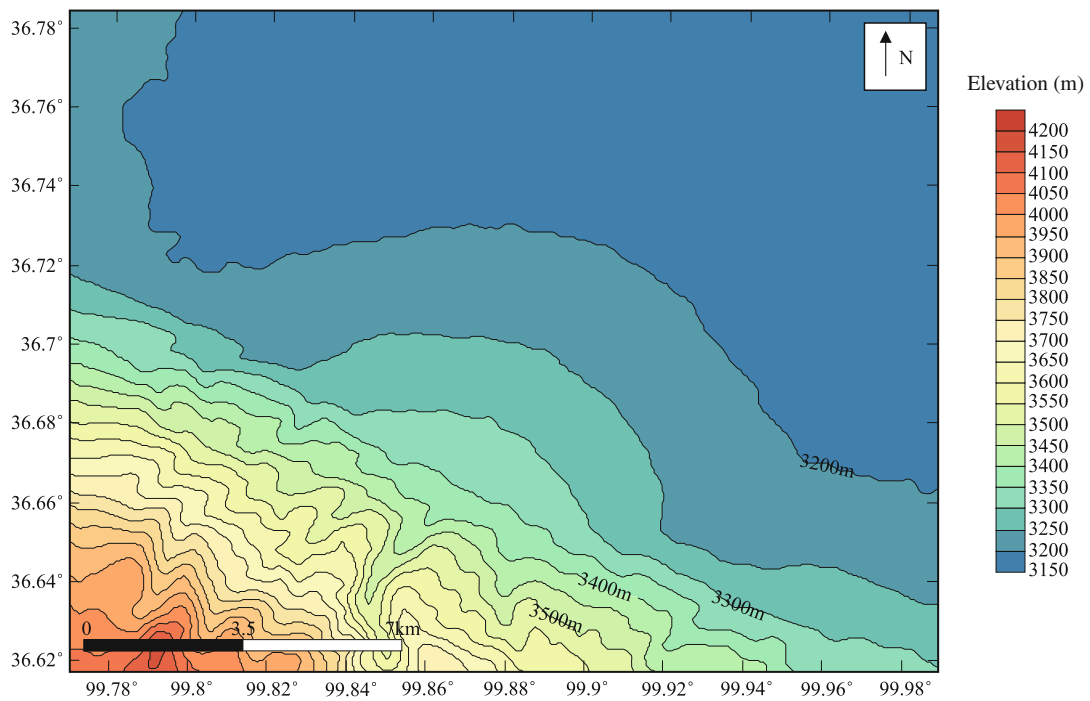


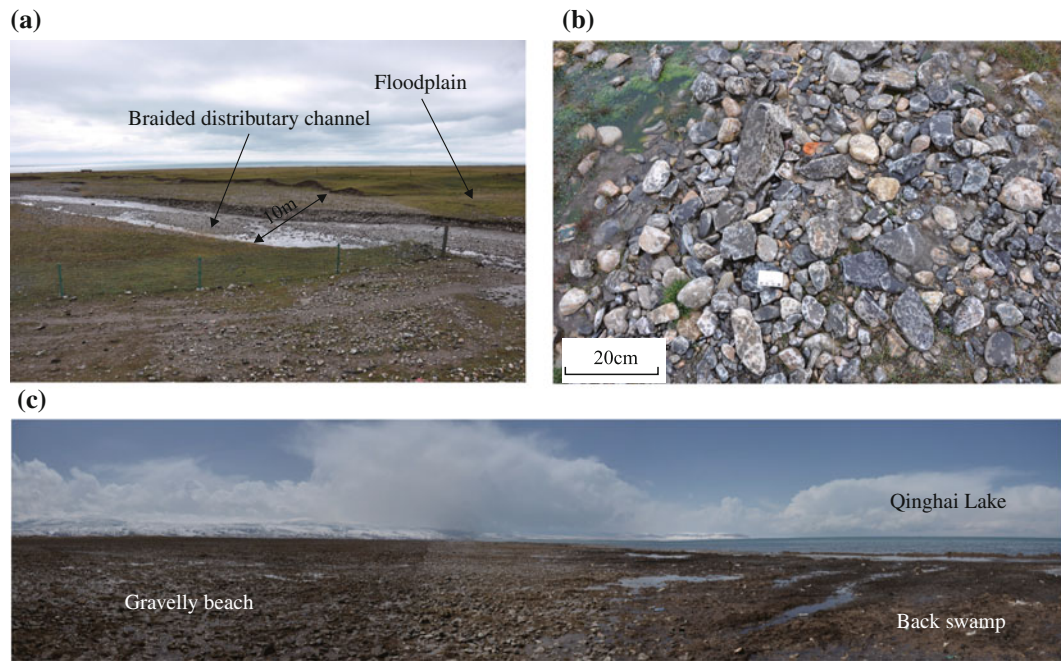**Fig. 3.22** Contour map of the fan delta plain on the southeast side of Heima River

**Fig. 3.23** **a** The braided river and flood plain of the fan delta plain southeast of Heima River. **b** Gravels on the channel bottom. **c** Flood plain swamps at the end of fan delta plain

and 20 cm. Gravels are miscellaneous sandstone and granite in lithology, with sub-angular shape and poor sorting. Water discharge at braided distributary channel is relatively small (Fig. 3.23b). Qinghai Nanshan is the main source region, and near-source accumulation is evident. Flood plains are developed between the braided distributary channels. Floodplain swamps are usually developed near the lake, in the lowland area of fan delta plain. Due to the insufficient supply of fine particles, floodplain swamps are small (Fig. 3.23c).

Field observation reveals that mouth bar is basically not developed at fan delta front. This may be related to the weak hydrodynamics of the fan delta. According to the Lanzhou Institute of Geology, the water depth at the Qinghai Lake sampling point 002 is 22.9 m, sediments are yellowish black muddy silt, and carbonate content is 31.8%. These features suggest the fan delta front may be smaller than 22.9 m. Remote sensing images suggest that the influence of the lake level on the fan delta plain is almost negligible. This may be because of the steep topography.

#### 3.2.2.4   Coast

Previous studies have done many researches on the evolution of Qinghai Lake coastline (Lanzhou Institute of Geology, CAS 1979; Yuan et al. 1990). Yuan et al. (1990) analyzed the ancient gravel and sand bars at Jiangxigou, east Erhai, and east Gahai. Combined with $^{14}$C dating of loess, they inferred the location of the Holocene lake coastline. The

location of late Pleistocene coastline was restored from the locations of lake terraces and erosion cliffs.

We found well-preserved lake terraces (Fig. 3.24a) and erosion cliffs (Fig. 3.24b) in the field. The location of the erosion cliffs is close to the inferred late Pleistocene lake coastline in previous study (Yuan et al. 1990). The first terrace is almost adjacent to the present shoreline of the Qinghai Lake, and can be regarded as the wet season coastline of modern coastal facies. The area between the first terrace and the late Pleistocene coastline can be regarded as ancient coastal facies. It should be noted that in the areas along the north, northwest, northeast coast of Qinghai Lake and the Heima River fan delta, previously formed ancient coastal facies is covered by alluvial fan, fan delta and river delta. The sand area of eastern lake also covers the sand and gravel deposits of ancient coastal facies.

At present, domestic and foreign scholars have basically reached a consensus on the depositional characteristics of the beach sand and bar sand. The thickness of beach sand is generally less than 2 m, and the sedimentary structure is mainly low angle cross bedding. The thickness of bar sand is generally larger than 2 m, and the sedimentary structure is mainly trough interlaced bedding (Jiang et al. 2015). The thickness of coastal sediments in this area is generally less than 2 m, without trough cross bedding structure. Therefore, the coastal facies of this area is mainly beach sand sediments (lake beach). The following discussion is focused on the modern and ancient coastal facies in this area.
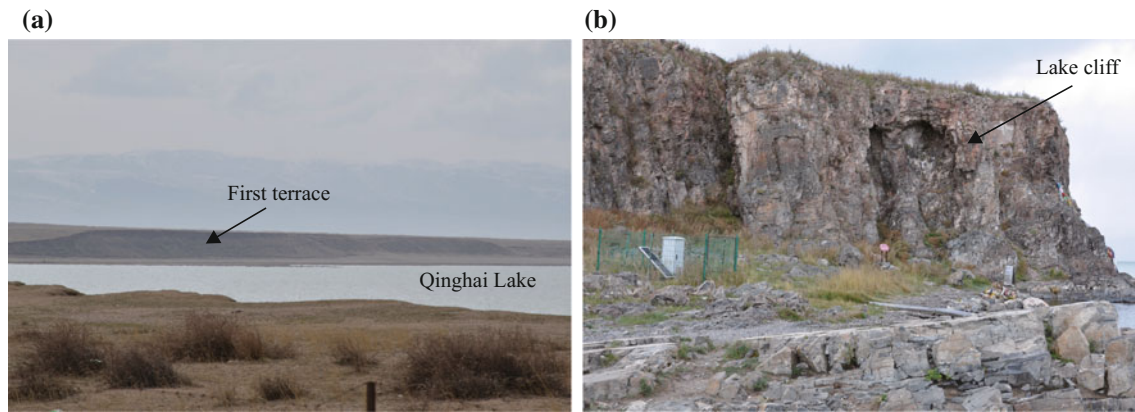
**Fig. 3.24** **a** The first lake terrace near Yilangjian. **b** The erosion cliff on the west side of Qinghai Lake

1. Modern coastal facies

The modern coastal facies can be divided into foreshore subfacies and shoreface subfacies by the surface of normal wave base. The lake beach sediments parallel to the shoreline are usually sheet like and have a large distribution area. Based on lithology, particle size and micro-landforms, the lake beach can be divided into beach ridge, inter beach ridge, sheet sand behind beach and lagoon behind beach.

Beach ridge is above average lake level and close to be horizontal. It is usually parallel to the shoreline, with linear (Fig. 3.25a), fin-like or hook-like (Fig. 3.25b) shape.

Beach ridge sediments are mainly gravel and sand. Some lake beaches have several beach ridges. Low-angle oblique bedding is commonly developed in the lake side of beach ridges (dip angle of $\sim 6°$), with aligned fine gravel. Inter beach ridge is between beach ridges, and is dominated by silt and fine sand sediments. Newly formed beach ridges at waterfront faces the lake, and often forms obstacle marks due to the swash/backwash effects of lake waves. The finer end of obstacle mark points to the water flow direction (Fig. 3.26a). The sheet sand behind beaches is located at the shore side of beach ridge, and is dominated by sand deposits. Erosional gully, which widens towards land, is commonly distributed on sheet sand (Fig. 3.26b). Lagoon behind beach is in the low area on the shore side of the sheet sand (Fig. 3.26b). Sediments in the lagoon are dominated by muddy sand, and water in the lagoon is from the lake during wet season.

According to the composition of sediments, lake beach can be divided into gravel beach and beach. Gravel beaches are mainly distributed beside the fan delta south of Heima River or along the erosinal shore. Plant residues are often found on gravel beaches, which are transported to the beach ridge by swash (Fig. 3.27a). Gravel beach can be divided into upper gravel beach and lower gravel beach based on hydrodynamism and grain size (Fig. 3.27b). The gravel content of upper gravel beach is about 60% (maximum gravel size is 15 cm), and sand content is about 35%. Sand is poorly sorted. Lower gravel beach have $\sim 28\%$ gravel (maximum gravel size is 4 mm). Sand accounts for 69%, and is well sorted. The flat surface of gravels dip towards lake, whereas the long axis is parallel to shoreline. In vertical direction, gravel beach shows reversed gradient. The composition of the gravel is
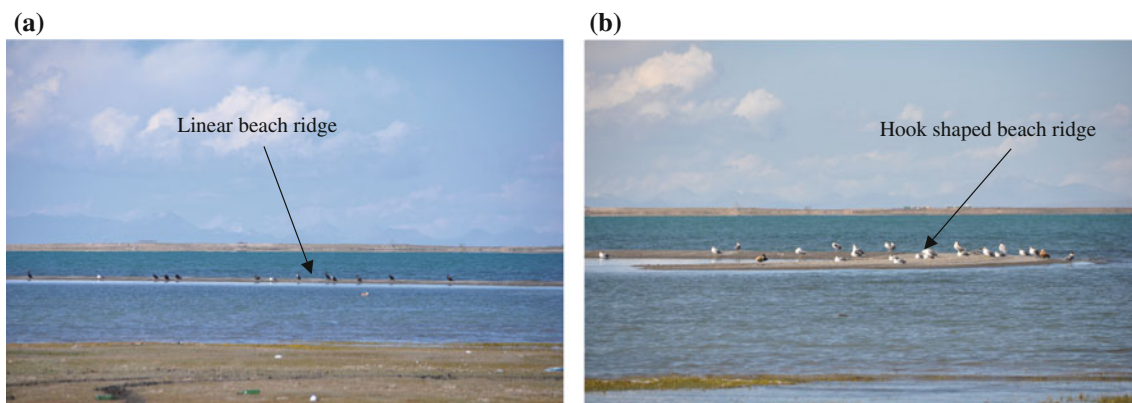


**Fig. 3.25** **a** Linear beach ridge. **b** Hook shaped beach ridge

**(a)** **(b)**
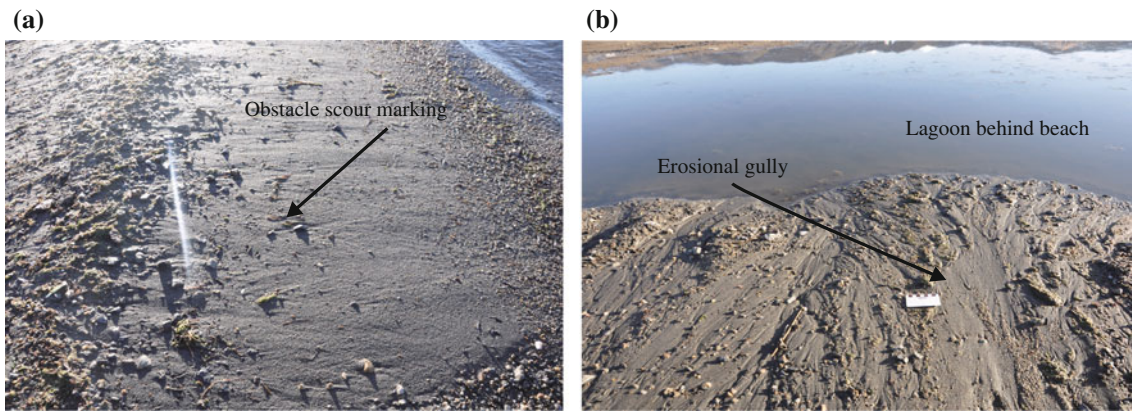


**Fig. 3.26** **a** Barrier mark. **b** Erosion gully and lagoon behind beach

**(a)** **(b)**
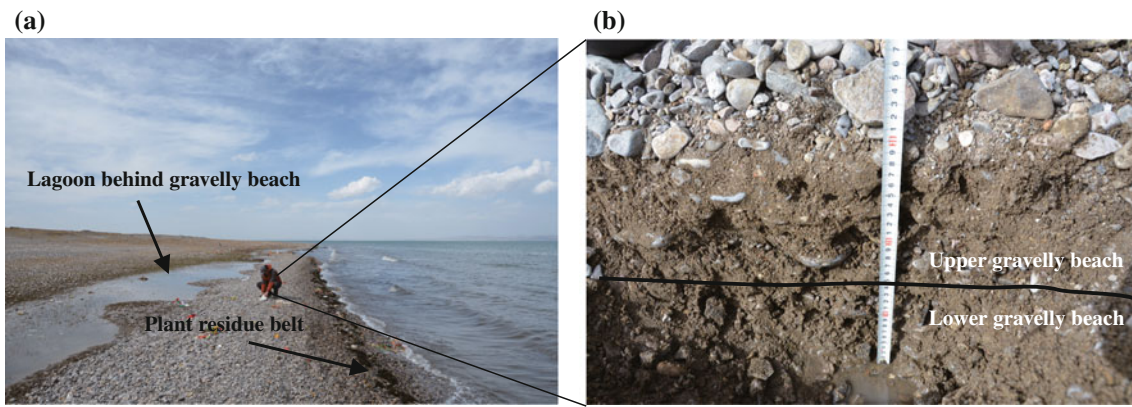


**Fig. 3.27** **a** Plant residue band on Heima River gravel beach. **b** Section of the gravel beach

dominated by limestone, reflecting an origin from the Triassic strata of Zhongwunong Mountain.

Sand beach is mainly distributed in the Erliangjian-Jiangxigou area. The beach sediments are mainly composed of gravel sand and sand. According to hydrodynamic characteristics and grain size, sand beach can be divided into upper sand beach and lower sand beach

(Fig. 3.28a). The upper sand beach contains about 35% gravel (maximum grain size ∼3 cm) and 62% sand (poor sorting). The lower sand beach has about 12% gravel (maximum grain size ∼4 mm) and 90% sand (medium sorting).

Both gravel beach and sand beach have reversed gradient, with coarse clasts deposited by swash on top and fine clasts deposited by backwash at bottom. Such reversed gradient

**(a)** **(b)**
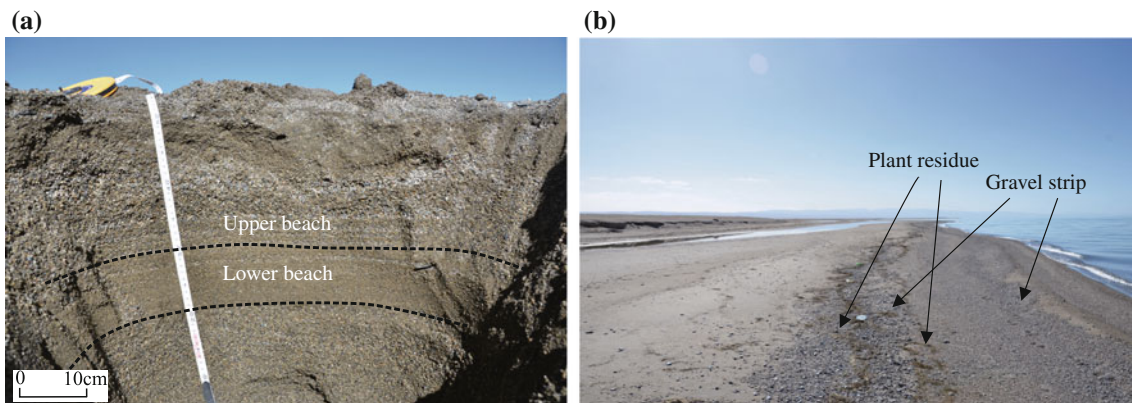


**Fig. 3.28** **a** Section of a sand beach in the Erlangjian-Jiangxigou area. **b** Plant residue and gravel band on the beach

appears rapidly in verticle section, and is shown as gravel or plant residue bands parallel to shoreline in the plane. These features indicate multiple fluctuation of lake water level and migration of lake shoreline (Fig. 3.28b).

2. Ancient coastal facies

The foreshore subfacies of the modern costal facies in this area is dominated by lake beach sedimentation. Due to the short deposition time, there is no obvious sedimentary structure in most sedimentary bodies. To further understand the lithology, sedimentary structure and evolution model of the lake beach sediments in this area, below we examine two representative cross sections in detail (observation point N4 and observation point N5).

Observation point N4 is a section at Yilangjian sandpit, and is located close to the tip of Yilangjian sandspit (N36° 38′ 56.8″, E100° 21′ 54.31″). The sediments is mainly gravel and sand, whose grain size and color are consistent with the loose sediments on the present lake beach. The section has a flat bottom and convex-shape top, with width of about 50 m and height of about 2 m (Fig. 3.29a).

The strike of the section is close to N-S. Large low angle cross bedding is developed (with dipping angle of about 9°). Single small layers have a tendency to converge southward. In the same layer, a thin layer of gravel is observed on the top. The long axes of the gravels have strike direction of 95°–130°, and dip direction of 5°–40°, which is equivalent to the thin gravel layer on the top part of the modern beach.

The internal stratification of the section can be divided into two parts: large low-angle cross bedding near the lake side (beach ridge), and parallel bedding away from the lake side (sheet sand behind beach). Low-angle cross bedding suggests repeated scouring bedding on the lake side of beach ridge by wave-generated underflow. Therefore, the sedimental bedding is near horizontal towards land and low-angle dipping towards lake.

Observation point N5 is a sandpit section on the east side of Erlangjian, which is located between the Erlangjian scenic area and Erlangjian sandspit, about 150 m from the current shoreline of Qinghai Lake. This section exhibit two sets of reversed cycle (Fig. 3.29b, c), which provides us convenience to study multi-stage beach sedimentation.



**Fig. 3.29** **a** Field picture of the section of Yilangjian sandpit (observation point N4). **b** Field picture of the section of Erlangjian east sandpit (observation point N5). **c** Sketch of the section

**(a)**



**(b)**



**(c)**



**(d)**



**Fig. 3.30** Sedimentary structure on the Erlangjian sandpit section. **a** The lower part is characterized by massive bedding (mud sedim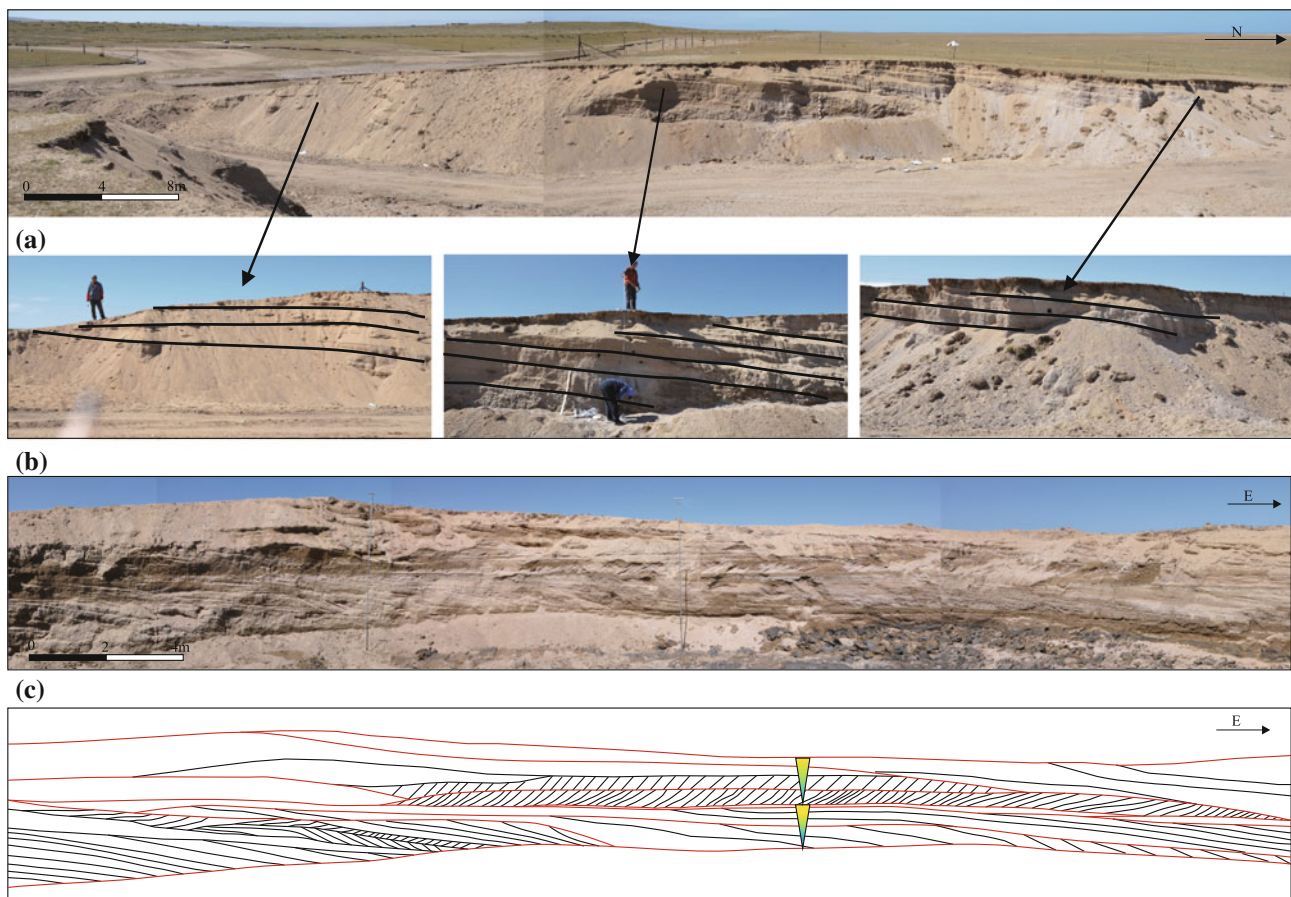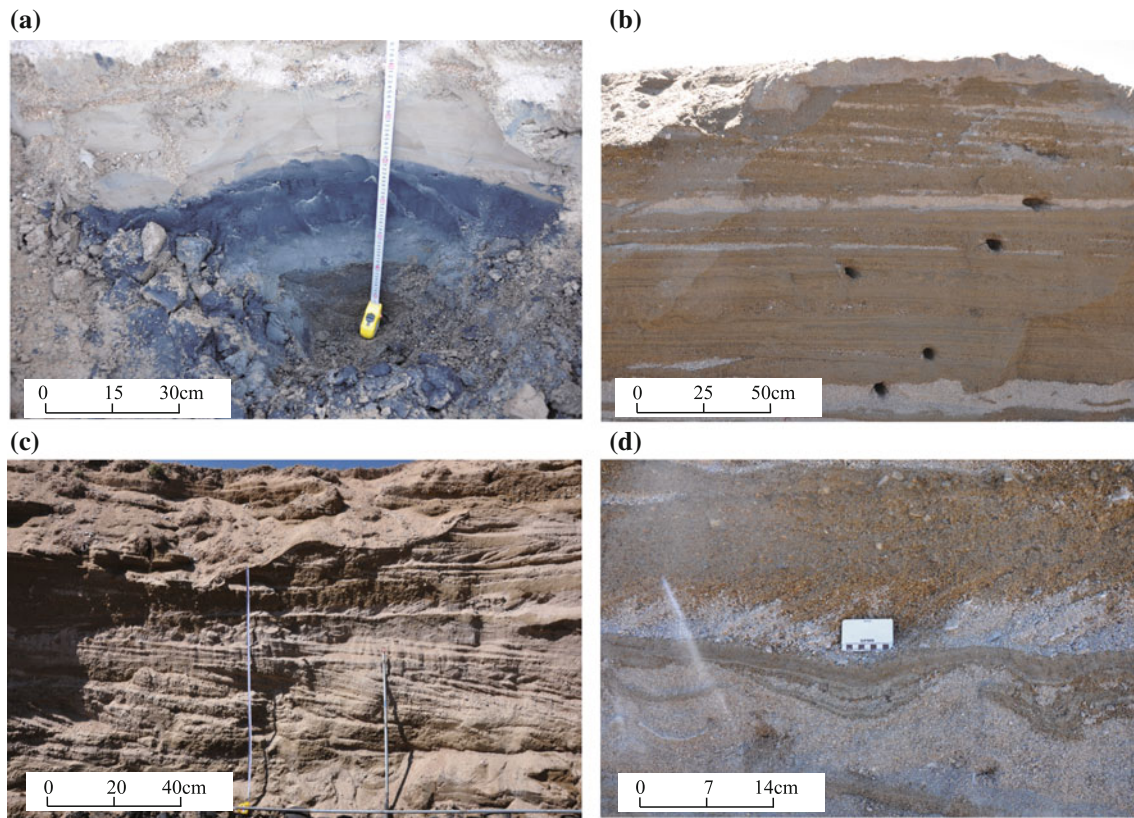ents), whereas the upper part is characterized by reversed gradient bedding (silt-sand-gravel sediments). **b** Parallel bedding (sand and gravel sediments). **c** The lower part is characterized by low-angle cross bedding dipping towards the lake, whereas the upper part is characterized by oblique bedding dipping towards the land. **d** Swash mark, which is overlaid by low-angle cross bedding dipping towards the land

There are many types of sedimentary structures, such as low-angle oblique bedding, flow mark, etc., in the complex bar. From bottom to top there are:

(1) Massive bedding. This is located at the bottom of the entire section, and the sediments are mainly dark gray mud, with uniform composition and structure and no lamellar structure. These features indicate this part is formed by rapid accumulation of suspended sediments (Fig. 3.30a).

(2) Reversed gradient bedding. It is located above the massive bedding, and is characterized by gradual changing of particle size. The layers are basically parallel to each other, without crossover. The particle size gradually increases from bottom to top, and these is no texture inside (Fig. 3.30a).

(3) Parallel bedding. Parallel bedding usually appears on the sections parallel to shoreline. The sediments are mainly coarse sand and gravel formed on a flat bed, indicating strong hydrodynamism (Fig. 3.30b).

(4) Low-angle cross bedding. Low-angle cross bedding appears in the middle of section, which is perpendicular to the shoreline. Sediments are dominated by coarse sand and gravel. The low-angle cross bedding can be divided into two groups (Fig. 3.30c): low-angle cross bedding dipping towards the lake (dipping angle $\sim 12°$), and oblique bedding dipping towards land (dipping angle $\sim 28°$). The former is formed by swash-backwash when the lake water level is constant or increasing. The later indicate beach ridges migrating towards the lake when water level decreases.

(5) Flow marks. Flow marks are between the two sets of low-angle cross bedding. Sediment is dominated by muddy silt. Flow marks are formed when the water flows on muddy sediments, flow separates and generates large eddy currents, resulting in differential erosion of the sediment surface (Fig. 3.30d).

A set of blue-black muddy sediments are developed at the bottom of the section. It is important to determine whether the muddy sediments are from shallow lake or lagoon behind beach. It will help us to study the multi-stage lake sedimentary processes. The muddy sediments dye hands and are rich in plant roots that grow upright. From the land side to the lake side, the thickness of the black mud gradually decreases from 50 to 8 cm.

In general, the muddy sediments of shallow lake gradually thicken toward the lake, whereas the muddy sediments of lagoon gradually thin toward the lake. Therefore, this set of blue-black muddy sediments is lagoon sediments
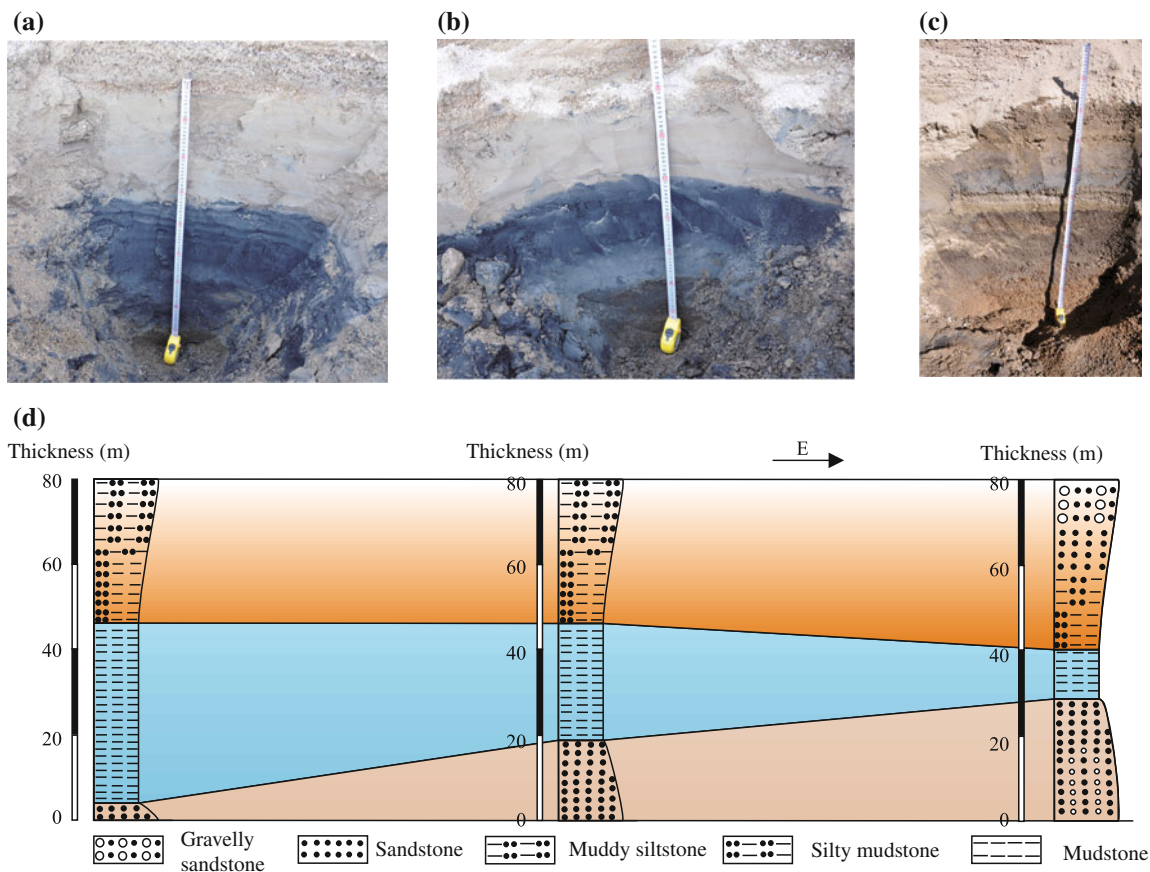
**Fig. 3.31** Comparison of the blue mud sediments at the bottom of Erlangjian section. **a** Field picture of the blue mud sediments at the land side of the section. **b** Field picture of the blue mud sediments at middle section. **c** Field picture of the blue mud sediments at the lake side of the section. **d** Correlative cross section based on (**a**), (**b**), and (**c**)

(Fig. 3.31). These muddy sediments are dated in the Beta laboratory in the United States, and yield $^{14}C$ age of $4840 \pm 30$ BP (Fig. 3.32).

As the section is arc-shaped, three lithologic columns are divided on the section (Log1, Log2 and Log3), which are representative of the multi-stage lake beach sediments from
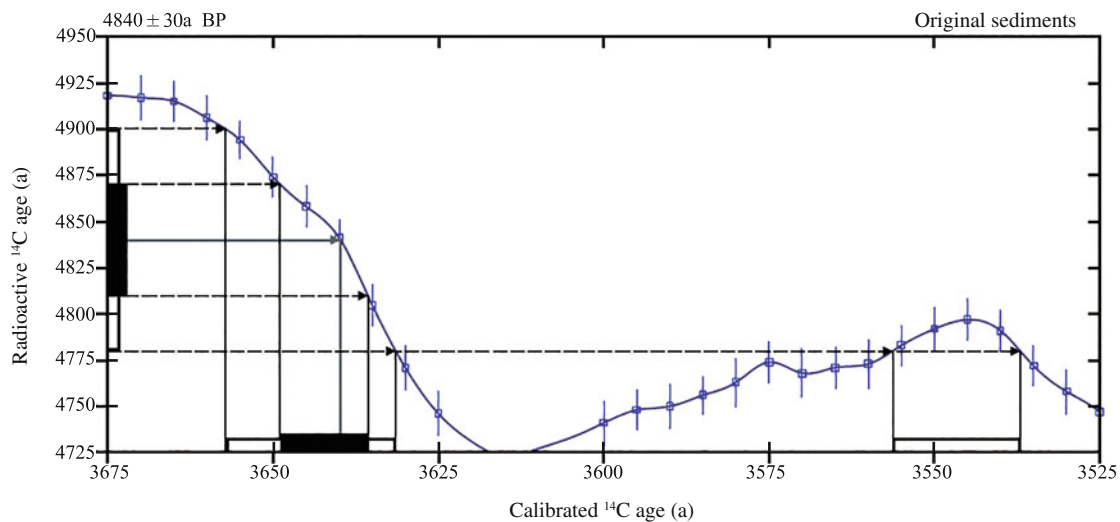


**Fig. 3.32** $^{14}C$ ages of the blue mud sediments
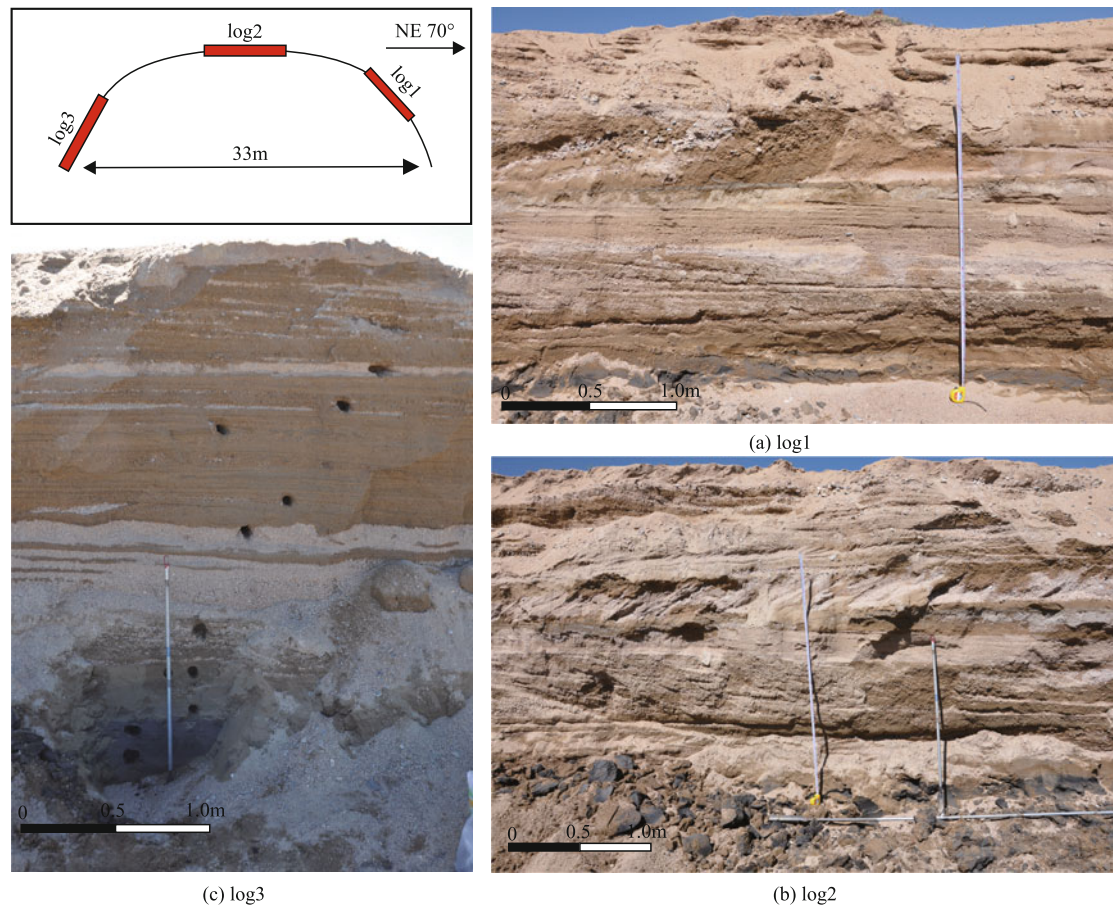
**Fig. 3.33** The location and field pictures of Log 1, 2, and 3 at observation point N5 (Erlangjian sandpit section)

lake to land. The shape of the sandpit is semi-circular, with diameter of 33 m, and half perimeter of 100 m. Log1 and the shoreline are oblique crossing. Log2 is perpendicular to the shoreline. Log3 is parallel to the shoreline, equivalent to lateral dissection of the bar (Fig. 3.33).

Log1: The black mud layer is the thinnest among all deposition profile, about 8 cm thick (Fig. 3.34). The mud layer is covered by about 6 cm thick brown muddy silt, which gradually transit into sandy sediments with reversed gradient, indicating gradually increased hydrodynamism. The next layer is low-angle oblique bedding dipping towards the lake, indicating the repeated swash of beach ridge as the lake water level increases. The next layer is a set of thin muddy sediments with flow marks, resulted from the erosion of beach ridge during wet season. The next layer is a set of oblique bedding dipping towards the land, suggesting the migration of beach ridge towards the lake as water level decrease. The tope layer is a set of sands (50 cm thick) with reverse gradient formed during rapid decrease of lake water level.

Log2: The black mud layer at the bottom is about 30 cm thick (Fig. 3.34). Above it is brown muddy slit about 15 cm thick. Like Log1, the sediments gradually transition to sand and gravel. The sand-gravel sediment layer with low-angle cross bedding structure and muddy sediment layer with flow marks are significantly thicker than those in Log1, indicating that this is the main part of the multi-stage lake sediments. The hydrodynamic conditions reflected in Log2 are similar to Log1.

Log3: The black mudstone layer at the bottom is the thickest among all logs (50 cm), reflecting this is closer to the deposition center of the lagoon (Fig. 3.34). The mudstone layer is covered by 30 cm thick brown muddy silt. The sedimentary structure above the muddy silt is dominated by parallel bedding. The parallel bedding in the middle part is mainly composed of interlayering of sandy sediments rich in heavy minerals. The parallel bedding of the lower part and the upper part shows interlayering of sand and gravel.

By comparing the lithologic columns of Log1, Log2 and Log3 (Fig. 3.34), the lake water level first rise and then fall.
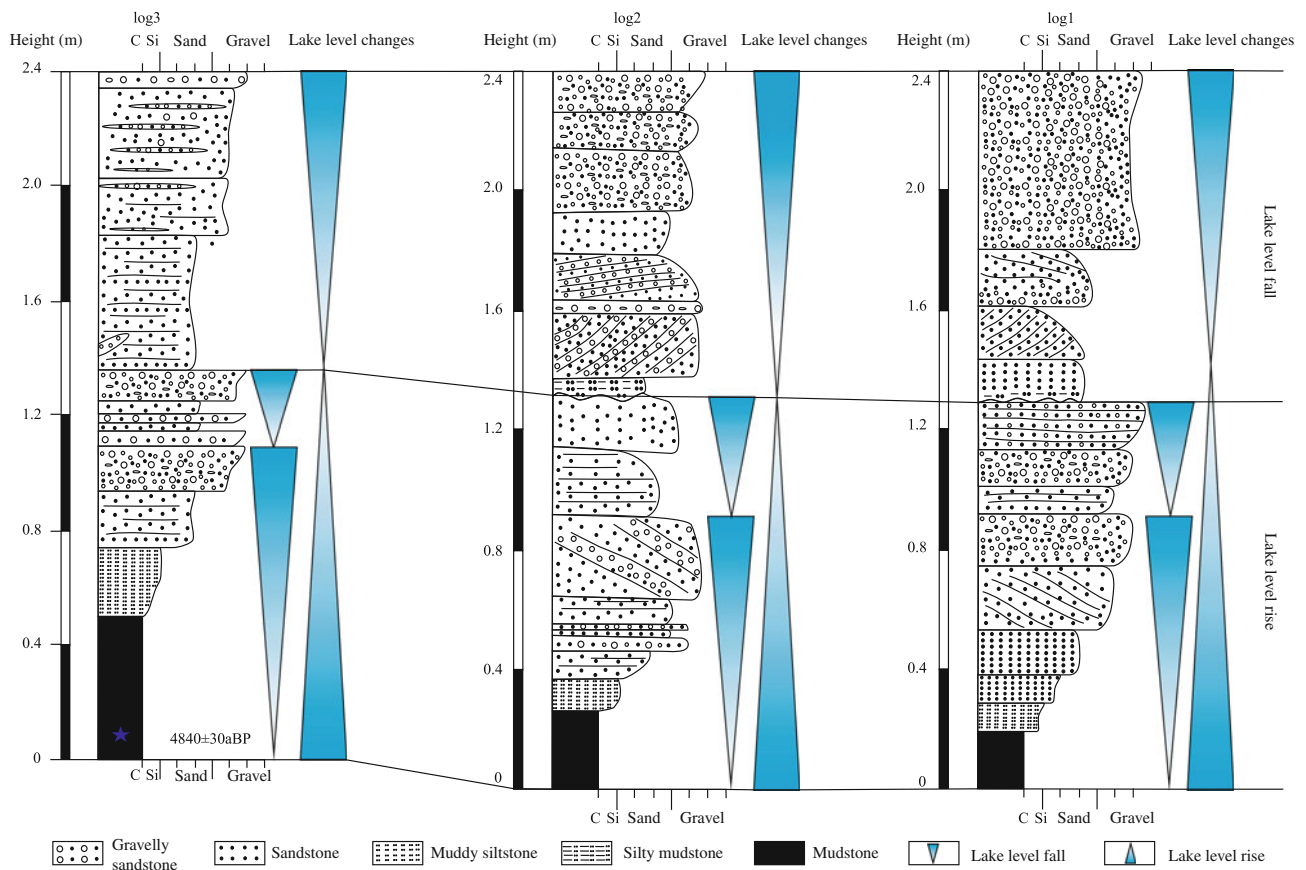
**Fig. 3.34**  Lithologic log and lake level variation of Log 1, 2, and 3

In addition, the lake water level did not rise continuously, but had some minor decrease in between.

The sedimentary evolution model of the research area is established based on the study of single-stage lake beach sedimentation and multi-stage lake beach sedimentation template (Fig. 3.35). The single-stage beach ridge is commonly characterized by low-angle cross bedding on the lake side and parallel bedding on the land side (Fig. 3.35a). The multi-stage sedimentation of lake beach is clearly controlled by the change of lake water level. About 4840 BP years ago (equivalent to the greenhouse period of mid-Holocene), muddy sediments are formed in the lagoon behind beach (Fig. 3.35b). As the lake rises, the beach ridge continues to descend towards the shore (Fig. 3.35c, d). When the lake reaches its highest level, beach ridge was scoured by waves during a short period of time, and formed a thin layer of muddy silt (Fig. 3.35e). The lake then descended, and the beach was eroded, leaving only bedding dipping towards the land (Fig. 3.35f, g).

### 3.2.2.5  Summary

The Qinghai Nanshan stretching hundreds of kilometers is the starting point of the "source-sink" system in this area. Due to different lithology and topography, the extent of weathering, erosion and transportation and sediment products are different at different piedmont area. The Heima river flow through Zhongwunong Mountain and Chakabei Mountain. Limestone is commonly outcropped at the drainage valleys of Heima River. Therefore, the gravels in Heima River is dominated by limestone. The small rivers on the south side of the Heima River mainly flow through strata composed of granite and clastic rocks, therefore contains abundant well rounded conglomerates and sandstone. The part of Qinghai Nanshan close to Jiangxigou area usually outcrop granitic diorite formed during late Indosinian, therefore volcanic gravels are commonly observed in alluvial fans. The Silurian clastic strata exposed before the Longbaoqian Mountain lead to the formation of alluvial fan by mudslide in front of the mountain.
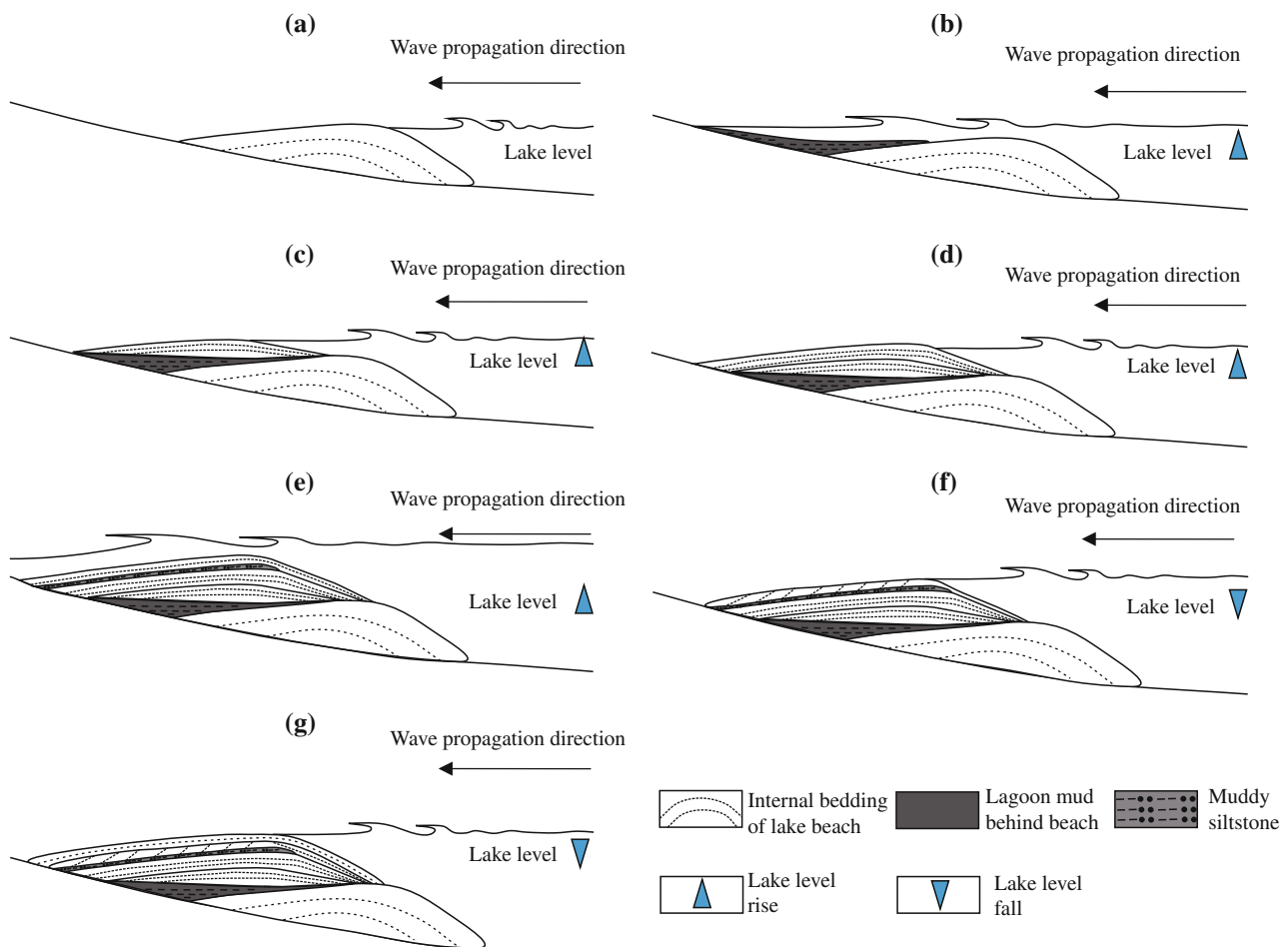
**Fig. 3.35** Multi-stage lake beach depositional model

The Heima River area is on windward slope, thus has high precipitation, high vegetation coverage. The vegetation is dominated by alpine meadow and shrub. The river system here is relatively stable, which leads to the development of fan delta. The precipitation of the Jiangxigou and Erlangjian area is lower than that of the Heima River. The vegetation coverage in this area is relatively low, dominated by shrub and low grass meadow. The rivers here are easy to dry up, resulted in development of alluvial fans formed by temporary flows (Fig. 3.36a).

In the coastal area along Erlangjian-Jiangxigou, the salinity and PH of soil are relatively high, and the maturity of the soil is low. Only salt-tolerant plants can grow on the soil. The coastal area near Heima River is flat and narrow. Soil in this region is fed by piedmont underground water, so the coastal area is usually covered by alpine meadow.

Although both coastal areas are formed by the retreat of the lake, due to the difference in vegetation type and coverage, the Erlangjian area has shown emergence of desert plants and desertification (Yao et al. 2015).

Based on field observations, remote sensing images, and comparison with previous studies, we complied the planimetric map of Qinghai Nanshan–Alluvial fan–fan delta depositional system (Fig. 3.36a) and the depositional cross-section (Fig. 3.36b). Alluvial fan, fan delta, and coastal facies are present before Qinghai Nanshan. Alluvial fan is located in the foothills, which often have small area and form alluvial fan skirt. Relatively stable braided distributary channels are widely developed on fan delta plains. Alluvial fan gradually transit to the ancient coastal facies towards the lake. The modern foreshore subfacies is mainly composed of beach sediments, which can be divided into

**(a)**



**(b)**
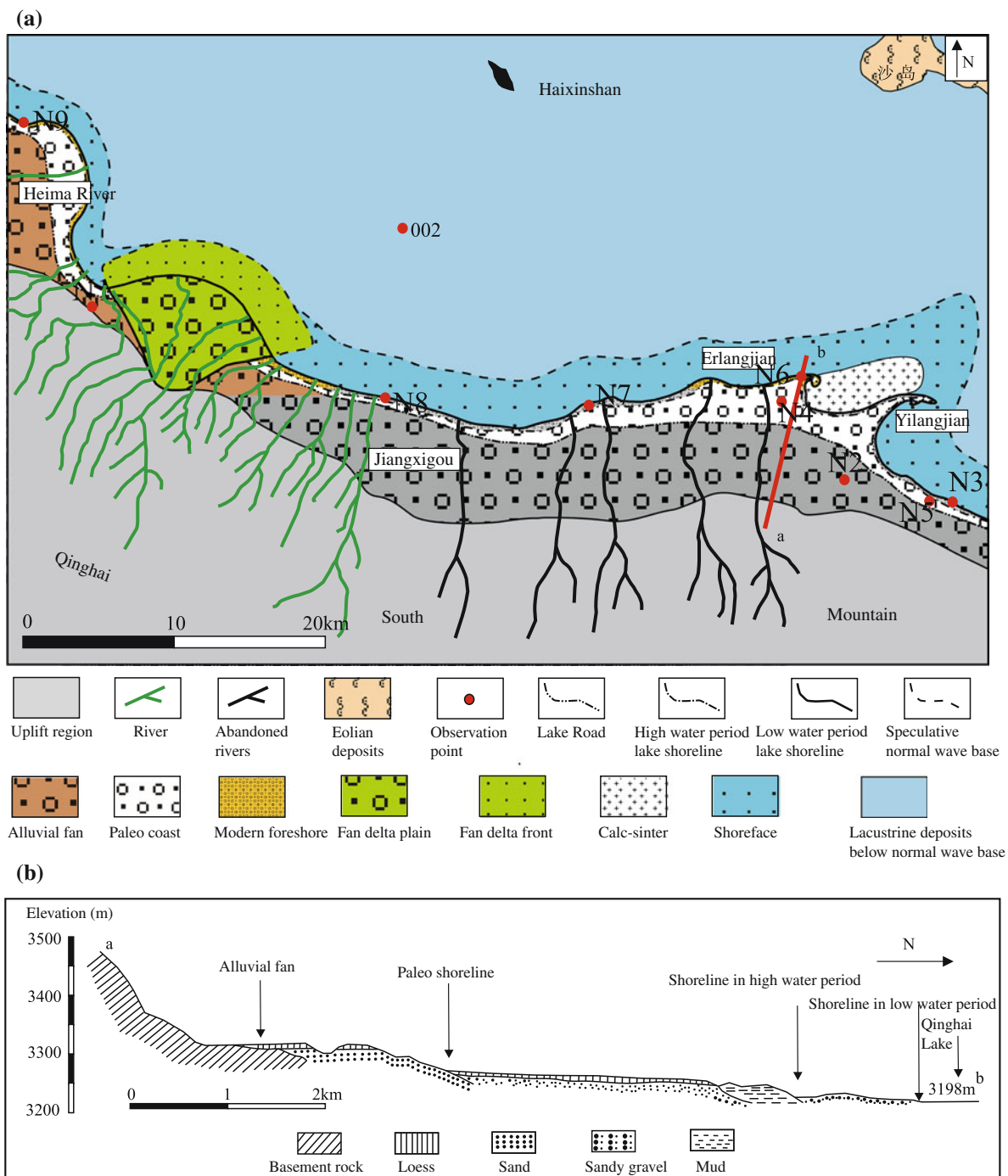


**Fig. 3.36  a** Qinghai Nanshan–Alluvial fan-fan delta/coastal depositional system. **b** Cross section a–b

beach ridge, inter beach ridge, sheet sand and lagoon. Based on the study of modern coastal facies and combined with two typical profiles, the characteristics of single- and multi-stage lake beach sedimentations are analyzed in detail, and the sedimentary evolution model of multi-stage lake beach sedimentation is established.

## 3.3 The Distribution of Modern Depositional System and Windfield-Source-Basin Dynamic Model of Qinghai Lake

### 3.3.1 The Distribution Characteristics of Modern Depositional System

In the "Qinghai Lake Comprehensive Investigation Report" published in 1979, the scientists from Lanzhou Institute of Geology, CAS and other institute conducted large-scale study of the Qinghai Lake for the first time. Their research focused on the formation and evolution of Qinghai Lake and the distribution of lake sediments, but did not compile a detailed planimetric map of the Qinghai Lake depositional system. In 1997, Wang et al. (1997) established the distributional map of the Qinghai Lake depositional system for the first time. They recognized 22 depositional facies, and describe the characteristics of each depositional facies (Fig. 3.37). Song et al. (1999) proposed for the first time that the coastal zone can be divided into microfacies including coastal gravel bar, mudflat, sand beach, and underwater wind sand accumulation and lagoon, based on field study of the coastal zone. Shi et al. (2008) divides the modern depositional system of Qinghai Lake into six sedimentary systems according to the distribution of water system and the characteristics of the sedimentary environment. They also put

forward the relationship between the distribution of modern depositions and the distribution of water system, tectonism and fault activity. Song et al. (2001) divided the modern delta of Qinghai Lake into river-controlled delta (Buha River Delta), wave-controlled delta (Haergai River Delta) and river-wave transitional delta (Shaliu River Delta), and further examined the sedimentary characteristics and control factors of formation of the first two types. Song et al. (2000) analyzed the characteristics and causes of the aeolian sand dune on the west coast of Qinghai Lake. An et al. (2006) analyzed the structure and sedimentary distribution at the lake bottom using seismic data. The previous studies of the modern sediments of Qinghai Lake provides a solid foundation for the research of the modern sedimentary system in this study.

In this study, we first introduce the "source-sink" system into the analysis of modern sedimentary systems. On the basis of studying depositional characteristics of "points" in different regions, we examine the pattern of sedimentary variation on each "line" in details, and established six "source-sink" and lake depositional systems. We also compile a new planimetric map of the modern depositional system of Qinghai Lake, based on the regional geologic map of Qinghai province (Qinghai Provincial Bureau of Geology and Mineral Resources 1991), the map of sediment distribution in Qinghai Lake (Lanzhou Institute of Geology, CAS 1979) and the map of shoreline migration of Qinghai Lake
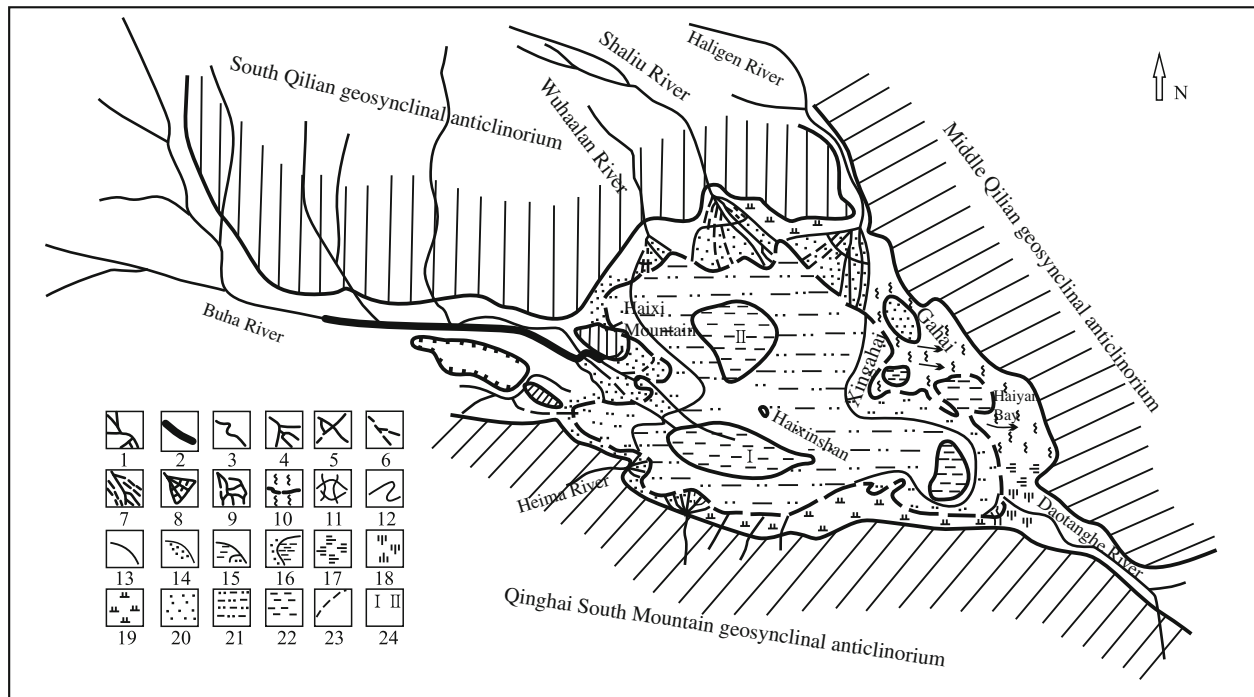


**Fig. 3.37** Depositional system of Qinghai Lake (modified from Wang et al. 1997). 1. Mountain river; 2. Braided river; 3. Meandering river; 4. Distributary channel; 5. Subaqueous river; 6. Abandoned channel; 7. Alluvial fan; 8. Fan delta; 9. Delta; 10. Eolian accumulation; 11. Lagoon; 12. Sand spit; 13. Sandy beach; 14. Gravelly beach; 15. Muddy beach; 16. Lake bay; 17. Swamp; 18. Salt marsh; 19. Alluvial plain; 20. Shallow lake; 21. Semi-deep lake; 22. Deep lake; 23. Shoreline; 24. Depression

(Yuan et al. 1990), which are combined with Google Earth remote sensing images, field study, and lake bottom measurement and sampling (Fig. 3.38).

Previous studies simply consider the source area as eroded area, when producing plan of the modern depositional system of Qinghai Lake. Based on the analysis of the source-sink system of the Qinghai Lake area, it is found that the petrological characteristics of the provenance area determine the type and supply of sediments in source-sink processes. Therefore, when compiling the plan of Qinghai Lake sedimentary system, we added in descriptions about the lithology, vegetation type and coverage, precipitation and evaporation of the source area, based on the geological map of Qinghai Lake and its surrounding area.

When the strata of the provenance area are Silurian (marine clastic rocks dominated by shale and sandstone), the strata are susceptible to erosion and transportation. Rivers passing those areas are enriched in sand and mud sediments, leading to formation of deltas by stable water flow (e.g., Buha River delta) and alluvial fans by temporary water flow (e.g., Guoluo alluvial fan). When the strata of the provenance area are granite and Triassic sandstone and conglomerate, the rocks are resistant to weathering and erosion. Sediments transported by rivers are dominated by gravels, and thus gravel-rich fan delta and alluvial fan are formed. When the strata of the provenance area are Jurassic (coal-bearing strata and sand/gravel strata), the eroded coal-bearing strata are rich in carbon and clay minerals, providing source sediments for downstream wetlands and swamps. When the strata of the provenance area are Mesoproterozoic (metamorphic rocks of amphibolite facies), the rocks are rich in unstable amphibole and biotite, and are susceptible to weathering and erosion.

Previous studies also failed to take into consideration of the migration of lake shoreline. In this study, we divided the costal deposition in modern coastal facies and ancient coastal facies by the first lake terrace. The modern coastal facies are further divided into foreshore and shoreface subfacies.

Based on field observation and water depth measurement, we revised some previous description of sedimentary facies: (1) The original Shaliu River fan delta is now divided into Gangcha alluvial fan, Gangche delta and Shahe River delta; (2) the distribution of Buha River delta front is re-outlined (3) the sedimentary facies at the lake inlet of the distributary north of Haergai River and their distribution and formation mechanism are refined.

From the 1960s to the early 20th century, the warm and dry climate in the Qinghai Lake area led to a decline in the water level and shrinking of lake area. The type and distribution of sedimentary facies have changed as following. (1) Buha River, which originally flow towards the northern depression, diverted to the south of the island, towards the southern depression and Tiebujia Bay. (3) As the Buha River delta continue to migrate towards the lake, the bird foot delta evolved to a lobate delta, and connected with Bird Island and Egg Island. The abandoned Buha delta plain (north of Bird Island) has formed aeolian sand dune. (4) Shaliu River delta continuously migrate towards the lake bay on the south side. (5) The originally isolated Sand Island has closed to form new Gahai, and the Haiyan Bay and Qinghai Lake is only connected by a long and narrow channel. (6) The sand spits at Erlangjian and Yilangjian migrate eastward (Fig. 3.38).

### 3.3.2 Main Controlling Factors of the Modern Depositional System of Qinghai Lake

Based on the description and analysis above, the controlling factors of the modern sedimentary system of Qinghai Lake include topography and geomorphology, lithology of the source area, water system, vegetation type and coverage, windfield, wave, lake current and water level (Fig. 3.39). The landscape of the mountains affects the distribution of water system and regional windfield. The landform of the lake bottom affects the direction of lake current. The type of sediments that are eroded and transported depends on the lithological characteristics of the provenance area. Vegetation types and coverage determine the stability of sediments in provenance areas. The runoff of the water system, the type of sediment supply and seasonal climate change affect the sediment transportation process. The ancient coastal sediments are eroded, transported and accumulated by wind to form eolian sand dunes. The characteristics of regional wind field are closely related to precipitation, which indirectly affects the vegetation type and coverage. Wave and the lake current control the plane distribution of sand bodies. Varying lake water level affects the accommodating space, and thus affects the depositional pattern.

To briefly summarize, the modern depositional system of Qinghai Lake is contemporarily influenced by the three factors: "windfield-source-lake basin". The following sections will discussion these three factors individually.

#### 3.3.2.1 Windfield

Climate refers to the state of the atmosphere of a region for several years. Climate factors include temperature, precipitation, evaporation, wind, etc. There are many previous studies on the temperature, precipitation and evaporation of the Qinghai Lake area (Li et al. 2002, 2005, 2008). However, few study had been done on the effects of windfield on the plane distribution of modern sediments at Qinghai Lake.

Although the Qinghai Lake and its drainage basin is located inland, precipitation in this area is higher than other inland areas due to the warm and wet air from southwest and plateau monsoon, coupled with the lake's own lake effects and the frequent transit of westerly belt. The annual
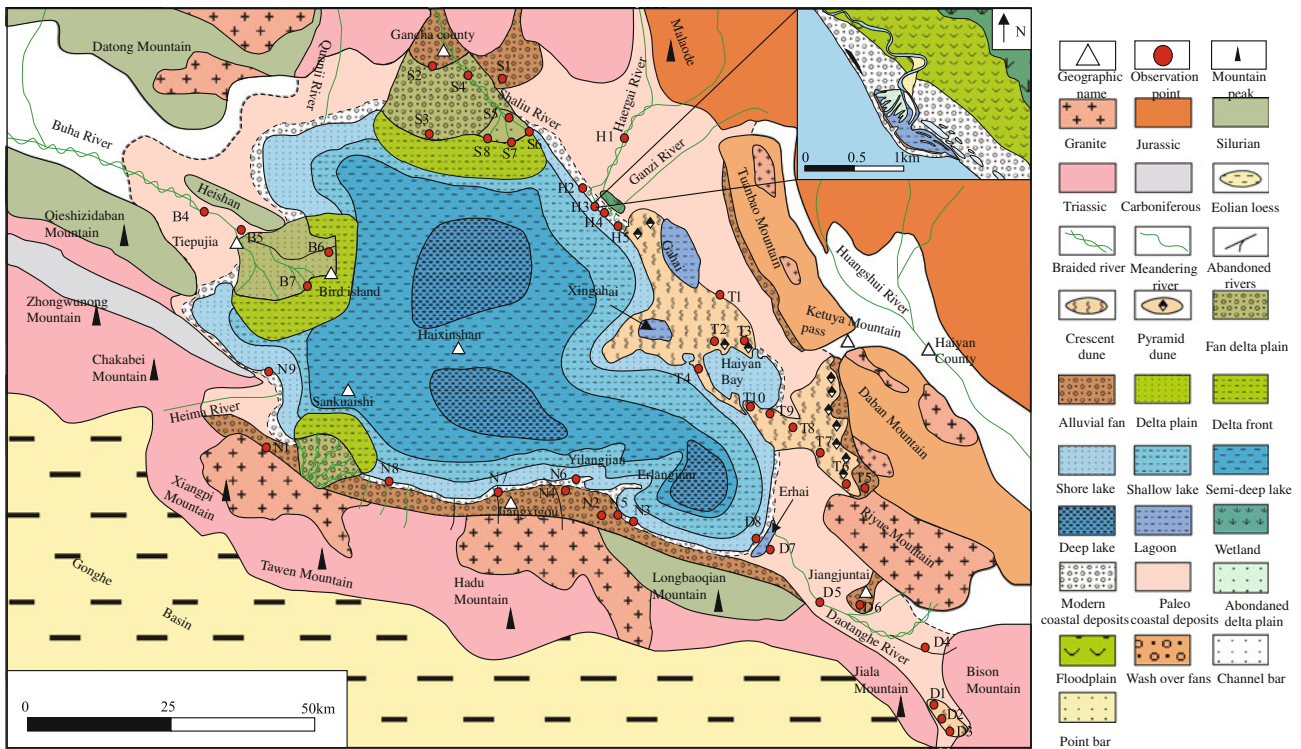
**Fig. 3.38** Modern depositional system of Qinghai Lake

**Fig. 3.39** The controlling factors of the modern depositional system of the Qinghai Lake
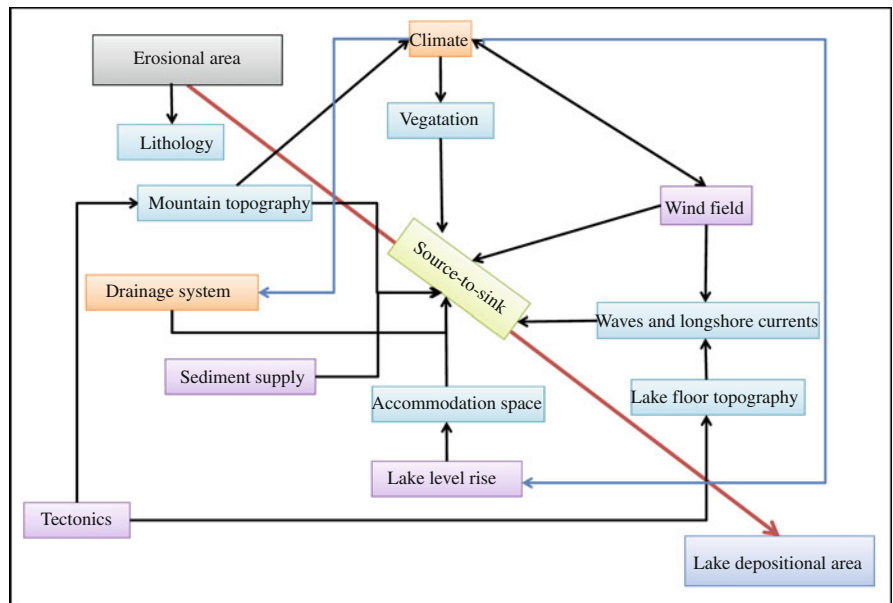


precipitation gradually decreases from the mountainous area north of the lake to south. However, the precipitation at Heima river is high (Fig. 3.40a), which is also indicated by the comparison of precipitation at Jiangxigou and Gangcha in previous discussion. This is likely because the terrain here is beneficial to ascending air, which facilitates precipitation.

Evaporation is the main path of water lose in the Qinghai Lake drainage basin. The average annual evaporation is 1000–1800 mm (20 cm caliber evaporation value) (Lanzhou Institute of Geology, CAS 1994). The variation trend of evaporation is opposite to that of precipitation, which gradually increase from north to south (Fig. 3.40b).
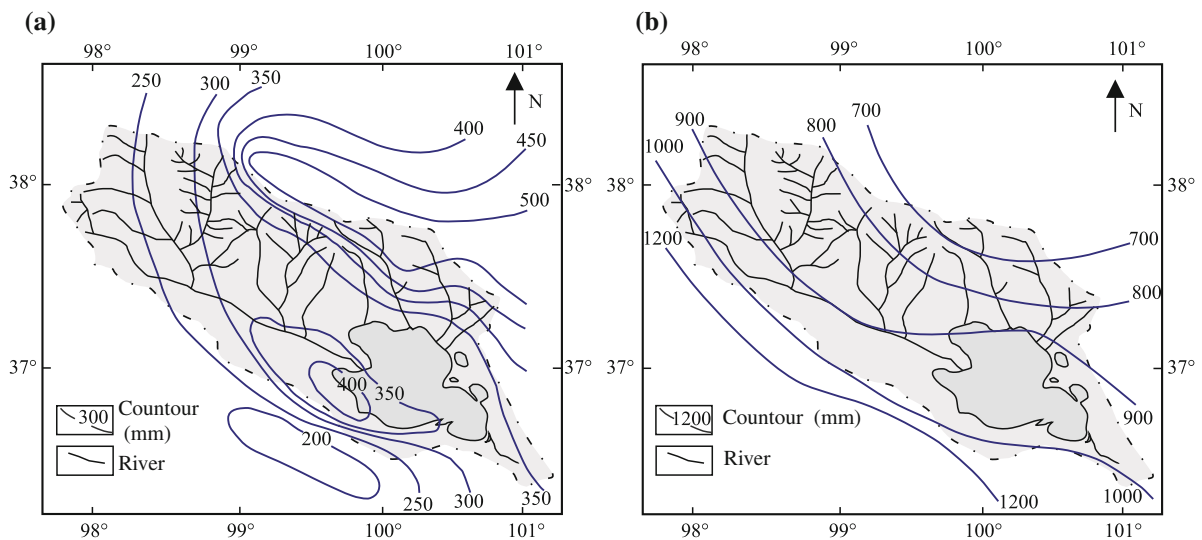
**Fig. 3.40** The annual mean precipitation (**a**) and evaporation (**b**) contour map of the Qinghai lake basin in recent years (from Chinese Academy of Sciences Lanzhou Geological Institute et al. 1994)

By comparison, the average annual evaporation of the Heima River area is similar to that of the eastern lake sand area. However, the average annual precipitation of the former is much higher than that of the later. Therefore, the surface humidity of the former is higher than that of the later. This is also reflected in the vegetation coverage and growth. Temperate steppe, which favors humid condition, is widely developed in the Heima River area. In contrast, the eastern lake sand area is dominated by shrub and sea buckthorn.

Because of the differences in surface humidity and vegetation coverage, and the sediment produced by weathering is also different. The west coast has higher vegetation coverage, therefore is more resistant to weathering, and the weathering products are mostly gravel. The east coast has lower vegetation coverage, which is easy to be weathered and eroded, and the weathering products are mostly sand. The differences in weathering products resulted in the deposition of gravel-sand lake beach sediments on the west

coast (Fig. 3.41a), and the development of large area eolian sand dunes on the east coast (Fig. 3.41b). The humid climate in the west coast leads to the development of gray-black muddy sediments (e.g., alluvial fan in front of Qinghai Nanshan) in mudslide deposits and coastal deposits. The dry climate in the east coast leads to the dominance of reddish-brown mud deposits and the presence of calcareous nodules (e.g., Guoluo alluvial fan).

Changes in the windfield is also controlled by geomorphology and lake-land wind formed by lake effect, in addition to the prevalent wind and monsoon changes.

There are obvious regional differences in the recent tectonism since the Late Tertiary. The uplift of Qinghai Nanshan is much greater than that of the TuanBao-Daban Mountain area. According to the DEM elevation remote sensing data, the three-dimensional geomorphic map of the west and east coast of Qinghai Lake is made. Qinghai Nanshan on the west coast of Qinghai Lake has relatively high landscape, with



**Fig. 3.41   a** Outcrop of the western bank of Qinghai Lake; **b** Outcrop of the eastern bank of Qinghai Lake

**(a)**                                          **(b)**
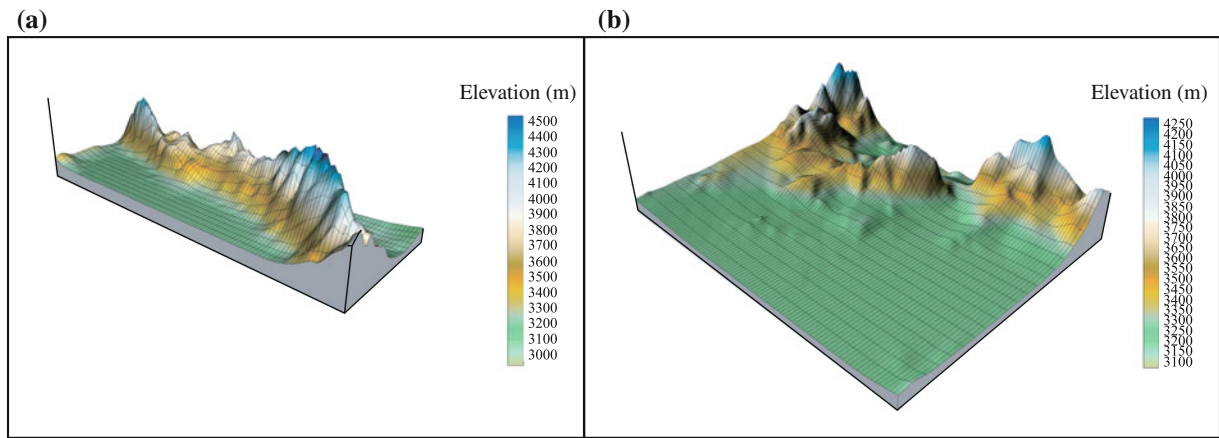


**Fig. 3.42** **a** The three-dimensional geomorphology of western bank of Qinghai Lake. **b** The three-dimensional geomorphology of eastern bank of Qinghai Lake

overall shape like a wall (Fig. 3.42a). The Riyue-Tuanbao Mountain on the east coast of Qinghai Lake has layered landform as a result of regional uplift (Fig. 3.42b).

The difference in topography and geomorphology, coupled with the role of lake-land wind, affects the regional windfield, which in turn affects the regional precipitation (Fig. 3.43). On the south side of Qinghai Nanshan is the vast Gonghe basin. When northwest wind dominates, with the effects of the terrain and thermodynamic effects of the Gonghe basin, southward airflow prevails on the ground of south side. The north side of Qinghai Nanshan is adjacent to Qinghai Lake. Under the effects of the prevailing northwest wind and lake wind, the airflow carrying water vapor leads to much higher

precipitation in the Jiangxigou-Heima River area than others. The Tuanbao-Riyue Moutain area has layered landform. Under the effects of the landform, airflow carrying water vapor is driven westward by high-altitude northwest airflow before the formation of rainfall, and then form precipitation in the Huangshui River valley on the east side.

The effect of wind on the modern coastal sediments is reflected by long-term wind wave, wind setup and longshore current generated by the prevailing northwest and north wind. Wind wave and coastal flow transport sediments from the Jiangxigou area to Yilangjian and Erlangjian and form sand spits. Wind wave and coastal flow also affect the estuary of the northern tributary of the Haergai River, and

**(a)**                                          **(b)**
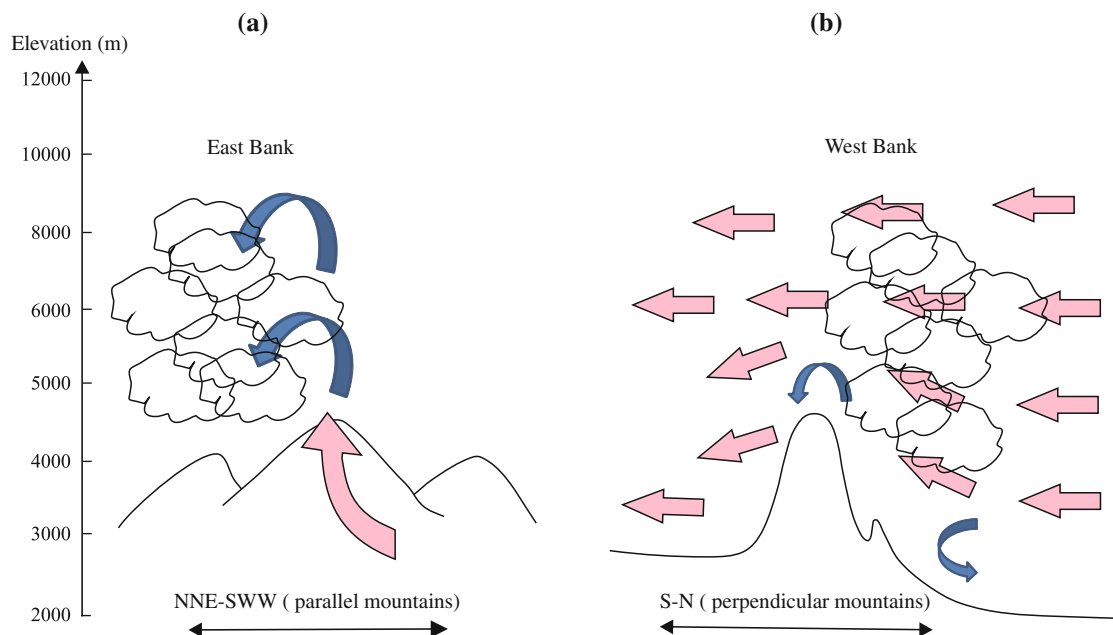


**Fig. 3.43** Conceptual model showing the interaction between cloud and landscape in the Qinghai Lake

form strip-shaped costal bar and lagoon, making the northern tributary cannot directly enter the Qinghai Lake. Wind surges affect the estuary of the Ganzi River, and forms barrier island-channel-lagoon deposition. Long-term effects of wave and longshore current also lead to closure of the Gahai and Erhai. As the lake level decreases, new Gahai and Haiyan Bay also gradually close. Therefore, the northeast-east-south coast of Qinghai Lake is widely affected by the wave and longshore current generated by northwest and north wind.

The wind not only affect the coastal zone below the lake level through wave, longshore current and wind setup, but also directly affect the coastal zone and piedmont area above the lake level. Because of the long-term effects of wind on the piedmont of and plain before the Tuanbao-Daban Mountain, combined with low precipitation, long sunshine duration and high evaporation, this area is easy to be weathered and eroded and form large eolian sand dune. The eolian sand dune on the west side of the Bird Island was formed by wind erosion, transportation and deposition of the delta plain, after the original plain was abandoned due to the avulsion of the Buha River. Long-term wind effect and warm and dry climate lead to the development of Langma Shegang sand area on the southeastern margin of the Daotanghe River valley, which is dominated by crescent-shaped sand dunes.

Therefore, the influence of wind direction and wind force on the sedimentary system of Qinghai Lake is reflected by the dry versus wet climate of the local area, sediment supply, and the intensity of wave and coastal flow. The difference in local climate lead to different degree of vegetation coverage, resulting in different resistance to weathering. The areas that are less resistant to weathering provide abundant sediment supply to eolian sand accumulation. The wave and longshore currents generated by prevailing winds have strong ability to transport and transform sand bodies in the lake.

### 3.3.2.2 Source

The source area is the basis of the "source-sink" depositional system. There are significant differences in the source area of different "source-sink" depositional system.

(1) Characteristics and controlling factors of the source areas in Riyue Mountain/Bison Mountain/Eastern Qinghai Nanshan: Granite at Riyue Mountain and Mid-lower Triassic slate and siltstone at Bison Mountain are the sediment source of the present Daotanghe River. The topography feature (high on the east side and low on the west side) is the direct cause of the current west side location of the Daotanghe River in the river valley. The warm and dry climate, low precipitation and low vegetation coverage lead to decreased runoff of the Daotanghe River, resulted in the massive revival of ancient sand dunes in the valley plain.

(2) Characteristics and controlling factors of source areas in western and middle Qinghai Nanshan: carbonate rocks are exposed at western Qinghai Nanshan; conglomerate, sandstone, dacite and granite are exposed at middle Qinghai Nanshan; Silurian shale and slate are exposed at northeastern Qinghai Nanshan. The precipitation and vegetation coverage in western Qinghai Nanshan is higher than those of middle Qinghai Nanshan. The water system in western Qinghai Nanshan is relatively stable mountain rivers. In contrast, the water system in middle Qinghai Nanshan is mostly temporary water flow. These features lead to formation of fan delta in front of western Qinghai Nanshan and alluvial fan in front of middle Qinghai Nanshan.

(3) Characteristics and controlling factors of source areas in the Buha River drainage basin: the catchment flows through granite strata; braided river and meandering river flow through limestone, sandstone, and shale strata. The NW high and SE low topography is the direct cause of the NW-SE flow direction of the Buha River. Ice and snow melt water, precipitation and underground water are the important water sources of Buha River. Soil along the river is mostly loose and easy to erode, which lead to high sediment load and provide sufficient sediment for the Buha River delta.

(4) Characteristics and controlling factors of the source areas in the western and eastern Datong Mountain: marine clastic rocks (mostly sandstone) are exposed at the outlet of Shaliu River; terrigenous marine clastic rocks (mostly slate and clay slate) are exposed near the Guoluo village. The sediments are derived from the water flow dominated Gangcha alluvial fan and mudslide dominated Guoluo alluvial fan. Higher annual evaporation rate lead to lower runoff of Shaliu River than Buha River. The relatively low vegetation coverage on both banks of the downstream leads to relatively low resistance to weathering, making the river channel easy to divert.

(5) Characteristics and controlling factors of the source areas in the northeastern Datong Mountain: Haergai River and Ganzi River flow through the middle Jurassic coal-bearing and clastic strata, which provide sediments for the wetlands and swamps near the estuary. Low annual evaporation helps preserve water in soil, and provide favorable conditions for formation of wetlands and swamps.

(6) The characteristics and controlling factors of the source areas in Tuanbao Mountain/Daban Mountain/western Riyue Mountain: the lithology of this area is mainly amphibolite facies metamorphic rocks that are susceptible to weathering. Low precipitation and high evaporation led to relatively dry climate in this area. The

relatively unitary vegetation type and low vegetation coverage lead to very week sand-fixing capacity. Lake of water system results in development of large area of eolian deposition.

To sum up, the controlling factors of the source area include lithology, geomorphology, climate (wind, precipitation, evaporation, etc.), vegetation type and coverage, water system, etc.

### 3.3.2.3 Lake Basin

The term "lake basin" contains two folds of meanings: lake basin topography and lake basin evolution. Lake basin topography can be divided into mountain landform and lake bottom landform. Mountain landform affects the distribution of water system and regional windfield. Lake bottom landform controls the propagation direction of lake current.

The direction of the main fault structure in the lake basin is NNW-NW-NWW, resulting in the mountainous region having strike direction of NW-SE. Therefore, the upstream of rivers in the lake area is mostly NW-SE (except the Daotanghe River and Heima River). The terrain (northwest high and southeast low) determines the slope of the rivers. The slope from the upstream to the downstream of Buha River is large, which is conducive to river undercutting. The slopes of the Haergai River, Ganzi River and Daotanghe River drainage basin are smaller, which lead to lower undercutting capacity and less obvious valley shape. Due to the greater elevation difference and longer transportation distance from source to estuary, more fine-grain sediments are unloaded at floodplain and delta plain of the Buha-Shaliu drainage basin than that of the Ganzi-Daotanghe drainage basin.

Qinghai Lake is characterized by three main clockwise transportation currents and other secondary counterclockwise transportation currents (e.g., lake bay, river). This is consistent with the geomorphology of the lake bottom, which have three depressions. In addition, the slope of the lake bottom is steeper on the south side due to tectonism, which lead to coarser costal sediments on the south side than on the north side.

The lake basin topography is the result of the combined effect of sedimentary background and tectonic activity. The role of tectonic activity in forming basin topography is as following: (1) determining the topographic height difference between sediment-carrying rivers and catchment basins, thus determining the rate and velocity of flow; (2) determining the abundance of sediment source (3) determining the plane distribution of lake sediments.

The evolution of lake basin affects the temporal variation of sedimentation. In turns of modern sedimentation, changing lake level can led to changing capacity, and thus affects depositional style. When the rate of capacity growth is higher than the rate of sediment supply, the Gangcha alluvial fan migrates towards the lake and form Gangcha delta. When the rate of capacity growth is close to the rate of sediment supply, the growth of Gangcha delta suspends. When the rate of capacity growth is lower than the rate of sediment supply, the abandoned Gangcha delta is cut by the Shaliu River, and transforms into ShaliuRiver delta that migrates towards the lake bay.

### 3.3.3 Application of the Windfield-Source-Basin Model

The controlling factors described above are not acting on the sedimentary system individually. Instead, the modern sedimentary system of the Qinghai Lake is the product of the comprehensive effects of the "windfield-source (provenance)-basin (basin geomorphology and basin evolution)" system. Sediment source is the material basis of the "windfield-source-basin" system. The wind is an important dynamic factor in the "windfield-source-basin" system. Wave and longshore current formed by wind control the distribution of sand body. Wind also influences the coastal zone that is often above lake level, where large-scale eolian sand accumulation can be formed. The geomorphology of the lake basin affects the transportation distance of rivers and the direction of lake currents. The varying lake level during the evolution of the lake basin affects the lake capacity, which in turn affects the depositional style of sediments.

The seven subsystems of the "windfield-source-basin" system described above can be applied to the modern sedimentary system of Qinghai Lake. (1) Wind controlled system: the piedmont region of the east lake sand area and Langma Shegang sand area are commonly characterized by wind eroded landform, therefore belongs to wind controlled system. (2) Source controlled system: the catchment area of river belongs to source controlled system. (3) Basin controlled system: the semi-deep and deep lake area and the travertine developing area is dominated by geological processes within the lake itself, which belongs to the basin controlled system. (4) Windfield-source system: eolian sand dunes in front of Tuanbao-Daban Mountain, on the Buha River delta plain, and in the Langma Shegang sand area are dominated by wind and its accompanying climate condition and sediment source supply, therefore belong to windfield-source system. (5) Wind-basin system: the oolite sand and gypsum-salt layer between sand dunes in eastern lake are influenced by wind and its accompanying climate condition and basin dynamics, and thus belongs to wind-basin system. (6) Source-basin system: this type of system widely existed in the surface dynamic processes from

source to sink, including alluvial fan, river, fan delta, and delta. (7) Windfield-source-basin system: this type of system is subjected to combined effects of windfield, sediment source and lake basin, and is mainly existed in the coastal shallow lake areas that are subjected to the effects of sediment source, including barrier coast (barrier island and trumpet-like estuary), lake beach and littoral deposition.

The modern depositional systems of Qinghai Lake are mainly source-basin system and windfield-source-basin system. We found that the depositional systems on the east coast and west coast are significantly different from each other.

The three "source-sink" sedimentary systems on the west coast of Qinghai Lake (Qinghai Nanshan–alluvial fan–fan delta/coastal sedimentary system, Buha River-delta sedimentary system and Datong Mountain-alluvial fan-fan delta/braided river-meandering river delta sedimentary system) have the following common characteristics. (1) Sediment supply is high, water system is well developed, and river runoff is large. (2) Constructive delta is often formed as rivers enter the lake (e.g., Gangcha delta, Buhahe delta). (3) Both modern and ancient coastal facies are dominated by lake beach deposition, indicating relatively week hydrodynamics. (4) The steep geomorphology on the west coast lead to relatively large elevation difference between the lake basin and sediment carrying rivers, which results in high flow rate and speed, and is favorable for sediment migration towards the lake. (5) Climate is relatively humid, precipitation is relatively high, and vegetation is well developed. (6) The three "source-sink" depositional systems are located on the leeward side (N-NW-W-SW) of the prevailing wind of Qinghai Lake area (northwest and north wind), and are subjected to limited effects of wind wave and longshore current.

The three "source-sink" sedimentary systems on the east coast of Qinghai Lake (Haergai River/Ganzi River–barrier coastal sedimentary system, Tuanbao Mountain/Daban Mountain–alluvial fan/coastal–wind sedimentary system and Riyue Mountain/Bison Mountain–Daotanghe–barrier coastal sedimentary system) have the following common characteristics. (1) Sediment supply is low, water system is not well developed, and river runoff is small and often dries up. Some sand dune areas even have no river. (2) These sedimentary systems have the characteristics of barrier coastal facies. For example, barrier bar is developed at the estuary of the tributary north of Haergai River. (3) Eolian sands accumulate in front of the Tuanbao Mountain and Daban Mountain, which account for about one fifth of the lake area. (4) The relatively flat geomorphology on the east coast lead to relatively small elevation difference between the lake basin and rivers, which is unfavorable for sediment migration towards the lake. (5) Climate is relatively dry, precipitation is relatively low, and vegetation is not well developed. (6) The three "source-sink" depositional systems

are located on the windward side (NE-N-SE-S) of the prevailing wind of Qinghai Lake area (northwest and north wind), and are subjected to strong effects of wind wave and longshore current.

Combined with previous discussion, the formation and distribution of the modern depositional system of Qinghai Lake is also influenced by wind direction and wind force in addition to the "source-sink" system. The "source-sink" sedimentary systems on the east coast have low sediment supply and are located on the windward side. In contrast, the "source-sink" sedimentary systems on the west coast have high sediment supply and are located on the leeward side. Therefore, the "windfield-source-basin" system of Qinghai Lake can be divided into "strong source-leeward" system and "weak source-windward" system.

The deposition model of the "strong source-leeward" system of the west coast is shown in Fig. 3.44. The west coast of Qinghai Lake is located at the steep slope on the short axis of the lake basin. Qinghai Nanshan terrain is relatively high, and is extensively weathered. A lot of clastic materials roll down from the hillside and form alluvial fans at mountain foot. The gravels in alluvial fan are poorly sorted and mainly subangular. As the sedimentary facies gradually transit into coastal facies, gravels are better sorted and more rounded. The coastal zone is subjected to the long-term effects of wave and longshore current, and forms large beaches. As the Erlangjian horst forms, the coastal sediments are transformed by wave and longshore current to form the Erlangjian sand spit. The tip of the sand spit continues to extend southeastward as the lake level increases. There are several mountain rivers in western Qinghai Nanshan, which have spread out from the mountain pass and formed typical mountain-based fan delta. The upstream tributaries of Buha River merge into catchment section, then flow downstream as braided river, which gradually transforms into meandering river after entering the plain area. As the slope further decreases, the distributary channels of delta plain further diverge and migrate, and form larger delta plain. In the 1970s, the Buha River flows before the Heishan Mountain, and then inject into the northern depression of Qinghai Lake. However, the current front of Buha River dalta is advancing towards the southern depression of Qinghai Lake, due to river diversion in the recent two decades. The Buha River delta in front of the Heishan Mountain has been abandoned, and form large eolian sand dune and coastal sand bar. The Buha River delta has large area but small front. The distribution area of estuarine bar and sheet sand is relatively narrow. The delta front slope, which is dominated by silty sediments, extends to semi-deep to deep lake. The north coast of Qinghai Lake is relatively flat. The Datong Mountain area has relatively high precipitation, well-developed water system, and multiple alluvial fans formed at mountain passes. The Gangcha alluvial fan (sand
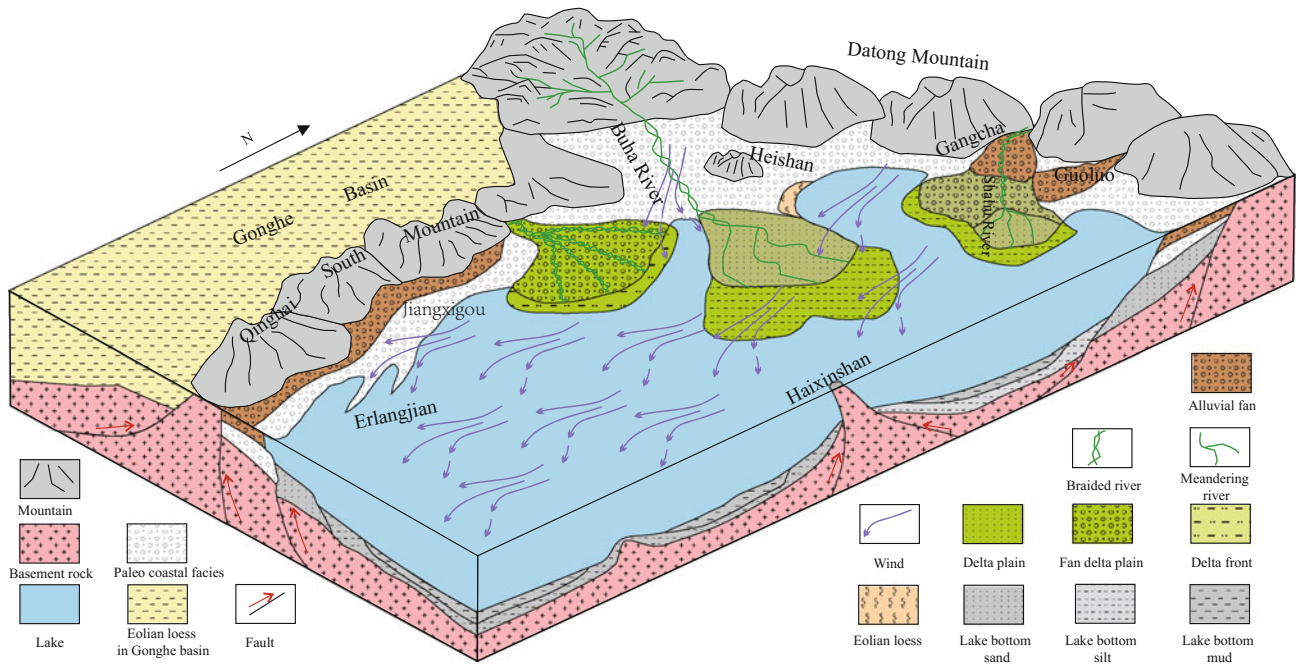
**Fig. 3.44** Depositional system of the leeward western bank of the Qinghai Lake under strong influence of sediment source

and gravel dominated) and Luoguo alluvial fan (mudslide dominated) gradually transit into Gangcha fan delta (sand and mud dominated). The fan delta is further away from the source area, thus has sediments that are well sorted and rounded during transportation. The present Shaliu river cut

into the old fan delta and forms the present Shaliu meandering river delta.

The deposition model of the "week source-windward" system of the east coast is shown in Fig. 3.45. The Haergai River and Ganzi River from Daban Mountain started as
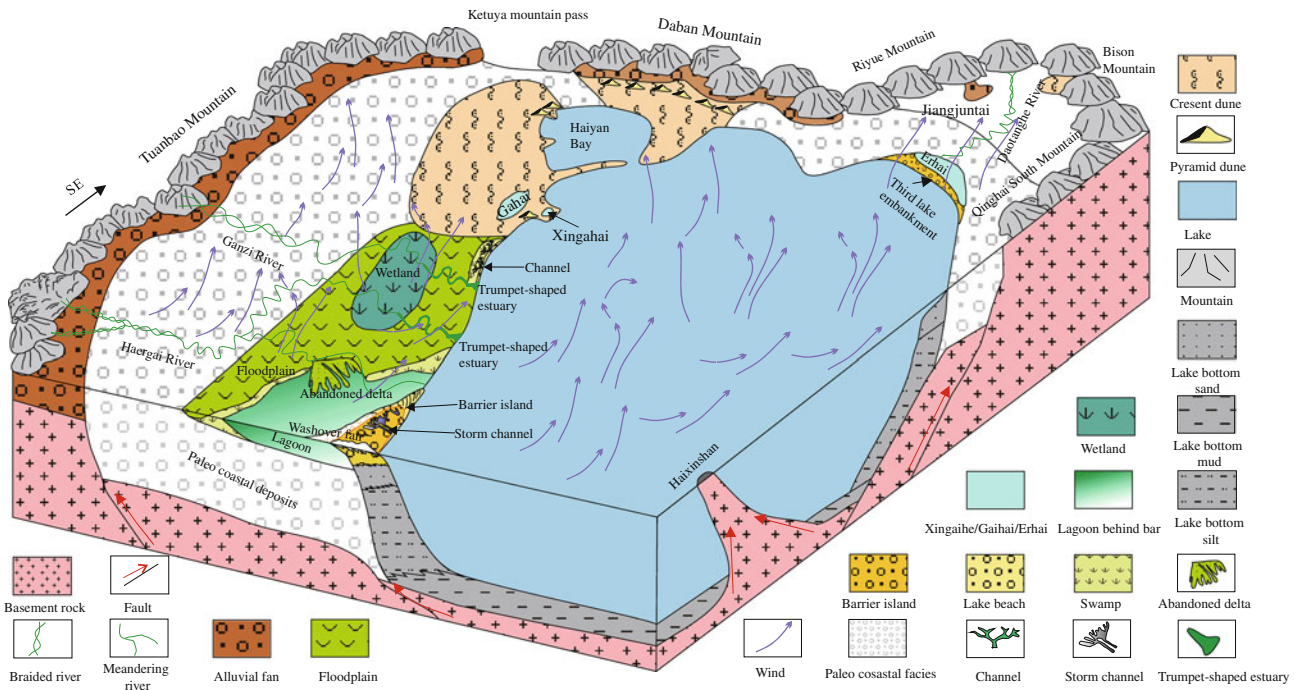


**Fig. 3.45** Depositional system of the windward eastern bank of the Qinghai Lake under weak influence of sediment source

braided river, and become "L" shaped meandering river after entering the plain area. The north tributary of Haergai River has relatively large runoff and high sediment load, therefore often form point bar. River sediments and coastal sediments are transported and reformed by the wave and longshore current generated by the prevailing northwest wind, and form a narrow barrier island. The barrier island hampered the further extension of delta towards the lake. Therefore, the delta formed by the north tributary of Haergai River only developed the plain part of delta. Under the effects of storm wave, over-flow gully and wash-over fan are formed on top of the barrier island. Lots of earlier coastal sand and gravel are transported to the lagoon behind the bar. Storm wave also cause lake water passes the barrier island and flows back into the river. The combined effects of wind setup and river lead to the formation of a trumpet-like estuary of the south tributary of Haergai River. Under the effect of wind setup, barrier bar-channel-lagoon deposition is also formed at the estuary of Ganzi River. The periodical wind setup brings the fine sediments from the lagoon to the coastal area before the barrier bar. Large eolian sand accumulation area is formed as the result of long-term wind erosion, transportation and accumulation of the east coast. Under the comprehensive effects of prevailing northwest wind, valley wind and lake-land wind, high pyramid dunes are formed at the wind intersection. The wave and longshore current generated by northwest wind act on the Sand Island and Haiyan Bay, and lead to formation of coastal sand bar. As lake level decreases, coastal bar is exposed and gradually closes to form barrier island-lagoon deposition. The uplift of Riyue Mountain and Bison Mountain leads to the invert of Daotanghe River and formation of Jiangjuntai alluvial fan. As the climate becomes warmer and drier, the runoff of Daotanghe River decreases and lake level drops. As the results of decreased lake level and the wave and longshore current generated by prevailing northwest wind, the third bank that separates Qinghai Lake and Erhai is formed (barrier island-lagoon deposition). Therefore, barrier island-lagoon depositions are developed on the NE-E-SE coast of Qinghai Lake, which is subject to long-term influence of waves and longshore currents that are generated by northwest and north wind.

# References

An ZS, Wang P, Shen J et al (2006) Geophysical study of the structure and sediment distribution of Qinghai Lake. Sci China Ser D Earth Sci 36(4):332–341

Anthony EJ, Julian M (1999) Source-to-sink sediment transfers, environmental engineering and hazard mitigation in the steep Var River catchment, French Riviera, southeastern France. Geomorphology 31(1):337–354

Bian QT, Liu JQ, Luo XQ et al (2000) Geotectonic setting, formation and evolution of the Qinghai Lake. Seismolog Geol 22(1):20–26

Chen KZ, Huang DF, Liang DG (1964) Formation and development of Qinghai Lake. Acta Geogr Sin 30(3):214–233

Chen JS, Tang QS, Dai ZY et al (2007) The comparison and identification of two different types of fan delta. J Southwest Pet Univ 29(4):1–6

Chen L, Chen KL, Liu BK, et al (2011) Characteristics of climate variation in Qinghai Lake basin during the recent 50 years. Journal of Arid Meteorology, 29(4):483–486

China Academy of Sciences Lanzhou Division, Research Center for Eco-Environmental Sciences, Chinese Academy of Sciences (1994). The evolution and prediction of the modern environment of Qinghai Lake. Science Press, Beijing, pp 69–149

Chinese Academy of Sciences Lanzhou Geological Institute, Chinese Academy of Sciences Shuisheng Biology Institute, Institute of Microbiology Chinese Academy of Sciences et al (1979) Comprehensive investigation report of Qinghai Lake. Science Press, Beijing, pp 1–165

Han YH, Li XY, Wang Q et al (2015) Hydrodynamic control of sedimentary systems in shore zone of Qinghai Lake. Acta Sedimentol Sin 33(1):97–104

Jiang ZX, Wang JH, Zhang YF (2015) Advances in beach-bar research: a review. J Palaeogeogr 17(4):427–440

Li L, Wang ZY, Qing YS et al (2002) Climate change and its impact on desertization around Qinghai lake. Plateau Meteorology 21(1):59–65

Li L, Zhu XD, Wang ZY et al (2005) Impacting factors and changing tendency of water level in Qinghai lake in recent 42 years. Journal of desert research 25(2):689–696

Li FX, Fu Y, Yang Q, et al (2008) Climate change and its environmental effects in the surrounding area of Qinghai lake. Resources Science 30(3):348–353

Li YT, Li XY, Cui BL et al (2010) Trend of streamflow in Lake Qinghai basin during the past 50 years (1956–2007)—take Buha River and Shaliu River for examples. J Lake Sci 22(5):757–766

Lin CS, Xia QL, Shi HS et al (2015) Geomorphological evolution, source to sink system and basin analysis. Earth Science Frontiers 22(1):9–20

Liu RX, Liu YJ (2008) Area changes of Lake Qinghai in the latest 20 years based on remote sensing study. J Lake Sci. 20(1):135–138

Moore GT (1969) Interaction of rivers and oceans: Pleistocene petroleum potential. AAPG Bull 53(12):2421–2430

Moreno C, Romero Segura MJ (1997) The development of small-scale sandy alluvial fans at the base of a modern coastal cliff: process, observations and implications. Geomorphology 18(2):101–118

PAN B T, GAO HS, LI BY, et al (2004) Step-like landforms and Uplift of the Qinghai-Xizang Plateau. Quaternary Sciences, 24(1):51–57

Qinghai Provincial Bureau of Geology and Mineral Resources (1991) Regional geology of Qinghai province. Beijing: Geological Publishing House, pp 1–379

Qinghai Geology and Mineral Resources Bureau (1991) Regional geology of Qinghai Province. Geological Publishing House, Beijing, pp 1–379

Shen HY, Yu JH (2007) Analysis of climatic change characteristics of wind in Qinghai Lake area. Qinghai Huanjing 17(4):170–172

Shi YM, Wang XM, Song CH (1996) Aeolian deposition on the Qinghai Lake region. Acta Sedimentol Sin 14(S1):234–238

Shi XH, Li L, Wang QC, et al (2005) Climate change and its influence on water level of Qinghai Lake. Meteorological science and technology 33(1):58–62

Shi YM, Dong P, Zhang YG et al (2008) Revelation of modern deposits in Qinghai Lake to precise exploration of lithologic hydrocarbon reservoirs. Nat Gas Ind 28(1):54–57

Somme TO, Helland-Hansen W, Martunsen OJ et al (2009) Relationships between morphological and sedimentological parameters in source-to-sink systems: a basis for predicting semi-quantitative characteristics in subsurface system. Basin Res 21(4):361–387

Somme TO, Jackson CA-L, Vaksdal M (2013) Source-to-sink analysis of ancient sedimentary systems using a subsurface case study from the Mor-Trondelag area of southern Norway: Part 1-depositional setting and fan evolution. Basin Res 25(5):489–511

Song CH, Wang XM, Shi YM et al (1999) Sedimentary characteristics and microfacies of shore zone in Qinghai Lake. Acta Sedimentol Sin 17(1):51–57

Song CH, Fang XM, Shi YM et al (2000) Characteristics and formation of Aeolian Dunes on Western Shore of the Qinghai Lake. J Desert Res 20(4):443–446

Song CH, Fang XM, Shi YM et al (2001) Sedimentary characteristics of modern Lacustrine Deltas in Qinghai Lake and their controlling factors. J Lanzhou Univ (Natural Sciences) 37(3):112–120

Sun JC (1938) Qinghai Lake. Geol Rev 3(5):122–134

Wang SM, Shi YF (1992) Review and discussion on the late quaternary evolution of Qinghai Lake. J Lake Sci 4(3):1–9

Wang ZJ, Wang ZS (1980) The discussion of Qinghai "Zhongwunong Mountain Group" and its related issues. Qinghai Geol 3:1–15

Wang XM, Song CH, Shi YM et al (1997) Modern sedimentary environment and sedimentary facies characteristics in Qinghai Lake. Acta Sedimentol Sin 15(S1):157–162

Wang YJ, Zhou XL, Ni SX, et al (2003) Analysis on climate change in the region of Qinghai Lake in the last 40 years. Journal of Nanjing Institute of Meteorology 26(2):228–235

Wu D, Zhu XM, Liu CN et al (2015) Discussion on depositional models of Fan Deltas in steep slope belt of the rift basin under the guidance of source-to-sink system theory: a case study from the Fula sub-basin, Muglad Basin, Sudan. Geol J China Univ 21(4):653–663

Xu HY, Li XY, Sun YL (2007) Climatic change in the lake Qinghai watershed in recent 47 years. Arid meteorology 25(2):50–54

Xu CG (2013) Controlling sand principle of source-sink coupling in time and space in continental rift basins: basin idea, conceptual systems and controlling sand models. China Offshore Oil Gas 25(4):1–21

Yan DX, Zhu BW, Xie QY et al (2011) Characteristics of temperature variation in regions around Qinghai lake. Meteorological science and technology 39(1):33–37

Yang HQ, Jiang DX (1965) The spore and pollen assemblages from the quaternary deposits of the Chinghai Lake basin and their significance. Acta Geogr Sin 4:321–335

Yao ZY, Li XY, Xiao JH (2015) Driving mechanism of sandy desertification around the Qinghai Lake. J Desert Res 35(6):1429–1437

Yuan BY, Chen KZ, Bowler JM et al (1990) The formation and evolution of the Qinghai Lake. Quat Sci 3:233–243

Zhang PX, Zhang BZ, Yang WB (1988) The evolution of the water body environment in Qinghai Lake since the postglacial age. Acta Sedimentologica Sinica, 6(2):1–14

Zhang K, Sun YG, Ju SC et al (2010) The neotectonic process causing the conversion of the Qinghai Lake from an outflow lake into an interior lake. Remote Sens Land Resour S1(86):77–81

Zhu GY, Jin Q, Zhang SC et al (2004) Combination characteristics of lake facies source rock in the Shahejie Formation, Dongying depression. Acta Geologica Sinic 78(3):416–427

# Paleogene Sedimentary System and Sedimentary Dynamics of Windfield-Source-Basin System in the Dongying Sag

## 4.1 Geology of the Dongying Sag

The Dongying Sag is a Mesozoic and Cenozoic petroliferous basin in the Jiyang Depression, Bohai Bay Basin. After dozens of years' petroleum exploration, the chronostratigraphy (Chen and Peng 1985; Pan et al. 2003), tectonic evolution (Allen et al. 1997; Hu et al. 2001; Lin et al. 2005; Feng et al. 2013), and paleogeographic evolution (Feng et al. 2013) in the Dongying Sag have been deeply studied, leaving abundant data. Massive drilling data (Fig. 4.1) are favorable to this study.

### 4.1.1 Tectonic Setting

As a Mesozoic and Cenozoic extension-shear half-graben basin located in the eastern Jiyang Depression, Bohai Bay Basin, the Dongying Sag trends NEE, with EW length around 90 km, SN width around 65 km, and area around 5700 km$^2$. The Dongying Sag is bounded by uplifts or highs, bordering the Binxian High and the Chenjiazhuang High to the north, the Luxi Uplift and the Guangrao High to the south, the Qingcheng High and the Linfanjia Structure to the west, and connecting with the Qingdong Sag to the east. The Dongying Sag is an asymmetric half-graben basin featuring northern faulted and steeper margin and southern hinged and gentler margin (Fig. 4.2). The Dongying Sag is divided into four negative geomorphic units, i.e., Boxing, Lijin, Minfeng, and Niuzhuang Sub-Sags, and is separated by the Chunhua-Caoqiao Faulted Nose Structure Belt and the central faulted anticline belt (Feng et al. 2006). Controlled by faults, the Dongying Sag has several positive structural belts, e.g., Gaoqing Faulted Structural Belt, Pingfangwang Burial-Hill Drape Structural Belt, Chunhua-Caoqiao Nose Structural Belt, Jinjia Nose Structural Belt, Chenguanzhuang–Wangjia Fault Structural Belt, and Bamianhe Nose Structural Belt (Fig. 4.2).

### 4.1.2 Stratigraphic Sequence

The Dongying Sag covers Paleozoic (Pz), Mesozoic (Mz), Paleogene (E), Noegene (N), and Quaternary (Q, Pingyuan Formation) from bottom to top. Among them, Paleogene strata are divided into Kongdian (Ek), Shahejie (Es), and Dongying (Ed) Formations, and Neogene strata are divided into Guantao (Ng) and Minghuazhen (Nm) Formations. Shahejie Formation is divided into Sha-4 (Es4), Sha-3 (Es3), Sha-2 (Es2), and Sha-1 (Es1) Members from bottom to top (Table 4.1).

Five large-scale depositional discontinuity occurred during the forming of Paleogene and Neogene (E + N) in the Dongying Sag, resulting in five planes of unconformity between the Mesozoic (Mz) and Kongdian Formation, Kongdian Formation and Sha-4 Member, Sha-4 Member and Sha-3 Member, Sha-2 Member and Sha-1 Member, and Dongying Formation and Guantao Formation, respectively. The unconformity between Guantao Formation and its underlying strata are the most extensive and can be traced almost across the whole Dongying Sag.

As a set of relatively complete formation in the Dongying Sag, the Paleogene strata has a maximum thickness of 8000 m and acts as the most important oil-generating and oil-bearing series (Feng et al. 2006). According to available drilling data, the regional stratigraphic characteristics of the Paleogene in the Dongying Sag are listed in Table 4.1. This study is targeted at Upper Sha-4 Submember.

### 4.1.3 Characteristics of Tectonic Evolution

Tectonic evolution of the Dongying Sag is divided into three phases (Fig. 4.3): paleogene rifting, post-rifting depression in Neogene Guantao Formation, and tectonic activation from Neogene Minghuazhen Formation to Quaternary. The first phase and the second phase constitute a basin-level tectonic
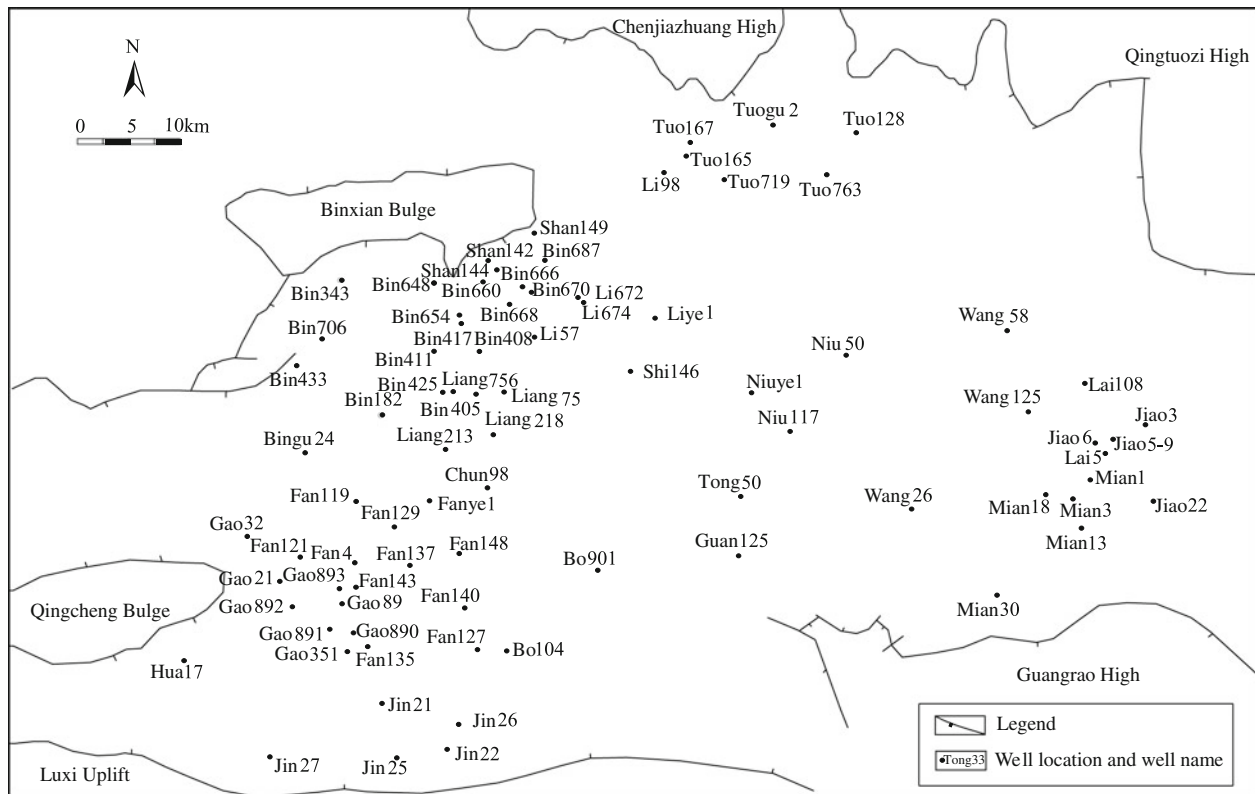
**Fig. 4.1** Location of part of wells in the Dongying Sag

subsidence cycle, which is divided into four stages, i.e., early-middle faulted depression, intense faulted depression, late faulted depression, and depression according to subsidence rate, which increased rapidly from zero to the maximum rate and decreased jumpily until a lag phase.

Rifting in large-scale Mesozoic and Cenozoic rift valleys or faulted basins in eastern China was episodic (Lin et al. 2005). Similarly, the tectonic subsidence in Paleogene rifting in the Dongying Sag was abrupt and intermittent, resulting in episode variation of basement subsidence rate: early initial rifting episode (rifting episode I), late initial rifting episode (rifting episode II), rifting extensional episode (rifting episode III) and rifting convergence episode (rifting episode IV). The faults, sags, and stratigraphic development and filling caused by tectonic movement are analyzed as follows.

(1)  Early initial rifting episode

Early initial rifting episode is the early-middle faulted depression stage of the Jiyang Depression and is equivalent to Kongdian Formation (Ek), corresponding to rifting episode I. In this episode, the Dongying Sag occurred as an extensional half-graben, where NWW faulting intensely occurred, resulting in the intense subsidence and extremely shallow lacustrine sedimentary formation of purplish red

mudstone and sandstone formed in shallow lacustrine swamp ($Ek^1$) in a dry climate. This sedimentary formation had locally developed halite and gypsum and was accompanied by erupted subalkaline tholeiite.

(2)  Late initial rifting episode

The late initial rifting episode corresponds to sedimentation of Sha-4 Member ($Es^4$), which was governed by NWW faults that were still active, and this episode stayed in a transition from dry climate to humid climate. In the early stage ($Es^{4x}$), the interbeds of red mudstone, gray mudstone, and sandstone intercalated with halite and gypsum were deposited. In the late Upper Sha-4 Member, a set of shallow lacustrine to semi-deep lacustrine biolithite limestone, shallow lacustrine beach bar, and oil shale was developed, accompanied by erupted subalkaline tholeiite. The target horizon, i.e., Upper Sha-4 Submember in the study was in this very stage of tectonic evolution.

Occurrence of both early and late initial rifting episodes was controlled by NWW faults resulted from NE-SSE tensile stress. Besides the main controlling faults intensively developed in northern boundary, a series of large-scale sedimentation-controlling faults were developed inside the Dongying Sag, resulting in multiple subsidence centers in the same sag.
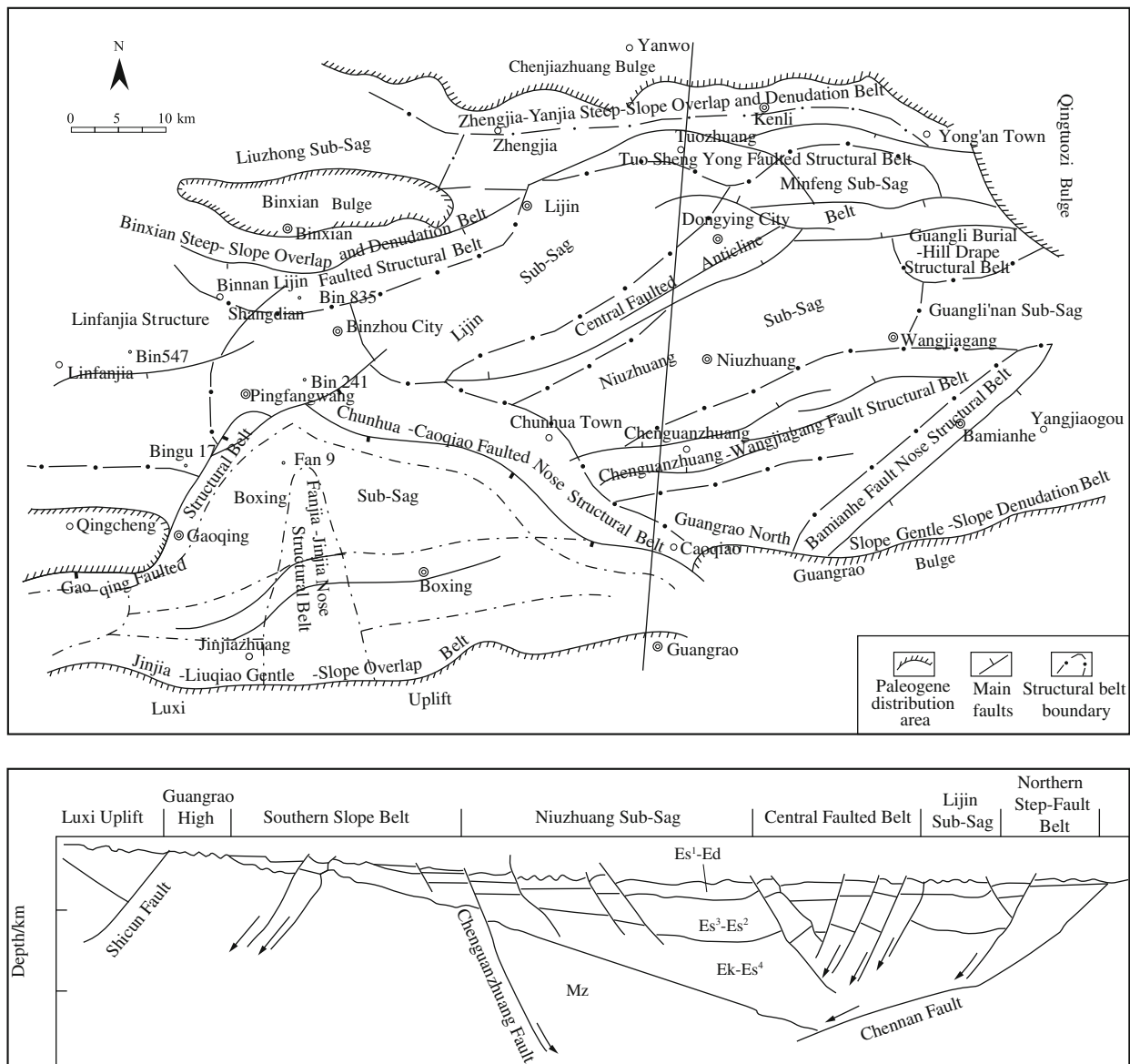
**Fig. 4.2** Outline map of regional structure (upper) (Li 2009) and NS geologic section (lower) (Wu 2015) in the Dongying Sag. Please refer to Sect. 4.2 for stratigraphic codes

### (3) Rifting extensional episode

The rifting extensional episode corresponds to sedimentation from Sha-3 Member to Lower Sha-2 Submember ($Es^3$-$Es^{2x}$), transition of regional tectonic stress field, with dominant NWW-SEE extensional stress and intense extensional rifting. In addition to successive activities of former faults, a series of new normal faults were developed, with synsedimentary characteristics. This episode corresponds to the intense faulted depression stage of the Jiyang Depression. Frequent NE and NEE faulting governed strata distribution. Due to varying subsidence volume, multiple subsidence centers were formed in the Dongying Sag. In this episode, the deposits dominated by deep lacustrine oil shale,

mudstone, turbidite fan, and delta-fluvial deposits indicating humid and warm climate were formed, accompanied by eruptions of olivine tholeiite and olivine basalt.

### (4) Rifting convergence episode

The rifting convergence episode corresponds to the sedimentation of Upper Sha-2 Submember to Dongying Formation ($Es^{2s}$–$Ed$), the late faulted depression of the Jiyang Depression. In this episode, the fault activities weakened. Affected by faults, many subsidence centers were far away from the main controlling boundary faults. The cutting action of later generated faults made activities of fault blocks complicated, and the Dongying Sag was uplifted and

**Table 4.1** Strata in the Dongying Sag (Li 2009)

| Strata | | | | | | Lithology | Contact relationship with the underlying formation | Thickness/m |
|---|---|---|---|---|---|---|---|---|
| Erathem | System | Series | Formation | Member | Submember | | | |
| Cenozoic | Quaternary | Holocene | Pingyuan Formation | | | Shallow yellow sandy clay intercalated with earthy yellow fine sandstone | Unconformity | 300–350 |
| | Neogene | Pliocene | Minghuazhen Formation | | | Brownish yellow, brownish red mudstone intercalated with loose sandstone | Disconformity | 700–760 |
| | | Miocene | Guantao Formation | | | Shallow brown, brownish yellow mudstone intercalated with siltstone and fine sandstone | Unconformity | 250–300 |
| | Palaeogene | Oligocene | Dongying Formation | | | Purplish red, brownish red mudstone, and a large set of massive sandstone | Disconformity | 410–510 |
| | | Eocene | Shahejie Formation | Sha-1 Member | | Gray, grayish green mudstone with thin-bedded dolomite, biolithite limestone, and thin-bedded sandstone | Disconformity | 120–195 |
| | | | | Sha-2 Member | | Dark gray mudstone and shallow gray siltstone and fine sandstone | Disconformity | 160–230 |
| | | | | Sha-3 Member | | Dark gray mudstone brown oil shale | Disconformity | 220–380 |
| | | | | Sha-4 Member | Upper Sha-4 | Gray, grayish green mudstone and siltstone, marlstone, pseudooolith limestone, and limy shale thin interbeds | Disconformity | 80–130 |
| | | | | | Lower Sha-4 | Blue gray mudstone with thin gypsum beds and red mudstone and siltstone interbeds | Disconformity | Not intersected |
| | | | Kongdian Formation | | | The upper part comprises shallow gray, brownish red siltstone, and purplish red mudstone interbeds, and the lower part comprises shallow gray, brownish red massive sandstone | Unconformity | Not intersected, intersected in a few wells |
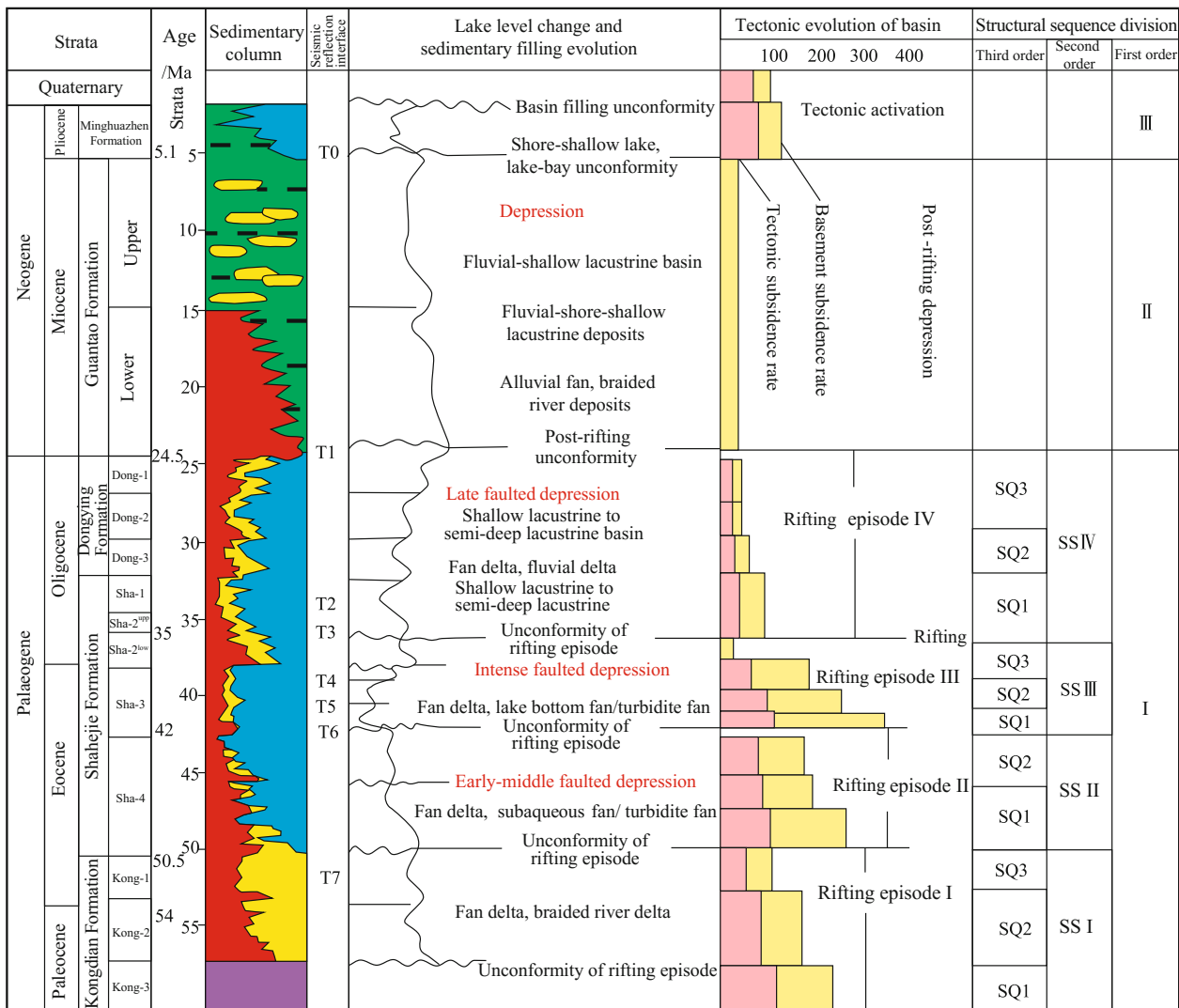
**Fig. 4.3** Cenozoic tectonic evolution and sequence division of the Jiyang Depression. Modified according to Lin et al. (2005)

corroded. In the early stage, a set of sediments dominated by shallow lacustrine facies were developed extensively in braided river plain. In the late stage, a set of sediments dominated by alluvial fan were developed, accompanied by large-scale alkali to strong alkali basalt, and alkaline ultramafic rocks.

Later on, the Dongying Sag together with the Bohai Bay Basin entered the stage of post-rifting filling. In Neogene, the depression stage of the Jiyang Depression, the burial depth increased, the faulting basically entered a lag stage, and the basin overall subsided due to isostasy, with subsidence range larger in the north and lower in the south. In the post-rifting depression stage (Ng), a set of braided river and meandering river deposits dominated by fine conglomerate, pebbly sandstone intercalated with grayish green and purplish red mudstone, and sandstone intercalated with grayish green and purplish red mudstone were stably developed in

the Bohai Bay Basin, accompanied by sedimentation of strong alkali basalt and basanite. In the tectonic activation stage (Nm), a set of alluvial deposits intercalated with ingression beds were developed (Feng et al. 2006).

## 4.2 Sequence Stratigraphic Division of Upper Sha-4 Submember in the Dongying Sag

### 4.2.1 Identification of Sequence Boundaries (SBs)

According to the unconformities and their corresponding interfaces resulted from tectonic episodes, second-order climate cycles, and second-order eustatic cycles of sedimentary

base level owing to source supply, paleogene structural sequence is divided into four sequence sets, i.e., SSI, SSII, SSIII, and SSIV. Among them, SSII comprises middle and lower Eocene Sha-4 Member, which is divided into two third-order sequences by third-order SBs: Sequence 1 (SQ1) and Sequence 2 (SQ2) corresponding to Lower Sha-4 Submember ($Es^{4x}$) and Upper Sha-4 Submember ($Es^{4s}$) of lithologic–biologic stratigraphic units.

The sequence of Upper Sha-4 Submember in the Dongying Sag was divided precisely with principles as follows (Zhu et al. 2003): (1) maximum discontinuity: the depositional discontinuity more obvious than SBs are not present within the sequence; (2) isochronism: all sequences are considered as products of synsedimentation and generally link with their corresponding tectonic subsidence; (3) uniformity: the sequence orders and types are unified within a certain range; and (4) consistency: the SBs divided according to different data are consistent and mutually verified.

1. Identification of SBs

SBs correspond to depositional discontinuity or unconformity and corresponding conformity, and the sedimentary environment below and above SB differs a lot. SBs are mainly identified by the following methods.

(1)  Seismic reflection markers

In seismic stratigraphy, a seismic reflecting interface indicates the chronostratigraphic interface on a stratigraphic sedimentary surface. Different pinch-out forms of strata correspond to different types of seismic event reflection termination in seismic data. Sequence stratigraphic analysis using seismic data is to identify the interfaces of stratigraphic units like sequences and system tracts using types of seismic reflection termination.

Seismic reflection interfaces are divided into concordant and discordant ones according to the reflection termination relationship of events above and below the interface. The discordant interface generally has angular unconformable contact with the seismic events below and above, which reflects that the interface is an unconformity or depositional discontinuity. Therefore, this kind of interfaces can be used to identify and classify SBs. According to morphological characteristics, the discordant interfaces are subdivided into truncation, toplap, onlap, and downlap.

In a seismic reflection profile, the seismic reflection near the SB along basin margin is characterized by truncation and onlap. For example, near Well Bin634 (Fig. 4.4), the sequence bottom boundary (T7′) shows truncation of seismic reflection waves below the boundary, and the sequence top boundary (T6′) shows onlap of the seismic reflection event below the boundary. The seismic reflection is characterized by rapid onlap from sag center to basin margin. As the interface between Upper and Lower Sha-4 Submember, T7 is characterized by strong wave crest, high amplitude, and good continuity, and corresponds to the first flooding surface (FFS) within the study area.

(2)  Markers of well logging curves

The well logging data, which have far higher resolution than seismic data, are used in high-resolution stratigraphic
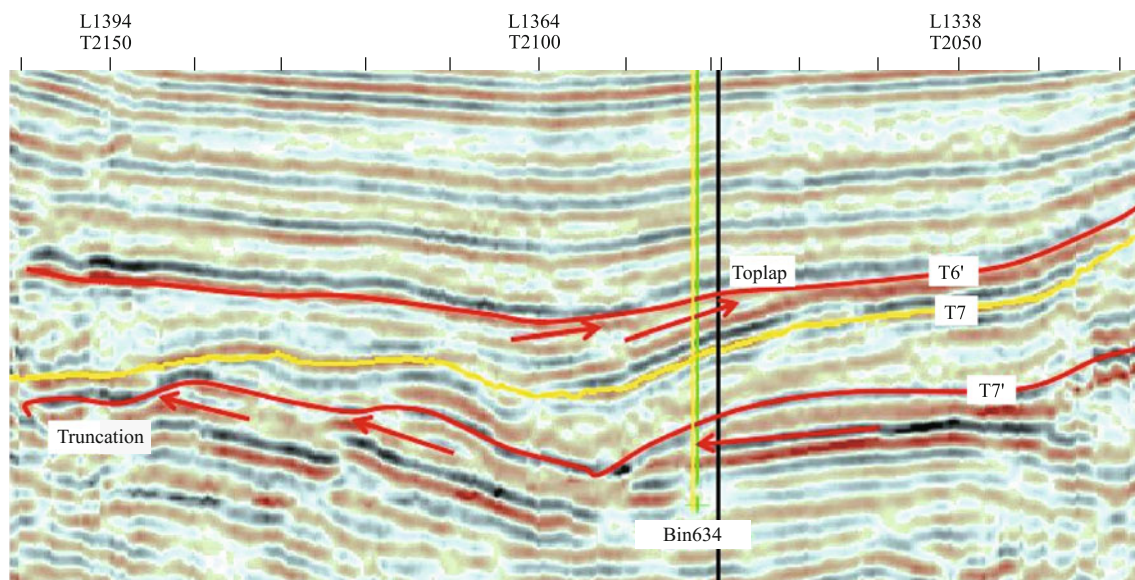


**Fig. 4.4**  Characteristics of seismic reflection across Well Bin634 in the Dongying Sag (south-north, and well location is shown in Fig. 4.1)

analysis of a whole well section. In combination with drilling coring and outcrop data, well logging data can be used for quantified and lateral correlation study. Therefore, the well logging data are widely applied in sequence stratigraphy and are basics for high-precision sequence stratigraphy research of coverage areas.

Stratigraphic unit interfaces can be identified with many types of well logging data, and spontaneous potential (SP), gamma ray (GR), and resistivity (R) curves have been commonly used before. Besides conventional well logging curves used for conventional analyses, the interval transit time, the cross plot of interval transit time and resistivity, and the wavelet time–frequency cycle have been used to identify SBs in this study.

(a) Identification of SBs by turning points in well logging curves

Sedimentary facies and lithology change greatly below and above an SB, resulting in an obvious turn in SP and R curves (Figs. 4.5 and 4.6). High self-potential value and low resistivity are above the SB, and the opposite case is below the SB, which is resulted from the difference in stratigraphic lithofacies and compaction below and above the SB.

(b) Response of interval transit time

Through analysis of Wyllie, Hubbert, and Ruley's results, Cao (2003) concluded that under normal burial and compaction, the logarithm of porosity in sedimentary strata is in linear relation with depth, so is the logarithm of interval transit time. With increasing burial depth, both porosity and interval transit time decrease, and this linear relation is shown as a straight line with a certain slope for continuous sedimentary strata of the same lithology in the same well. However, obvious differences in sediment characteristics and compaction below and above the discontinuity plane can
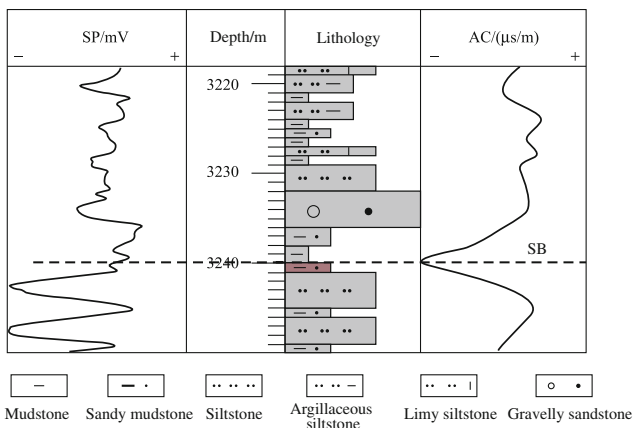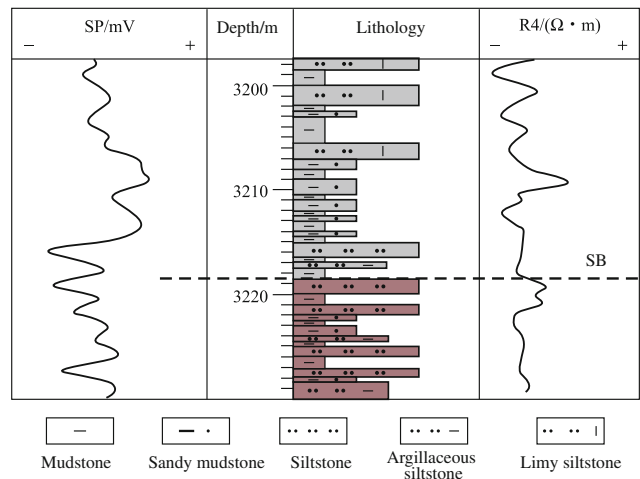


**Fig. 4.6** SB in Well Fan138

cause a dislocation in the curve of interval transit time and depth (Fig. 4.7). Hence, for some wells, the curve of logarithm of interval transit time and depth is not simply a straight line but a broken line or faulted line segments. This provides a theoretical basis to identify planes of unconformity or SBs.

(c) Cross plot of interval transit time curve and resistivity curve

On the basis of measured core data scaling, many researchers identify organic-rich source rocks and measure total organic

**Fig. 4.7** Characteristics of interval transit time in Well Wang26





**Fig. 4.5** SB in Well Fan143
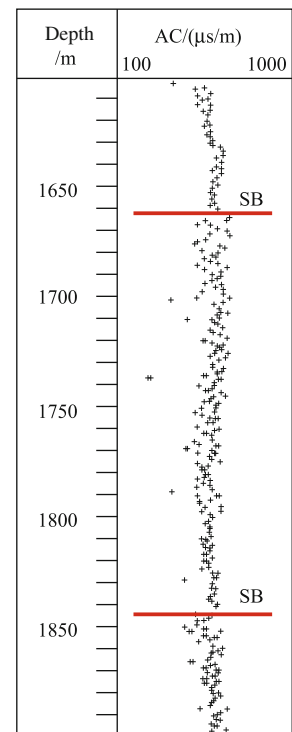
carbon (TOC) using well logging data (Passey 1990; Zhang and Zhang 2000). The porosity curve (generally interval transit time curve) of an appropriate scale is overlapped with the resistivity curve. For organic-rich fine-grained source rocks, two curves show the certain difference of amplitude defined as $\Delta$logR (Passey 1990), which is generally in direct proportion to TOC of source rocks.

Vertically, TOC changes periodically within the sequence stratigraphic framework. In a single sequence stratigraphic section, the peak of TOC corresponds to the maximum sea (lake) flooding surface, and the SB corresponds to the low of TOC. Therefore, $\Delta$logR corresponds well to the SB and condensed section (CS). An SB corresponds to the low value interval of $\Delta$logR, CS corresponds to the high value interval of $\Delta$logR, and MFS corresponds to the high peak interval of $\Delta$logR (Fig. 4.8).

(d)   Wavelet time–frequency cycle

Sediments with different rhythmic characteristics constitute strata and cycles of different orders. Cycle-induced changes of physical properties are well reflected in the frequency domain in well logging data. Continuous wavelet transform is performed on well logging curves, and the relation between well logging signals and depth is transformed to that between depth and scale domain. By studying the periodic oscillation characteristics of wavelet coefficient

curves at varying scales, their relation with SB, system tract interface, and parasequence set interface are established (Fig. 4.9).

(3)   Abrupt change of sediment color and sedimentary facies

Coring and cutting logging data are also used to identify and divide interfaces of stratigraphic sequence. According to Walther's Law of Facies, only the facies adjacent laterally in a concordant sedimentary series is continuously overlapped and not interrupted in the vertical sequence. Hence, the facies types far apart laterally but close vertically indicate depositional breaks among strata, exhibiting abrupt changes of lithology, color, etc., below and above SB. On the contrary, within each sequence, the strata are characterized by successive sedimentation, continuous sedimentary facies, gradual change of lithology, color, etc., and rhythmic variation of stratigraphic thickness, which are all considered as markers of sequence stratigraphic interfaces.

At the SB, the sedimentary environment changed, so did the sedimentary facies types and stratigraphic superimpositions. Below the interface is the relatively shallow water sedimentary facies, and above the interface is the relatively deepwater sedimentary facies. For example, in Well Mian1, below the sequence bottom interface lithologically occurs the red mudstone, reflecting a sedimentary environment of



**Fig. 4.8**  $\Delta$logR variation and identification of SBs and system tract interfaces

(a) Well Wang125
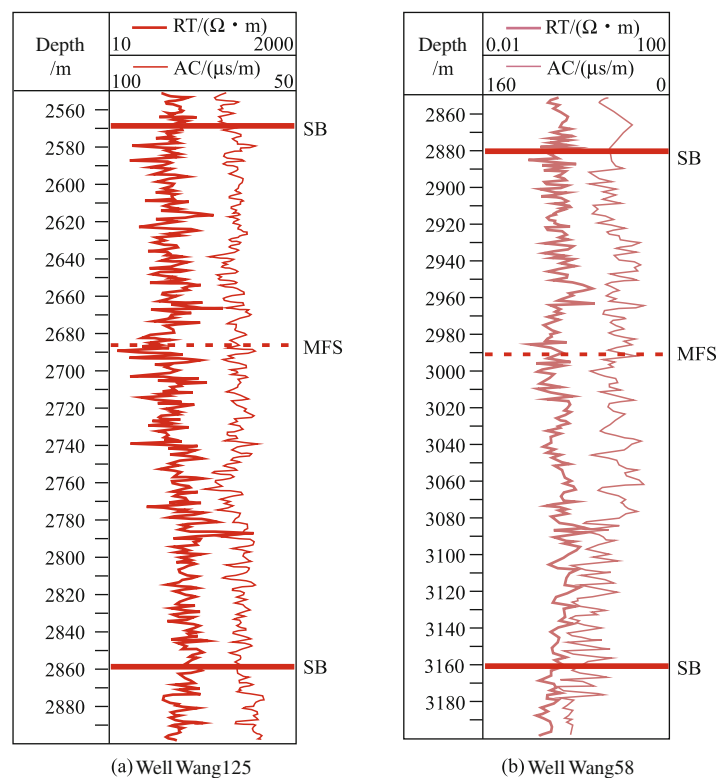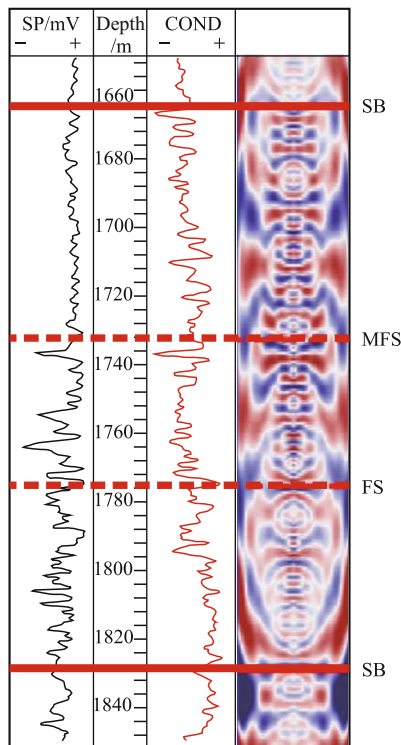
(b) Well Wang58

**Fig. 4.9** Identification of SBs and system tract interfaces with wavelet time–frequency cycle in Well Wang26

river alluvial plain, and above the interface is gray mudstone, reflecting a sedimentary environment of shore-shallow lacustrine (Fig. 4.10).

(4) Paleontological characteristics

In terms of paleontology, a great variation exists in the biological assemblages below and above the SB, reflecting staged biological evolution and abrupt environment variation. The paleontological characteristics are used for identifying sequence boundaries (Fig. 4.11).

2. Systems tract

Systems tract is a three-dimensional assembly of synsedimentary systems. According to first flooding surfaces (FFS) and maximum flooding surface (MFS), a third-order sequence is divided into lowstand systems tract (LST) between FFS and sequence bottom boundary, transgressive systems tract (TST) between FFS and MFS, and highstand systems tract (HST) between MFS and sequence top boundary. Therefore, to identify system tract interfaces is to locate FFS and MFS.

FFS is the first significant flooding surface when lake level rises due to factors such as basin tectonism and climate change after it decreases to the lowest point. FFS indicates

that the water level starts to rise, and there is an obvious difference of sedimentary water depth below and above FFS. Above FFS, the mudstone gets darker, and a retrogradation parasequence is developed, corresponding to the first onlap point in seismic data. Additionally, FFS can also be determined by the obvious differences in lithology, lithofacies, and drilling data of strata below and above FFS: (a) lithologies, lithofacies, and sedimentary types below and above FFS are obviously different. For example, in TST across Well Wang125, the water depth increased abruptly. Shore-shallow lacustrine sediments are dominant below FFS, while semi-deep-deep lacustrine sediments above FFS (Fig. 4.12); (b) stratigraphic superimposition below and above FFS is obviously different. For example, LST below FFS is dominated by progradation, and TST above FFS occurs as retrogradation.

MFS is the interface with maximum water level, where the water depth reaches its peak, and CS is developed. MFS is identified mainly via following methods: (a) greatly different stratigraphic superimpositions above and below MFS, i.e., the dominant progradation or aggradation above MFS, and the dominant retrogradation below MFS; (b) at the top TST occured the thin-bedded condensed deposits, which are dominated by shallow, semi-deep and deep lacustrine dark mudstone, oil shale, and limy shale, with thickness increasing toward the deep lake and color lighter toward the shore; the logging curves are characterized by high gamma ray, high self-potential, spike-like high resistivity, high density, and high strength acoustic wave, corresponding to the peak interval of TOC($\Delta$logR) (Fig. 4.8), and representing sedimentary production of MFS.

3. Parasequence Set (Fourth-Order Sequence)

Low-order sequence stratigraphic units are divided, traced, and correlated according to transgressive surfaces or transgressive–retrogradation transformed interfaces, etc. Therefore, a high-precision sequence stratigraphic framework is established by identifying and tracing FSs or transgressive surfaces in various cycles. The systems tract is divided into several parasequence sets according to significant FSs. Each parasequence set consists of several parasequences superimposed in a certain style and bounded by FS.

Within the study area, FS corresponding to a parasequence boundary features mudstone between continuous sediment of sandstone, e.g., the mudstone drape at the top of middle-distal bar and river mouth bar in the delta sedimentary system, and the mudstone between shore-shallow lacustrine beach bar sandstone.

According to superimposition of parasequences, the parasequence sets are divided into progradational, retrogradational, and aggradational parasequence sets.
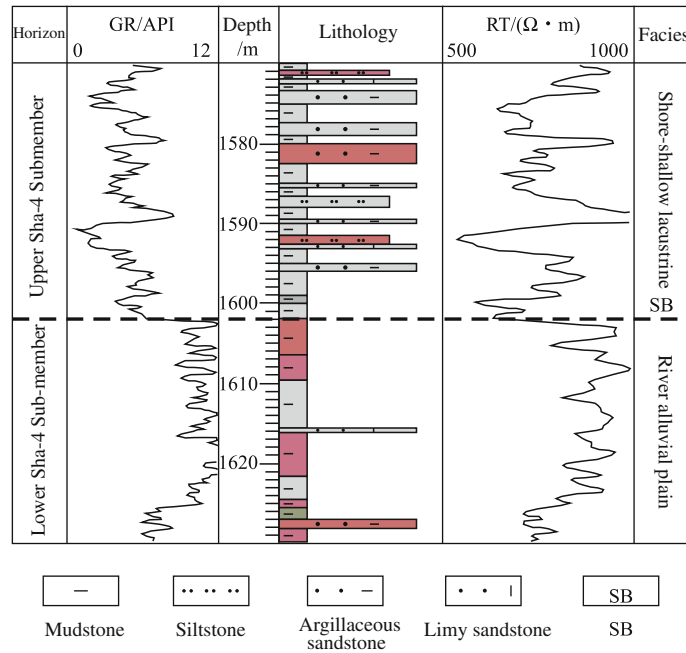
**Fig. 4.10** Abrupt change of sediments color at sequence bottom in Well Mian1
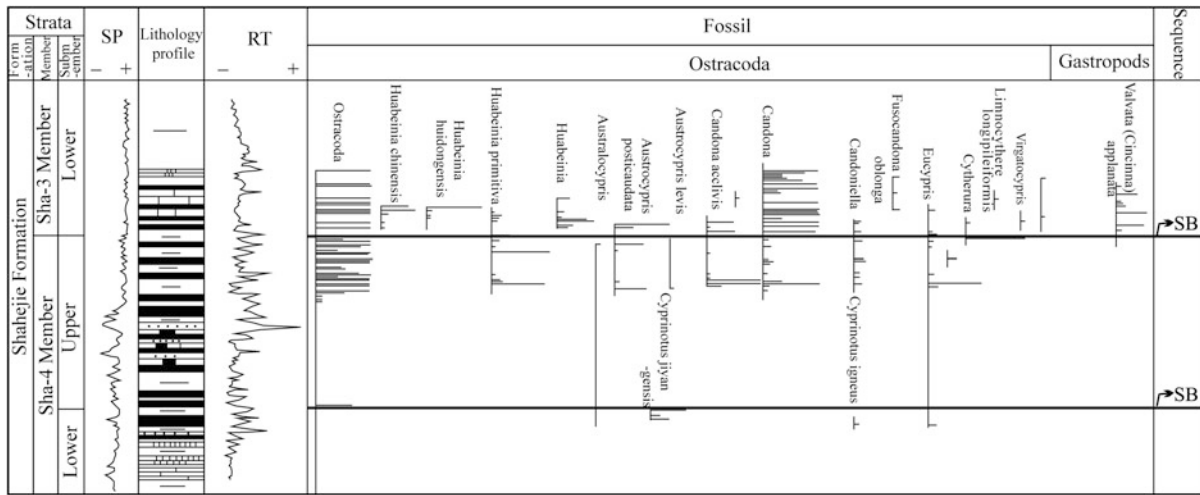


**Fig. 4.11** Relation between palaeobios and SB in Well Chun11 according to Feng et al. (2006)

(1) Progradational parasequence set (Figs. 4.13 and 4.14): when the shoreline advances toward the lake center, and the sedimentary center moves toward the lake basin center, from bottom to top the sandbodies gradually thicken and the grains coarsen, with most logging curves indicating coarsening-upward sequence, generally corresponding to continuous descent of relative lake level in LST.

(2) Retrogradational parasequence set (Figs. 4.15 and 4.16): when the lake shoreline sways landwards, and the sedimentary center moves toward the lake shoreline, from bottom to top the sandbodies become gradually thinner and the grains become finer, with most logging curves indicating fining-upward sequence, generally corresponding to continuous rising of relative lake level in TST.

**Fig. 4.12** Abrupt change of sediments color in FFS across Well Wang125
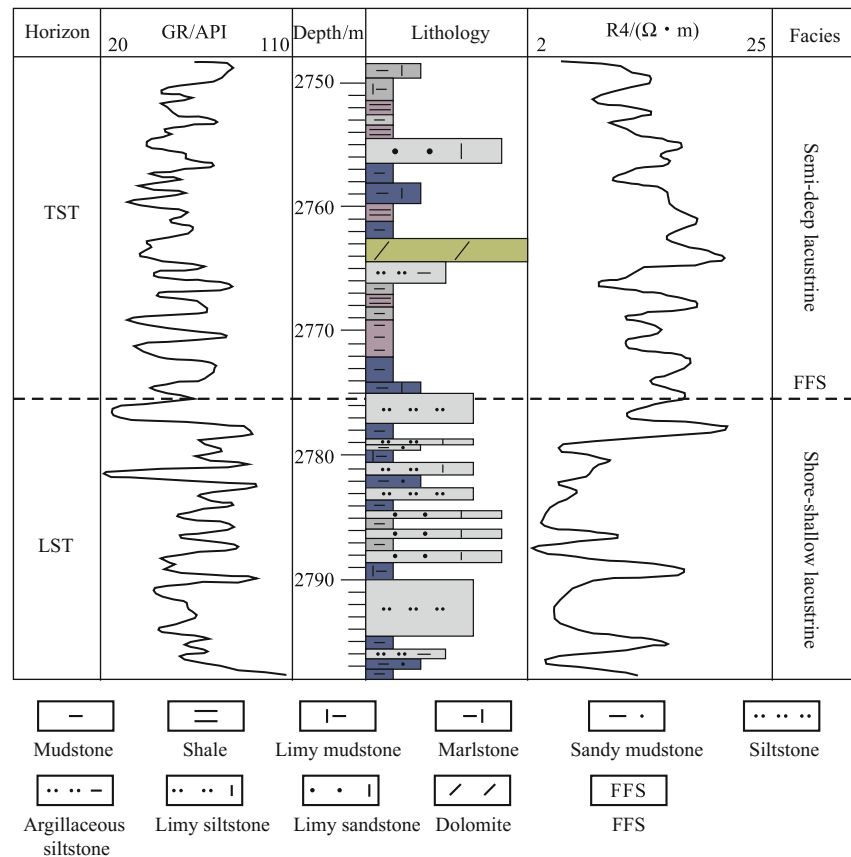


(3) Aggradational parasequence set (Figs. 4.17 and 4.18): when the lake basin shoreline is relatively stable and the lake water depth changes little, most sandbodies are superimposed vertically, with little change of thickness and sediment grains, and the aggradational parasequence set consists of superimposition of similar parasequences, generally formed in HST.

### 4.2.2    Division of Sequence in the Typical Wells

(1)    Integrated analysis of sequence across Well Gao89

Well Gao89 is located in the Boxing Sub-Sag. Upper Sha-4 Submember across Well Gao89 has depth between 2850 and 3120 m and total thickness of 270 m, and it is a third-order sequence. The lithological section is dominated by sandstone–mudstone, with local argillaceous limestone. According to sandstone content, stratigraphic superimposition, and analysis of SP and GR curves, Upper Sha-4 Submember is divided into two parts at depth of 2992 m, below which is LST with high sandstone content and stratigraphic superimposition dominated by progradation, and above 2992 m is TST and HST dominated by argillaceous

limestone, dark gray mudstone, and grayish brown oil shale, reflecting an abrupt increase in water depth. Thus, FFS was located at 2992 m. Similarly, according to the oil shale at 2922 m and corresponding high GR and SP, TST and HST were identified. Moreover, according to lithologic combination and logging curve characteristics, LST was divided into three progradational parasequence sets, TST was divided into two retrogradational parasequence sets, and HST was divided into one progradational parasequence set and one aggradational parasequence set. Accordingly, Upper Sha-4 Submember across Well Gao89 was identified as a third-order sequence and further divided into three system tracts and seven parasequence sets (Fig. 4.19).

LST: it has depth between 2992 and 3120 m, consists of No. 1, No. 2, and No. 3 parasequence sets from bottom to top, and is dominated by shallow lacustrine lacustrine beach and bar deposits. No. 1 parasequence set has depth between 3069.5 and 3120 m and is dominated by interbeds of dark gray mudstone, and siltstone, with obviously small thickness of but upward increasing content of sandstone. No. 1 parasequence set is a progradational parasequence set. Above 3069.5 m, the lithological combination and logging curve configuration change greatly, and the dark gray mudstone at 3069.5 m represents termination of FS and No. 1 parasequence set. No. 2 parasequence set has depth
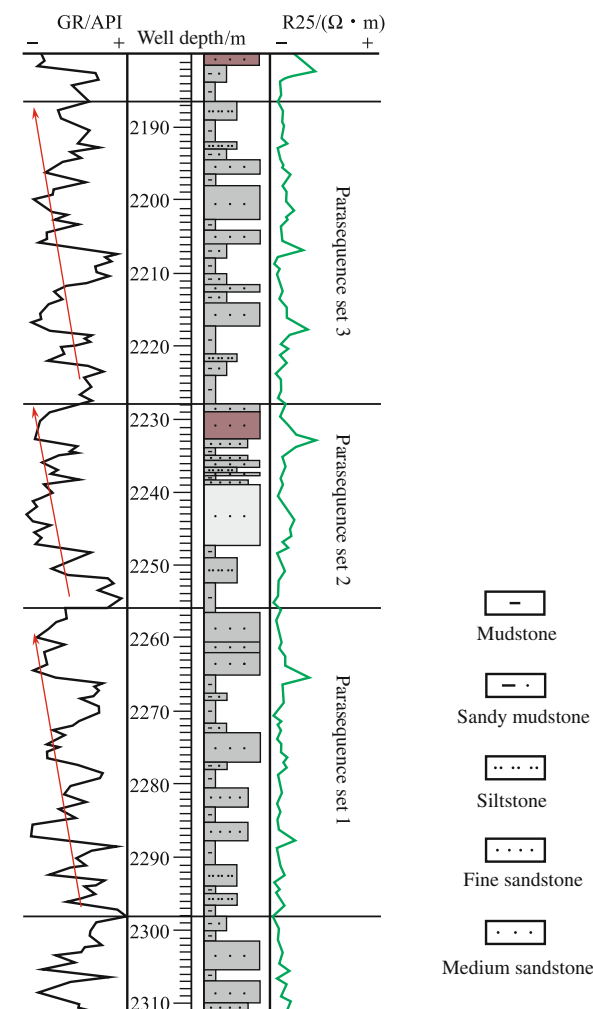
**Fig. 4.13** LST progradational parasequence set across Well Liang90

No. 4 parasequence set, at depth between 2964 and 2992 m, is a retrogradational parasequence set and is lithologically dominated by shallow lacustrine subfacies deposits composed of marlstone, shale, and mudstone at the bottom, beach sand deposits of thin-bedded limy siltstone in the middle, and interbeds of semi-deep to deep lacustrine dark gray mudstone and shale at the top. No. 5 parasequence set has depth between 2922 and 2964 m and is dominated by interbeds of semi-deep to deep lacustrine dark gray mudstone and shale.

HST: it has depth between 2850 and 2922 m and consists of No. 6 and No. 7 parasequence sets from bottom to top. No. 6 parasequence set has depth between 2895.5 and 2922 m and is a progradational parasequence set. No. 7 parasequence set has depth between 2850 and 2895.5 m and is an aggradational parasequence set. This HST is dominated by interbeds of semi-deep and deep lacustrine dark gray mudstone and shale, and one set of turbidite is developed between No. 6 and No. 7 parasequence sets.

(2)   Integrated analysis of sequence across Well Gao894

Well Gao894 is located in the Boxing Sub-Sag. Upper Sha-4 Submember across Well Gao894, a third-order sequence, has depth between 3150 and 3451 m and total thickness of 301 m. The lithological section is dominated by sandstone–mudstone, with local marlstone and dolomite. The mudstone encountered by this well is basically dark gray, representing relative deepwater environment with shallow lacustrine subfacies, semi-deep to deep lacustrine subfacies, and beach bar deposits developed. According to sandstone content, stratigraphic superimposition, and analysis of SP and GR curves, Upper Sha-4 Submember is subdivided into two parts at 3325.5 m, below which is LST with high sandstone content and stratigraphic superimposition dominated by progradation. Above 3325.5 m are TST and HST dominated by marlstone, dark gray mudstone, and grayish brown oil shale, reflecting an abrupt increase in water depth. Thus, FFS was located at 3325.5 m. The gray-brown oil shale at 3262 m and corresponding high GR represent MFS, where HST and LST are divided. Furthermore, according to lithologic combination and well logging curve characteristics, LST is divided into three progradational parasequence sets, TST is divided into two retrogradational parasequence sets, and HST is divided into one progradational parasequence set and one aggradational parasequence set. Accordingly, Upper Sha-4 Submember across Well Gao894, as a third-order sequence, is similarly subdivided into three system tracts and seven parasequence sets (Fig. 4.20).

LST: it has depth between 3325.5 and 3451 m, consists of No. 1, No. 2, and No. 3 parasequence sets from bottom to top, and is dominated by beach and bar deposits.

between 3024 and 3069.5 m and is lithologically dominated by interbeds of dark gray mudstone, fine sandstone, and medium sandstone. Compared with No. 1 parasequence set, No. 2 parasequence has larger grain size and thicker single layer of sandstone, and it is a progradation type. Above 3024 m, the lithologic combination and logging curve configuration change obviously again. The dark gray mudstone at 3024 m represents termination of FS and No. 2 parasequence set. No. 3 parasequence set has depth between 2992 and 3024 m and is lithologically dominated by interbeds of gray, dark gray mudstone and medium sandstone. Compared with No. 1 and No. 2 parasequence sets, No. 3 has obviously lower sandstone content, reflecting an increase in relative lake level. The well developed marlstone at 2992 m represents termination of LST.

TST: it has depth between 2922 and 2992 m, consists of No. 4 and No. 5 parasequence sets from bottom to top, and is dominated by beach and shallow lacustrine deposits.

**Fig. 4.14** LST progradational parasequence set across Well Gao892
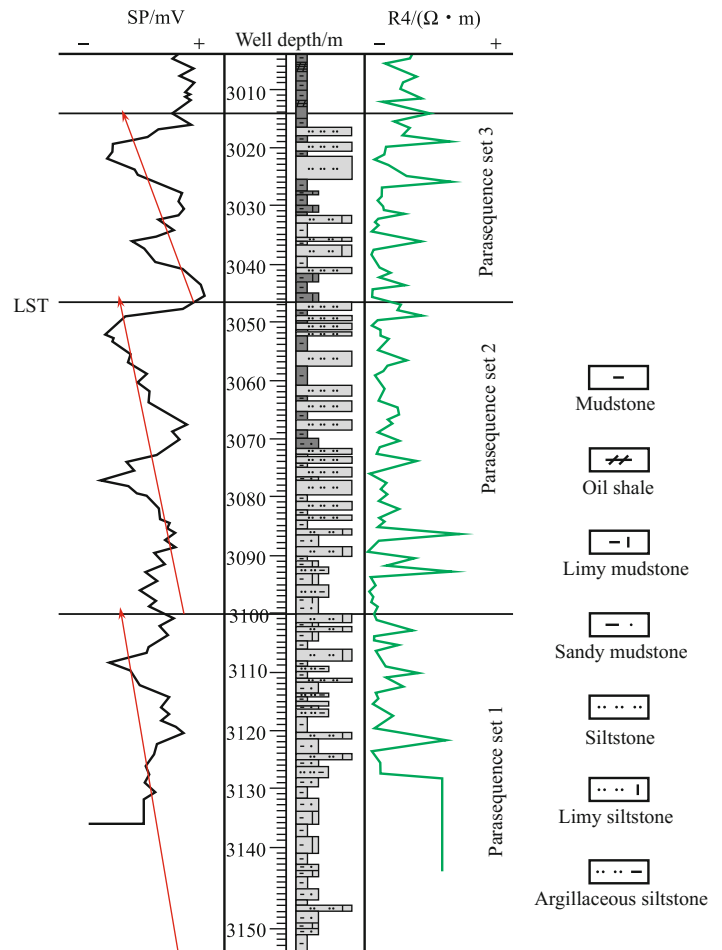


No. 1 parasequence set has a depth between 3410 and 3451 m and is lithologically dominated by interbeds of gray, dark gray mudstone, and siltstone, with obviously small thickness of sandstone but increasing sandstone content upward. No. 1 parasequence set is a progradation type. Above 3410 m, the lithologic combination and logging curve configuration change greatly. The gray mudstone at 3410 m represents termination of FS and No. 1 parasequence set. No. 2 parasequence set has depth between 3369 and 3410 m, and it is lithologically dominated by interbeds of gray, dark gray mudstone, and siltstone. Compared with No. 1 parasequence set, No. 2 parasequence set has thicker single layer of sandstone and is a progradational parasequence set. Above 3369 m, the lithologic combination and logging curve configuration change obviously again. The dark gray mudstone at 3369 m represents termination of FS and No. 2 parasequence set. No. 3 parasequence set has depth between 3325.5 and 3369 m and is lithologically dominated by interbeds of gray, dark gray mudstone, and siltstone, with minor marlstone. No. 3 parasequence set is a weak progradational parasequence set. Above 3325.5 m, the

lithologic combination and logging curve configuration change greatly, the gray mudstone at 3325.5 m represents termination of FFS and No. 3 parasequence set.

TST: it has depth between 3262 and 3325.5 m and consists of No. 4 and No. 5 parasequence sets from bottom to top. The lower part is dominated by shore-shallow lacustrine subfacies deposits and gradually evolves into semi-deep to deep lacustrine deposits when reaching MFS upward. No. 4 parasequence set, at depth between 3292.5 and 3325.5 m, is a retrogradational parasequence set, with a sedimentary cycle of thin-bedded sandstone-shallow lacustrine mudstone from bottom to top till occurrence of brown oil shale, indicating termination of No. 4 parasequence set. No. 5 parasequence set has depth between 3262 and 3292.5 m, and it is a retrogradational parasequence set, with thin-bedded sandstone at the bottom and thick semi-deep and deep lacustrine dark gray mudstone, limy mudstone, and shale at the top. The upper boundary is marked by brown oil shale, representing MFS.

HST: it has depth between 3150 and 3262 m, and consists of No. 6 and No. 7 parasequence sets from bottom to
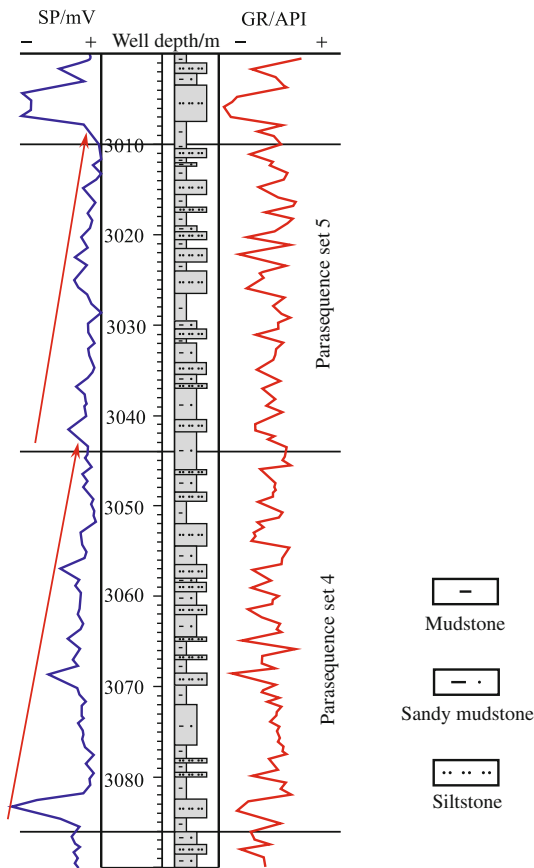
**Fig. 4.15** TST retrogradational parasequence set in Well Bin423

**Fig. 4.16** TST retrogradational parasequence set in across Well Fan138
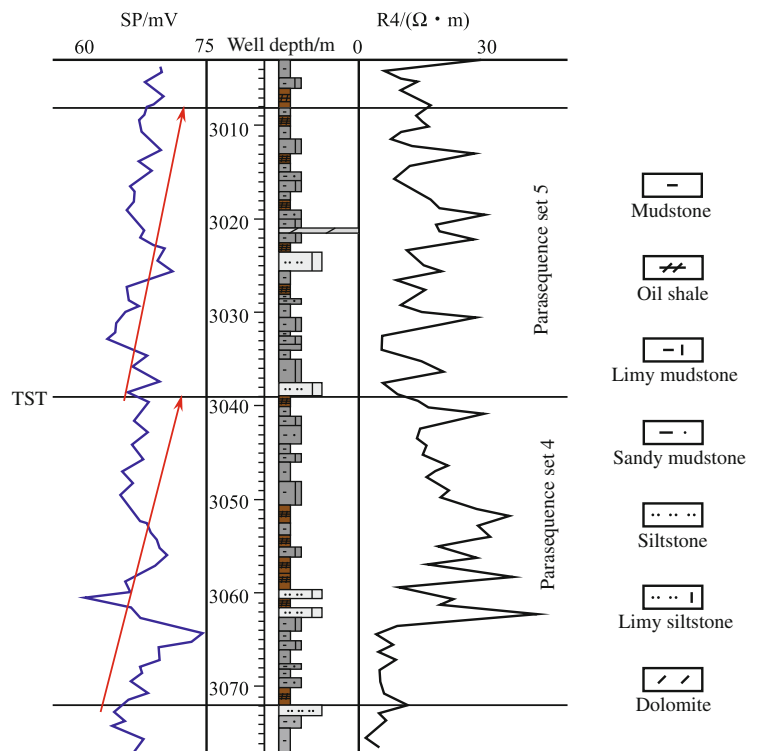


**Fig. 4.17** HST progradational parasequence set across Well Bin438

top, dominated by gray-dark gray mudstone and dolomite. No. 6 parasequence set has depth between 3229 and 3262 m and it is a progradational parasequence set, with thick semi-deep and deep lacustrine dark gray mudstone, limy mudstone, and shale at the bottom, and thin-bedded turbidite at the top. No. 7 parasequence set has depth between 3150 and 3229 m, and it is an aggradational parasequence set. This HST is dominated by semi-deep and deep lacustrine subfacies dark gray mudstone, shale, limy mudstone and thin-bedded limy dolomite, dolomite, and marlstone.
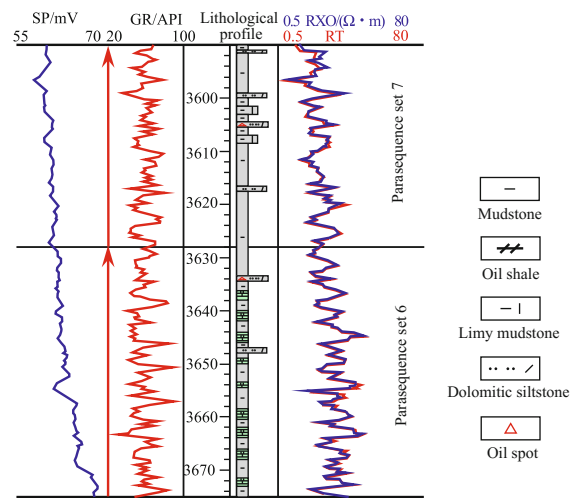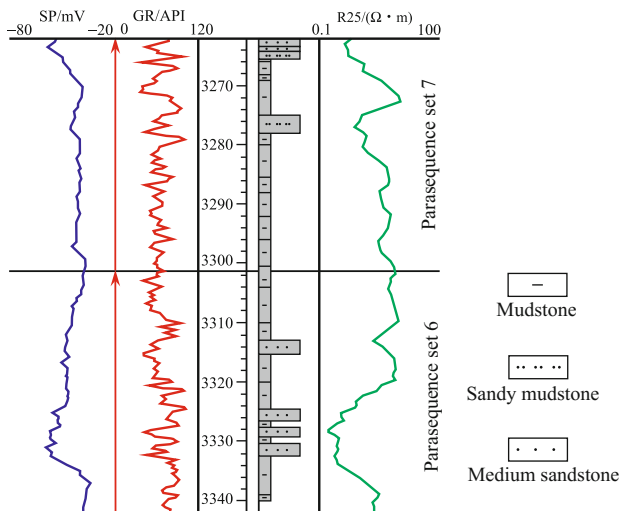
**Fig. 4.18** HST progradational parasequence set across Well Bin668

(3)  Integrated analysis of sequence across Well Gao32

Well Gao32 is near the Qingcheng High and adjacent to the Gaoqing Fault Belt. Upper Sha-4 Submember across Well Gao32 has depth between 2358 and 2622 m and total thickness of 264 m, and it is a third-order sequence. The lithology is dominated by mudstone, with local limestone. The mudstone is gray. Well Gao32, located to the west of the Dongying Sag, has sandstone density obviously higher than that of Well Gao89 and Gao894, and generally comprises delta deposits. According to (siltstone) sandstone content and stratigraphic superimposition, and combining with analysis of SP and GR curves, FFS and MFS were identified, respectively, at 2481 m and 2422 m, and accordingly, LST, TST, and HST were identified. Furthermore, according to lithologic combination and logging curve characteristics, LST is divided into three progradational parasequence sets, TST is divided into two retrogradational parasequence sets, and HST is divided into two aggradational parasequence sets. Accordingly, Upper Sha-4 Submember across Well Gao32 was identified as a third-order sequence and similarly subdivided into three system tracts and seven parasequence sets (Fig. 4.21).

LST: has depth between 2481 and 2622 m, and consists of No. 1, No. 2, and No. 3 parasequence sets from bottom to top, dominated by delta-front subaqueous distributary channel and river mouth bar deposits. No. 1 parasequence set has SP logging curve with combined shape of funnel and box, and comprises a progradational cycle of river mouth bar-subaqueous distributary channel from bottom to top. No. 2 parasequence set consists of two sedimentary cycles of river mouth bar-subaqueous distributary channel from bottom to top; the river mouth bar is a coarsening-upward cycle composed of siltstone, argillaceous siltstone, and sandy mudstone, with logging curve of funnel shape; the subaqueous distributary channel is composed of thick siltstone, with logging curve of box shape. No. 3 parasequence set is a progradational type composed of river mouth bar and subaqueous distributary channel; the lower river bar is dominated siltstone, limy sandstone, and thin-bedded sandy mudstone, with logging curve of funnel shape; the upper distributary channel comprises interbeds of thick limy sandstone and siltstone, with logging curve of box shape.

TST: has depth between 2422 and 2481 m, and consists of No. 4 and No. 5 parasequence sets from bottom to top, dominated by delta front subaqueous distributary channel, and river mouth bar deposits. No. 4 parasequence set is a retrogradational parasequence set composed of subaqueous distributary channel-river mouth bar-interdistributary bay deposits from bottom to top. The subaqueous distributary channel deposits mainly consist of siltstone and limy sandstone, the river mouth bar comprises sandy mudstone-siltstone-limy sandstone from bottom to top, and the interdistributary bay is dominated by sandy mudstone. No. 5 parasequence set is dominated by compound subaqueous distributary channel deposits.

HST: it has depth between 2358 and 2422 m, consists of No. 6 and No. 7 parasequence sets from bottom to top, and is dominated by delta front subaqueous distributary channel and river mouth bar deposits. No. 6 parasequence set is dominated by a set of river mouth bar deposits, lithologically dominated by sandy mudstone, siltstone, and limy sandstone from bottom to top, with logging curve of funnel shape. No. 7 parasequence is mainly a set of subaqueous distributary channel deposits, dominated by siltstone and limy sandstone, with logging curve of toothed box shape.

(4)  Integrated analysis of sequence across Well Bo104

Well Bo104 is located in the central west of the Boxing Sub-Sag. Upper Sha-4 Submember across Well Bo104 has depth between 1991.5 and 2228.4 m and total thickness of 236.9 m, and it is a third-order sequence. The lithology is dominated by gray-dark gray (limy) mudstone, (limy) siltstone, (limy) fine sandstone, and dolomite in shore-shallow lacustrine beach bar sandbody and argillaceous deposits. According to (siltstone) sandstone content and stratigraphic superimposition, and combining with analysis of SP and GR curves, FFS and MFS were identified, respectively, at 2137 m and 2074 m, and accordingly, LST, TST, and HST were identified. According to lithologic combination and logging curve characteristics, LST is divided into three progradational parasequence sets, TST is divided into two retrogradational parasequence sets, and HST is divided into two aggradational parasequence sets. Accordingly, Upper Sha-4 Submember across Well Gao32 was identified as a
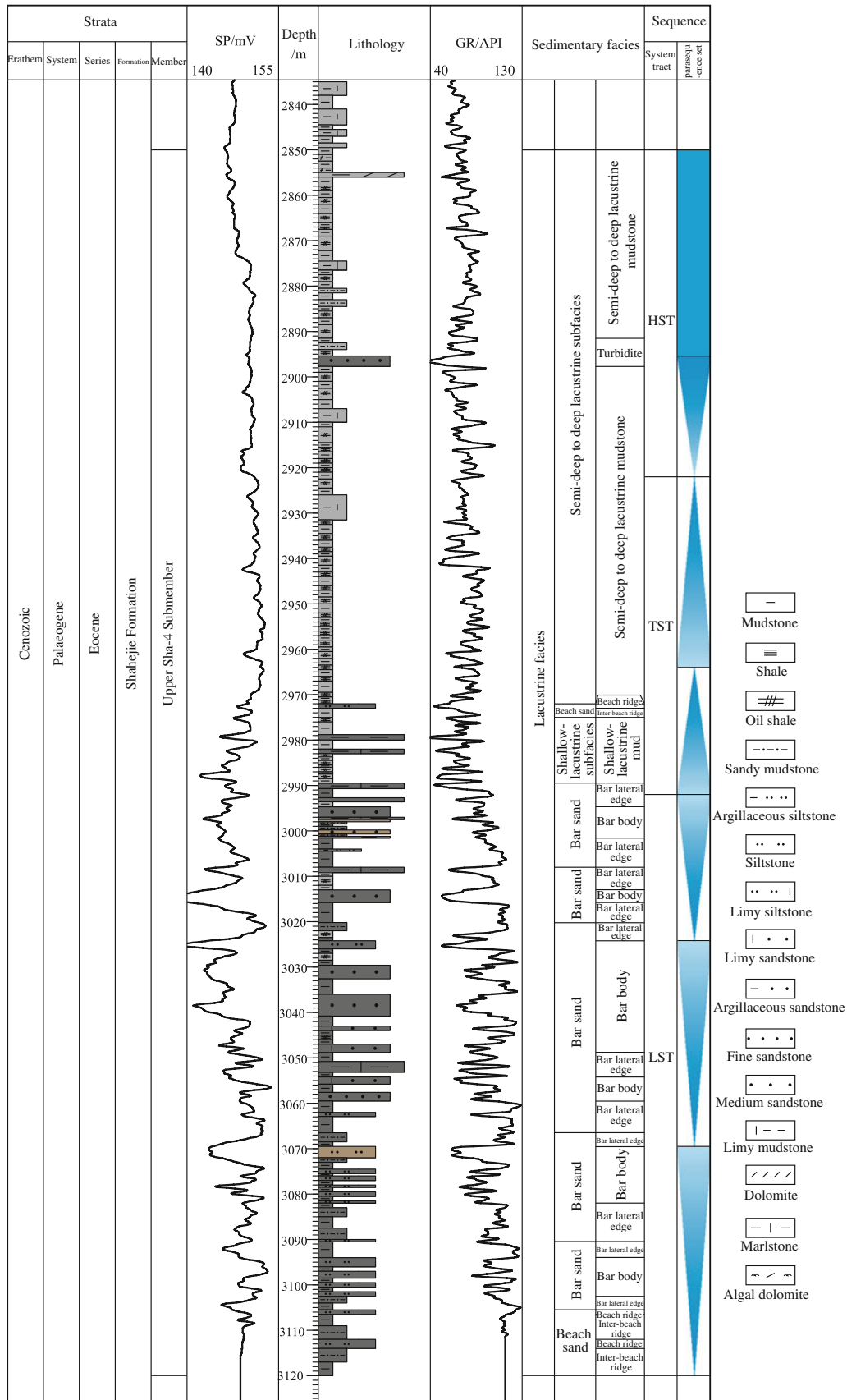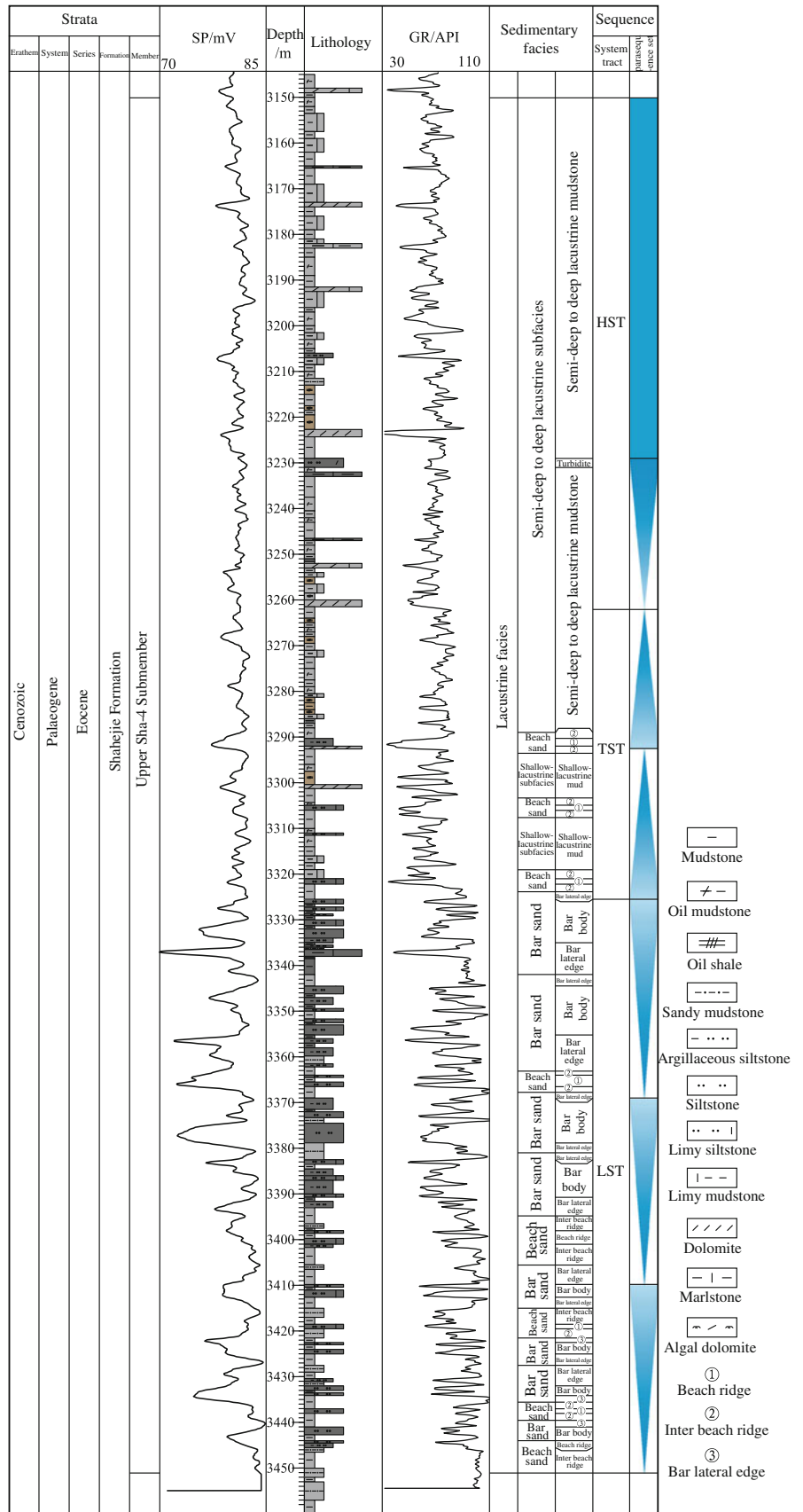
**Fig. 4.19** Integrated analysis of facies across Well Gao89

**Fig. 4.20** Integrated analysis of facies across Well Gao894

**Fig. 4.21** Integrated analysis of facies across Well Gao32

third-order sequence and similarly divided into three system tracts and seven parasequence sets (Fig. 4.22).

LST: it has depth between 2137 and 2228.4 m, consists of No. 1, No. 2, and No. 3 parasequence sets from bottom to top, and is dominated by beach and bar deposits. No. 1 parasequence set, at depth between 2196 and 2228.4 m, is a progradational parasequence set and has a high sandstone/strata thickness ratio; its lithology is coarse-grained and is dominated by fine sandstone and limy sandstone, with logging curve of toothed funnel shape, and bar deposits are mainly developed. No. 2 parasequence set, at depth between 2177 and 2196 m, is a progradational parasequence set and is dominated by bar deposits. No. 3 parasequence set, at depth between 2137 and 2177 m, is a progradational parasequence set and is a compound cycle of mudstone-siltstone-limy siltstone-sandy mudstone-mudstone from bottom to top, being beach bar deposits.

TST: it has depth between 2074 and 2137 m, consists of No. 4 and No. 5 Parasequence sets from bottom to top, and is dominated by beach bar deposits and shallow lacustrine mudstone deposits. No. 4 parasequence set, at depth between 2103.5 and 2137 m, is a retrogradational type; the bottom is dominated by interbeds of limy siltstone, argillaceous sandstone, and mudstone, which are shallow lacustrine beach and bar deposits; the top is dominated by gray mudstone, marlstone, and dark gray shale, which are shallow lacustrine deposits. No. 5 parasequence set, at depth between 2074 and 2103.5 m, is a retrogradational type, and it is dominated by gray mudstone, marlstone, sandy mudstone, dolomite, and dark gray shale, which are of shallow lacustrine subfacies deposits.

HST: it has depth between 1991.5 and 2074 m, consists of No. 6 and No. 7 parasequence sets from bottom to top, and is dominated by beach bar deposits and shallow lacustrine mudstone deposits, with a thin-bedded biological beach. No. 6 parasequence set, at depth between 2034 and 2074 m, is an aggradational parasequence set; the bottom is compound cycle deposits composed of sandy mudstone-limy siltstone-siltstone- mudstone-marlstone from bottom to top, being bar deposits; the middle is the shallow lacustrine deposits composed of dolomite and mudstone interbeds, and the top is a set of beach deposits composed of limy sandstone. No. 7 parasequence, at depth between 1991.5 and 2034 m, is an aggradation dominated by interbeds of dark gray marlstone and gray mudstone, being shallow lacustrine deposits; additionally, the bottom has biological beach deposits of algal dolomite which is approximately 1 m thick.

(5)  Integrated analysis of sequence across Well Jin22

Well Jin22 is located in the south of the Boxing Sag, and adjacent to the Luxi Uplift. Upper Sha-4 Submember across

Well Jin22 has depth between 875 and 1004 m and total thickness of 129 m, and it is a third-order sequence. The lithology is dominated by gray mudstone-siltstone-fine sandstone and variegated conglomerate, which are generally onshore gravelly beach bar deposits. According to sandstone and conglomerate content and stratigraphic superimposition, and combining with GR curves analysis, FFS and MFS were identified, respectively, at 953 and 928 m, and accordingly LST, TST, and HST were identified. According to lithologic combination and logging curve characteristics, LST is further divided into three progradational parasequence sets, TST is divided into two retrogradational parasequence sets, and HST is divided into one aggradational parasequence set and one progradational parasequence set. Accordingly, Upper Sha-4 Submember across Well Jin22 was identified as a third-order sequence, and similarly divided into three system tracts and seven parasequence sets (Fig. 4.23).

LST: it has depth between 953 and 1004 m, and consists of No. 1, No. 2, and No. 3 parasequence sets from bottom to top. No. 1 parasequence set, at depth between 979 and 1004 m, is a progradational parasequence set, which is dominated by two sets of >10 m thick conglomerate intercalated with thin-bedded argillaceous siltstone, and it is the deposits of gravelly beach bar body, with logging curve of box shape. No. 2 parasequence set, at depth between 965 and 979 m, is a progradational parasequence set and consists of coarsening-upward mudstone-siltstone-conglomerate from bottom to top, which are the deposits of bar body, with logging curve of funnel shape. No. 3 parasequence set, at depth between 953 and 965 m, is a progradational parasequence set, dominated by coarsening-upward cycle composed of mudstone-siltstone-conglomerate, with logging curve of funnel shape.

TST: it has depth between 928 and 953 m and consists of No. 4 and No. 5 parasequence sets from bottom to top. No. 4 parasequence set, at depth between 938 and 953 m, is a progradational parasequence set and is basically a coarsening-upward cycle of sandy mudstone-argillaceous siltstone, mudstone-conglomerate-fine sandstone from bottom to top; the lithology coarsens, and sand layer thickens from bottom to top. No. 4 parasequence set is composed of gravelly beach bar lateral-margin deposits. No. 5 parasequence set, at depth between 928 and 938 m, is a retrogradational parasequence set. No. 5 parasequence set is basically composed of argillaceous siltstone intercalated with thin sandy mudstone and mudstone, which are gravelly deposits of beach bar lateral margin.

HST: it has depth between 875 and 928 m, and consists of No. 6 and No. 7 parasequence sets from bottom to top. No. 6 parasequence set, at depth between 893 and 928 m, is an aggradational parasequence set and is
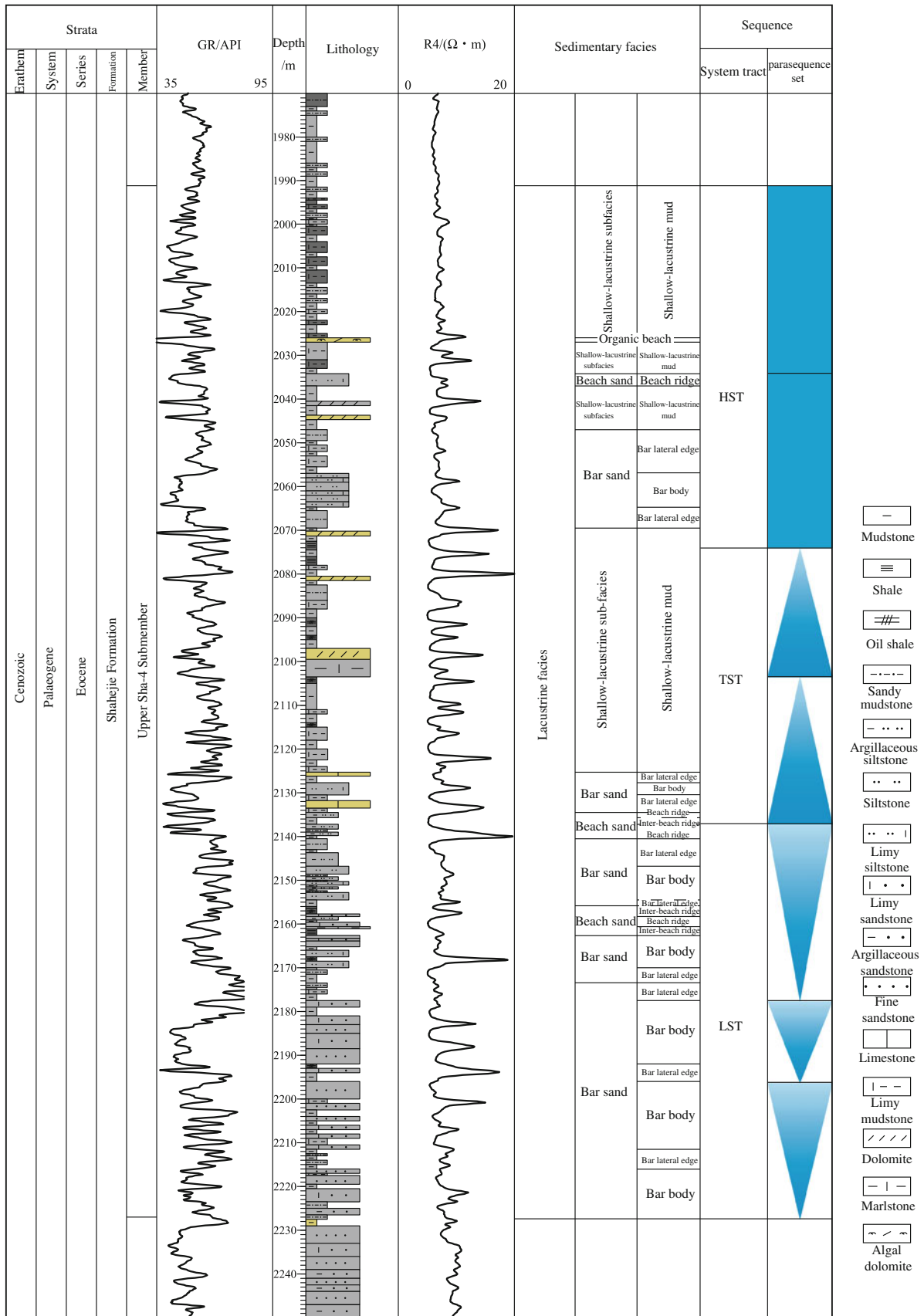
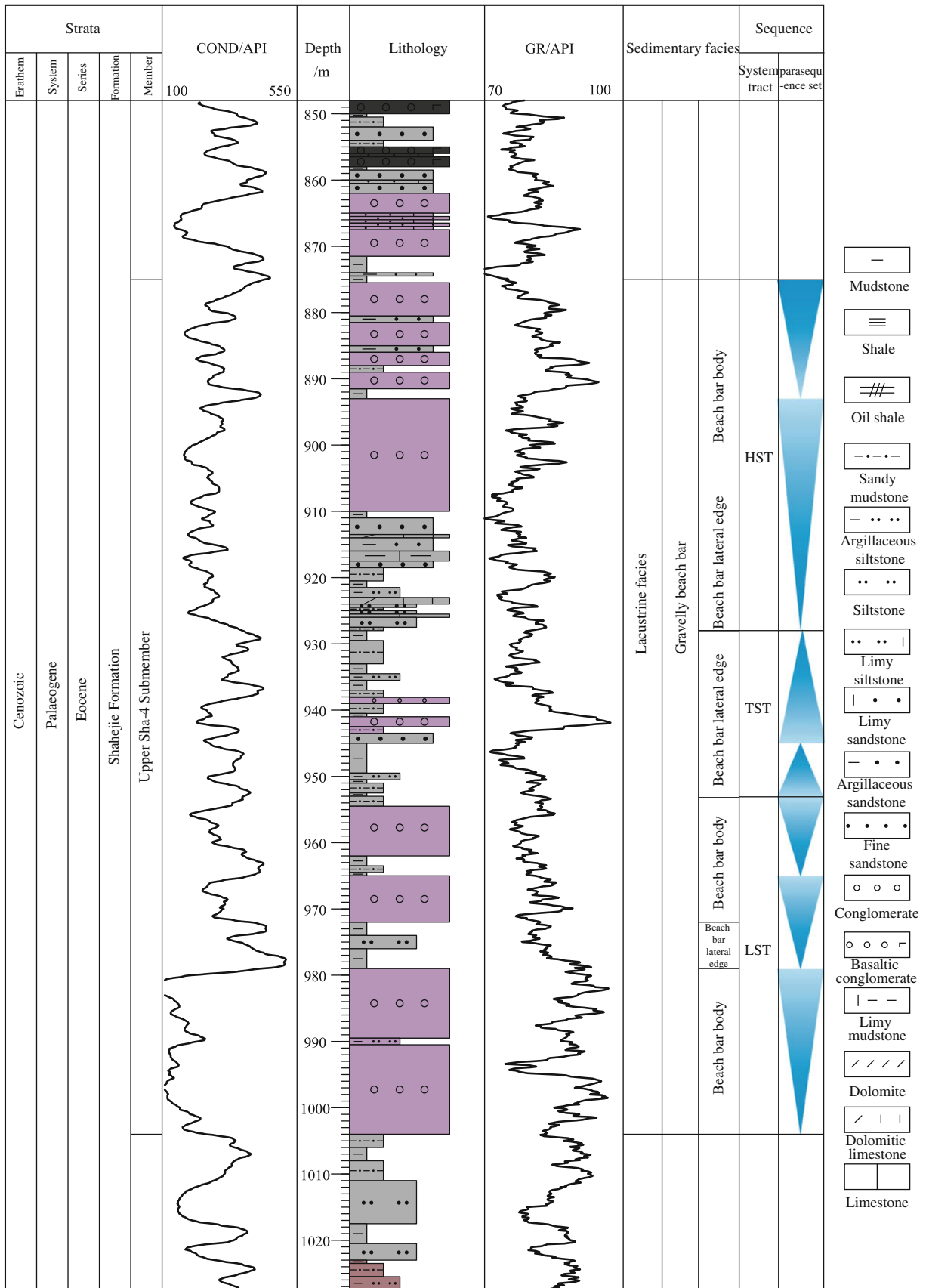**Fig. 4.22** Integrated analysis of facies across Well Bo104

**Fig. 4.23**  Integrated analysis of facies across Well Jin22

dominated by thick conglomerate, with logging curve of box shape. It is composed of gravelly beach bar body deposits. No. 7 parasequence set, at depth between 875 and 893 m, is an aggradational parasequence set, dominated by thick conglomerate and thin mudstone, sandy mudstone or silty mudstone interbeds, with logging curve of toothed box shape. No. 7 parasequence set is composed of gravelly beach bar body deposits.

(6) Integrated analysis of facies across Well Bin435

Well Bin435 is located in the west of the Lijin Sag. Upper Sha-4 Submember corresponds to the interval between 3206 and 3500 m. The lithology is dominated by sandstone-mudstone. Similarly, according to sandstone content and stratigraphic superimposition, and combining with analysis of logging curves, the target horizon is divided into two parts at 3288 m, below which is LST dominated by progradation and aggradation superimposition with high sandstone content. Above 3288 m are TST and HST dominated by dark gray mudstone and limy mudstone, with certain-scale oil shale. Therefore, FFS was identified at 3288 m, reflecting an abrupt increase in water depth. According to lithologic combination and logging curve characteristics, LST is further divided into three parasequence sets. Similarity, two parasequence sets are divided in TST and HST. Upper Sha-4 Submember across Well Bin435 was identified as a third-order sequence and divided into three system tracts and seven parasequence sets (Fig. 4.24).

LST: it has depth between 3288 and 3500 m. No. 1 parasequence set corresponds to the interval between 3452 and 3500 m, and the lithology is interbed of dark gray mudstone and gray sandstone, with sandstone content increasing obviously upward, and single sand layer thickness around 1 m. The deviation amplitude between GR and SP logging curves and the baseline indicates decreasing water depth and multiple parasequences of aggradation–progradation upward. Above 3452 m, a sharp increase in mudstone content and GR value indicates FS. According to the structural location and sedimentary environment of Well Bin435, and combining with finger-shaped, funnel-shaped GR curve, and relatively obvious coarsening-upward cycle, No. 1 parasequence set was identified as deposits of shallow lacustrine mudstone and shallow lacustrine beach bar. No. 2 parasequence set corresponds to the interval between 3369 and 3452 m, and the lithology is the interbed of gray mudstone and gray sandstone, without greatly increasing sandstone content and single sand layer thickness. The deviation amplitude between GR and SP logging curves and the baseline reflects low stand aggradation–poor progradation. Above 3369 m, the mudstone content and GR value increase sharply again, indicating FS. Combining with the

structural location and sedimentary environment of Well Bin435, and according to the location of sequence stratigraphic framework, and finger-shaped, finger-like funnel-shaped GR and SP curves characterized by obvious reverse cycle, No. 2 parasequence set was identified as shallow lacustrine mud and shallow lacustrine beach bar deposits. No. 3 parasequence set corresponds to the interval between 3288 and 3369 m and is interbeds of gray, dark gray mudstone, and gray sandstone, in which sandstone content increases greatly, reflecting lowstand progradation. The thickness of a single sand layer generally varies between 1 and 3 m. Above 3288 m, the mudstone content and GR value increase sharply, and mudstone darkens, indicating FFS. Core observation shows that the lower part is dominated by wave-formed structures, e.g., wavy bedding and charcoal fragments, indicating the depositional environment of shallow water. In the upper part, the mudstone darkens, and structures reflecting storm action occurs, e.g., truncation structure and boulder clay. The upper part (3369–3350 m) was identified as shore-shallow lacustrine mud and shore-shallow lacustrine beach bar, and the upper part (3350–3288 m) was identified as semi-deep lacustrine mud and storm deposits.

No. 4 (3270–3288 m), No. 5 (3252–3270 m), No. 6 (3236–3252 m), and No. 7 (3206–3236 m) parasequence sets have nearly 100% mudstone above 3288 m, with large sets of oil shale, and SP curves close to shale baseline, reflecting depositional environment of deepwater, poor provenance, and reduction. Deposits of these parasequence sets are identified as semi-deep lacustrine argillaceous deposits.

(7) Integrated analysis of sequence across Well Liang754

Well Liang754 is located in the southwest of the Lijin Sag, far away from provenance, and it is tectonically to the north of the central faulted anticline belt and the Chunhua-Caoqiao Fault Belt. Upper Sha-4 Submember corresponds to the interval between 3090 and 3332 m. The lithology is dominated by dark gray sandstone–mudstone. Similarly, according to sandstone content, stratigraphic superimposition, and combining with analysis of logging curves, the target horizon is divided into two parts at 3190 m, below which is LST with superimposition of progradation and aggradation of high sandstone content. The part above 3190 m comprises TST and HST dominated by dark gray mudstone, and limy mudstone, and certain-scale oil shale. FFS was identified at 3190 m, indicating an abrupt increase in water depth. According to lithologic combination and logging curve characteristics, LST is divided into three parasequence sets. Similarly, two parasequence sets are also divided from TST and HST. Upper Sha-4 Submember across Well Liang754 is

**Fig. 4.24** Integrated analysis of facies across Well Bin435

identified as a third-order sequence and divided into three system tracts and seven parasequence sets (Fig. 4.25).

No. 1 parasequence set corresponds to the interval between 3303 and 3332 m, and the lithology is dominated by interbed of gray mudstone and gray sandstone, with aggradation superimposition in lithologic section. The single sand layer thickness is generally around 1 m. The deviation amplitude between GR and SP logging curves and the baseline generally indicates upward aggradation. Above 3303 m, sharply increasing mudstone content and GR value indicate FS. According to the structural location and sedimentary environment of Well Liang754, and combining with its finger-shaped, finger-like funnel-shaped GR curve and relatively obvious coarsening-upward cycle, No. 1 parasequence set is identified as shore-shallow lacustrine mudstone and shallow lacustrine beach deposits.

**Fig. 4.25** Integrated analysis of facies across Well Liang754

No. 2 parasequence set corresponds to the interval between 3229 and 3303 m; the lithology is interbeds of gray mudstone and gray sandstone, in which the sandstone content and single sandstone bed thickness do not increase greatly. The amplitude of GR and SP logging curves deviating from the baseline reflects low stand aggradation–weak progradation characteristics. From 3229 m upward, mudstone content and GR value increase sharply again, indicating FS. Combining with the structural position and sedimentary environment of Well Liang754, the location of sequence stratigraphic framework, finger-shaped, finger-like funnel-shaped GR and SP curves with obvious coarsening-upward cycle, No. 2 parasequence set was identified as shallow lacustrine mud and shallow lacustrine beach sediments.

No. 3 parasequence set corresponds to the interval between 3288 and 3369 m, and the lithology is interbeds of gray, dark gray mudstone, and gray sandstone. The sandstone content increases obviously, with characteristics of lowstand progradation. The single sand layer thickness generally varies between 1 and 3 m. Above 3190 m, the mudstone content and GR value increase sharply and mudstone darkens, and FFS is identified at 3190 m. According to core observation, the upper part is dominated by argillaceous siltstone, accompanied by truncation structures, characterized by storm action. The lower part (3210–3229 m) was identified as shore–shallow lacustrine mud and shore-shallow lacustrine beach bar deposits. The upper part (3210–3190 m) was identified as semi-deep lacustrine mudstone and storm deposits.

No. 4 (3170–3190 m), No. 5 (3146–3170 m), No. 6 (3110–3146 m), and No. 7 (3090–3110 m) parasequence sets have nearly 100% mudstone above 3288 m, with the mudstone content almost reach 100%, and a large set of oil shale occurs, the SP curve is closed to the mudstone baseline, reflecting a deepwater, poor source, reducing environment; these parasequence sets were identified as semi-deep lacustrine argillaceous deposits.

(8)  Integrated analysis of facies across Well Shi146

Well Shi146 is located in the central southwest of the Lijin Sag, adjacent to the deep low-lying area of the sag, and tectonically to the north of central faulted anticline belt. Upper Sha-4 Submember corresponds to the interval between 3749 and 3922 m.

The lithology is dominated by sandstone–mudstone. Similarly, according to sandstone content and stratigraphic superimposition, and combining with analysis of multiple logging curves, the target horizon is divided into two parts at 3808 m, below which is LST with high sandstone content, and strata of progradation and aggradation superimposition.

The part above 3808 m is TST and HST dominated by dark gray mudstone and limy mudstone, with certain-scale oil shale. FFS is identified at 3808 m, reflecting an abrupt increase in water depth. According to lithologic combination and logging curve characteristics, LST is divided into three parasequence sets. Similarly, two parasequence sets are divided from TST and HST. Upper Sha-4 Submember across Well Shi146 was identified as a third-order sequence and similarly divided into three system tracts and seven parasequence sets (Fig. 4.26).
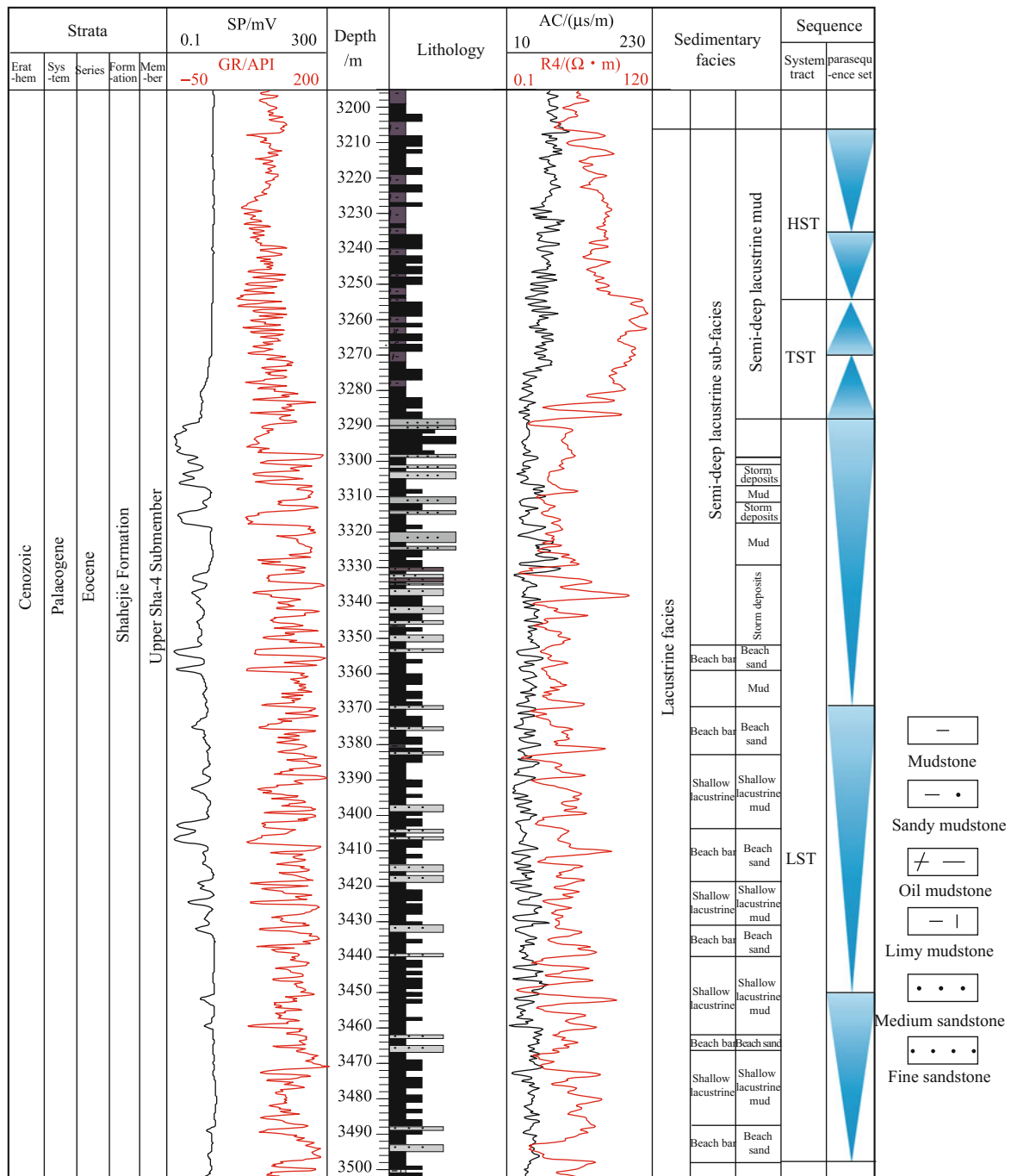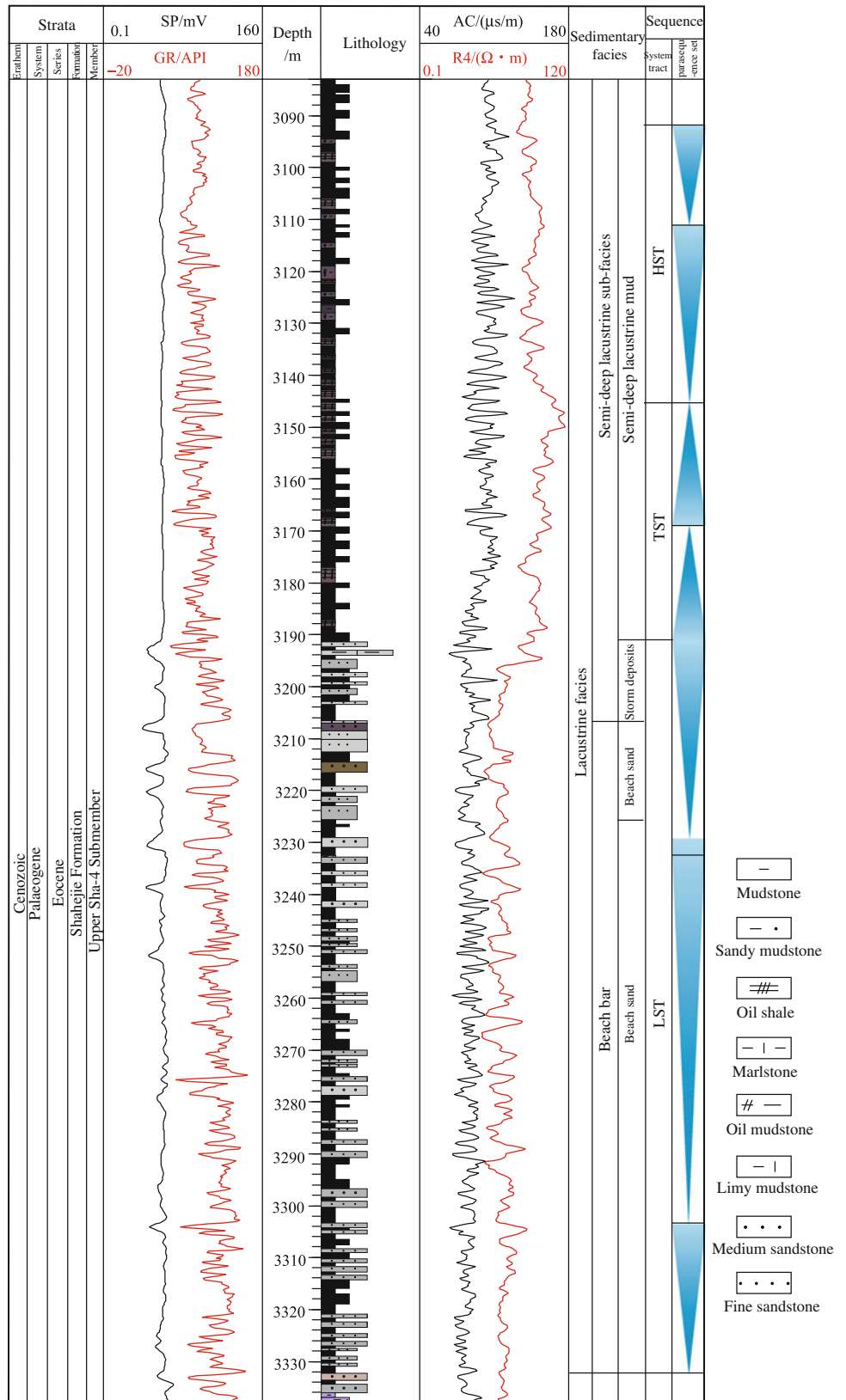
No. 1 parasequence set corresponds to the interval between 3303 and 3332 m, and the lithology is the interbed of gray mudstone and gray sandstone, with superimposition of aggradation–poor progradation in lithologic section. The single sand layer thickness is generally around 1 m. The deviation amplitude between GR and SP logging curves and the baseline generally also shows upward aggradation. Above 3303 m, the sharply increasing mudstone content and GR value indicate FS. According to the structural location and sedimentary environment of Well Shi146, and lithology dominated by mudstone and argillaceous sandstone, with high shale content, No. 1 parasequence set is identified as semi-deep lacustrine storm deposits.

No. 2 parasequence set corresponds to the interval between 3846 and 3890 m, and the lithology is interbed of gray mudstone and gray sandstone, without greatly increasing sandstone content, and increasing single sand layer thickness. The lithologic section indicates low stand aggradation–poor progradation. Above 3846 m, the mudstone content and GR value increase sharply again, indicating FS. Combining with the structural position and sedimentary environment of Well Shi146, and the location in the sequence stratigraphic framework, No. 2 parasequence set was identified as semi-deep lacustrine storm deposits.

No. 3 parasequence set corresponds to the interval between 3808 and 3846 m; the lithology is gray, dark gray mudstone, and gray sandstone interbeds; the sandstone content increases obviously, reflecting low stand, progradation characteristics. The single sand layer thickness is up to 14 m. Above 3808 m, the mudstone content and GR value increase sharply, mudstone darkens, and FFS is identified at 3808 m. According to core observation, the upper part is lithologically dominated by argillaceous siltstone, accompanied by muddy rip-up clasts and deformation structures characterized by storm action. No. 3 parasequence set was identified as shore-shallow lacustrine mud and storm deposits.

No. 4 (3790–3808 m), No. 5 (3777–3790 m), No. 6 (3768–3777 m), and No. 7 (3749–3768 m) parasequence sets have nearly 100% mudstone above 3808 m, with SP curve closed to shale baseline, reflecting a deepwater, poor
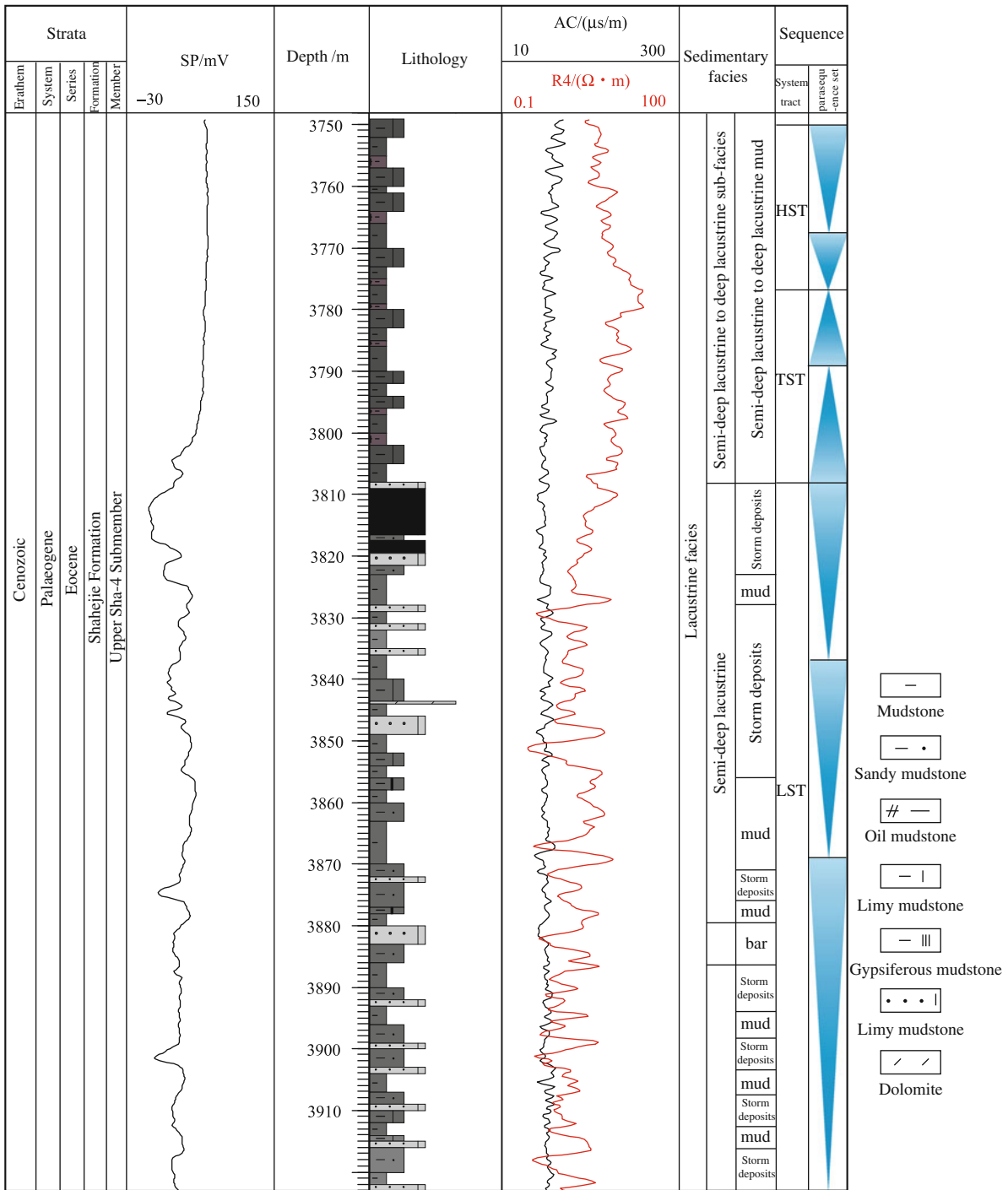
**Fig. 4.26** Integrated analysis of facies across Well Shi146

provenance, and reduction environment, and they are identified as semi-deep lacustrine argillaceous deposits.

(9)  Integrated analysis of sequence across Well Li672

Well Li672 is located in the central Lijin Sag. Upper Sha-4 Submember corresponds to the interval between 3872 and 4192 m. The lithology is dominated by sandstone–mudstone. Similarly, according to sandstone content and stratigraphic superimposition, and combining with analysis of logging curves, the target horizon is divided into two parts at 3970 m, below which is LST of progradation and aggradation superimposition with high sandstone content. The part above 3970 m is TST and HST dominated by dark gray

mudstone, and limy mudstone, with certain-scale oil shale. FFS is identified at 3970 m, indicating an abrupt increase in water depth. According to lithologic combination and well logging curve characteristics, LST is divided into three parasequence sets. Similarly, two parasequence sets are also divided from TST and HST. Upper Sha-4 Submember across Well Li672 was identified as a third-order sequence and similarly divided into three system tracts and seven parasequence sets (Fig. 4.27).

No. 1 parasequence set corresponds to the interval between 4124 and 4192 m, and its lithology is interbed of dark gray mudstone and gray sandstone, with greatly increasing sandstone content upward and relatively high single sand layer thickness between 2 and 8 m. Additionally, the deviation amplitude between GR and SP logging curves and the baseline generally shows water depth decreasing upward and multiple parasequence sets characterized by aggradation–progradation. Above 4124 m, the increasing sharply mudstone content and GR value indicate FS. Core observation shows dark mudstone indicates deepwater deposits, interbeds of sandstone, and GR curve of finger-like bell shape, and obvious fining-upward cycle characteristics; thus, No. 1 parasequence set was identified as semi-deep lacustrine mudstone and storm deposits.

No. 2 parasequence set corresponds to the interval between 4050 and 4124 m; the lithology is interbeds of gray mudstone and gray sandstone, with sandstone content increasing greatly upward, but generally lower than that of No. 1 Parasequence Set, and greatly decreasing single sand layer thickness generally lower than 2 m, indicating deepwater, which is due to that Well Li672 is near the lake basin center. The deviation amplitude between GR and SP logging curves and the baseline indicates shallowing water depth upward and multiple parasequence sets of aggradation–progradation. Above 4050 m, mudstone content and GR value increase sharply again, indicating FS. Core observation shows massive wave-origin sedimentary structures, including ripple bedding, wave-formed sand bedding, etc., and some horizons also show sedimentary characteristics of relatively deepwater, including storm-formed structures, etc., indicating shallow water–deep water alternating deposits. Besides, GR curve is characterized by multiple sets of finger-like funnel shape and obvious reverse cycles. Thus, No. 2 parasequence set was identified as semi-deep lacustrine mudstone and shallow lacustrine beach bar, and some beds were identified as storm deposits and semi-deep lacustrine mud.

No. 3 parasequence set corresponds to the interval between 3970 and 4050 m, and the lithology is interbeds of dark gray, gray mudstone, and gray sandstone, with the increasing sandstone content, which is obviously higher than that of No. 2 parasequence set, reflecting lake basin shrinkage and sand progradation. The single sand layer thickness is relatively low, generally between 1 and 2 m.

GR, SP logging curves, etc., reflect multiple parasequence sets of aggradation–progradation. Above 3970 m, mudstone content and GR value increase sharply, indicating FFS. Core observation shows that the lower part is dominated by wave-formed sedimentary structures, including ripple bedding, wave-formed sand bedding, ripple mark, etc., reflecting relatively shallow water deposits. Besides, GR curve is characterized by finger-like funnel shape and obvious reverse cycle, and No. 3 parasequence set is identified as shore-shallow lacustrine mud and shore-shallow lacustrine beach bar. The central upper part (3970-4030 m) is characterized by relatively deepwater sediments and storm-origin sedimentary structures, and it is identified as semi-deep lacustrine mud and storm deposits.

No. 4 (3932–3970 m), No. 5 (3912–3932 m), No. 6 (3892–3912 m), and No. 7 (3872–3892 m) parasequence sets have nearly 100% mudstone above 3970 m upward, with a large set of oil shale, and SP curve closed to the mudstone baseline, indicating a deepwater, poor provenance, reduction environment. They are identified as semi-deep lacustrine argillaceous deposits.

(10)   Integrated analysis of sequence across Well Liang218

Well Liang218 is located in the central low high of transition area from the Lijin Sag to the Boxing Sag. Upper Sha-4 Submember corresponds to the interval between 3050 and 3249 m, with total thickness of 199 m. Upper Sha-4 Submember is wholly identified as a third-order sequence (Fig. 4.28), which is divided into LST (three parasequence sets), TST (two parasequence sets), and HST (two parasequence sets) from bottom to top. Upper Sha-4 Submember mudstone is shallow gray-dark gray, and it is dominated by beach bar deposits, semi-deep lacustrine tempestite, and semi-deep lacustrine mudstone deposits (Fig. 4.28).

LST: it corresponds to the interval between 3150 and 3249 m, consists of No. 1, No. 2, and No. 3 parasequence sets from bottom to top, and is dominated by beach bar deposits and semi-deep lacustrine tempestite. No. 1 parasequence set has a depth between 3196.5 and 3249 m and a thickness of 52.5 m, with beach ridge, beach inter-ridge, and beach ridge from bottom to top. The beach inter-ridge is lithologically dominated by limy siltstone, dolomitic siltstone, and argillaceous siltstone, with finger-like logging curve, shallow lacustrine mudstone 18 m thick, intercalated with limy mudstone. The mudstone top is thin-bedded beach inter-ridge sandstone, which is lithologically dolomitic sandstone and argillaceous siltstone. No. 2 parasequence set has a depth between 3175 and 3196.5 m and a thickness of 21.5 m, with three layers of beach sand intercalated with two beds of mudstone. The beach sand is mainly thin-bedded beach inter-ridge sandstone intercalated with thin-bedded mudstone, and it is lithologically dolomitic sandstone,

**Fig. 4.27** Integrated analysis of facies across Well Li672
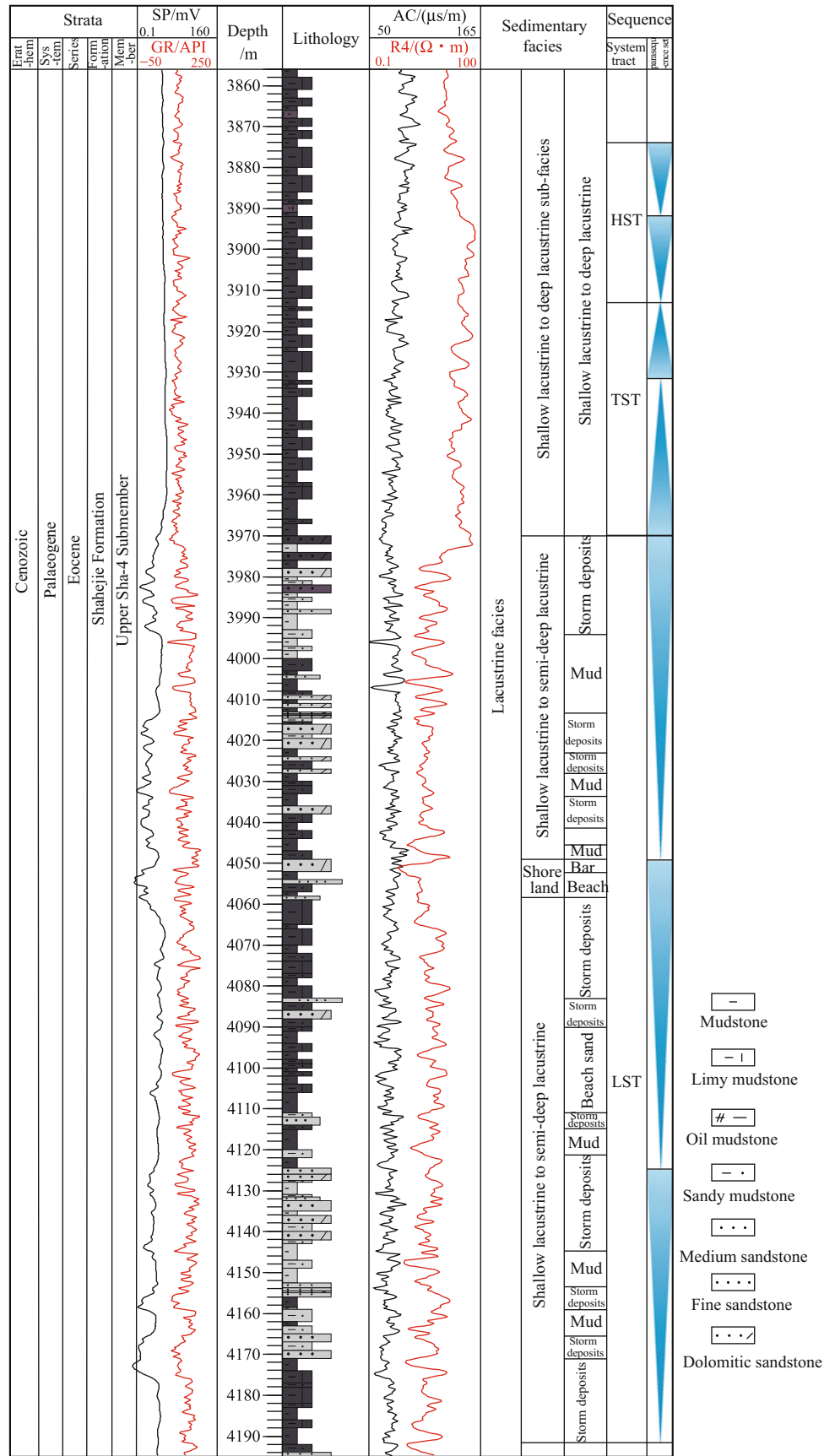
**Fig. 4.28** Integrated analysis of facies across Well Liang218

siltstone, and argillaceous siltstone, with logging curve of jogged or low-amplitude finger shape, with thick shallow lacustrine mudstone intercalated with dolomitic mudstone. No. 3 parasequence set has a depth between 3150 and 3175 m and a thickness of 25 m, and it is a set of semi-deep lacustrine storm deposits. Storm deposits are lithologically dolomitic sandstone, with oil stains at the top. The single sand layer is 3.5 m thick, with jogged logging curve, and dolomitic sandstone intercalated with mudstone and silty mudstone.

TST: it corresponds to the interval between 3095 and 3150 m, and consists of No. 4 and No. 5 Parasequence sets from bottom to top. No. 4 parasequence sets, which are storm deposits, have a depth between 3128.5 and 3150 m and a thickness of 21.5 m. The lithology is dominated by dolomitic sandstone with minor argillaceous sandstone; the dolomite is developed at the top, with finger-like logging curve. No. 5 parasequence set has a depth between 3095 and 3128.5 m and a thickness of 33.5 m, dominated by storm deposits and semi-deep lacustrine mudstone. The storm deposits are lithologically dominated by dolomitic sandstone, with finger-like logging curve, and there is another layer of siltstone approximately 3.5 m thick; the semi-deep lacustrine mudstone comprises dolomitic mudstone, limy mudstone and silty mudstone.
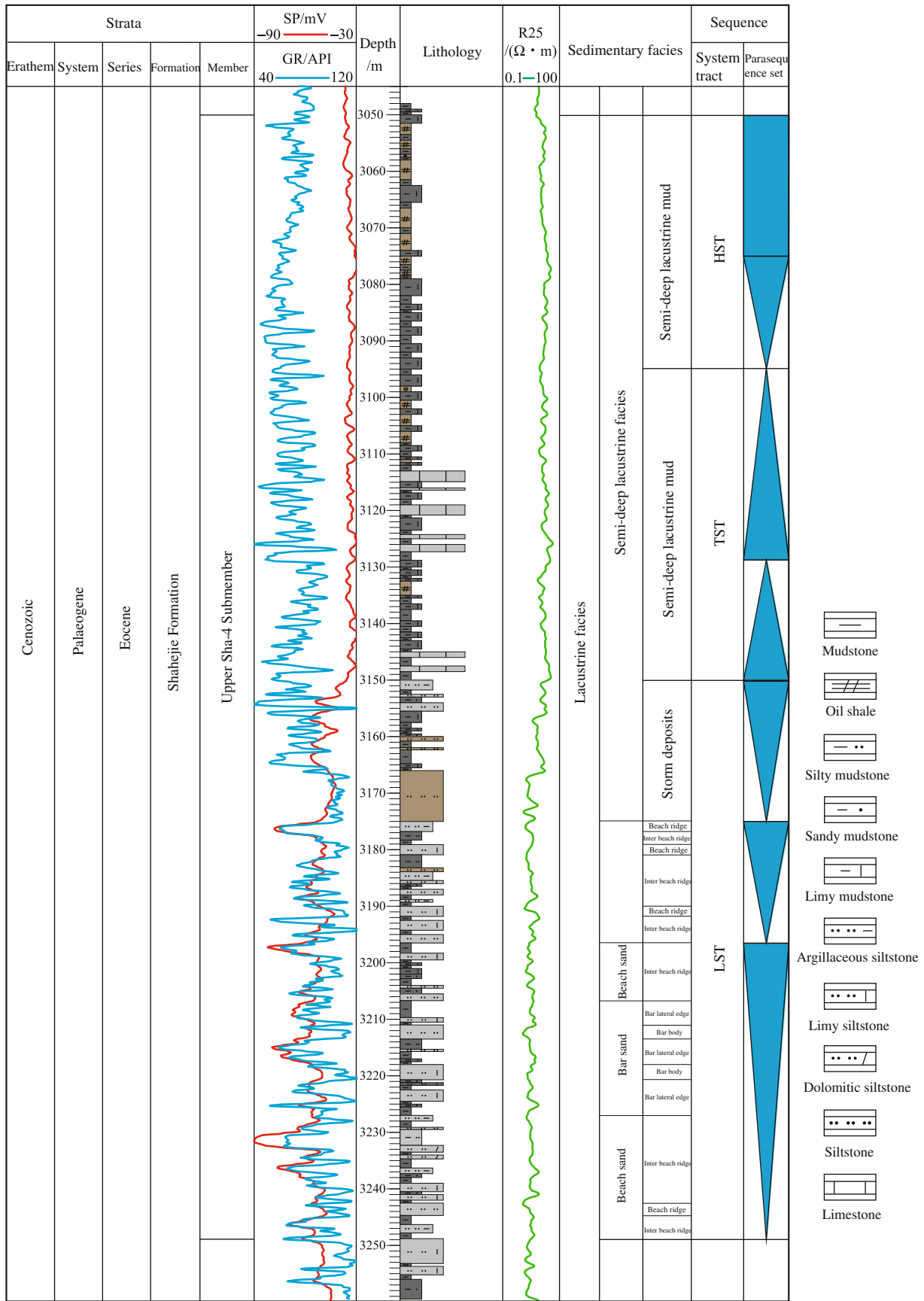
HST: it corresponds to the interval between 3050 and 3095 m and consists of No. 6 and No. 7 parasequence sets from bottom to top. No. 6 parasequence set has a depth between 3075 and 3095 m and a thickness of 20 m, with shallow lacustrine mud-beach inter-ridge-shallow lacustrine mud from bottom to top, dominated by mudstone. The beach ridge is lithologically dolomitic sandstone and dolomite, with logging curve of wide-amplitude thick finger shape. No. 7 parasequence has a depth between 3050 and 3075 m and a thickness of 25 m, with beach ridge-shallow lacustrine mud-beach ridge-beach inter-ridge facies from bottom to top. The beach ridge lithology comprises siltstone, and limy sandstone, with logging curve of wide-amplitude thick finger shape. The beach inter-ridge lithology is thin interbeds of argillaceous siltstone, limy sandstone and mudstone, limy mudstone, and silty mudstone, with logging curve of thin finger shape.

### 4.2.3   Division of Sequence Stratigraphy

According to integrated analyses of sequence division of Upper Sha-4 Submember in the Dongying Sag, the Lijin and Boxing Sub-Sags feature different geomorphology, while the southeastern gentle slope belt in the Dongying Sag and the Boxing Sub-Sag have similar paleo-geomorphological features. Affected by the Binxian Bulge, Linfanjia Bulge, the Pingfangwang Paleo-Burial-Hill Drape Structural Belt,

Central Anticline Belt and the transitional low salient area from the Lijin Sub-Sag to Boxing Sub-Sag, the Lijin Sub-Sag features complex topography, greatly varying thickness, and steepness along side slopes, fluctuated terrain within sub-sags, and deep low-lying parts of sub-sags. Upper Sha-4 Submember was deposited in deep lake. The maximum thickness in the northeastern sub-sags indicates the sedimentary and subsidence centers of the Dongying Sag in the sedimentary period of Upper Sha-4 Submember. Relatively stable thickness in the Boxin Sag and relatively flat paleo-terrain indicate shallow lake water during deposition of Upper Sha-4 Submember. Due to relatively flat terrain during sedimentation of the southeastern gentle slope, the thickness varied little along EW and increased regularly along NS. Varying paleo-terrain and paleo-water depth controlled different sedimentation of the Dongying Sag.

Based on sequence correlation in single-well and well-tie sections, the sequence stratigraphic framework of Upper Sha-4 Submember is established (Fig. 4.29). According to stratigraphic superimposition, logging curve variation, and seismic reflections, Upper Sha-4 Submember is identified as a third-order sequence and subdivided into LST, TST, and HST. The interface between LST and TST was identified as FFS, mainly based on (a) no obvious denudation and sedimentary discontinuity above and below FFS; (b) transition of stratigraphic superimposition from poor progradation to retrogradation; (c) the greatly increasing shale content and darker mudstone above FFS; and (d) abrupt change of logging curve at FFS. The interface between TST and HST is identified as MFS and corresponds to the widespread oil shale. According to stratigraphic superimposition, Upper Sha-4 Submember is divided into seven parasequence sets, which is used for good correlation of drill hole sections in whole area (Fig. 4.30).

In LST, the relative lake level descended, shoreline and wave base migrated toward the lake basin center, and sediments prograded, resulting in widely developed sandstone, with delta, fan-delta, beach bar and shore-shallow lacustrine and semi-deep lacustrine fine-grained lithology. In TST, the relative lake level rose, shoreline and wave base migrated toward continent, with expanded water area and increased water depth, resulting in thick and widely distributed semi-deep and deep lacustrine mudstone, oil shale, and limestone in a fining-upward retrogradation sequence. HST is dominated by shore-shallow lacustrine and semi-deep lacustrine mudstone, beach bar sandstone, and limestone in aggradation–poor progradation. Sandbodies migrated slightly toward lake basin center and were mainly distributed in LST, i.e., below FFS. As water was relatively shallow in LST, and sandbodies prograded inside basin, favorable sandbodies of LST advanced toward the lake basin center and were remodified by lake basin water, resulting in secondary transportation and sedimentation and forming
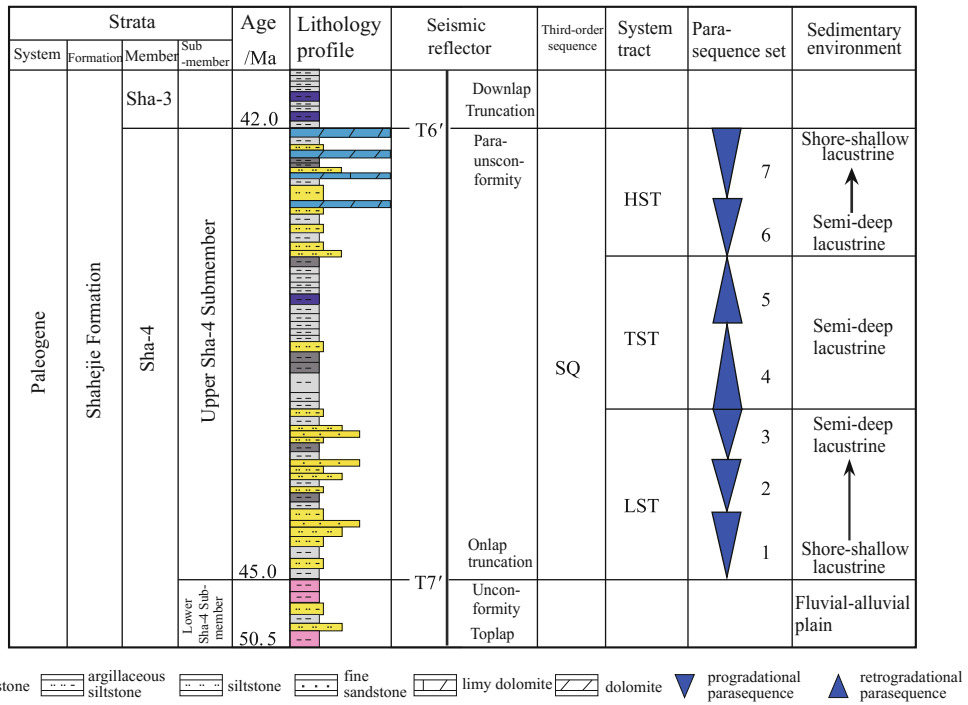
**Fig. 4.29** Division of sequence stratigraphy of Upper Sha-4 Submember in the Dongying Sag according to Li (2009). 1—Mudstone; 2 —argillaceous siltstone; 3—siltstone; 4—fine sandstone; 5—limy dolomite; 6—dolomite; 7—progradation parasequence; 8—retrogradation parasequence; HST—highstand systems tract; TST—transgressive systems tract; LST—lowstand systems tract
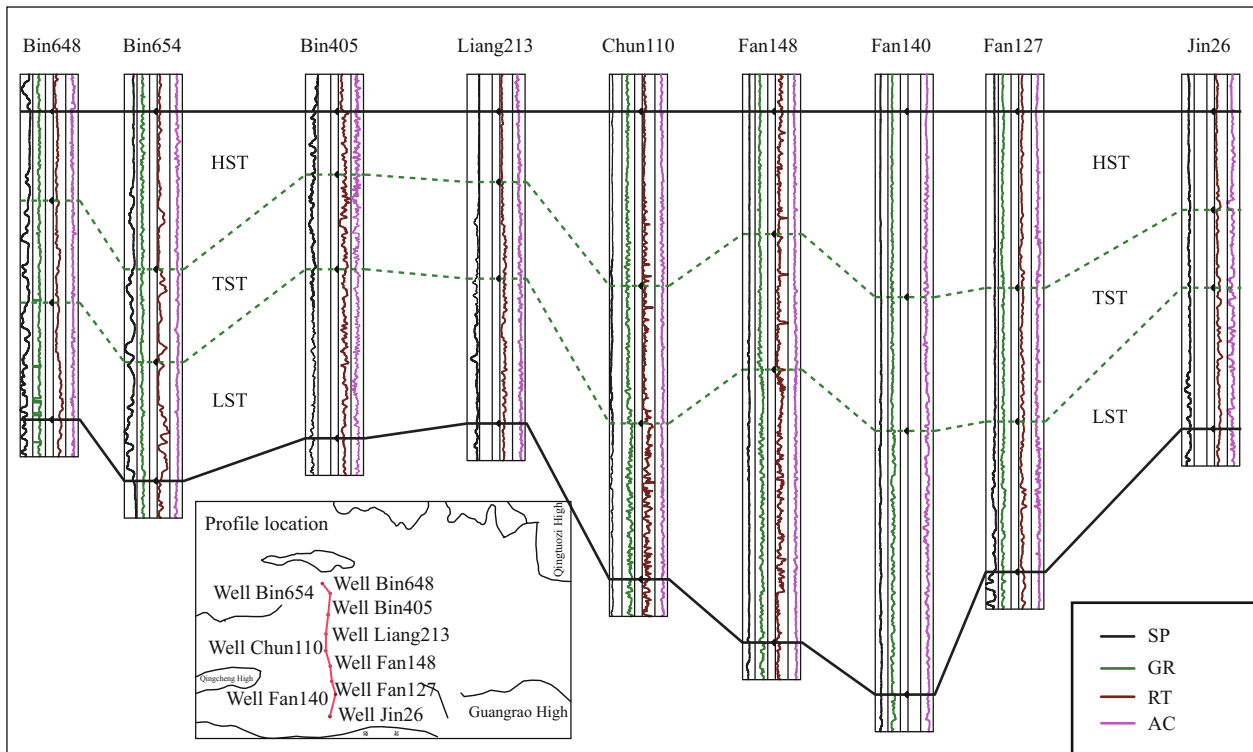


**Fig. 4.30** Comparison of stratigraphic sequence of backbone profile of Upper Sha-4 Submember in the Dongying Sag

relatively shallow water sedimentary facies assemblage widely distributed in the lake basin.

## 4.3    Sedimentary Facies of Upper Sha-4 Submember in the Dongying Sag

On the basis of core observation, logging curves pattern, and lithofacies assemblage analysis, we have studied and summarized the sedimentary facies of Upper Sha-4 Submember in the Dongying Sag combining with the previous research results. First, we determined main sedimentary facies through identification of facies markers in single wells; then, we selected a backbone profile and determined distribution of sedimentary facies in lines and surfaces successively with contour of sand content and isopach of sandstone; we further conducted research on control of various sedimentary facies by each element in windfield-source-basin system. The

sedimentary facies of Paleogene Upper Sha-4 Submember in the Dongying Sag and their general distribution are shown in Table 4.2.

The following sections focus on fan-delta, subaqueous gravity flow, delta, shore and shallow lake, carbonate beach bar, storm deposits, and semi-deep and deep lacustrine fine-grained sedimentary facies, and characteristics of those sedimentary facies developing in sequence stratigraphic framework with system tract as the unit.

### 4.3.1    Fan-delta

The fan-delta is mainly developed in the southern slope of Binxian Bulge. Based on lithofacies assemblage and well log/mud log characteristics, the lithofacies assemblage is characterized by a set of coarsening-upward cycle dominated by medium- to fine-grained conglomerate, pebbly sandstone,

**Table 4.2** Table of sedimentary facies division of Upper Sha-4 Submember in the Dongying Sag (refer to Figs. 4.1 and 4.2)

| Facies | Subfacies | | | Wells | Sequence position | Plane position |
|---|---|---|---|---|---|---|
| fan-delta | Plain, front, frontal fan-delta | | | Shan142, Bin654, etc. | LST, TST, HST | North part of western segment, southern slope of Binxian Bulge |
| Delta | Front, frontal delta | | | Gao32, Hua17, etc. | LST, TST, HST | Eastern and western sides of south part, axial edge of sag |
| Subaqueous fan | Inner fan, middle fan, outer fan | | | Li98, Tuo167, Yan 227, etc. | LST, TST, HST | North part, downthrow side of Chennan Fault |
| Gravelly beach bar | / | | | Jin22, Jin25, etc. | LST, TST, HST | Western side of south part, north side of Luxi Uplift |
| Sandy beach bar | Beach | Outer beach | | Fan129, Fan148, etc. | LST, TST, HST | Boxing Sub-Sag in south part, Bamianhe Area, western side of Lijin Sub-Sag |
| | | Inter-bar beach | | Gao893, etc. | | |
| | | Coastal beach | | Bo104, Gao890, etc. | | |
| | Bar | Coastal bar (or beach ridge) | | Jin22, Jin25, etc. | LST, TST, HST | |
| | | Nearshore bar | | Fan135, Bo104, etc. | | |
| | | Offshore bar | | Fan143, Fan137, etc. | | |
| Storm deposits | / | | | Bin670, Li672, Wang58, etc. | LST, TST | Lijin Sub-Sag, Niuzhuang Sub-Sag |
| Limestone beach | / | | | Bin182, etc. | HST | Pingwangzhuang Area |
| Biodetritus beach bar | / | | | Bin706, Bin433, etc. | HST | Pingwangzhuang Area |
| Lacustrine | Shore-shallow lacustrine | | | / | LST, TST, HST | Whole area |
| | Semi-deep lacustrine | | | / | | |
| | Deep lacustrine | | | / | | |

and coarse sandstone and followed by gray-green mudstone, gray mudstone, and dark gray mudstone (Figs. 4.31 and 4.32). On the seismic profile, the fan-delta appears as the wedge reflection configuration. The fan-delta plain is rarely preserved, and fan-delta front deposits and pre-fan-delta deposits are mainly preserved.

1. Fan-delta plain subfacies

Due to denudation, the on-water deposits of fan-delta is rarely preserved. The preserved lithofacies assemblage is dominated by positive cycle composed of medium—to fine-grained conglomerate, and coarse—to fine-grained
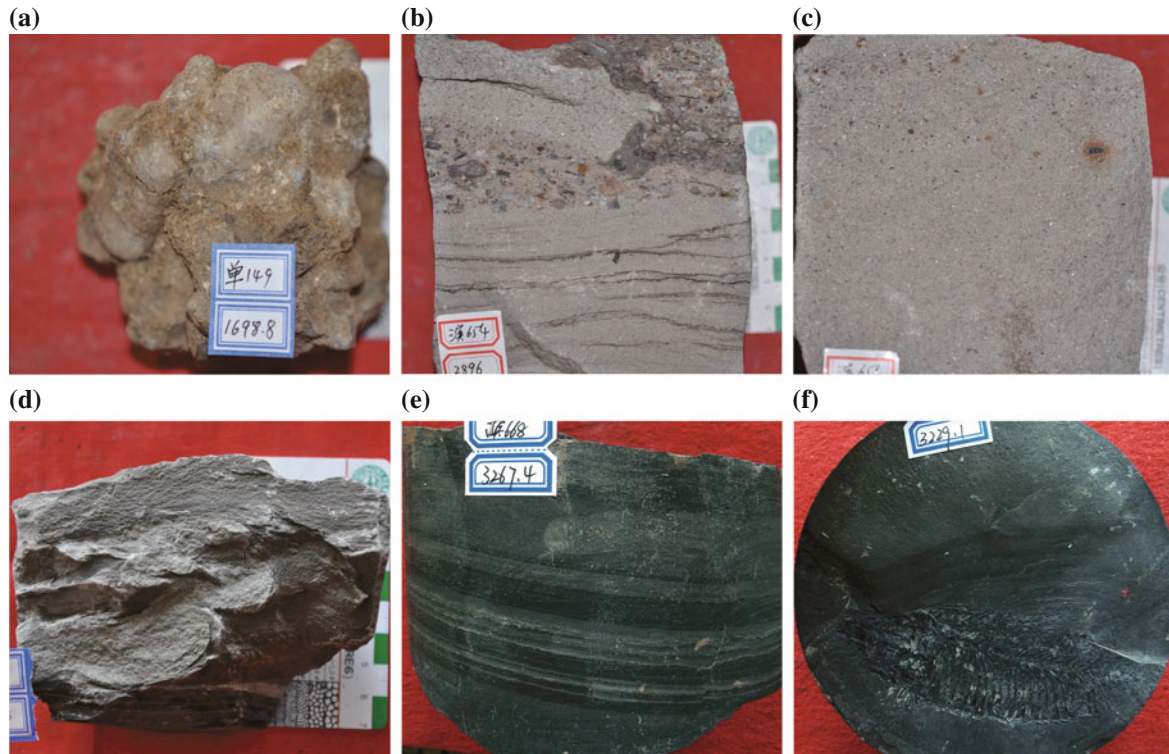


**Fig. 4.31** Characteristics of fan-delta sedimentary core. **a** Shan149, at 1698.8 m, randomly arranged gravels; **b** Bin654, at 2896 m, upper conglomerate, and bottom ripple bedding; **c** Bin654, at 2895 m, gray sandstone, coarsening-upward; **d** Bin687, at 3335.3 m, slump deformation; **e** Bin668, at 3267.4 m, horizontal bedding; **f** Bin668, at 3229.1 m, dark gray mudstone, backbone fossil
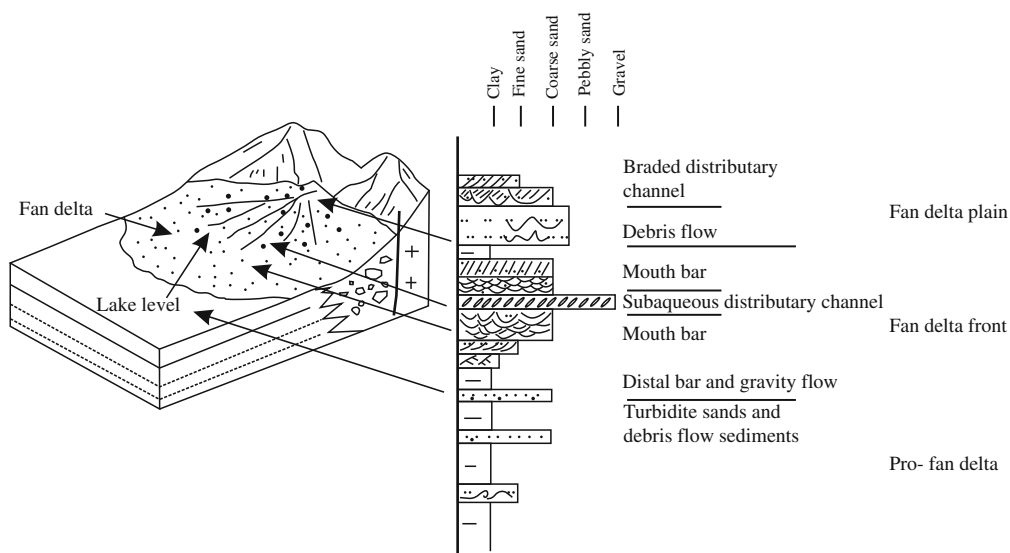


**Fig. 4.32** Sedimentary model and sequence of fan-delta in the Dongying Sag according to Feng et al. (2006)

sandstone interbedded with gray-green mudstone, and occasionally purplish red mudstone. The fan-delta plain is divided into debris flow deposits and braided channel deposits.

(1) Debris flow deposits

The debris flow deposits is dominated by bulk medium- to fine-grained conglomerate, and the gravel diameter (in an axle) reaches 100 mm, and is generally between 2 and 70 mm. Upright, inclined, and flat gravels are arranged chaotically, with subrounded and rounded shapes (Fig. 4.31a), indicating a certain distance from provenance. These gravels include boulder clay, granite gravel, and metamorphic gravel, with sandy mudstone as matrix.

(2) Braided channel deposits

The braided channel deposits are always associated with debris flow and dominated by positive cycle composed of pebbly sandstone and sandstone. The bottom is erosive surface, which is always pebbly coarse sandstone with subangular-sub rounded gravel, and characterized by directional alignment, forming bottom gravel layer of braided channel. The sandstone with fining-upward graded bedding constitutes bar deposits of braided channels, with massive and cherry plant stems seen.

2. Fan-delta front subfacies

The fan-delta front subfacies is characterized by the inverse cycle composed of thick (pebbly) sandstone, and siltstone interbedded with mudstone. According to lithofacies assemblages and characteristics of sedimentary tectonics, the fan-delta front subfacies is further divided into subaqueous braided channel, interdistributary bay, river mouth bar, sheet sand, and slump deposits (Fig. 4.31b–f).

(1) Subaqueous braided channel

The subaqueous braided channel is the subaqueous extension of fan-delta plain braided channel. The lithology is dominated by gray, and gray-green pebbly sandstone, and coarse- to medium-grained sandstone, forming a positive cycle. The bottom is erosive surface (Fig. 4.31b), where the directionally aligned granule conglomerate, parallel bedding, and cross-bedding interbedded with pebbly sandstone, and coarse- to medium-grained sandstone are developed.

(2) Subaqueous braided interchannel (interdistributary bay)

Subaqueous braided interchannels are low-lying lands between subaqueous braided channels and are connected with lakes. Their sedimentation is dominated by suspension and settling. Their lithology is dominated by dark gray, dark gray-green silty mudstone, mudstone, and limy mudstone, with horizontal bedding and small ripple bedding (Fig. 4.31e), reflecting weak reduction-reduction environment, and big biological remains are also seen (Fig. 4.31f).

(3) Mouth bar

A mouth bar is formed when the sand carried by water deposits in the river mouth as braided channel merges with the lake and flow rate decreases and is characterized by coarsening-upward structure composed of medium thick pebbly sandstone, and fine- to coarse-grained sandstone (Fig. 4.31c), with cross-bedding, wavy bedding, massive bedding, etc. The top is bounded by erosive surface.

(4) Sheet sand

The sediments of subaqueous braided channel, and river bar formed previously were migrated horizontally by wave and connected, forming sheet sand. The lithology is dominated by gray fine sandstone, and the sedimentary structure is dominated by wavy bedding, wavy rippled bedding, etc., with high angle organism burrows and carbon dust, reflecting shallower sediments.

3. Pro-fan-delta subfacies

The Pro-fan-delta sediment is dominated by dark gray mudstone and silty-fine mudstone, with horizontal bedding, and occasionally slump turbidite sandbody wrapped in frontal fan-delta dark gray mudstone. It is difficult to distinguish fine-grained sediments in frontal fan-delta subfacies and semi-deep lacustrine mudstone in normal sedimentation.

## 4.3.2 Subaqueous Gravity Flow Deposits

Northern boundary faults of the Dongying Sag covers Lijin Fault, Chennan Fault, and Shengbei Fault, with paleogeographic framework of large topographical elevation difference and short distance from provenance in northern Dongying Sag, and deepwater environment was formed in the downthrown side of the faults. Meanwhile, the semiarid-muggy climate was favorable to mechanical weathering of parent rock, with abundant supply of sediments and development of near-provenance sandy conglomerate fans, e.g., nearshore subaqueous fan and sublacustrine fan. The lithology is dominated by dark gray mudstone and gray-dark gray silty-fine sandstone, medium- to coarse-grained sandstone, pebbly sandstone, etc. The gravel is characterized by complex components, uneven size,
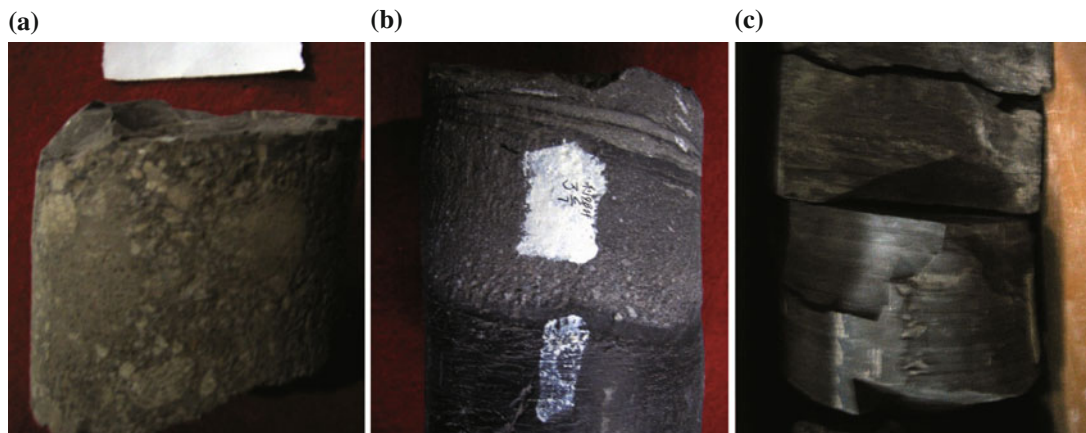
**Fig. 4.33** Characteristics of cores from nearshore subaqueous fan. **a** Well Li98, at 3434.0 m, matrix-supported sandy conglomerate, with poorly sorted and non-oriented gravel; **b** Well Li98, at 3277.8 m, gravel-bearing medium- to coarse-grained sandstone, fining-upward sequence, with bottom erosion surface; **c** Well Li98, at 3428.4 m, dark gray siltstone and siltstone-fine sandstone

subangular-subrounded shape, poor sorting (Fig. 4.33a), and low compositional maturity and textural maturity.

1. Nearshore subaqueous fan

The nearshore subaqueous fan is developed in the downthrown side of the Chennan Fault, i.e., the basin-controlling fracture in the north of the basin, which is further divided into the inner fan, middle fan, and outer fan. The inner fan is dominated by thick layers of massive glutenite with gravels chaotically arranged (Fig. 4.33a), which is the result of high-density turbidity current deposits, and the main water channel is developed in the inner fan. The middle fan is composed of medium- to coarse-grained pebbly sandstone, with the graded bedding, parallel bedding, and basal scour structure commonly seen (Fig. 4.33b). Braided water channels are primarily developed in the middle fan. The channel migration has caused vertical formation of erosive surface-divided and superimposed sandstone layers barely or never with argillaceous interlayers; thus, the middle fan generally features the gravelly high-density turbidity current deposits. The outer fan is accumulated with mudstone intercalated with thin siltstone and silty-fine sandstone, with parallel bedding and current ripple bedding (Fig. 4.33c), and it is dominated by sequence of low-density turbidity current deposits.

2. Sublacustrine fan

Sublacustrine fans are developed extensively in the downthrown side of the Shengbei Fault (Liu and Wang 2010; Yuan et al. 2012) (Fig. 4.34) and are formed when factors like gravity, earthquakes, and floods exert force on the nearshore subaqueous fans. The near-provenance part of sublacustrine fans is mainly a set of poorly sorted, massive, and matrix-supported mingled conglomerates (Liu and Wang 2010), deposited by the gravity flow along the main water channel. The middle fan dominated by pebbly sandstone and massive sandstone intercalated with thin mudstone has graded bedding and deformed bedding and is mainly deposited by flows along braided water channels and between channels. The braided water channel deposition is featured by bottom erosive surfaces, and the interchannel deposits are dominated by fine sediments with structures like incomplete Bouma sequences, ripple cross-bedding, and soft-sediment deformation. The middle fan constitutes the main body of the sublacustrine fan. The outer fan is at the far end of the sublacustrine fan and is mainly composed of fine-grained sediments featured by dark mudstone intercalated with thin siltstone and fine sandstone, with horizontal bedding developed. The sublacustrine fan as a whole is overlaid upward in sequence by the inner fan, middle fan, and outer fan, mostly a fining-upward cycle (Liu and Wang 2010).

3. Channel turbidite

The channel turbidite, developed in the fault trough at the downthrown side of the boundary fault (Liu and Wang 2010) (Fig. 4.34), is mainly composed of sandstone and pebbly sandstone intercalated with thin mudstone and has the gravity flow generated depositional structures like (superimposed) graded bedding, slump deformation, and muddy rip-up clasts. The channel turbidite generally connected the nearshore subaqueous fan near the provenance and the sublacustrine fan at the distal end and acted as the sediment movement channel from semi-lacustrine area to deep lacustrine area, resulting in composite deposition of nearshore subaqueous fan, channel turbidite, and sublacustrine fan.
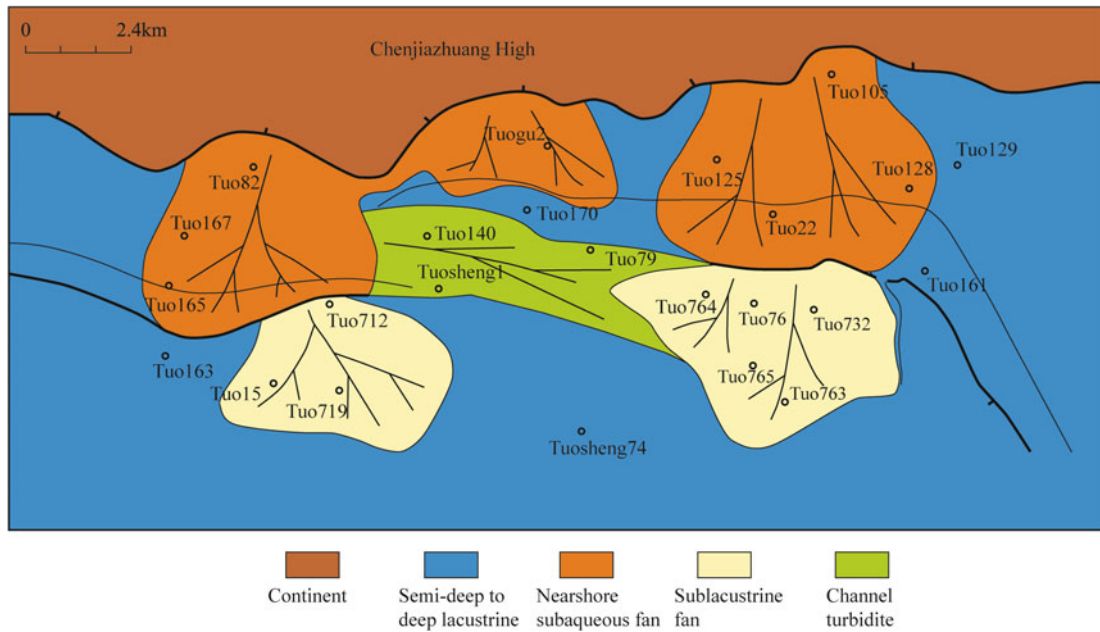
**Fig. 4.34** Characteristics of planar distribution of sedimentary facies of Upper Sha-4 Submember in the Dongying Sag (Liu and Wang 2010)

### 4.3.3 Delta

The delta in the Dongying Sag is confined to Qingcheng Bulge to the northwest of Boxing Sub-Sag, Guangrao Bulge in the east of slope area of southern Dongying Sag, and surrounding area toward lake. According to previous research (Tian and Jiang 2009; Jiang et al. 2011; Yang et al. 2011), delta deposits dominated by delta front are encountered by Well Block Jiao3, Jiao6, Jiao22, Lai5, Mian1, Mian3, Mian18, Mian13, Gao21, and Fan121 in study layers (Fig. 4.1). The lithology is dominated by gray fine sandstone, silty-fine sandstone intercalated with mudstone, with good sorting and roundness and development of sedimentary structures, e.g., parallel bedding, cross-bedding, lentoid bedding, wavy bedding, and flaser bedding. The

coarsening-upward sequence has log curve reflections of box shape and funnel shape, etc. (Fig. 4.35).

The delta front was developed in LST, TST, and HST of Upper Sha-4 Submember in the Dongying Sag (Tian and Jiang 2009). The delta front is divided into subaqueous distributary channel, mouth bar, sheet sand, etc. The subaqueous distributary channel is characterized by scouring bottom and filling of gravel-bearing sandstone, with fining-upward sequence and SP curve of bell or toothed bell shapes. The mouth bar sandstone has much better sorting compared with subaqueous distributary channel and is dominated by medium- to fine-grained sandstone, characterized by coarsening-upward sequence and SP curve of funnel or toothed funnel shapes (Fig. 4.35). The mouth bar and subaqueous distributary channel are oftentimes associated (Fig. 4.35).

**Fig. 4.35** Logging profile of delta front (modified from Jiang et al. 2011)
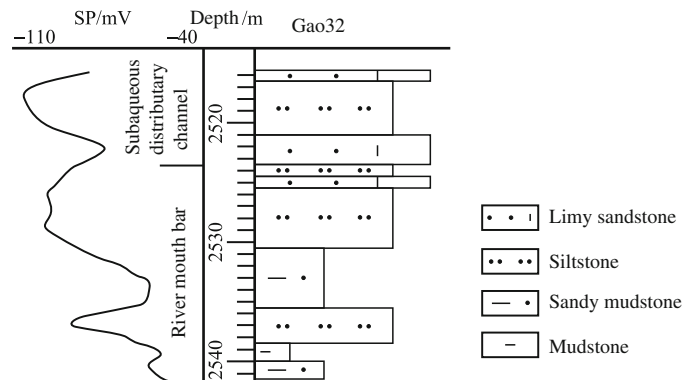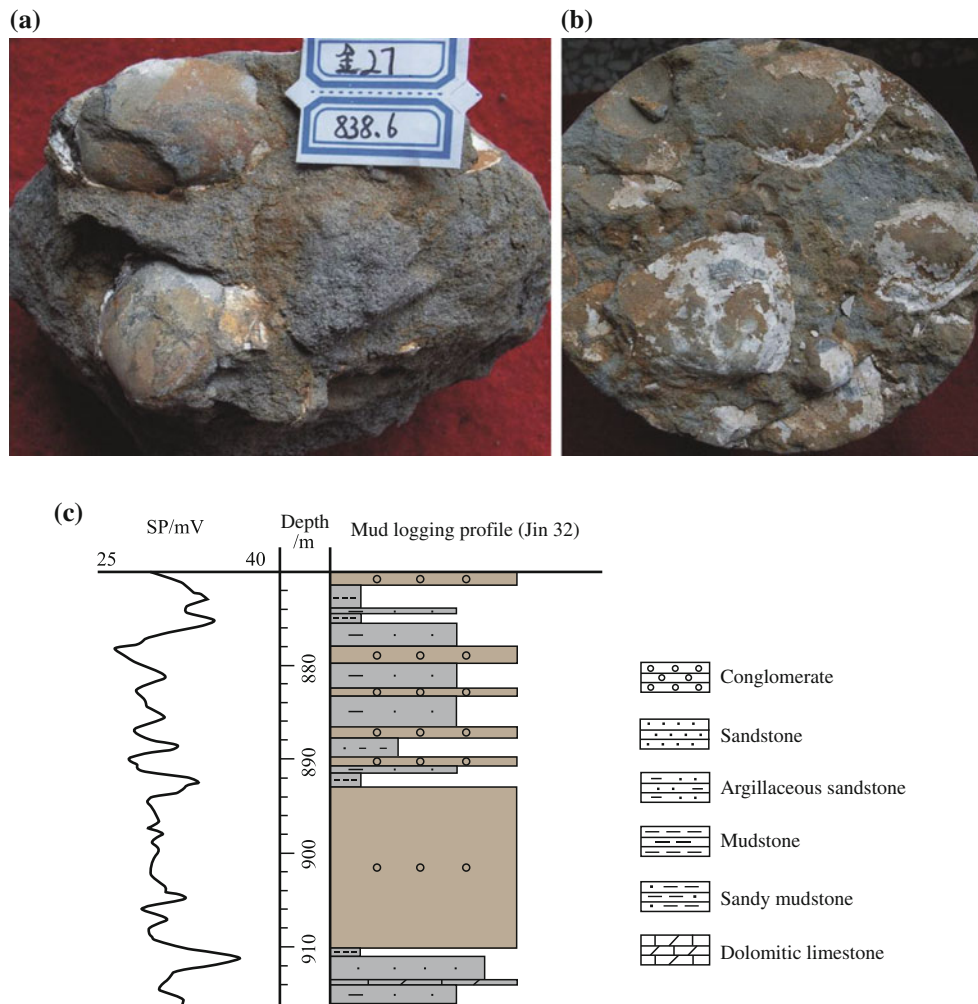
**Fig. 4.36** Characteristics of gravelly beach bar (Modified from Wang et al., 2018). **a** gravel, subrounded-rounded, Well Jin27, at 838.6 m; **b** fossil of bivalve biological remains, Well Jin27, at 839.6 m; **c** typical well logging and mud logging profile of gravelly beach ridge, well Jin22

### 4.3.4   Clastic Beach Bar

beach bar sandbodies, the general term for beach sand and bar sand, are common along the shore-shallow lake area. Upper Sha-4 Submember of the Paleogene in Dongying Sag, especially during the LST, is gentle in palaeogeomorphology and abundant in provenance supply, and a large area of beach bar was developed under interaction of provenance and waves.

1. Gravelly beach ridge

Gravelly beach bar is developed in the littoral zone near the Luxi Uplift in Boxing Sub-Sag (Li 2009). It is dominated by medium-grained conglomerate and gravel-bearing coarse-grained sandstone. Subround-round (Fig. 4.36a) gravels generally have the diameter of 2–30 mm (an axis). Relatively intact shell fossil and snail fossil layers are preserved in the

rocks (Fig. 4.36b). Their logging curve reflections are generally of toothed box or toothed funnel shapes (Fig. 4.36c).

2. Sandy beach bar

A large area of sandy beach bar is developed in the LST of Upper Sha-4 Submember in Dongying Sag (Jiang et al. 2011, 2014) and is mainly distributed in Boxing Sub-Sag, the southeast of Niuzhuang Sub-Sag, the west of Lijin Sub-Sag, and central high belt of the transition region from Lijin Sub-Sag to Boxing Sub-Sag. Focusing on the core and logging, this study summarizes the features and interprets hydrodynamic mechanism of the beach bar from the aspects of cores lithology, sedimentary structure (Fig. 4.37), grain size analysis and logging response (Fig. 4.38). By observing the cores from the cored wells in different locations, the beach sand and the bar sand are distinguished and then subdivided according to the hydrodynamic mechanism,
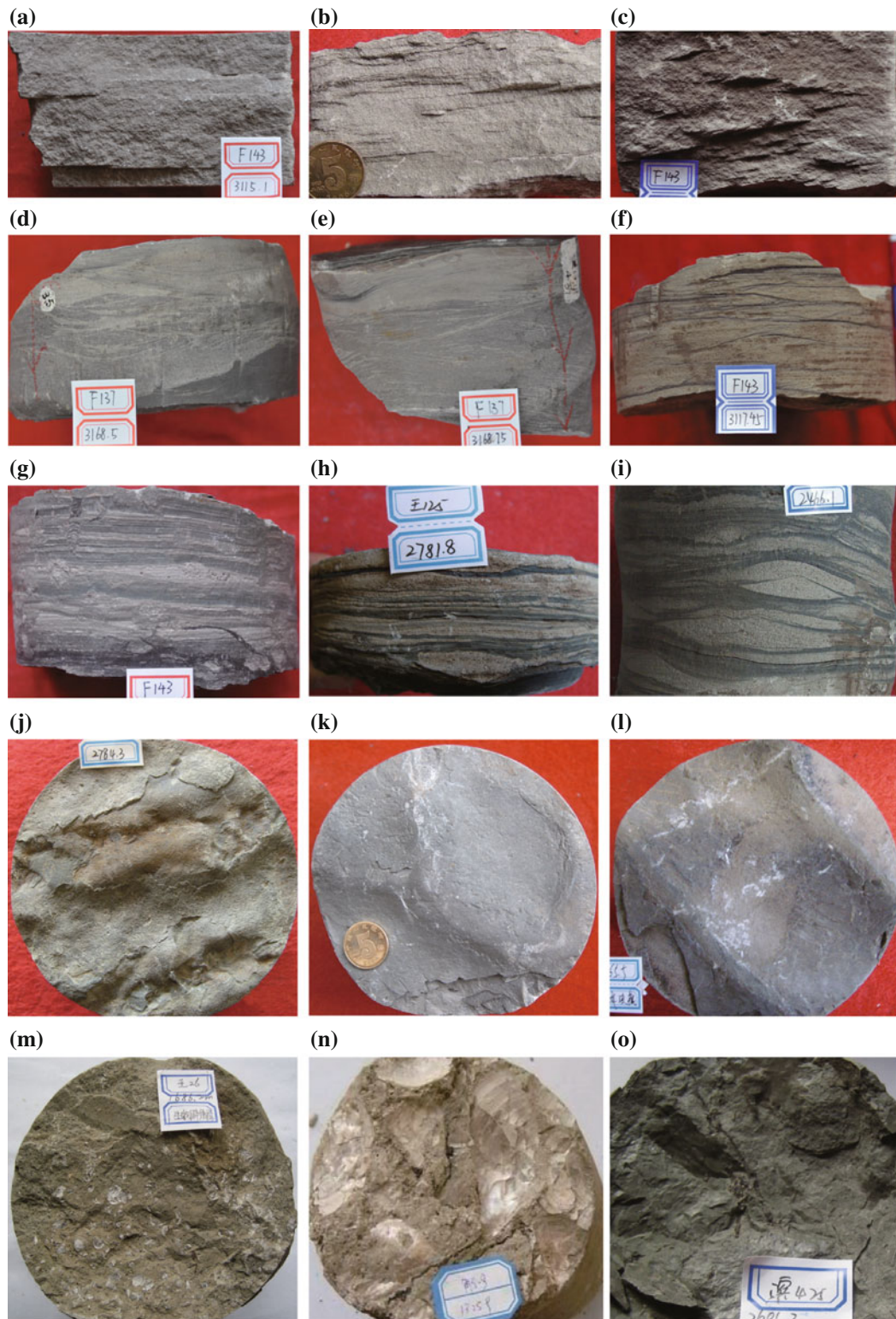
**Fig. 4.37** Typical cores of Upper Sha-4 Submember beach bar in the Dongying Sag. **a** Sandstone with parallel bedding, Well Fan143, at 3115.1 m; **b** sandstone with swash cross-bedding, Well Bo104, at 2149.8; **c** sandstone with (tabular) cross-bedding, Well Fan143, at 3117.25 m; **d** sandstone with wave ripple cross-bedding, at Well Fan137, at 3168.5 m; **e** sandstone with wave ripple cross-bedding, Well Fan137, at 3168.5 m; **f** argillaceous sandstone with ripple cross-bedding, Well Fan143, at 3117.45 m; **g** lenticular bedding, with vertical organism burrows, Well Fan143, at 3110.95 m; **h** lenticular bedding, Well Wang125, at 2781.8 m; **i** lenticular bedding, Well Bo901, at 2466.1 m; **j** wave ripple, Well Wang125, at 2784.3 m; **k** wave ripple, Well Fan119; **l** wave ripple, Well Bin666, at 3065.5 m; **m** bivalve biodetritus layer, Well Wang26, at 1686.2 m; **n** bivalve biodetritus layer, Well Jiao5-9, 1325.9 m; **o** plant root, stem breeze, Well Bin425, at 2601.2 m

**Fig. 4.38** Characteristics of sandy beach bar sediments of Upper Sha-4 Submember in the Dongying Sag (modified from Jiang et al. 2011). **a** Beach sand; **b** bar sand

(a) beach sand encountered by Well Gao89

(b) bar sand encountered by Well Gao892

Mudstone    Limy mudstone    Sandy mudstone    Siltstone    Limy siltstone
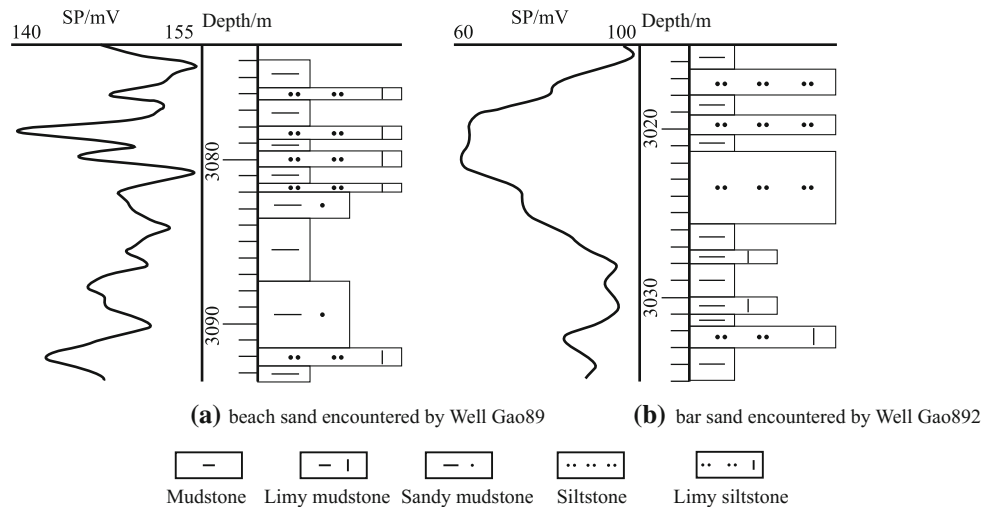
lithology, and texture. Sedimentary features of beach sand and bar sand are as follows.

(1) Sandy beach deposits

The beach sand is dominated by silty-fine sandstone, followed by a small amount of argillaceous siltstone with gravel occasionally seen; its typical bedding structures include wavy bedding, micro-wavy bedding, swash cross-bedding, lenticular bedding, wave ripple bedding, etc. The main bedding plane structures are ripple marks. Dense carbon debris layers or the roots, stems, and leaves of plants as well as intact biological fossils like snail fossil are frequently found, and biological burrow is developed; the logging curves mainly show as thin finger-like with high-medium amplitude (Fig. 4.38a); the colors of mudstone intercalations between sandbodies is both light gray, gray, gray-green, motley, or even red that reflects shallow water or intermittently exposed environments and dark gray that reflects relative deepwater environments, and the thickness of a single sand layer is generally less than 2 m. The grain-size probability curve is dominated by bouncing section and suspending section, followed by the rolling section because some beach sand contains relative coarse components transported by rolling.

(2) Sandy bar deposits

Generally, bar sand is surrounded by beach sand and is coarser than beach sand. Bar sand is mainly composed of medium- to fine-grained sandstone and siltstone, with a small amount of pebbly sandstone. Its major sedimentary structures include parallel bedding, wedge-shaped bedding, wavy bedding, lenticular bedding, and massive bedding. The bedding plane structures are ripple marks and parting lineation,

etc. A small amount of carbon debris and scarce biological fossils are observed. The thickness of a single sand layer is larger than that of the beach sand. The logging curves mainly show as toothed funnel-like, toothed box-like, or wide amplitude thicker finger-like (Fig. 4.38b). Colors of mudstone are mainly dark gray that reflects relative deepwater, with gray-green, and relatively homogeneous colors. The grain-size probability curves are dominated by dual-section curve of bouncing + suspending, and tri-section curve of rolling + bouncing + suspending is occasionally found with limited rolling part generally accounting for 1–5%.

The general comparison of beach sand and bar sand is shown in Table 4.3.

(3) Planar assemblage pattern of beach bar in the Dongying Sag

Once the wave is generated, it will propagate toward the shore, and prior to reaching the zone above wave base, wave shoaling, breaker, regeneration-breaker, surf, and swash occur successively. Based on the genetic mechanism of bar, the bar is developed along the breaker line and shoreline with concentrated sediments, and the wave shoaling zone, wave regeneration zone, and swash zone are dominated by beaches; in plane, the bar is basically surrounded by sheet-like beach (Fig. 4.39).

Besides the difference between beach sand and bar sand, bar sand (beach sand) of different locations in wave action zones with varying hydrodynamic characteristics (Sect. 2.1.4) has varying sediment textures and structures (see Sect. 2.1.4). According to different positions and sedimentary characteristics of beaches and bars, a model which reflects the hydrodynamic zoning and beach bar distribution in shoreland area of the Dongying Sag is established (Fig. 4.39).

**Table 4.3** Difference between beach sand and bar sand (modified according to Tian and Jiang 2009)

| Identification mark | Beach sand | Bar sand |
|---|---|---|
| Thickness of single sandbody | Thin single-layer, frequent interbedding vertically | Thick single bar sand, less frequent interbedding vertically |
| Distribution area | Generally parallel shoreline, relatively wide, with large area, with beach between bars | Mostly rod-like, parallel, and cross shoreline |
| Typical bedding | Wavy compound bedding, wave ripple bedding, lenticular bedding, ripple mark; swash cross-bedding developed in swash zone | Parallel bedding, groove, tabular cross-bedding, wave ripple bedding, ripple mark |
| Characteristics of well logging curves | Medium–high amplitude, thin finger, and sharp knife shapes | Medium–high amplitude, funnel shape |
| Phytolith | Abundant phytolith, with stratified kish carbon | Rare phytolith |

(1) Coastal bar (or beach ridge). Beach ridge is developed around shoreline. Due to nearby provenance and asymmetric wave, the coarse clasts tend to be transported toward the shore, forming a train of bar along the shoreline. Thus, the beach ridge in Upper Sha-4 Submember of the Dongying Sag is dominated by gravels (Fig. 4.36) typically in Well Jin21, Jin22, Jin25, and Jin 26 (well location is shown in Fig. 4.1).

(2) Offshore bar. The offshore bar is formed in breaker zone where the first breaker occurs. Since most of wave energy was depleted here, the sandstone with parallel bedding was formed by strong hydrodynamics. In the breaker zone, sediments are transported by onshore current and offshore current and accumulated at the breaker line; the breaker zone is composed of sediments of similar granularity and specific gravity, with relatively good sorting. Therefore, the grain-size probability curves are characterized by relatively steep slope and are dominated by bouncing + suspending components (Fig. 4.39b) typically in Well Fan137 and Well Fan143, etc. (well location is shown in Fig. 4.1).

(3) Nearshore bar. The nearshore bar is formed in surf zone or the breaker zone under small wave (good weather), with limited wave scale and energy weaker than that of offshore bar. Due to asymmetric waveform during wave propagation, the coarse clasts were transported toward the shore. Consequently, compared with the offshore bar, the nearshore bar has the rolling component (Fig. 4.39c) and worse sorting of sediments especially in Well Fan135, Gao890, etc. (well location is shown in Fig. 4.1).

(4) Inter-bar beach. Inter-bar beach is formed between offshore bar and nearshore bar and is caused by first regenerated oscillatory wave resulted from first breaker, with relatively low energy, fine sediments, and sedimentary structure dominated by wavy bedding (Fig. 4.39d) typically in Well Gao893, etc. (well location is shown in Fig. 4.1).

(5) Coastal beach. The coastal beach is formed in swash zone, where wave energy is depleted thoroughly. The surf and decelerated backwash caused by the inertia of surf, and repeated flush on sediments by strong hydrodynamism resulted in high energy coastal beach. The typical sedimentary structure is low angle cross-bedding (Fig. 4.39e) typically in Wells Bo104, Gao890, Wang26, etc. (well location is shown in Fig. 4.1).

The inter-bar beach sand was formed in shoreland. Besides, as the wave encountered subaqueous uplifts during the propagation, the wave energy was attenuated because of feeling bottom. Thus, sedimentation occurred, and ripple was formed under wave action, with features of subaqueous beaches. The beach bar sandbodies of the above origin were developed in central uplift area of Sha-4 Member in the Dongying Sag (Li 2009).

### 4.3.5 Carbonate Beach Bar

In depositional period of parasequence sets 6 and 7 of HST in Upper Sha-4 Submember of the western Dongying Sag, the carbonate beach bar was developed in the uplift of Pingfangwang Burial-Hill Drape Structural Belt and partial well area between Boxing Sub-Sag and Niuzhuang Sub-Sag, with limited distribution area. Usually, such areas are located at the uplifts far from provenances. The lithology is dominated by reef limestone, limestone, dolomitic limestone, and algal mound limestone, which are composed of carbonate matter like lake organism, ooid, and intraclasts (Li 2009), with locally developed brecciated limestone and oolitic limestone (Li 2009).

For example, Well Bin182, a typical coring well in carbonate beach bar (Figs. 4.40 and 4.1), is located at the eastern flank of Pingfangwang Structure of Shangdian-Pingfangwang Burial-Hill Drape Structural
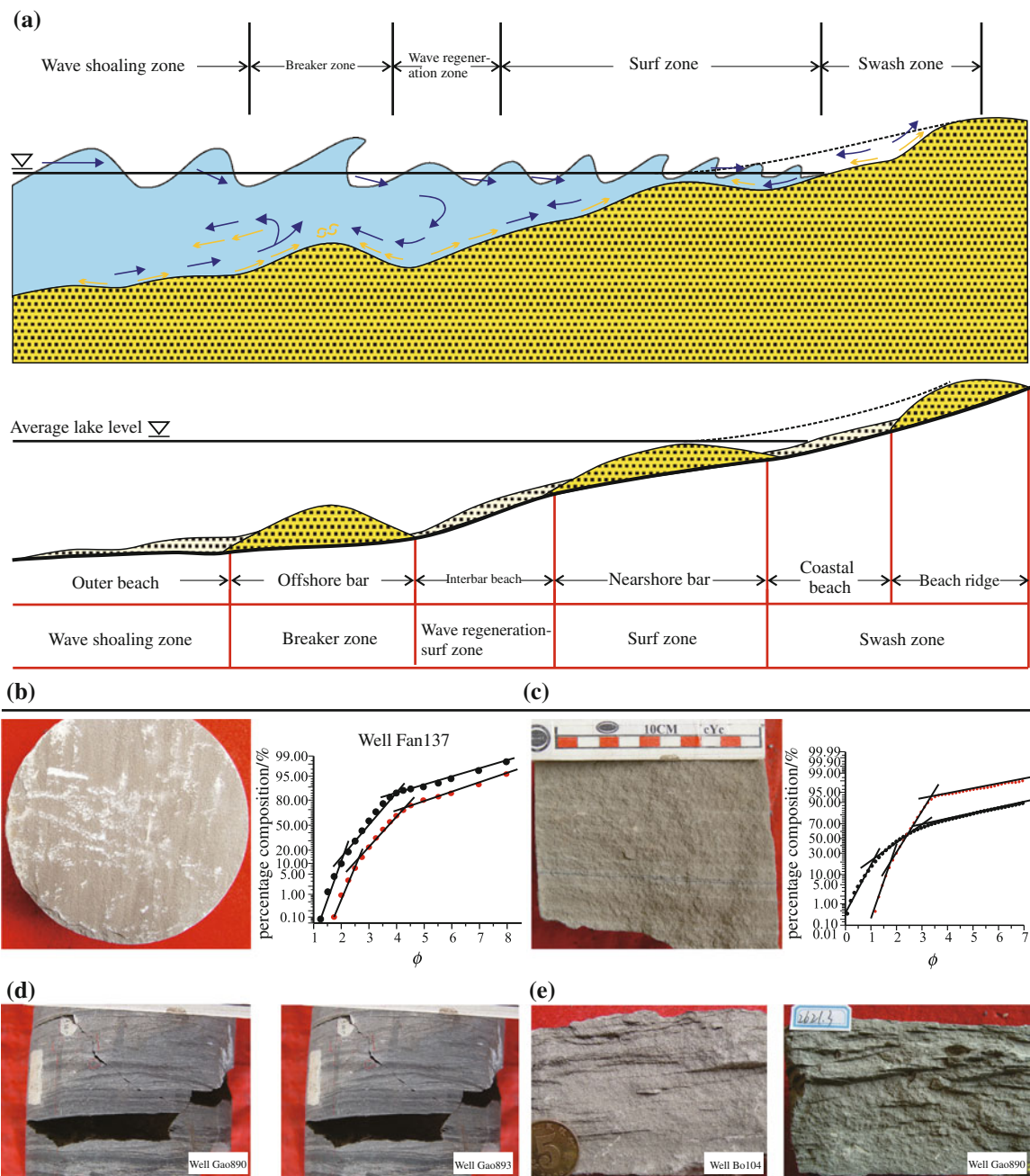
**Fig. 4.39** Division of beach bar microtopography of Upper Sha-4 Submember in the Dongying Sag and its characteristics. **a** Shoreland hydrodynamic zones and their corresponding microtopography distribution model of beach bar; **b** core and grain-size characteristics of offshore bar; **c** core and grain-size characteristics of nearshore bar; **d** characteristics of inter-bar beach; **e** characteristics of coastal beach

Belt in the western Dongying Sag (Fig. 4.2). According to core observation, the oil immersed biohermal limestone and the typical carbonate beach bar deposits are, developed, respectively in interval between 1631.4–1637.0 m and 1640.3–1650.0 m in Well Bin182.

In sedimentary period of Upper Sha-4 Submember in western Dongying Sag, minor biodetritus beach bar is developed in some well blocks, where the biodetritus is dominated by ostracoda, which is frequently interbedded with limestone, marlstone, and dolomitic limestone, with thickness of single layer less than 2 m and limited distribution; the oil-bearing biolithite caves were developed in some region (Li 2009).

From the view of sequence stratigraphy, the carbonate beach bar is mainly developed in HST, which was previously explained that in this period, the deficient terrigenous clast benefits forming carbonate beach bar (Li 2009).
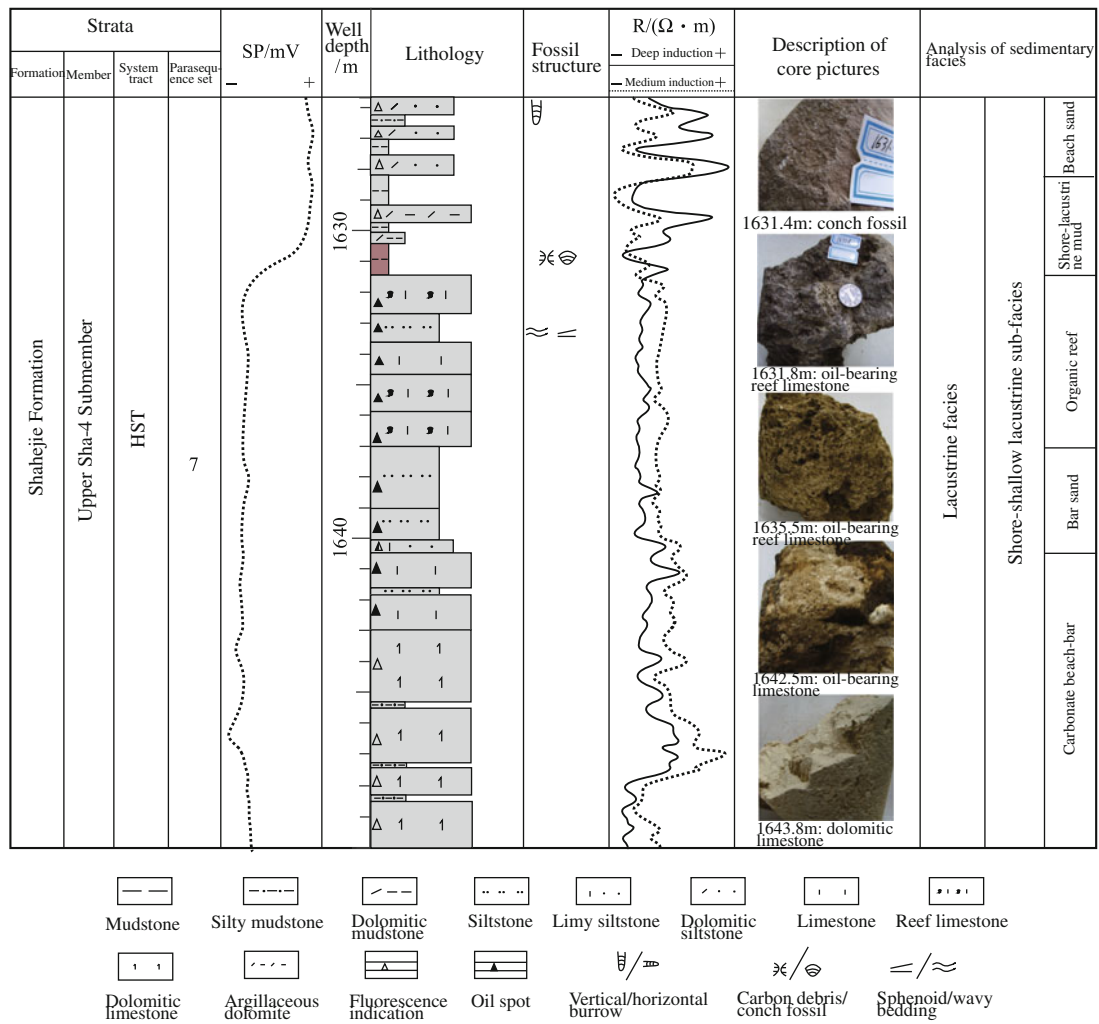
**Fig. 4.40** Analysis of cores facies across Well Bin182 (Li 2009)

## 4.3.6 Storm Deposits

The storm results in large-scale wave and fluctuation of lake water, causing oscillation of lake, which is due to continuous storm action that comes from a certain direction. The backwater is formed on the windward side, where lake level raises; on the contrary, the lake level declines on the leeward side. When storm weakens, the water will move in the reverse direction, forming lake oscillation until the lake levels off. The oscillation of lake erodes and re-suspends the shoreland sediments, and the sediments are transported to and deposited in the deepwater zone by water oscillation, forming storm deposits.

The drilling/logging data show that in the middle of Lijin Sub-Sag, Upper Sha-4 Submember of the Dongying Sag is dominated by a large number of thin interbeds developed under background of dark gray mudstone, and scour structure, deformation structure, and hummocky cross-bedding which were not in shore lacustrine facies zone, but in the

deeper aquatic environments. Analysis shows that the thin interbeds are resulted from the actions of storm and wave, with following references: (1) universally dark mudstone are, i.e., dark gray; (2) scour structure that reflects deepwater environment, e.g., muddy rip-up clasts and gutter cast; (3) hummocky cross-bedding, truncated structure, etc., that reflect storm action; (4) penecontemporaneous deformation structures, e.g., load cast and corrugated deformation; (5) structures like bulky sandstone and biological escape structure that reflect rapid aggregation; and (6) the lithofacies assemblage successively composed of bulky (siltstone) sandstone (fining-upward), parallel bedding (siltstone) sandstone, hummocky cross-bedding (siltstone) sandstone, asymmetrical–symmetrical wavy bedding (siltstone) sandstone and mudstone from bottom to top, indicating hydrodynamic variation of gravity flow–unidirectional flow–compound flow–oscillatory flow (Fig. 4.41).

Storm deposits in study area are dominated by siltstone and argillaceous siltstone with minor fine sandstone and
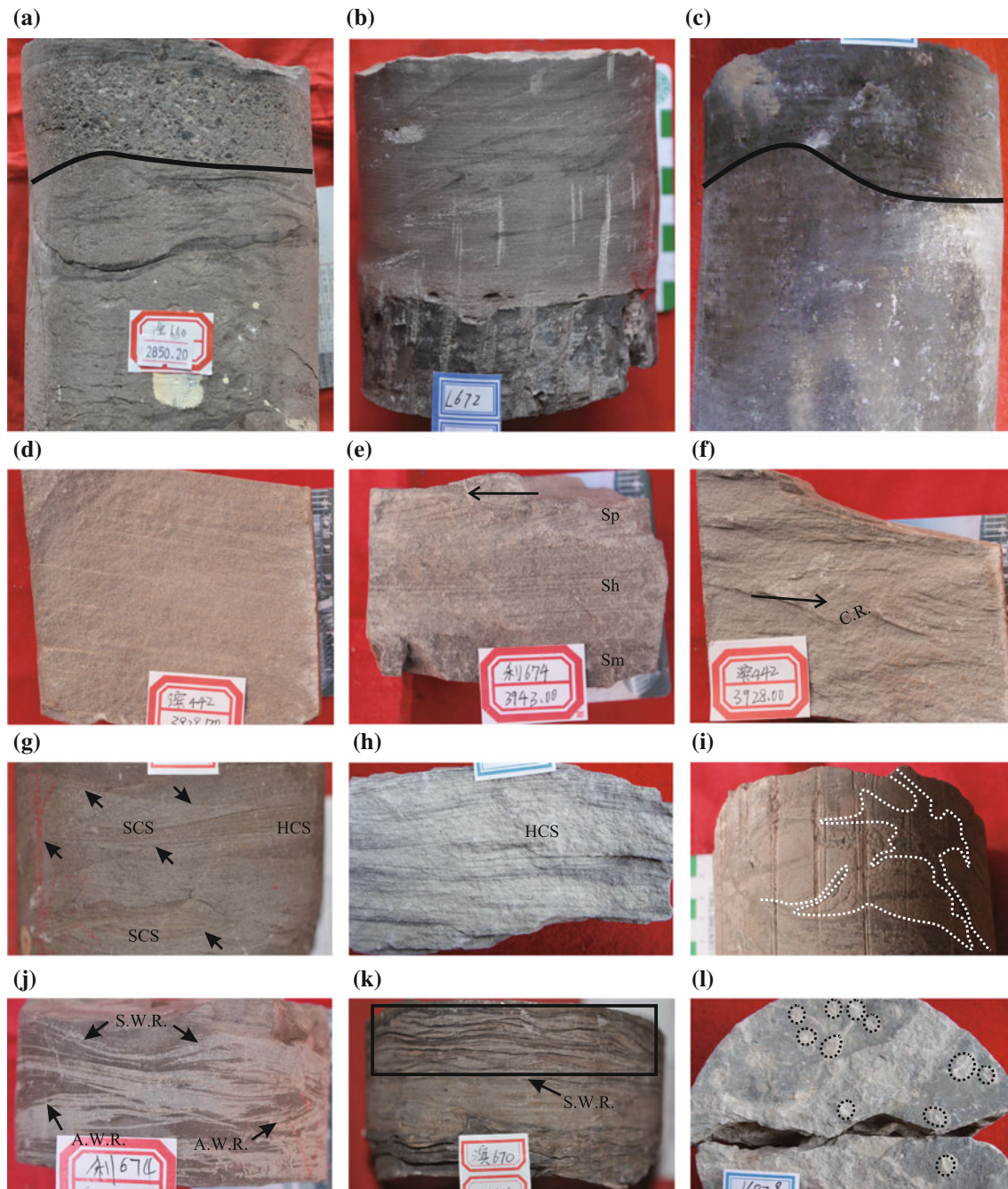
**Fig. 4.41** Identification mark of storm deposits cores. **a** Erosion surface and lag deposits, Well Bin660, at 2850.2 m; **b** Gutter cast and muddy rip-up clasts, Well Li672, at 4132.5 m; **c** truncation structure, Well Bin666, at 3097.3 m; **d** parallel bedded sandstone, Well Bin442, at 3929.7 m; **e** bulk sandstone-parallel bedded sandstone-tabular cross-bedded sandstone, Well Li674, at 3934 m; **f** climbing ripples, Well Bin442, at 3928 m; **g** hummocky-swaley cross-bedded sandstone, Well Bin670, at 3282 m; H Hummocky cross-bedded sandstone, Well Bin182, at 1684.5 m; **i** deformation structure, Well Bin440, at 3848.15 m; **j** asymmetric–symmetric rippled lamina, Well Li674, at 4072.49 m; **k** symmetric rippled lamina, argillaceous sandstone, Well Bin670, at 3268.6 m; **l** vertical organism burrow, Well Bin182, at 1687.8, Sp plannar cross-bedded sandstone; Sh, parallel bedded sandstone; Sm, massive sandstone; C.R. climbing ripple; HCS, Hummocky cross stratification; SCS, swaley cross stratification; S.W. R., symmetric wave ripple; A.W.R., asymmetric wave ripple

often bears boulder clay; the sedimentary structures include bottom erosive surface that reflects erosive action, accompanied by tool marks like gutter cast, deformation structures reflecting gravity flow, parallel bedding reflecting unidirectional flow, wave ripple bedding reflecting unidirectional and oscillatory flows, sinusoidal wavy bedding and hummocky bedding reflecting oscillating flow, and dark gray mudstone reflecting suspended deposits, which occur
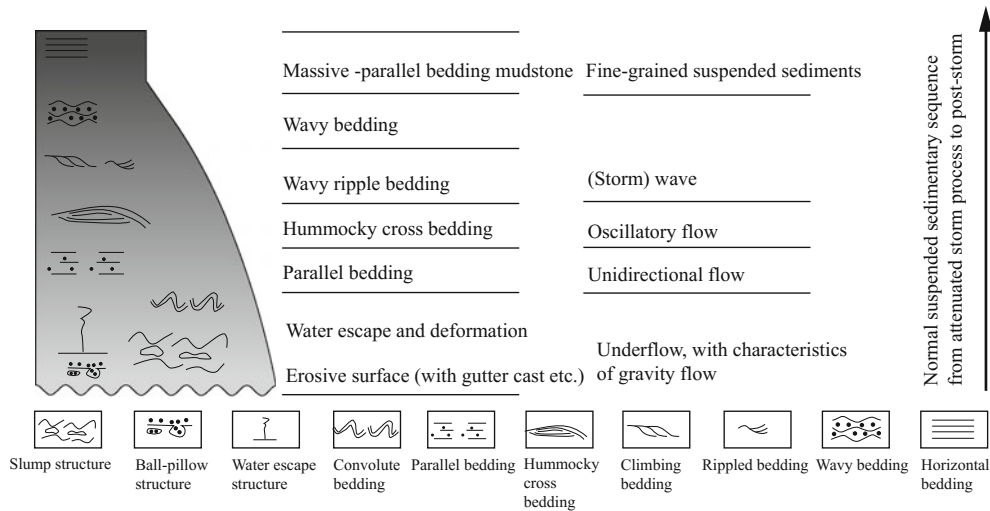
**Fig. 4.42** Para-Bouma sequence of storm deposits (Modified from Wang et al. 2015)

vertically in a certain order and constitute a para-Bouma sequence (Fig. 4.42). Carbonaceous fragments layers or roots, stems, and leaves of plants are occasionally seen, and biological escape traces are observed. Curves of well logging mainly show as densely thin finger-like, toothed bell-like, and those for single sand layer show as thin finger-like or sharp knife-like with high and medium amplitude. The mudstone is basically dark gray that reflects deepwater environment. The grain-size probability curves are characterized by multi-bouncing and one suspension, indicating the influence of complex hydrodynamics on storm deposits.

According to analysis of sedimentary facies and sequence stratification in a single well, storm deposits were mainly developed in the late period of LST, when the lake began to expand and waterbody energy increased. Meanwhile, continuous progradation of sediments (fan-delta) provided sufficient provenance, and storm deposits were more likely formed under storm action. In planar distribution, from near-provenance to far-provenance area, the storm deposits on the south slope of Binxian Bulge shows varying sedimentary characteristics (Fig. 4.43): near-provenance storm deposits have coarser grain (fine gravel-fine sand) and mainly show gravity flow–unidirectional flow–compound flow sedimentary sequence, among which gravity flow and unidirectional flow play a dominant role. Far-provenance storm deposits have finer grain (fine sand) and are largely controlled by gravity flow and unidirectional flow, with the
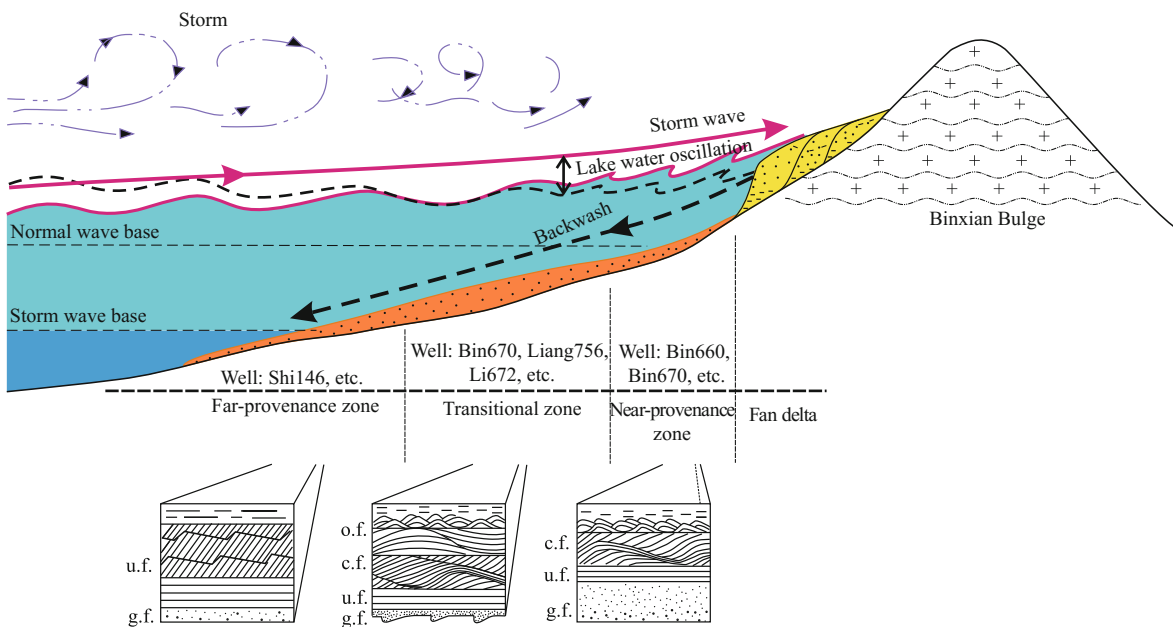


**Fig. 4.43** Pattern of storm deposits origin (Wang et al. 2015). o.f. oscillatory flow induced deposits; c.f. combined-flow induced deposits; u.f. unidirectional flow induced deposits; g.f. gravity flow induced deposits

sedimentary structures caused by wave-induced oscillatory flow rarely seen. The complete semi-Bouma sequence occurs in the storm deposits between near-provenance area and far-provenance area (Wang et al. 2015).

## 4.3.7   Fine Grain Deposits (Semi-Deep Lake-Deep Lake)

Apart from relatively shallow depositional systems like gravelly deposits, Upper Sha-4 Submember in the Dongying Sag also has broad semi-deep and deep lacustrine deposits featured by fine-grained rock (sediments smaller than silt; Wu 2015). Wu (2015), depending on the thin-section observation and X-ray diffraction analysis of cores from Wells Niuye1, Fanye1, and Liye1 at the center of the

Dongying Sag (well location is shown in Fig. 4.1), divides the fine-grained lithofacies in the study area into 12 types on the basis of rock component (silt, clay, and carbonate as three terminals), petrogenesis, sedimentary features, TOC, etc. (Table 4.4).

Wu (2015) further established the depositional patterns of fine-grained lithofacies in the study area in terms of the carbonate compensation depth (CCD) and lysocline (Fig. 4.44): (1) Below CCD, the rapider dissolution than the supply of carbonate incurred unsaturated carbonate. The minerals are dominated by clay. The organic matters are reserved in the waterbody of strong reducibility, and horizontal foliation is developed in the quite waterbody. Hence, the lithofacies are dominated by deep lacustrine organic shales. (2) Above CCD, the dissolution of carbonate equals supply, resulting in carbonate precipitation and dissolution,

**Table 4.4** Categories of fine-grained rock in Upper Sha-4 Submember in the Dongying Sag (Wu 2015)

| Categories | Subcategories | |
|---|---|---|
| Siltstone (Type I) | beach bar siltstone (TypeI-1) | |
| | Turbidite massive siltstone (Type I-2) | |
| Carbonatite (Type II) | High organic content laminated limestone (Type II-1) | |
| | Medium organic content laminated limestone (Type II-2) | |
| | Low organic content laminated limestone (Type II-3) | |
| Clay rock (Type III) | High organic content laminated clay rock (Type III-1) | |
| | Medium organic content laminated clay rock (Type III-2) | |
| | Low organic content laminated clay rock (Type III-3-1) | |
| | Low organic content massive clay rock (Type III-3-2) | |
| | Low organic content laminated gypsiferous clay rock (Type III-3-3) | |
| Mixed fine-grained rock (Type IV) | Laminated carbonate mixed fine-grained rock | Laminated limy mixed fine-grained rock (Type IV-1) |
| | | Laminated dolomitic mixed fine-grained rock (Type IV-2) |
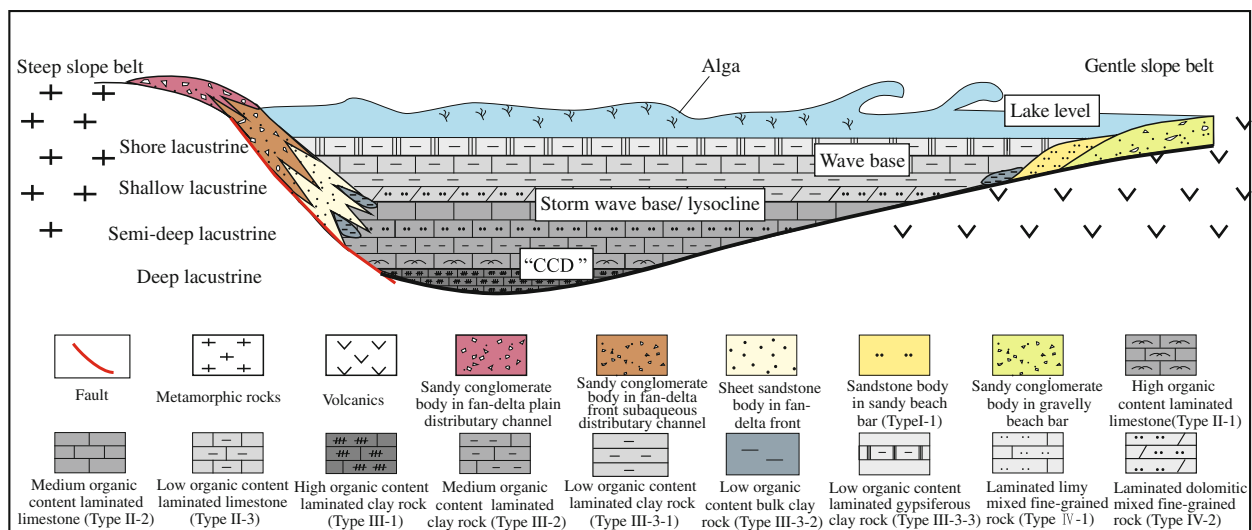


**Fig. 4.44** Sedimentary model of lithological facies of Upper Sha-4 Submember in the Dongying Sag (Wu 2015)

and increasing the carbonate content, with deepwaterbody of reducibility, and high organic content. And the foliation was developed in fine-grained sandstone. With the water bottom uplifting, the deposits were somewhat affected by terrigenous clasts and waterbody disturbance, occasionally with fluctuation of microwaves. According to the depth of waterbody where deposition occurred, the semi-deep lacustrine high organic content laminated limestone, medium organic content laminated clay rock, laminated limy fine-grained rock, and medium organic content laminated limestone were developed in sequence from bottom to top. (3) In the deposits area above the lysocline, the carbonate is in hypersaturated state due to quicker supply than dissolution, and the minerals are dominated by carbonate, intercalated with minor clay and terrigenous clasts. In shallow waterbody of weak reducibility, the organic matters were insufficiently supplied and not easily reserved. Affected by terrigenous clasts and water kinetics, the fine-grained sandstone is characterized by laminae of wave pattern with occasional foliation. The lithofacies is dominated by shallow lacustrine laminated dolomitic mixture fine-grained sandstone, low organic content laminated clay, and low organic content laminated limestone from bottom to top. (4) In the dry weather, the gypsiferous deposits were deposited due to evaporation, with low organic content, and fine-grained sandstone with foliation and great fluctuation. The lithology is dominated by the shore lacustrine low organic content

laminated gypsiferous clay. Accompanied by increasing terrigenous input, the quartz and feldspar content in fine-grained sandstone were increased, and the lithofacies are dominated by beach bar sandstone and delta frontal sheet sand, etc. (Wu 2015).

## 4.3.8  Framework of Sedimentary System

### 4.3.8.1  Framework of Profile Sedimentary System

A well-tie profile for sedimentary facies comparison across Well Jin22, Fan127, Fan140, Fan148, Chun108, Liang218, Li57, and the Chenjiazhuang Bulge is utilized to illustrate the distribution of depositional systems in the study area (Fig. 4.45).

This profile trends nearly SN and connects Well Jin22 near the root of the Luxi Uplift, Well Fan127, Fan140, and Fan 148 in the Boxing Sub-Sag, Well Chun108 and Liang 218 in the low belt of highs of the Chunhua-Caoqiao Nose Structure between the Lijin Sub-Sag and Boxing Sub-Sag, Well Li57 in the Lijin Sub-Sag and until the Chenjiazhuang Bulge in the north successively from south to north. Covering all structural units in western Dongying Sub-Sag and crossing whole Dongying Sub-Sag, the profile shows the distribution characteristics, vertical evolution of sedimentary systems of Upper Sha-4 Submember in western Dongying
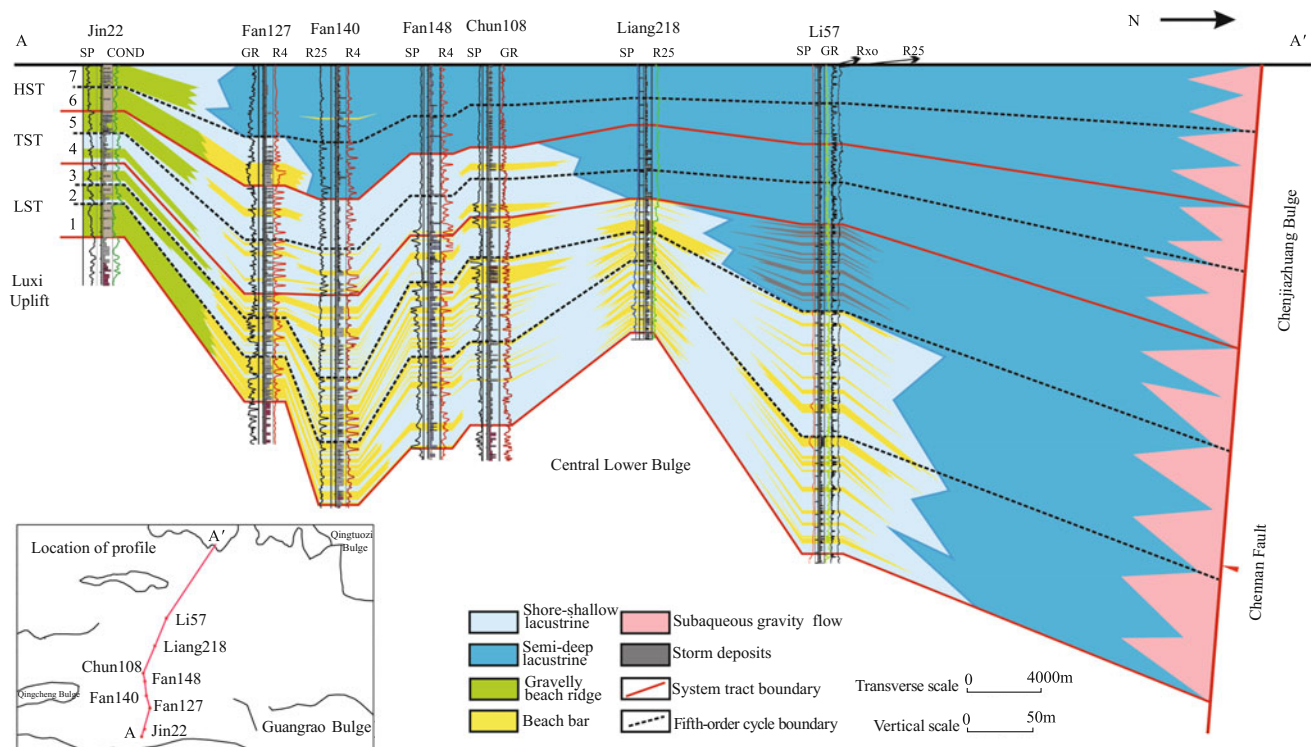


**Fig. 4.45** Comparison profile of well-tie sedimentary facies across Jin22-Fan127-Fan140-Fan148-Chun108-Liang218-Li57-Chenjiazhuang High

Sag, and spatial distribution of all sedimentary facies, and it is representative.

According to the profile, the strata thickens northwards, reflecting macroscopic palaeogeomorphology of northern steeper margin and southern gentler margin in the Dongying Sag. But the central uplift belt between the Boxing Sub-Sag and Lijin Sub-Sag is obviously thinner and plays the role of separation. The Boxing Sub-Sag in the south has relatively thinner strata, with smaller thickness differences between wells, indicating smooth lakebed with less fluctuation and generally shallow waterbody. The Lijin Sub-Sag, however, has large thickness differences between wells, indicating great landform relief at lakebed. The strata steepen abruptly toward north and stretch to the deep sag.

This profile covers gravelly beach bars, sandy beach bar, storm deposits, subaqueous gravity flow, and shore-shallow lacustrine and semi-deep and deep lacustrine fine-grained deposits. The gravelly beach bars were mainly developed on the north side of Luxi Uplift in LST, TST, and HST, and are interpreted as near-provenance apron-shaped alluvial fans reformed by wave (Li 2009). The sandy beaches and bars are developed extensively in the Boxing Sub-Sag, central low high belt, and Lijin Sub-Sag, especially in the Boxing Sub-Sag almost covered by sandy beaches and bars. They were developed mainly in LST with wide shore-shallow

lacustrine distribution, and less in TST and HST where the waterbody deepened and shore-shallow lacustrine range shrinked. The subaqueous gravity flow deposits are in the front of the Chenjiazhuang Bulge in the northern Lijin Sub-Sag and close to the downthrown side of the Chennan Fault and are composed of nearshore subaqueous fan, channel turbidite, and sublacustrine fans in LST, TST, and HST. In addition, storm deposits developed in the late depositional period of LST (LST-3) are encountered by Well Block Li57 in the Lijin Sub-Sag.

### 4.3.8.2  Analysis of Planar Sedimentary Facies

(1)  Sedimentary facies in LST

According to contour of sandstone/strata thickness ratio (Fig. 4.46) and contour of sandstone thickness (Fig. 4.47), the high sandstone content is distributed in the downthrown side of fault in the north boundary, the north slope of the Luxi Uplift in the south, and both sides of the Qingcheng Bulge along basin axis, and between the Qingtuozi Bulge and Guangrao Bulge. On the whole, along the south side of the Chenjiazhuang Bulge and southward, the sandstone/strata thickness ratio reduces sharply (>70% to 0) together with the sandstone thickness (>80 m to 0), and the shale
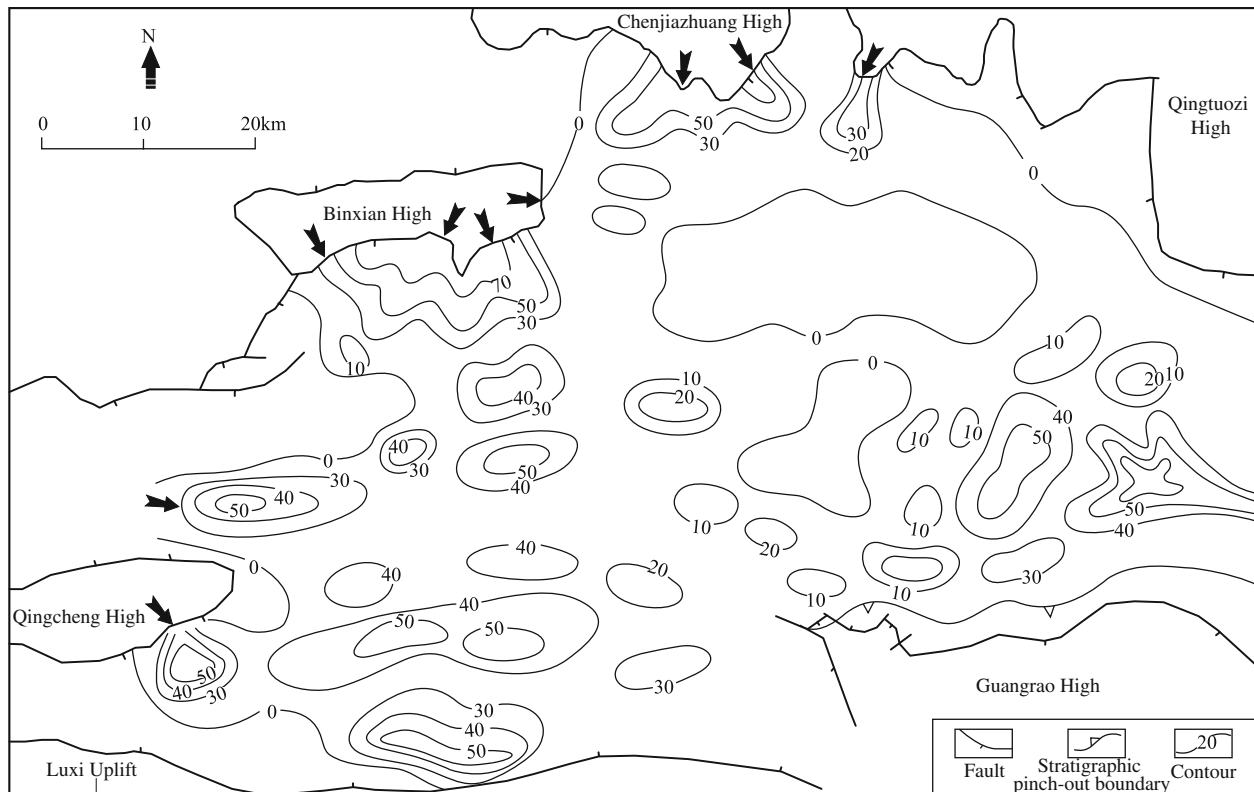


**Fig. 4.46**  Contour of LST sandstone/strata thickness ratio

content increases sharply, indicating deepening waterbody, and relatively steep downthrown side of Chennan boundary basin-controlling fault. The eastern Lijin Sub-Sag and Minfeng Sub-Sag, therefore, are located in the deep sub-sag area of the Dongying Sag. As for other study areas, from the periphery (the sandstone/strata thickness ratio >50% and the sandstone thickness around 50 m) to the center (the sandstone/strata thickness ratio between 10 and 40% and the sandstone thickness between 10 and 20 m) of the sag, the sandstone contents tend to slowly decrease, with the local area of high sandstone content (the accumulative sandstone thickness of 40–50 m), most with strip or potato shape.

The contour of sandstone/strata thickness ratio is combined with investigation on structural and depositional setting to conduct analysis of planar facies in the study area (Fig. 4.48). The subaqueous gravity flow deposits (including the nearshore subaqueous fans, channel turbidite, and sublacustrine fans) was mainly developed in south slope of the Chenjiazhuang Bulge in the north steep slope belt, with provenance mostly from the Chenjiazhuang Bulge, and it was gradually changed to the semi-deep and deep lacustrine deposits toward the basin center. The provenance from the Bingxian Bulge formed a fan-delta on the south slope with beach bar deposits (in gentle slope) and storm deposits (in steep slope) in the front. The provenance from the Luxi Uplift successively formed the longshore gravelly coastal bar, nearshore and offshore bar, inter-bar and outer-bar

beaches from the near to the distant. The provenance between the Qingtuozi Bulge and the Guangrao Bulge formed delta, with beach bar deposits in its front. Besides, the provenance from the Qingcheng Bulge along the axis deposits also formed delta (Fig. 4.48).

LST is characterized by extensive beach bar sandbodies, which were developed in the Boxing Sub-Sag, central low high belt, front belt of the Binxian Bulge, and south boundary of the Niuzhuang Sub-Sag, and the beach bar is characterized by distribution High alongshore line in the lake basin boundary (Fig. 4.48).

(2) Sedimentary facies in TST

Similarly, according to the contour of sandstone/strata thickness ratio (Fig. 4.49) and contour of sandstone thickness (Fig. 4.50), it is concluded that the provenance in TST inherits the features in LST, i.e., high sandstone content in the downthrown side of fault in the north boundary, north slope of the south Luxi Uplift, both sides of the Qingcheng Bulge along a basin axis, and between the Qingtuozi Bulge and Guangrao Bulge. Along the south side of the Chenjiazhuang Bulge and southward, the sandstone/strata thickness ratio abruptly reduces from 60% to 0 and the sandstone thickness from >30 m to 0. The eastern Lijin Sub-Sag and Minfeng Sub-Sag were still located in the deep sag of the Dongying Sag. In the other areas, the depression was
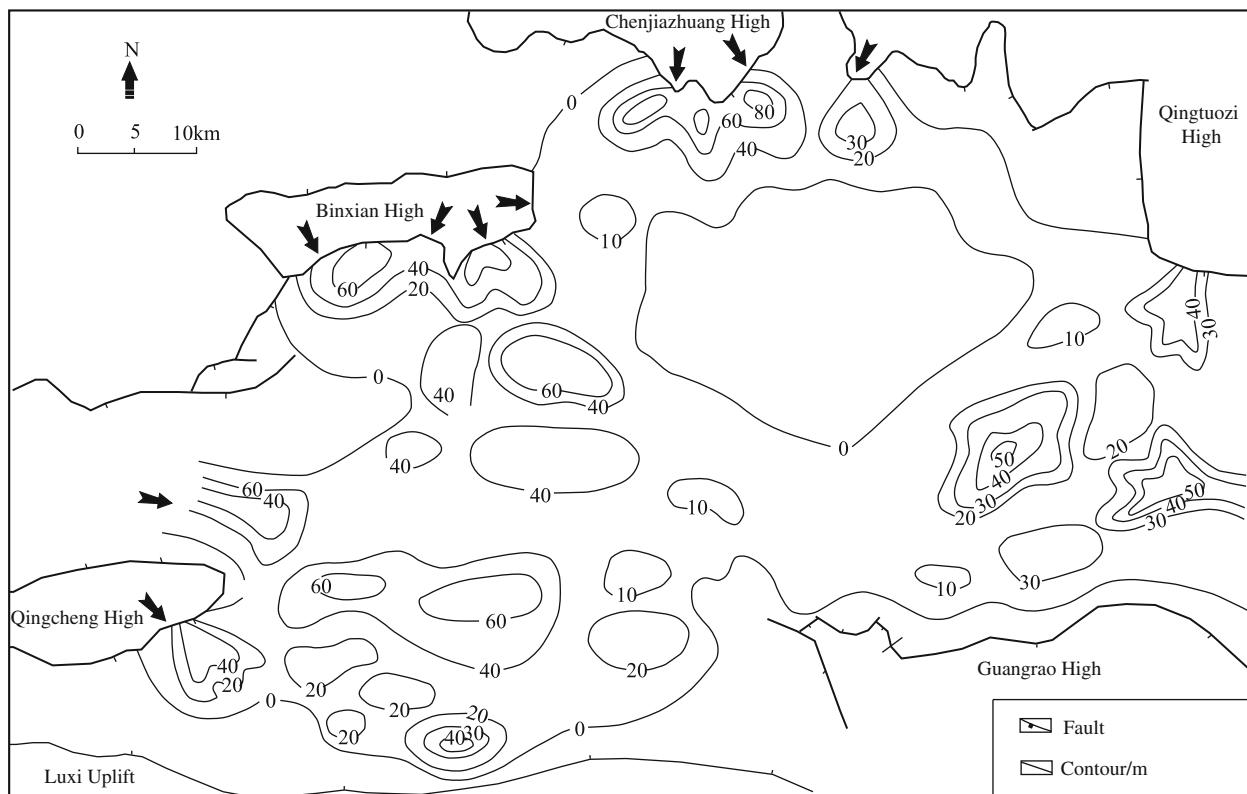


**Fig. 4.47** Contour of LST sandstone thickness

**Fig. 4.48** Sedimentary facies of LST in the Dongying Sag
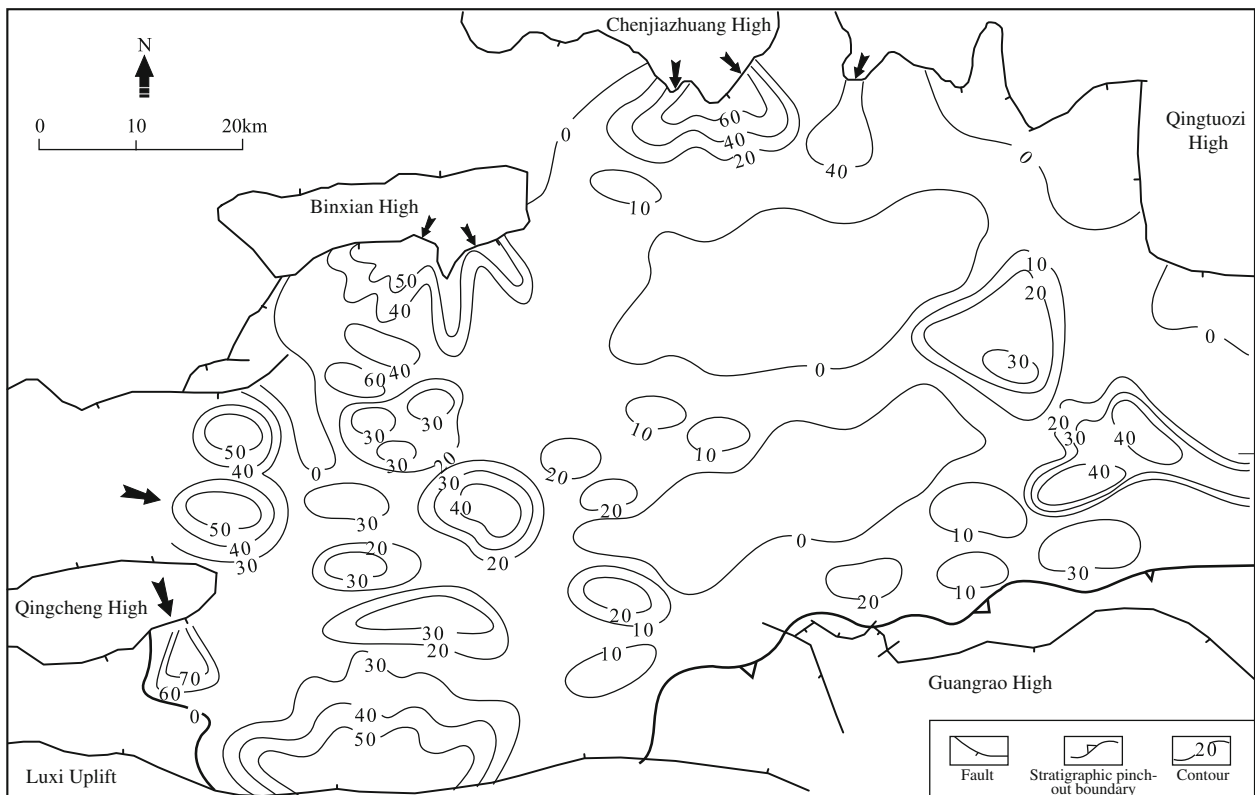


**Fig. 4.49** Contour of TST sandstone/strata thickness ratio
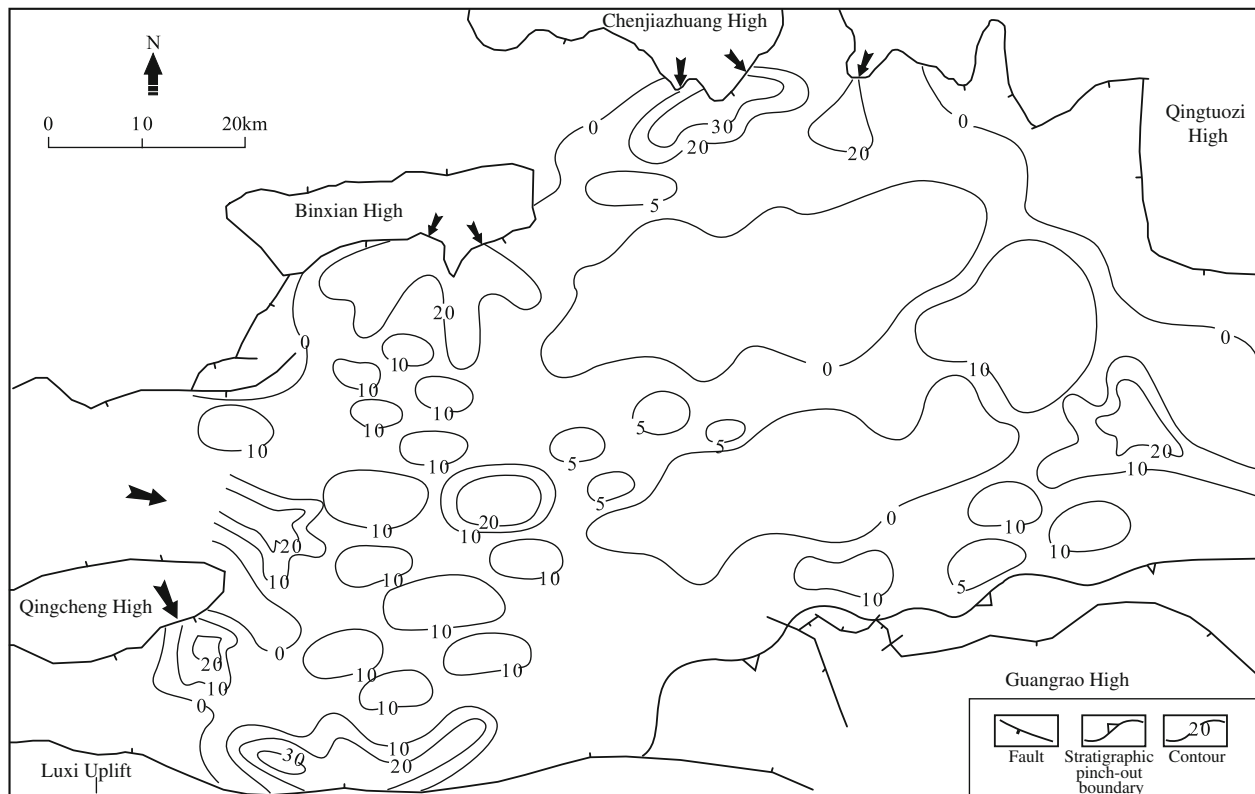
**Fig. 4.50**  Contour of TST sandstone thickness

deposited with gradually reduced sandstone from the periphery to the center, with local high content of sandstone, mostly with the strip or potato pattern. On the whole, the sandstone thickness in TST is less than that in LST, with larger area of zero sandstone content (extended to the Niuzhuang Sub-Sag), indicating weakened provenance effect.

Similarly, according to the contour of sandstone/strata thickness ratio combined with investigation on structural and depositional setting, the planar facies in the study area was analyzed (Fig. 4.51). The subaqueous gravity flow deposits (including the nearshore subaqueous fans, channel turbidite, and sublacustrine fans) were mainly developed in south slope of the Chenjiazhuang Bulge in the north steep slope belt, with sediments mostly from the Chenjiazhuang Bulge, and gradually changed to semi-deep and deep lacustrine deposits toward the basin center. The provenance from the Bingxian Bulge formed a fan-delta on the south slope with beach bar deposits and storm deposits in the front. The provenance from the Luxi Uplift successively formed the longshore gravelly beach ridge, nearshore and offshore bar, inter-bar, and outer-bar beaches from the near to the distant, with scale obviously smaller than that in LST. The provenance between the Qingtuozi Bulge and the Guangrao Bulge

formed delta, with beach bar deposits in its front. Besides, the provenance from the Qingcheng Bulge along the axis deposits also formed delta. Due to rise of lake level, the area of semi-deep lake was enlarged obviously (Fig. 4.51).

In TST, the deposits of subaqueous gravity flow, delta, and fan-delta have smaller scale, with the beach bar only in Well Blocks Gao89, Bin182, Mian30, etc. (well locations shown in Fig. 4.1), but the semi-deep and deep lacustrine deposits are expanded, with turbidite fan deposits in the Niuzhuang Sub-Sag (Fig. 4.51).

(3)  Sedimentary facies in HST

Similarly, according to the contour of sandstone/strata thickness ratio (Fig. 4.52) and contour of sandstone thickness (Fig. 4.53), it is concluded that HST is characterized by high sandstone content in the downthrown side of fault in the north boundary, north slope of the south Luxi Uplift, both sides of the Qingcheng Bulge along a basin axis, and between the Qingtuozi Bulge and Guangrao Bulge. Along the south side of the Chenjiazhuang Bulge and southward, the sandstone/strata thickness ratio abruptly reduces from 60% to 0, and the sandstone thickness from >40 m to 0. The eastern Lijin Sub-Sag and Minfeng Sub-Sag were still
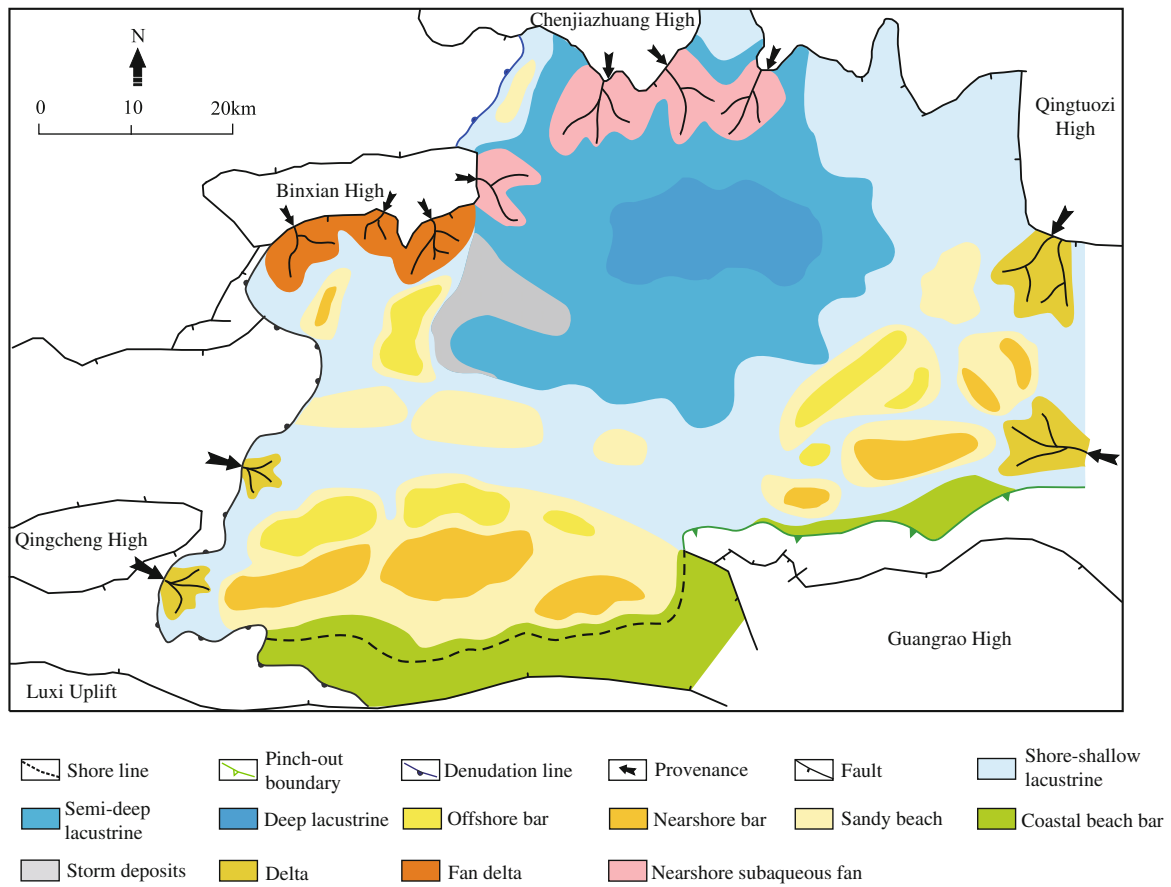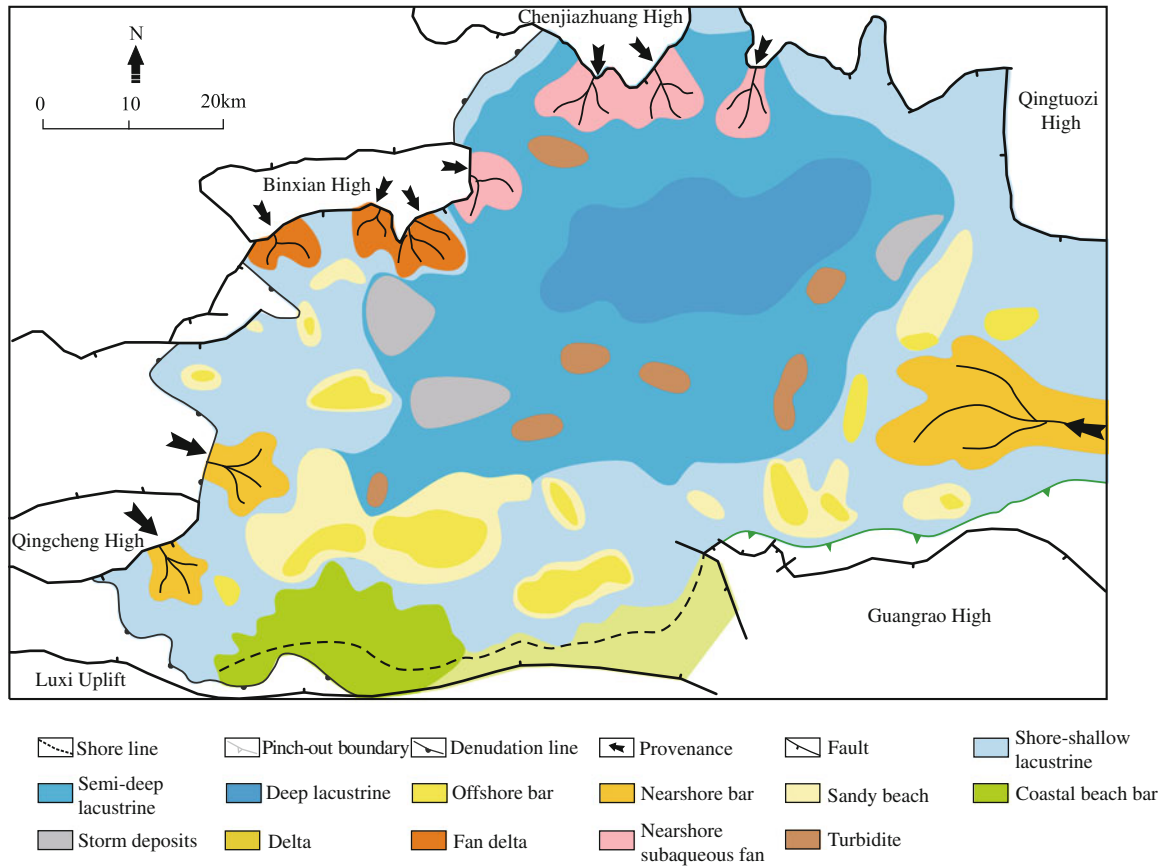
**Fig. 4.51** Sedimentary facies of TST in the Dongying Sag
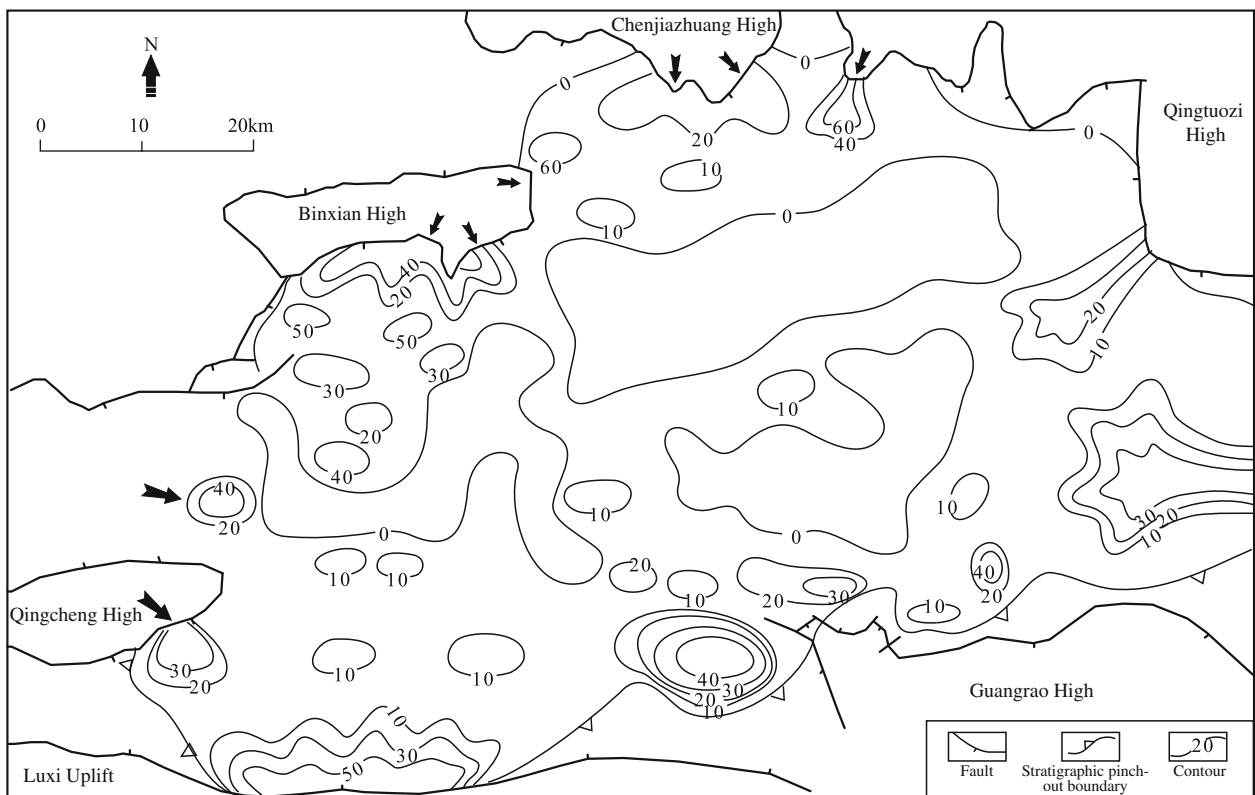


**Fig. 4.52** Contour of HST sandstone/strata thickness ratio
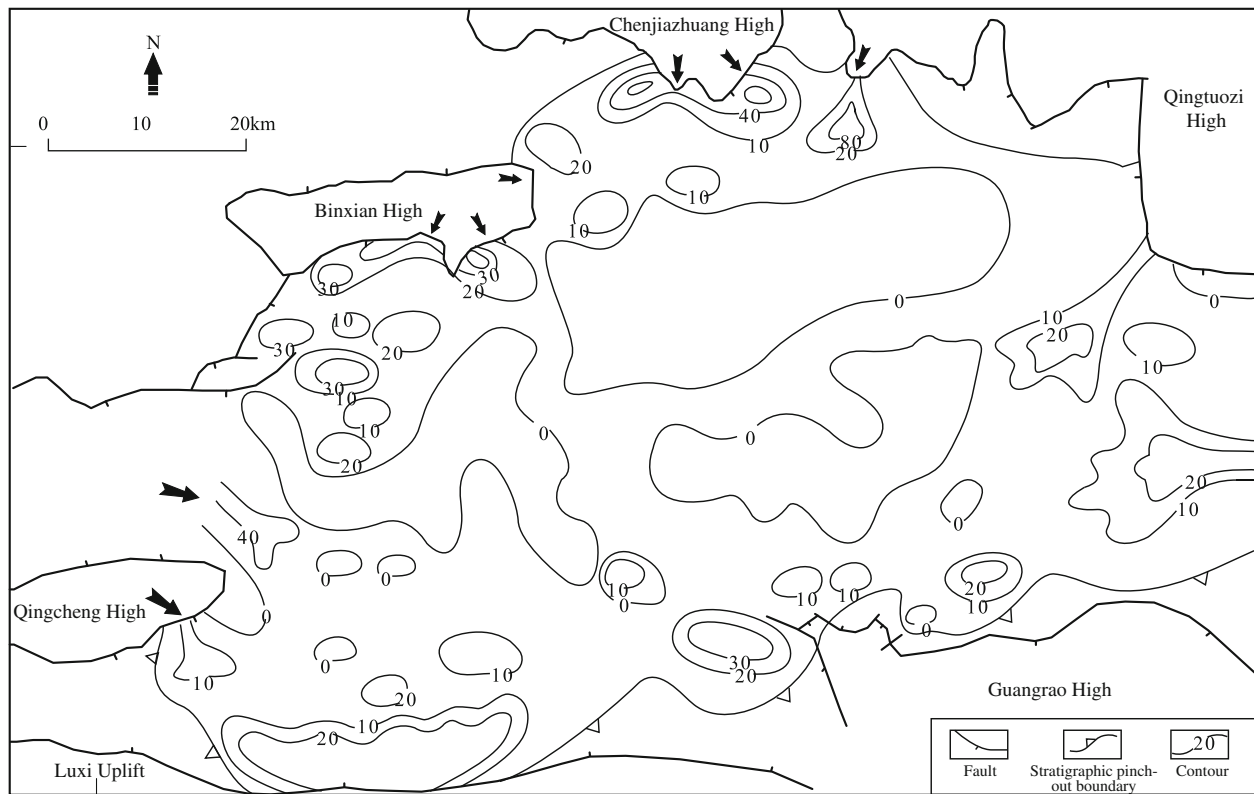
**Fig. 4.53** Contour of HST sandstone thickness

located in the deep sag of the Dongying Sag. In the other areas, the depression was deposited with sandstone gradually decreased from the periphery to the center, with local high content of sandstone, mostly with the strip or potato pattern. On the whole, the sandstone thickness in HST is less than that in LST, without big difference with TST, and with larger area of zero sandstone content (extended to the Niuzhuang Sub-Sag and central low high).

Similarly, according to the contour of sandstone/strata thickness ratio combined with investigation on structural and depositional setting, the planar facies in the study area was analyzed (Fig. 4.54). The subaqueous gravity flow deposits (including the nearshore subaqueous fans, channel turbidite, and sublacustrine fans) were mainly developed in south slope of the Chenjiazhuang Bulge in the north steep slope belt, with provenance mostly from the Chenjiazhuang Bulge, and it was gradually changed to the semi-deep and deep lacustrine deposits toward the basin center. The provenance from the Bingxian Bulge formed a fan-delta on the south slope with beach bar deposits and storm deposits in the front. The provenance from the Luxi Uplift successively formed the longshore gravelly beach ridge, nearshore and offshore bar, inter-bar, and outer-bar beaches from the near to the distant, with scale obviously smaller than that in LST. The provenance between the Qingtuozi Bulge and the Guangrao

Bulge formed delta, with beach bar deposits in its front. Besides, the provenance from the Qingcheng Bulge along the axis deposit also formed delta. It is worth noticing that in HST the diminished provenance effects result in development of the carbonate beach bar (limestone beach) in Pingfangwang and Chenguanzhuang area (Fig. 4.54).

In HST, the provenance direction is similar to that in LST and TST, and the subaqueous gravity flow, delta, and fan-delta are larger than those in LST and TST. The limestone beach was developed in Well Block Bin182, limited lacustrine deposits near Well Block Bingu24, and beach bar near Well Block Fan143, Liang213, Mian30, etc. (Fig. 4.54) (well location is shown in Fig. 4.1).

On the whole, the shoreline and wave base in LST generally moved toward the lake basin center, and the accompanying sediments progradation resulted in the extensively deposited sandbodies, most of which are delta, fan-delta, beach bar, and shallow shore lacustrine mudstone. In the late depositional period of LST, the storm deposits occurred due to deepened water (below wave base). In TST, the shoreline and wave base moved toward the continent, with expanded water area and deepened waterbody, and sediments were dominated by semi-deep lacustrine storm deposits and fine-grained sedimentary rocks. The lake shoreline moved toward the continent, and a fining-upward retrogradational
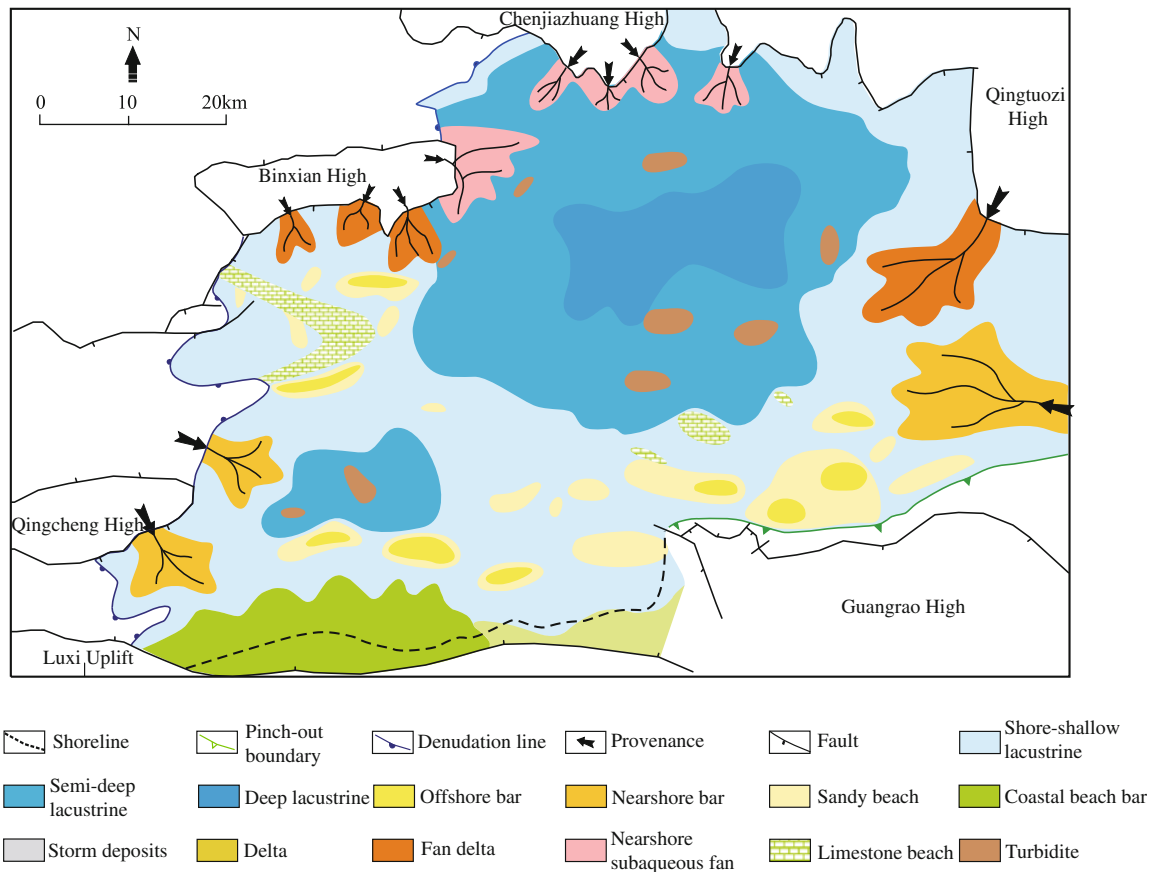
**Fig. 4.54** Sedimentary facies of HST in the Dongying Sag

sequence was formed. HST is characterized by sediment aggradation and weak progradation, with sandbodies migrated toward the basin center, and the carbonate rocks in HST are different from those in LST and TST. According to the sequence stratigraphy, main sandbody is in LST, i.e., below first flooding surface. Due to shallower waterbody in LST, the sandbody progradation occurred toward the basin center, which pushed the favorable sandbodies in LST moving toward basin center, and being reformed by the waterbody of lake basin, causing secondary migration and deposition, resulting in broad distribution in the lake basin, and forming shallower water sedimentary facies and their assemblies.

## 4.4   Dynamics of Windfield-Source-Basin System in Upper Sha-4 Submember

The shore-shallow lacustrine beach bar sandstone is dominated by many factors, and its distribution is also influenced by multiple factors, e.g., paleo-structure-paleo-geomorphology, paleo-windfield-hydrodynamic condition, variation of paleo-sedimentary base level, and massive shoreline variation. Reconstruction of single factor covers paleo-water

depth, paleo-geomorphology, paleo-provenance, and paleo-windfield. Among them, reconstruction of paleo-geomorphology is completed by calibration with result of paleo-water depth, and it provides reference for provenance analysis, and reconstruction of paleo-windfield needs parameters of paleo-water depth and paleo-slope. This chapter successively describes paleo-water depth, paleo-geomorphology, paleo-provenance, and paleo-windfield in "windfield-source-basin system".

### 4.4.1   Reconstruction of Paleo-Water Depth

Conventional reconstruction of paleo-water depth is completed with multiple proxies of sediments, e.g., lithology, sedimentary structure, paleontological types, ecological characteristics, geochemical parameters, etc., which just realizes qualitative estimation of paleo-water depth, with larger error. The shore-shallow lacustrine beach bar is always formed in shallow environment, and it is sensitive to waterdepth variation; thus, the qualitative reconstruction could not accurately reflect the paleo-water depth. The micropaleontology (Refer to Sect. 2.3.3.2) (Su et al. 2012), a proprietary technology for construction of paleo-water

depth, is used to reconstruct paleo-water depth of LST in Upper Sha-4 Submember (Li 2009) combining with phase sequence method.

The aquatic paleontological data found in the cores of Shahejie Formation in the Jiyang Depression cover ostracoda, microbody alga, gastropods, and a small amount of fish bone, among which ostracoda and microbody alga are dominate. In the previous study, the oryctocoenosis diversity or dominance almost realizes quantitative reconstruction of paleo-water-depth (Fig. 2.20) (Li et al. 2005). However, current paleontological data in the target intervals do not meet statistics requirements of calculating diversity or dominance (except regional strata or well locations) and could only realize approximate estimation of water depth. The criteria of water depth corresponding to those paleontological data were determined by Su et al. (2012), as shown in Table 4.5.

It is noticed that Su et al. (2012) determined distribution of ostracoda fossil with different occurrence (Table 4.5) according to depth range of modern ostracoda in South American Lake Titicaca and by reference to zoning of relative water depth of paleo-lake of Upper Sha-4 Submember in the Dongying Sag. However, in the relatively shallow water area, especially in lacustrine-shore area with strong activity of wave and alongshore current, ostracoda and other hard shell biology are always migrated by strong wave and water flow (Su et al. 2012), other than preserved in situ, which does not accurately reflect paleo-water depth.

In order to accurately obtain the mark of primitive environment, Su et al. (2012) have conducted an unprecedented paleontology analysis of benthic macroalgae. Benthic algae have two features: (1) fixation in water bottom, not resistance to migration, and a good reflection of primitive environment; (2) living in the water bottom with photosynthesis. Varied types of benthic algae live at varying water depth with varying light intensity. Thus, the water depth can be distinguished with benthic alga types. For example, red light is effective for photosynthesis of green algae and is about 0.5–3 m deep, while red algae prefer weak light and can still be found in 200 m deep seawater (Su et al. 2012). Thus, according to the research results of Su et al. (2012), the water depth of corresponding algae is determined (Table 4.5).

With "Multi-discipline biological superimposition depth" and "Weighted comprehensive determination of depth", the ultimate absolute depth is determined based on

**Table 4.5** Criteria scale for estimation of palaeobios and paleo-water depth of Upper Sha-4 Submember in the Dongying Sag (Su et al. 2012)

| Fossil category | Fossil subcategory | Possibly lowest water depth (m) | Possibly highest water depth (m) |
|---|---|---|---|
| Microbody alga | Stonewort | 0 | 2 |
| | Green alga | 0 | 5 |
| | Pediastrum duplex/leiosphaeridia | 0 | 2 |
| | Grainflat/mesh aegagropila linnaei | 4 | 10 |
| | Limes marginis alga | 10 | 20 |
| | Transition of microbody alga (rare shallow water types/rare deepwater types) | 3 | 9 |
| | Deflandrea | 10 | 20 |
| Benthic macroalga | Microbial mat | 8 | 26 |
| | Blue algae lamina | 13 | 26 |
| | Red alga | 5 | 30 |
| | Moss | 0 | 1 |
| Ostracoda | Several individual and rare types | 0 | 3 |
| | No ostracoda | 3 | 5 |
| | No living individual | 3 | 7 |
| | High disparity and abundance | 7 | 13 |
| | Many individual and sparse types | 13 | 20 |
| | Rare individual and types | 20 | 30 |
| | No fossil | >30 | |
| | Some austrocypris | 4 | 7 |
| | Austrocypris, with high abundance | 4 | 10 |
| Other fossils | Abundant pleopod | 0 | 3 |
| | Abundant fishbone (Still water lagoon) | 1 | 3 |
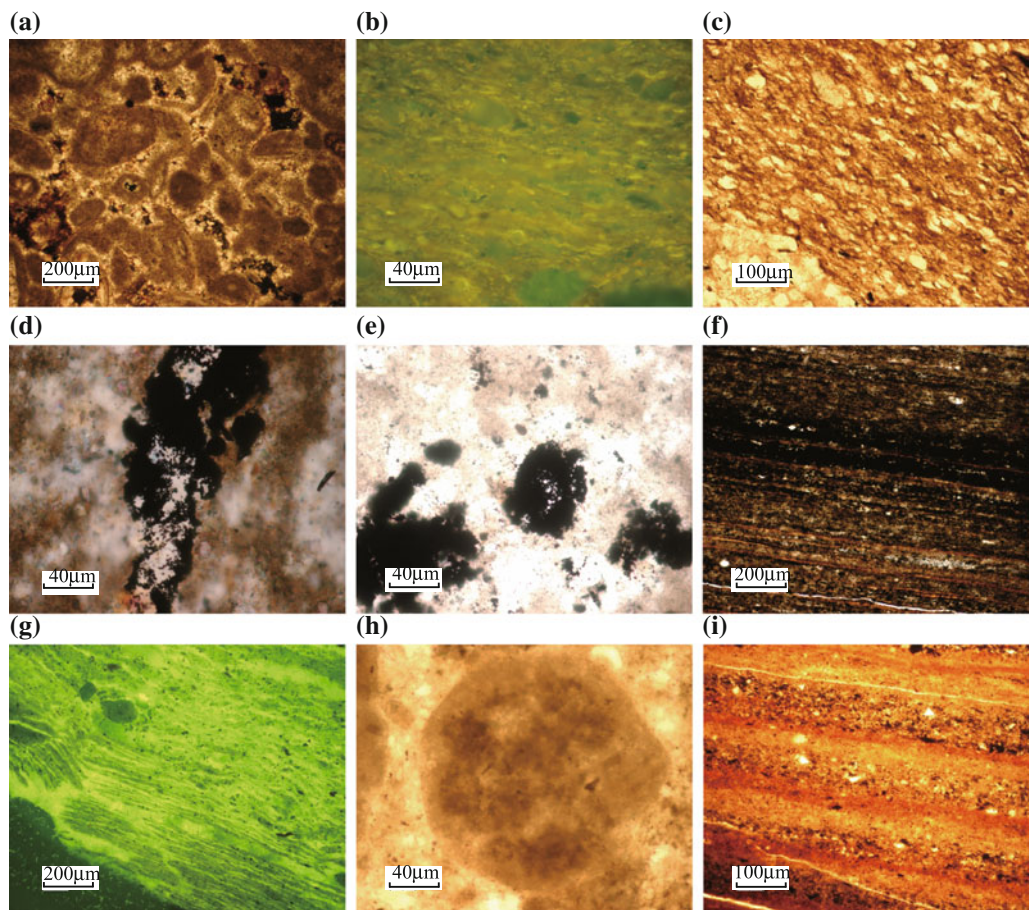
**Fig. 4.55** Part of microbody paleobios and interpretation of corresponding water depth (according to Jiang Zaixing). **a** Well Bin182, at 1632.6 m, water depth of ostracoda-bearing alga-gobbet limestone between 2 and 4 m; b Well Bin654, at 2964 m, microspore, water depth between 2 and 5 m; **c** Well Bin668, at 3391.3 m, water depth of blue alga between 2 and 5 m; **d** Well Bin668, at 3207.8 m, section of red alga, water depth around 20 m; **e** Well Bo901, at 2473 m, red alga pseudoparenchyma, red alga multicellularity pseudoparenchyma, water depth around 20 m; **f** Well Bo901, at 2453.1 m, red alga mat, water depth around 25 m; **g** Well Lai108, at 2484 m, brown alga mat, water depth around 30 m; **h** Well Gao351, at 2447.4 m, colony of brown alga micelle, water depth between 2 and 5 m; **i** Well Wang58, at 3032 m, red alga mat, water depth at 20 m

paleontological data of more than 50 wells in LST of Upper Sha-4 Submember in the Dongying Sag (Fig. 4.55). The value of paleo-water depth in the hole is projected to the Dongying Sag, and the quantized contour of water depth of LST of Upper Sha-4 Submember in the Dongying Sag is obtained (Fig. 4.57) with results of reconstruction of paleo-water depth of LST of Upper Sha-4 Submember with phase sequence (Li 2009) (Fig. 4.56), and combining with distribution of sedimentary facies and lithology.

The water depth varies between 0 and 30 m, and generally, Shallow water area is larger than the deepwater area, which indicates that in early period of Upper Sha-4 Submember sedimentation, the Dongying Sag is dominated by shore-shallow lacustrine. Specifically, the water depth >8 m is mainly distributed in the central part of northern Dongying Sag (Lijin-Minfeng Sub-Sag), which is characterized by "deep in the north and shallow in the south". In addition, the isobaths are denser in the north part than in southern part of the Dongying Sag, reflecting the geomorphology of "northern steeper margin and southern gentler margin". For example, Chenjiazhuang Bulge rapidly transits from shore lacustrine zone about 1–2 m deep to shallow lacustrine or semi-deep lacustrine >10 m, reflecting steep lakebed slope. Moreover, the isobaths are sparse in the southeast and southwest parts, with depth variation of 2 m within 1 km. The geomorphology of water depth differentiation is verified in previous research on sedimentology (Su et al. 2012). The reconstruction of paleo-water depth in target horizon with microbody paleobios and its result are shown in reference (Su et al. 2012).
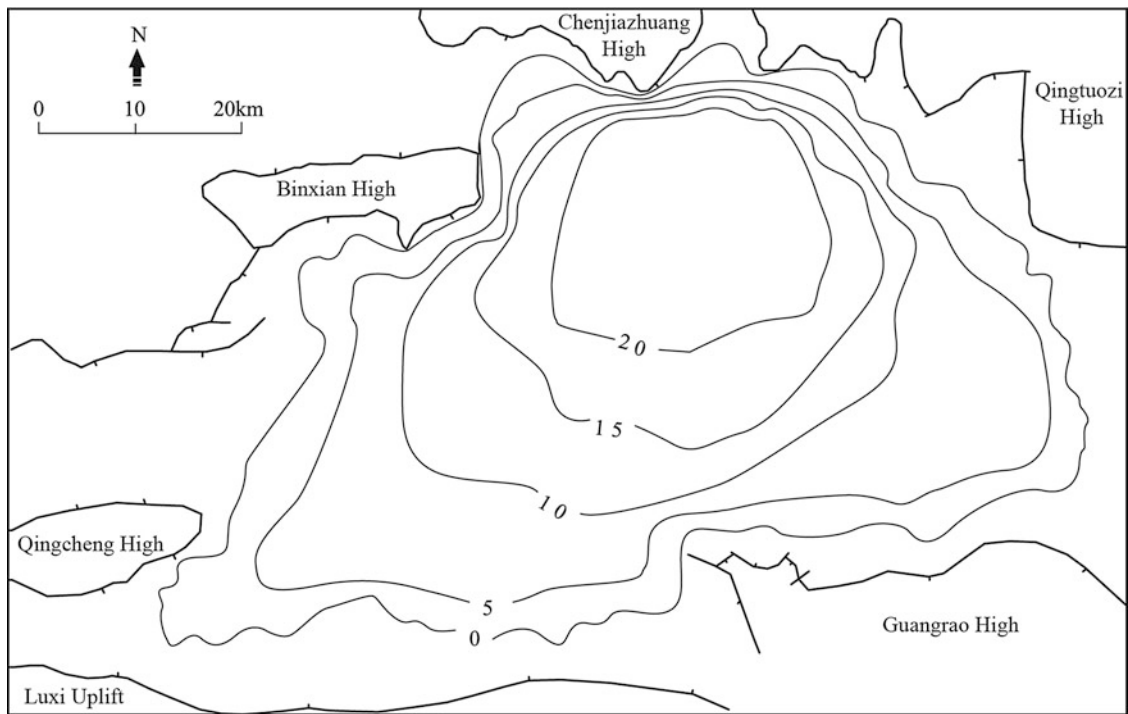
**Fig. 4.56** Contour of paleo-water depth of LST in Upper Sha-4 Submember in the Dongying Sag determined by phase sequence (Li 2009)
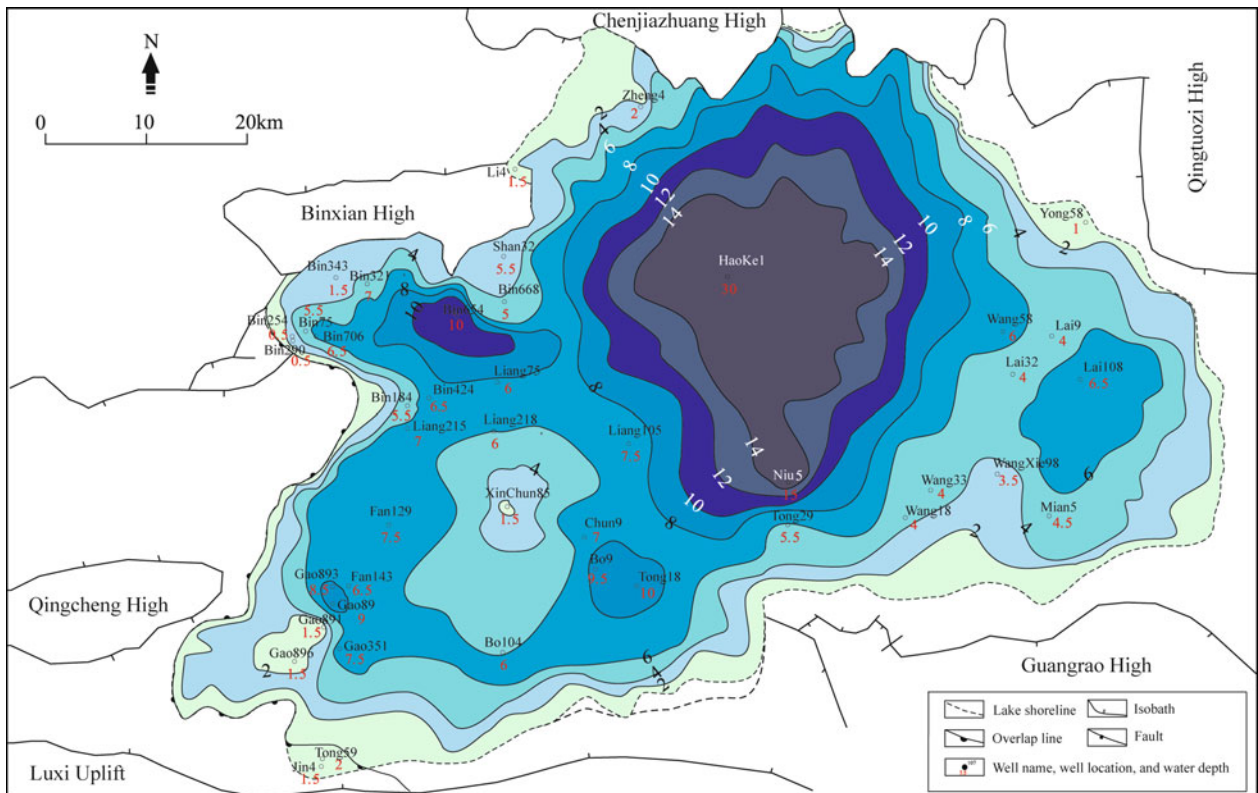


**Fig. 4.57** Quantization contour of paleo-water depth of LST in Upper Sha-4 Submember in the Dongying Sag (Su et al. 2012)
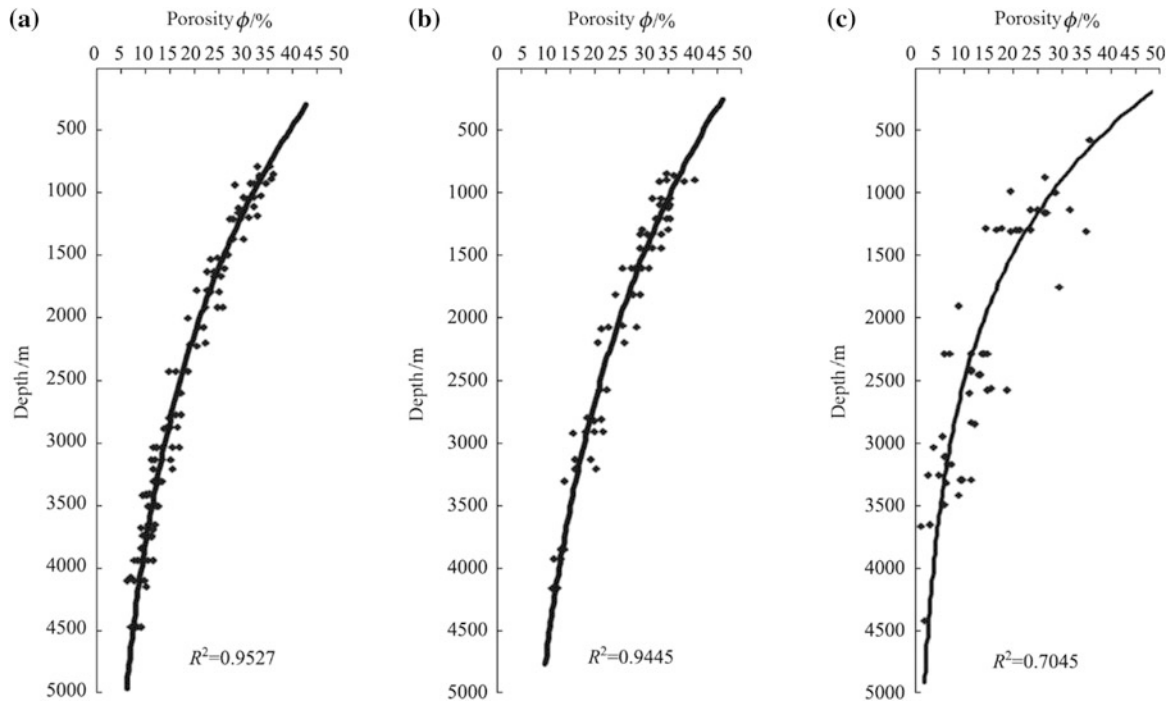
**Fig. 4.58** Relation of $\Phi$-D in sandstone **a**, siltstone **b**, and mudstone **c** in the Dongying Sag (Hu 2008; Gui 2008; Jiang et al. 2009)

## 4.4.2 Reconstruction of Paleo-Geomorphology

During Upper Sha-4 Submember period, unconformity planes were not developed in large areas of Dongying Sag. Therefore, denudation quantity of basin margin in this period is not taken into account. Based on such a premise, paleo-geomorphology of Upper Sha-4 Submember in LST is reconstructed in terms of structure and deposition (Fig. 2.18) with lithology-physical property data, logging data, seismic prospecting data, as well as the aforementioned results of paleo-water depth reconstruction.

Techniques used in this paleo-geomorphology reconstruction mainly include the following: (1) compaction reconstruction technique: compaction is reconstructed by setting up compaction formulas for different series of strata and lithologies and by utilizing three-dimensional basin simulation; (2) balanced cross section reconstruction technique: differential compaction and paleo-structure are reconstructed by loading sedimentary microfacies and isochronous surfaces, etc.; and (3) paleo-geomorphology reconstruction is calibrated by paleo-water depth reconstruction results.

Compaction formulas are extremely important for compaction reconstruction. For the surrounding area of Dongying Sag, Guo et al. (2009), Hu (2008), and Jiang et al. (2009) present porosity-depth cross plot of three lithologies (sandstone, siltstone, and mudstone) (Fig. 4.58) according to measured porosity values.

Based on these cross plots, $\Phi$-D formulas (Formula 4.1 to 4.3), initial porosity, and compaction coefficients of sandstone, siltstone, and mudstone (Table 4.6) are obtained. Thus, porosity at any depth of any lithology on the stratigraphic section in the study area is obtained, which is the basis for further compaction reconstruction.

$$\text{Sandstone}: \Phi = 48.569e^{(-0.000412*D)} \quad (4.1)$$

$$\text{Siltstone}: \Phi = 50.92e^{(-0.000353*D)} \quad (4.2)$$

$$\text{Mudstone}: \Phi = 58.445e^{(-0.000686*D)} \quad (4.3)$$

Based on calibration of true thickness, compaction reconstruction, balanced cross section reconstruction, calibration of paleo-water depth reconstruction results, as well as

**Table 4.6** Initial porosity and compaction coefficient of sandstone, siltstone, and mudstone (Jiang et al. 2009)

|  | Sandstone | Siltstone | Mudstone |
| --- | --- | --- | --- |
| Initial porosity (%) | 48.569 | 50.92 | 58.445 |
| Compaction coefficient | 0.000412 | 0.000353 | 0.000686 |
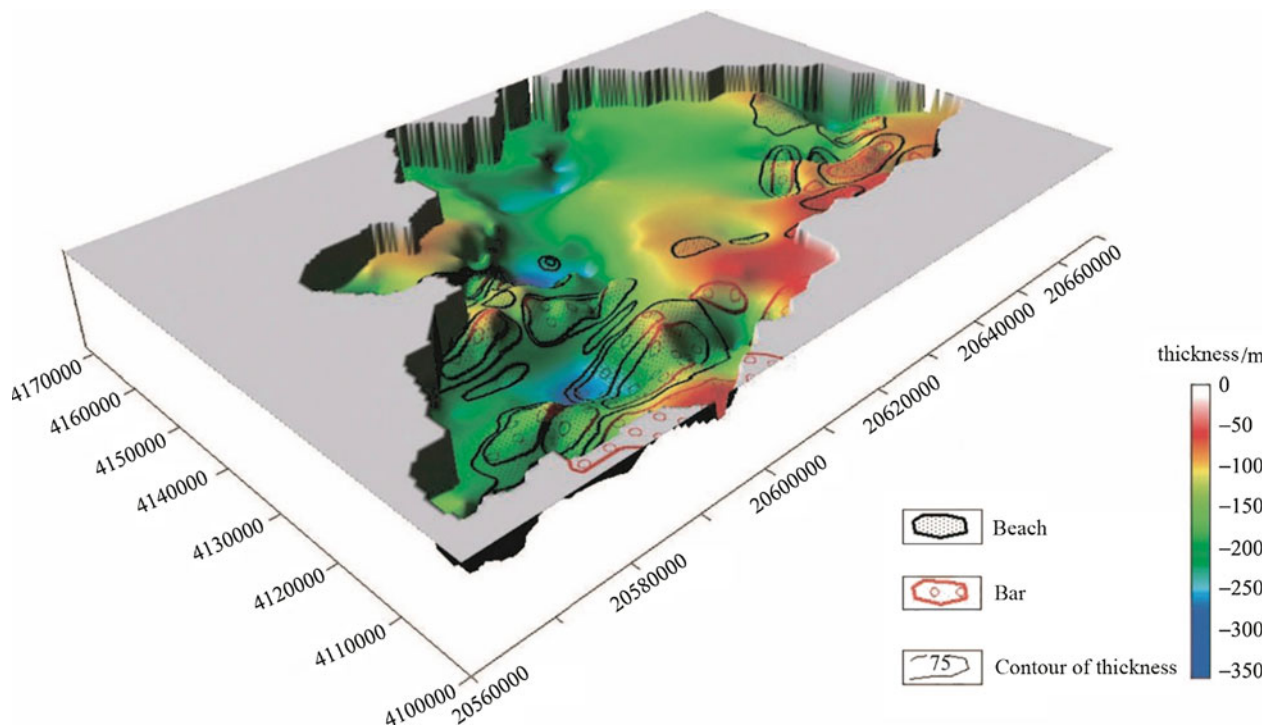
**Fig. 4.59** Result of reconstruction of LST paleo-geomorphology in the Dongying Sag (according to internal data of Jiang)

analysis data such as sedimentary facies, sandbody distribution, and paleo-thickness reconstruction, paleo-geomorphology of Paleogene Upper Sha-4 Submember in the Dongying Sag during the sedimentation period is reconstructed (Fig. 4.59) and the contour of paleo-slope is also obtained (Fig. 4.60). The reconstructed paleo-geomorphology clearly shows steeper and deeper landform in the north and gentler and shallower landform in the south, which well matches with the paleogeography of this area (Fig. 4.2). The distribution of beaches and bars is greatly controlled by paleo-geomorphology and sandbodies are mostly distributed in gentle slope belt in the south of the Dongying Sag (Figs. 4.59 and 4.60). The distribution of beach bar sandbodies has a certain correspondence with microtopography, and sandbodies are concentrated in the surrounding area of positive reliefs and slopes.

### 4.4.3  Analysis of Paleo-Provenance

1. Paleo-geomorphology

The Dongying Sag is a half-graben basin with EW axis and northern steeper margin and southern gentler margin and was developed in the tectonic setting of extension and rifting (Yang et al. 2011) (Fig. 4.2). It can be divided into northern steep slope belt (the southern slope of Chenjiazhuang Bulge-Binxian Bulge), southern gentle slope belt (the

northern slope of Luxi Uplift-Guangrao High), and EW axial belt. Sediments were supplied from lake basin edge of above belts: the northern steep slope belt is controlled by basin edge faulting and has coarse detrital glutenite fans such as near-provenance fan-deltas, nearshore subaqueous fans, and associated deepwater gravity flow deposits; the southern gentle slope belt has linear alluvial fan aprons; EW axial belt has deltas. Paleo-geomorphology features determine the process of sedimentation and further determine the direction, pattern, and scale of sediment transportation (Li 2009) (Fig. 4.2).

2. Rock debris analysis

Sedimentary petrology is one important aspect for provenance analysis. Yang et al. (2011) summarizes features of rock debris in the study area and conducts research on provenance with debris classification. Research results show that rock debris of Upper Sha-4 Submember in the Dongying Sag includes metamorphic rock debris, sedimentary rock debris, and extrusive rock debris. Statistics of debris content show that metamorphic rock debris content is the highest in the whole sag and the content other two types of debris is lower. Based on this, the division criteria of debris content are set (Yang et al. 2011) (Table 4.7), and the Dongying Sag is divided into nine provenances based on the division criteria (Fig. 4.61).
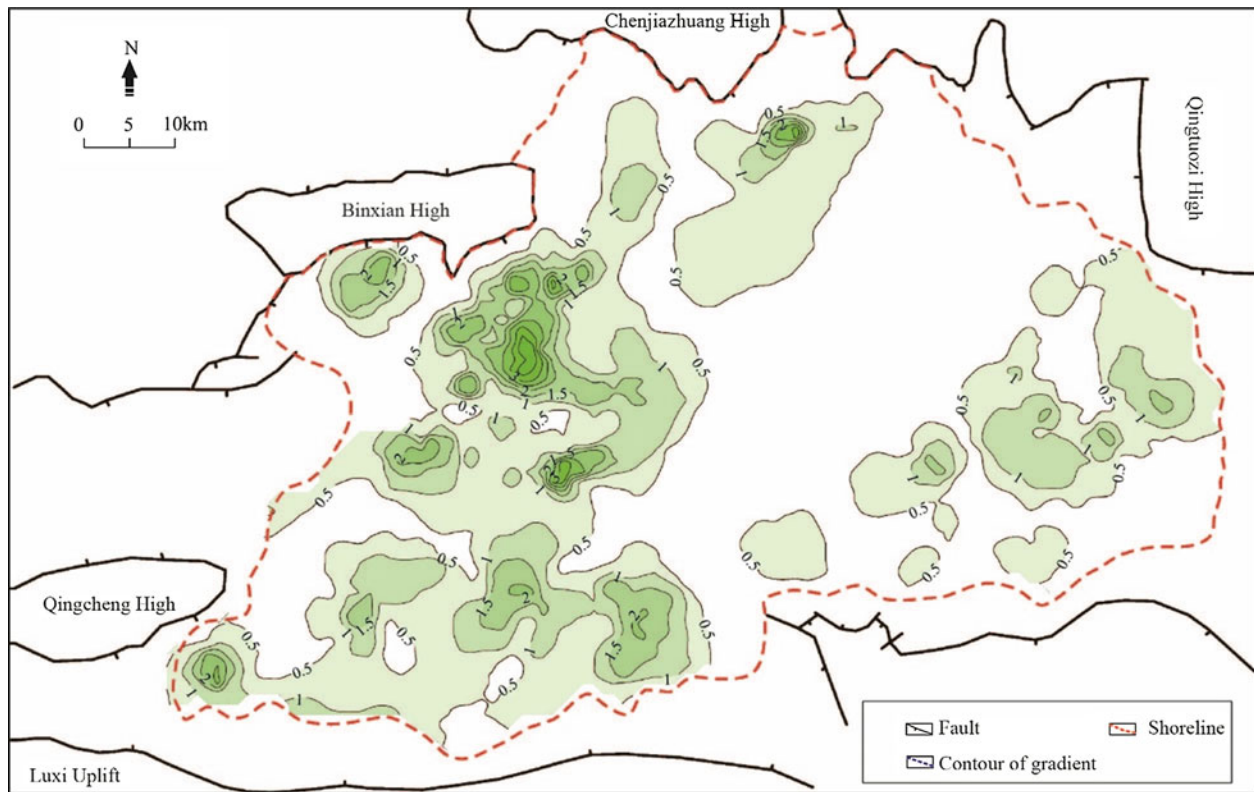
**Fig. 4.60** Contour of paleo-slope of Paleogene Upper Sha-4 Submember in the Dongying Sag (according to internal data of Jiang)

**Table 4.7** Criteria of debris content division in Upper Sha-4 Submember in the Dongying Sag (Yang et al. 2011)

| Debris types | Content (volume fraction, %) | | |
|---|---|---|---|
| | High | Medium | Low |
| Metamorphic rock | >70 | 50–70 | <50 |
| Extrusive rock | >25 | 10–25 | <10 |
| Sedimentary rock | >25 | 10–25 | <10 |

3. Sandstone content

In normal sedimentary differentiation, clast particles become gradually finer along the sediments supply direction. Therefore, in an ideal basin, coarse-grained detrital sediments are distributed at the basin edges, while fine-grained sediments are distributed in the central part of the basin, i.e., the area away from the provenance. The sandstone content in the sedimentary strata gradually decreases from the edge to the center of a basin, and the provenance location can be traced according to variation gradient of sandstone content. The direction and location of provenances can be estimated with planar variation of sandstone content in the sedimentary strata (Yang et al. 2011).

According to lithology data from around 400 wells in the study area, sandstone content and sandstone thickness contour maps are drawn (Figs. 4.46, 4.47, 4.49, 4.50, 4.52 and 4.53). It is clearly shown that all surrounding highs supply

sediments for the basin in the study area. With sedimentary facies study (Figs. 4.48, 4.51 and 4.54), the eastern area of the Dongying Sag is mainly controlled by Qingtuozi Bulge and Guangrao Bulge. The Guangrao Bulge has gentle terrain and shallower water bodies with normal deltas developed (Fig. 4.35) and the Qingtuozi Bulge has fan-delta–normal delta due to steeper terrain and deeper water bodies, stably supplying sediments for forming beaches and bars. The northwestern Lijin Sub-Sag is mainly influenced by Binxian Bulge and has poorly rounded and poorly sorted gravel mingled with sand and high shale content. With geomorphology and cores features, fan-deltas are mainly developed in this area (Figs. 4.31 and 4.32), supplying sediments to forming beach bars and storm deposits of southwestern Lijin Sub-Sag. As for northeastern Lijin Sub-Sag which is close to the basin-controlling fault, i.e., Chennan Fault, coarse debris directly run into deep lake area and subaqueous gravity flow system is formed (Figs. 4.33 and 4.34). Boxing Sub-Sag is
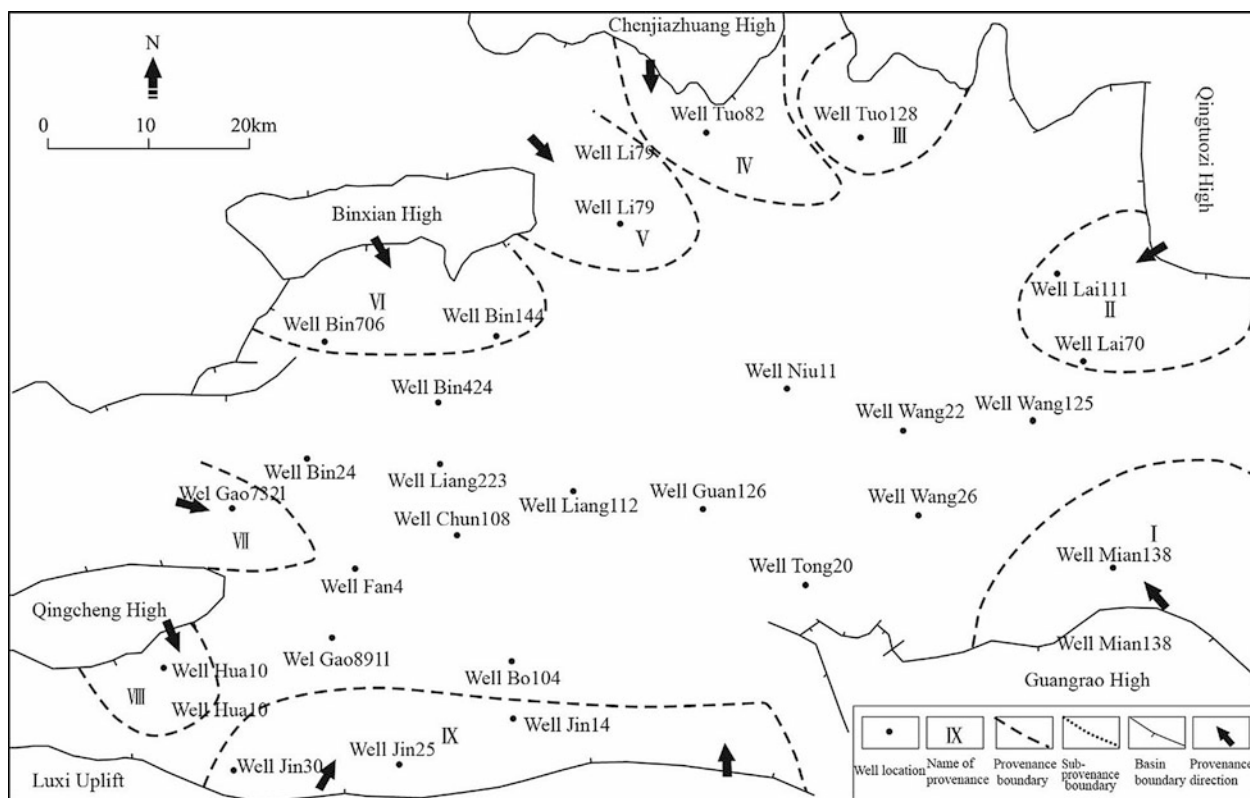
**Fig. 4.61** Provenance of Upper Sha-4 Submember in the Dongying Sag (Yang et al. 2011). I is the intermediate magmatite-intermediate metamorphic rock-intermediate sedimentary rock debris area; II is the intermediate magmatite-high metamorphic rock-low sedimentary rock area; III is the intermediate magmatite-intermediate metamorphic rock-intermediate sedimentary rock debris area; IV is the low magmatite-high metamorphic rock-low sedimentary rock debris area; V is the high magmatite-low metamorphic rock-high sedimentary rock debris area; VI is the intermediate magmatite-intermediate metamorphic rock-high sedimentary rock debris area; VII is the low magmatite-high metamorphic rock-low sedimentary rock debris area; VIII is the low magmatite-intermediate metamorphic rock-high sedimentary rock debris area; and IX the high magmatite-intermediate metamorphic rock-low sedimentary rock debris area

controlled by Luxi Uplift and Gaoqing Bulge. The Gaoqing Bulge has normal delta and the Luxi Uplift has beaches of poorly sorted, well-rounded, and subrounded-rounded gravel sediments (Fig. 4.36). Due to many provenances and linear supply of the Luxi Uplift, Boxing Sub-Sag is full of sand.

4. Maturity index

During the water transportation of detrital material, the content of unstable component decreases and compositional maturity increases as the transportation distance is longer. Quartz is a relative stable mineral in rocks, and its relative content compared with other minerals increases as it is increasingly away from the provenance area. Based on this, maturity coefficient is used: maturity coefficient = [quartz + chert (%)]/[feldspar + debris (%)] (Yang et al. 2011).

Based on the above maturity coefficient, Yang et al. (2011) draw the contour map of compositional maturity index of Upper Sha-4 Submember in the Dongying Sag (Fig. 4.62) and sediment supply directions are marked on this map. Guangrao Bulge and Qingtuozi Bulge control the provenance supply in the east; Luxi Uplift and Qingcheng Bulge supply provenance for Boxing Sub-Sag; Binxian Bulge mainly supply provenance for the west of Lijin Sub-Sag; and Chenjiazhuang Bulge is the major provenance for the north of Dongying Sag. Main provenance directions reflected by the compositional maturity index is in line with the counterparts reflected by sandstone content.

Based on aforementioned analysis of paleogeomorphology, rock debris, sandstone content, and maturity index, it is held that Upper Sha-4 Submember of Dongying Sag has nine provenance areas (I–IX), four sub-provenance areas (sub-provenance area A–D), and two barren provenance areas (barren provenance area A, B) (Yang et al.) (Fig. 4.63). In order to better reflect the relation between beach bar sediments and provenances, the development areas of beach bar sand are defined as sub-provenance areas. Sub-provenance area A is mainly controlled by provenance areas I and II. Sub-provenance area B is controlled by provenance areas IX and VIII. Sub-provenance area C is mainly controlled by provenance
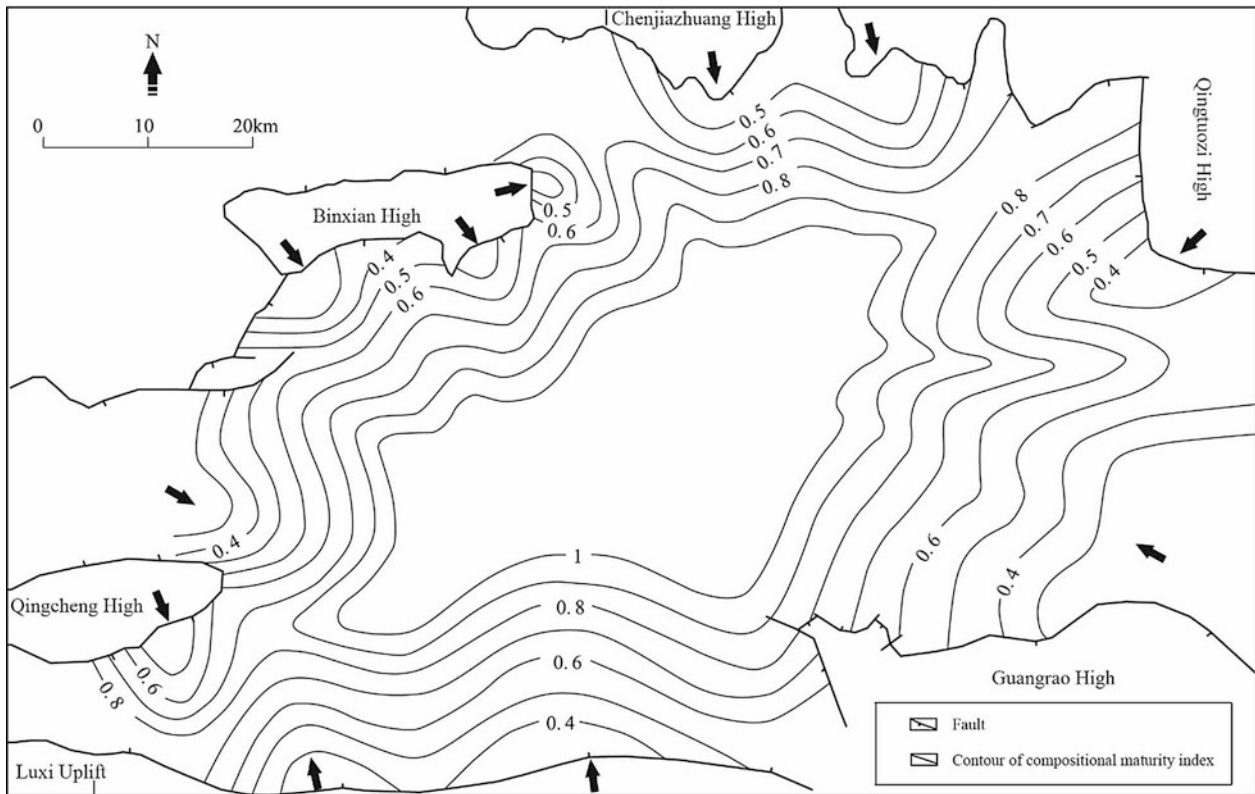
**Fig. 4.62** Contour of compositional maturity index of Upper Sha-4 Submember in the Dongying Sag according to Li (2009), Yang et al. (2011)
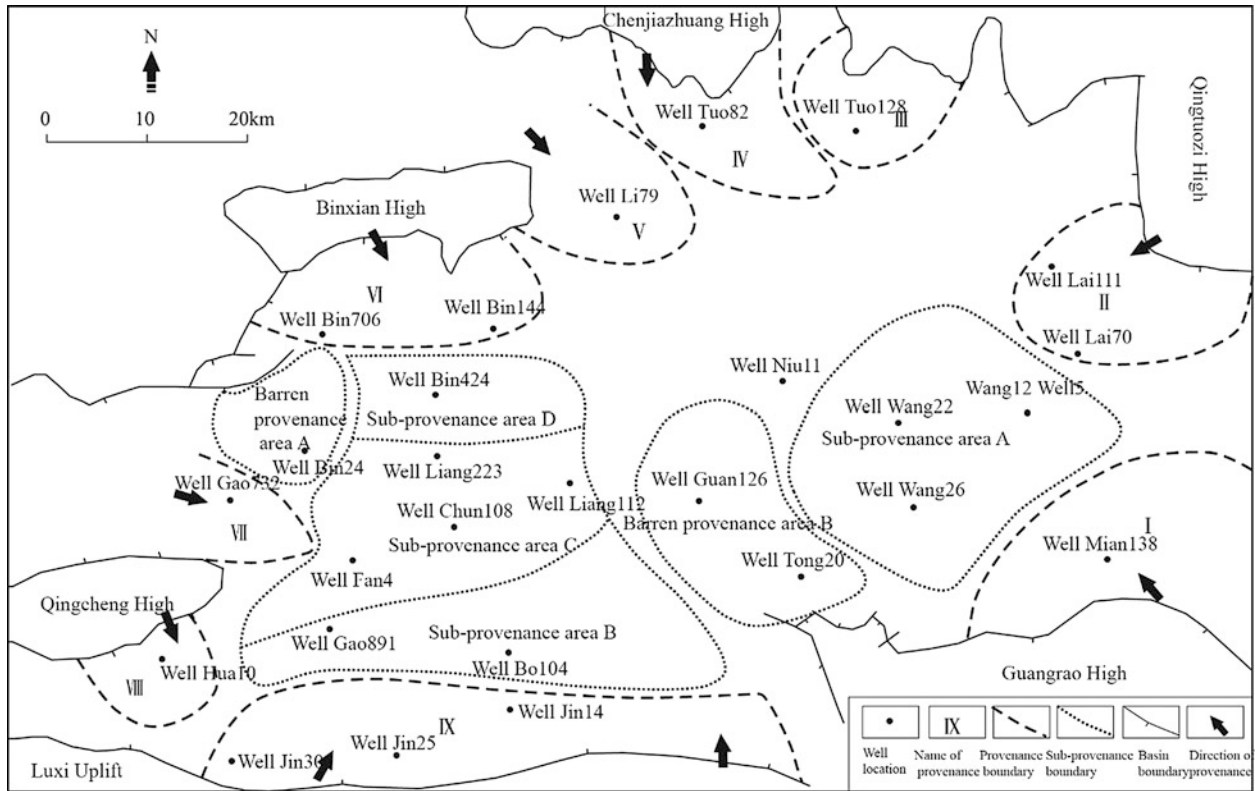


**Fig. 4.63** Distribution of Upper Sha-4 Submember provenance in the Dongying Sag (Li 2009; Yang et al. 2011)

area VII. Sub-provenance area D is mainly controlled by provenance area VI. Far from and barely affected by provenance areas, barren provenance areas lack terrigenous detrital supply and are major development areas of carbonatite sediments.

## 4.4.4   Reconstruction of Paleowind Force

Beach bar sandbodies consist of sand beach and bar (Jiang et al. 2011). According to evolution characteristics of wave, the bars are further divided into offshore bar (breaker zone), nearshore bar (surf zone) and coastal bar (beach ridge) (Jiang et al. 2014) (Fig. 2.10). In 45.0 Ma ago, the Dongying Sag was evolved into an open faulted lake basin with massive beach bar sandbodies developed by wind-wave action (Jiang et al. 2011, 2014). The wind-wave dynamic model of the beach bars in Dongying Sag was constructed (Fig. 4.64): the waves shoal and deform near wave base, and the wave height increases as the water depth gradually decreases during propagation to the shore. When the water depth decreases to a limit, wave steepness reaches the maximum, and then the waves begin to roll back and being broken, forming breaker. On the one hand, the waves from the wave shoaling zone carry sediments to the breaker zone. On the other hand, the broken waves toward the shore may form oscillatory waves and then form circulating current in the onshore side of breaker line. In addition, the offshore compensation flows (bottom flows) are formed during propagation of waves to the shore. Therefore, in the breaker zone, the water flows to the breaker line from two directions (confluence) and transports sediments from the shore and from the ocean (lake) gather near the breaker line, which results in bars (offshore bars) and groove behind bars. This is the "breaker model" or "self-organization model" of bars. After first break, waves are often reconstructed and oscillatory waves are formed again in deep groove behind bars. Before reaching the surf zone, the regenerated waves may be broken for second or even third time, forming inner breaker zone, and bar (nearshore bar).

The breaker ultimately becomes swash, forming "swash zone". Lake water rushes toward the shore by force of inertia, and goes back along the slope, forming undertow or backwash until when the water vanishes or the wave collides with next surf. In swash zone, the transportation capacity of swash is greater than that of backwash, and waves effectively carry coarse sediments to the shore. The silt is carried upward to the highest position of upwash and then accumulated over there, forming bars along the shore, and the bars are called coastal bar.

Multibars were developed in LST in the Dongying Sag, which fits well with above model (Fig. 4.39). The bars developed in the breaker zone are called offshore bar; those developed in the surf zone and inner breaker zone are nearshore bars; those developed behind the swash zone are beach ridges. Beaches are between or in front of bars (Fig. 4.64).

The typical beach bar depositional system developed in Upper Sha-4 Submember in the Dongying Sag provides excellent conditions for reconstruction of paleo-windfield. According to Sect. 2.1.6 of Chap. 2 where the paleo-wind force is reconstructed with the breaker bar (longshore bar) thickness and the gravelly beach ridges thickness, the paleo-windfield of Upper Sha-4 Submember is quantitatively reconstructed. (1) The wave conditions and evenly the wind conditions of LST in Upper Sha-4 Submember are reconstructed by detailed analysis of the offshore bars in LST; (2) the north wind speed throughout whole Upper Sha-4 Submember is reconstructed by analysis of the longshore gravelly beach ridges in LST-HST. Details are as follows.

### 4.4.4.1   Reconstruction of Paleowind Force with Thickness of Breaker Bar (Offshore Bar)

In LST of Upper Sha-4 Submember in the Dongying Sag, where breaker bars are developed, two well-tie profiles almost perpendicular to the trend of breaker bars, i.e., BB' (Bin420-Bin411-Bin417-Bin408-Shi146) and CC' (Gao891-Gao89-Fan143-Fan4), are selected for research (Fig. 4.64a). According to Sect. 2.1.6.2 where the paleo-wind force is reconstructed with the breaker bar (offshore bar) thickness and the gravelly beach ridge thickness, we can the paleo-wind force is calculated with accurate acquisition of breaker bar thickness, fetch, and gradient of paleo-topography in geological records.

(1)   Identification of breaker bars and acquisition of their thickness

The main idea is to accurately identify the breaker bars from geological records and measure the maximum thickness of the single-stage breaker bar, and the original thickness can be obtained after compaction calibration. Details are as follows.

The whole breaker bar deposits correspond to a parasequence, and both top and bottom surfaces correspond to the converted surface—FS, where the depth of water increases suddenly. This cycle basically reflects evolution of gradually decreasing water depth; therefore, the breaker bars generally show a coarsening-upward sequence in vertical direction and sometime show a composite sequence of "fine-coarse-fine grain size", which indicates the water environment of decreasing wave energy after forming bar and gradual
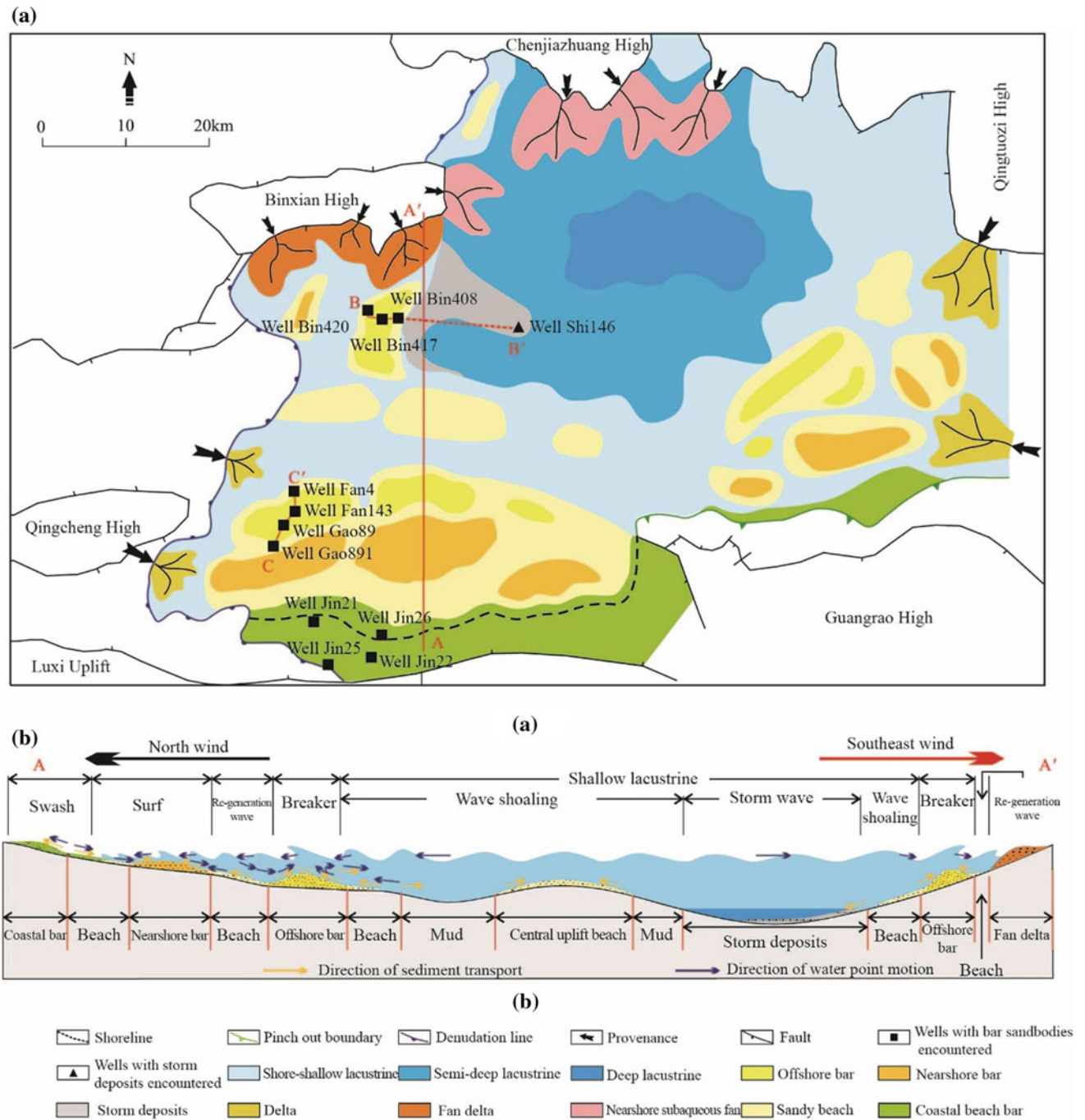
**Fig. 4.64** Sedimentary facies **a** and model of beach bar **b** of LST in the Dongying Sag

transition to suspended deposits after wind-wave action. In the deposits records, the flooding surface corresponds to the lithofacies converted surface. For the sake of narration, on basis of research by Taylor and Ritts (2004) and combining with common lithofacies and sedimentary structures in data of core of about 900 m in 30 wells in this area, a set of plate (Fig. 4.65) and corresponding lithofacies codes (Table 4.8) are established.

According to process of forming breaker bars, and combining with detailed observation and description of cores (Fig. 4.66), it is considered that the lithofacies assemblage of an ideal complete breaker bar from bottom to top is "Fmh-Fm-Fsl-Fsw-Fsr-Fsm-Sly-Saw-Sr-Sp-Sm-Sh-Sr-Fsr-Fsw-Fm" (Fig. 4.66, lithofacies codes shown in Table 4.8) during pre-formation, full development, and termination of development. Fmh-Fm represents suspended deposits, i.e., OSM (offshore mudstone) in static water with the maximum
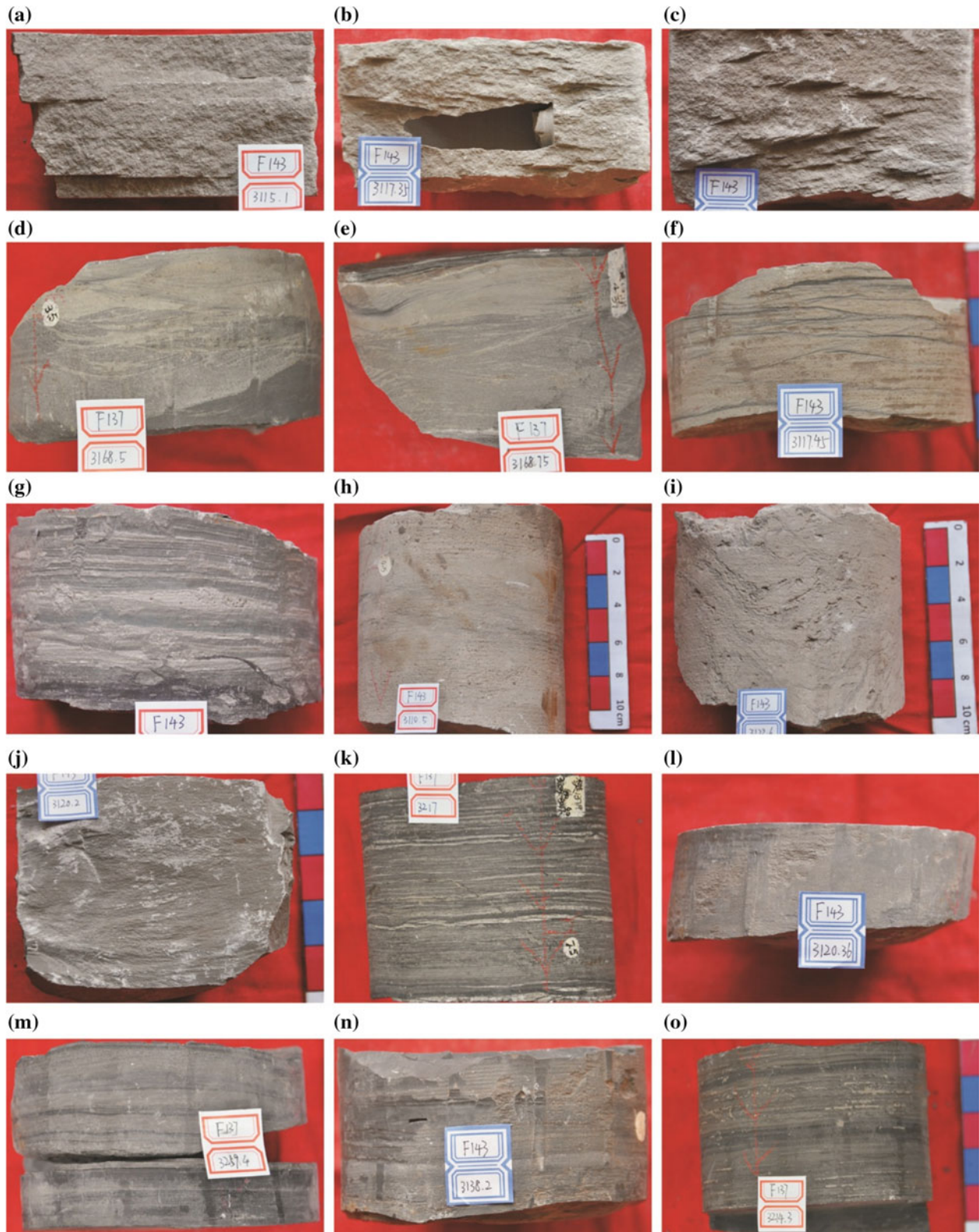
**Fig. 4.65** Lithologies in breaker bar. **a** Parallel bedded fine sandstone (Sh), Well Fan143, at 3115.1 m. **b** Low angle cross-bedded fine sandstone (Sl), Well Fan143, at 3117.35 m. **c** Wedge cross-bedded fine sandstone (Sp), Well Fan143, at 3117.25 m. **d** Wave ripple cross-bedded fine sandstone (Sr), Well Fan137, at 3168.5 m. **e** Hummocky cross-bedded fine sandstone (Shc), Well Fan137, at 3168.75 m. **f** Wavy bedded fine sandstone (Sw), Well Fan143, at 3117.45 m. **g** Lenticular bedded fine sandstone (Sli), organism burrows, Well Fan143, at 3110.95 m. **h** Massive fine sandstone (Sm), Well Fan143, at 3110.5 m. **i** Deformed fine sandstone (Sd), Well Fan143, at 3122.6 m. **j** Wave ripple bedded siltstone (Fsr), Well Fan143, at 3120.2 m. **k** Lenticular bedded siltstone (Fsl), Well Fan137, at 3217 m. **l** Massive siltstone (Fsm), Well Fan143, at 3120.36 m. **m** Horizontal bedded siltstone-wavy bedding siltstone (Fsh-Fsw), Well Fan137, at 3289.4 m. **n** Massive mudstone (Fm), Well Fan148, at 3138.2 m. **o** Horizontal bedded mudstone (Fh), Well Fan137, at 3214.3 m

**Table 4.8** Division of breaker bar lithology

| Lithology code | Lithology | Sedimentary structure | Hydrodynamic force |
|---|---|---|---|
| Sh (Fig. 4.65a) | Fine-coarse sandstone | Parallel bedding, with stripping line between bedding | High flow regime, Fr > 1 |
| Sl (Fig. 4.65b) | Fine-medium sandstone | Low angle cross-bedding (<10°) | Transitional flow, low angle wash sand dune |
| Sp (Fig. 4.65c) | Fine-medium sandstone | Tabular or wedge cross-bedding | Unidirectional migration of subaqueous sand wave or sand dune |
| Sr (Fig. 4.65d) | Fine-medium sandstone | Wave ripple cross-bedding | Low flow regime, small-scale bed form unidirectional migration |
| Shc (Fig. 4.65e) | Fine-medium sandstone | Hummocky cross-bedding | Oscillatory flow or composite flow resulted from tempestuous wave |
| Sw (Fig. 4.65f) | Fine-medium sandstone | Wavy bedding | Abundant suspended deposits, low flow regime |
| Sli (Fig. 4.65g) | Fine-medium sandstone | Lenticular bedding | Low flow regime, and insufficient supply of silt |
| Sm (Fig. 4.65h) | Fine-coarse sandstone | Massive | Rapid sedimentation or bioturbation |
| Sd (Fig. 4.65i) | Fine-medium sandstone | Soft-sediment deformation | Gravity flow, or in situ tempestuous wave liquidation deformation |
| Fsr (Fig. 4.65j) | Siltstone | Wave ripple cross-bedding | Small-scale bed form unidirectional migration (silt) |
| Fsl (Fig. 4.65k) | Siltstone | Lenticular bedding | Low flow regime, and insufficient supply of silt |
| Fsm (Fig. 4.65l) | Siltstone | Massive | Rapid sedimentation or bioturbation |
| Fsw (Fig. 4.65m) | Siltstone | Wavy bedding | Abundant of argillaceous sediment, low flow regime |
| Fsh (Fig. 4.65m) | Siltstone | Horizontal bedding | Slow suspension and sedimentation of silt |
| Fm (Fig. 4.65n) | Mudstone | Massive | Rapid sedimentation or bioturbation |
| Fmh (Fig. 4.65o) | Mudstone | Horizontal bedding | Slow argillaceous sediment suspension and sedimentation |

depth. Fsl-Fsw-Fsr-Fsm represents gradually swallowing water when waves begin to act on lake bottom in wave shoaling zone with weak hydrodynamic force and is OSS (offshore siltstone) mainly caused by increasingly enhanced wave action on silty bed. Sly-Saw-Sr-Sp-Sm-Sh represents further decreasing water depth when waves broke, and longshore bar (LSB) (offshore bar) was mainly formed and was formed by stronger wave action on silty bed. Sh represents the highest flow regime, i.e., the shallowest water on top of breaker bar. It should be noted that breaker bar formed in heavy wind-wave had two lithofacies, i.e., She and Sd. Sr-Fsr-Fsw represents the flooding surface after forming breaker bars and was buried and preserved as OSS in deepened water. In the stage of Fm, water depth further increased when OSM was formed till next similar sedimentary cycle. The SP curve reflections of above lithofacies assemblages are of funnel shape in lower part and bell shape in upper part (Fig. 4.67). Practically, such a complete sequence is rare or changed in one or two orders, but this is enough to help identify a fully developed breaker bar (Fig. 4.68) from drilling data.

Based on this, and compared with well-tie profiles perpendicular to the trend of breaker bar, the vertical development stage and lateral morphological features of breaker bar in this period are displayed (Fig. 4.67).

Therefore, 20 stages of breaker bars in BB' profile, 14 sets of storm deposits of same period in deeper water (Fig. 4.68a), and 26 stages of breaker bars in CC' profile (Fig. 4.68b) were identified. Before calculation, the thicknesses of 46 stages of breaker bars were summarized by lithology, and decompaction calibration was conducted to gain original thicknesses.

(2) Decompaction calibration of present thickness of breaker bar

Compaction calibration is needed after accurate identification of breaker bars and acquisition of their thickness with well data. Assuming that the rock skeleton volume is constant during burial, compaction calibration is operated with initial porosity of the lithology of breaker bars and corresponding depth (Formula 4.4).

**Fig. 4.66** Interpretation of coring intervals in Well Fan143. Description and interpretation of Eocene breaker bar formed in 45 Ma–44.3 Ma ago. Codes of lithology are shown in Table 4.8

$$t_0 = \frac{1 - \Phi}{1 - \Phi_0} t \qquad (4.4)$$

where $t_0$ is the original thickness of breaker bar (m); $t$ is the present thickness of breaker bar (m); $\Phi_0$ is the initial porosity of breaker bar (%); and $\Phi$ is the present porosity of breaker bar (%).

The breaker bar is dominated by sandstone and siltstone, and correspondingly, two compaction formulas are needed. According to the measured porosity data in the Jiyang Depression, the relationship between depth and porosity of sandstone and siltstone was plotted (Fig. 4.58), obtaining compaction equations and initial porosity of sandstone and siltstone (Jiang et al. 2009). According to compaction equations (Eqs. 4.1 and 4.2), the initial porosity of sandstone and siltstone are, respectively, 48.569 and 50.92%, and the porosity at any depth is be obtained. Using Eq. 4.4, the thickness of breaker bar (46 in total, Fig. 4.68) at a specified depth is corrected (Tables 4.9 and 4.10).

(3)  Paleo-wind direction index

Assume that the trend of breaker bar is almost perpendicular to the propagation direction of waves (consistent with wind direction in most cases) (Jiang et al. 2014; Orme and Orme 1991), with steep and short leeward side of breaker bar and gentle and long windward side and in the cross section. Therefore, on basis of planar distribution (Fig. 4.64a) and thickness of single-stage breaker bar in cross section (Fig. 4.68a, b), the paleo-wind direction is obtained. The breaker bar in Fig. 4.68a strikes NE-SW in horizontal plane, and the single-stage bar is thick in NW and thin SE, which indicates dominance by the southeast wind. The breaker bar shown in Fig. 4.68b nearly extends EW, and the single-stage bar is thick in the south and thin in the north, which indicates dominance by the north wind. Therefore, it is concluded that there were both southeast wind and north wind in this period. In addition, thin layer of sandstone and siltstone was developed upon dark gray mudstone in the northwest of Dongying

**Fig. 4.67** Vertical sequence of ideal breaker bar (offshore bar), which is divided into three parts: the first is sediment formed before breaker bar, which is mainly OSM (Fmh-Fm from bottom to top) and OSS (Fsh-Fsl-Fsw-Fsr-Fsm from bottom to top), representing sedimentary environment of shallowing water depth before forming breaker bar; the second is main body of breaker bar, with lithology of Sli-Sw-Sr-Sp-Sm-Sh from bottom to top, representing main stage of breaker bar, and shallowest water depth; the third is the sediment formed after breaker bar, with deepening water depth, with lithology of frontal LSB (Sr), OSS (Fsr-Fsw), and OSM (Fm) from bottom to top. The curve of spontaneous potential log shows funnel shape in the bottom and bell shape in the top. Codes of lithology are shown in Table 4.8

Sag, with massive sedimentary structures, e.g., erosion, soft sedimentary deformation, hummocky cross-bedding, and wavy bedding, which are similar to Bouma sequence vertically, and interpreted as the semi-deep lacustrine storm deposits (Fig. 4.64a, b). However, the storm deposits reflecting strong paleo-wind-wave action is rare in southern Dongying Sag. Thus, the origin and distribution of storm deposits (Fig. 4.64a) reflects the impact of southeast storm action, which is due to the impact of the typhoon from northwest Pacific Ocean.

(4) Acquisition of the paleo-fetch parameters

On basis of acquisition of paleo-wind direction, the radial rays (Fig. 4.69) are made at the interval of 6 degree within ±45° in the direction against the wind, at the position where breaker bars were developed, and the average projected length of the rays in the paleo-wind direction is determined as fetch (CERC 1977; Orme and Orme 1991). With this method, the fetches corresponding to the breaker bars developed in Well Gao89, Fan4, Bin408, Bin417, Bin411
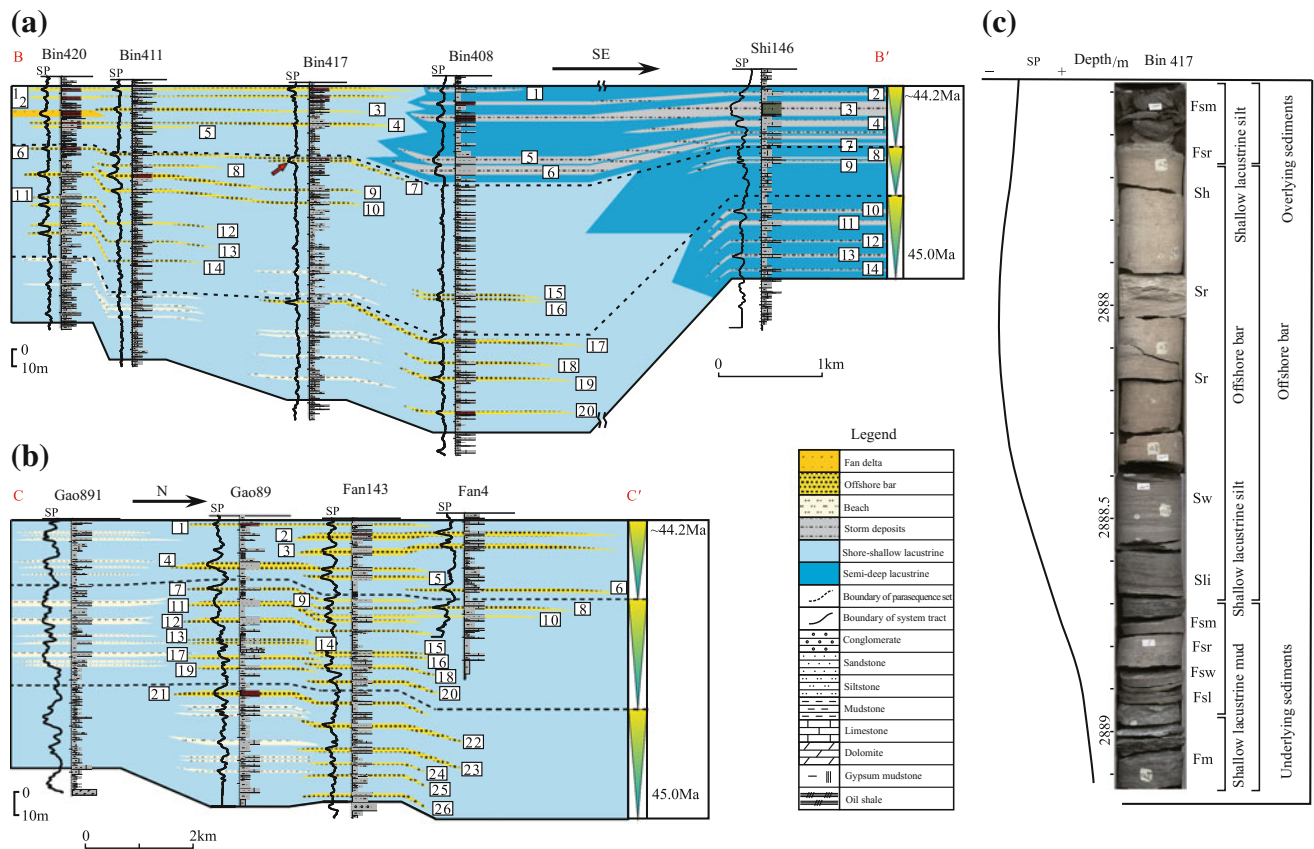
**Fig. 4.68** Identification of breaker bar in drilling and logging data. **a** Identification and comparison of breaker bar and storm deposits in Profile BB' (Bin420- Bin411-Bin417-Bin408-Shi146, and the location of profile is shown in Fig. 4.64a), the red arrow indicates the position of core in **c**; **b** identification and comparison of breaker bar and storm deposits in Profile CC' (Gao891-Gao89-Fan143-Fan4, and the location of profile is shown in Fig. 4.64a); **c** core from Bin417, which indicates sediments of complete breaker bar, and the location is indicated by red arrow in Fig. 4.64a)

and Bin420 are, respectively, 25,869, 26,225, 23,169, 48,164, 49,074, 49,913, and 50,609 m (Tables 4.11 and 4.12).

(5)  Acquisition of paleo-gradient

Paleo-gradient is directly read from the paleo-gradient contour map (Fig. 4.60). The gradients of the breaker bars developed in Well Gao89, Fan143, Fan4, Bin408, Bin417, Bin411, and Bin420 are, respectively, 1°, 1°, 1°, 2°, 1°, 1.2°, and 1.5°.

(6)  Calculation of paleo-wave condition and paleo-wind force

On basis of identification of thickness of breaker bars after compaction calibration, combining parameters of paleo-topographic gradient and paleo-fetch, the breaker depth, wave height of breaker, wave height of deepwater, shear coefficient of wind, wind speed and vertical variation

of wind force, and wind scale corresponding to breaker bar were obtained with Formulas 2.4, 2.5, and 2.6 (Tables 4.11 and 4.12).

According to calculation, LST (about 45.0–44.2 Ma ago) of Upper Sha-4 Submember in the Dongying Sag was dominated by both SE wind of 6–12 m/s (4–6 level) and northerly wind of 8–22 m/s (4–9 level) (Table 4.12), which were paleo-East Asian monsoons. This is the earliest direct evidence to support existence of the paleo-East Asian monsoon, illustrating that the paleo-East Asian monsoon is earlier to 45 Ma. Therefore, it is believed that the paleo-East Asian monsoon already formed had begun to act on the Dongying Sag in middle Eocene (about 45 Ma ago). The speed of north wind had experienced two cycles of "increase–decrease–increase" with a lower peak (about 18 m/s) in the early-middle period and a higher peak (about 22 m/s) in the latter period, while the southeast wind has two cycles of "decrease–increase–decrease" in the same period, and the speed of southeast wind is lower in general. The wind forces of southeast wind and the northerly wind show an
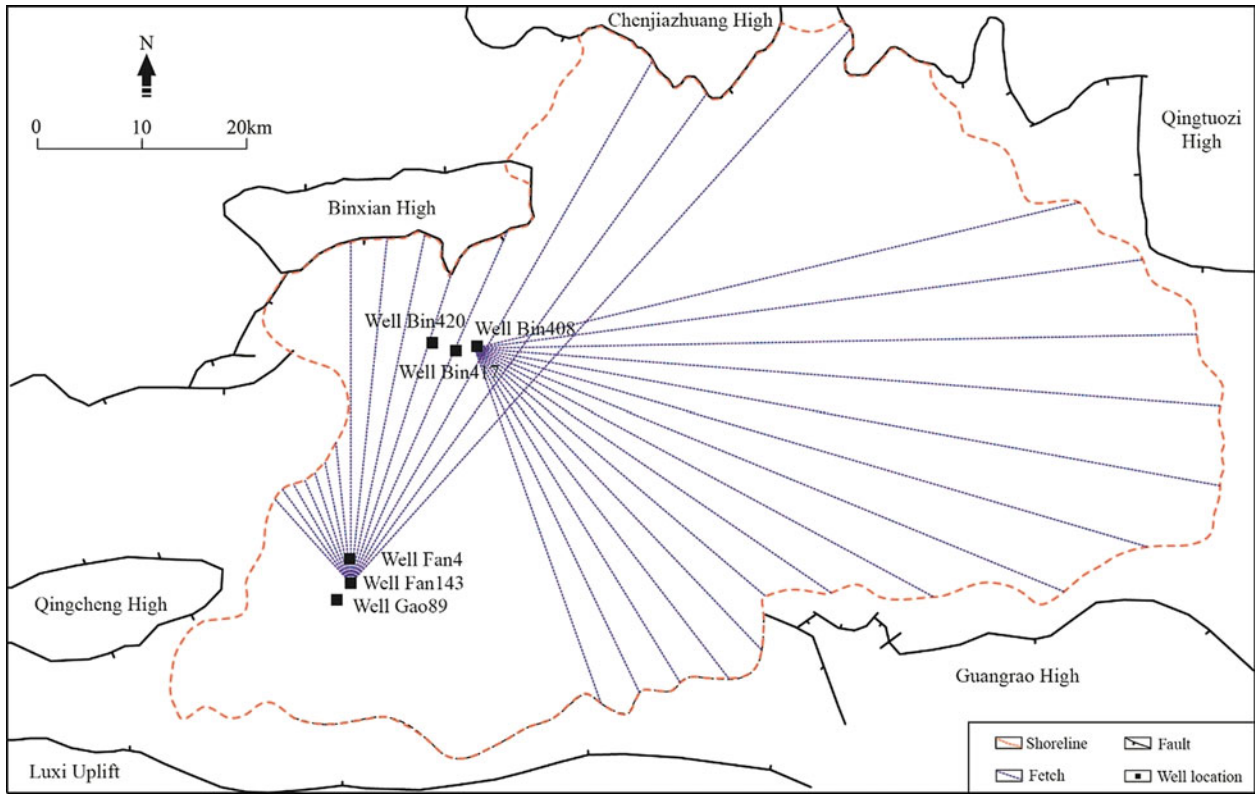
**Fig. 4.69** Method of measuring paleo-fetch (Well Fan143 and Well Bin408)

**Table 4.9** Decompaction calibration of 20 stages of breaker bars in Profile BB'

| Bar No. | Well No. | Depth (m) | Current bar thickness (m) | Sandstone thickness (m) | Siltstone thickness (m) | Sandstone porosity (%) | Siltstone porosity (%) | Sandstone thickness calibration (m) | Siltstone thickness calibration (m) | Breaker bar thickness calibration (m) |
|---|---|---|---|---|---|---|---|---|---|---|
| 1 | Bin417 | 2844.00 | 1.70 | 0.00 | 1.70 | 15.05 | 18.66 | 0.00 | 2.82 | 2.82 |
| 2 | Bin420 | 2653.00 | 1.30 | 0.00 | 1.30 | 16.28 | 19.96 | 0.00 | 2.12 | 2.12 |
| 3 | Bin411 | 2598.00 | 2.00 | 1.00 | 1.00 | 16.65 | 20.35 | 1.62 | 1.62 | 3.24 |
| 4 | Bin417 | 2865.50 | 1.75 | 0.00 | 1.75 | 14.92 | 18.52 | 0.00 | 2.91 | 2.91 |
| 5 | Bin420 | 2670.00 | 1.00 | 0.00 | 1.00 | 16.17 | 19.84 | 0.00 | 1.63 | 1.63 |
| 6 | Bin420 | 2683.00 | 1.40 | 0.00 | 1.40 | 16.08 | 19.75 | 0.00 | 2.29 | 2.29 |
| 7 | Bin417 | 2887.00 | 1.10 | 0.90 | 0.20 | 14.78 | 18.38 | 1.49 | 0.33 | 1.82 |
| 8 | Bin411 | 2631.50 | 1.20 | 0.70 | 0.50 | 16.43 | 20.11 | 1.14 | 0.81 | 1.95 |
| 9 | Bin411 | 2637.50 | 2.80 | 2.50 | 0.30 | 16.38 | 20.07 | 4.06 | 0.49 | 4.55 |
| 10 | Bin420 | 2698.00 | 2.60 | 2.60 | 0.00 | 15.98 | 19.65 | 4.25 | 0.00 | 4.25 |
| 11 | Bin420 | 2712.00 | 1.20 | 0.00 | 1.20 | 15.89 | 19.55 | 0.00 | 1.97 | 1.97 |
| 12 | Bin420 | 2716.50 | 1.50 | 0.00 | 1.50 | 15.86 | 19.52 | 0.00 | 2.46 | 2.46 |
| 13 | Bin420 | 2728.00 | 1.50 | 0.00 | 1.50 | 15.78 | 19.44 | 0.00 | 2.46 | 2.46 |
| 14 | Bin420 | 2733.00 | 1.60 | 0.00 | 1.60 | 15.75 | 19.40 | 0.00 | 2.63 | 2.63 |
| 15 | Bin408 | 3285.00 | 1.05 | 0.00 | 1.05 | 12.55 | 15.97 | 0.00 | 1.80 | 1.80 |
| 16 | Bin408 | 3287.50 | 0.90 | 0.00 | 0.90 | 12.54 | 15.95 | 0.00 | 1.54 | 1.54 |
| 17 | Bin408 | 3313.00 | 1.60 | 1.20 | 0.40 | 12.40 | 15.81 | 2.04 | 0.69 | 2.73 |
| 18 | Bin408 | 3325.50 | 1.50 | 1.50 | 0.00 | 12.34 | 15.74 | 2.56 | 0.00 | 2.56 |
| 19 | Bin408 | 3335.00 | 1.90 | 1.90 | 0.00 | 12.29 | 15.69 | 3.24 | 0.00 | 3.24 |
| 20 | Bin408 | 3355.00 | 1.50 | 1.50 | 0.00 | 12.19 | 15.58 | 2.56 | 0.00 | 2.56 |

**Table 4.10** Decompaction calibration of 26 stages of breaker bars in Profile CC'

| Bar No. | Well No. | Depth (m) | Current bar thickness (m) | Sandstone thickness (m) | Siltstone thickness (m) | Sandstone porosity (%) | Siltstone porosity (%) | Sandstone thickness calibration (m) | Siltstone thickness calibration (m) | Breaker bar thickness calibration (m) |
|---|---|---|---|---|---|---|---|---|---|---|
| 1 | Fan143 | 3111.50 | 1.00 | 1.00 | 0.00 | 13.48 | 16.98 | 1.68 | 0.00 | 1.68 |
| 2 | Fan143 | 3117.00 | 3.20 | 2.20 | 1.00 | 13.45 | 16.94 | 3.70 | 1.69 | 5.39 |
| 3 | Fan143 | 3123.50 | 3.00 | 2.20 | 0.80 | 13.41 | 16.91 | 3.70 | 1.35 | 5.06 |
| 4 | Gao89 | 3015.50 | 3.00 | 3.00 | 0.00 | 14.02 | 17.56 | 5.02 | 0.00 | 5.02 |
| 5 | Fan143 | 3134.60 | 1.65 | 1.15 | 0.50 | 13.35 | 16.84 | 1.94 | 0.85 | 2.78 |
| 6 | Fan4 | 3479.30 | 1.45 | 0.70 | 0.75 | 11.58 | 14.91 | 1.20 | 1.30 | 2.50 |
| 7 | Gao89 | 3025.50 | 1.20 | 0.00 | 1.20 | 13.96 | 17.50 | 0.00 | 2.02 | 2.02 |
| 8 | Fan4 | 3487.00 | 1.20 | 1.20 | 0.00 | 11.55 | 14.87 | 2.06 | 0.00 | 2.06 |
| 9 | Fan143 | 3147.80 | 1.00 | 0.00 | 1.00 | 13.28 | 16.76 | 0.00 | 1.70 | 1.70 |
| 10 | Fan143 | 3151.50 | 1.10 | 0.00 | 1.10 | 13.26 | 16.74 | 0.00 | 1.87 | 1.87 |
| 11 | Gao89 | 3032.00 | 2.00 | 2.00 | 0.00 | 13.93 | 17.46 | 3.35 | 0.00 | 3.35 |
| 12 | Gao89 | 3039.00 | 1.95 | 1.95 | 0.00 | 13.89 | 17.42 | 3.26 | 0.00 | 3.26 |
| 13 | Gao89 | 3047.30 | 0.70 | 0.70 | 0.00 | 13.84 | 17.37 | 1.17 | 0.00 | 1.17 |
| 14 | Gao89 | 3049.00 | 1.00 | 1.00 | 0.00 | 13.83 | 17.36 | 1.68 | 0.00 | 1.68 |
| 15 | Fan143 | 3167.00 | 0.90 | 0.00 | 0.90 | 13.17 | 16.65 | 0.00 | 1.53 | 1.53 |
| 16 | Fan143 | 3168.50 | 1.05 | 0.00 | 1.05 | 13.17 | 16.64 | 0.00 | 1.78 | 1.78 |
| 17 | Gao89 | 3055.00 | 1.60 | 1.60 | 0.00 | 13.80 | 17.32 | 2.68 | 0.00 | 2.68 |
| 18 | Fan143 | 3173.30 | 1.50 | 1.20 | 0.30 | 13.14 | 16.61 | 2.03 | 0.51 | 2.54 |
| 19 | Gao89 | 3159.50 | 1.40 | 1.40 | 0.00 | 13.21 | 16.69 | 2.36 | 0.00 | 2.36 |
| 20 | Fan143 | 3180.00 | 1.50 | 1.10 | 0.40 | 13.10 | 16.57 | 1.86 | 0.68 | 2.54 |
| 21 | Gao89 | 3070.75 | 2.50 | 0.00 | 2.50 | 13.71 | 17.22 | 0.00 | 4.22 | 4.22 |
| 22 | Fan143 | 3199.00 | 2.00 | 2.00 | 0.00 | 13.00 | 16.46 | 3.38 | 0.00 | 3.38 |
| 23 | Fan143 | 3209.50 | 1.95 | 1.65 | 0.30 | 12.94 | 16.40 | 2.79 | 0.51 | 3.30 |
| 24 | Fan143 | 3215.30 | 1.00 | 0.00 | 1.00 | 12.91 | 16.37 | 0.00 | 1.70 | 1.70 |
| 25 | Fan143 | 3220.50 | 1.05 | 0.00 | 1.05 | 12.89 | 16.34 | 0.00 | 1.79 | 1.79 |
| 26 | Fan143 | 3229.00 | 1.30 | 0.00 | 1.30 | 12.84 | 16.29 | 0.00 | 2.22 | 2.22 |

approximate cyclic inverse correlation with two cycles (Fig. 4.70), which is similar to present East Asian monsoons. Storm is more frequent with significant difference between speeds of winter wind and summer wind (Fig. 4.70).

### 4.4.4.2 Reconstruction of Paleo-Wind Force with Thickness of Gravelly Beach Ridge

In LST-HST of Upper Sha-4 Submember in the Dongying Sag, the gravelly beach ridges were developed in southern shoreline and formed by waves propagated southward resulted from north wind. The thickness of gravelly beach ridges is used to reconstruct the paleo-wind force. According to reconstruction of paleo-wind force by thickness of gravelly beach ridges in Sect. 2.1.6.2, the paleo-north wind force is calculated only with accurate parameters of thickness of

beach ridge, fetch, paleo-water depth, and angle between wind direction and normal line of shoreline.

(1)  Acquisition of thickness of beach ridge

Fence diagram across Well Jin 21, Jin 22, Jin 25, and Jin 26 is drawn in the position where the longshore gravelly beach ridges were developed (Fig. 4.71, well locations are shown in Fig. 4.64a) were drawn. In the fence diagram, 26 stages of gravelly beach ridges are identified for calculation, with 10 in HST, 2 in TST, and 14 in LST. Due to little impact of compaction on thickness of gravelly beach ridges, the present thickness rather than the corrected thickness is used for calculation.

Detailed thickness is listed in Table 4.13.

**Table 4.11** Paleo-wave and wind speed of paleo-southeast wind corresponding to 20 stages of breaker bars in Profile BB'

| Bar No. | Well No. | Bar initial thickness (m) | Gradient | Breaker water depth (m) | Breaker wave height (m) | Offshore significant wave height (m) | Fetch (m) | Wind shearing factor (m/s) | Wind speed (m/s) |
|---|---|---|---|---|---|---|---|---|---|
| 1 | Bin417 | 2.82 | 0.02 | 4.57 | 2.74 | 1.37 | 49,074 | 12.11 | 10.03 |
| 2 | Bin420 | 2.12 | 0.03 | 3.39 | 2.04 | 1.02 | 50,609 | 8.85 | 7.78 |
| 3 | Bin411 | 3.24 | 0.02 | 5.23 | 3.14 | 1.57 | 49,913 | 13.74 | 11.12 |
| 4 | Bin417 | 2.91 | 0.02 | 4.71 | 2.83 | 1.41 | 49,074 | 12.48 | 10.29 |
| 5 | Bin420 | 1.63 | 0.03 | 2.61 | 1.57 | 0.78 | 50,609 | 6.82 | 6.29 |
| 6 | Bin420 | 2.29 | 0.03 | 3.66 | 2.20 | 1.10 | 50,609 | 9.56 | 8.28 |
| 7 | Bin417 | 1.82 | 0.02 | 2.95 | 1.77 | 0.89 | 49,074 | 7.82 | 7.03 |
| 8 | Bin411 | 1.95 | 0.02 | 3.15 | 1.89 | 0.94 | 49,913 | 8.27 | 7.36 |
| 9 | Bin411 | 4.55 | 0.02 | 7.34 | 4.41 | 2.20 | 49,913 | 19.29 | 14.65 |
| 10 | Bin420 | 4.25 | 0.03 | 6.80 | 4.08 | 2.04 | 50,609 | 17.74 | 13.69 |
| 11 | Bin420 | 1.97 | 0.03 | 3.15 | 1.89 | 0.94 | 50,609 | 8.21 | 7.32 |
| 12 | Bin420 | 2.46 | 0.03 | 3.94 | 2.36 | 1.18 | 50,609 | 10.27 | 8.78 |
| 13 | Bin420 | 2.46 | 0.03 | 3.94 | 2.36 | 1.18 | 50,609 | 10.28 | 8.78 |
| 14 | Bin420 | 2.63 | 0.03 | 4.20 | 2.52 | 1.26 | 50,609 | 10.97 | 9.26 |
| 15 | Bin408 | 1.80 | 0.03 | 2.84 | 1.70 | 0.85 | 48,164 | 7.59 | 6.87 |
| 16 | Bin408 | 1.54 | 0.03 | 2.43 | 1.46 | 0.73 | 48,164 | 6.51 | 6.06 |
| 17 | Bin408 | 2.73 | 0.03 | 4.31 | 2.59 | 1.29 | 48,164 | 11.53 | 9.64 |
| 18 | Bin408 | 2.56 | 0.03 | 4.04 | 2.42 | 1.21 | 48,164 | 10.80 | 9.14 |
| 19 | Bin408 | 3.24 | 0.03 | 5.12 | 3.07 | 1.54 | 48,164 | 13.68 | 11.08 |
| 20 | Bin408 | 2.56 | 0.03 | 4.04 | 2.43 | 1.21 | 48,164 | 10.82 | 9.15 |

(2) Acquisition of paleo-fetch parameters

The above method (in Sect. 4.4.4.1) is used to obtain the parameters of paleo-fetch. The north fetch corresponding to Well Jin21, Jin22, Jin25, and Jin26 are, respectively, 35,977 m, 51,231 m, 43,158 m, and 49,948 m (Table 4.13).

(3) Acquisition of paleo-water depth parameters

The gravelly beach ridges were developed in whole Upper Sha-4 Submember, including LST, TST, and HST where there were obvious differences of water depth; therefore, different water depth parameters are used in calculation. On basis of the reconstruction of paleo-water depth (Sect. 4.4.1 and Fig. 4.57), 15 m is selected as an average water depth in LST. According to reconstruction of paleo-lake basin water depth using the dominance diversity of Ostracoda by Li et al. (2005), the average water depth of the Dongying Sag in early depositional period of Sha-3 Submember was 50 m. Therefore, the paleo-water depth of 50 m in HST is adopted. Assuming that the water depth increases linearly during evolution from LST to HST, 32.5 m, the median of both water depth mentioned above, is adopted as the paleo-water

depth in TST. These three parameters are optimum depth (Table 4.13) currently.

(4) Estimation of the angle between wind direction and normal line of shoreline

Here, the angle is estimated as follows: assuming the north paleowind and EW shoreline, the angle between paleowind direction and normal line of shoreline is 0 (Eq. 2.12 shows that β value has little effect on calculation result).

(5) Calculation of paleowave conditions and paleowind force

After identification of thickness of beach ridge, and combining with paleo-fetch and paleo-water depth, Formula 2.12 is used to obtain the effective wave height of deepwater, wind backwater height, height of wave surge, wave run-up, wind shear coefficient, wind speed, and variation of wind force and wind scale on the time sequence corresponding to each beach ridge (Table 4.13; Fig. 4.72).

Reconstruction shows two cycles of "increase–decrease" of the north wind speed in LST (Fig. 4.72), which is in

**Table 4.12** Paleo-wave and wind speed of paleo-southeast wind corresponding to 26 stages of breaker bars in Profile CC'

| Bar No. | Well No. | Bar initial thickness (m) | Slope | Breaker water depth (m) | Breaker wave height (m) | Abyssal region effective wave height(m) | Fetch (m) | Wind shearing factor (m/s) | Wind speed (m/s) |
|---|---|---|---|---|---|---|---|---|---|
| 1 | Fan143 | 1.68 | 0.02 | 2.73 | 1.64 | 0.82 | 26,225 | 9.89 | 8.51 |
| 2 | Fan143 | 5.39 | 0.02 | 8.75 | 5.25 | 2.62 | 26,225 | 31.71 | 21.95 |
| 3 | Fan143 | 5.06 | 0.02 | 8.20 | 4.92 | 2.46 | 26,225 | 29.73 | 20.83 |
| 4 | Gao89 | 5.02 | 0.02 | 8.13 | 4.88 | 2.44 | 25,869 | 29.68 | 20.80 |
| 5 | Fan143 | 2.78 | 0.02 | 4.52 | 2.71 | 1.35 | 26,225 | 16.37 | 12.82 |
| 6 | Fan4 | 2.50 | 0.02 | 4.06 | 2.44 | 1.22 | 23,169 | 15.66 | 12.37 |
| 7 | Gao89 | 2.02 | 0.02 | 3.27 | 1.96 | 0.98 | 25,869 | 11.94 | 9.92 |
| 8 | Fan4 | 2.06 | 0.02 | 3.35 | 2.01 | 1.00 | 23,169 | 12.91 | 10.57 |
| 9 | Fan143 | 1.70 | 0.02 | 2.75 | 1.65 | 0.83 | 26,225 | 9.97 | 8.57 |
| 10 | Fan143 | 1.87 | 0.02 | 3.03 | 1.82 | 0.91 | 26,225 | 10.97 | 9.26 |
| 11 | Gao89 | 3.35 | 0.02 | 5.43 | 3.26 | 1.63 | 25,869 | 19.82 | 14.98 |
| 12 | Gao89 | 3.26 | 0.02 | 5.29 | 3.17 | 1.59 | 25,869 | 19.29 | 14.65 |
| 13 | Gao89 | 1.17 | 0.02 | 1.90 | 1.14 | 0.57 | 25,869 | 6.94 | 6.38 |
| 14 | Gao89 | 1.68 | 0.02 | 2.72 | 1.63 | 0.82 | 25,869 | 9.91 | 8.53 |
| 15 | Fan143 | 1.53 | 0.02 | 2.48 | 1.49 | 0.74 | 26,225 | 8.98 | 7.87 |
| 16 | Fan143 | 1.78 | 0.02 | 2.89 | 1.74 | 0.87 | 26,225 | 10.48 | 8.92 |
| 17 | Gao89 | 2.68 | 0.02 | 4.35 | 2.61 | 1.30 | 25,869 | 15.87 | 12.50 |
| 18 | Fan143 | 2.54 | 0.02 | 4.11 | 2.47 | 1.23 | 26,225 | 14.91 | 11.88 |
| 19 | Gao89 | 2.36 | 0.02 | 3.83 | 2.30 | 1.15 | 25,869 | 13.98 | 11.28 |
| 20 | Fan143 | 2.54 | 0.02 | 4.12 | 2.47 | 1.24 | 26,225 | 14.92 | 11.89 |
| 21 | Gao89 | 4.22 | 0.02 | 6.84 | 4.10 | 2.05 | 25,869 | 24.95 | 18.06 |
| 22 | Fan143 | 3.38 | 0.02 | 5.49 | 3.29 | 1.65 | 26,225 | 19.88 | 15.02 |
| 23 | Fan143 | 3.30 | 0.02 | 5.36 | 3.22 | 1.61 | 26,225 | 19.42 | 14.73 |
| 24 | Fan143 | 1.70 | 0.02 | 2.76 | 1.66 | 0.83 | 26,225 | 10.02 | 8.60 |
| 25 | Fan143 | 1.79 | 0.02 | 2.90 | 1.74 | 0.87 | 26,225 | 10.52 | 8.95 |
| 26 | Fan143 | 2.22 | 0.02 | 3.60 | 2.16 | 1.08 | 26,225 | 13.03 | 10.65 |

accordance with above reconstruction of the north wind using breaker bar (Fig. 4.70). However, the differences are as follows: (a) the earlier peak (about 23.5 m/s) is obviously higher than the latter peak (about 17.5 m/s); (b) the paleo-north wind reconstructed by longshore gravelly beach ridge is stronger than that reconstructed by the breaker bar in the early period of LST, but weaker in the late period of LST, which is possibly caused by the errors in calculation or parameters acquisition. The analysis is as follows.

According to Fig. 4.73, the result of the paleowind force reconstructed by longshore gravelly beach ridge varies with the water depth: when the water depth is less than 18 m, the wind speed increases sharply as the water depth increases; when the water depth is more than 18 m, the wind speed no longer varies as the water depth increases. Therefore, according to our analysis: the average water depth in LST is determined as 15 m, but the actual water depth in the early

period of LST approaches <15 m and that in the late period of LST approaches >15 m. In other words, the wind speed in the early period of LST is overestimated, and the wind speed in the late period of LST is underestimated when reconstructing paleowind force with sandy and gravelly beach ridge. However, in TST and HST, the water depth is more than 18 m, and the errors caused by water depth parameters can be neglected.

### 4.4.5   Paleo-Windfield and Sedimentary Environment

#### 4.4.5.1   Evolution of Paleo-Climate Affected by Paleo-Windfield

Eocene Upper Sha-4 Submember in the Dongying Sag, eastern China was deposited in about 45-42 Ma ago, during
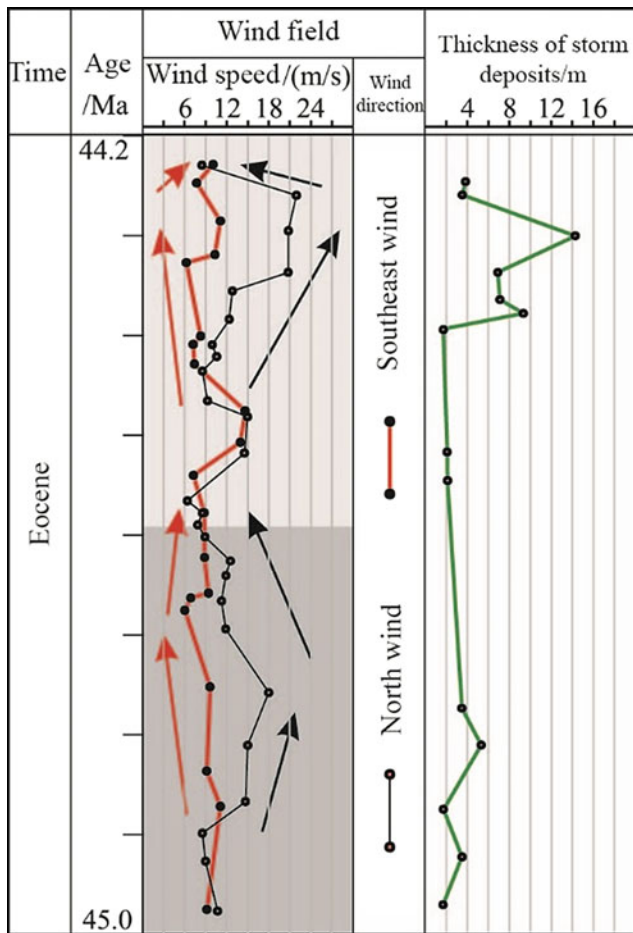
**Fig. 4.70** Curve of wind speed determined by thickness of LST breaker bar (offshore bar) in Upper Sha-4 Submember in the Dongying Sag and frequency (strength) of storm activity reflected in storm deposits

which obvious monsoon climate had appeared in eastern China, according to the latest study on the paleo-climate in the Dongying Sag in this period (Quan et al. 2011; Huber and Goldner 2012; Quan et al. 2012a, b; Wang et al. 2013), which is in accordance with this paper. According to the study by Quan et al. (2012a). During 45 Ma-42 Ma, the evolution of paleo-temperature in northern China was transited from relatively cold to relatively warm. The period of relatively cold (45–43.5 Ma) roughly corresponds to the depositional period of LST in Upper Sha-4 Submember, indicating frequent influence by strong winter wind from the polar region, which is in accordance with the significantly higher north wind speed in LST shown in Fig. 4.72. According to the previous study on the paleo-climate in this area, such as the geochemical data (Wu 2015; Song 2005), in LST of Upper Sha-4 Submember, the paleo-climate in the Dongying Sag was relatively dry and cold, providing further evidences for the north wind-dominated paleo-windfield, and the dry-cold environment caused by low-temperature

and steam-short airflow from the northern inland. The global deep-sea oxygen isotope curve also shows a slight fall in global temperature during 45 Ma–44 Ma (Zachos et al. 2001, 2008), which is consistent with the result of reconstruction. However, the reconstruction more detailed shows two increases of strength of north wind (winter wind) and two decreases of strength of southeast wind (summer wind) in LST.

The study by Quan et al. (2012a) also shows an obvious warming in eastern China during 43.5 Ma–42 Ma, which roughly corresponds to TST and HST. According to the geochemical data (Wu 2015; Song 2005), the paleo-climate in Dongying Sag became warm and humid in TST–HST. It is consistent with obviously lower north wind speed in LST and HST than in LST, as shown in Fig. 4.72, which supports the paleo-windfield in which the north wind was restricted. In addition, the global deep-sea oxygen isotope curve (Zachos et al. 2001, 2008) shows a trend of decrease in global temperature in about 42.5 Ma, which corresponds to an obvious increase in north wind speed during late depositional period of HST (close to 42.5 Ma), as shown in Fig. 4.72, and indicates another increase in the winter wind speed in late depositional period of HST. Therefore, the reconstruction is consistent with the paleo-climate at that time.

It is inferred that the variation in temperature and humidity in this area is caused by the relative strength of north wind and southeast wind. In LST, the north wind (winter wind) may be dominant, correspondingly making the climate dry and cold with low temperature and lack of rainfall. In TST, the north wind was restricted, and the summer wind may be dominant on the basis of correlation of monsoon in summer and winter (Fig. 4.70), correspondingly making the climate warm and humid, with high temperature and increase of rainfall. In HST, there was another increase in winter wind speed and a decrease in warmth and humidity, which led to a relatively warm and humid climate (Wu 2015).

### 4.4.5.2  Control of Sedimentation by Paleo-windfield

Lithofacies development was controlled by sedimentary environment. Therefore, the lithofacies and variation in lithofacies assemblage indicate the change in sedimentary environment. Differences among lithofacies in three system tracts correspond to the changes of paleo-climate caused by paleo-windfield.

According to the research by Wu (2015), in LST, the lithofacies of fine-grained rocks were dominated by stratiform evaporate, low organic content laminated gypsiferous clay rock, and low organic content laminated limestone, which are all rich in quartz and feldspar. Massive beach bar siltstone was also developed in LST. The dominant winter
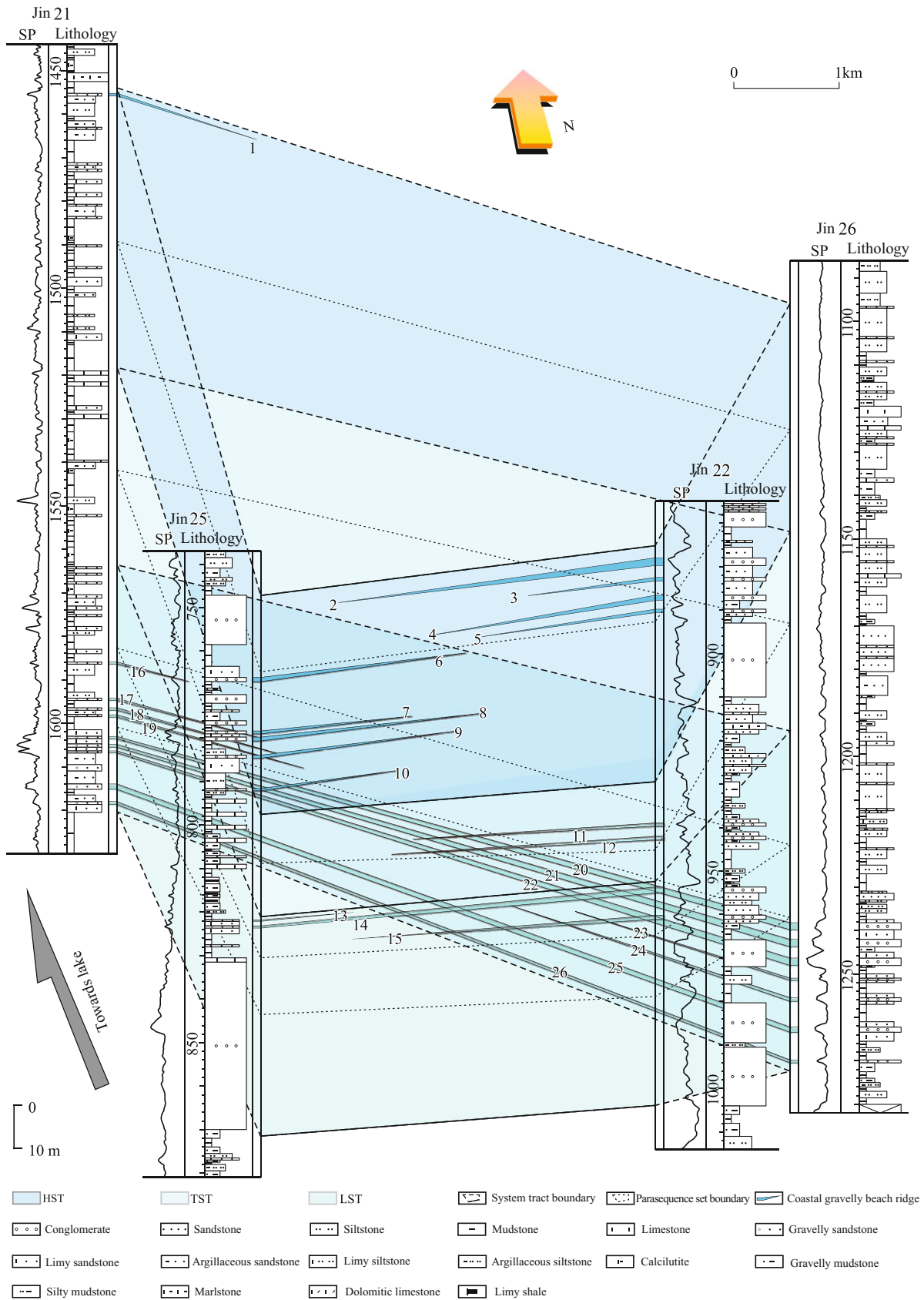
**Fig. 4.71** Fence diagram of gravelly beach ridge of Upper Sha-4 Submember in the Dongying Sag. Twenty-six stages of gravelly beach ridges are identified, including 10 in HST, 2 in TST, and 14 in LST. Well locations are shown in Fig. 4.64a

**Table 4.13**  Paleo-wave and paleo-north wind speed of 26 gravelly beach ridges bars in Fig. 4.71

| No. | Well No. | Thickness (m) | Fetch (m) | Water depth (m) | Angle between wind direction and the normal line of shoreline (°) | Wind speed (m/s) | Wind pressure coefficient (m/s) | Offshore significant wave height (m) | Wind surge (cm) | Wave setup (cm) | Wave run-up (cm) |
|-----|----------|--------------|-----------|-----------------|------|-------|--------|------|------|------|------|
| 1 | Jin21 | 0.50 | 35,977 | 50.0 | 0 | 10.32 | 12.54 | 1.22 | 0.01 | 0.12 | 0.36 |
| 2 | Jin22 | 1.55 | 51,231 | 50.0 | 0 | 21.85 | 31.54 | 3.65 | 0.09 | 0.36 | 1.09 |
| 3 | Jin22 | 0.60 | 51,231 | 50.0 | 0 | 10.32 | 12.53 | 1.45 | 0.02 | 0.14 | 0.43 |
| 4 | Jin22 | 1.10 | 51,231 | 50.0 | 0 | 16.68 | 22.63 | 2.62 | 0.05 | 0.26 | 0.79 |
| 5 | Jin22 | 0.75 | 51,231 | 50.0 | 0 | 12.32 | 15.59 | 1.80 | 0.03 | 0.18 | 0.54 |
| 6 | Jin25 | 0.95 | 43,158 | 50.0 | 0 | 15.95 | 21.41 | 2.27 | 0.04 | 0.23 | 0.68 |
| 7 | Jin25 | 0.60 | 43,158 | 50.0 | 0 | 11.07 | 13.67 | 1.45 | 0.02 | 0.15 | 0.44 |
| 8 | Jin25 | 0.75 | 43,158 | 50.0 | 0 | 13.23 | 17.01 | 1.81 | 0.03 | 0.18 | 0.54 |
| 9 | Jin25 | 0.65 | 43,158 | 50.0 | 0 | 11.80 | 14.78 | 1.57 | 0.02 | 0.16 | 0.47 |
| 10 | Jin25 | 0.45 | 43,158 | 50.0 | 0 | 8.80 | 10.30 | 1.09 | 0.01 | 0.11 | 0.33 |
| 11 | Jin22 | 0.60 | 51,231 | 32.5 | 0 | 10.17 | 12.31 | 1.42 | 0.03 | 0.14 | 0.43 |
| 12 | Jin22 | 0.75 | 51,231 | 32.5 | 0 | 12.13 | 15.30 | 1.77 | 0.04 | 0.18 | 0.53 |
| 13 | Jin25 | 0.35 | 43,158 | 15.0 | 0 | 6.91 | 7.65 | 0.81 | 0.03 | 0.08 | 0.24 |
| 14 | Jin22 | 1.30 | 51,231 | 15.0 | 0 | 17.47 | 23.95 | 2.77 | 0.19 | 0.28 | 0.83 |
| 15 | Jin22 | 0.90 | 51,231 | 15.0 | 0 | 13.26 | 17.06 | 1.97 | 0.11 | 0.20 | 0.59 |
| 16 | Jin21 | 0.50 | 35,977 | 15.0 | 0 | 9.82 | 11.80 | 1.14 | 0.04 | 0.11 | 0.34 |
| 17 | Jin21 | 0.45 | 35,977 | 15.0 | 0 | 9.06 | 10.68 | 1.04 | 0.04 | 0.10 | 0.31 |
| 18 | Jin21 | 0.55 | 35,977 | 15.0 | 0 | 10.57 | 12.91 | 1.25 | 0.05 | 0.13 | 0.38 |
| 19 | Jin21 | 0.55 | 35,977 | 15.0 | 0 | 10.57 | 12.91 | 1.25 | 0.05 | 0.13 | 0.38 |
| 20 | Jin26 | 1.60 | 49,948 | 15.0 | 0 | 20.60 | 29.33 | 3.35 | 0.26 | 0.34 | 1.01 |
| 21 | Jin26 | 1.75 | 49,948 | 15.0 | 0 | 22.00 | 31.81 | 3.63 | 0.30 | 0.36 | 1.09 |
| 22 | Jin26 | 1.90 | 49,948 | 15.0 | 0 | 23.38 | 34.27 | 3.92 | 0.33 | 0.39 | 1.17 |
| 23 | Jin26 | 0.60 | 49,948 | 15.0 | 0 | 9.85 | 11.83 | 1.35 | 0.06 | 0.14 | 0.41 |
| 24 | Jin26 | 0.95 | 49,948 | 15.0 | 0 | 13.96 | 18.18 | 2.08 | 0.12 | 0.21 | 0.62 |
| 25 | Jin21 | 1.10 | 35,977 | 15.0 | 0 | 17.92 | 24.71 | 2.40 | 0.14 | 0.24 | 0.72 |
| 26 | Jin26 | 0.60 | 49,948 | 15.0 | 0 | 9.85 | 11.83 | 1.35 | 0.06 | 0.14 | 0.41 |
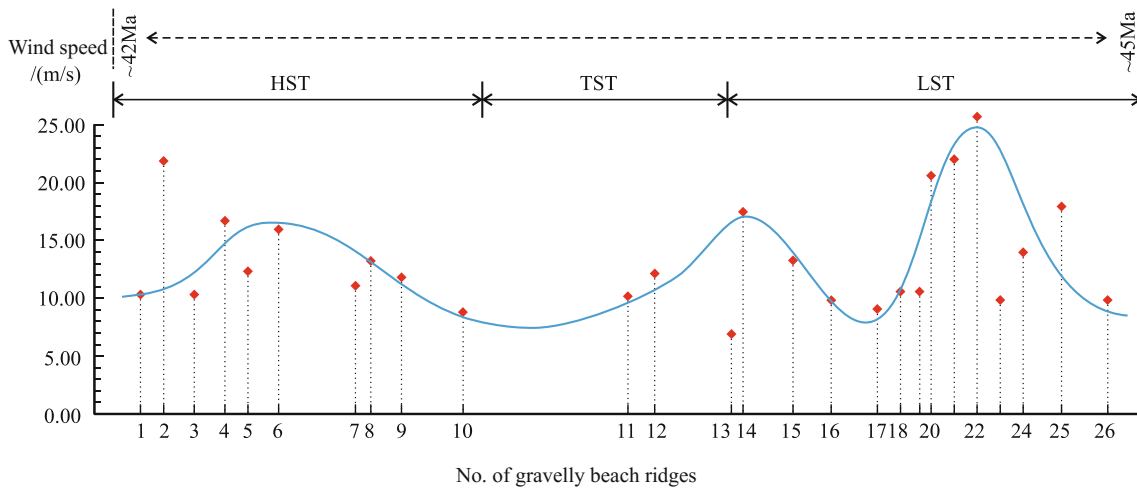


**Fig. 4.72**  Wind speed of paleo-north wind reconstructed with longshore gravelly beach ridges (modified from Wang et al., 2018)
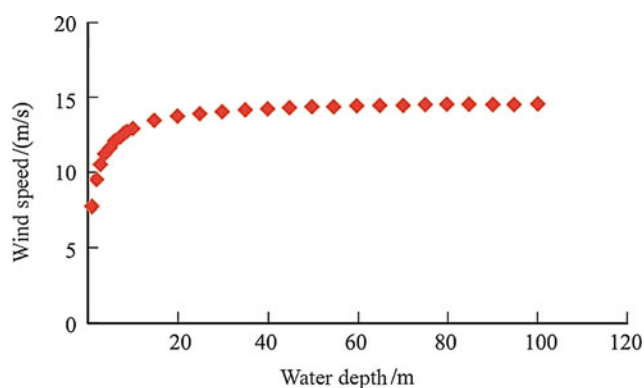
**Fig. 4.73** Relation between wind speed and water depth in Formula 2.12. Other parameters are typified as: beach ridge thickness 0.8 m, fetch 40,000 m, angle between wind direction and the normal line of shoreline 0°

wind, dry and cold climate, and shallow lake basin in LST led to (a) relatively strong provenance and abundant terrigenous detritus transported into the lake through delta; (b) low biological productivity, weak water reductivity, and less content of organic matters which are not preserved well in sediments; (c) strong evaporation, salts precipitation with high salinity and stratification in the lake water, and the lithology of fine-grained rocks dominated by siltstone and low organic content laminated creaming clay rocks; and (d) strong windfield and full development of beach bar deposits controlled by wind-wave action (Fig. 4.48).

In TST, the lithofacies of fine-grained rocks are dominated by laminated dolomitic mixed fine-grained rocks and low-high organic content laminated limestone, with content of organic matter and pyrite significantly increased in sediments. The humid and warm climate dominated by the summer wind led to (a) weaker provenance, rapid rise of lake basin waterbody, retrogradation of delta, and beach bar from the lake margin to the continent, and decreasing input of terrigenous clasts, and fine-grained rocks in TST not dominated by quartz and feldspar; (b) obviously decreased gypsiferous deposits and algal bloom which provide abundant organic matters with warm and humid climate; the gradually deepening waterbody and stronger reducibility provides better preservation conditions of organic matters and increases content of organic matters in sediment; and (c) weaker windfield, and restricted development of beach bar controlled by action of wind and wave (Fig. 4.51).

Among the lithofacies of fine-grained rocks in HST, the laminated limestone with high organic content is not developed, and the laminated limestone with medium organic content decreases greatly. Early and middle depositional period of HST, the lithofacies assemblage was dominated by laminated limy mixed fine-grained rocks and low organic content laminated limestone. In late period of HST, the lithofacies assemblage was dominated by medium

to low-organic content laminated limestone, which is due to another strong north wind, lower temperature, reduced rainfall (warmer and more humid than in LST, relatively stable lake level, and another enhancement of provenance. Another weak progradation or aggradation of delta and beach bar in the lake margin toward the lake leads to increase of terrigenous detrital content and non-dominance of lime. Algae decreases and content of organic matter in deposits reduced, and not easily preserved. Beach bar deposits were more abundant than in TST but less abundant than in LST (Fig. 4.54).

### 4.4.6  Analysis of Factors Controlling Distribution of Beach Bar Sandbodies

The development of beach bar is controlled by many factors, e.g., geomorphologic conditions (macroscopic and microscopic geomorphologies), sequence evolution, conditions of water depth, storm wave, and provenance supply, etc.

#### 4.4.6.1  Control of Beach Bar by Paleo-Structure and Paleo-Geomorphology

The distribution of sandbodies is mainly controlled by tectonic movement of basin. The development of beach bar system is closely related to tectonic movement episode of basin. In faulted basin, for example, a vast shoreland belt is developed in the period of relatively stable tectonic movement and flat paleo-geomorphology (e.g., early phase of rift and fault-depression conversion period), which benefits forming beach bar (Lin et al. 2010).

Dongying Sag, a typical continental faulted basin, has experienced fault-depression–extinction. In the sedimentary period of Upper Sha-4 Submember, Dongying Sag stays in the initial fault period (Fig. 4.3), i.e., early period of fault basin, with relatively weak tectonic movement of basin, flat topography, and shallow waterbody, and the basin is characterized by large lake area, flat lakebed, and vast shoreland belt, which benefits developing and forming beach bar (Sun et al. 2003; Li 2009).

The paleo-geomorphology controlled by tectonic movement plays an important role in formation and distribution of beaches and bars (Sun et al. 2003; Chang et al. 2004). In the sedimentary period of Upper Sha-4 Submember in the Dongying Sag, from a macroscopic view, faults developed along the margin of or inside the lake basin controlled the sedimentary environment and sedimentary system of lake basin, and the lake basin can be divided into north steep slope belt, south gentle slope belt, EW axial belt, central high belt, and Boxing, Lijin, Niuzhuang, and Minfeng Sub-Sags. The north steep slope belt has a narrow shoreland zone, which was not favorable to massive beach bar development. Beach bar deposits were widely developed in the

south gentle slope belt and central high belt (Figs. 4.48, 4.51 and 4.54). In terms of structural location, beaches and bars were mostly developed in the relatively flat area. The development of beach bar was also controlled by microscopic paleo-geomorphology (Wang et al. 2011). The small-scale protruding topography acted as energy dissipation zone of wave, where the hydrodynamic force decreases, and the sediments tend to deposit. Overall, the periphery of positive geomorphic units is favorable to beach bar development, which is confirmed by beach bar deposits developed in the subaqueous paleo-uplifts in the Dongying Sag (Fig. 4.59). Thus, the beaches and bars were greatly controlled by paleo-geomorphology and were better developed in gentle slope shoreland zone and on slopes of positive geomorphic units.

Thus, paleo-structure and paleo-geomorphology is one of the factors influencing formation and distribution of beach bar sandbodies.

### 4.4.6.2   Control of Distribution of Beach Bar Sandbody by Sequence Stratigraphic Framework

The beach bar system is developed in the shoreland zone between wave base level and shoreline, and the distribution of beach bar sandbody is controlled by location of shoreline and wave base level, which is migrated significantly due to variation in sea (lake) level. Thus, the beach bar system is sensitive to variation in accommodation space in basin resulted from variation in sea (lake) level (Lin et al. 2010). In LST, the shoreline and wave base level is massively migrated toward the center of lacustrine basin, and correspondingly moved toward shoreland zone, with progradation

of beach bar; during lacustrine transgression, the shoreland zone is moved toward continental, resulting in retrogradation of beach bar sandbody toward shore; during HST, the beach bar sandbody is stabilized, and vertically aggraded or slightly migrated toward the center of lake basin (Tian and Jiang 2012).

In Upper Sha-4 Submember of the Dongying Sag, for example, the beach bar sandbodies are developed in varying degrees in different system tracts. The gravelly beach bars are mainly developed in LST and less in TST and HST, and the carbonate beach bars are locally developed in HST (Figs. 4.45 and 4.74). The deposition of Upper Sha-4 Submember in the Dongying Sag occurred during the initial development stage of fault basin, when the fault basin was basically formed. During forming LST, water bodies in the basin were in high-frequency oscillation and slowly rose, and conditions such as water depth, provenance, and hydrodynamic force are favorable to beach bar development. Thus, the beach bar sandbodies are generally well developed in LST, with wide and continuous planar distribution mainly in southwestern Lijin Sub-Sag, Boxing Sub-Sag, and southeastern Dongying Sag (Fig. 4.47) and high sandstone/ strata thickness ratio between 20 and 60% (Fig. 4.46).

However, in TST and HST, the massive beach bar is hardly formed in most lake basin due to increase in water-body depth. In TST, the beach bar always shows the isolated stripped shape and limited planar distribution due to deepened water, enlarged lake basin, and insufficiently supply of terrigenous debris (Fig. 4.50), with sandstone/strata thickness ratio between 10 and 30% (Fig. 4.49). In HST, the gravelly beach bar is rarely developed, with isolated elliptical sandbody (Fig. 4.53), and sandstone/strata thickness
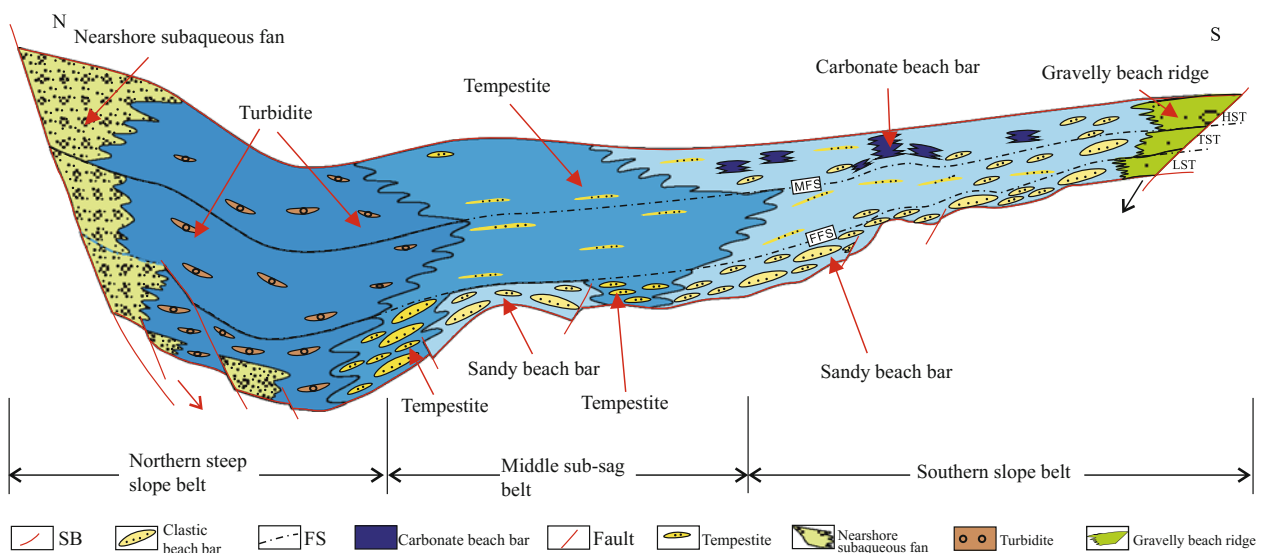


**Fig. 4.74**   Distribution model of beach bar sandbodies in the western Dongying Sag (Tian and Jiang 2012)

ratio between 10 and 50% (Fig. 4.52). However, the carbonate beach bar is developed in the periphery of Pingfangwang High and part of Niuzhuang Sub-Sag (Fig. 4.54).

### 4.4.6.3  Control of Beach Bar by Lake Level Fluctuation and Transition of Shoreline

The beach bar is potentially developed in the shoreland between normal wave base and shoreline (flood level), and the shoreline limits progradation of beach bar toward continent, and the wave base limits development of beach bar toward sea (lake). Due to variation in relative water level resulted from episodic tectonic movements and periodic climatic change, the lake shoreline varies correspondingly. The distribution of beach bar is controlled by migration of shoreline, and the terrain and rise and fall of lake level. Gentle slope, large rise, and fall of water level results in large migration of shoreline, and wide distribution of beach bar. Conversely, the beach bar has a narrow distribution. With flat paleotopography in south Dongying Sag, the vertical change of lake level would results in large migration of shoreline (Tian and Jiang 2012). Frequently, large variation in paleo-shoreline causes large-scale planar distribution and vertical superimposition of sandbody (Jiang and Liu 2010).

The beach bar sandstone is developed in wholly shallow water, and the sedimentary structure is characterized by wave mark structure, wave rippled bedding, and bioturbation in shallow water (Fig. 4.37). With relatively small accommodation space, the frequent vibration of water depth plays important role in development and preservation of beach bar. In short term of base level decline, the role of provenance is strengthened, forming beach bar, which is possibly preserved in the period of rise. Thus, the beach bar is possibly preserved around transitional surface of fall/rise of short-term base level.

A complete parasequence of beach bar represents an evolution cycle of beach bar sedimentation, and the top and bottom correspond to surrounded FS (Cao et al. 2009). The mudstone interlayer between beach bars represents small-scale flood surface. Each sequence of beach bar sandbody corresponds to fall of lake level, and preservation of beach bar indicates rise of lake level. In LST, the beach bar sandbody is characterized by vertical superimposition (Figs. 4.45 and 4.47), indicating that beach bar sandbody of LST is controlled by lake level of high-frequency oscillation. The lake level of LST in the Dongying Sag stays in condition of "high-frequency oscillation", and during fall of relative lake level, the detrital material is migrated to off bank from near bank, forming beach bar; during rise of relative lake level, the beach bar is preserved. Thus, "high-frequency oscillation" causes vertically frequent thin interbed, and massive plane distribution of beach bar sandbody (Jiang et al. 2011).

During lacustrine transgression, the water depth is increased, and the shoreline and wave base are wholly migrated to continent, and the relative lake level shows weak oscillation, resulting in retrogradation of beach bar sandbody toward shoreline (Fig. 4.51). In HST, the lake level is stabilized, and the beach bar sandbody is prograded toward the center of lake basin (Fig. 4.54). Thus, the beach bar is less developed in TST and HST than LST. In addition, the paleo-water depth is an important factor controlling development of carbonate beach bar. The paleo-water depth governs forming carbonatite. Shallow water depth provides little space for accommodation of carbonatite, which is poorly preserved. Thus, in TST and HST, the content of carbonatite is increased significantly, and evenly the carbonatite beach bar is developed in HST (Fig. 4.54).

### 4.4.6.4  Control of Beach Bar by Paleo-Wind (Wave) Dynamical Conditions

The second modification of wave directly makes beach bar form. In the continental lake basin, hydrodynamic force is mainly from wind force; thus, both are closely related.

In windward side of basin, the deepwater wave changes to shallow water wave from deepwater to shallow water area and further to shoreline, causing changes of wave. The wave shoaling, breaker, wave regeneration, breaking of regenerated wave, surf, and swash occur successively inside the area shallower than wave base (Figs. 2.10 and 4.64b). Beaches and bars alternate in wave dynamic zones (Figs. 2.10, 4.39 and 4.64). The shape of bars in shallow water zone will change correspondingly when wave parameters change and new wave is formed. The accumulation of beaches and bars shows obvious zoning due to different hydrodynamic forces. In addition, the propagation direction of wind waves governs the beach bar distribution. Generally, the normally injected wave always results in beach bar parallel to the shoreline, while the wave obliquely crossing the shoreline always results in beach bar obliquely crossing the shoreline (Fig. 1.13d).

According to hydrodynamic characteristics and development location, the beach bar in the study area is divided into coastal bar (beach ridge developed in the swash zone), coastal beach (swash zone), nearshore bar (surf zone), inter-bar beach (wave regeneration zone or inner breaker zone), offshore bar (breaker zone), and outer beach (wave shoaling zone) (Figs. 4.39a and 4.64b).

The south gentle slope belt of Boxing Sub-Sag—Niuzhuang Sub-Sag has gentle topography and wide distribution and has strong hydrodynamic force due to winter monsoon (northerly wind), which is similar to hydrodynamic characteristics of non-barrier coastal zone in marine environment, with obvious hydrodynamic zoning. The wave shoaling zone, breaker zone, wave regeneration zone, surf zone, and swash zone occur successively from interior lake to shore

bank. Varied wave characteristics and hydrodynamic force strength govern different forming and zoning of sediments. Thus, extensive beaches and bars are developed in shore-shallow lacustrine area of southern gentle slope belt of Boxing Sub-Sag—Niuzhuang Sub-Sag (Fig. 4.64).

However, in the belt from Binxian Bulge-Chenjiazhuang Bulge southward, the summer monsoon (southerly winds) is weak, with low wind speed and weak wave energy, which had limited influence on secondary distribution of nearshore sandbodies (e.g., fan-delta front sandbodies). The beach bar has narrow distribution due to limited transport capacity and short transport distance of wave (Fig. 4.64).

The irregular shoreline and complex subaqueous topography cause refraction of wave and thus dispersion or concentration of wave energy. Figure 4.59 shows that the surrounding area of convex bank and positive structural units and the windward side of slope units are favorable places for beach bar development, and the difference of wave energy causes microfacies differentiation of beaches and bars along the shoreline.

According to above discussion (Sect. 4.4.5), the paleo-windfield not only impacts the waterbody and produces wave but also the activities of paleo-atmospheric flow field, governing the temperature and humidity of climate and controlling the beach bar in a certain way. For example, during the LST period dominated by north wind, the climate was dry and cold with strong physical weathering, and the beach bar was mainly terrigenous detrital. However, in TST and HST periods controlled by southeast wind, the climate was warm and humid with strong chemical weathering, and the biological action was intense in the lake, resulting in high yield of carbonatite and obviously higher content of carbonatite in the beach bar, and even carbonate beach bar in HST.

#### 4.4.6.5 Control of Beach Bar by Paleo-Source Conditions

The provenance is one of basic factors controlling sediment types and distribution and is the material basis. Especially in the shore-shallow lacustrine beach bar resulted from secondary transport and sedimentation, the provenance is originated from modification and secondary distribution of surrounding sandbodies by wave. Thus, the enrichment degree of provenance determines the forming of beach bar. With abundant provenance supply, the sandy beach bar is extremely developed, but the carbonate beach bar is often formed when provenance supply is deficient (Fig. 1.6).

The Dongying Sag is bounded by uplifts or highs, adjoining Chenjiazhuang and Binxian Bulges to the north, and Luxi Uplift and Guangrao Bulge to the south, Qingcheng Bulge to the west, and Qingtuozi Bulge to the east, with sediments supplied from several directions. However, due to weak tectonic activities of Upper Sha-4 Submember

sedimentary period, the detrital material was only deposited as small deltas and fan-deltas at the margin of the basin. These sandbodies provided limited material basis for forming sandy conglomeratic beach bar (Li 2009). Affected by wave, the beach bar sandbodies were formed in the front edge of fan-delta in western Lijin Sub-Sag, south slope area of Boxing Sub-Sag and Niuzhuang Sub-Sag. On the plane, Binxian Bulge in the north slope belt is near provenance, with development of fan-delta. Affected by the wave, these sandbodies provided material for the formation of beach bar, but had limited distribution due to topographic slope and wind wave force. The linear alluvial fans were developed near the slope toe of Luxi Uplift in the south slope area of Boxing Sub-Sag (Li 2009), and these fan sediments were screened by the wave caused by strong north wind. The gravels were locally sorted, rounded, and accumulated, with coastal gravelly beach bar formed, and the silt-medium sand was migrated to the shoreland zone, with nearshore bar, inter-bar beach, offshore bar, and outer beach formed (Fig. 4.64). Similarly, the beach bar developed in south slope of Niuzhuang Sub-Sag was formed with sediments from near-provenance delta and southward wave action. However, the central belt between Lijin Sub-Sag and Boxing Sub-Sag stayed in area with poor provenance or secondary provenance supply and with insufficient terrigenous detrital supply and had relatively high content of limy cement in beaches and bars (Li 2009).

Inside sequence stratigraphic framework, the supply of provenance is sufficient and the beach bar is developed in LST. However, in TST and HST, the poor provenance limits the development of sandy beach bar, but benefits the forming of carbonate beach bar. In HST, the carbonate beach bar is even locally developed in Pingfangwang Bulge and Niuzhuang Sub-Sag and is dominated by reef limestone, biolithite limestone, oolitic limestone, micrite, and dolomitic limestone.

### 4.4.7 Division of Windfield-Source-Basin System

The evolution of Upper Sha-4 Submember in the Dongying Sag is interpreted with "windfield-source-basin" system. According to development background of sedimentary system, the sedimentary system of Upper Sha-4 Submember in the Dongying Sag is subdivided into four subsystems (Fig. 4.75).

(1) Basin-controlled system

During the sedimentary period of Upper Sha-4 Submember in the Dongying Sag, the low-lying area with water depth >15 m (Figs. 4.56 and 4.57) was far from provenance, and the water depth was greater than storm wave base. The
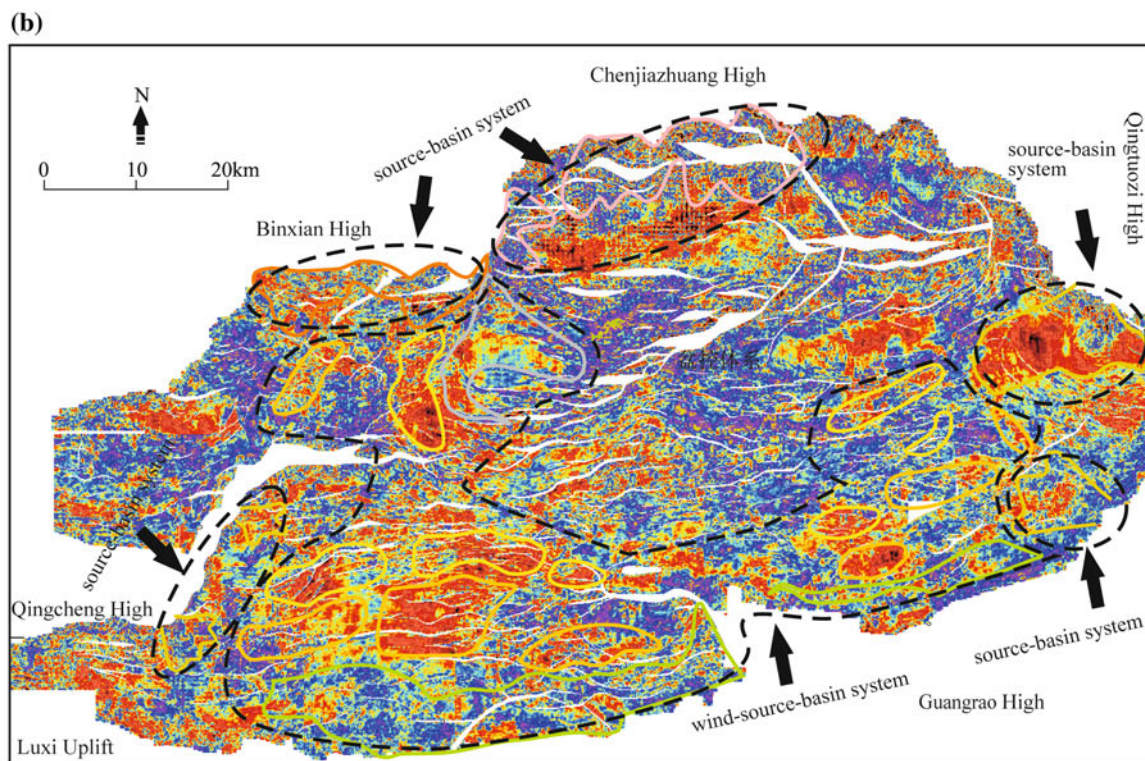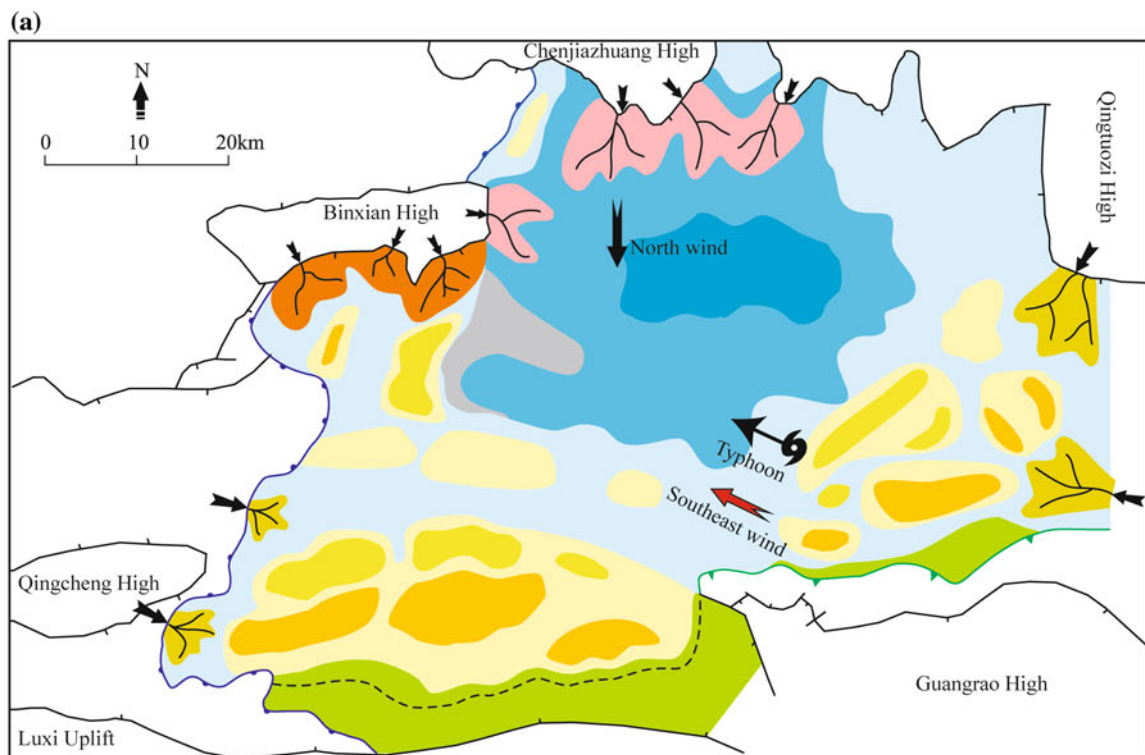
**Fig. 4.75** Model of Upper Sha-4 Submember windfield-source-basin system in the Dongying Sag (LST). **a** Distribution of LST sedimentary facies and prevailing wind direction; **b** properties of LST dominant amplitude and division of wind-source-basin system

sedimentation there was dominated by the geological agent of the basin itself, and the impact of provenance and wind force was negligible. The basin was controlled by its own processes such as suspension and settling of sediments, and chemical rock forming controlled by biological and chemical action. The study area was controlled by laminated limestone and laminated clay rock with medium–high organic matter (Fig. 4.44) mainly developed in eastern Lijin Sub-Sag and Minfeng Sub-Sag (Wu 2015).

(2) Source-basin system

The Dongying Sag is a typical half-graben faulted lake basin, and the basin edge is divided into steep slope belt, gentle slope belt, axial belt, with different genesis and distribution of sandbodies. When the wind dynamics is negligible, if the windfield of Upper Sha-4 Submember in Dongying Sag is controlled by monsoon system with the winter monsoon (north wind) stronger than summer monsoon (south wind), different sedimentary systems will be formed with varying provenances in different paleo-geomorphologic backgrounds in the windward side of lake basin edge (along northern boundary fault) with weak wind and the lake basin edge (EW axis edge) without wind dynamics. The sedimentary system is divided into three categories. The first is subaqueous gravity flow system in the downthrown side of Chennan Fault. It is controlled by marginal faults and is near high mountain abrupt cliff, with large water depth gradient. The provenance provided by the Chenjiazhuang Bulge directly flowed into deepwater area as gravity flow, forming subaqueous gravity flow system, e.g., nearshore subaqueous fan and sublacustrine fan (Figs. 4.48, 4.51 and 4.54). The second is the fan-delta system in the south slope of Binxian Bulge. The fault displacement in the northern boundary fault of the Dongying Sag gradually decreases from east to west, and thus, the gradient of northern steep slope belt decreased from east to west (Fig. 4.59). Toward the south slope of Binxian Bulge, the gradient of paleotopography slows down, and the water depth gradient decreases compared with eastern side (Figs. 4.56 and 4.57), with fan-delta system dominated (Figs. 4.48, 4.51 and 4.54). The third is EW axial delta system. The entrance of provenance in the long axis of basin in eastern and western sides (Figs. 4.59 and 4.60) is characterized by gentle slope (Figs. 4.59 and 4.60), small water depth gradient (Figs. 4.56 and 4.57), and fluvial process stronger than water storing, forming a normal delta system (Figs. 4.48, 4.51 and 4.54).

(3) Windfield-basin system

The Upper Sha-4 Submember of Dongying Sag also includes the sedimentary system controlled by windfield and basin,

when the terrigenous detrital import is negligible. The windfield-basin system is formed by its sediments under wind dynamics. The sedimentary system in Upper Sha-4 Submember in Dongying Sag has locally developed biodetritus beach bar (Bin706 Well Block) and ooid limestone beach (Li 2009), indicating the dominance of windfield-basin system. The windfield-basin system is active in HST.

(4) Windfield-source-basin system

The detrital beach bar sediments and storm deposits are typical products resulted from interaction between end members of "windfield-source-basin" system, which is well manifested in Upper Sha-4 Submember in Dongying Sag: (1) the windward side, abundant provenance, gentle slope belt, positive topography, and transition of lake level tend to result in the massive and thick beach bar sandbodies. Boxing Sub-Sag and the south slope of Niuzhuang Sub-Sag were in such a sedimentary setting. Boxing Sub-Sag is characterized by gentle landform and local highs (Fig. 4.59). Linear alluvial fan apron developed at the toe of Luxi Uplift provided massive terrigenous clasts, forming massive beaches and bars due to southward wave resulted from prevailing winter monsoon (Figs. 4.48, 4.51 and 4.54). The sedimentation in LST was characterized by frequent oscillation of lake level and vertical superimposition of beach bar sandbodies (Fig. 4.45). Similarly, the south slope of Niuzhuang Sub-Sag was filled with abundant terrigenous clasts from surrounding deltas. Massive and vertically superimposed beach bar sandbodies were formed in the front and at the edge of deltas under aforementioned background of paleo-geomorphology, paleo-windfield, and sequence evolution (Figs. 4.48, 4.51 and 4.54). The south slope of Binxian Bulge and the edge of fan-deltas also had above sedimentary background, but were mainly controlled by the wave resulted from summer monsoon (south wind). Generally, the summer monsoon was weaker than winter monsoon (Fig. 4.70); thus, the beach bar was less developed in the north slope than in the south slope of the Dongying Sag; (2) the storm action, abundant provenance, deepwater depth, and steep slope were favorable to the development of storm deposits. The western Lijin Sub-Sag had a large amount of clasts supplied by the near-provenance fan-deltas (Figs. 4.48, 4.51 and 4.54) and is near basin edge fault, with steep slope (Fig. 4.58) and large water depth gradient (Figs. 4.55 and 4.56). Due to cyclone (typhoon) from western Pacific, seiche occured, and storm deposits were formed and preserved below normal wave base (Fig. 4.43).

Affected by single factor or multiple factors of wind, source, and basin, different sedimentary systems were formed in different locations in the sedimentary period of Upper Sha-4 Submember in Dongying Sag.

## 4.5  Significance of Research on Windfield-Source-Basin System and Prospect of Its Application

### 4.5.1  Significance of Paleo-Climate

The methods of paleo-windfield reconstruction are further applied to the Upper Sha-4 Submember, a classical block of beach bar development in the Dongying Sag. Main applications are as follows.

(1) The trend and lateral asymmetry of breaker bar and the thickness of breaker bar are used to reconstruct the paleowind direction and force, respectively. By applying the methods to Upper Sha-4 Submember of Boxing Sub-Sag, it is found that during LST (ca. 45 Ma) of Upper Sha-4 Submember, north wind of 6.4–21.9 m/s coexisted with southeast wind of 6.3–14.6 m/s, which are interpreted as the paleo-East Asian monsoon. The wind force of the north wind (winter wind) and the southeast wind (summer wind) showed cyclic inverse correlation (Fig. 4.70). The speed of north wind had two cycles of "increase–decrease", while the southeast wind had two cycles of "decrease–increase" in the same period. The southeast wind generally had a lower speed than the north wind, which is very similar to the features of present East Asian monsoon. In addition, storm processes were more frequent when there was a large difference in speed between winter wind and summer wind, which is the earliest direct evidence for the existence of the paleo-East Asian monsoon. The age of paleo-East Asian monsoon is estimated back to 45 Ma.

(2) The thickness of the longshore gravelly beach ridges is used to quantitatively reconstruct the paleowind force. By applying this method to the longshore gravelly beach ridges of the south slope of Boxing Sub-Sag of Upper Sha-4 Submember in Dongying Sag, it is found that during the depositional period of Upper Sha-4 Submember, the paleo-north wind (winter wind) witnessed two increases (the early peak of 20–25 m/s and the later peak of 15–20 m/s) in LST, a decrease (to 7–10 m/s) in TST, and another increase (to 13–17 m/s) in HST (Fig. 4.72). The evolution of the paleo-windfield matches well with the evolution of other paleo-climate parameters such as temperature and humidity and has global comparability (4.4.5.1). The study shows that during the depositional period of Upper Sha-4 Submember in Dongying Sag, the windfield controlled the changes of climate parameters such as temperature and humidity and controlled the lithofacies of fine-grained sedimentary rocks (4.4.5.2).

### 4.5.2  Significance for Petroleum Geology

(1) Basin system controlled petroleum sources

Laminated limestone with medium–high organic content was developed in the low-lying areas in TST and HST of Upper Sha-4 Submember in Dongying Sag (Wu 2015) and was distributed with the thickness from tens of meters to hundreds of meters in the low-lying areas of Lijin Sub-Sag and Minfeng Sub-Sag. These source rocks have carbonate rock content more than 50% and clay content generally less than 15–20%. Among these fine-grained rocks, high-quality source rocks are those with total organic carbon (TOC) of 3–5.1%, organic matter types dominated by I–II1, good kerogen types, vitrinite reflectance (Ro) of 0.6-1.0% and high degree of evolution (Wang et al. 2012). In addition, the laminated limestone with medium–high organic content in the study area was formed in a relatively warm and humid climate controlled by weak windfield when an algal bloom provided abundant I–II1 organic matter, which helped the formation of high-quality source rocks.

Meanwhile, these source rocks also acted as cap rocks. For example, source rocks acted as seal when they supplied oil to lithologic traps. Distributed in the sub-sag belt, steep slope belt, gentle slope belt, and the flank of central anticline belt of Sha-4 Submember in Dongying Sag, the lithologic reservoirs are mainly "self-source rocks and self-reservoirs".

(2) (Windfield) source-basin system controls reservoirs and migration
① Windfield-source-basin system controls the quality of reservoirs

Large delta or fan-delta systems are developed along the long axis of Dongying Sag and their sandbodies host a part of petroleum in Gaoqing Oilfield, Guangli Oilfield, and Wangjiagang Oilfield. Fan-delta system and subaqueous gravity flow system are developed along the northern steep slope belt and their sandbodies host a part of petroleum in Shengtuo Oilfield, Binnan Oilfield, and Shanjiasi Oilfield. All the oilfields mentioned above are found in thick sandbodies controlled by major provenances.

In addition to frame sandbodies along the sediment supply direction from major provenances, the sandbodies of shoreland beach bar outside the major provenances can also have high-quality reservoirs (Li 2009). The formation of these sandbodies is closely related to the windfield-source-basin system, and a part of petroleum in Zhenglizhuang Oilfield

and Daluhu Oilfield exists in them. Beach bar sandbodies have become new domains for reserve and production ramp-up, with fairly good exploration and development effect in eastern basins of China.

② Basin system controls petroleum migration pathways

Frame sandbodies are the main places for petroleum accumulation and migration. The frame sandbodies which are widespread, superimposed and good in physical properties have high efficiency of petroleum migration. Once hydrocarbons are out of source rocks, they will migrate from high potential belts to low potential belts after entering frame sandbodies and accumulate. Petroleum migration pathways are closely related to the fault belts formed by tectonism for they can link up the sandbodies of poor vertical connectivity. For example, the Dongying Sag is a half-graben faulted basin with well-developed fault structures: the first-order faults such as Gaoqing-Pingnan Fault and Chennan-Yong'an-Qingtuozi Fault were developed earlier and controlled the formation of sags; the second-order faults such as Shengbei fault belt, Chenguanzhuang-Wangjiagang fault belt, Liangjialou-Xianhe fault belt, and Boxing fault belt generally control the stratigraphic development and petroleum accumulation of their own structural belts; the third-order faults derived from the second-order faults are small in fault throw, short in extension, and large in number. Numerous are 4–5 order faults and even lower order faults and fractures that cannot be identified by normal seismic profiles. Many fault belts (such as Dongying-Xinzhen complex fault belt) were continuously active after the main hydrocarbon expulsion stage of source rocks, and these faults and fractures will be crucial petroleum migration pathways in the Dongying Sag if they link source rocks with reservoirs.

③ Accumulation dynamics in basin-source system

The abnormal high pressure in strata often becomes the driving force of petroleum migration, behind which one of the reasons could be the change of provenance properties. For example, in the Dongying Sag, the under-compaction of fore-deltas and deep lacustrine mudstone of Sha-3 and Sha-4 Submember was formed due to the rapid progradation of Dongying deltas after the deposition of Sha-4 Submember. Then, dense shells or sealing layers were formed by full compaction between thick overlying delta sandstone and the lower thick mudstone, and abnormal high pressure occurred in strata from the depth of 2200 m (Feng et al. 2006; Wang

et al. 2012), with an abnormal pressure compartment in Sha-3 Member to Upper Sha-4 Submember (Wang et al. 2012). These abnormal high-pressure belts are usually in the deep part (such as sub-sag belts) of the second-order structural belts. Fluid pressure in the pressure compartment continuously increased during the hydrocarbon generation and clay mineral transformation and it would flow from high potential belts (source rock belts) to low potential belts (reservoir belts) when it was close to or over the bursting pressure of boundary rock strata.

(3) Windfield-source-basin system and petroleum accumulation

According to the influence of windfield-source-basin system on sources, reservoirs, caps, and migration mentioned above, there are good source-reservoir- seal assemblages in Upper Sha-4 Submember in Dongying Sag. Taking western Boxing Sub-Sag as a specific example, analyses are as follows (Fig. 4.76): ① the high-quality source rocks in TST and HST are both source rocks of high quality and efficiency and good overlying caprock; ② Lijin Sub-Sag is advantageous in space allocation of sources and reservoirs since it is located in the steep slope zone, close to the provenance, and has rapid facies change from coarse-grained fan-delta sandbodies to deepwater mudstone deposits, close to potential source rocks; shore-shallow lacustrine beach bar are favorable to reservoir development because it is repeatedly flushed by waves, resulting in high degree of sorting and roundness; storm beach bar is beneficial to forming lithologic reservoirs for its sediments are from fan-deltas (a small part from shore-shallow lacustrine beach bar) and it is developed in deeper water along steep slope under the action of storm waves, with source rocks surrounded; ③ under the abnormal high pressure in Upper Sha-4 Submember and Sha-3 Member, petroleum migrated along frame sandbodies, boundary faults, fractures, and fissures near the second-order faults and accumulated in reservoirs of relatively low pressure.

Under the above action, from low oil-generating sub-sags to structural highs of sub-sag margin, with gradually shallower depth and lower strata pressure, the lenticular lithologic reservoirs gradually change to updip pinch-out lithologic reservoirs and fault-rollover anticline reservoirs (structural reservoirs), with decreasing petroleum filling degree, and reservoirs without edge water, bottom water or oil (dry reservoirs) gradually change to reservoirs with oil-water interbeds and obvious edge water and bottom water (Fig. 4.76).
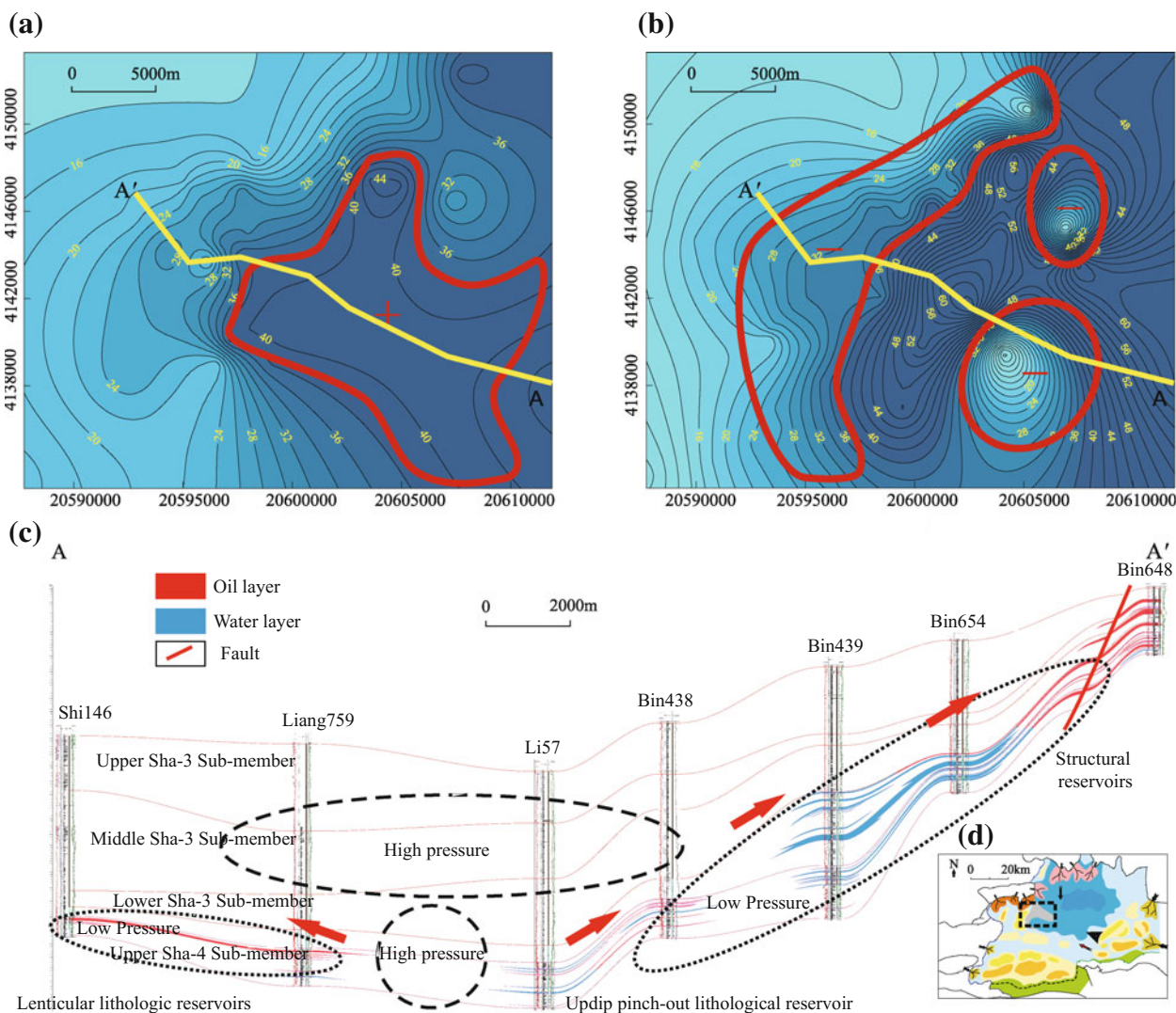
**(a)**

**(b)**

**(c)**



**Fig. 4.76** Accumulation model of western Lijin Sub-Sag in the Dongying Sag. **a** Distribution of sedimentary facies of LST in Upper Sha-4 Submember in the Dongying Sag, black dashed line represents location of **b** and **c**; **b** contour of formation pressure of Sha-3 Member (Unit: MPa), the black dashed box in A indicates location of blocks, "+" indicates high-pressure area; **c** contour of formation pressure of Upper Sha-4 Submember (Unit: MPa), the black dashed box in A indicates location of blocks, "−" indicates low-pressure area; **d** AA' reservoir profile, yellow full line in **b** and **c** indicates profile location

## References

Allen MB, Macdonald DIM, Xun Z et al (1997) Early Cenozoic two-phase extension and late Cenozoic thermal subsidence and inversion of the Bohai Basin, Northern China. Mar Pet Geol 14 (7):951–972

Cao YC (2003) Study on the sequence stratigraphy and its forming mechanism of Paleogene in Jiyang depression. Graduate University of Chinese Academy of Sciences, Guangzhou Province

Cao YC, Wang J, Liu HM et al (2009) Sedimentary characteristics and models of beach-bar sandbodies in the upper part of the fourth member of Paleogene in the south slope of Dongying depression. J China Univ Petrol 33(6):5–10

CERC (1977) Shore Protection Manual, vol 3. U.S. Army Coastal Engineering Research Center, Fort Belvoir, VA

Chang DS, Lu GC, Kong FD et al (2004) Analysis on exploration of Lake shallow-water beach and bar oil and gas reservoirs in Dagang exploration area. China Petrleum Explor 2:26–33

Chen DG, Peng ZC (1985) K-Ar ages and Pb, Sr isotopic characteristics of Cenozoic volcanic rocks in Shandong, China. Geochimica 4:293–303

Feng YL, Li ST, Zou CN (2006) Sequence stratigraphy of continental fault basins: a case study of Dongying sag in Bohai Bay Basin. Science Press, Beijing

Feng Y, Li S, Lu Y (2013) Sequence stratigraphy and architectural variability in late Eocene lacustrine strata of the Dongying depression, Bohai Bay Basin, Eastern China. Sed Geol 295:1–26

Gui BL (2008) The palaeogeomorphologic reconstruction of Es2 in Zhuangxi area, Bohai Bay Basin. China University of Geosciences, Beijing

Guo YX, Sui FG, Lin HX et al (2009) Discussion on the division and correlation of glutinite sedimentary period by time-frequency analysis—a case study of Sha4 to Sha3 member of northern abrupt slope zone in Bonan Depression. Petrol Geol Recovery Effi 16 (5):8–11

Hu XY (2008) The palaeogeomorphologic reconstruction of Es4s in Zhuangxi area, Bohai Bay Basin. China University of Geosciences, Beijing

Hu S, O'Sullivan PB, Raza A et al (2001) Thermal history and tectonic subsidence of the Bohai Basin, Northern China: a Cenozoic rifted and local pull-apart basin. Phys Earth Planet Inter 126(3):221–235

Huber M, Goldner A (2012) Eocene monsoons. J Asian Earth Sci 44:3–23

Jiang ZX, Liu H (2010) Lacustrine palaeoshoreline and its controls on sandbodies and hydrocarbon. J Palaeogeogr 12(5):589–598

Jiang ZL, Deng HW, Lin HX et al (2009) Methods and application of paleo-geomorphologies rebuilding: an example of the second member of Shahejie formation, Zhuangxi Area, Jiyang Depression. Geoscience 23(5):865–871

Jiang ZX, Liu H, Zhang SW et al (2011) Sedimentary characteristics of large-scale lacustrine beach-bars and their formation in the Eocene Boxing Sag of Bohai Bay Basin, East China. Sedimentology 58:1087–1112

Jiang ZX, Liang SY, Zhang YF et al (2014) Sedimentary hydrodynamic study of sand bodies in the upper subsection of the 4th member of the Paleogene Shahejie formation in the Eastern Dongying depression, China. Petroleum Sci 11:189–199

Li GB (2009) Study on the sedimentary system of beach and bar in the upper fourth member of Shahejie formation of the Paleogene in the Western Dongying Sag. China University of Geosciences, Beijing

Li SJ, Zheng DS, Jiang ZX et al (2005) Water depth of palaeo-lacustrine basin recovered by dominance diversity of Ostracoda: an example from sedimentary period of the Member 3 of Shahejie formation of Paleogene in Dongying Sag, Shandong Province. Journal of Palaeogeography 7(3):399–404

Lin CS, Liu JY, Zhang YZ et al (2005) Sequence stratigraphy and tectono stratigraphic analysis of tectonically active basins: a case study on the Cenozoic-Mesozoic lacustrine basins in China. Earth Sci Front 12(4):365–374

Lin HX, Deng HW, Qin YQ et al (2010) Control of sequence stratigraphic evolution on the distribution and hydrocarbon accumulation of beach and bar reservoirs. Petrol Explor Dev 37(6):680–689

Liu H, Wang SL (2010) Provenance systems and their control over sandbodies in the upper Es4 of the Shengtuo area in the Dongying Sag, the Bohai Bay Basin. Oil Gas Geol 31(5):602–609

Orme AJ, Orme AR (1991) Relict barrier beaches as paleoenvironmental indicators in the California desert. Phys Geogr 12(4):334–346

Pan YL, Zong GH, Guo YX et al (2003) Terrestrial sequence stratigraphy and lithological deposit group of sandstone in Jiyang faulted Lacustrine Basin. Acta Petrolei Sin 24(3):16–23

Passey QR (1990) A practical model for organic richness from porosity and resistivity logs. AAPG Bull 74(12):1777–1794

Quan C, Liu C, Utescher T (2011) Paleogene evolution of precipitation in Northeastern China supporting the Middle Eocene intensification of the East Asian monsoon. Palaios 26:743–753

Quan C, Liu Y, Utescher T (2012a) Eocene monsoon prevalence over China: a paleobotanical perspective. Palaeogeogr Palaeoclimatol Palaeoecol 365–366:302–311

Quan C, Liu YSC, Utescher T (2012b) Paleogene temperature gradient, seasonal variation and climate evolution of northeast China. Palaeogeogr Palaeoclimatol Palaeoecol 313:150–161

Song MS (2005) Sedimentary environment geochemistry in the Shasi section of southern ramp, Dongying depression. J Mineral Petrol 25 (1):67–73

Su X, Ding X, Jiang ZX et al (2012) Using of multi-microfossil proxies for reconstructing quantitative paleo-water depth during the deposit period of LST of Es4s in Dongying depression. Earth Sci Front 19 (1):188–199

Sun XN, Liu Y, Man Y et al (2003) Hydrocarbon accumulation conditions in beach-bar sandstones of the fourth member of Shahejie formation in West Dongying depression. Foreign Oilfield Eng 19(7):24–25

Taylor AW, Ritts BD (2004) Mesoscale heterogeneity of fluvial-lacustrine reservoir analogues: Examples from the Eocene Green River and Colton Formations, Uinta Basin, Utah, USA. J Pet Geol 27(1):3–25

Tian JJ, Jiang ZX (2009) Sequence stratigraphy characteristics and sedimentary system evolution of Upper Es4 in the Dongying depression. Acta Geologica Sin 83(6):836–846

Tian JJ, Jiang ZX (2012) Comparison and analysis of beach bars sedimentary characteristics of Upper Es4 in Huimin and Dongying depression. J Jilin Univ (Earth Science Edition) 42(3):612–623

Wang YZ, Song GQ, Wang XZ et al (2011) Controlling effect of paleogeomorphology on deposition of beach and bar sand reservoir —case study of south slope, east Dongying depression. Petrol Geol Recovery Effi 18(4):13–16

Wang YS, Liu HM, Gao YJ et al (2012) Sandbody genesis and hydrocarbon accumulation mechanism of beach-bar reservoir in faulted-lacustrine-basins: a case study from the upper of the fourth member of Shahejie Formation, Dongying Sag. Earth Sci Front 19 (1):100–107

Wang D, Lu S, Han S et al (2013) Eocene prevalence of monsoon-like climate over eastern China reflected by hydrological dynamics. J Asian Earth Sci 62:776–787

Wang J, Jiang Z, Zhang Y (2015) Subsurface lacustrine storm-seiche depositional model in the Eocene Lijin Sag of the Bohai Bay Basin, East China. Sed Geol 328:55–72

Wang J, Jiang Z, Xian B et al (2018) A method to define the palaeowind strength from lacustrine parameters. Sedimentology 65:461–491

Wu J (2015) The study on sedimentary characteristics and sequence stratigraphy of fine-grained rocks of the upper fourth member of Paleogene Shahejie formation, Dongying depression. China University of Geosciences, Beijing

Yang YQ, Qiu LW, Jiang ZX et al (2011) A depositional pattern of beach bar in continental rift lake basins: a case study on the upper part of the fourth member of the Shahejie Formation in the Dongying Sag. Acta Petrolei Sin 32(3):417–423

Yuan GH, Cao YC, Wang YZ (2012) Sedimentary facies and their evolution of the 4th -middle 3rd members of Shahejie Formation in Minfeng area, Dongying Sag. Oil Gas Geol 33(2):277–286

Zachos J, Pagani M, Sloan L et al (2001) Trends, rhythms, and aberrations in global climate 65 Ma to present. Science 292 (5517):686–693

Zachos JC, Dickens GR, Zeebe RE (2008) An early Cenozoic perspective on greenhouse warming and carbon-cycle dynamics. Nature 451(7176):279–283

Zhang ZW, Zhang LH (2000) A method of source rock evaluation by well-logging and its application result. Petrol Explor Dev 27(3):84–87

Zhu XM, Kang A, Wang GW (2003) Sequence stratigraphic models of depression and faulted-down lake basins. Acta Sedimentol Sin 21 (2):283–287

# Depositional Systems and Windfield-Source-Basin System Dynamics of the West Sag, Liaohe Depression, Bohai Bay Basin

## 5.1 Geologic Setting

### 5.1.1 Tectonic Divisions

The Liaohe Depression, located in the northeast of Bohai Bay Basin, is a Mesozoic to Cenozoic continental rift basin formed on pre-Mesozoic base. Its onshore part is further divided into seven units: (1) West Sag, (2) East Sag, (3) Damintun Sag, (4) Shenbei Sag, (5) Central High, (6) West High, and (7) East High (Fig. 5.1) (Hu et al. 2005; Qi et al. 2013), among which the West Sag is the most important oil-producing area (*ca.* 82 vol.%).

The West Sag, located in the southwest of the depression, is bounded by the Damintun Sag to the north, the West High to the west, the Central High to the east, and the Bohai Sea to the south. It has a length, width, and area of 135, 15–30 km, and 2560 km$^2$, respectively. The sag successively experienced the rift stage (Paleogene) and depression stage (Neogene) (Table 5.1) (Li et al. 2004). Thus, it is characterized by a half-graben structure, with the border-fault and flexural margins in the western and eastern parts, respectively. Three sags develop along the border-fault margin belt; they are successively Niuxintuo Sub-sag, Panshan-Chenjia Sub-sag and Qingshui Sub-sag from north to south. Along the flexural margin part, it is successively (1) Gaosheng, (2) Shuguang, (3) Dujiatai, (4) Qijia, and (5) Huanxiling sub-highs develop from north to south (Fig. 5.2) (Bao et al. 2009; Feng et al. 2009a, b).

### 5.1.2 Strata Characteristics

The strata are composed of Archean and Paleoproterozoic basement and Cenozoic deposits. The basement includes: (1) mixed granites, granites, gneiss of the Archean to Paleoproterozoic strata, (2) quartzite, black shale, slate as well as dolomite, limestone and clastic rock from the Mesoproterozoic to Neoproterozoic, (3) dolomite, limestone and mudrock in the Paleozoic, and (4) volcanic rocks, tuff, and clastic rock in the Mesozoic. The Cenozoic deposits (9400 m thick) are composed of Paleogene Fangshengpao, Shahejie and Dongying Formations, Neogene Guantao and Minghuazhen Formations and Quaternary Pingyuan Formation. The deposits vertically presents cyclical properties with multi-hydrocarbon layers (e.g., the Niuxintuo, Gaosheng, Dujiatai, Lianhua oil layers).

The Es$_4$ strata are the target layer of this chapter; they are formed in the early rift stage. In the Niuxintuo area, the strata are interbedded black basalt and green mudrock in the lower Es$_4$ strata (named as Niuxintuo oil-layer) but thick mudrock in the middle and upper Es$_4$ strata. In the Gaosheng area, gray-, green-gray, brown-gray mudrock, oil shale and dolomitic limestone with interbedded thin silt layers develop in Es$_4$ strata, named as Gaosheng oil layer. In the Huanxiling and Qijia areas, the upper Es$_4$ strata are composed of interbedded conglomerate, sandstone and mudrock, named as Dujiatai oil layer (Liu et al. 2015). The uncovered thickness of the Es$_4$ strata reaches 646 m with an average depositional rate of 97 m/Ma, and shows unconformity with the underling Fangshenpao Formation.

## 5.2 Sequence Stratigraphy Framework

Sequence stratigraphy reveals the time-parallel framework of the strata. Currently, the exploration target has transformed from structural hydrocarbon reservoir to lithologic reservoir, making it more important in exploration process.

### 5.2.1 Recognition of Sequence Boundaries

#### 5.2.1.1 Third-Order Sequence Boundaries

The formation of sequence boundaries is presented by a rapid change in strata unit and stacking pattern. The lithology, facies, wireline characteristics, seismic reflection properties commonly show abrupt changes in sequence boundaries, acting as the proofs in recognizing sequence units (Jiang et al. 2010a, b).
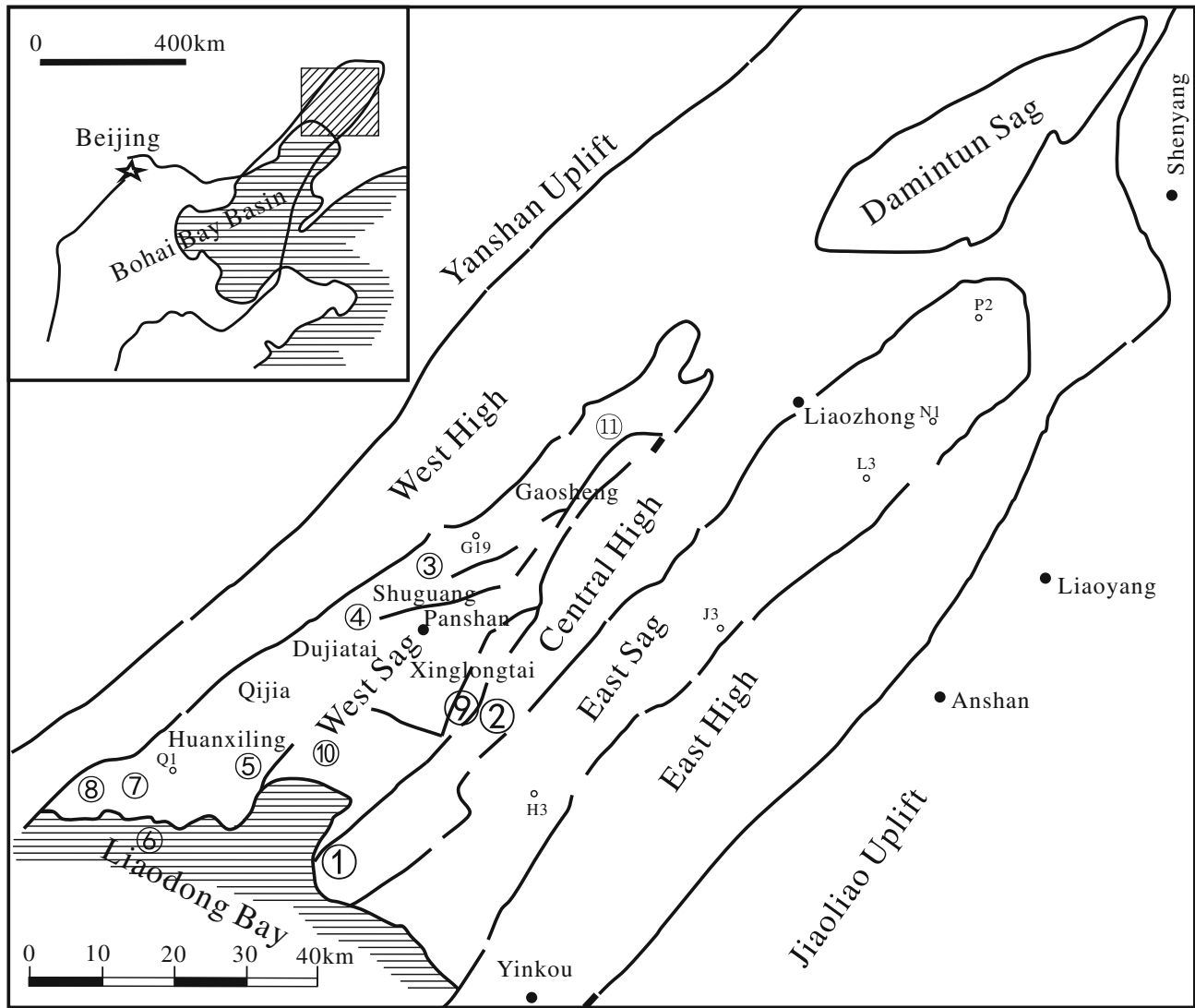
**Fig. 5.1** Geologic map of the West Sag, Liaohe Depression. The main fault systems in the West Sag include: (1) Taian-Da'ao fault system, (2) Lengjiabu fault system, (3) Shu95-Gao10 fault system, (4) Shu27 fault system, (5) Shuangtaizi fault system, (6) Yuanyanggou fault system, (7) Jin2-Huan5 fault system, (8) Jin4 fault system, (9) Xinglongtai-Maquanzi fault system, (10) Shuangtaizi fault system from north to south, (11) Gaosheng fault system

(1)  Seismic data

Seismic data are the basic method for the preliminary evaluation of subsurface fill, including overall structure, stratigraphic architecture, and fluid properties. The development of seismic exploration technique resulted for the transition from classical stratigraphy to seismic stratigraphy (the precursor of sequence stratigraphy) in the 1970s (Vail 1975; Payton 1977), and led to establishing criteria for interpreting seismic stratigraphic and sequence stratigraphic units (Vail et al. 1977). The termination properties in seismic data are key proofs in sequence stratigraphy study (Jiang et al. 2009), including onlap, toplap, downlap, and truncation surfaces etc. (Fig. 5.3). An obvious third-order sequence boundary is recognized in seismic reflection sections of the West Sag (Fig. 5.3); it divides the sequence into SQ1 and SQ2, with the boundaries named as SB1, SB2, and SB3 in ascending order. Among them, SB1 and SB3 corresponds to the lower boundaries and upper boundaries of $Es_4$ strata, respectively. In addition, the SQ1 is truncated in southern part of the sag.

(2)  Well logging data

In wireline logs, the sequence stratigraphy presents as rhythmic pattern, with the boundaries showing sharp changes. Spontaneous curve (SP) commonly has high values with a funnel-shape below the sequence boundaries, but resistivity curve mostly has low values with a bell-shape. Above

**Table 5.1** Strata characteristics of the Paleogene West Sag, Liaohe Depression

| Strata | | | Lithology | Thickness (m) |
|---|---|---|---|---|
| Ed | Ed$_1$ | | Yellow-green, gray-green mudrock with some pale-green glutenite | / |
| | Ed$_2$ | | Interbedded sandstone and mudrock in the lower section, and dark mudrock in the upper section | 50–100 |
| | Ed$_3$ | | Sandstone and mudrock in the lower section, and thick interbedded dark mudrock and sandstone as well as glutenite in the upper section | / |
| Es | Es$_1$ | | Interbedded sandstone and mudrock | 30–50 |
| | Es$_2$ | | Light-gray, pale-gray conglomerate with interbedded maroon mudrock | 100–200 |
| | Es$_3$ | $O_r$ | Dominating gray-black mudrock | 2500 |
| | | $O_{dl}$ | Dominated by dark-gray, brown-gray mudrock and pale-gray sandstone | |
| | | $O_l$ | Feldspar-rich sandstone and conglomerate in shallow lake, but interbedded gray-black mudrock, oil shale and calcitic shale in deep lake | |
| | Es$_4$ | $O_d$ | Thin sandstone and mudrock layers in the lower section, sandstone deposits with some thin mudrock layers in the middle section, gray mudrock and sandstone in the upper section | 646 |
| | | $O_g$ | Sandstone, conglomerate layers interbedded by thin gray, green-gray mudrock as well as some oil shale | |
| | | $O_n$ | Pale-gray conglomerate, sandstone, brown-gray mudrock, calcitic shale, oil shale, dolomitic limestone with thin interbedded silty layers | |
| Ef | Ef$_1$ | | Purple mudrock and glutenite with thin interbedded mudrock in the southern and northern part of the sag, and red mudrock in the middle part of the sag | / |
| | Ef$_2$ | | Basalt in the northern and southern part of the sag, but purple mudrock in the middle part of the sag | |

*Notes Ed* Dongying Formation, *Es* Shahejie Formation, *Ef* Fangshengpao Formation. *$O_r$* Rehetai oil layer, *$O_{dl}$* Dalenghe oil layer, *$O_l$* Lianhua oil layer, *$O_d$* Dujiatai oil layer, *$O_g$* Gaosheng oil layer, *$O_n$* Niuxintuo oil layer. "/" No data

the sequence boundaries, *SP* value is medium to low with finger-shape, but resistivity curve is medium to high with box-shape. The lithology also shows sharp change as recorded in borehole logging. It is thick gray mudrock, oil shale below SB2, but thin interbedded sandstone and mudrock above the SB2 (Fig. 5.4) (Cao et al. 1996).

(3) Geochemistry data

The seismic data, core data and well logging data have some limitations in studying sequence stratigraphy, as follows: (1) seismic data are limited by resolution, (2) cores are expensive for collection, (3) well logging data may lead to multi-interpretations in many cases. To avoid this, geochemistry data are also used in analyzing sequence stratigraphy here.

(1) ΔlogR

Some well logging data reflect the organic matter characteristics, thus are useful in recognizing organic-rich source rock and interpreting TOC content. This method is based on overlapping of well log curves, in which "porosity curve" (e.g., AC curve) is overlapped to the resistivity curve. Obvious amplitude difference exists between the two curves in organic-rich intervals, whereas the two are parallel to each other or overlapped in organic-poor intervals. This is caused

by the low density and low velocity of kerogen (high AC values) and the response of strata water, and the amplitude difference is defined as ΔlogR (Orr et al. 1981).

The calculating equation of ΔlogR is shown as follows:
$$\Delta \log R = log(R/R_{\text{base line}}) + (\Delta t - \Delta t_{\text{base line}})/164.$$

Among them, Δlog*R* = the value of measured space in well logging curves at a logarithm resistivity coordinate (Ω m); R = measured resistivity in the well logging instrument (Ω m); R$_{\text{base line}}$ = the corresponding resistivity of the base line (Ω m); Δt = the measured spread time (us/m); Δt$_{\text{base line}}$ = the corresponding spread time of the base line; 1/164 = the Δt of every 164 us/m, also equivalent to a logarithm coordinate of Rt.

Δlog*R* value is generally positively correlated to TOC content in source rock. TOC content and source rock properties is commonly closely related to sequence stratigraphy framework. TOC content vertically shows cyclical properties in sequence stratigraphy. The peak value of TOC content commonly matches maximum flooding surface (MFS), as a result of low depositional rate. Below or above the surface, the high depositional rates dilute the organic matter (Wang et al. 2003). Hence, well logging data can be used to judge the layers with highest TOC content, which is actually maximum flooding surface (MFS) in sequence stratigraphy. In addition, sequence boundaries commonly have low TOC values. Δlog*R* shows closely relationship with sequence stratigraphy (Fig. 5.5). Sequence boundaries mostly have
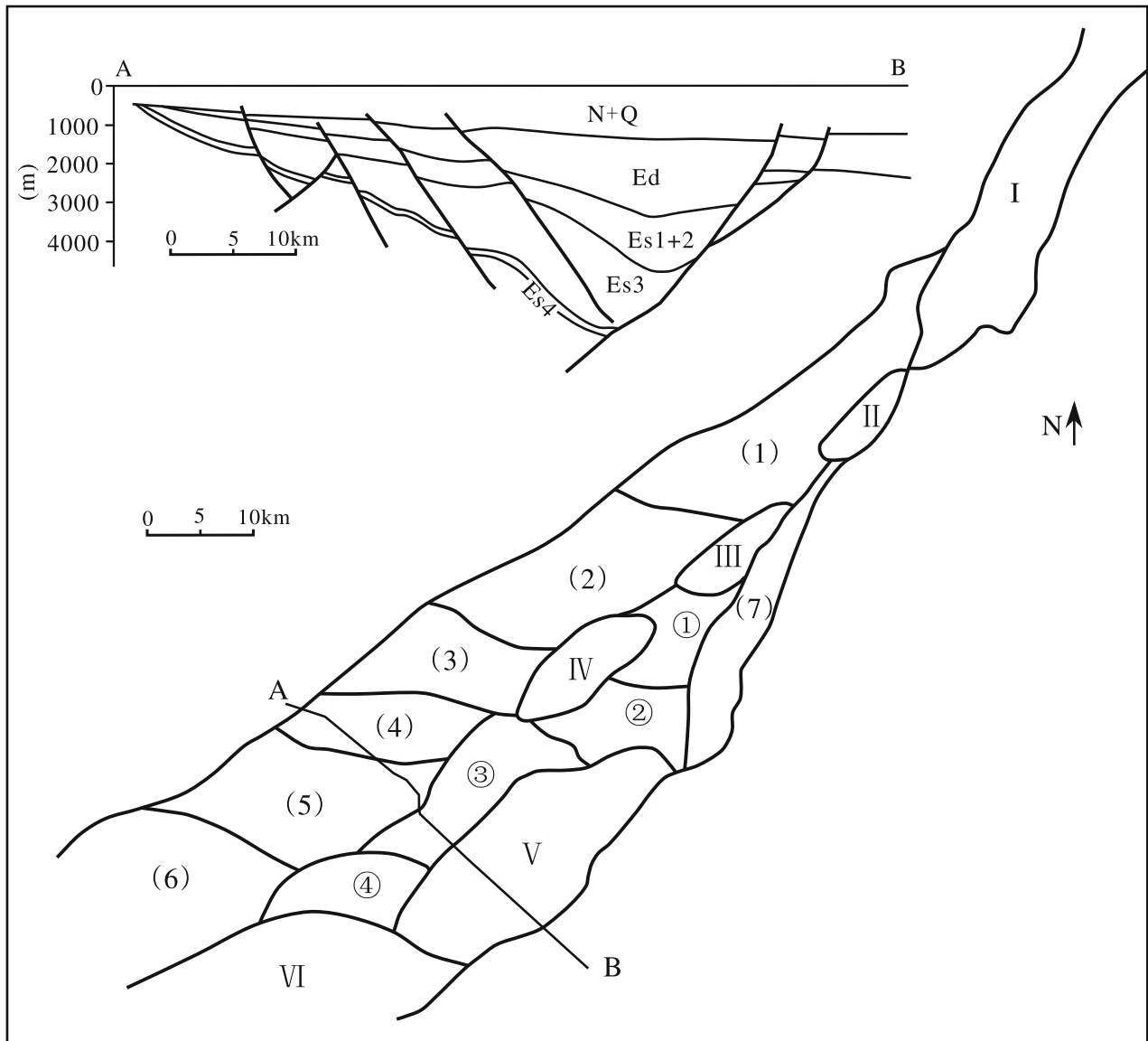
**Fig. 5.2** Tectonic divisions of the West Sag, Liaohe Depression. I. Niuxintuo sub-sag; II. Taian sub-sag; III. Chenjia sub-sag; IV. Panshan Sub-sag; V. Qingshui Sub-sag; VI. Yuanyanggou sub-sag. ① Xinglongtai anticline structural belt; ② Maquanzi anticline structural belt; ③ Shuangtaizi anticline structural belt; ④ Shuangnan fault anticline structural belt. (1) Gaosheng nose-like High; (2) Shuguang nose-like High; (3) Dujiatai nose-like High; (4) Qijia nose-like High; (5) Huanxiling nose-like High; (6) Xibaqian slope belt; (7) Lengjia twisted belt
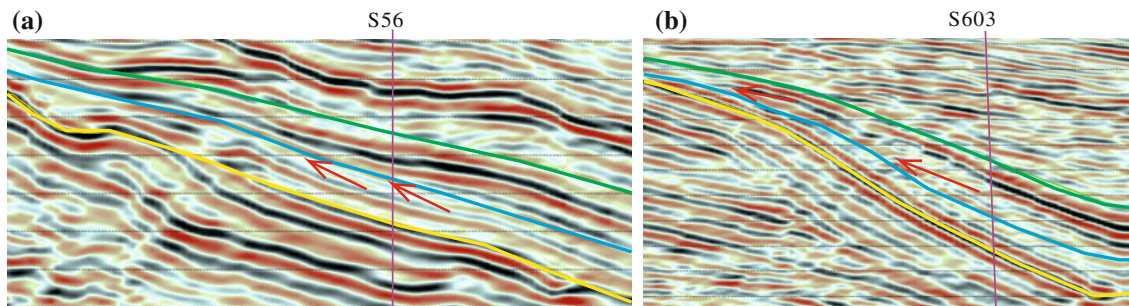


**Fig. 5.3** Onlap characteristics in seismic sections

**Fig. 5.4** The sharp lithology changes between SQ1 and SQ2. SQ = Third-order sequence, ST = System tract, PSS = Parasequence set
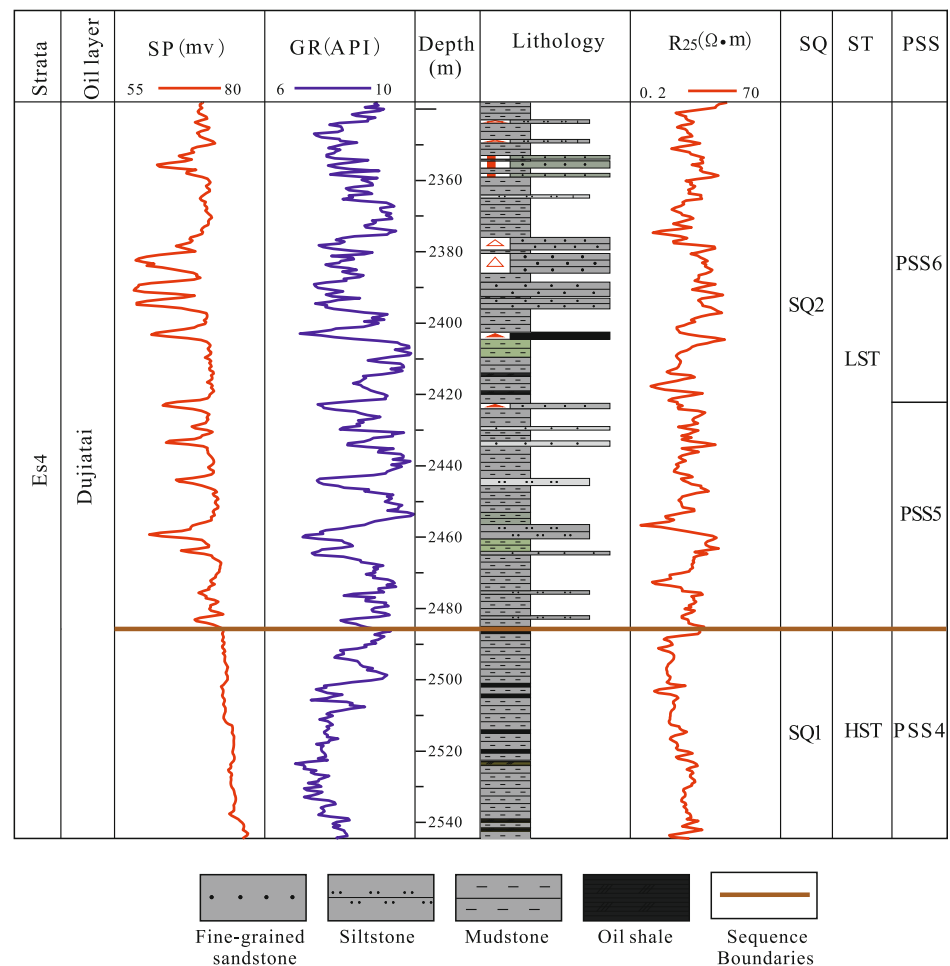


low ΔlogR values, but condensate section (CS) mainly has high ΔlogR values.

**(2)  Th/U and U/K**

Thorium (Th), uranium (U) and potassium (K) curves in Gamma Spectrum curves reflect the water depth changes, and thus can be used to reflect the sequence unit (Wang et al. 2007). Th/U, Th/K and U/K ratios are employed in this study; they are closely related to water depth, water dynamics, and source rock properties, respectively (see Table 5.2) (Dai et al. 1995).

Th/U value is commonly high in LST, caused by the relatively shallow-water and oxygen-rich environment. However, Th/U is low in TST caused by the relatively high deep-water and oxygen-poor environment. The excellent source rock potential in CS results in high U/K value. Hence, these ratios reflect the changes in sequence units.

In well Du 305 of the West Sag, both Th/U and U/K curves reflect the changes in sequence unit of SQ2. In well Du305, Th/U values in the interval of 2606–2697 m are high with a peak value of 36, indicating an oxic and relatively

shallow water environment; the values in 2575–2606 m are composed of mudrock and oil shale with low Th/U values (mostly <5), indicating an anoxic environment in TST interval. These ratios suggest the interval of 2557–2696 as a complete third-order sequence.

### 5.2.1.2  System Tract and Parasequence Set Boundaries

The division of system tract is based on accurately recognize the first flooding surface (FFS), maximum flooding surface (MFS), and sequence boundaries. Therein, FFS is the surface that the ratio between accommodation space and sediment supply (A/S) changes from dynamically equilibrium to increase. The parasequence set is mostly aggradation below this surface but mainly progradation above it. The MFS divides the TST and HST. It refers to the surface with highest A/S, mainly composed of fine-grained sediments. In MFS, *GR* curve has high values but *SP* and resistivity curves have low values. In seismic section, the MFS show good lateral continuity and high amplitude (Jiang 2012).

A complete third-order sequence should include LST, TST and HST according to vail' division of system tracts.

**Fig. 5.5** The response of $\Delta \log R$ to sequence boundaries. SQ = Sequence, ST = System tract, PSS = Parasequence set

**Table 5.2** Sedimentary environment and source rock properties indicated by Th/U, Th/K, U/K ratios

| Th/U | >30 | 10–30 | 4–10 | <4 |
|---|---|---|---|---|
| Environment | Oxic | Dysoxic | Suboxic | Anoxic |
| Th/K | >10 | 6–10 | 3–6 | <3 |
| Hydrodynamic | High | Medium | Low | Still water |
| U/K | <0.4 | 0.4–0.7 | 0.7–1.2 | >1.2 |
| Source rock potential | Poor | Fair | Good | Excellent |

LST is the beginning of a sequence, in which water depth is relatively shallow. TST is the middle part of a sequence, divided by FFS at the lower boundaries and MFS at the upper boundaries. HST is the uppermost part of a sequence, divided by MSF at the lower interface. In the Es$_4$ strata of Liaohe Depression, SQ1 is composed of LST, TST and HST, whereas SQ2 is only composed of LST and TST.

Parasequence set refers to a set of genetically correlated and particularly stacked parasequences. It is recognized by flooding surfaces as well as the corresponding surfaces at the upper and lower interfaces. A system tract is composed of several parasequence set in areas with high subsidence rate and depositional rate. A parasequence set contains three types: (1) progradation, (2) transgression, (3) aggradation, according to the ratio between depositional rate and newly added accommodation space. Each of the above three types can be recognized in the Liaohe Depression. The characteristics are as follows. (1) progradational parasequence set shows shallow-upward in water depth, and thus thicken-upward of sandstone layers and thinning-upward of mudrock layers. It mostly distribute in HST and LST. (2) Transgressional parasequence shows deepen-upward of water depth, and thus thinning-upward of sandstone layers but thicken-upward of mudrock layers. It mostly distribute in TST. (3) Aggradational parasequence set is formed in a relatively stable water level, with relatively stable sandstone and mudrock thickness as well as their ratio from bottom to top. It is mostly in HST and LST (Figs. 5.6 and 5.7).

### 5.2.2 The Establishment of Sequence Stratigraphy Framework by Combination of Wells and Seismic Data

In the West Sag of Liaohe Depression, sequence stratigraphy framework is established at a distance of 10 × 10 grid in seismic data. The recognition of seismic stratigraphy is mainly based on its reflection properties (e.g., toplap, truncation, onlap, downlap) as well as the general reflection properties in seismic section. The interfaces of SQ1 and SQ2 are recognized in the West Sag, which are SB1, SB2 and SB3 in ascending order, respectively. Meanwhile, the two

parasequence set interfaces in LST of SQ2 is also recognized, named as PSS6 and PSS7 from bottom to top. Unfortunately, the interfaces of other parasequene set are unrecognizable from seismic data limited by the resolution. The following three paragraphs show two seismic sections along and perpendicular to the source direction, respectively.

The section along the source direction includes successively wells S14, S606, SG18, S68, and S66 from northwest to southeast. Terrigenous debris flowed into the lake from west. The thickness is relatively thin at the west part of the section, and increases eastward. A buried hill exists between wells S606 and SG18, making the strata pinch off around this buried area (Fig. 5.8).

The section perpendicular to the source include successively wells D131, D139, D129, S52, S100, S54, SG19, and S134 from southwest to northeast. The section route is parallel to the shoreline and also far from the shoreline. The strata thickness gradually becomes thick from south to north (Fig. 5.9).

The Es$_4$ strata in the West Sag is composed of two third-order sequences (SQ1, SQ2), 5 system tracts, and 8 parasequence sets as recognized in wells. SQ1 is composed of LST, TST and HST; its LST comprise PSS1 and PSS2, and the TST and HST comprise PSS3 and PSS4, respectively. LST and TST of SQ2 locate in the ES$_4$ strata, whereas HST locates in the Es$_3$ strata; its LST is composed of two parasequence set (PSS5 and PSS6), and TST composed of two parasequence set (PSS7 and PSS8). Note SQ1 is missing at the south of Dujiatai area (Fig. 5.10).

## 5.3 Sedimentary Systems and "Windfield-Source-Basin System" Depositional Dynamics

Based on sequence stratigraphy framework, the sedimentary systems and "Windfield-Source-Basin System" depositional dynamics in the West Sag are studied based on wells, cross-section, and seismic facies. This study clearly defined the distribution and controlling factors of sandbodies (Li et al. 2008b).
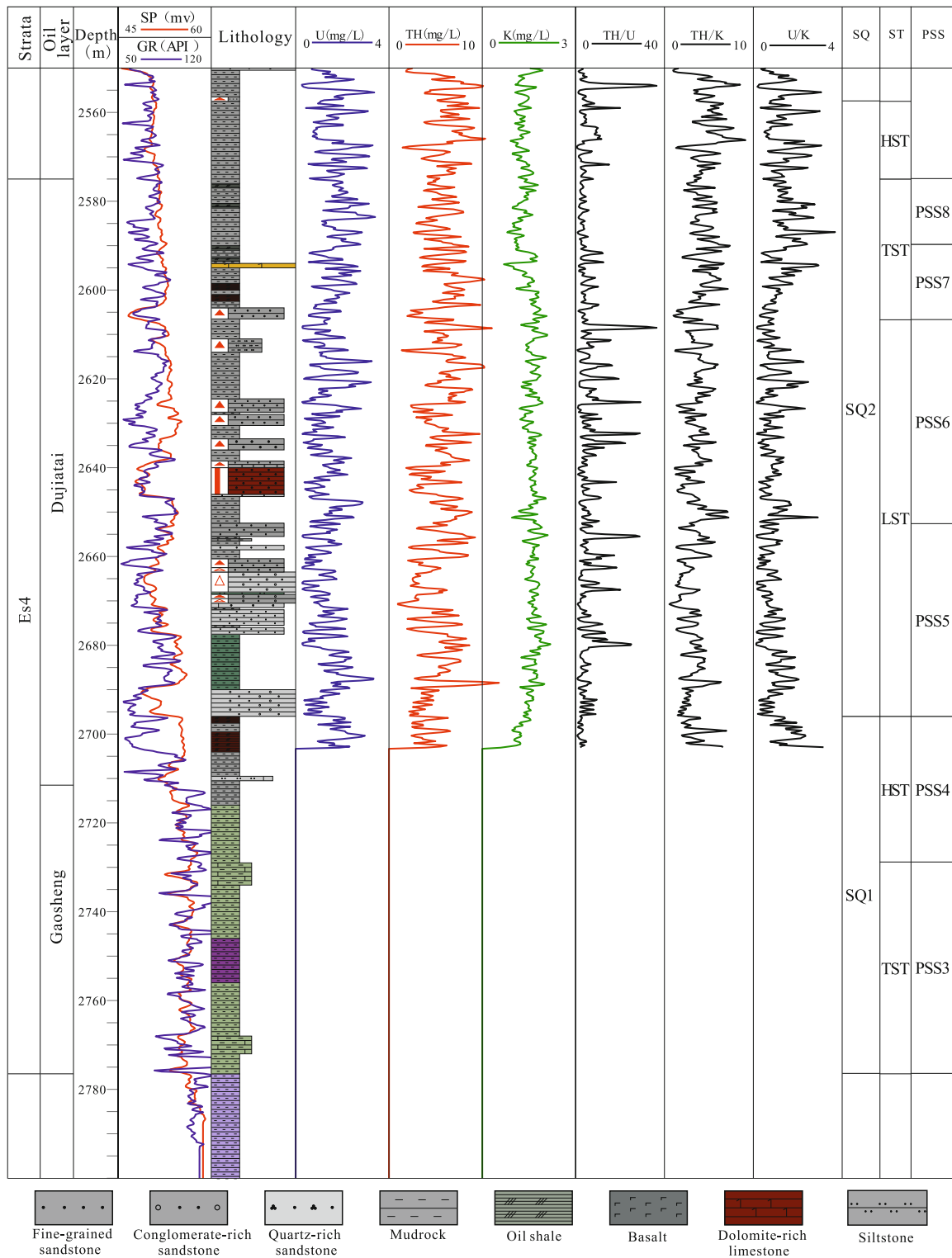
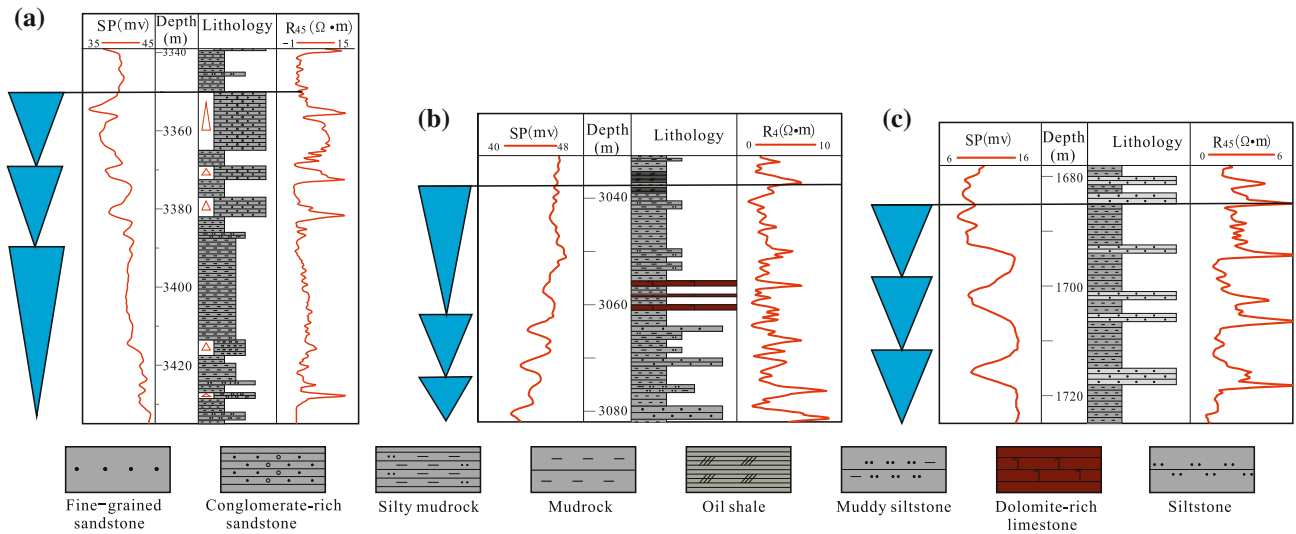**Fig. 5.6** Th/U, Th/K, and U/K curves in well D305. SQ = Sequence, ST = System tract, PSS = Parasequence set

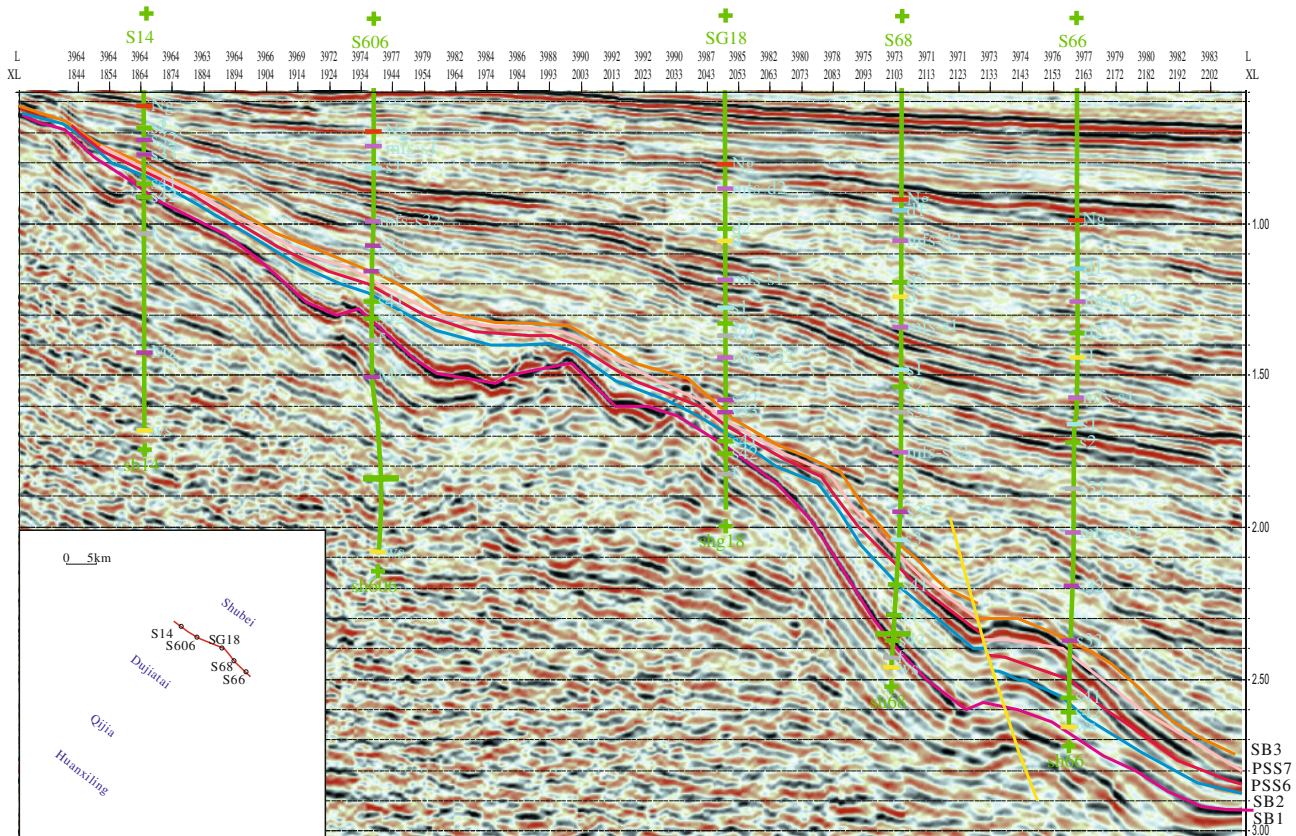**Fig. 5.7** Parasequence set characteristics in **a** LST of well H631, **b** TST of well D146, and **c** HST of well Q106



**Fig. 5.8** Seismic section along the source direction in the West sag, Liaohe Depression
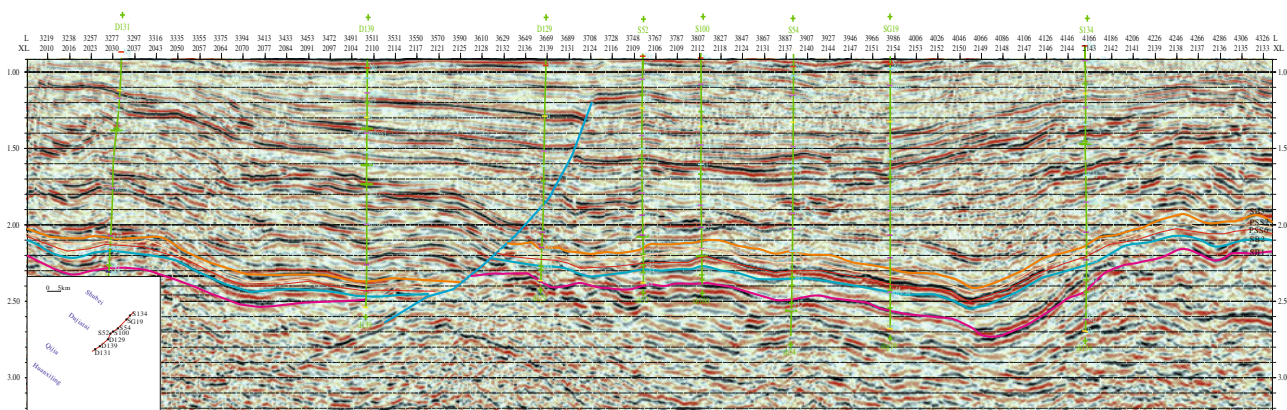
**Fig. 5.9** Seismic section perpendicular to the source direction in the West sag, Liaohe Depression

## 5.3.1 Sedimentary Facies

### 5.3.1.1 Wells

(1)  Shubei Area (Well S66)

Well S66 is a representative well in the eastern Shubei Area (The Shubei Area refers to the northern part of the Shuguang Area). The Es$_4$ interval is 2923.5–3365 m, composed of two third-order sequence from bottom to top.

SQ1 contains 3217–3365 m, divided to LST, TST, and HST. Its LST (3295.5–3365 m) is composed of PSS1 and PSS2, characterized by overflowing basalt. The TST (3258–3295.5 m) includes PSS3, composed of deep-water oil shale and gray-dark mudrock. The HST (3217–3258) includes PSS4, composed of interbedded shallow-water sandstone and mudrock.

SQ2 contains 2923.5–3217 m. The LST is 3021–3217 m, composed of PSS5 and PSS6. PSS5 is dominated by thin sandstone and mudrock layers, with sandstone layers 0.5–7 m thick. Typical characteristics include cross-bedding, and large amounts of coal debris. The *SP* curve shows coarsening-upward characteristics and resistivity curve has abnormally high amplitude with finger-shape peaks. PSS6 are similar to PSS5 in lithofacies association, characterized by thin sandstone layers (<4 m). The TST (2923.5–3021 m) is composed of PSS7 and PSS8. During PSS7 (2973–3021 m), a thin sandstone layer (*ca*. 1 m) exist in the first flooding surface (FFS), recognized as beach-bar deposits formed by submerging of lake water (Yang et al. 2011). It is mainly brown oil shale with some gray mudrock of semi-deep lake during PSS8 (2923.5–2973 m). A sandstone layer with a thickness of 10 m also exists in PSS8, probably formed by storms.

Most of the sandstone layers, recognized as beach-bar deposits, in well S66 exist in the LST of SQ2 (Fig. 5.11).

(2)  Dujiatai Area (Well D305)

Well D305 is located in central Dujiatai Area. The depth interval is 2575–2776.5 m, composed of SQ1 and SQ2. SQ1 ranges from 2710.5 m to 2776.5 m, with dominant mudrock in its TST and HST (Fig. 5.12).

The depth interval of SQ2 is 2575–2710.5 m, composed of LST, TST, and HST (HST is actually in the Es$_3$ strata) as recognized in the lithofacies association. The LST (3201.5–3379.5 m) is composed of PSS5 and PSS6 according to the sedimentary cycles. The depth interval of PSS5 is 2646.5–2710.5 m. In well logs, it is mainly gray conglomerate, gray fine-grained sandstone, green-gray mudrock, gray-dark mudrock. The *SP* curve shows box-shape, whereas resistivity curve show sharp contact with the underlying layers. The PSS5 in the Dujiatai area is mainly braid-delta. PSS6 is similar to in PSS5 in sedimentary characteristics, also dominated by braid-delta deposits. The TST is dominated by oil shale, dark-gray mudrock, indicating relatively deep water environment.

(3)  Qijia Area (Well Q18)

Well Q18 is located in central Qijia Area. The burial depth of Es$_4$ strata is 2005–2152 m. Only SQ2 develops in this well. According to the lithology changes, it is divided into LST, TST, and HST, with HST in the Es$_3$ strata (Fig. 5.13). The burial depth of LST is 1667.5–1807 m. It includes PSS5 and PSS6 according to the sedimentary cycles. The PSS5 (1746–1807 m) is thin interbedded pale-gray fine-grained sandstone and gray mudrock. The *SP* curve shows coarsen-upward characteristics, and resistivity curve composed of a set of stacked finger-shape cycles. The PSS6 corresponds to a burial depth of 1667.5–1746 m, with the sedimentary characteristics similar to PSS5. The lithology is pale-gray fine-grained sandstone, with wavy cross-bedding and plant debris. The TST has high clay content, indicating a

**Fig. 5.10** Sequence units
division of the Es₄ West sag,
Liaohe Depression.
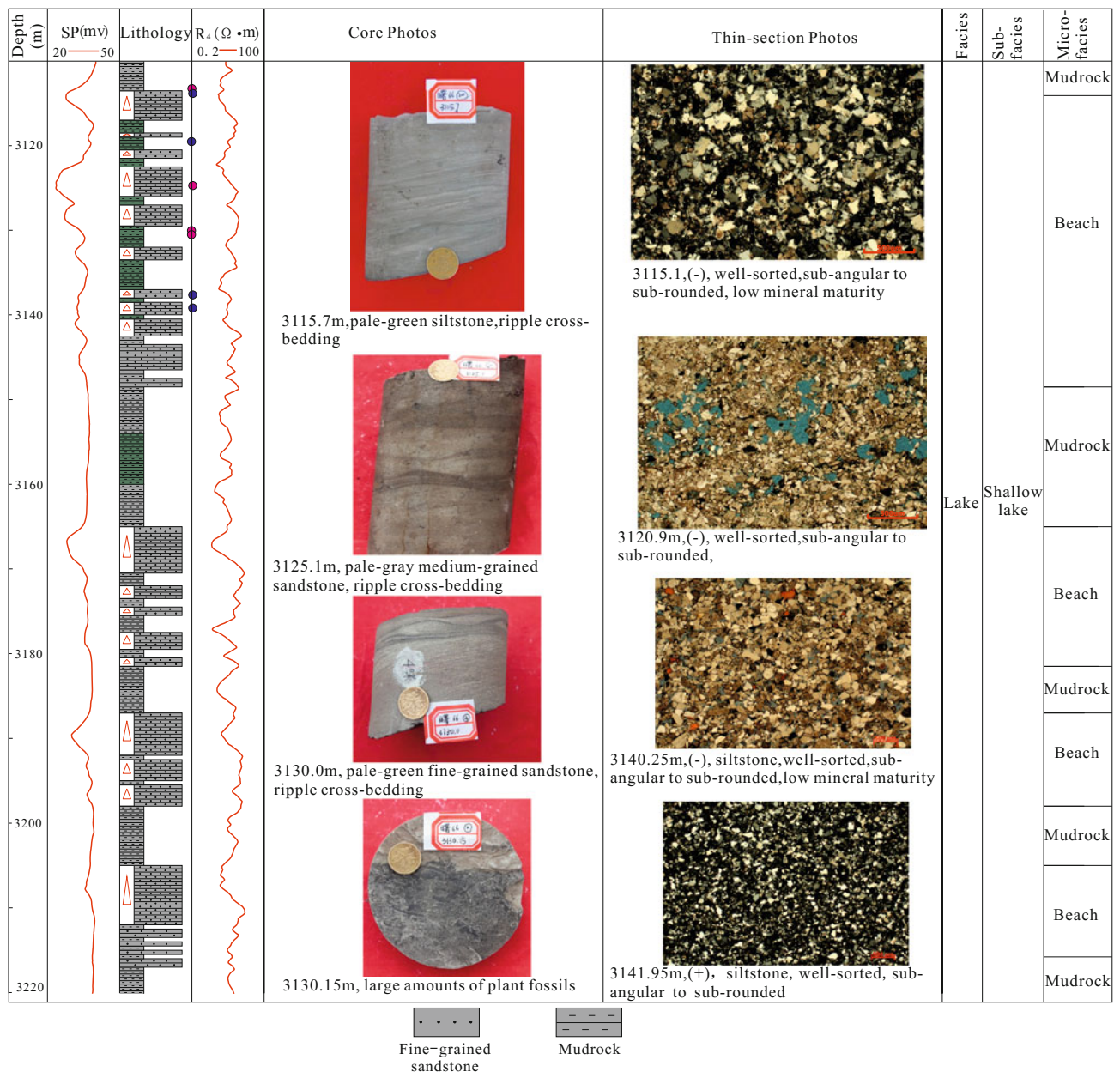SQ = Sequence, ST = System
tract, PSS = Parasequence set
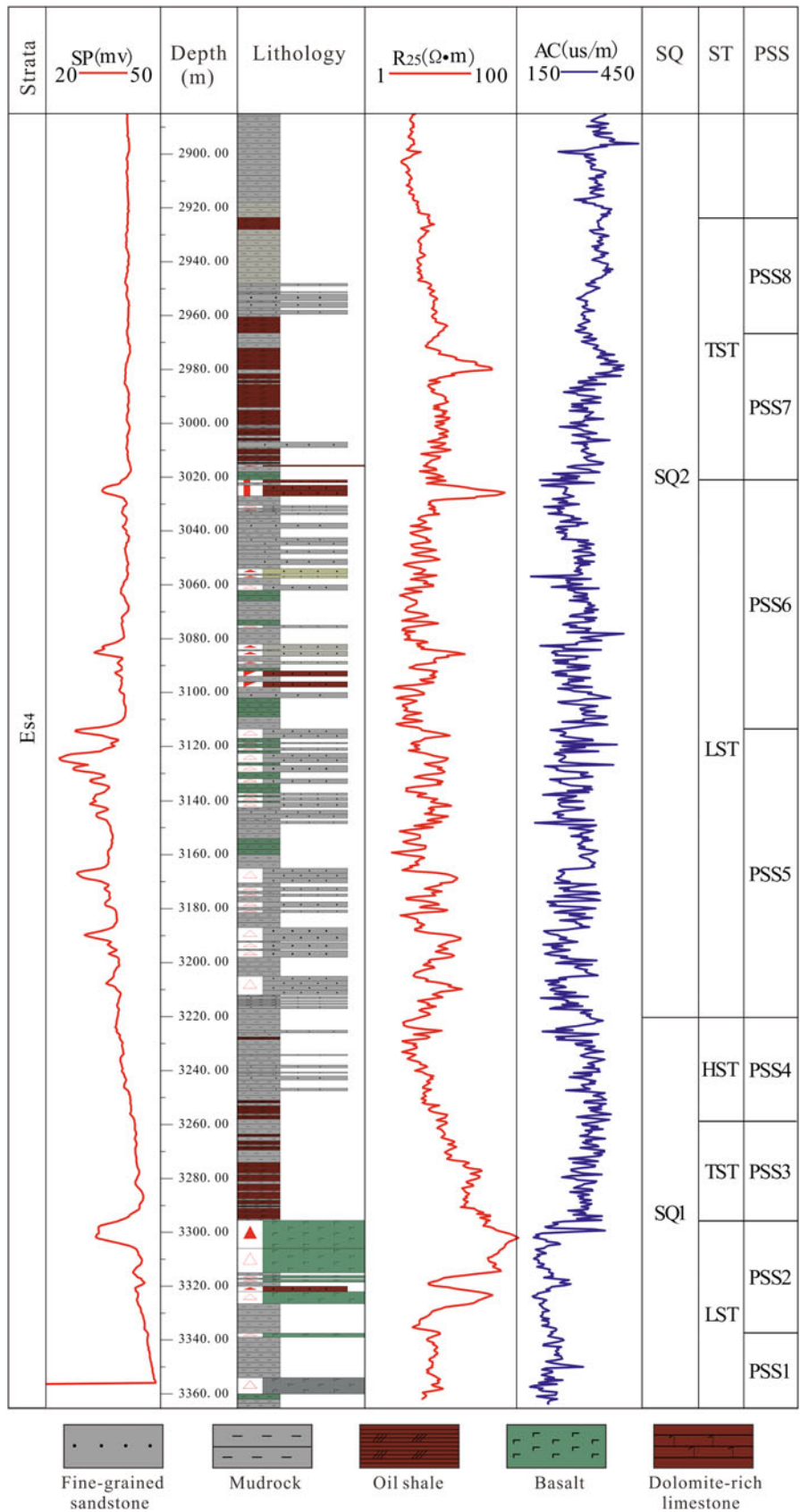
**Fig. 5.11** Petrology and facies interpretation of well S66 in the Es$_4$ strata

deeper water than LST. Note the Es$_4$ strata of well Q18 have no channel deposits.

To sum up, the SQ2 period of well Qi16 is mostly shallow-lake beach-bar deposits. As it is close to the shoreline, it is probably converted from bedrock by waves.

(4)  Huanxilin Area (Well H631)

Well H631 is located in eastern Huanxilin Area. The burial depth of Es$_4$ strata is 3188–3436 m. The SQ1 is missing, and

only SQ2 develops. The SQ2 is divided into LST, TST, and HST, with HST in the Es$_3$ strata (Fig. 5.14). The LST corresponds to 3227–3436 m, and is further divided into 2 parasequence sets (PSS5 and PSS6). The PSS5 includes 3321–3436 m, composed of gray conglomerate-bearing sandstone and fine-grained sandstone, and dark-gray mudrock. The *SP* curve shows blocky shape, and resistivity curve show bell-shape with a sharp bottom contact. The PSS6 corresponds to 3225–3321 m, composed of gray glutenite, pale-gray fine-grained sandstone, pale-gray muddy siltstone,
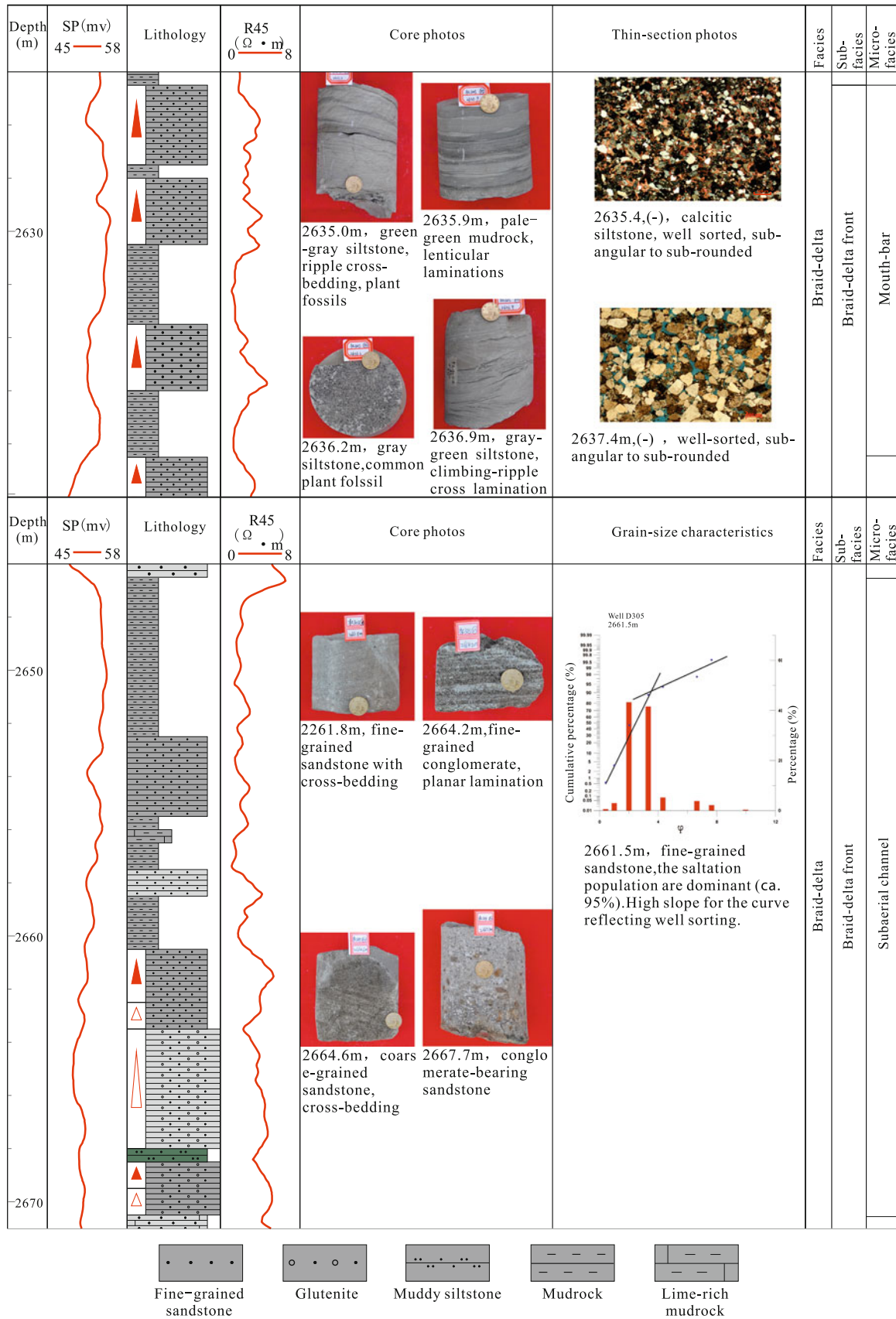
**Fig. 5.12** Petrology and facies interpretation of well D305 in the Es$_4$ strata
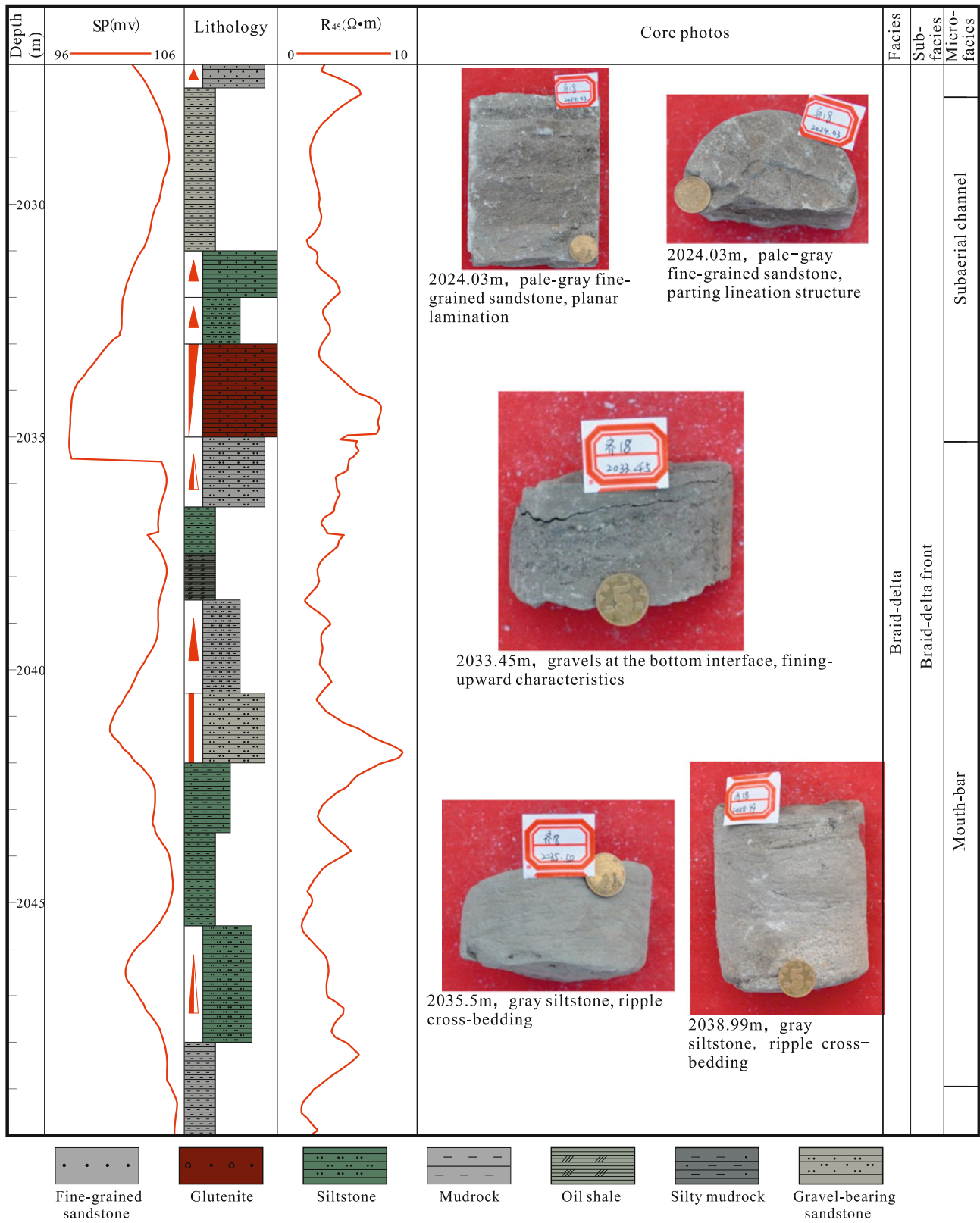
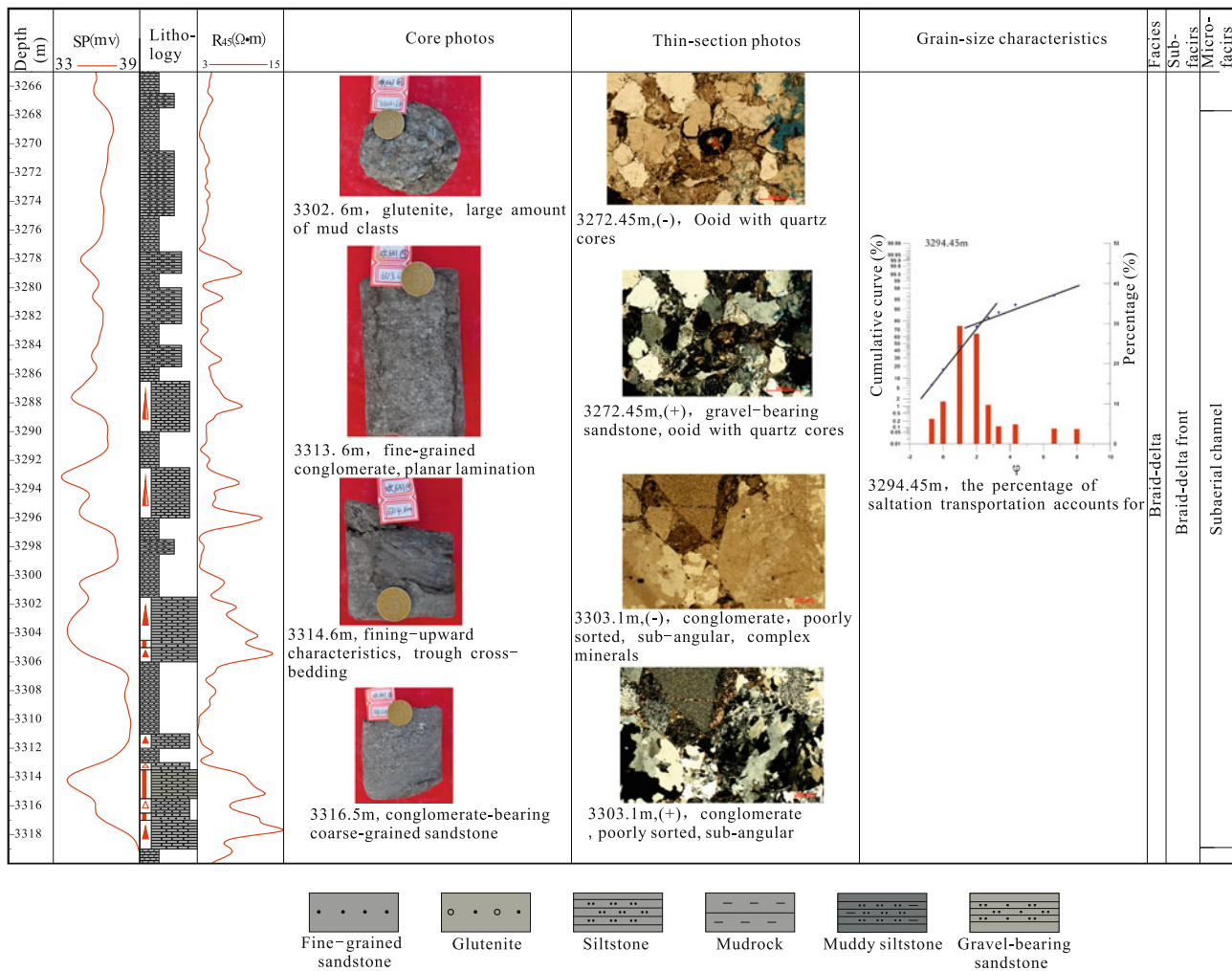**Fig. 5.13** Petrology and facies interpretation of well Q18 in the Es₄ strata

The figure columns (left to right): Depth (m); SP(mv) 33—39; Lithology; $R_{45}(\Omega \cdot m)$ 3—15; Core photos; Thin-section photos; Grain-size characteristics; Facies; Sub-facies; Micro-facies.

Core photos:
- 3302. 6m，glutenite，large amount of mud clasts
- 3313. 6m，fine-grained conglomerate, planar lamination
- 3314.6m, fining-upward characteristics, trough cross-bedding
- 3316.5m, conglomerate-bearing coarse-grained sandstone

Thin-section photos:
- 3272.45m,(-)，Ooid with quartz cores
- 3272.45m,(+)，gravel-bearing sandstone, ooid with quartz cores
- 3303.1m,(-)，conglomerate，poorly sorted, sub-angular, complex minerals
- 3303.1m,(+)，conglomerate, poorly sorted, sub-angular

Grain-size characteristics:
- 3294.45m
- 3294.45m，the percentage of saltation transportation accounts for
- Cumulative curve (%); Percentage (%)

Facies: Braid-delta; Sub-facies: Braid-delta front; Micro-facies: Subaerial channel

Legend: Fine-grained sandstone; Glutenite; Siltstone; Mudrock; Muddy siltstone; Gravel-bearing sandstone

**Fig. 5.14** Petrology and facies interpretation of well H631 in the Es$_4$ strata

and dark-gray mudstone. Cores are collected from this PSS6. Fining-upward sequence with trough cross-bedding, ripple cross-bedding are common in cores. Microscope observation shows a poorly sorted characteristics. To sum up, LST of well H631 is braid-delta front, further divided into subaerial distributary channel and mouth-bar. TST consists of oil shale, and dark-gray mudrock of semi-deep lake.

### 5.3.1.2   Cross-sections

#### (1)   Wells D66-D83-D139-D126

This section is parallel to the direction of source. From west to east, it is successively wells D66, D83, D3, D139, and D126. The subaerial channel sandstone is relatively close to the lake margin, whereas mouth-bar and sheet sandstone is relatively close to lake center. The deeper water and intensive wave trigged the reconstruction of deposits in braid-delta front,

forming beach-bar deposits. In TST, the rising lake level reformed the deposits of LST, and so caused the formation of beach-bar around wells D139 and D126 (Fig. 5.15).

#### (2)   Wells H13-Q108-D414-D83-D16-D24-S30-SG17

This section is perpendicular to the source direction, extending from the southern Huanxiling Area to the northern Shubei Area. From south to north, it is successively wells H13, Q108, D414, D83, D16, D24, S30, and SG17. This cross-section passed several areas, and almost revealed the main sedimentary bodies in the West Sag, Liaohe Depression (Fig. 5.21). Well H13 in the Huanxiling Area and well D414 in the Dujiatai Area are dominated by braid-delta front, whereas well Q18 in the Qijia Area is dominated by beach-bar deposits formed from bedrocks. Well S30 in the Shubei Area is also dominated by beach-bar deposits, which were sourced from delta sandstone as well as bedrocks by waves (Fig. 5.16).
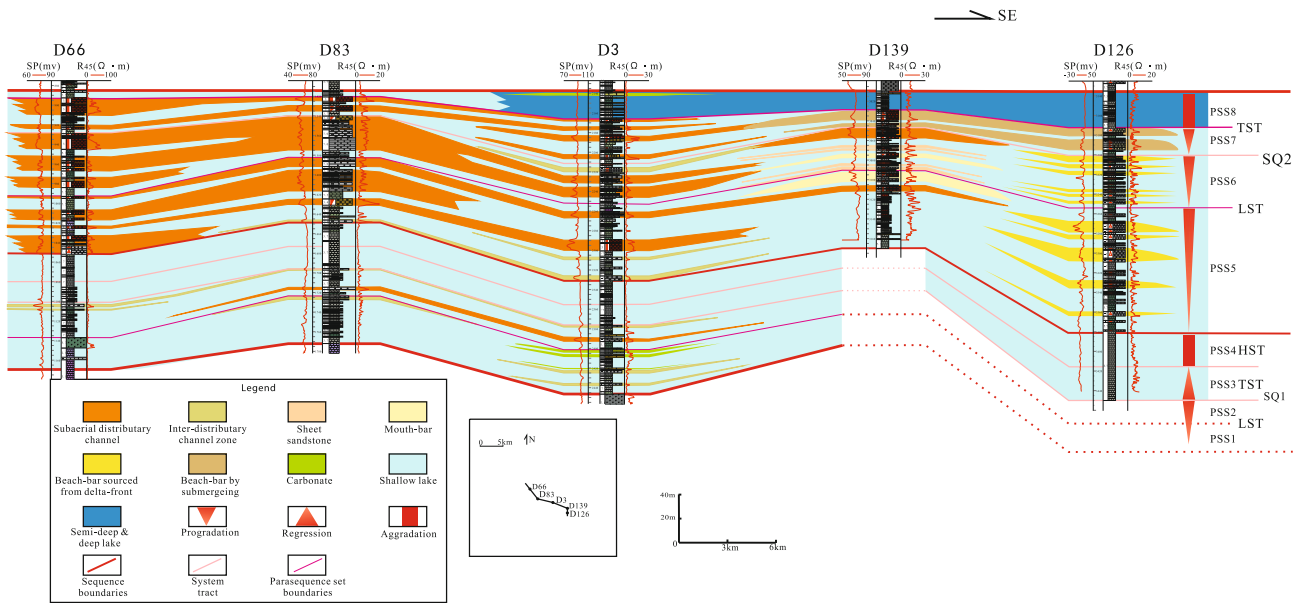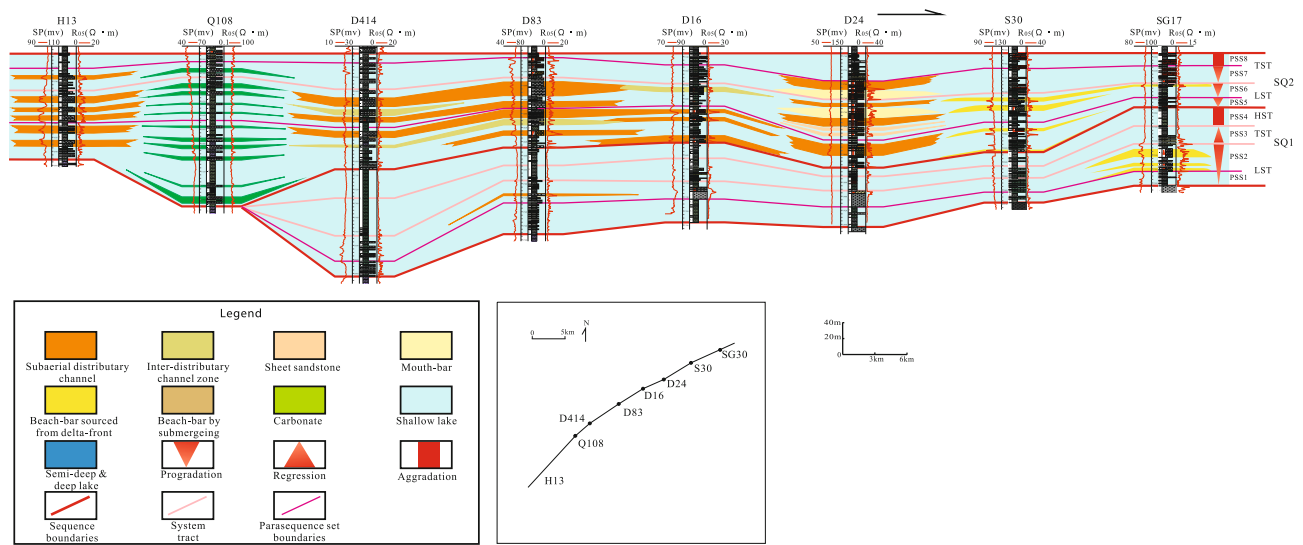
**Fig. 5.15** Cross-section of wells D66-D83-D139-D126



**Fig. 5.16** Cross section of wells H13-Q108-D414-D83-D16-D24-S30-SG17

### 5.3.1.3 Seismic Attributes Analysis

Core and well-log data can precisely characterize the sedimentary characteristics, but can hardly reflect the flat distribution of facies. In regards to beach-bar deposits, the lateral distribution is far higher than the thickness, making it difficult to characterize the lateral distribution by traditional seismic section. Seismic sedimentology is thus employed here to solve above problems (Zeng and Hentz 2004), which makes the thin-bedded sandstone bodies recognizable.

90° Phase Rotation

Zero-phase is traditionally regarded as the final result of seismic data processing. However, thin-bedded sandstone doesn't corresponded to phase axis one by one. 90° phase rotation, however, can enable the phase axis consistent to the sandstone layers (Zeng and Backus 2005). The target layer in this chapter is characterized by interbedded thin sandstone (<10 m thick) and mudrock layers. The strata velocity is *ca.*
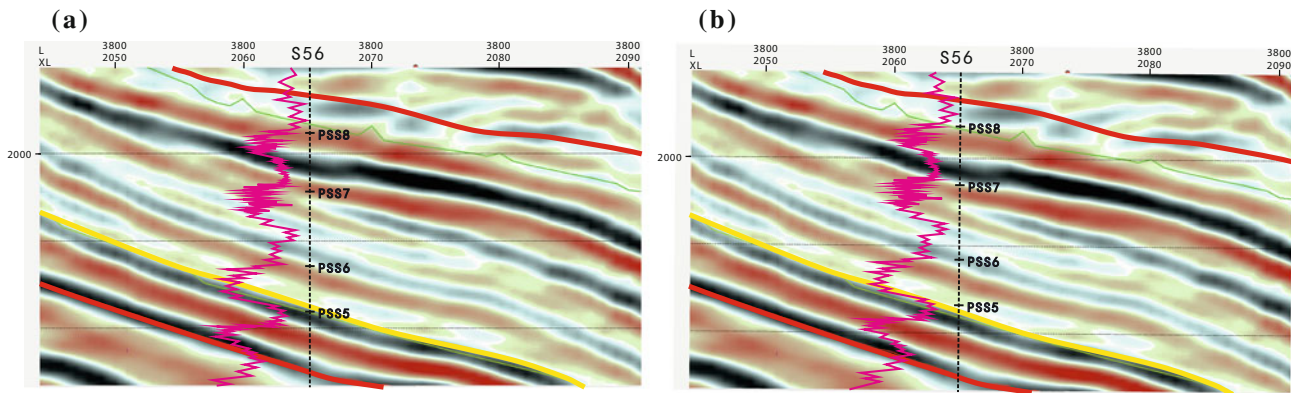
**Fig. 5.17**  **a** 0° phase seismic section; **b** Seismic section after 90° phase rotation

4000 m/s, with a tuning thickness of 30 m ($\lambda/4$). These thin-bedded sandstone layers can hardly be recognized in traditional seismic section, but can be recognized after 90° phase rotation. Figure 5.17 is a cross-section along the source direction. It is shown that well logs and seismic data are not well matched in zero-phase condition (Fig. 5.17a), but well matched after 90°-phase rotation (Fig. 5.17b).

In addition, the amplitude in seismic section matches with lithology interpretation in well logs after the 90°-phase rotation. However, petro-physical analysis is also necessary for predicting lithology in strata slice. The target is characterized by sandstone and mudrock, with sandstone and mudrock show high and low impedance, respectively. Figure 5.18 is the rendezvous plot between impedance and *GR*. As shown in this figure, sandstone and mudrock are obviously different in impedance. The relationship between impedance-polarity/amplitude and lithology layers are established based on the response of impedance association to lithology association. Therein, medium to high impedance indicates sandy deposits, and low impedance indicates muddy deposits.

Strata Slice Analysis

Strata slice method is based on inserting a series of surfaces between two time-parallel surfaces to study the flat distribution of facies and sedimentary systems. It is getting much more important along with the transformation from exploring structural reservoir to lithologic reservoir. The method extracts the seismic amplitude in these continually inserted surfaces, which show the evolution of sedimentary systems. The principle is based on the distribution area of sedimentary bodies is much higher than thickness, and the lateral resolution is commonly much higher than vertical resolution for seismic data. Hence, these sedimentary bodies can be recognized well in flat map, although unrecognizable in seismic section. For example, the beach-bar can be clearly recognized in flat map (Fig. 5.19) (Zeng et al. 1998).
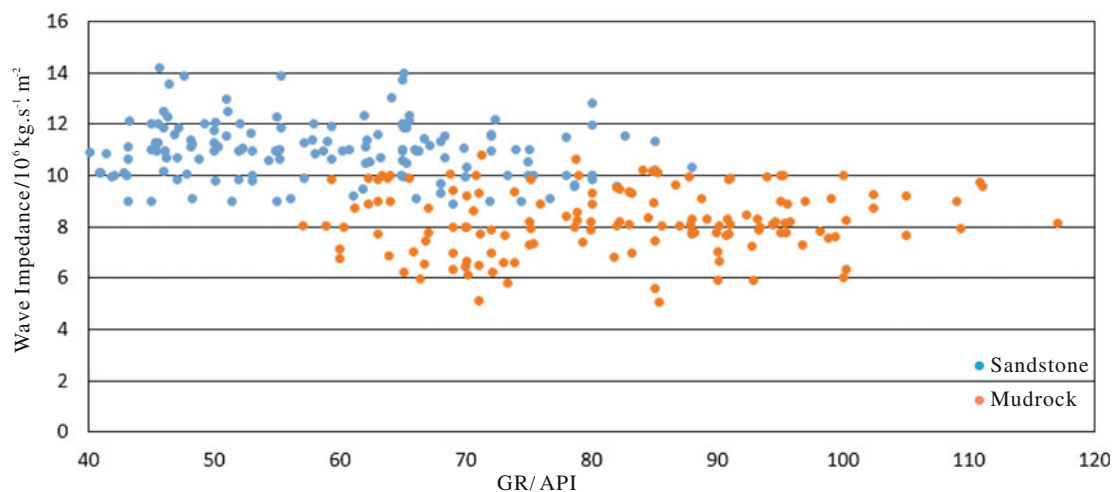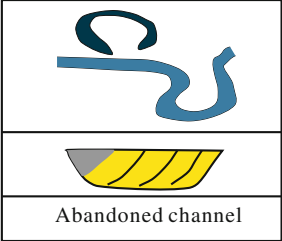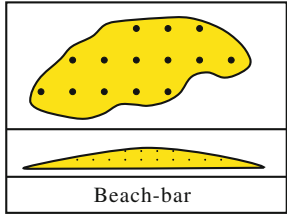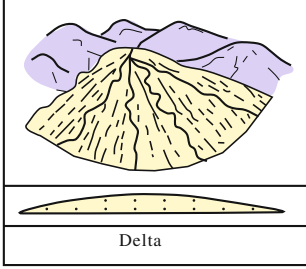


**Fig. 5.18**  The GR-wave impedance plot of well S56, the SQ2 of West Sag, Liaohe Depression

**Fig. 5.19** Vertical to horizontal proportions of sedimentary bodies



| Horizontal≈Vertical | Horizontal＞＞Vertical |
|---|---|
| Abandoned channel | Beach-bar |
| | Delta |
| 1% | 99% |

The selection of time-parallel phase axis is the base to obtain strata slice. In the West Sag of Liaohe Depression, sequence boundaries and MFS is recognizable. As a consequence of the complex tectonic background and frequent variation of sedimentary bodies, the mutual verification from several phase axis can lower the risks of incorrect interpretation. Once the time-parallel surface is determined, a linear geology-time model can be defined. The X, Y axis of this model is same to the original seismic data, but its Z axis corresponds to time. All the phase-axis in the seismic data are horizontal. The amplitude slices along time-parallel surfaces constitute the data bodies. This chapter extracted 135 strata slices in an interval of 1 ms in the Es$_4$ West Sag. Each of the above slices is converted to seismic section to compare with the strata, and also mutually confirmed with well, core data. Thus, the most representative and clear strata slice is selected in each parasequence set.

Here more than ten types of seismic attributes are extracted and compared. The results shows that root mean square amplitude is the most sensitive in the West Sag, and can clearly reflect the distribution of sandbodies. Figure 5.20 is the root mean square amplitude extracted from SQ2-PSS5. The negative-amplitude (red color) presents as belt and flake shape. The seismic facies of six red-colored areas are recognized. Therein, the Shubei Area is characterized by medium-amplitude and medium-continual seismic facies, with the long elongate parallel to lake margin. Cores and borehole logging data show this area is dominated by thin fine-grained sandstone, siltstone with interbedded mudrock. Sedimentary structures such as wave ripples are common. Hence, the Shubei Area is recognized as shallow-water beach-bar

deposits. The Dujiatai Area is characterized by medium-high amplitude and medium continual lenticular seismic facies. In the western part of the area, it is conglomerate beach-bar deposits as recognized in seismic facies. Huanxiling Area is characterized by medium to high amplitude and medium-continual progradational seismic facies, recognized as braid-delta front deposits. This blue area of the figure is characterized by low amplitude and medium-continual seismic facies, recognized as shallow lake deposits (Fig. 5.20). The seismic facies of PSS2 is similar to those in PSS1; it indicates the sedimentary characteristics of PSS2 are similar to those in PSS1, but with smaller sandbody scale. In TST-PSS3, medium-amplitude and medium-continual lenticular seismic facies widely distribute in the eastern Dujiatai Area. It is also beach-bar deposits as recognized in wells and seismic data.

### 5.3.2 Depositional Model of Beach-Bar Deposits in the West Sag, Liaohe Depression

Five types of beach-bar deposits are recognized in the sag by depositional mechanisms. They are reformed from (1) the side edge of delta, (2) distal part of delta-front, and (3) bedrocks, or formed by (4) submerging of previously deposits during lake-level rising, and (5) storm events.

Type 1

It commonly distribute along the side edge of delta-front. As river flows into lake, the dynamics from river becomes weak, instead, wave dynamics enhanced. Thus, delta-front
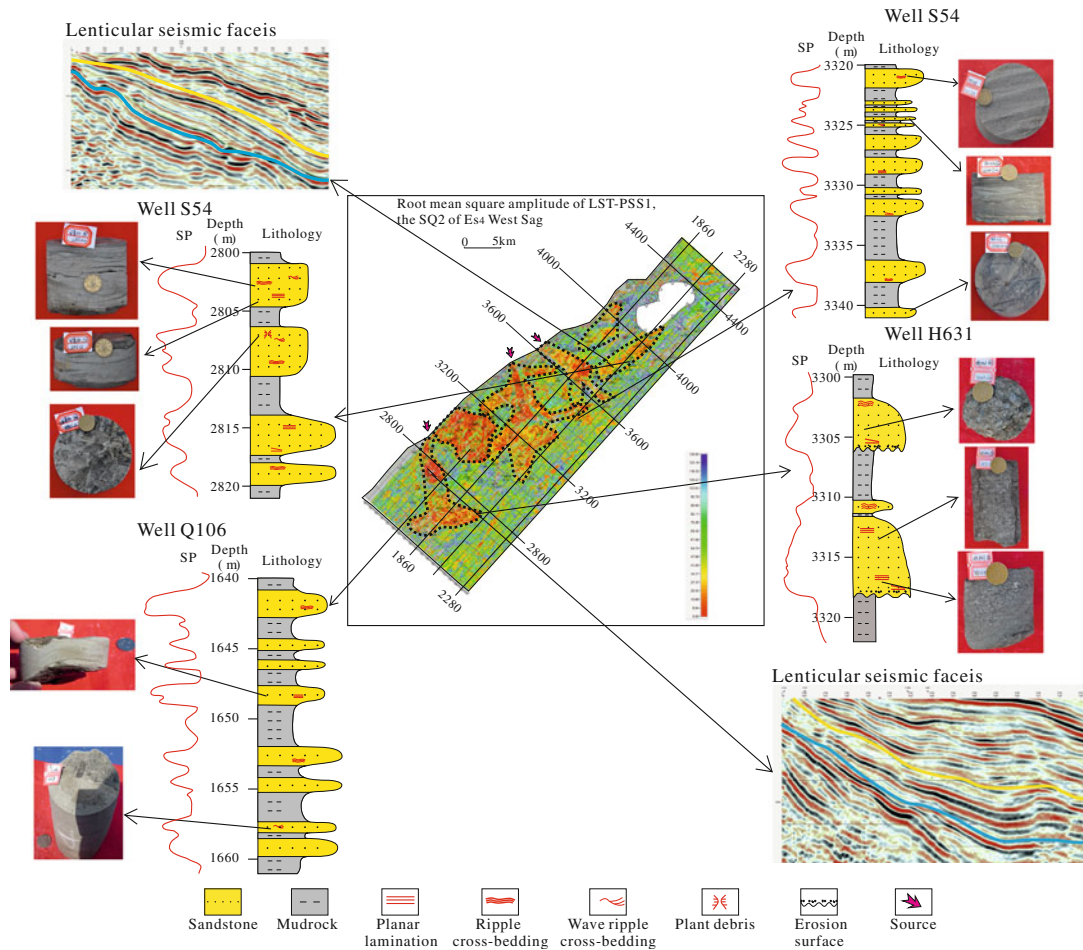
**Fig. 5.20** Facies interpretation and seismic slice calibration of SQ2-LST-PSS5, the West Sag of Liaohe Depression

sandbodies is easily influenced by wave that are parallel to shoreline. It re-transported deposits to the side edge of delta, forming beach-bar deposits. In addition, burial hill develops between deltas, facilitating the re-deposition of sand around the hills. In type 1, the sandstone layers are thin-bedded (0.5–7 m thick). Mudrocks are green-gray, indicating a relatively shallow water environment. Sedimentary structures such as wave cross-bedding, parallel cross-bedding, wash cross-bedding are common. The *SP* curve shows coarsen-upward characteristics. The resistivity curves show abnormally high finger-shape properties (Fig. 5.21).

### Type 2

It commonly distribute in front of delta-front. In the early rift stage, the lake is relatively shallow, and the delta sandbodies only extends a short distance from the shoreline. The wave dynamics are relatively strong in comparison to river dynamics in areas of delta-front, influencing the sandbodies.

Hence, beach-bar deposits formed in front of delta-front sandbodies. Type 2 deposits is similar to type 1 deposits in sedimentary structures. However, some horizontal plant fossils present in Type 2 deposits, indicating a depositional environment far from the shoreline (Fig. 5.22).

### Type 3

It is mostly conglomerate in grain size, formed by erosion of bedrocks in shoreline areas with weak source input. In addition, the conglomerate by terrigenous input were also converted to beach-bar deposits in lake level shrinking. Type 3 deposits commonly formed in areas between two sources. In lithology profile, it is mostly thick mudrock with some thin-bedded sandstone and glutenite. Wavy cross-bedding and plant fossil are common in cores. The *SP* curve shows coarsening-upward characteristics; the resistivity curve shows finger-shape. In seismic section, it presents as lenticular shape (Fig. 5.23).
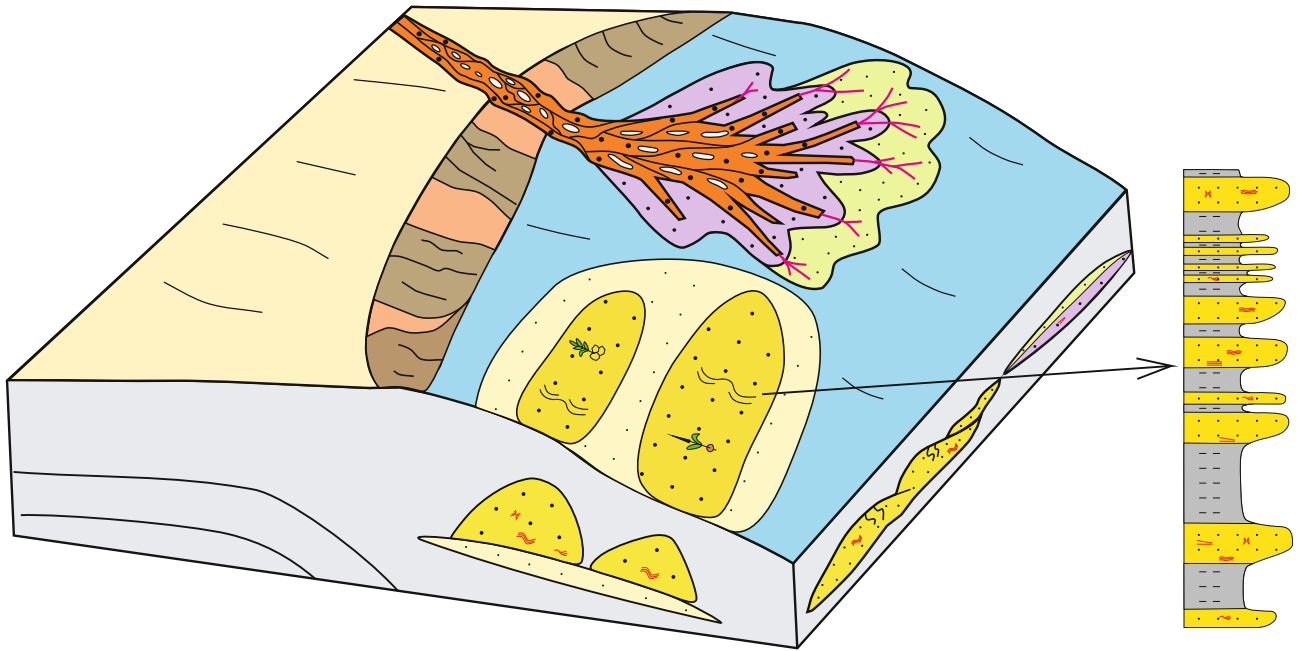
**Fig. 5.21** Formation model of beach-bar deposits at the side ridge of braid-delta
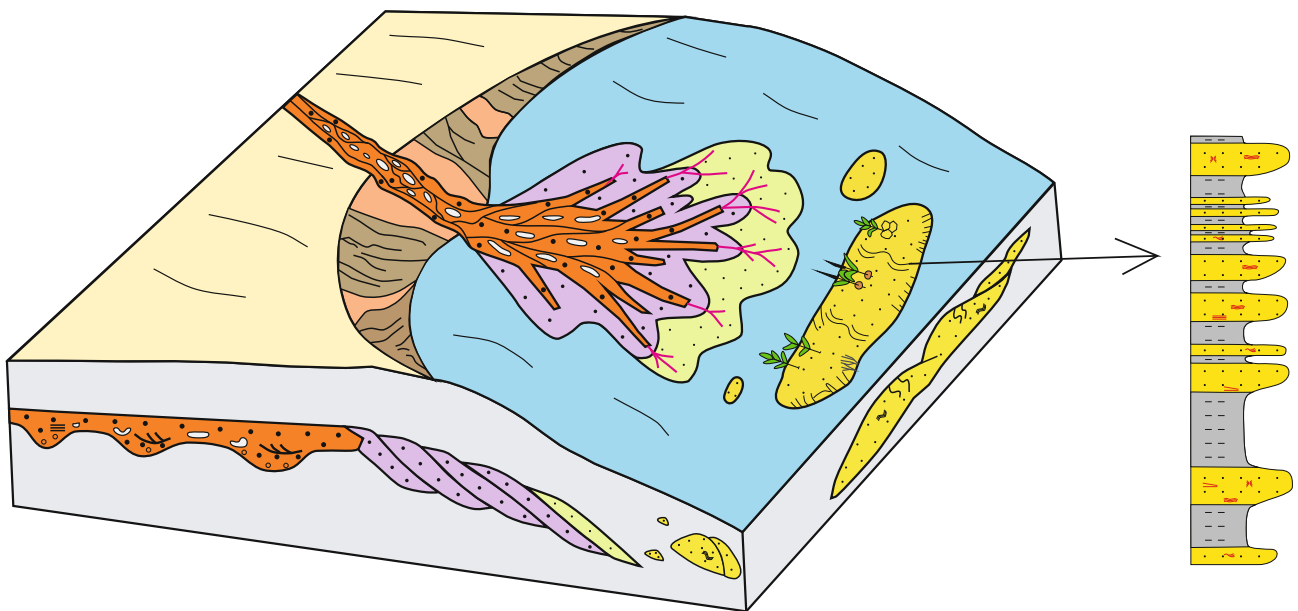


**Fig. 5.22** Formation model of beach-bar deposits in front of braid-delta front

Type 4

Type 4 was formed in early TST. The enhancement of wave dynamics by rising lake level reformed the previous deposits of LST, forming beach-bar deposits. In lithology profiles, it is brown muddy fine-grained sandstone and gray mudrock, indicating a relatively rising lake level. Wave ripple cross-bedding, and plant fossils are common. SP curve

shows coarsening-upward characteristics; resistivity curve shows abnormally high finger-shape (Fig. 5.24).

Type 5

In the Es$_4$ period of West Sag, some beach-bar also formed in semi-deep to deep-water environment deposited by storm events. The lithology is mainly fine-grained sandstone,
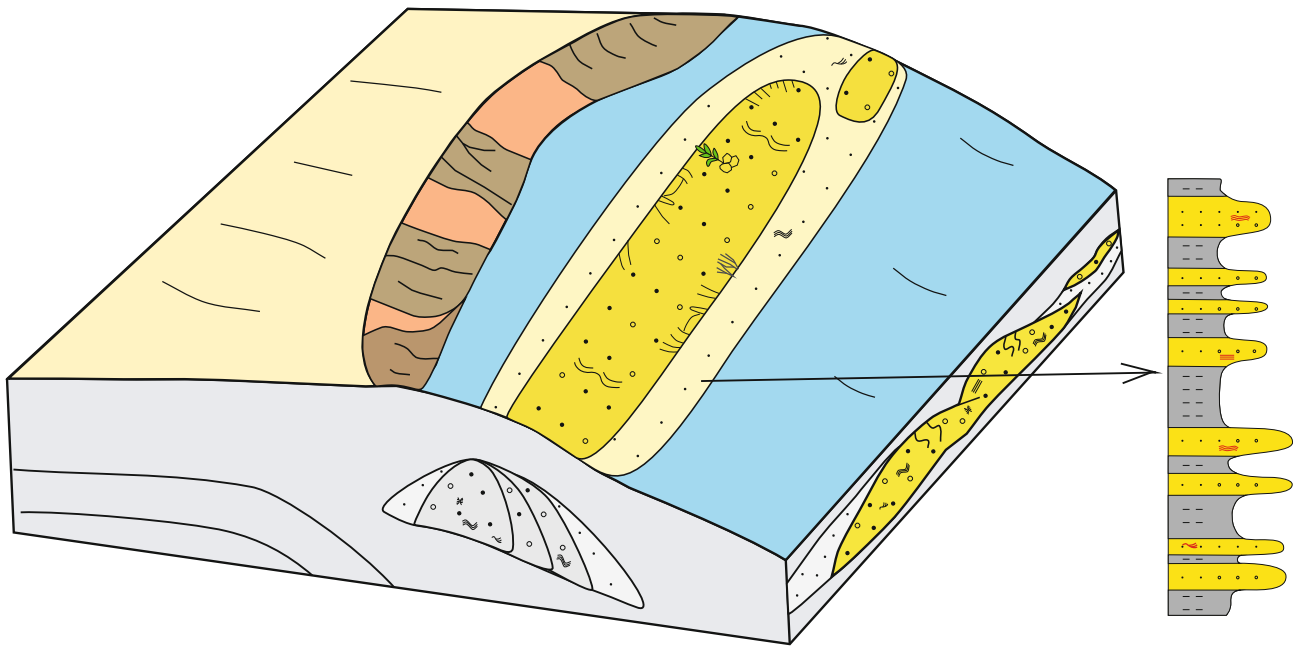
**Fig. 5.23** Formation model of beach-bar deposits sourced from bedrock
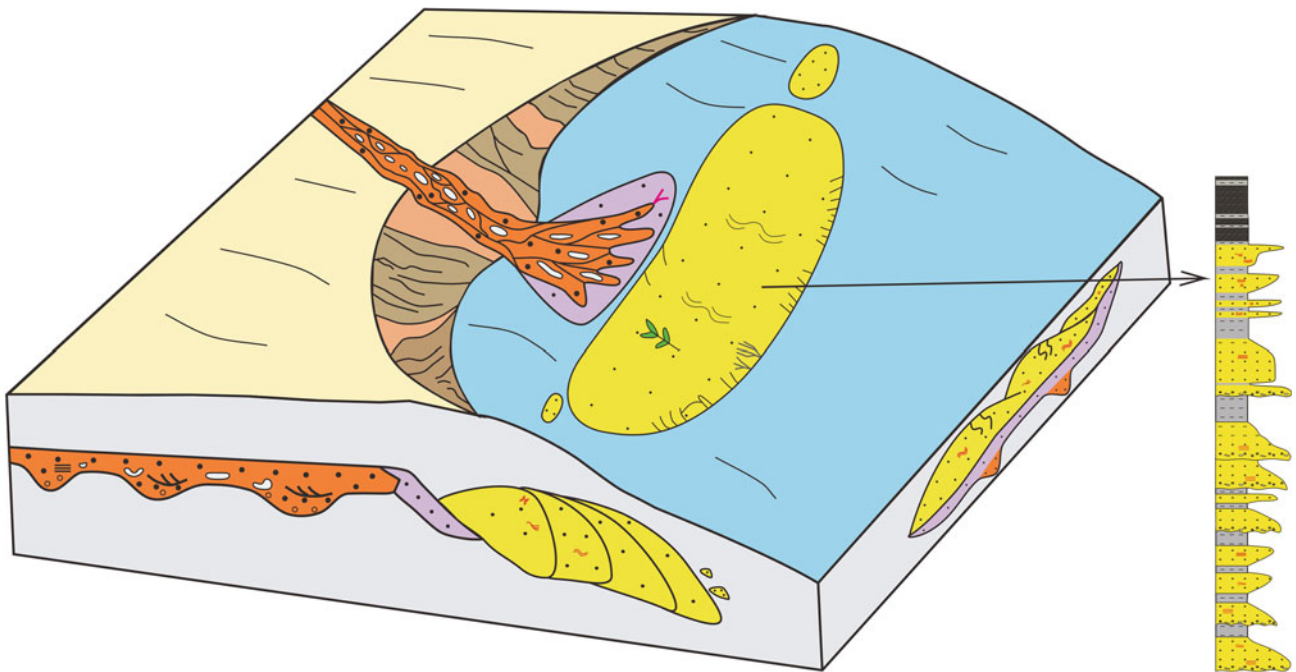


**Fig. 5.24** Formation model of beach-bar deposits formed from submerging

siltstone, and gray mudrock. Sandstone and mudrock frequently alternates. It is mostly fining-upward in a facies sequence. Sedimentary structures of storms deposits (e.g., hummocky cross-bedding, teared mud clasts, biological escape structures) (Wang et al. 2015). The *SP* curve shows box-shape with minor serrated characteristics (Fig. 5.25).

### 5.3.3 Windfield-Source-Basin System in the Upper Es$_4$ West Sag, Liaohe Depression

The "Windfield-Source-Basin" System controlled the distribution of sedimentary facies and sedimentary systems.
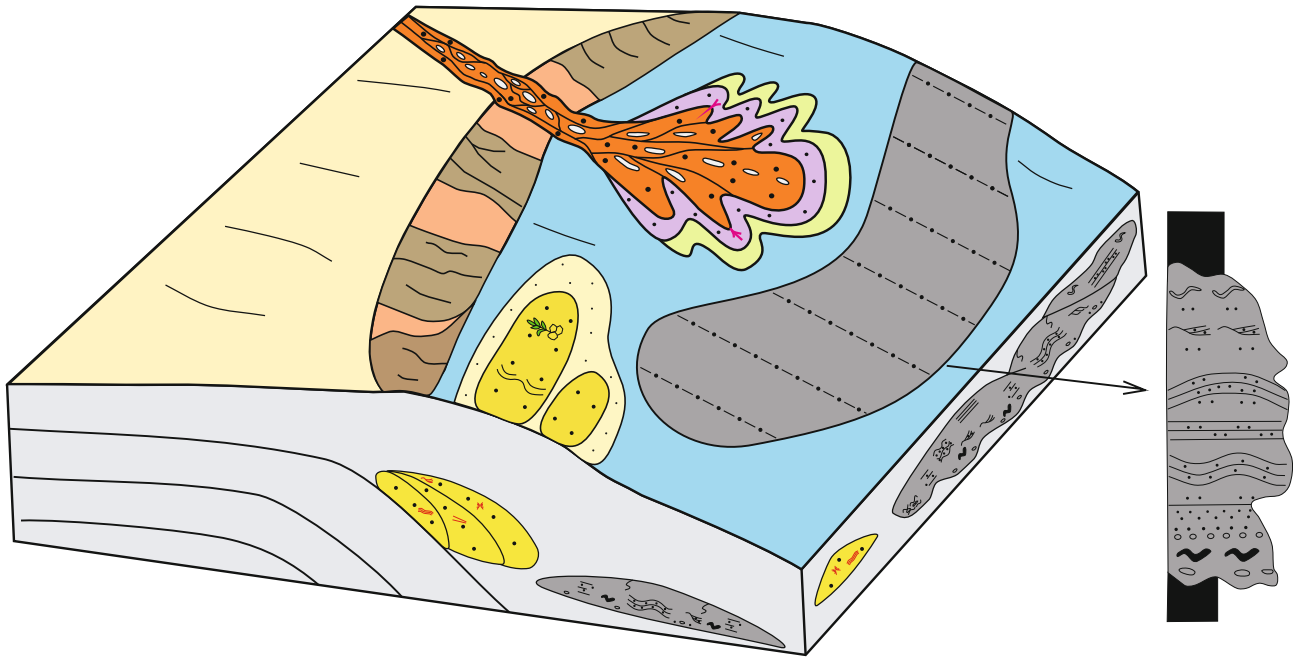
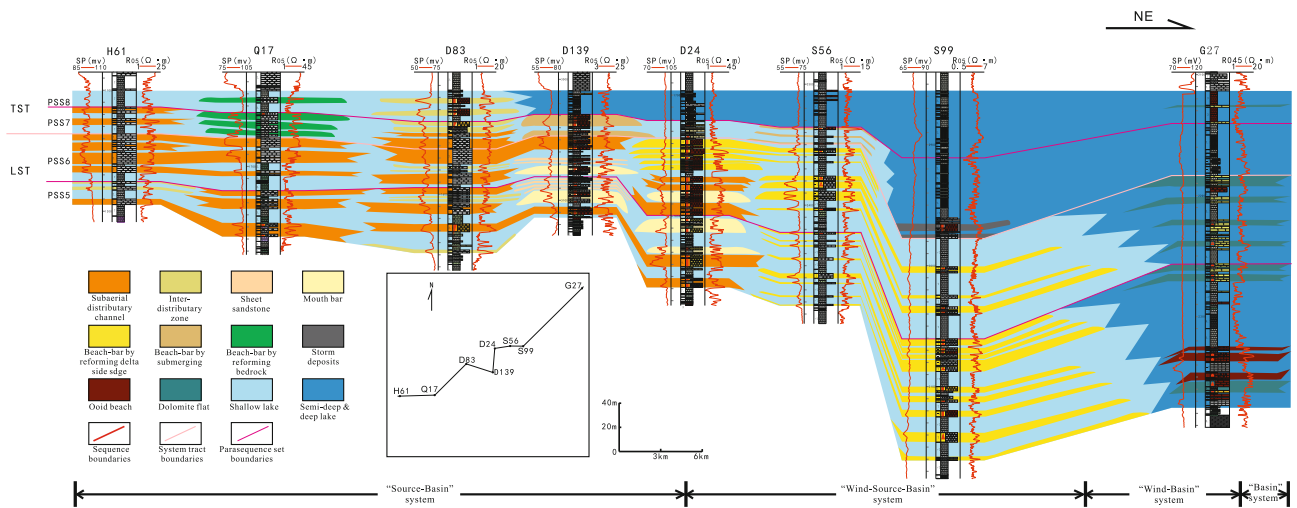**Fig. 5.25**  Formation model of beach-bar deposits formed by storms



**Fig. 5.26**  Cross-section sedimentary facies of wells H61-Q17-D83-D139-D24-S56-S99-G27

Cross-sections of wells are used here to analysis the controlling factors of each sedimentary system (Fig. 5.26). Four sedimentary systems are thus defined here.

Source-Basin Sedimentary System

The Liaohe Depression is a half-graben basin with an elongate shape. The paleo-geomorphology is relatively high in the southern part and low in the northern part. Correspondingly, water depth gradually increases from south to north, which controlled the distribution of sandbodies. Source and basin properties controlled the sedimentary

systems of the Huanxiling, Qijia, and Dujiatai Areas in the southern part of the sag. Three main "point" sources developed from the West High to West Sag. Because of the gradient formed by tectonic activities, braid-delta developed in the lake margin, acting as the main facies in the above three areas. Therein, Huanxiling Area has the shallowest water depth, in which source property is the main controlling factors. The effect of source gradually decreased from south to north, as a result of increasing water depth. Thus, braid-delta is relatively small in the Dujiatai Area. Instead, the wind from southeast direction effected the sandbodies, forming beach-bar deposits in front of the delta-front.

Windfield-Source-Basin Sedimentary System

Beach-bar deposits widely distribute in the Es$_4$ strata in Shubei Area. The factors of wind, source, and basin co-controlled the distribution of beach-bar deposits. "Wind" refers to the paleo-windfield in the depositional period. In some cored wells (e.g., S52, S103, S603), ripple mark, and wave ripple cross-bedding are common, indicating a strong wave dynamic by wind. In the TST of some cored wells (e.g., S66, S99, and S100), truncated structures, escape structures, and hummocky cross-bedding are common, suggesting the deposition by storm events. "Source" refers to the original minerals and grains for beach-bar deposits. In the Shubei Area, the source mainly come from the reform of the side edge of braid-delta in the Dujiatai area. Meanwhile, the erosion of exposed buried hill also provides some sources. "Basin" refers to the paleo-geomorphology and paleo-water depth. Therein, beach-bar deposits prefer to deposit on or around the subaerial hills, slope, and platform. In the Shuguangbei Area, the burial hill in its northern part is ideal for beach-bar deposition. The paleo-water depth is 4–6 m through calculating the wave ripple and bar thickness (see Chap. 4 for methods). Generally, wind induced waves, and then the wave dynamics controlled the distribution of beach-bar deposit; the distribution of source controlled the flat distribution and model of beach-bar. The evolution of paleo-geomorphology and paleo-water depth controlled the location and layers of beach-bar deposits.

Wind-Basin System

Terrigenous input is poor in the Es$_4$ Gaosheng Area because of semi-deep to deep water environment. Ooid beach (wells G27, SG84) and biological debris beach (wells G19, G25) presents in the LST of some part of this area. This beach-bar type is mainly controlled by paleo-climate and basin properties, which mainly formed in environment with little terrigenous input. A relatively arid climate promotes the evaporation, thus facilitating the chemical deposition of calcitic minerals. Meanwhile, *Ostracoda*, *Gastropoda*, algal, and some benthic fossil widely distribution in such condition, thus facilitating the formation of biological carbonate. The waves formed by wind is also important for the deposition of allochemical grains. Paleo-geomorphology is the primary controlling factor on carbonate deposition; the subaerial hills and slope with little terrigenous input is the ideal environment for carbonate beach-bar. In addition, paleo-water depth controlled the productivity and preservation of carbonates.

Basin System

The Gaosheng Area in the West Sag is closed to some degree in water current circulation. Water current is weak in the TST period, thus the deposits are mainly laminated to massive limestone and mudrock.

## 5.4    Detailed Study of Beach-Bar Deposits

The Es$_4$ Shubei Area is a typical example in studying beach-bar, because: (1) it contains many types, (2) the sedimentary characteristics are typical, and (3) the controlling factors varies among different types. Therefore, a more detailed characterization of sequence stratigraphy and sedimentary systems is conducted on the beach-bar deposits in the Shubei Area.

### 5.4.1    High-Resolution Stratigraphy Framework

Parasequence is the basic unit in sequence stratigraphy analysis. It is typically several to tens of meters thick, with a time period of tens to hundreds of thousand years. In a parasequence unit, water depth gradually decreases upward. Other phenomena include: (1) single layer thickness gradually increases upward, (2) the bioturbation intensity gradually decrease upward, and the water dynamics gradually becomes strong upward. Cores, outcrops, and wells log data are effective ways to recognize parasequence unit.

According to these principles, the stratigraphy framework in typical beach-bar areas are further divided at a resolution of parasequence (LST of SQ2 in the Shubei Area) (Fig. 5.27).

High-resolution stratigraphy framework in the Shubei Area is established based on cores, well logs, and seismic data. It contains two third-order sequence (SQ1 and SQ2 from bottom to top). The detailed division is shown in Table 5.3.

### 5.4.2    Sedimentary Systems of Beach-Bar in the Shubei Area

1. Facies in cores and well logs

Cores of beach-bar deposits from seven wells are observed. Therein, well S52 is analyzed here as a typical well.

Well S52 is located in southern Shubei Area, close to the Dujiatai Area. Three cored sections are collected in the Es$_4$ strata. Generally, SQ1 belongs to shallow lake environment, with the LST dominated by green basalt and gray mudrock, and the TST and HST dominated by thick gray mudrock and oil shale.

The LST of SQ2 is dominated by thin-bedded sandstone and gray-green mudrock, indicating a relatively shallow
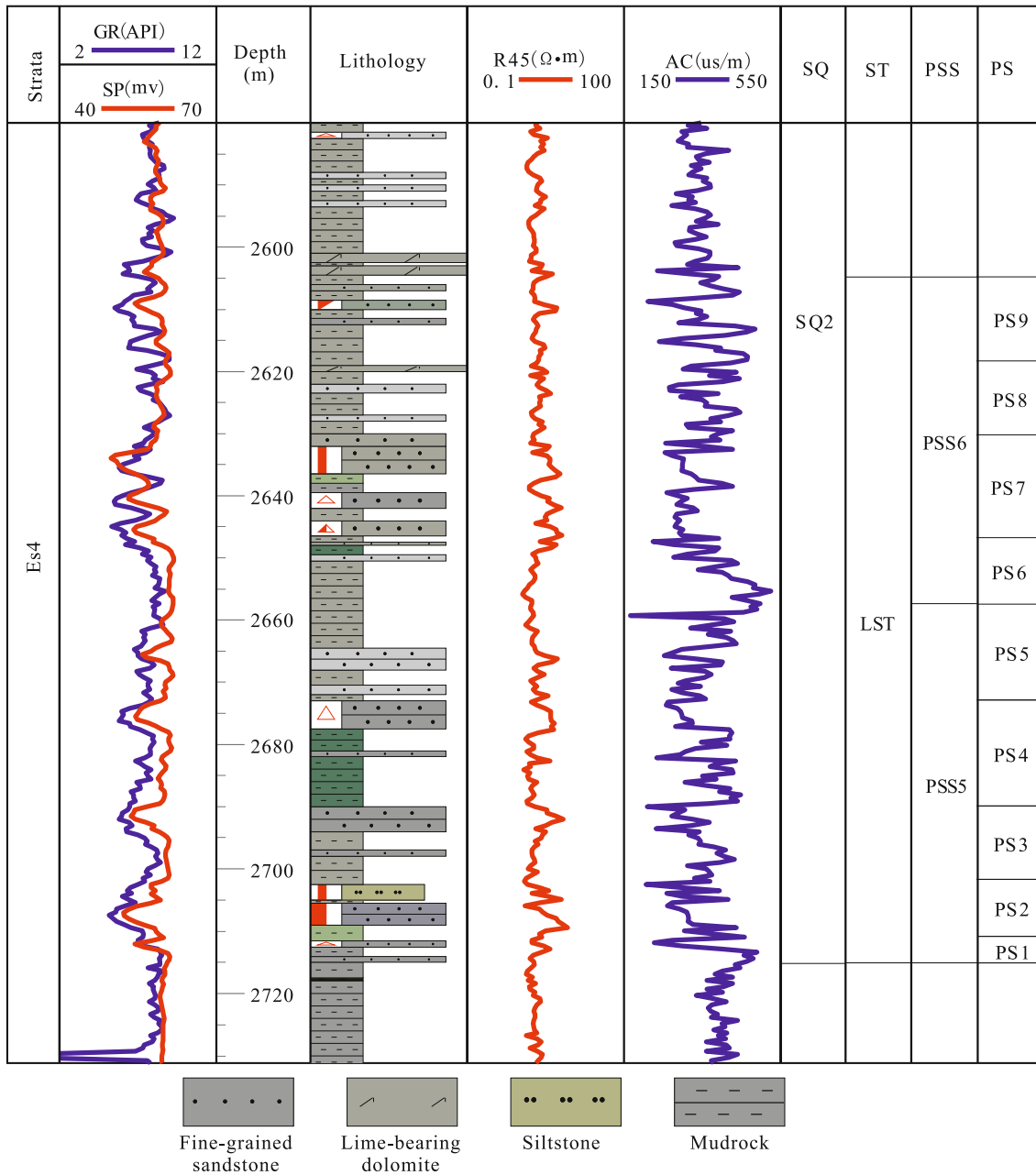
Fig. 5.27 Parasequence units in the LST of SQ2, well S52. SQ = Sequence, ST = System tract, PSS = Parasequence set, PS = Parasequence

water environment. The beach-bar deposits commonly show finger-shape in well logs (Li et al. 2008a). Ripple cross-bedding, planar lamination, and wash cross-bedding are common in cores, indicating strong wave dynamics (Tian and Jiang 2012). Therefore, beach-bar prefer to deposit in LST. According to well log characteristics and bar thickness, the main bar-body and bar-edge is thus defined.

Lake level rose in the TST of SQ2, and the sandstone were mainly formed by storm events (Fig. 5.28).

2. Flat distribution of beach-bar sandbodies

The analysis of flat distribution of sandbodies is conducted at a resolution of parasequence set. Here we take PSS5 as an example (Fig. 5.29). PSS5 locates in the lowermost LST of SQ2. The water is relatively shallow at this time, and beach-bar widely distribute in this period. Two rows of beach-bar distribute in the Shubei Area in PSS5, which are close to and far from the shoreline, respectively. The

**Table 5.3** High-resolution stratigraphy framework in the $ES_4$ West Sag, Liaohe Depression

| Strata | Sequence | System tract | Parasequence set | Parasequence |
|---|---|---|---|---|
| $ES_4$ | SQ2 | TST | PSS8 | |
| | | | PSS7 | |
| | | LST | PSS6 | PS9 |
| | | | | PS8 |
| | | | | PS7 |
| | | | | PS6 |
| | | | PSS5 | PS5 |
| | | | | PS4 |
| | | | | PS3 |
| | | | | PS2 |
| | | | | PS1 |
| | SQ1 | HST | PSS4 | |
| | | TST | PSS3 | |
| | | LST | PSS2 | |
| | | | PSS1 | |

sandbodies are thick at this time, with the total thickness higher than 20 m. The bar far from the shoreline reaches *ca.* 40 m. The sandstone/strata thickness ratios of the bars are 30–40% and >40% for the rows close to the shoreline and far from the shoreline, respectively. The beach sandstone distribute around the bar sandstone, with a large distribution area.

## 5.5 Controlling Factors for the Distribution of Beach-Bar Deposits

More than half of the beach-bar deposits distribute in the Shubei Area, with a total area of 60 km². Several factors such as paleo-geomorphology, paleo-source, paleo-water depth, and paleowindfield co-controlled the distribution of beach-bar in this area.

The $Es_4$ period belongs to the early rift stage, with a gentle slope and shallow water depth. The Shubei Area is far from the main source. Waves converted the braid-delta into beach-bar. The subaerial hill here also facilitates the beach-bar deposition. Generally, wind (paleo-wind force, paleo-wind direction)-source (paleo-source)-basin (paleo-geomorphology, paleo-water depth) co-controlled the beach bar depositional process and sedimentary systems.

### 5.5.1 Reconstruction of Paleo-Geomorphology

Paleo-geomorphology is co-controlled by a set of factors such as tectonic background and paleo-climate. Paleo-geomorphology in the Shubei Area is rugged because of the volcanic activities were earlier than the $Es_4$ period.

The paleo-geomorphology reconstruction for $Es_4$ strata can be used to analysis its effect on beach-bar deposition.

The reconstruction of paleo-geomorphology is based on the following four steps. Firstly, the residual strata thickness is made and regulated in wells and seismic data. Secondly, the eye thickness is corrected. Thirdly, Basin Mod 1D software is used to reconstruct the burial history and compaction effect. Finally, the paleo-geomorphology map is made using 3D software.

Calculation and Regulation of Remaining Thickness

A correct calculation of remaining strata thickness is necessary for reconstructing the paleo-geomorphology. The remaining thickness refers to the strata thickness after compaction, erosion, and tectonic events. It is the base to reconstruct the paleo-thickness, which can generally reflect the distribution characteristics of paleo-geomorphology.

The base of remaining strata should be the bottom surfaces for beach-bar deposition, and the top of strata should be the surface after beach-bar deposition. According to the sequence stratigraphy characteristics of $Es_4$ Shubei Area, the bottom boundary of SQ2 is chosen as the strata bottom surface, and MFS of SQ2 as the strata top surface.

Well-seismic data calibration and tendency compensation of inter-wells paleo-geomorphology are used in reconstructing strata thickness. This method uses well data as controlling point, and seismic data to predict the information between wells. The process includes following four steps: (1) well calibration of multi-wells, and calibration of target layers in the seismic data; time-depth calibration is made to get the strata thickness data, (2) gridding the strata thickness from seismic data, and also extract the data from well. The

**Fig. 5.28** Lithology, well-logging, and facies interpretation of well S52. SQ = Sequence, ST = System tract, PSS = Parasequence set, PS = Parasequence
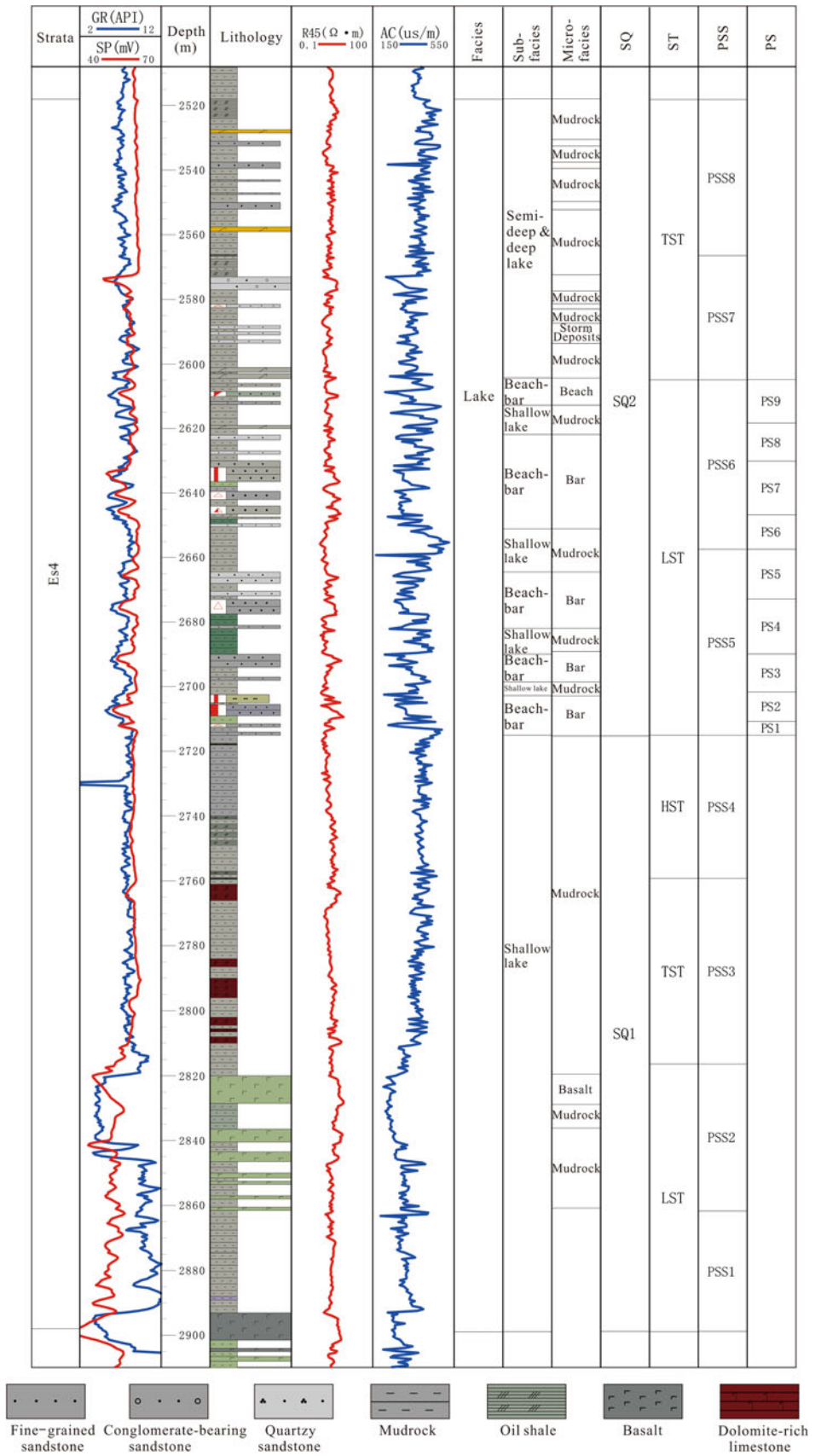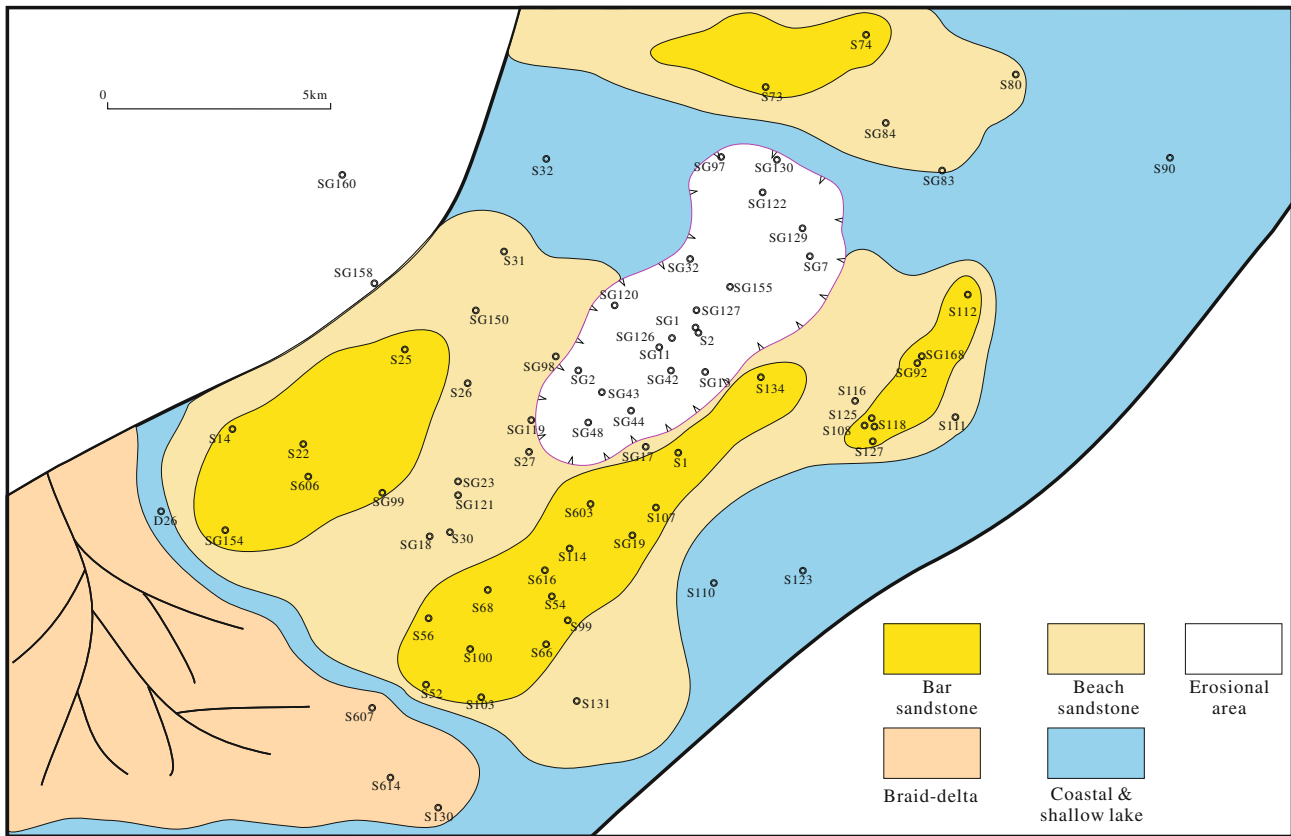
**Fig. 5.29** Sedimentary facies of parasequence set 5 at the SQ2, the Shubei Area

deviations between data from seismic grid and wells are calculated, and then fitted using linear equations, (3) merging the grid data with strata thickness map, and finally get the flat isoline map.

According to the above method, the strata layer data from 3D seismic data and *ca.* 80 wells are used and the finally get the remaining strata thickness of each strata.

Dip Angle Correction

Seismic data are used to calculate the dip angle of strata top surface. The time surfaces in seismic data is converted to burial depth surface through time-depth calibration. Then, gridding the data from the surface and extract the dip angle data. Please see Figs. 2.19 and 2.20 of Sect. 2.3.2 in this book for detailed principles and methods.

Compaction Reconstruction

The physical compaction during burial lowers the porosity, and thus strata thickness decreases. The calculation of original strata thickness is necessary for paleo-geomorphology

reconstruction. According to Eq. 2.16 in Sect. 2.3.2 of this book, the $\Phi$-$H$ relationship is made by using the porosity of cores, thus the primary $\Phi_o$ and compaction factor $C$ can be calculated. The lithology influences the $C$ and $\Phi_o$ values. The SQ2 in Shubei Area is dominated by beach-bar deposits and oil shale. Therefore, the $C$ and $\Phi_o$ values of each lithology are calculated based on the measured porosity and $\Phi$-$H$ relationship.

The porosity curve along with depth changes is thus made using $\Phi$-$H$ data (Fig. 5.30), and thus the primary $C$ and $\Phi_o$ values of each lithology is calculated (Table 5.4).

The calculated compaction factor and primary porosity can be used to reconstruct compaction degree. Currently, there is not a special software to reconstruct compaction degree. However, there are some software to do the burial history. The compaction degree can be calculated in these software for burial history.

Here we take well S52 as an example. The thickness and ratio of each lithology within a strata is defined after defining the top layer and bottom layers of strata. The related data are inputted to Basin Mod software, and thus the burial history and compaction degree is calculated (Fig. 5.31). The
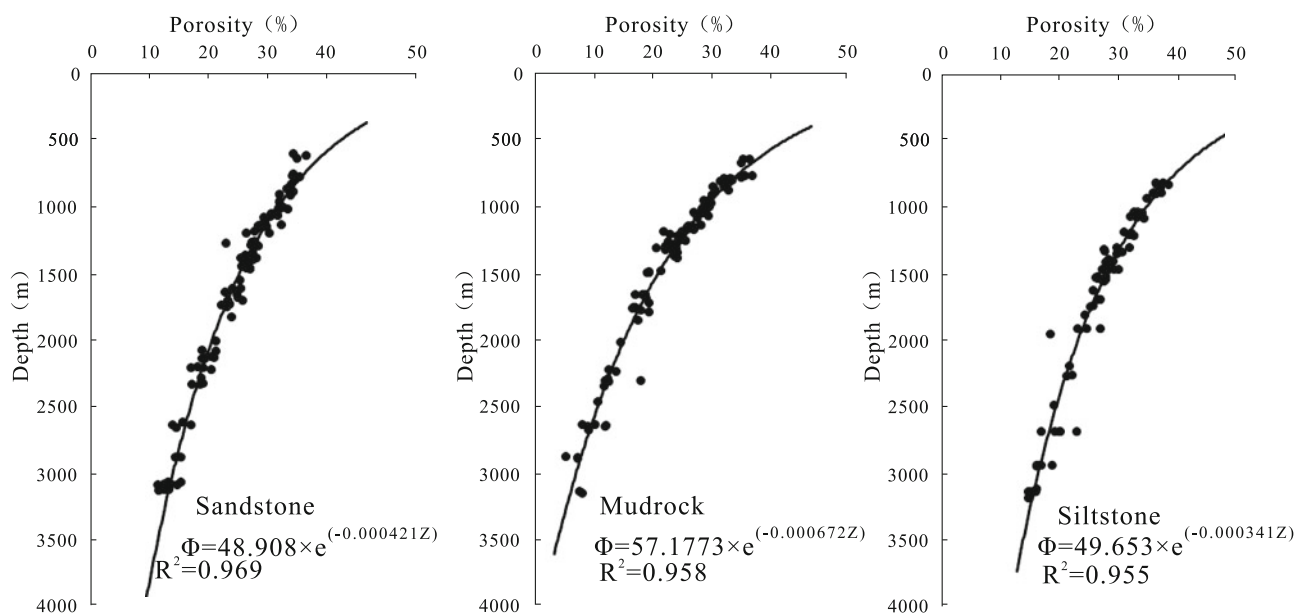
**Fig. 5.30** $\Phi$-H relationship of **a** sandstone, **b** siltstone, and **c** mudrock

**Table 5.4** Primary porosity and compaction factor of sandstone, mudrock, and siltstone

| Lithology | Primary porosity (%) | Compaction factor ($10^{-3}$/m) |
|---|---|---|
| Sandstone | 48.908 | 0.421 |
| Mudrock | 57.177 | 0.672 |
| Siltstone | 49.653 | 0.341 |

compaction degree of 62 wells are calculated in the study area.

Determining the Erosional Area

MFS layer is ideal for reconstructing paleo-geomorphology. However, lake water is shallow in LST and has relatively small areas. In such a condition, some areas for beach-bar deposition may expose to air. Hence, the recognition of erosional area is essential.

The slope in the Shubei Area is uneven influenced by the buried hill. According to the sequence stratigraphy framework, the LST of SQ1 and SQ2 is above the buried hill. In many wells, the dark mudrock and oil shale directly overlies the basalt of Fangshenpao Formation (Fig. 5.32). The areas of buried hill is defined according to sequence stratigraphy framework and the reconstructed strata thickness data. The buried hill was exposed to air at the LST of SQ2, dominated by erosion. From TST of SQ2, the buried hill was submerged, and then dominated by deposition.

The Results of Paleo-geomorphology Reconstruction

The strata data are shown in a 3D map after the above four steps. The paleo-geomorphology map for beach-bar

deposition of the SQ2 is thus determined after the defining of erosional areas (Fig. 5.33).

## 5.5.2  Reconstruction of Paleo-Water Depth

The common methods for paleo-water reconstruction include sedimentology, geochemistry, and paleontology. The Shubei Area is dominated by beach-bar deposits. Therefore, two methods are employed here to calculate paleo-water depth, including: (1) wave ripples (Diem 1985), and (2) beach-bar thickness.

Wave-Ripple in Reconstructing Paleo-Water Depth

Six typical cores with wave ripple were selected to calculate paleo-water depth (Table 5.5). The results show that water depth for beach-bar was mostly shallower than 8 m. In such a water depth, wave current is very strong and thus facilitating beach-bar deposition.

Bar Thickness in Reconstructing Paleo-Water Depth

Bar thickness is also useful in reconstructing paleo-water depth. Here we take well S66 as an example. The thickness
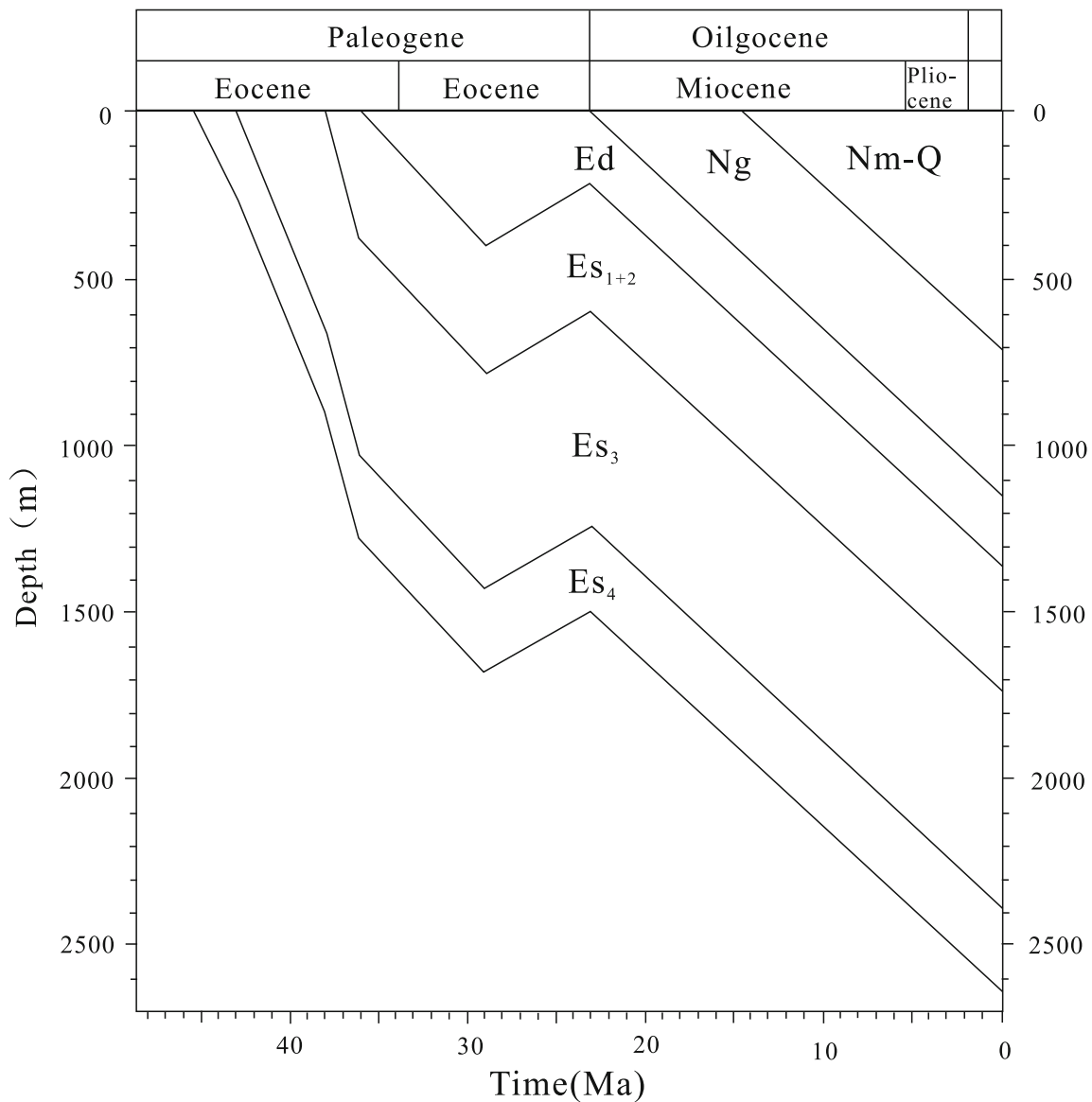
**Fig. 5.31** Burial history of well S52 in the Shubei Area

for inner bar and outer bar is *ca.* 3.49 m, 2.5 m in average, respectively (Fig. 5.34). The compaction factor is 0.59 in well S66. The calculated water depth is 0–1.69 m for scour-backflow belt, and 7.59–11.85 m for broken wave belt is 7.59–11.85 m after regulation. Because the wave base reaches 11.85 m, mostly of the bars located above the wave base. However, storms events can also form beach-bars below the wave base. An integrated beach-bar includes three rows according to the distance from the shoreline, including: (1) coastal bar, (2) inner bar, and (3) outer bar. The paleo-water depth reconstruction shows that beach-bar mostly distribute at a water depth of 2–10 m, which should be coastal and shallow lake.

### 5.5.3 Reconstruction of Paleo-Source

Source analysis is the basic content in reconstructing paleo-geography and paleo-basin properties. It can be used to: (1) judge the existence of paleo-land and erosional area, (2) show the paleo-attitude characteristics, (3) reconstruct the sedimentary systems, (4) define the source properties and tectonic background.

The methods for paleo-source analysis generally include two types. They are: (1) petrology and paleontology observation, including lithofacies, mineral constitution, maturity, fossils etc., and (2) geochemistry analysis, including major, minor, and trace element and isotope data etc.

**Fig. 5.32** Strata characteristics of well SG129 located at the buried hills of Shubei Area. SQ = Sequence, ST = System tract, PSS = Parasequence set
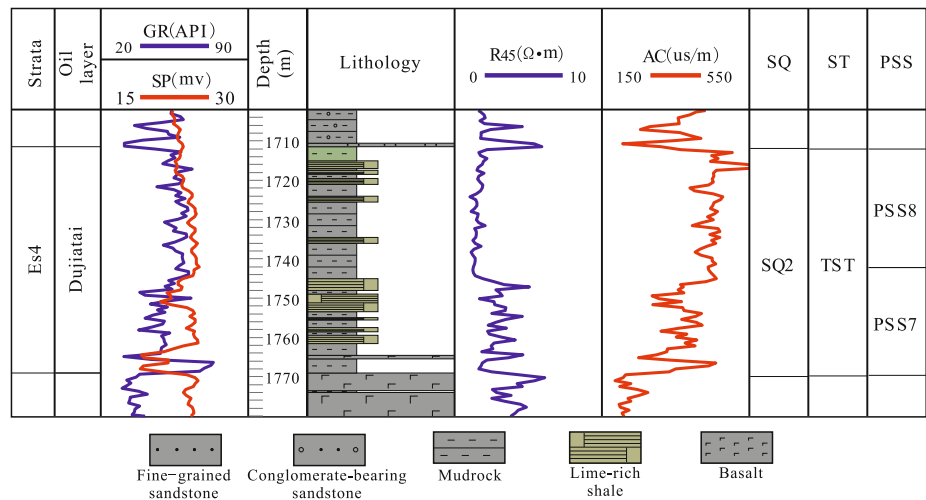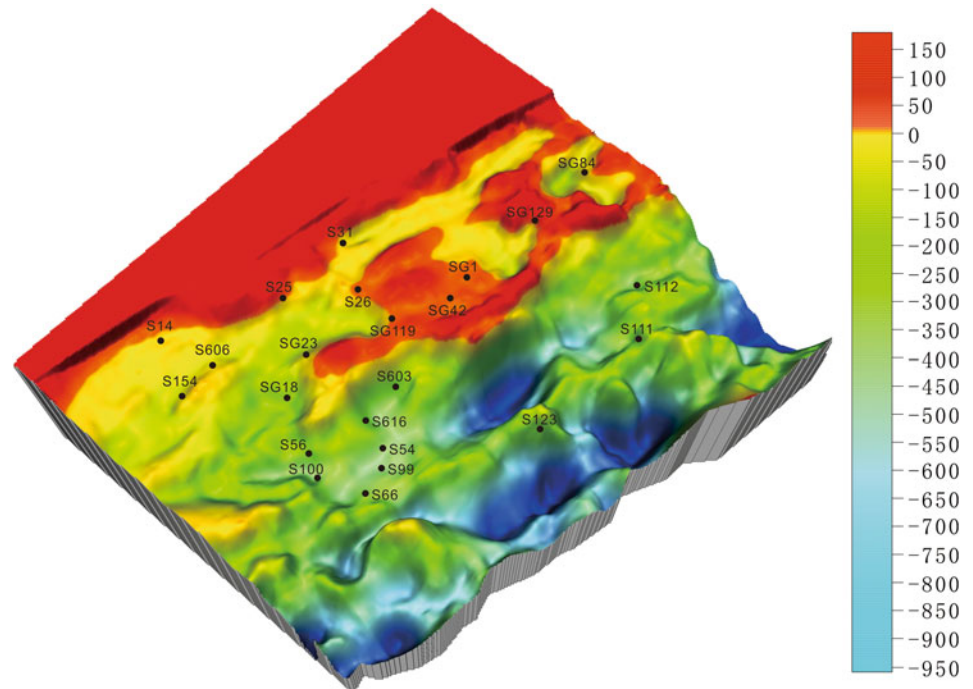


**Fig. 5.33** Paleo-geomorphology characteristics of SQ2 at the Es$_4$ of Shubei Area



The source of Shubei Area is mainly from west. However, burial hills in LST of SQ1 and SQ2 in the Shubei Area were exposed to air, and then submerged in TST and HST. Hence, the buried hill can act as the source in a relatively long period. Lithics and seismic section are used to analysis the source properties.

Lithic Composition and Maturity Analysis

Lithic is the direct proof to analysis petrology characteristics. This chapter analyzed 18 cored wells. Here we take well S100 as an example (Fig. 5.35). This well contains complex lithic constiution, with various lithics observed in thin-sections. In regards to sedimentary rocks, quartz and dolomitic lithics are common. Typical lithics from volcanic rocks such as basalt are also common. The lithics from slate are also common. Lithic composition is very complex in well S100, with low maturity. It suggests this well is close to the source, and the source comes from several locations.

The andesite, rhyolite, and volcanic clastic rocks widely distribute in the late Jurassic to early Cretaceous of eastern China. In the Miocene period, volcanic events decreases, and lithology became basalt. If the beach-bar deposits is only sourced from the braid-delta in the south, all the sources

**Table 5.5** Wave ripple data and their reconstructed paleo-water depth

| Core photos | Wells and depth (m) | Average grain size (mm) | Density ($\times 10^3$kg/m$^3$) | Ripple wavelength (cm) | Paleo water depth (m) |
|---|---|---|---|---|---|
|  | Well S52 2711.15 m | 0.1 | 2.31 | 4.56 | 6.31 |
|  | Well S52 2806.3 m | 0.21 | 2.30 | 5.96 | 6.34 |
|  | Well S66 3130.0 m | 0.12 | 2.27 | 4.77 | 6.29 |
|  | Well S66 3125.1 m | 0.29 | 2.26 | 6.26 | 5.49 |
|  | Well S99 3074.93 m | 0.13 | 2.23 | 4.78 | 6.25 |
|  | Well S51 2455 m | 0.097 | 2.3 | 3.71 | 4.61 |

come from strata earlier than the Mesozoic. In such a condition, there should be no lithics from basalt in the beach-bar deposits. However, typical lithics from basalt also exist in the beach-bar deposits, suggesting the Shubei buried hill also provided the source for the beach-bar deposits.

The Shubei buried hill is the source area. Hence, the lithics from basalt decreases with the increasing distance from the buried hill, but the lithic from braid-delta decreases from south to north. According to the systematically observation, the lithics from basalt are common in beach-bar deposits in the slope at the south of Shubei buried hill, and decrease southward. The lithics became andesite and rhyolite in the Dujiatai area. The results matches the explanation that buried hill in the Shubei Area acted as the source. In addition, the large amounts of andesite and rhyolite lithics in the

beach-bar deposits suggest the braid-delta in the south also acted as the source.

Seismic Section Characteristics

Two seismic sections crossing the buried hill belt were observed (Fig. 5.36). The thickness of Es$_4$ strata sharply decreases above the buried hill, and the deposits show pinch off characteristics above the slope. The above characteristics can be observed in both seismic section (Fig. 5.36). It corresponds to the only TST and HST deposited above the buried hill.

Both of the above two methods show the buried hill in Shubei Area was exposed and eroded, and acted as the source the surrounding beach-bar deposits. The beach-bar deposits in the LST of SQ2 was mostly sourced from the

**Fig. 5.34** Lithology, well logging, and facies interpretation of well S66



| Strata | Oil layer | SP(mv) 20 — 50 | Depth (m) | Lithology | Facies |
|---|---|---|---|---|---|
| Es4 | Dujiatai | | | | Shallow lake |
| | | | 3120 | | Coastal bar |
| | | | 3122 | | |
| | | | 3124 | | Inner bar |
| | | | 3126 | | |
| | | | 3128 | | Outer bar |
| | | | 3130 | | Shallow lake |

Fine−grained sandstone          Mudrock
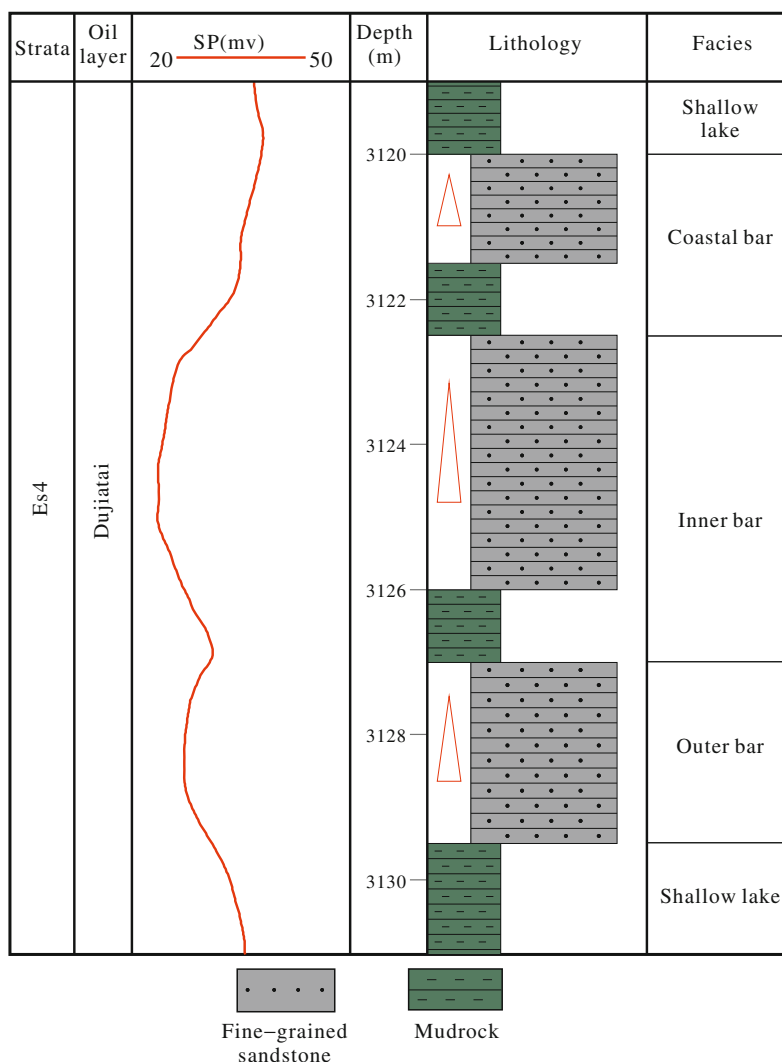
buried hill. From the TST of SQ2, the lake level rise, and then the buried hill was submerged. Hence, deposition began from TST of SQ2.

### 5.5.4  Reconstruction of Paleo-Windfield

The formation of beach-bar deposits was mostly influenced by waves, and then shoreline-parallel current (Jiang et al. 2011). Wind induced the formation of waves. Hence, paleo-wind field reconstruction is significant in studying beach-bar deposits. This reconstruction includes paleo-wind power reconstruction and paleo-wind direction reconstruction.

Paleo-Wind Power Reconstruction

The reconstruction of paleo-wind power is based the equation between wind and wave. Here we take 2711.15 m of well S52 as an example, in which the reconstructed paleo-water depth is 6.57 m and wave height is 1.55 m. The wind distance is 20,000 m according to the geologic background. The calculated wind speed 17.665 m/s. Other cores are also calculated with this method. The results are presented in Table 5.6. The wind power are divided by shown in Table 5.6.

Paleo-Wind Power Reconstruction

The paleo-climate shows obvious belt characteristics with different latitude in the Eocene period, suggesting the paleo-climate was influenced by planetary wind rather than monsoon. Actually, the monsoon did not appear until the middle Oligocene. According to the geography locations and climate belt characteristics, the Bohai Bay Basin was located between the west wind belt of planetary wind and subtropical high-pressure belt. Influenced by the planetary wind, the west wind belt of north hemisphere commonly show cyclone

**Fig. 5.35** Thin-section characteristics of well S100



(a) 2675.3m,quartz and chert lithics
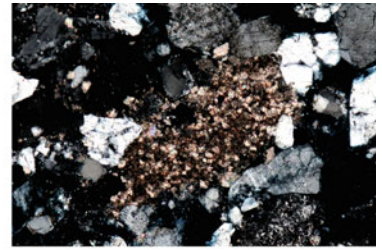


(b) 2675.3m,dolomite lithics



(c) 2684.5m,silica cementation



(d) 2675.3m,basalt lithics



(e) 2578.5m,quartz from extrusive rock



(f) 2578.5m,quartz porphyry lithics
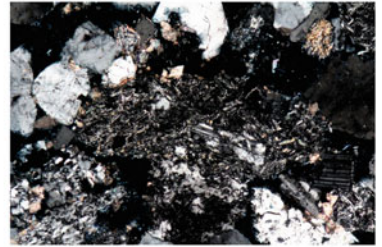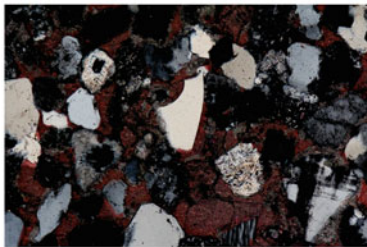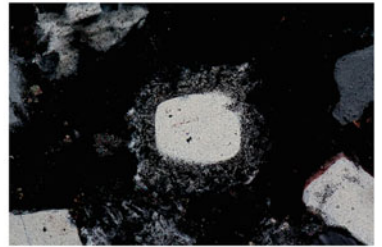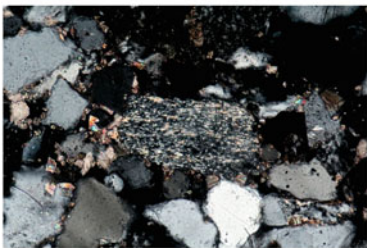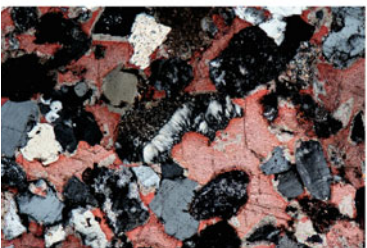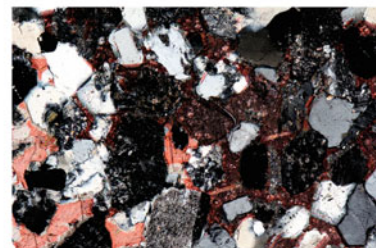


(g) 2684.5m,slate lithics



(h) 2684.5,cherts



(i) 2578.5m,tuff deprivation



(j) 2578.5m,quartz replaced by calcite
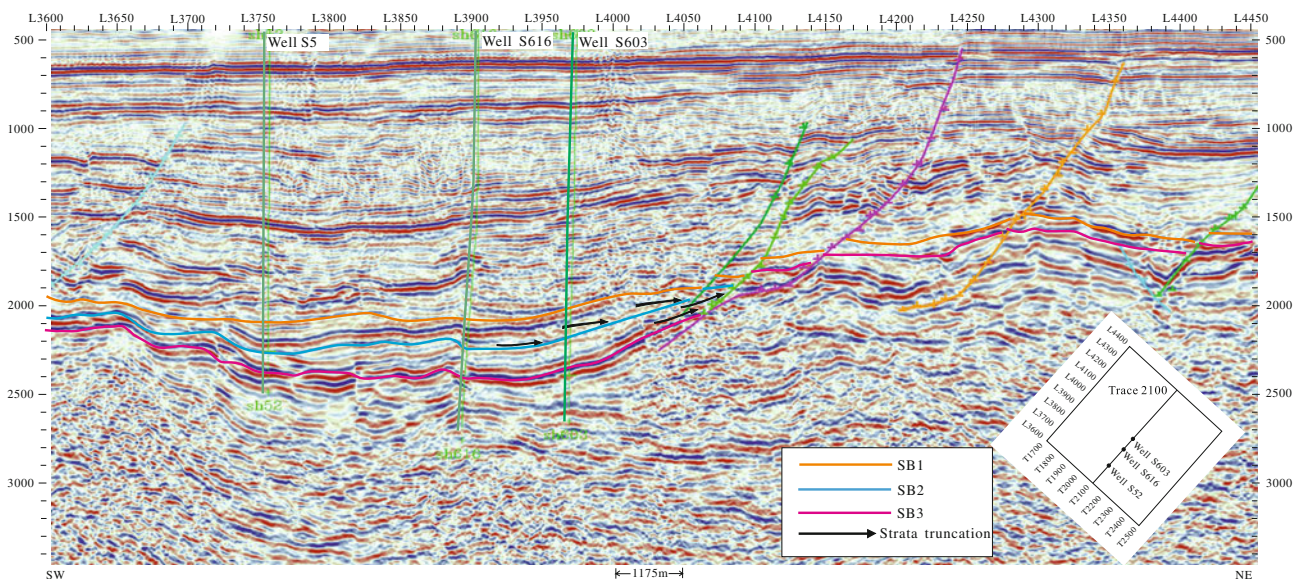
**Fig. 5.36** Seismic interpretation results of line 2100

**Table 5.6** Calculated results of paleo-wind power

| Well | Depth (m) | Water depth (m) | Wave height (m) | Wind speed (m/s) | Wind power |
|------|-----------|-----------------|-----------------|------------------|------------|
| S52  | 2711.15   | 6.57            | 1.55            | 17.655           | 8          |
| S54  | 2806.30   | 6.67            | 1.66            | 20.034           | 8          |
| S66  | 3130.00   | 6.88            | 1.62            | 18.207           | 8          |
| S66  | 3125.10   | 5.49            | 1.44            | 19.531           | 8          |
| S99  | 3074.93   | 6.25            | 1.50            | 18.096           | 8          |
| S51  | 2455.00   | 4.61            | 1.12            | 13.941           | 7          |

of clockwise direction, when it encountered the high-pressure belt of the subtropical belt. In such a condition, the west wind changed to northwest wind or north wind. According to the above characteristics, northwest wind or north wind is dominant in the Eocene Bohai Bay Basin (Liu and Jiang 2011).

The elongate of beach-bar deposits was parallel to the spread direction of waves, which is controlled by the wind direction. Hence, the elongate of beach-bar deposits can used to reconstruct paleo-wind direction (Li et al. 2010). Beach-bar deposits mainly distribute in two areas at the LST of SQ2 in the Es$_4$ period, which is (1) the nearshore area at the northwest of Shuguang buried hill, and (2) the slope area at the southeast of Shuguang Area. The elongate of beach-bars in the two areas are generally parallel to the elongate of the West Sag.

Previous studies suggested that only northwest of north wind existed in the Eocene West Sag. In such a condition, wave transported to southeast; sheltered by the buried hill, the wave energy decreases along with transportation. Hence, no beach-bar deposits should exist in the southeast of the buried hill. This is actually contradict to the distribution of beach-bar in the Eocene West Sag. Hence, southeast wind should also exist in this period. Note the monsoon is southeast wind in this period. The co-existence of northwest wind and southeast wind suggest both planetary wind and monsoon influenced the beach-bar deposition.

## 5.5.5 Controlling Effect of Windfield-Source-Basin System on Beach-Bar Deposition

The formation of beach-bar deposits is co-controlled by three factors: (1) wind, (2) source, and (3) basin (Jiang et al. 2015). Theoretically, the ideal environment for beach-bar deposition should include the following elements: (1) a consistent wind that can induce strong waves, (2) relatively shallow water depth in which the waves can influence lake floor, (3) the source comes from the reform of early deposits rather directly from land, (4) a gentle slope (Jiang et al. 2014).
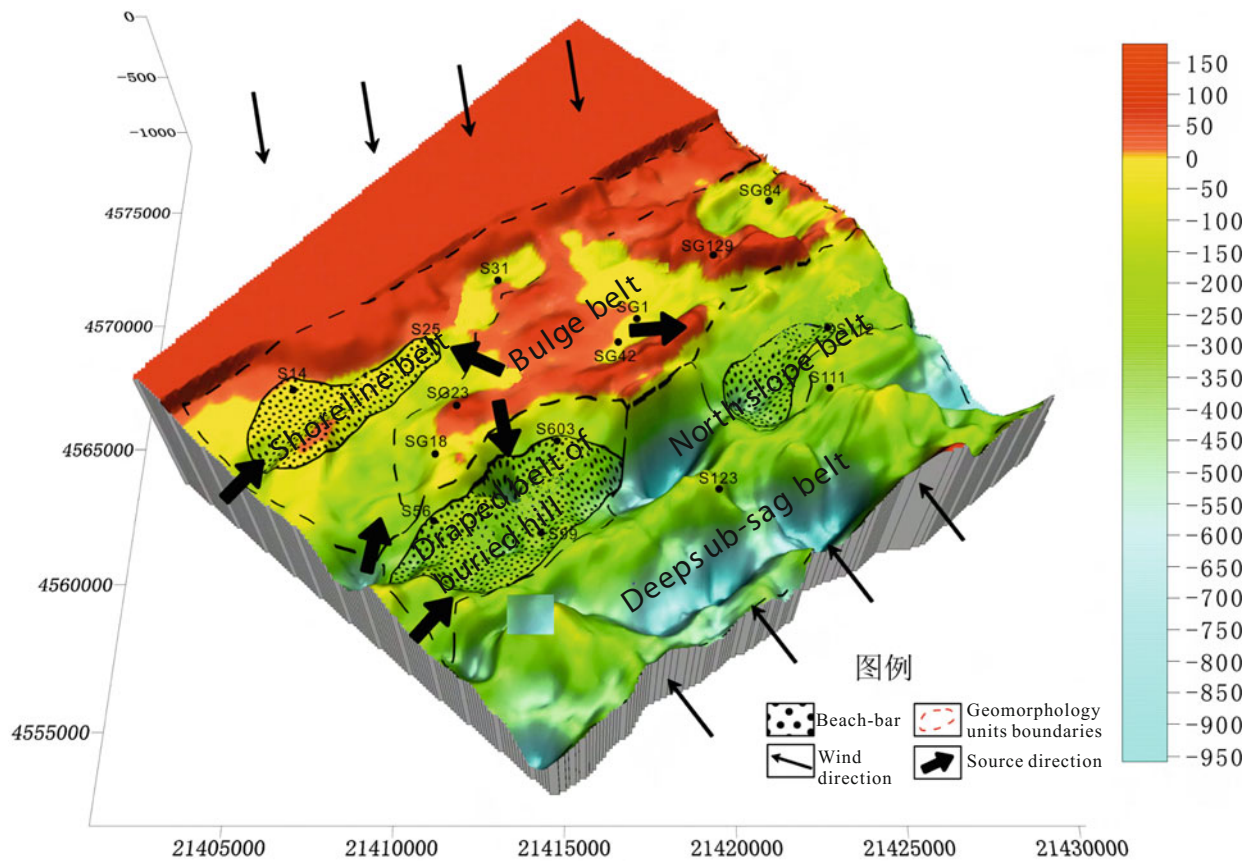
**Fig. 5.37** The paleo-geomorphology factor for beach-bar deposition in the Shubei Area. The color bar >0 refers to higher than lake level, whereas the color bar <0 refers to lower than lake level

In the Shubei Area, five belts are recognized, as follows: (1) near-shore belt, (2) subaerial hill belt, (3) draped belt of buried hill, (4) northern slope belt, and (5) deep sub-sag belt (Fig. 5.37).

Near-Shore Belt

This belt has gentle slope, with a relatively shallow water. From south to north, the paleo-geomorphology gradually increases. Hence, the northern part of the sag was exposed and eroded. This belt is close to the shoreline. Because of the shelter by Shubei buried hill, north wind is the dominant trigger mechanism of waves. The wind distance is very short because this belt is close to mountains, and thus the wave dynamics is also weak. The sources come from the braid-delta at the southern West Sag and buried hill from eastern part of the Sag. Generally, the near-shore belt has excellent wave dynamics, source, and geomorphology conditions for beach-bar deposition. Limited by the relatively shallow water and weak water dynamics, the beach-bar layers are thick and dominated by beach deposits. As shown in well S14 (Fig. 5.38), thin-bedded beach-bar deposits widely distribute in the LST of SQ2. In addition, well S26 also has thin beach-bar layer.

Buried Hill Belt

The buried hill was exposed to air in LST of SQ2, and thus providing the source for beach-bar. Because of the relatively short period for deposition, many layers

**Fig. 5.38** Lithology, well logging, and sequence units of well S14 located in the near-shore area. SQ = Sequence, ST = System tract, PSS = Parasequence set
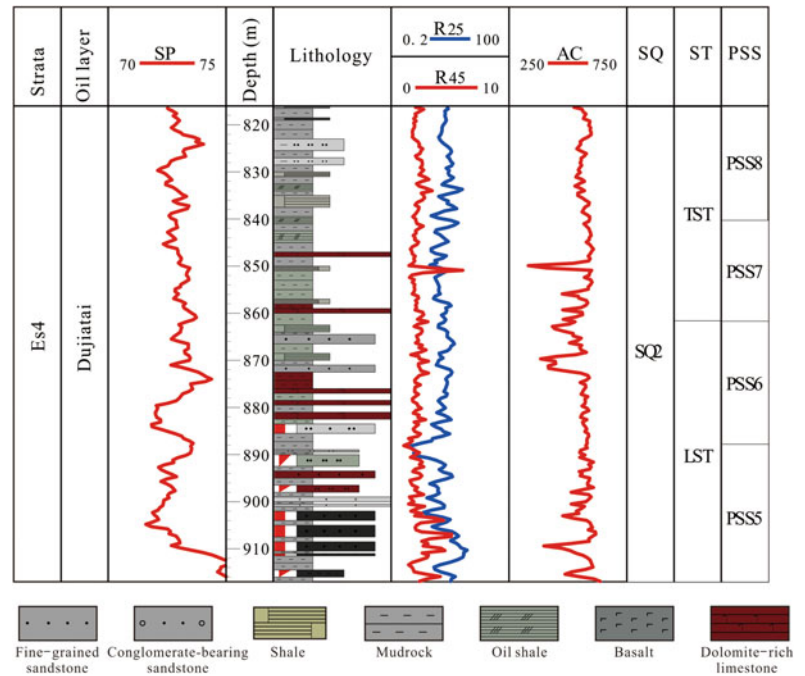


of the Es$_4$ strata are missing. The subaerial hill acted as the source, but there is no beach-bar deposits. Typical depositional characteristics at buried hill belt are shown in Fig. 5.39.

Draped Belt of Buried Hill

This is the subaerial slope areas in the southeast Shuguang buried hill. The slope are gentle, with the water depth increasing southward. The source includes the braid-delta from south and the buried from Shuguang Area. The water depth gradually increases from buried hill to southeast of the sag. Three rows of beach-bar deposits (coastal bar, inner bar, and outer bar) develops in this belt. Therefore, water-depth, geomorphology, source, and wave dynamics are all excellent for beach-bar deposition, acting as excellent area for beach-bar. As shown in well S66 (Fig. 5.3), beach-bar deposits widely distribute with interbedded mudrock. The early TST also has some beach-bar deposits.

Northern Slope Belt

This belt located in the northeast of buried hill. The geomorphology characteristics are similar to that of draped belt of buried hill. The water dynamics were controlled by southeast wind. No braid-delta from south sourced to this area in comparison to the draped belt of buried hill, because of the deep-buried. Therefore, there is no large scale beach-bar deposits in this belt, but some small scale beach-bar deposits also develop in the belt.

Deep Sub-sag Belt

This belt has a relatively large water depth, and the wave cannot reach the lake floor. Therefore, typical beach-bar deposits formed by traction flow cannot develop in such condition. However, storms can also trigger some beach-bar deposits in this environment; these deposits are commonly fine-grained sandstone and siltstone, interbedded with thick dark oil shale.

**Fig. 5.39** Lithology,
well-logging, and sequence units
of well S66 at the Draped belt of
buried hill. SQ = Sequence,
ST = System tract,
PSS = Parasequence set
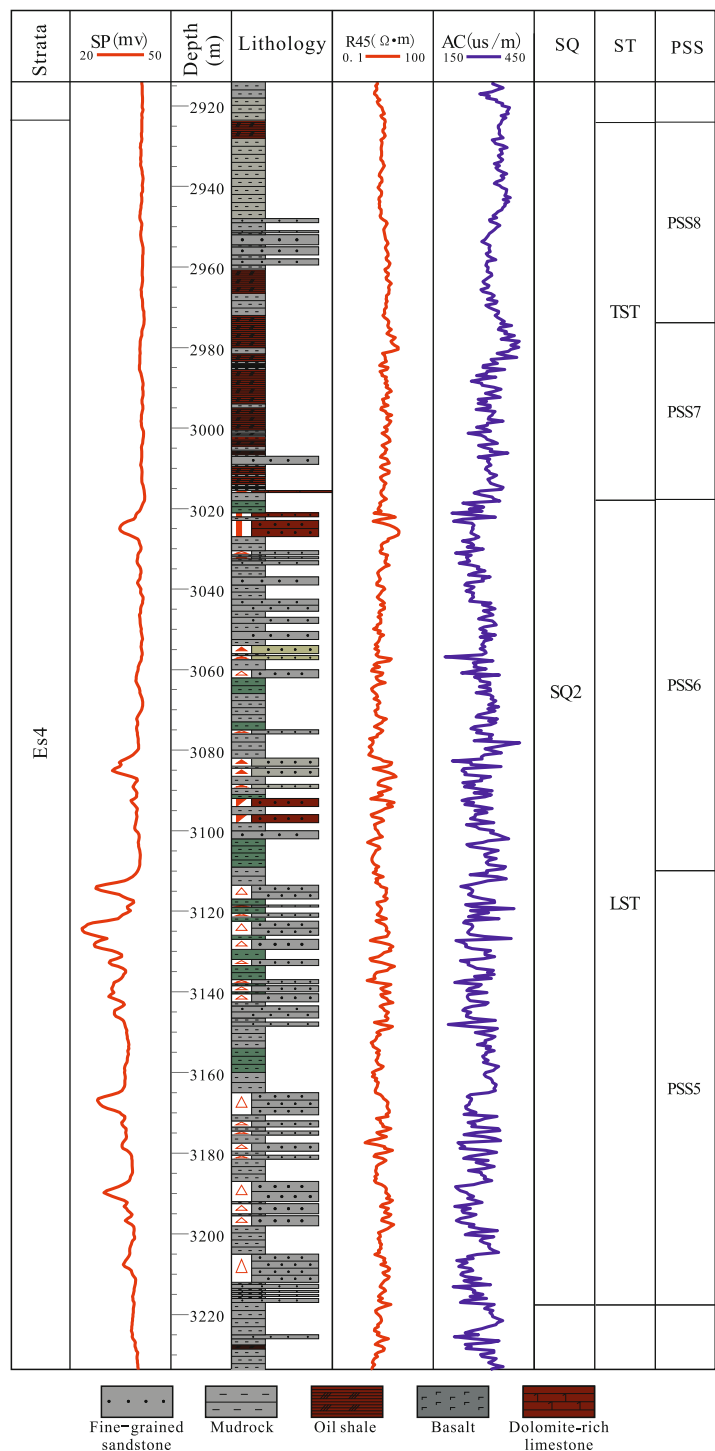


## References

Bao Z, Zhao L, Wang Y et al (2009) Controlling factors of reservoir sandstone in half-graben lake basin: example from the Eocene West Sag, Liaohe Depression. Geoscience 23(4):676–682 (in Chinese with english abstract)

Cao Y, Jiang Z, Wang L et al (1996) The recognition of sequence unit and boundaries in half-graben lake basin. J China Univ Petrol 20 (4):1–5 (in Chinese with english abstract)

Dai D, Tang Z, Chen X et al (1995) The geochemistry and well-log response of uranium in hydrocarbon exploration. Nat Gas Ind 15 (5):21–24 (in Chinese with english abstract)

Diem B (1985) Analytical method for estimating palaeowave climate and water depth from wave ripple marks. Sedimentology 32:705–720

Feng L, Jiang Z, Tian J (2009a) Sequence stratigraphy framework of the upper Es$_4$ Dongying Sag. Spec Oil Gas Reservoir 16(1):16–19 (in Chinese with english abstract)

Feng Y, Lu W, Men X (2009b) Sequence stratigraphy and distribution of lithologic reservoir in the Eocene western Liaohe Depression. Acta Sedimentologica Sin 27(1):57–63 (in Chinese with english abstract)

Hu L, Fuhrmann A, Poelchau HS et al (2005) Numerical simulation of petroleum generation and migration in the Qingshui sag, western depression of the Liaohe Basin, Northeast China. AAPG 89 (12):1629–1649

Jiang Z (2010a) Sedimentology (2nd ed). Petroleum Industry Press, Beijing (in Chinese)

Jiang Z (2010b) The current status and prospecting of sedimentary systems and sequence stratigraphy. Oil Gas Geol 31(5):535–541 (in Chinese with english abstract)

Jiang Z (2012) The development of sequence stratigraphy: summary of the international sequence stratigraphy Seminar. Geosci Front 19 (1):1–9 (in Chinese with english abstract)

Jiang Z, Xiang S, Chen X et al (2009) Sequence stratigraphy model of the Eocene Shahejie Formation in the Diannan area. Acta Sedimentol Sin 27(5):931–938 (in Chinese with english abstract)

Jiang Z, Liu H, Zhang S et al (2011) Sedimentary characteristics of large-scale lacustrine beach-bars and their formation in the Eocene Boxing Sag of Bohai Bay Basin, East China. Sedimentology 58:1087–1112

Jiang Z, Liang S, Zhang Y et al (2014) Sedimentary hydrodynamic study of sand bodies in the upper subsection of the 4th Member of the Paleogene Shahejie Formation in the Eastern Dongying Depression, China. Pet Sci 11:189–199

Jiang Z, Wang J, Zhang Y (2015) The summary on the development of beach-bar. J Palaeogeogr 17(4):427–440 (in Chinese with english abstract)

Li W, Sun H, Tang W (2004) Sequence stratigraphy and distribution of hydrocarbon reservoirs in the Eocene East Sag, Liaohe Depression. J China Univ Petrol 28(5):1–5 (in Chinese with english abstract)

Li G, Jiang Z, Chen S et al (2008a) Sedimentary characteristics and controlling factors of beach-bar deposits in upper Es4 Lijin Sag. Geol China 35(5):911–921 (in Chinese with english abstract)

Li G, Jiang Z, Yang S et al (2008b) Sedimentary facies and evolution of the upper Es4 Lijin Sag. Spec Oil Gas Reservoir 15(5):35–39 (in Chinese with english abstract)

Li G, Jiang Z, Wang S et al (2010) Quantitative prediction of thin-bedded beach-bar sandbodies: example from the upper Es4

Dongying Sag. Geol China 37(6):1659–1671 (in Chinese with english abstract)

Liu L, Jiang Z (2011) The development of reconstructing paleo-wind direction. Prog Geogr 30(9):1099–1106 (in Chinese with english abstract)

Liu S, Jiang Z, Wang X et al (2015) Reservoir characteristics and digenesis of the west slope in the West Sag, Liaohe Depression. Geosciences 29(3):692–701 (in Chinese with english abstract)

Orr FM Jr, Yu AF, Lien CL (1981) Phase behavior of $CO_2$ and crude oil in low-temperature reservoirs. SPE J 21(4):480–492

Payton C (1977) Seismic stratigraphy-applications to hydrocarbon exploration. AAPG 26:63–81

Qi J, Li X, Yu F et al (2013) Tectonic deformation and characteristics of "Tanlu rift zone" in the Miocene West Sag, Liaohe Depression. Sci China (D Series) 43(8):1324–1337 (in Chinese with english abstract)

Tian J, Jiang Z (2012) The comparison of sedimentary characteristics of beach-bar deposits in the Huiming and Dongying Sags. J Jilin Univ 42(3):612–623 (in Chinese with english abstract)

Vail P (1975) Eustatic Cycles from Seismic Data for Global Stratigraphic Analysis. Houston Geol Soc Bull 18(2):16–16

Vail P, Mitchum R, Thompson S (1977) Seismic Stratigraphy and Global Changes of Sea Level, Part 3: Relative Changes of Sea Level from Coastal Onlap 1. Seismic Stratigraphy

Wang L, Jiang Z, Cao Y et al (2003) The use of well-logs in recognizing sequence boundaries. J Southwest Univ 25(3):1–4 (in Chinese with english abstract)

Wang L, Jiang Z, Feng L, et al (2007) Identification of sequence reservoir section in deep-water lake basins: Taking Fula depression in Muglad basin as an example. Petroleum Geology & Oilfield Development in Daqing 26(6):24–27

Wang J, Jiang Z, Zhang Y (2015) Subsurface lacustrine storm-seiche depositional model in the Eocene Lijin Sag of the Bohai Bay Basin, East China. Sed Geol 328:55–72

Yang Y, Qiu L, Jiang Z et al (2011) Sedimentary model of beach-bar in half-graben lake basin: example from the upper Es4 Dongying Sag. Acta Petrolei Sin 32(3):417–423 (In Chinese with English Abstract)

Zeng H, Backus MM (2005) Interpretive advantages of 90°-phase wavelets: Part 1—modeling. Geophysics 70(3):7–15

Zeng H, Hentz TF (2004) High-frequency sequence stratigraphy from seismic sedimentology: applied to Miocene, Vermilion Block 50, Tiger Shoal Area, offshore Louisiana. AAPG Bull 88(2):153–174

Zeng H, Backus MM, Barrow KT et al (1998) Stratal slicing Part 1: realistic 3-D seismic model. Geophysics 63(2):502–513

# The Sedimentary Characteristics of Paleogene Conglomerates and Their Sedimentary Dynamics in Source-to-Sink System in the Langgu Sag

## 6.1 Geologic Background

The Langgu Sag is a Paleogene NE-SW-oriented half graben, located in the northern Jizhong Depression of the Bohai Bay Basin. The Langgu Sag is separated from the Dachang sag to the north, from Daxing high to the west, from the Wuqing sag to the east, and to the south by the Niutuozhen high. The Langgu sag is about 90 km long in the N-S direction, 20–40 km wide in the E-W direction and 2600 km$^2$ in exploration areas (Jin et al. 2006; Wang and Liu 2008) (Fig. 6.1).

The basement of the Langgu Sag consists of a pre-Mesoproterozoic crystalline basement and a Mesoproterozoic-Mesozoic sedimentary basement. The present tectonic pattern is mainly the result of the combined actions of Yanshanian movement and Himalayan tectonic movement. The Yanshan movement at the end of the Mesozoic was mainly composed of left-lateral shear extrusion, fold deformation and uplifting and denudation, which developed a series of NE and NNE strike-slip faults and its associated NW and NWW faults. They laid the foundation for the extensional fault-depression in the Cenozoic basins and the depressions, which has important implications for the tectonic setting of the Paleogene basin and its sedimentary distribution of its overlying strata (Gao 2004; Yang 2004).

In the Paleogene, the west of Langgu sag was dominated by the Daxing fault, which is a detachment with the strike of NNE and dip of SEE. It is combined with a normal fault whose dip is NW, forming an inverse Y-shaped extensional fault system. The sag underwent a strong subsidence near the Daxing fault side and gradually lift upward to the east, forming a half graben. Affected by early tectonics and regional stress, there are two main sets of faults in the Langgu sag. One set of faults trends nearly NE-SW and NNE-SSW, paralleling to the long axis of the sag, including the Daxing fault, Jiuzhou fault, Jiuzhoudong fault, Caojiawu fault, Yangshuiwu fault, and Hedong fault. The other set of faults trending nearly E-W include the Tongbozhen fault,

Liuqiying fault, Banjiehe fault, and Niubei fault. Faults have many composition styles in the section, such as "Y"-shaped, inverse "Y"-shaped, "cabbage"-shaped, horst and so on. Class I faults, which controlled the sag, consists of the Daxing fault and the Hedong fault. Class II faults, which controlled the second tectonic belts of the sag, consists of the Tongbozhen fault, Jiuzhou fault, Caojiawu fault, and Niubei fault (Yang 2004; Song et al. 2006). Under the controlling of the major faults, the Langgu sag is divided into five primarily tectonic belts by six faults above: the Jiuzhou-Gu'an belts, the Liuquan-Caojiawu belts, the Hexiwu belts, the Niubei slop, and the Fengheying belts (Zheng et al. 2006).

The Daxing fault in western sag is a boundary fault, controlling the evolution of tectonics and sediments of the Langgu sag. It began acting in the Paleogene Kongdian Formation ($E_k$) and reached its maximum activity intensity during Third member of the Paleogene Shahejie Formation ($Es^3$)and the fourth member of the Paleogene Shahejie Formation ($Es^4$) (Zhao and Liu 2003). Under the control of the Daxing fault, the basement of the Langgu sag formed a westward-dipping fault block, whose west is low and east is high. The Paleogene strata cover the Cambro-Ordovician carbonate rocks and Carboniferous-Permian coal-bearing strata, which form a buried hill structural belt and a regional unconformity (Jin et al. 2006). It developed Paleogene extensional fault-depression type sedimentary system dominated by inland fluvial and lacustrine, which gets deeper and thicker from east to west. From bottom to top, the Paleogene strata consist of the Kongdian Formation (Ek), the Shahejie Formation (Es), and the Dongying Formation (Ed). The Shanhejie Formation can be divided into four members from bottom to top according to rock properties: $Es^4$, $Es^3$, $Es^2$, and $Es^1$ (Fig. 6.2). $Es^4$ and $Es^3$ members are the major oil-bearing series (Zhao and Liu 2003; Song et al. 2007).

Paleogene conglomerates of the Langgu sag are mainly located in the Gu'an-Jiuzhou tectonic belts. And they are named as "Daxing conglomerate", whcich refers to conglomerate group that is formed in several geological periods,
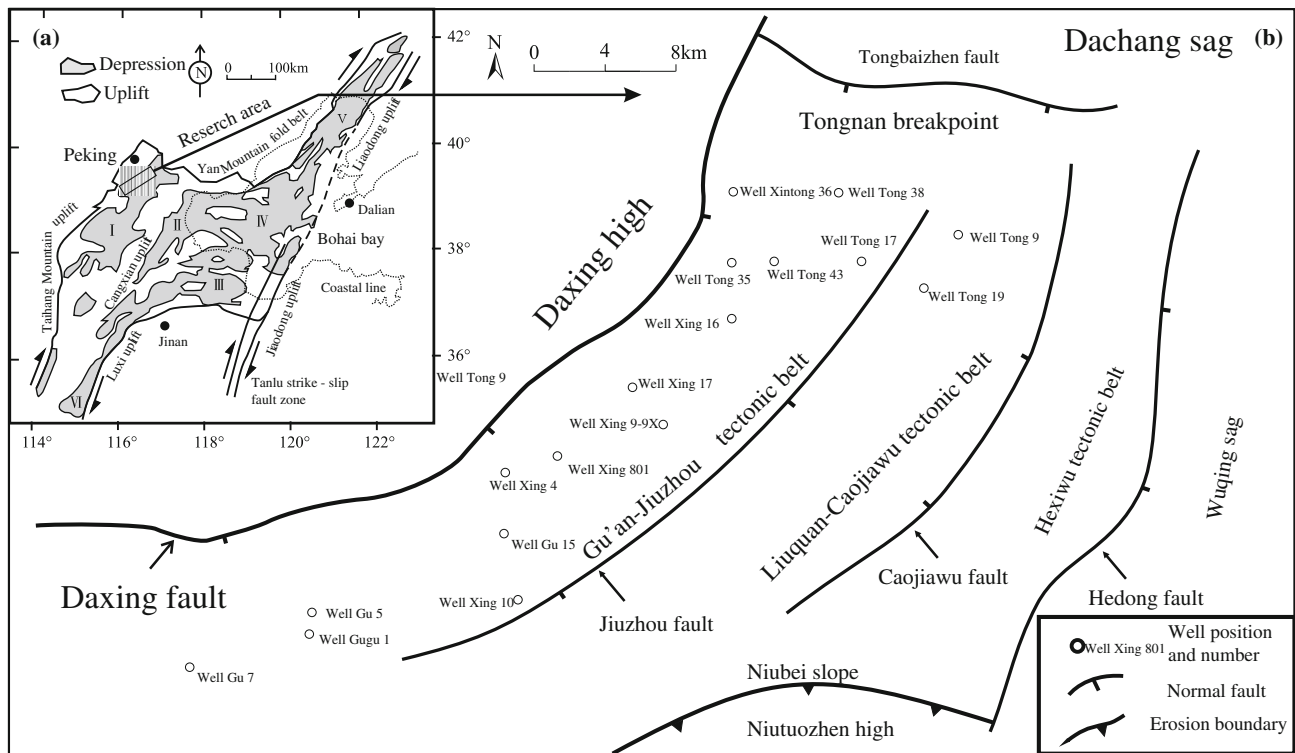
**Fig. 6.1** The location (**a**) (Modified from Jiang et al. 2007) and the tectonic (**b**) of the Langgu sag. I-Jizhong depression; II-Huanghua depression; III-Jiyang depression; IV-Bozhong depression; V-Liaohe depression; VI-Dongpu depression

overlapped vertically, and spreads along the Daxing fault in NE-SW direction. The development and distribution of the Daxing conglomerate is primarily controlled by the Daxing fault. The Daxing fault acted intensively in the early period of Es$^3$ member (Zhang et al. 1998; Zhao and Liu 2003), and the Daxing high lifted continuously, which resulted in strong weathering and denudation of the overlying Cambrian—Middle and Upper Proterozoic strata. The weathering products were carried into the deep lake by floods, forming multi-phase superimposed nearshore subaqueous fans (Zhu et al. 2003b; Song et al. 2006, 2007) (Fig. 6.3a), namely "the Daxing conglomerate". The nearshore subaqueous fans, showing skirt-like shape, contiguously distributed along the Daxing fault (Fig. 6.3b). The compositions of gravels in these fans are primarily limestone and dolomite, with angular to sub-round in respect of roundness, no sorting, and out of order. Between fans, dark gray organic-rich mudstone with some oil shale and marl is developed, and rich in *Huabei-estheria* (Dong et al. 2002), indicating that the Daxing conglomerate developed in the semi-deep to deep lake sedimentary environments.

The Daxing conglomerate is mainly developed in the lower Es$^3$, and some developed in the upper Es$^4$ and middle Es$^3$. They are in contact with or surrounded by a large set of mature source rocks, thus, having great resource potential. The drilling results indicated that part of the conglomerates have good porosities and active oil-gas shows, and good development benefits were gotten in the conglomerate body from the Xing 9 well area. According to the rolling evaluation in the past two years, the drilling of Well Xing 9 conglomerate body has achieved remarkable results, and high-yield industrial oil-gas flow is obtained in Well Xing 9-7, Well Xing 9-2, and Well Xing 9-6.

## 6.2 Sedimentary Characteristics of the Conglomerate Body

Conglomerate, belonging to coarse detrital rock, primarily consists of coarse detrital particles and gravels, which determines its a series of characteristics. Firstly, most of its grains are lithic fragments rather than mineral debris. Secondly, the coarse particles are easy to study in the field or core. The interstitial matrix is commonly developed. Compared with the sandstone, the upper size limit of the interstitial matrix has been increased, usually are fine-grained sand, silt, and clay material. They deposited simultaneously or almost simultaneously with coarse debris. Cements are

**Fig. 6.2** Sedimentary facies and sequence framework of the Paleogene Langgu sag (modified after Zheng et al. 2006)
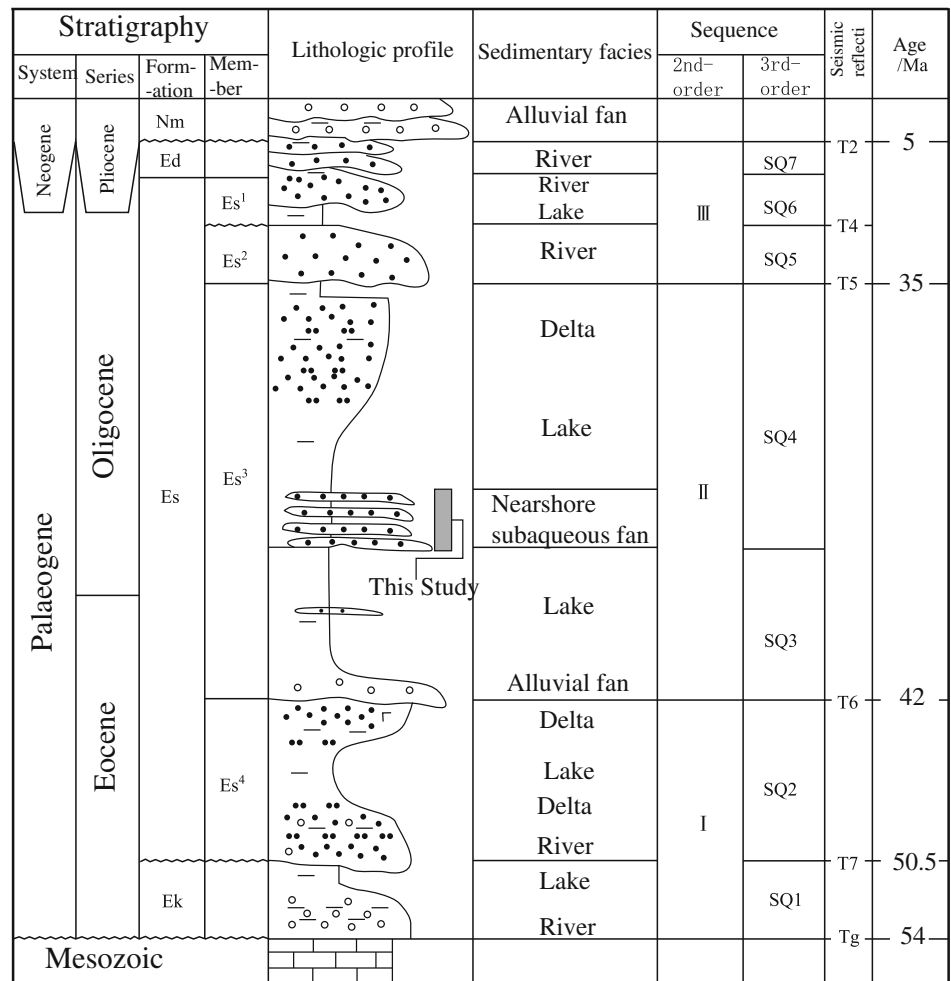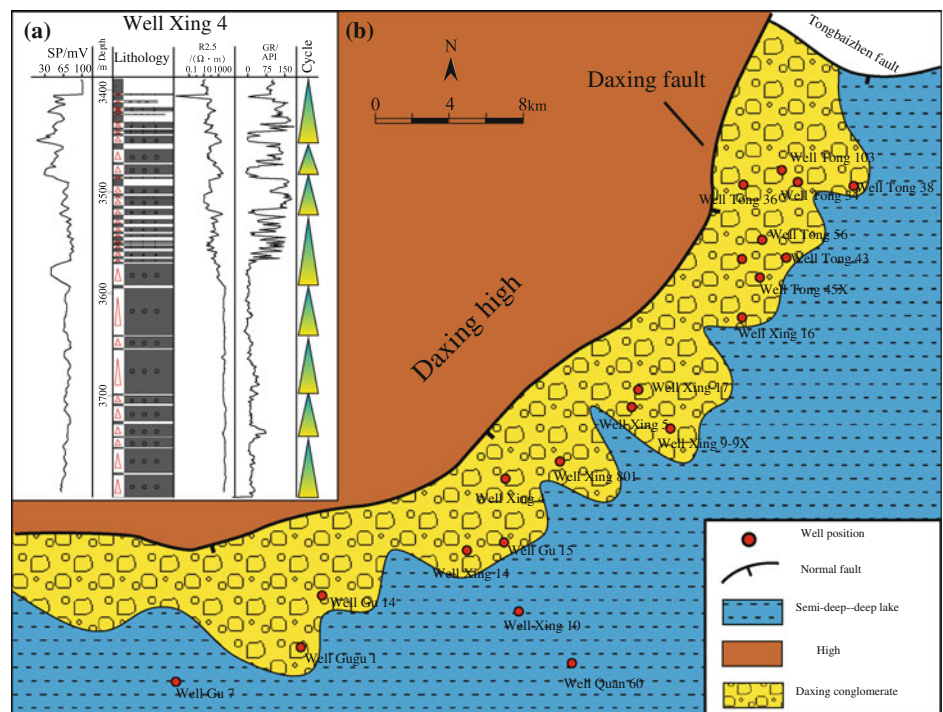


**Fig. 6.3** Distribution and vertical sequences of the Daxing conglomerate (modified from Liu et al. 2012b)

chemical materials precipitated from solutions or colloidal solutions, such as calcite, silica, ferric hydroxide etc. Sedimentary structures are common large-scale cross-bedding and graded bedding, and sometimes massive bedding when bedding is not obvious (Jiang 2010).

### 6.2.1 Rock Type

According to core observation, thin section identification, and logging analysis, rock types of the Daxing conglomerate are analyzed from different classification aspects.

According to the gravel size, there are four types of conglomerate: fine conglomerate, gravels 2–10 mm in diameter; Medium conglomerate, gravels 1–10 cm in diameter; Coarse conglomerate, gravels 1–10 dm in diameter; Boulder conglomerate, gravels more than 1 m in diameter (Fig. 6.4). In the study area, main types are medium conglomerates and fine conglomerates with a few coarse conglomerates and boulder conglomerates.

According to conglomerate compositions, the Daxing conglomerates are primarily oligomictic conglomerates, consisting of single component gravels. The gravel of carbonate is more than 90%. The conglomerate bodies are mainly formed by the rapid accumulation locally or after short distance transportation of sediments which were formed by weathering and fragmentation of unstable rocks (limestone) in the eroded area.

According to the support type of the particles, the rock types of the Daxing conglomerate can be divided into matrix-supported conglomerate and grain-supported conglomerate (Fig. 6.5). The matrix in the matrix-supported conglomerate is dominated by mud and silt, and plenty of matrix make gravels "floating". The grain-supported conglomerate has high gravel content and grains are mainly point and line contacts. The matrix in grain-supported conglomerate is mainly composed of carbonate silt, which is similarly with gravels.

### 6.2.2 Texture Characteristics

The Daxing conglomerate is mainly developed in the middle and lower $Es^3$. Gravel compositions are dominated by carbonate, with some clastic rock. The detrital particles are characterized by non-sorting to medium sorting and angular to sub-angular, which indicating sedimentary characteristics of nearby provenances (Fig. 6.6a) and low texture maturity. In the matrix-supported conglomerate, grains do not contact each other and the cementation type is mainly basal cementation, which generally reflects rapid accumulation of density flow. In grain-supported conglomerate, grains contact each other in point-line and the cementation type is mainly porous cementation or contact cementation. In addition, conglomerates often have complex dual-mode structures or multiple-modal structures. That is, all or part of the spaces between gravels were filled by sand particles, and the pores between sand grains were filled by clay particles (Fig. 6.6b).

### 6.2.3 Sedimentary Structures

The sedimentary structures of the Daxing conglomerate are unitary, mainly consisting of massive bedding, graded bedding, and syngenetic deformation sedimentary structures, which reflect gravity flow deposition characteristics. Beddings, wave mark, exposure structure, chemical structure, and biological relics are normally not developed (Liu et al. 2012a).

1. Massive bedding

Massive bedding refers to bedding that has homogeneous material, showing no differences in compositions and textures and no laminae structure. Massive bedding is often found in mudstone and thick coarse detrital rocks. The Daxing conglomerate develops lots of massive beddings (Fig. 6.7). They are caused by the rapid deposition of coarse



(a) Well Gu 15 , 3905.65m, fine conglomerate

(b) Well Tong 35 , 2714.05m, medium conglomerate

(c) Well Xing 4 , 3647.37m coarse conglomerate

(d) Well Xing 9-9X , 4093.15 ~ 4096.57m, boulder conglomerate
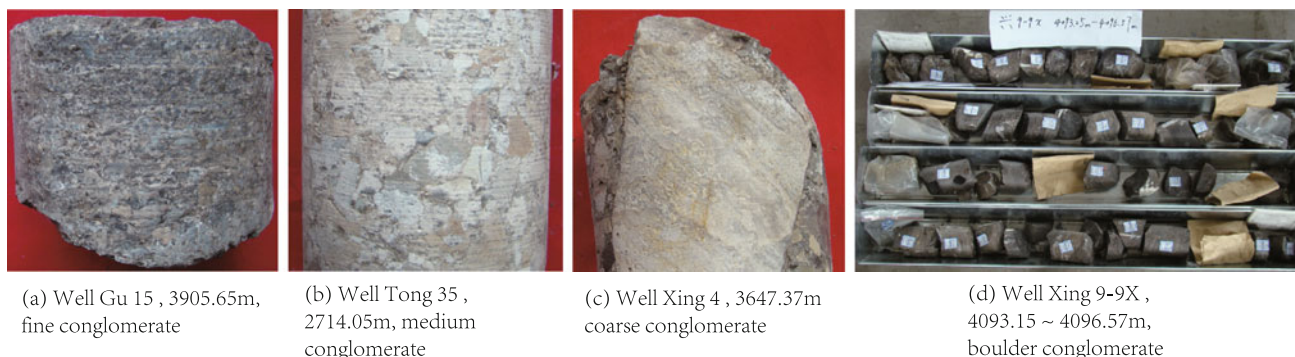
**Fig. 6.4** The types of conglomerates (from gravels size)

(a) Well Gugu 1 , 4082.24m, matrix-supported
conglomerate

(b) Well Tong 45X , 3015.4m, grain-supported
conglomerate
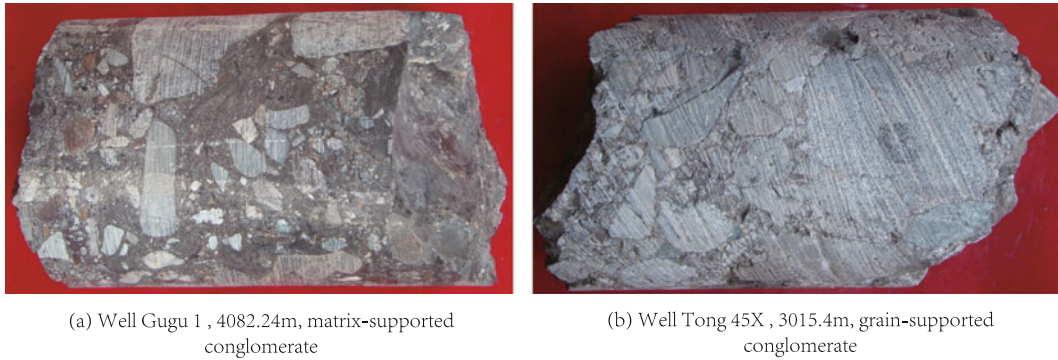
**Fig. 6.5**  The types of conglomerates (from supported types)



(a) Well Gu 15 , 3903.54m

(b)Well  Tong 43 , 2619.84m
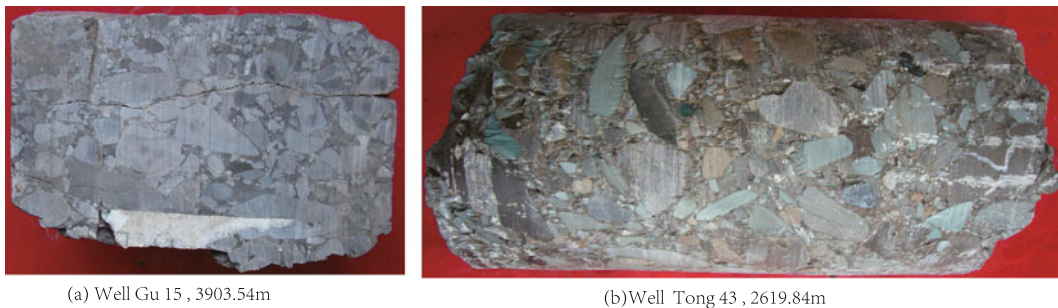
**Fig. 6.6**  The texture characteristics of the Daxing conglomerate



(a) Well Gugu 1 , 4082.24m

(b) Well Tong 35 , 2734.05m
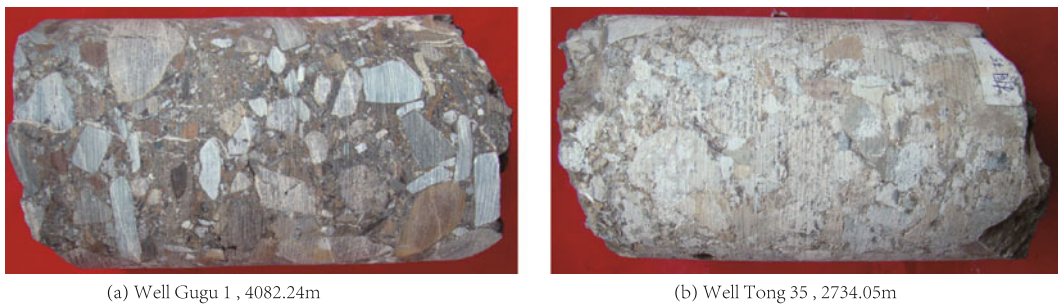
**Fig. 6.7**  Sedimentary structure—massive bedding

conglomerates. They are very common in conglomerates of Caiyu, Jiuzhou and Gu'an, and are the major sedimentary structures in the study area.

2.  Graded bedding

The Daxing conglomerate belongs to the typical gravity flow deposits. The graded bedding is very developed in the Daxing conglomerate (Fig. 6.8). Graded bedding is dominated by normal graded bed sequence, and usually found in fine conglomerate or the rock which is in the transition from fine conglomerate to thin sandstone, caused by weakening water power in the late of gravity flow. It is few developed in thick medium or coarse conglomerates.

3.  Scour surface

Because of the development of channel microfacies, the Daxing conglomerate has developed a lot of scour surfaces (Fig. 6.9). The scour surface is generally at the bottom of normal graded bed sequence and shows erosion of underlying fine-grained sediments by overlying sand-gravel sediments.

(a) Well Gu 15 , 3902.21m       (b) Well Gugu 1 , 4701.25m       (c) Well Tong 37 , 1480.6m       (d) Well Tong 103, 1671.15m

**Fig. 6.8** Sedimentary structure—graded bedding



(a) Well Gu 15, 3903.59m            (b) Well Tong 35 , 2342.31m            (c) Well Tong 103 , 1671.15m

**Fig. 6.9** Sedimentary structure—scour surface

4. Truncated structure

Due to the changes of hydrodynamic conditions and provenance supply conditions, the Daxing conglomerate body, as an event sedimentary body, also develops some truncated structures (Fig. 6.10). It is mainly manifested as the mud cutting on sandy sediments or fine gravel sediments, which is a symbol of sudden change of hydrodynamic conditions.

5. Load, flame and ball-pillow structure

The load and flame structures in the Daxing conglomerate body are not often found. This is associated with dominated thick conglomerates in the Daxing conglomerate. Some load and flame structures can be found in the fan edges or the lithologic combination in the interbedding of sand-gravel sediments and mud sediments between channels (Fig. 6.11). Sand-ball structures are more rarer than load cast in the

Daxing conglomerate and are only found in local fine sediments (Fig. 6.11).

6. Sandstone veins

The Daxing conglomerate also developed some sandstone or conglomerate veins. Sandy (gravel) material irregularly distributed in dark mudstone as fine veins (Fig. 6.12). The veins are vertical or inclined to strata, with width from a few millimeters to several centimeters. These veins were caused by injection of pore-water-rich sandy (gravel) sediments into the mud sediments under pressure, commonly indicating deep water environment.

7. Slump deformation structure

The Daxing conglomerate, as event gravity flow sediment, also develops a lot of slump deformation structure. These slump deformation structures generally appear at the edges of
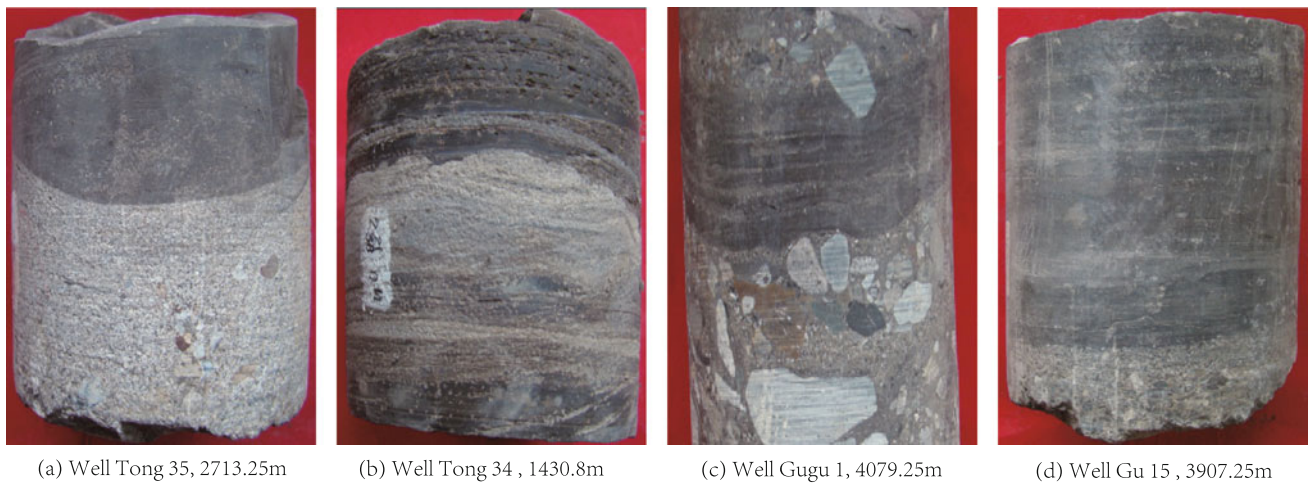
(a) Well Tong 35, 2713.25m        (b) Well Tong 34 , 1430.8m        (c) Well Gugu 1, 4079.25m        (d) Well Gu 15 , 3907.25m

**Fig. 6.10** Sedimentary structure—truncated structure



(a) Well Tong 34 , 1427.5m, load structure

(b) Well Tong 53 , 2291.96m, load structure

(c) Well Gugu 1 , 4073.04m, ball-and-pillow structure

(d) Well Tong 33 , 1668.05m, ball-and-pillow structure

**Fig. 6.11** Sedimentary structures—load and ball-pillow structures

the fan bodies or between the channels, manifesting mixed deposits of sandstone and mudstone. Some sandstone trips were strongly distorted and shaped like snakes and bowels.

8. Mud gravel and mudstone tear debris

Mud gravels and mudstone tear debris are most common in gravity-flow or storm-flow sedimentary environments. The Daxing conglomerate also developed some mud gravels which were formed by coarse sediments stiring semi-consolidated muddy sediments. Mud gravels are most dark gray mud gravels, with a few amaranth mud gravels (Fig. 6.13).

The Daxing conglomerate also developed lots of dark gray mudstone tear debris (Fig. 6.13). The mudstone tear debris have curved sheet, swirling, tear-like shape, and unevenly distribute in the sandstone and fine conglomerate.

9. Plant debris or charcoal

In the Daxing conglomerate, there are almost no biological relics and bioturbation, but there are abundant plant debris or

charcoal on rock surfaces. And some plant debris even preserve intact plant leaves and stems (Fig. 6.14). Some charcoal layers contain sulfides, which can be used as a good sign of deep water deposition.

### 6.2.4   Gravel Compositions

Gravels are important parts of conglomerate. The nature, content, and combination of gravels can reflect the material source of the conglomerate, and influence reservoir properties of the conglomerate to a certain extent. Therefore, the gravel compositions of conglomerate are considered as an important study aspect of conglomerate. The study of the gravel compositions is mainly by core observation, thin section analysis (conventional thin section and casting thin section), scanning electron microscope, and whole rock X-ray diffraction analysis.

The gravel compositions of the Daxing conglomerate include carbonate gravels and clastic gravels. More than 90% of the Daxing conglomerate are composed mainly of carbonates gravels, including limestone and dolomite

(a) Well Gugu 1 ,
4068.36m, sandstone veins

(b) Well Gugu 1 , 4071.06m, sandstone
veins

(c) Well Tong 33 , 1835.06m,
deformation structure

(d) Well Gugu 1 , 4217.32m,
deformation structure

**Fig. 6.12**  Sedimentary structures—sandstone vein and slump deformation structure



(a) Well Tong 34 ,
1431.7m, mud gravel

(b) Well Tong 43 ,
1972.2m, mud gravel

(c) Well Xing 8 , 2870.3m,
mudstone tear debris

(d) Well Tong 45 X ,
3015.54m, mudstone
tear debris

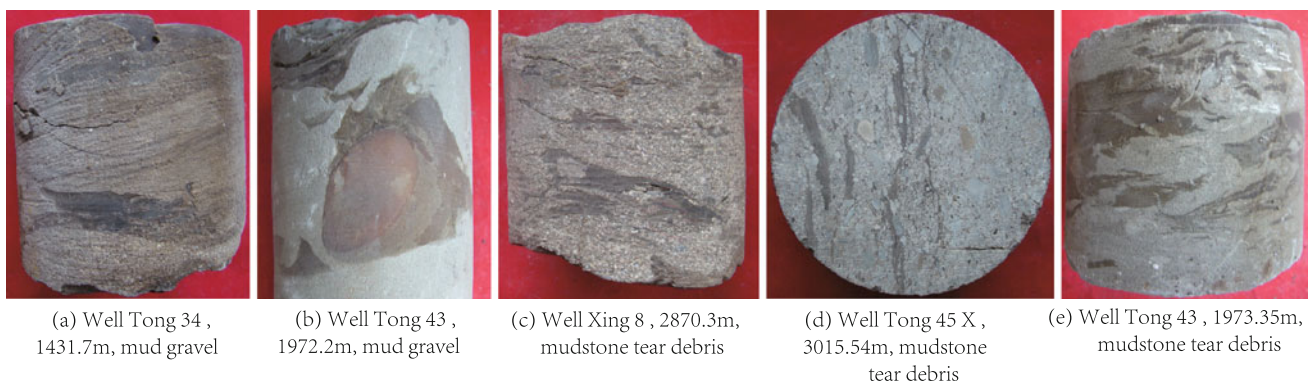(e) Well Tong 43 , 1973.35m,
mudstone tear debris

**Fig. 6.13**  Sedimentary structures—mud gravel and mudstone tear debris

gravels. Clastic gravels, including mudstone and siltstone gravels, develop only in local areas, having varied types but low content (Liu et al. 2012b).

1. Limestone gravels

(1)  Grain limestone

The grian limestones make up approximate 30% of the limestone gravels. The grain limestones are generally 0.5–10 cm in diameter and include edgewise limestone (Fig. 6.15a), oolitic limestone (Fig. 6.15b, c), algal limestone (Fig. 6.15d), and bioclastic limestone (Fig. 6.15e, f). The edgewise limestones (Fig. 6.15a) are mainly composed of limestone pebbles and microcrystalline calcite cement, in which limestone pebbles are flat and arranged in a micro-parallel configuration. The size of the pebbles is 2–20 mm in length. Ooids in the oolitic limestone (Fig. 6.15b, c) are generally 0.3–1.0 mm in size. The cores of the ooids

are intraclast, a few are terrigenous clasts, and cements are mainly microcrystalline and sparry calcite. Algal limestones are characterized by lump limestone (Fig. 6.15d). Lumps are generally 0.05–0.3 mm in size and are cemented by microcrystalline and sparry calcites. Bioclasts in bioclastic limestone are mainly derived from metacrinus, brachiopoda, trilobites, sponges (Fig. 6.15e, f), and the cement is mainly micrite and microcrystalline calcite.

(2)  Micrite

Micrites make up approximate 45% of the limestone gravels. The gravel size is generally smaller than grain limestone gravel, usually 0.5–5 cm in diameter. The composition of micrite limestone is uniform and almost entirely composed of lime mud (Fig. 6.15g), which sometimes includes a few lithochemical particles (<5%). In this structure, the micrite is similar to the terrigenous claystone. Some micrites have yellow irregular stripes caused by uneven dolomitization.
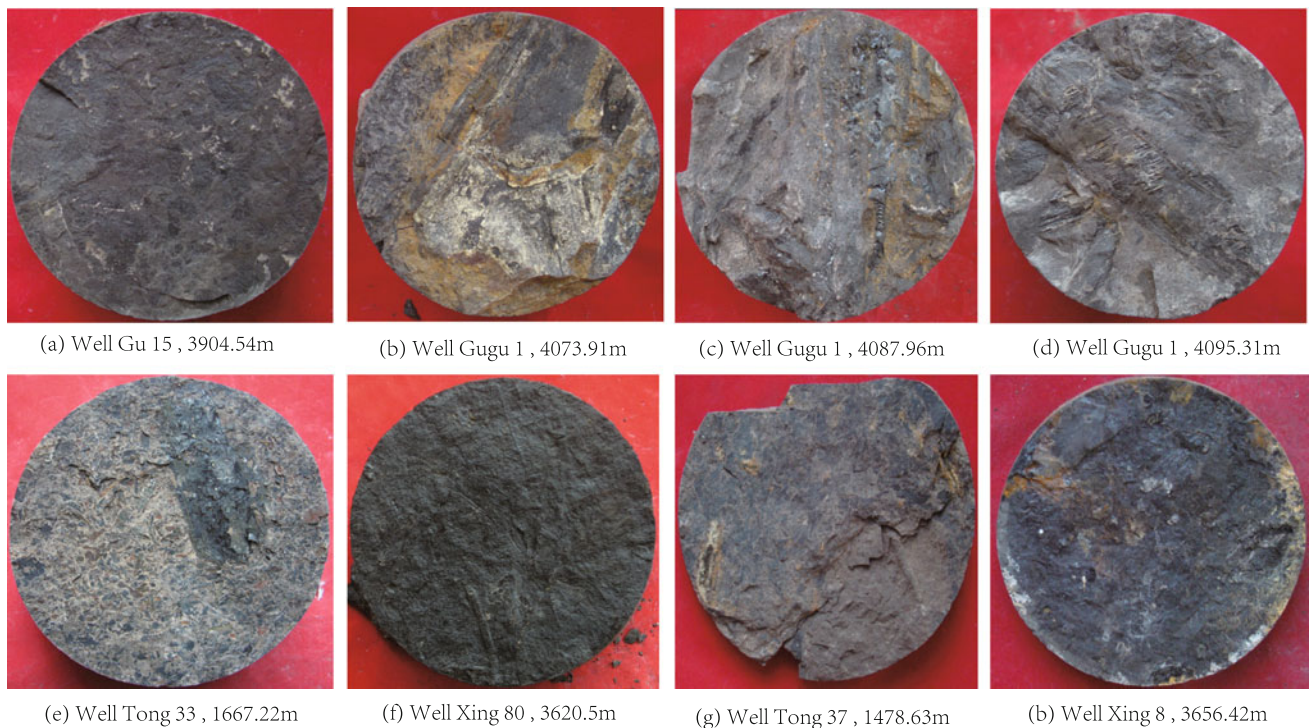
(a) Well Gu 15 , 3904.54m     (b) Well Gugu 1 , 4073.91m     (c) Well Gugu 1 , 4087.96m     (d) Well Gugu 1 , 4095.31m

(e) Well Tong 33 , 1667.22m     (f) Well Xing 80 , 3620.5m     (g) Well Tong 37 , 1478.63m     (b) Well Xing 8 , 3656.42m

**Fig. 6.14**  Plant debris and charcoal

(3)  Muddy limestone

Muddy limestones (Fig. 6.15h) make up about 25% of the limestone gravels. The gravel size is generally 0.3–2 cm in diameter. The muddy limestones mainly consist of lime mud and siliceous terrigenous clasts at 70 and 30% fraction, respectively.

2.  Dolomite gravels

(1)  Grain dolomite

The percentage of grain dolomites in dolomite gravels is very small, less than 5%. The gravel size is generally 0.5–2.5 cm in diameter. The main type of grain dolomite is sparite algal lump dolomite (Fig. 6.15i), in which the lumps have similar sizes (about 0.2 cm) and clear outlines. The lumps are dominated by microcrystalline texture dolomite and cemented by sparry calcites.

(2)  Fine crystalline dolomite

Fine crystalline dolomites account for 15% of the dolomite gravels, which are generally 0.5–5 cm in diameter. Fine crystalline dolomites are characterized by metasomatic or recrystallized dolomite crystals, which have a well-defined crystalline granular texture and are generally automorphic to

hypautomorphic mosaic-like or occasionally allomorphic mosaic-like. Parts of the dolomite crystals have a zonal structure with a hazy core and luminescent edge (Fig. 6.15j).

(3)  Powder crystalline dolomite

Powder crystalline dolomites make up about 30% of dolomite gravels and are 0.5–7 cm in diameter. Powder crystalline dolomites mainly consist of automorphic to hypautomorphic powder crystals (Fig. 6.15k), which have clear crystalline granular textures and dotted contacts.

(4)  Dolomicrite

Dolomicrites generally account for about 30% of the dolomite gravels and are 0.5–10 cm in diameter. They are composed of micro-crystals as well as a few fine crystals and powder crystals. Dolomicrites have a homogeneous microcrystalline structure, and the tiny crystalline grains are mainly hypautomorphic to allomorphic (Fig. 6.15l, m).

(5)  Siliceous dolomite

Siliceous dolomites make up approximately 20% of the dolomite gravels and are 1–20 cm in diameter. They are characterized by micro-crystal dolomites and siliceous clastics with a homogeneous structure. Dolomite crystals
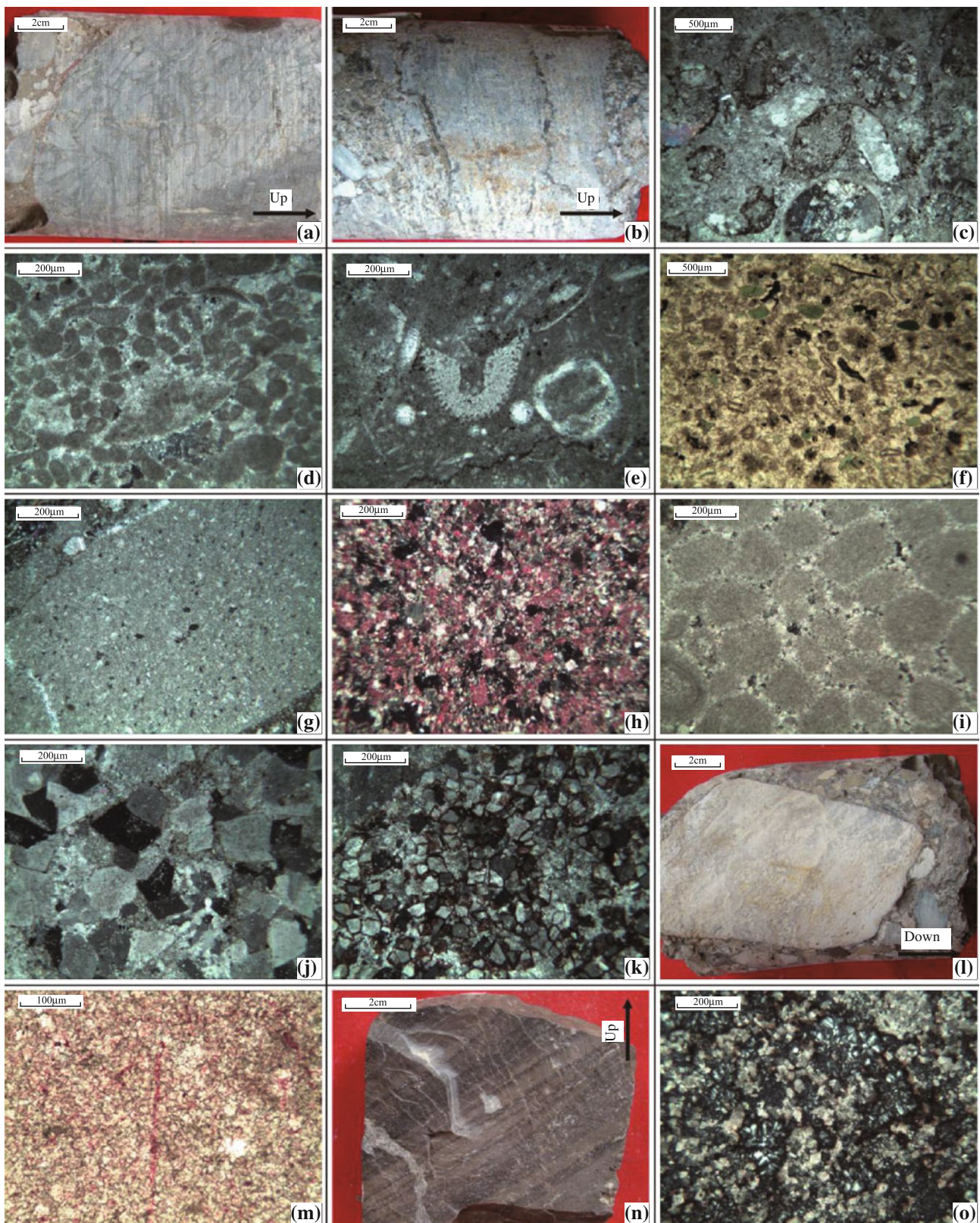
**Fig. 6.15** Composition types and characteristics of gravels in the Daxing conglomerate (from Liu et al. 2012b). **a** Edgewise limestone, Well Tong 103, 2095.85 m; **b** Oolitic limestone in cores, Well Tong 56X, 2977.11 m; **c** Oolitic limestone in thin-sections (+), Well Xing 4, 3647.37 m; **d** Algal limestone (+), Well Tong 56X, 2976.5 m; **e** Bioclastic limestone (+), Well Tong 35, 3017.5 m; **f** Bioclastic limestone (−), Well Tong 103, 2090.0 m; **g** Micrite (+), Well Tong 35, 3208.5 m; **h** Muddy limestone (+), Well Tong 35, 3209.6 m; **i** Algal lump dolomite (+), Well Tong 45X, 3015.54 m; **j** Fine crystalline dolomite (+), Well Tong 34, 1518.25 m; **k** Powder crystalline dolomite (+), Well Xing 801, 3410.8 m; **l** Dolomicrite in the cores, Well Xing 4, 3647.37 m; **m** Dolomicrite in thin-section (−), Well Xing 9-9X, 4095.4 m; **n** Siliceous dolomite in the cores, Well Xing 9-9X, 4094.5 m; **o** Siliceous dolomite in thin-sections, Well Xing 4, 3648.02 m

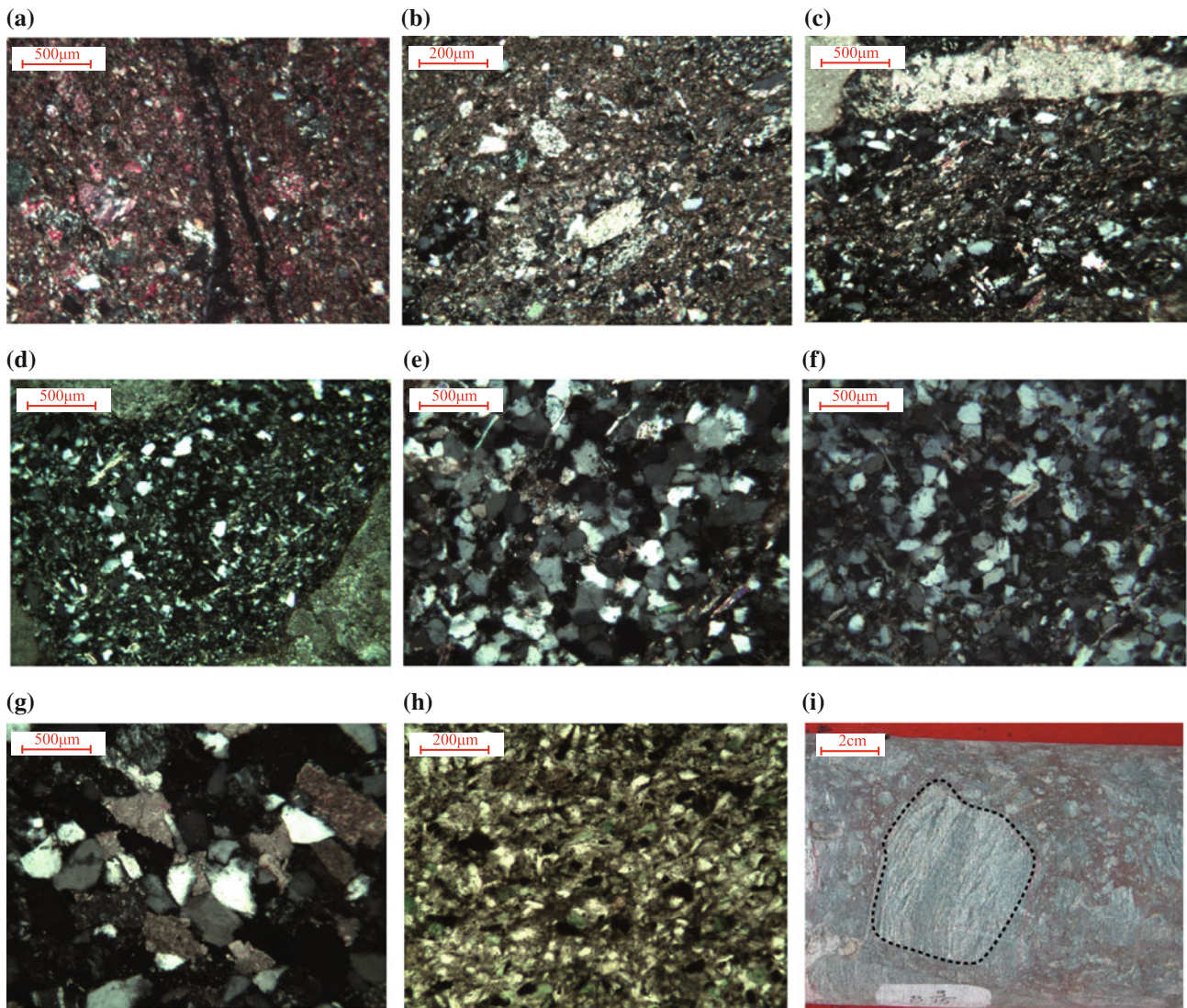**Fig. 6.16** Clastic gravels in the cores

generally account for 60% of siliceous dolomite, whereas siliceous components account for 40% and are mainly quartz (Fig. 6.15n, o).

3. Clastic rock gravels

In addition to the primary carbonate gravels, there are some (10%) clastic rock gravels in the Daxing conglomerate (Fig. 6.16). The gravels mainly include mudstone, muddy siltstone, siltstone, quartz sandstone, calcareous quartz sandstone, glauconitic quartz sandstone. Although these clastic rock gravels are relatively low content, they have important significance of provenance, especially in the Gu'an area of the southern Langgu sag. These clastic gravels and a large amount of muddy matrix are likely to indicate

that the provenance of the conglomerates in the Gu'an area is mainly Mesozoic clastic strata.

(1) Mudstone

Mudstones account for about 60% of the kind of mudstone gravels and are 0.2–5 cm in diameter, mainly including purple, gray, and dark gray mud-debris. Particles have strong plasticity and are often squeezed deformation into a flat or tear-like shape (Fig. 6.16).

(2) Silty mudstone

The silty mudstones account for about 40% of the kind of mudstone gravels and are 0.5–2 cm in diameter, mainly

including gray gravel particles. The silty mudstones can be found that contain a certain amount of quartz particles under microscope (Fig. 6.16).

(3) Siltstone

The siltstones account for about 25% of the kind of sandstone gravels and are 0.5–2.5 cm in diameter. The siltstones can be found that consist mainly of tiny quartz particles under microscope (Fig. 6.16), and parts have few mud.

(4) Quartz sandstone

Quartz sandstones account for about 10% of the kind of sandstone gravels and are 0.2–5 cm in diameter. Quartz sandstones can be found that are mainly composed of quartz, almost no mud under microscope (Fig. 6.16).

(5) Calcareous quartz sandstone

Calcareous quartz sandstone accounts for about 20% of the kind of sandstone gravels and are 0.5–5 cm in diameter. Under microscope, calcareous quartz sandstone is mainly composed of quartz, almost no mud, and cement is mainly calcareous. The calcareous cements provide a material base for late secondary dissolution (Fig. 6.16).

(6) Glauconitic quartz sandstone

Glauconitic quartz sandstones account for about 45% of the kind of sandstone gravels and are 0.5–7 cm in diameter. The most striking feature of the specimen is that the gravels are light green. Glauconitic quartz sandstones mainly consist of quartz and a certain amount of glauconite under observation of microscope. Glauconitic quartz sandstones have a directive function, indicating that these gravels mainly from the Qingbaikou System of the Upper Algonkian (Fig. 6.16).

## 6.2.5 Interstitial Components

Interstitial components in the Daxing conglomerate can be divided into two categories, including calcareous and argillaceous. The cements include calcareous, siliceous, and clay minerals. The matrix is mainly composed of muddy and silty matrix, with a small amount of calcareous matrix (Table 6.1).

1. Cements

(1) Calcareous cement

Carbonate mineral are the dominated cement in the study area, representing a diagenetic environment of alkaline fluids. There are mainly three types: microcrystalline calcite, sparry calcite and dolomite (Fig. 6.17).

Microcrystalline calcite has relatively high content, up to 35%, and abroad distribution. They mainly occupy the intergranular pores in the form of dispersion. Sparry calciteshows granular and inlaid forms. Dolomite mainly distributed in Jiuzhou area, having deep burial depth, and was mainly lining-like and pectinate shape.

(2) Argillaceous cement

The authigenic clay minerals have relatively low content and two forms including pore lining (clay minerals grow vertically to grain edge) and pore filling. In the area, authigenic clay minerals include kaolinite and illite (Fig. 6.18). Under scanning electron microscopy, kaolinite showed a variety of forms, including hexagonal sheet, book grating or granular, and occurred as pore filling or replacing other minerals. The precipitation of authigenic kaolinite requires sufficient $SiO_2$ and $Al^{3+}$ in the pore water, as well as acidic pore water properties, which are mainly derived from circulating pore water. Illite mainly appears in the form of silk thread, and the aggregates

**Table 6.1** The interstitial components in the conglomerate

| Interstitial components | Type | Subtype | Content (%) |
|---|---|---|---|
| Cement | Calcareous cements | Microcrystalline calcite | 35 |
| | | Sparry calcite | 25 |
| | | Dolomite | 10 |
| | Clay minerals | Kaolinite | 10 |
| | | Illite | 5 |
| | Siliceous cements | | 5 |
| Matrix | Muddy matrix | Kaolinite | 40 |
| | | Illite | 10 |
| | Silt sandstone | | 40 |
| | Calcareous matrix | Microcrystalline calcite | 10 |

(a) Microcrystalline calcite cements (-), Well Xing 5 , 2978.05m

(b) Sparry calcite cements (+), Well Tong 56X , 2976.5m

(c) Sparry calcite cements (+), Well Gu 15 , 3908.64m

(d) Dolomite cements (+), Well Xing 9-9X , 4095.57m

(c) Intergranular calcite, Well Tong 35 , 2714.75m

(f) Dolomite crystal,  Well Xing 9-9X , 4095.5m

**Fig. 6.17**  Calcareous cements



(a) Book palisade kaolinite, Well Xing 9 , 2571.9m

(b) Grain kaolinite, Well Tong 43 , 2574.77m

(c) Sheet kaolinite and illite, Well Tong 35 , 2714.75m

(d) Kaolinite and iilite, Well Gugu 1 , 4079.9m
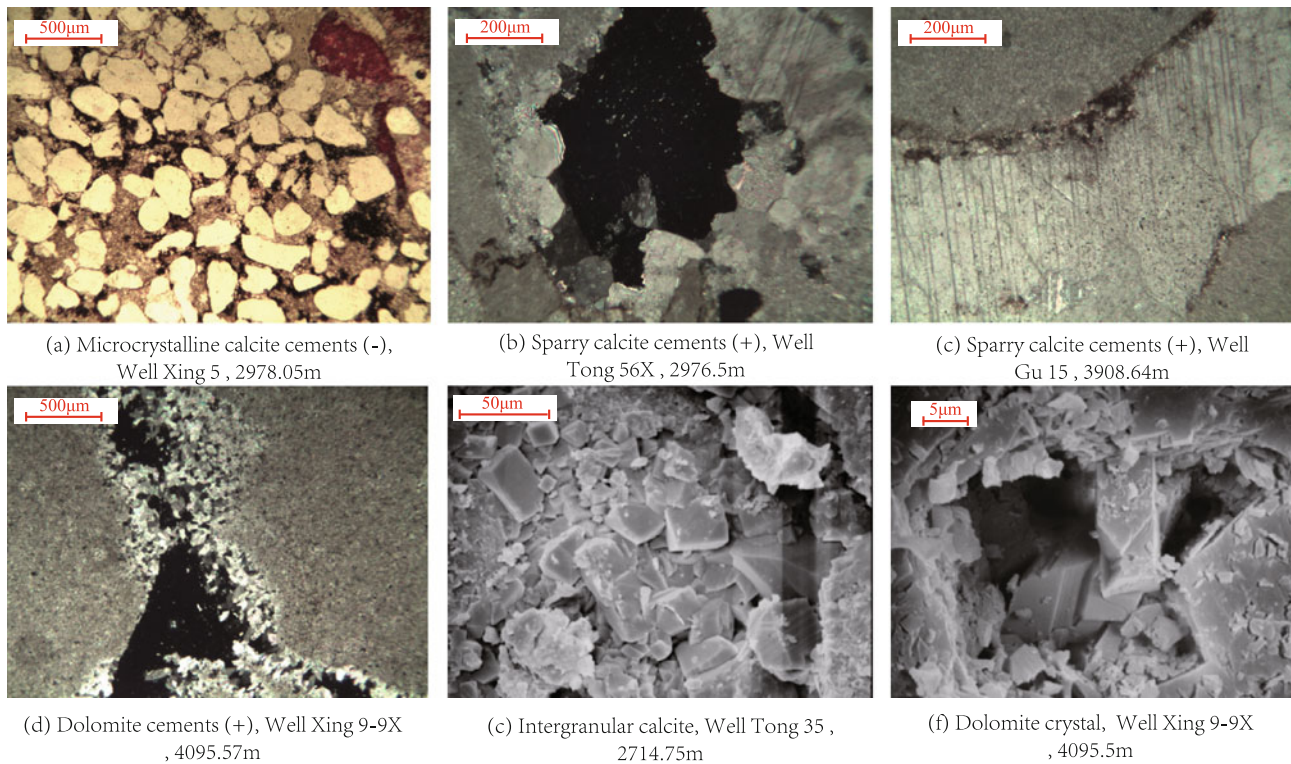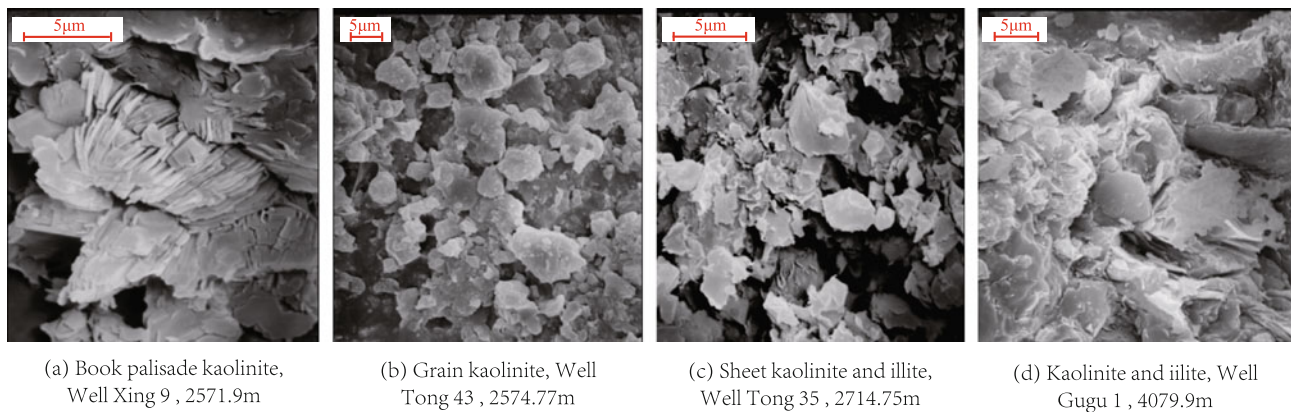
**Fig. 6.18**  Argillaceous cements

appear in the form of scaly, fragmented and feathery. Illite is formed in potassium ions-rich weakly alkaline solution, or transformed from other minerals during diagenesis.

(3)   Siliceous cement

Siliceous cements include cristobalite, quartz and quartz overgrowth (Fig. 6.19). Cristobalite generally appears as fibrous crystal. Besides precipitation from solution directly, cristobalite can also transform from opal. Quartz overgrowth

is mainly controlled by temperature and pressure, which increases with the increase of the depth and diagenesis. It begins in the form of crystallite on the clastic quartz particles, and have obvious dust line.

2.  Matrix

Based on core observation, the matrix in the Daxing conglomerate is dominated by argillaceous and calcareous matrix (Fig. 6.20).
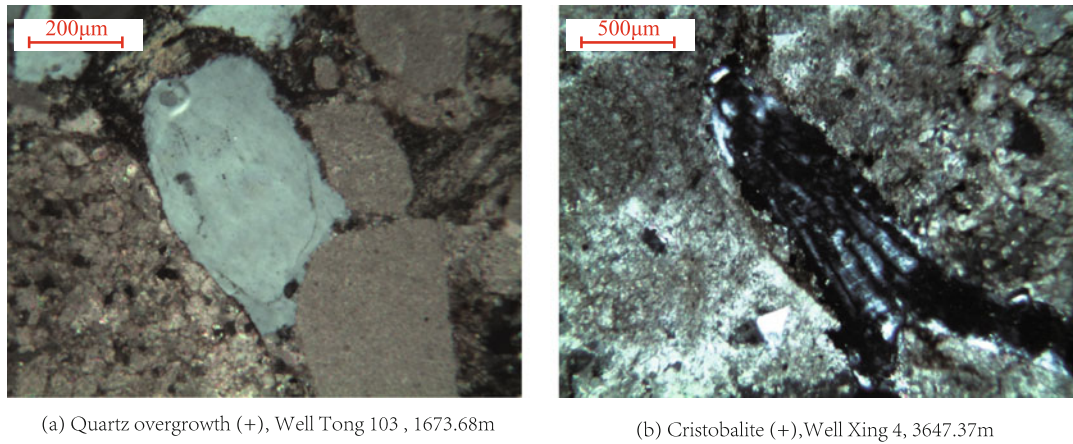
(a) Quartz overgrowth (+), Well Tong 103 , 1673.68m

(b) Cristobalite (+),Well Xing 4, 3647.37m

**Fig. 6.19** Siliceous cements



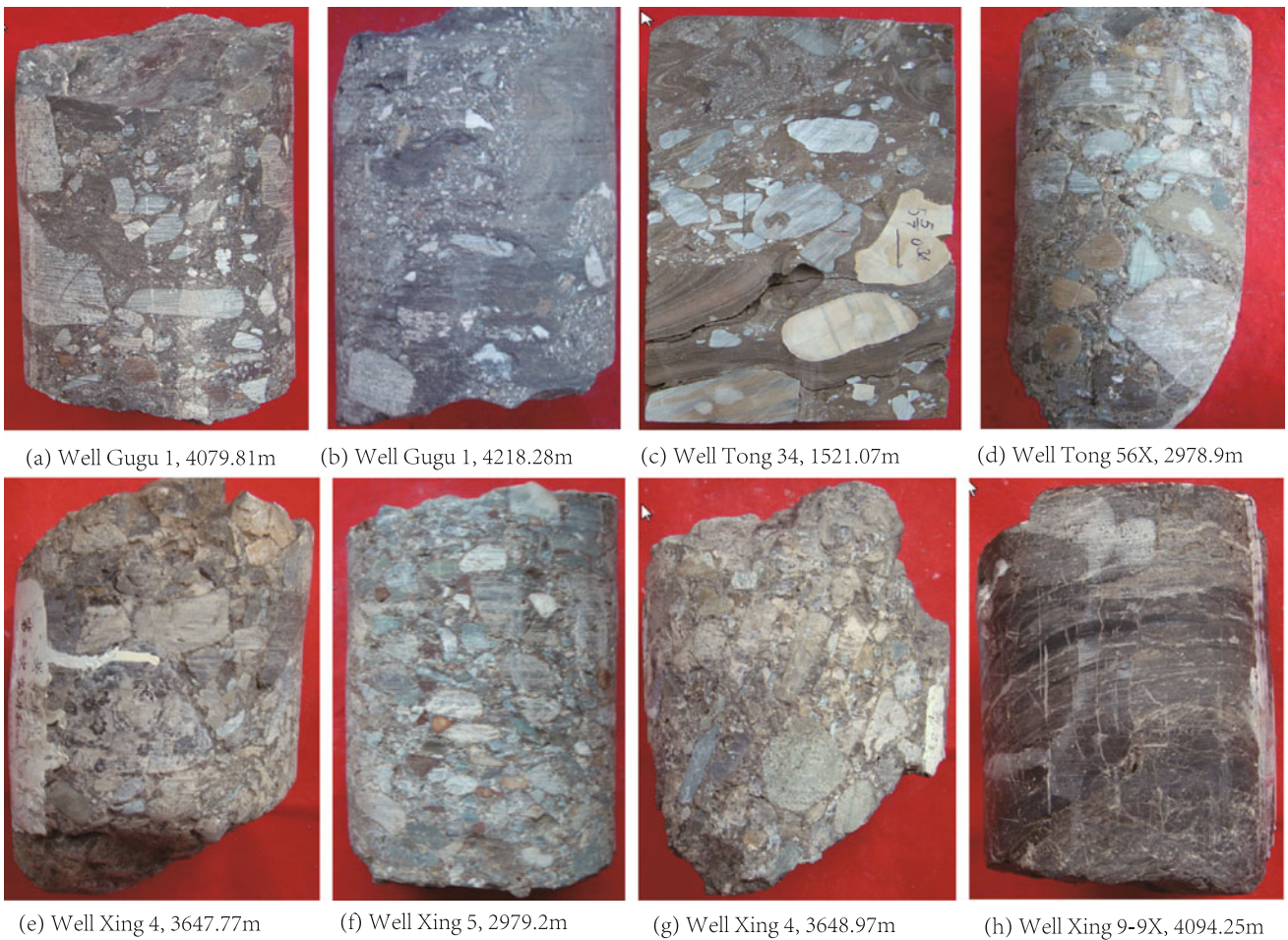(a) Well Gugu 1, 4079.81m	(b) Well Gugu 1, 4218.28m	(c) Well Tong 34, 1521.07m	(d) Well Tong 56X, 2978.9m

(e) Well Xing 4, 3647.77m	(f) Well Xing 5, 2979.2m	(g) Well Xing 4, 3648.97m	(h) Well Xing 9-9X, 4094.25m

**Fig. 6.20** Types of matrix in the Daxing conglomerate. **a–d** Argillaceous matrix; **e–h** calcareous matrix

Muddy matrix is mainly distributed in conglomerate in some parts of Gu'an and Caiyu areas. The existence of muddy matrix determines that the conglomerate is mainly matrix-supported conglomerate. As matrix-supported conglomerate, detrital particles are mostly not in contact with each other and are floating-like and isolated distribution in the matrix.

Calcareous matrix are mainly distributed in the grain-supported conglomerate in the Jiuzhou area. Content
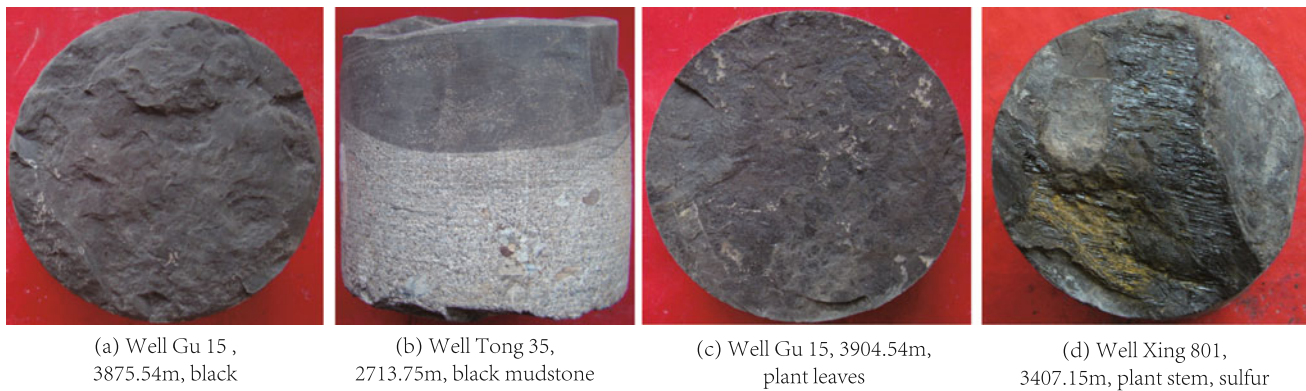
(a) Well Gu 15 , 3875.54m, black | (b) Well Tong 35, 2713.75m, black mudstone | (c) Well Gu 15, 3904.54m, plant leaves | (d) Well Xing 801, 3407.15m, plant stem, sulfur

**Fig. 6.21**  Mudstone between Daxing conglomerate

of this matrix is less. In conglomerate, types of cementation are primary porous cementation and contact cementation, and supporting style are mainly point-contact, line-contact, and local is suture contact.

### 6.2.6    Mudstone Between Conglomerates

There are many organic-rich mudstone, sometimes oil shales, between conglomerates (Fig. 6.21). The mudstone is mainly dark gray, gray and gray-black in color. Most of the mudstone is massive, while some has horizontal layers. In the surface of beddings, there are lots of carbonized plant debris, and some intact plant leaves and stems can be found. Some mudstone contains yellow powder sulfide (Fig. 6.21). According to predecessors' research results, the mudstone contains lots of *Huabei-estheria* fossils (Dong et al. 2002), indicating that the Daxing conglomerate is developed in semi-deep to deep lake sedimentary environments.

## 6.3    Palaeogeomorphology Restoration

Palaeogeomorphology is one of the key factors to control the development of sedimentary system, which determines the basic pattern and development history of the provenance and sedimentary system. The study of paleomorphology can help to reveal the relationship between the provenance, sedimentary system and their spatial patterns. That is benefit to guide the next step in oil and gas exploration. In this chapter, the paleogeomorphology of the Langgu sag is restored from the three aspects of highs, basin controlling faults, and sag.

### 6.3.1    Residual Topography of Highs

The paleogeomorphic restoration of residual topography of in the Daxing high was mainly accomplished according to

the data of Bouguer gravity anomaly. The larger the value is, the higher the terrain is. On the contrary, the smaller the value is, the lower the terrain is. The denser the contour is, the steeper the terrain is. On the contrary, the sparser the contour is, the flatter the terrain is. According to the Bouguer gravity anomaly contour map on the Daxing high (Fig. 6.22), the Daxing high has a northeast-southwest strike. The northern Daxing high is high while the southern is low and has alternation of groove and beam. On the Daxing high, there are two high points in the north. The height and slope is gradually reduced from the center-north to the south and north. There develop a number of paleo-gullies on the Daxing high, and these paleo-gullies are major channels for coarse debris on the Daxing high to get into basin. Using the software surfer 8.0, the geomorphic features of the residual strata on the Daxing high are plotted on the basis of the data of Bouguer gravity anomaly (Fig. 6.23). In the 3D map, the paleogeomorphic terrain features of the Daxing high are more clear and obvious.

### 6.3.2    Morphology of the Basin Controlling Fault

The restoration of the Daxing fault surface helps to study the distribution and source direction of the conglomerates. The fault surface of the Daxing fault is restored according to buried depth of the fault surface. First, fine interpretation of the Daxing fault has been conducted according to the seismic data, and then extract depth data of the Daxing fault surface (Fig. 6.24), and finally use software surfer 8.0 to map the fault surface (Fig. 6.25). In the 3D map of the Daxing fault surface, there were a lot of gullies on the Daxing fault surface, which can act as channels tof clastic materials getting into the basin. The development of the conglomerate bodies has a good correspondence with the paleo-gullies. For example, the resource channels can be found along the direction of the conglomerate bodies to the high on the Well Xing 8, Well Xing 9, Well Gu'gu 1 and so on.

**Fig. 6.22** Bouguer gravity anomaly contour map of the Daxing high (arrow indicates possible paleo-gullies)

**Fig. 6.23** 3D map of residual paleotopography of the Daxing high (arrow indicates the possible paleo-gullies)



### 6.3.3 Basin Paleomorphology

1. The methods to recover the paleomorphology

At present, methods to study the paleomorphology mainly include structural analysis, sedimentology analysis and a combination of the two methods (Deng et al. 2001; Lu et al.

2005). The sedimentology analysis method can further elicit the high-resolution sequence stratigraphic method (Wang et al. 2003; Zhao et al. 2003). To data, the study of paleo-geomorphic restoration is mostly in the qualitative stage. The more the recovery data is, the more accurate the restoration is. Some quantitative methods need to be further developed. In addition, the different lithological compaction rate should be considered to calculate original thickness of

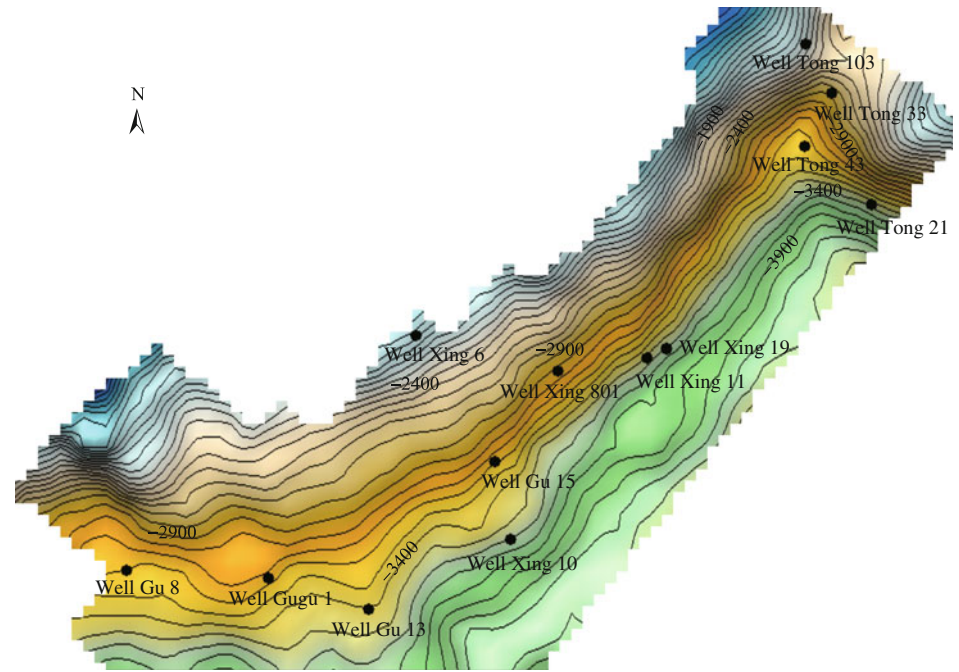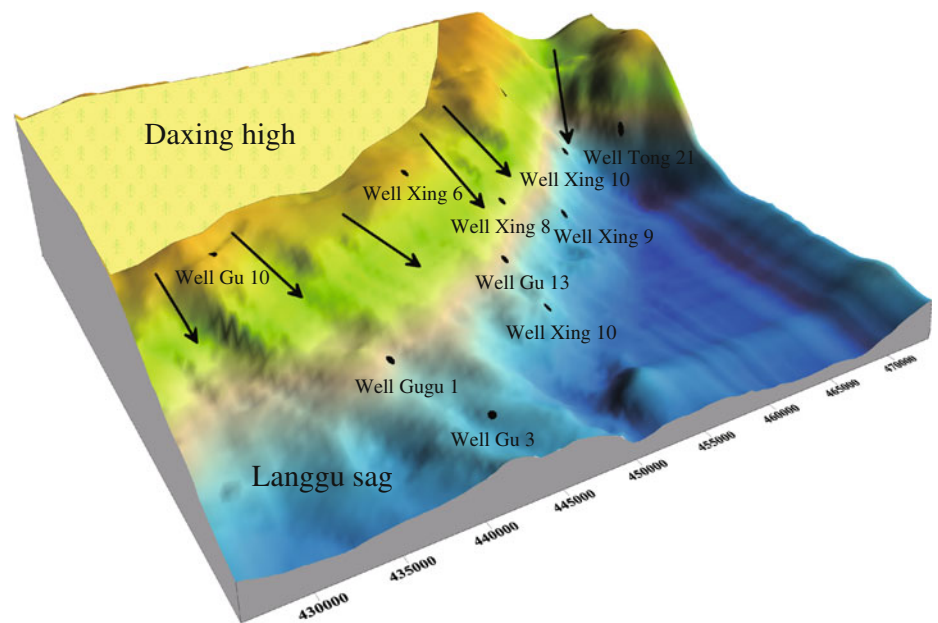**Fig. 6.24** Buried depth contour map of the Daxing fault surface



**Fig. 6.25** Daxing fault surface geomorphic features (remnant paleogeomorphic, arrow indicates possible paleo-gullies)

the deposition, that would make the restoration more accurately (Qi and Yang 2001; Davies et al. 2007).

This book is mainly based on the sedimentological research method and consider depositional thickness as an important parameter of the restoration of paleogeomorphology. An important assumption to use this method is that the sedimentary surface is flat after deposition, namely, a roughly horizontal deposition surface after sediments filling the sedimentary areas. Therefore, under the assumption, the depositional thickness can be used to recover the paleogeomorphology. The depth of the sag is deep where the thickness of the sediment is large. The depth of the sag is shallow where the thickness of the sediment is small.

In order to restore the paleogeomorphology more accurately, it is usually necessary to recover original thickness by correcting apparent bed thickness. These corrections generally include apparent thickness correction, denudation recovery, and compaction recovery (Perrier and Quilbier

1974; Jia et al. 2007). Without pursuit of precision, paleogeomorphology can be restored qualitatively through apparent bedding thickness, if no erosion occurred in the formation, the inclination of the formation changes little, and the lithology is similar. The paleogeomorphology restoration by this mothed can qualitatively reflect the overall height fluctuation and the source direction information.

In the depositional period of middle and lower Es$^3$ in the study area, a conglomerate body in contact with the deep lake facies was developed in the descending plate of the Daxing fault and the sediments were not eroded in the later stage of tectonic evolution. Therefore, this chapter uses the present apparent bedding thickness to restore the paleogeomorphology of the Langgu sag qualitatively. During this study, the top's and bottom's time of each formation on the seismic profile was confirmed firstly, and then the time was transformed into depth according to the time-depth relationship (Formula 6.1). Then we can get the thickness of each formation. Finally, based on t the strata thickness, the paleogeomorphology of the middle and lower Es$^3$ in the Langgu sag can be qualitatively restored.

$$Z = 2649.0 \times \exp(0.000329t)^{-1} \qquad (6.1)$$

Z—depth of formation, t—seismic time.

2. The palaeogeomorphic features of the basin

Using the seismic data to calculate the thickness of the middle and lower Es$^3$, and then using software surfer 8.0 for

mapping, the palaeogeomorphy of the Daxing conglomerate during the main depositional period can be restored (Figs. 6.26 and 6.27).

During the depositional period of the lower Es$^3$, the Paleogeomorphic features of the basin is characterized by "high mountain and deep lake", and the terrain elevation difference is more than 2000 m. In the Caiyu area, the landform is characterized by the fault trough which was controlled by high and fault. The slope of the terrain is slow, and some gullies are developed on the Daxing high. Under the control of the trough fault, it is easy to form the detrital material supply system along the direction of axis of the basin when the debris input into the basin. In the Jiuzhou region, the geomorphic unit is relatively simple, showing the characteristics of the "high mountain-canyon (gully)-deep lake". Terrain slope is steep. There develop typical nearshore fan-shaped sediments with coarse debris. In the Gu'an area, the characteristics are similar to the Jiuzhou area. Due to the earlier fault activity in the area, some conglomerate deposits were developed in the early period (the deposition period of the Es$^4$). As a result, the gully cuts deeper in the direction of the high, and the early conglomerates locally shows the relative high ground underwater, such as Well Gugu 1 area (Fig. 6.26).

During the depositional period of the middle Es$^3$, the geomorphological pattern of the basin inherited the geomorphic features of the lower Es$^3$, but there are also some differences. Experienced the erosion in the lower Es$^3$ and the Daxing fault continued movement toward the high direction, the height of the Daxing high was reduced and the
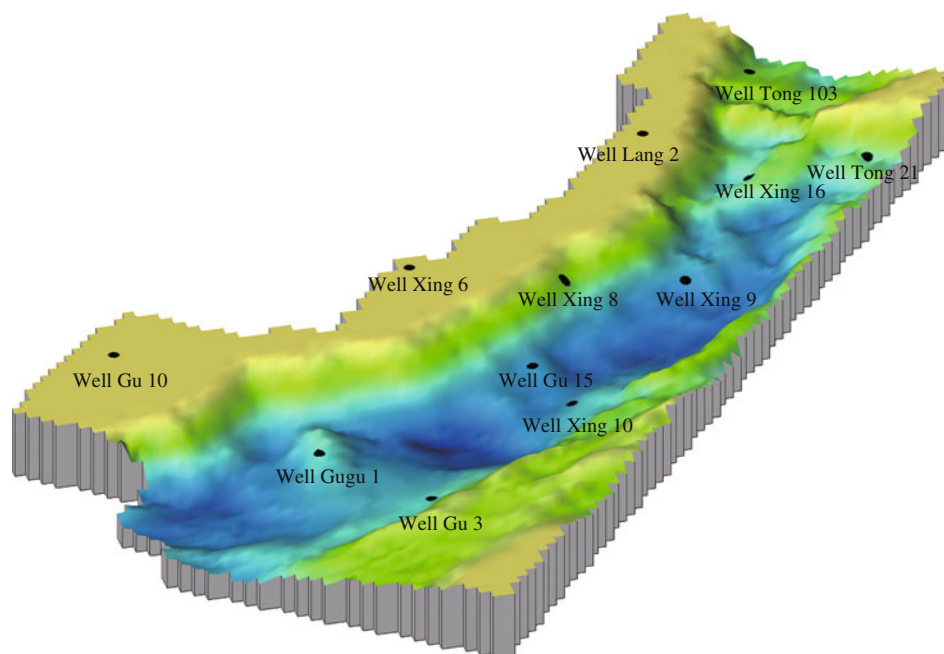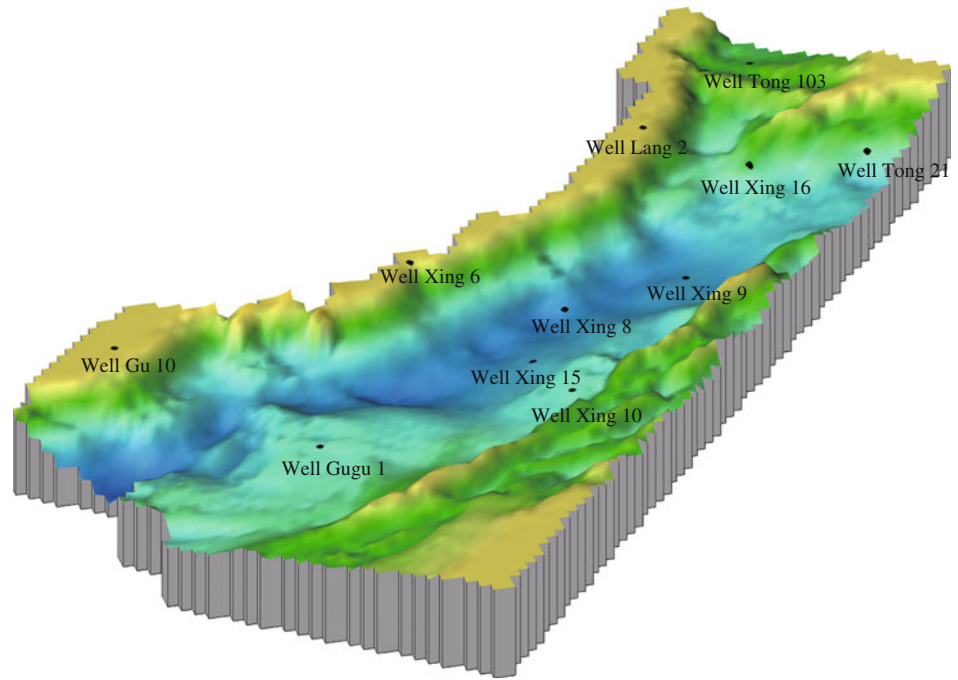


**Fig. 6.26** Paleogeomorphy of the Langgu sag in the lower Es$^3$ (modified from Liu et al. 2012a).

**Fig. 6.27** Paleogeomorphy of the Langgu sag in the middle Es$^3$



paleo-gullies were further cut toward the high direction. Therefore, the slope gradient of the sag are lower compared to lower Es$^3$, and the terrain becomes relatively flat. The overall characteristics of the basin landforms of the Caiyu area, the Jiuzhou area and the Gu'an area are similar to those in the lower Es$^3$. The northern terrain is flat and is characterized by the trough fault; the central area has simple landforms with steep slope and the fans were developed under controlling of paleo-gullies; and the gradient degree in southern terrain is between the northern area and the central area, the paleo-gullies act also as the source channel, and fan developed in the deep lake area (Fig. 6.27).

### 6.3.4 Paleomorphology Models

The paleogeomorphological model of the Daxing conglomerate during the depositional period was established by integrating the characteristics of residual strata, the Daxing fault, and the sag in the middle and lower Es$^3$ (Fig. 6.28). The paleogeomorphic background of the Daxing conglomerate is characterized by "high mountain, steep slop, many canyons and deep water". During the Daxing conglomerate depositional period, the height difference between the high and the sag was very big; the slope was steep, and there were many canyons among mountains; The coarse debris from

**Fig. 6.28** Paleogeomorphic model during depositional period of the Daxing conglomerate
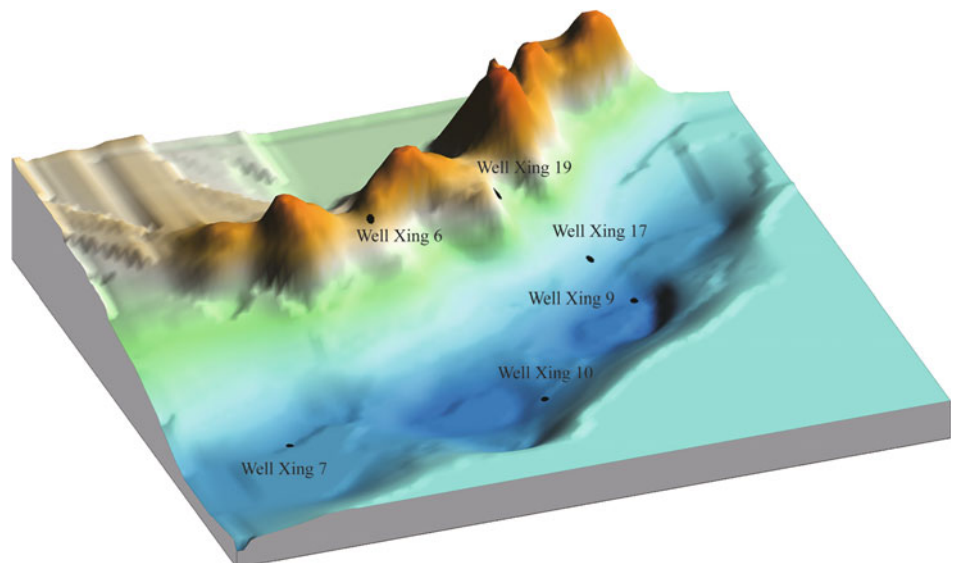
high was transported into the deep lake by short distance via paleo-gullies and formed locally stacked conglomerate bodies near provenance.

## 6.4  Paleo-Provenance Restoration

The Daxing high controlled the material source of the Daxing conglomerate in the Langgu sag. Study of the paleogeographic evolution of the Daxing high in the Paleogene is conductive to study debris material compositions and its vertical trend in the Daxing conglomerate. And it has a macroscopic guiding effect and realistic exploration significance for the prediction of sedimentary characteristics and reservoir type in the Daxing conglomerate.

The paleogeomorphological features of the basin indicate that the coarse debris on the highs is mainly carried out through the paleo-gullies and formed the conglomerate body near the provenance. So the paleogeological features of the highcan be recoveried approximately by analyzing the compositions of gravels in the conglomerate body and reversing these gravels to the high. Based on the analysis of the Paleogene residual strata in the Daxing high and the gravel types and their compositions of the Daxing conglomerate, the lithologic characteristics of the high can be recoveried by reversing gravels compositions to the high along the direction of provenance, following the principle of "sedimentary reverse order". Then the paleogeological characteristics and evolution of the Daxing high during the depositional period of the Daxing conglomerate can be restored.

### 6.4.1  Residual Strata

So far, the wells drilling in the basement on the Daxing high include wells Gu 10, Xing 6, Xing 19, Xing 1 and Xiang 2. At the bottom of the well Gu 10, siliceous dolomite and dolomite strata of the mesoproterozoic Jixian system developed, with a drilling thickness of 227 m. At the bottom of the well Xing 6, the Archean gneiss strata was dilled, with a drilling thickness of about 200 m. At the bottom of well Xing 19, Archean granite was drilled, with a drilling thickness of about 400 m. In addition, according to the "Petroleum Geology of China—Volume 5—Huabei Oilfield" and drilling records, siliceous dolomite of the upper and middle the Proterozoic Jixian system was drilled in well Xing 1 and Archean granite in the well Xiang 2. In this paper, combining the paleogeographic map of the pre-Paleogene of the Jizhong area (Fig. 6.29), the paleogeographic map of the Daxing high and the Langgu sag was established. In the Daxing high, residual stratas are mainly Archean eonothem, as well as the Mesoproterozoic Changcheng system, Jixian

system, Qingbaikou system, with NE-SW strike. These stratas get newer from southeast to northwest.

### 6.4.2  Distribution of Gravel Components in Conglomerate

#### 6.4.2.1  Gravel Composition Characteristics

More than 90% of Daxing conglomerate are composed mainly of carbonate gravels. Some clastic gravels (<10%), like quartz sandstone and mud pebble, are also developed in the Daxing conglomerate. The carbonate gravels include limestone and dolomite gravels. The limestone gravels are composed of grain limestone, micrite and muddy limestone, whereas the dolomite gravels include grain dolomite, fine crystalline dolomite, powder crystalline dolomite, dolomicrite and siliceous dolomite (Table 6.2). In addition to carbonate rock gravel, there are some (<10%) clastic gravels (Table 6.2). The lithologies of these gravels include mudstone, muddy siltstone, siltstone, quartz sandstone, calcareous quartz sandstone, glauconitic quartz sandstone. Although these clastic gravels are ratively low content, they are important indications of provenance, especially in the Gu'an area of the southern Langgu sag. These clastic gravels and a large amount of muddy matrix probably indicate that the provenance strata of the conglomerate in the Gu'an area is mainly Mesozoic clastic strata. Details of the various gravels are discussed in Sect. 6.2.4.

The gravel compositions of the Daxing conglomerate have obvious zoning characteristics in the plane. (1) In the middle $Es^3$, the gravel compositions of the conglomerates in the northern sag are mainly silt mudstone, siliceous dolomite, and power crystalline dolomite, with a few glauconitic quartz sandstone, siliceous rock, and mudstone. The gravels compositions of the conglomerates in the central sag are mainly power crystalline dolomite, siliceous dolomite, and followed by micrite. The conglomerate is not developed in the southern Gu'an area (Fig. 6.30). (2) In the lower $Es^3$, the graves compositions of the conglomerates in the northern sag are mainly micrite and grain limestone, followed by power crystalling dolomite, with a few glauconitic quartz sandstone and micrite. The gravel compositions of the conglomerates in the central sag are mainly power crystalline dolomite, followed by siliceous dolomite and micrite. The gravels compositions of the conglomerates in the southern sag are mainly micrite, power crystalline dolomite, and mudstone, with a few siliceous dolomite and glauconitic quartz sandstone (Fig. 6.31).

#### 6.4.2.2  Gravel Age Characteristics

According to the lithologic assemblage characteristics of gravels and fossils, and referring lithology and fossils

**Fig. 6.29** Paleogeographic map of pre-Paleogene in the Daxing high and Langgu sag. Ar-Archean; Ch-Changcheng system; Jx-Jixian system; Qb-qingbaikou system; €-Cambrian; O-Ordovician; C-P-Carboniferous-Permian; J-Jurassic; Mz-Mesozoic
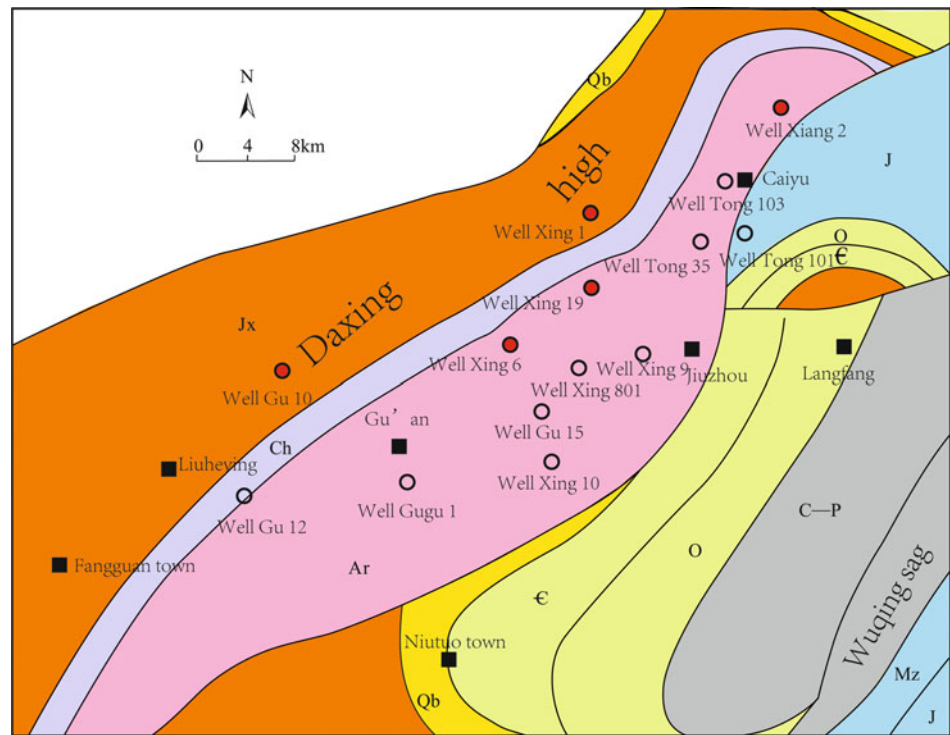


**Table 6.2** Compositions of the Daxing conglomerate gravels

| Gravel types | Lithology | Content (%) | Diameter (cm) |
|---|---|---|---|
| Limestone | Grain limestone | 30 | 0.5–10/3 |
| | Micrite | 45 | 0.5–5/1.5 |
| | Muddy limestone | 25 | 0.3–2/3 |
| Dolomite | Grain dolostone | 5 | 0.5–2.5/1.5 |
| | Fine crystalline dolomite | 15 | 0.5–5/2 |
| | Power crystalline dolomite | 30 | 0.5–7/4 |
| | Dolomicrite | 30 | 0.5–10/5 |
| | Siliceous dolomite | 20 | 1–20/10 |
| Mudstone | Mudstone | 60 | 0.2–5/2 |
| | Silt mudstone | 40 | 0.5–2/1 |
| Sandstone | Siltstone | 25 | 0.5–2.5/1 |
| | Quartz sandstone | 10 | 0.2–5/2 |
| | Calcareous sandstone | 20 | 0.5–5/2 |
| | Glauconitic quartz sandstone | 45 | 0.5–7/3 |

characteristics of provenance areas (Table 6.3), the age of these gravels and their distribution were analyzed (Figs. 6.32 and 6.33).

In the middle Es$^3$, the gravels of conglomerates in the northern area primarily come from the Cambrian limestone strata and the upper-middle Proterozoic Jixian system dolomite strata, followed by the Ordovician limestone, the upper-middle Proterozoic Qingbaika clastic rock strata, and a small amount of Mesozoic clastic rock strata. The gravels of conglomerates in the central area are mainly from the dolomite strata of the Jixian system in the upper-middle Proterozoic, followed by the Cambrian and Ordovician limestone strata. In the southern area, the conglomerates are not developed. In the lower Es$^3$, the gravels of conglomerates in the northern area are mainly from the Cambrian limestone strata, followed by the Ordovician limestone, and part of the gravels are from the upper-middle Proterozoic Jixian system dolomite strata. The gravels of conglomerates
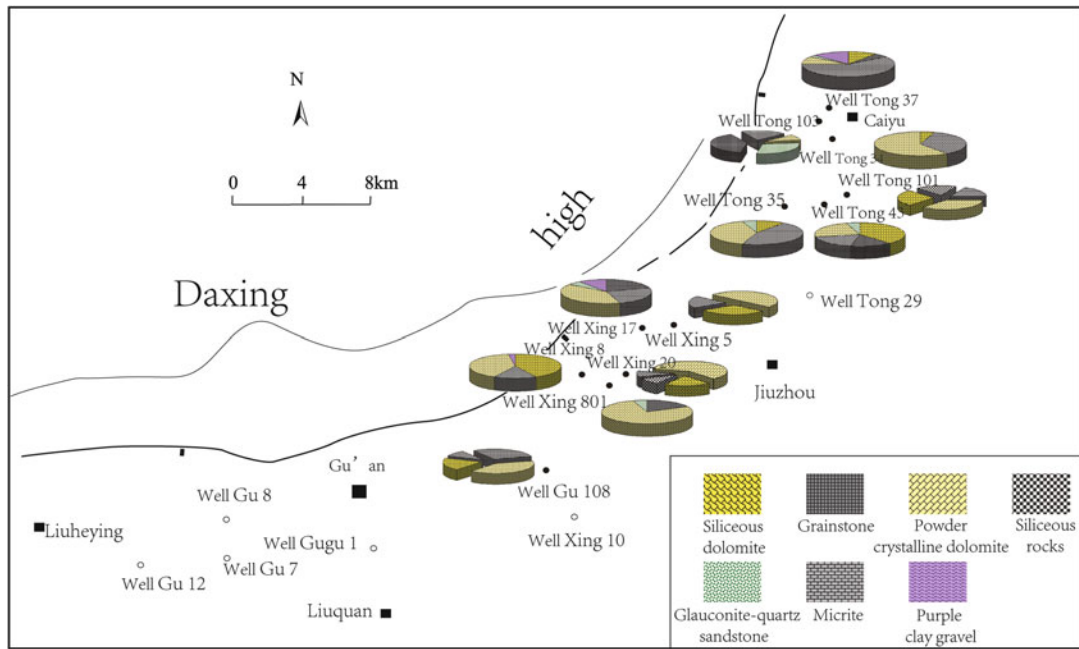
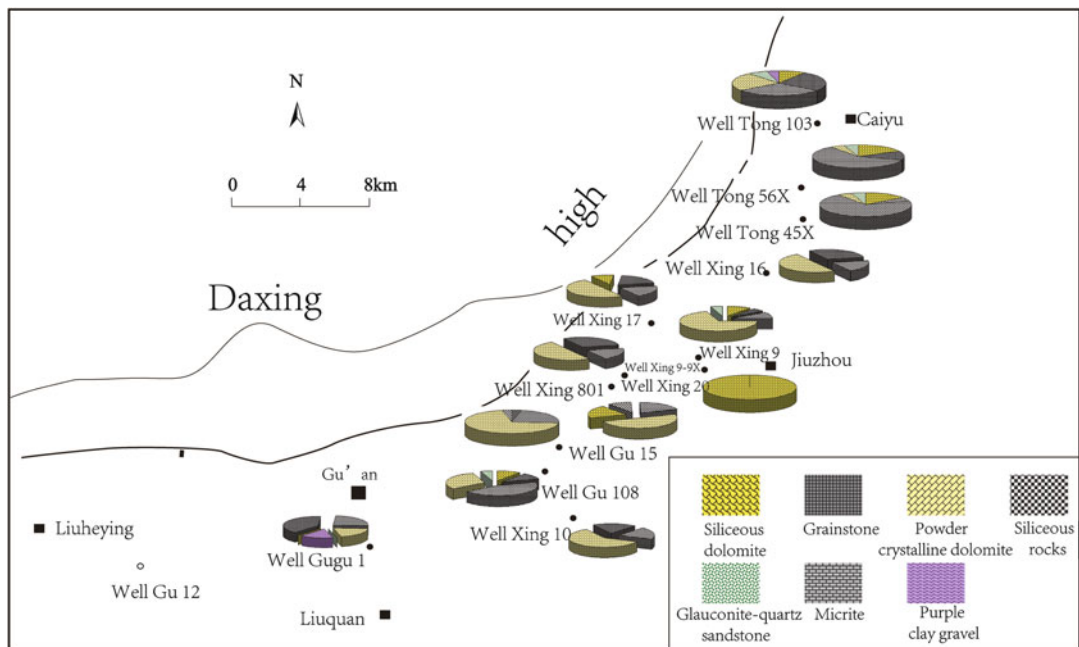**Fig. 6.30** Distribution of gravel compositions of conglomerates in the Langgu sag in the middle $Es^3$



**Fig. 6.31** Distribution of gravel components of conglomerates in the Langgu sag in the Lower $Es^3$

in the central area mainly come from the dolomite strata of the Jixian system in the upper-middle Proterozoic, followed by Cambrian and Ordovician limestone strata. Gravels of conglomerates in southern area come mainly from the Cambrian limestone strata, followed by the dolomite strata of the Jixian system in the upper-middle Proterozoic and Mesozoic clastic rock formation.

## 6.4.3   The Paleogeologic Evolution of the Daxing High

Based on the analysis of the palaeogeomorphology, the residual strata of the high, the composition and age of gravels, the paleogeologic evolution of the Daxing high can be rebuilt during the depositional period of conglomerates.

**Table 6.3** Lithology characteristics and fossil assemblages in main provenance strata of the Daxing conglomerate North China Oilfield geological record preparation group (1988)

| Provenance strata | Lithologic characteristics | Fossil assemblages |
|---|---|---|
| Mesozoic | Red sandstone, mudstone, pebbly sandstone, glutenite | |
| Ordovician | Lime dolomite, dolomicrite, mottled dolomitic limestone | Graptolite, nautilus |
| Cambrian | Muddy limestone, edgewise conglomerate, oolitic limestone, micrite, bioclast limestone (trilobite), algal limestone, fuchsia shale, siltstone | Trilobites; spines, thorn fossils |
| Qingbaikou system | Glauconite quartz sandstone, micrite | Large individual (50–100 μm), combination of micro-ancient plants with rough surface |
| Jixian system | Siliceous dolomite, siliceous rock, powder crystalline dolomite, black and yellow-green shale, algal dolomite | Thick film, 10–50 μm, micro-ancient plant combination with rough surface or verrucous pattern |
| Changcheng system | Flint dolomite, quartz sandstone, muddy siltstone, some volcanic breccia, muddy dolomite | Simple form, combination of tiny (molecular class) micro-ancient plant |
| Archean eonothem | Granite, metamorphic rocks of the Miyun group | |
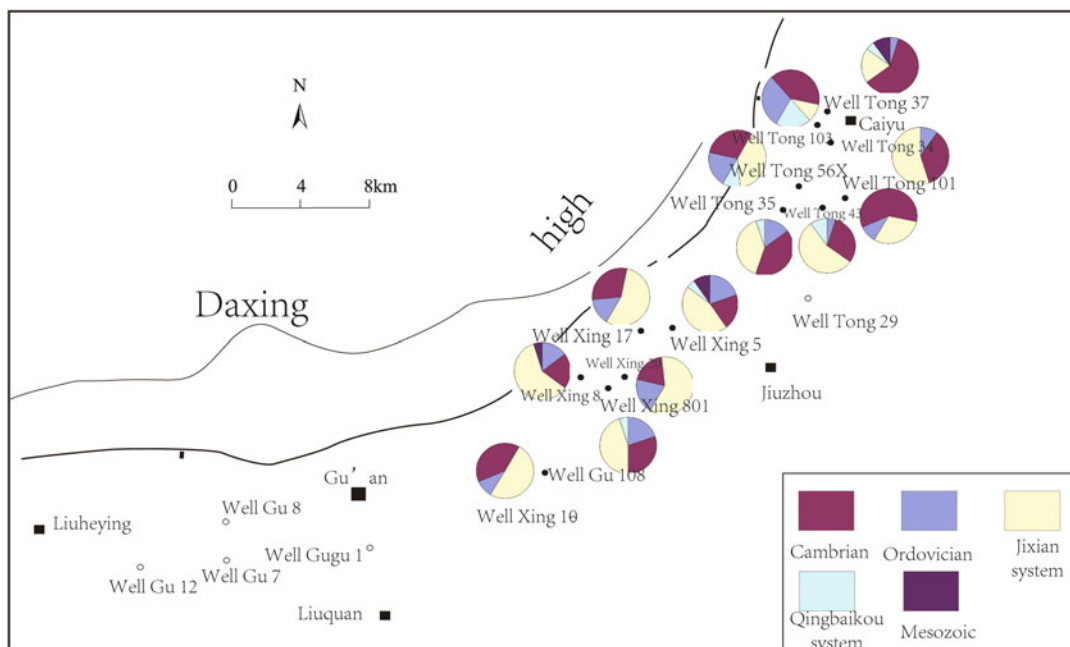


**Fig. 6.32** Distribution of gravel age in the middle Es$^3$ of the Langgu sag

Before the deposition of the lower Es$^3$, the Daxing high developed the Middle-Upper Proterozoic Jixian system, Qingbaikou system, Paleozoic Cambrian, Ordovician, and Mesozoic from southeast to northwest (Fig. 6.34). The Cambrian and Ordovician strata have a wide distribution and large exposure area, followed by the Middle-Upper Proterozoic Jixian system. These strata constitute the main provenance stratigraphy of the Daxing conglomerate during the depositional period of the lower Es$^3$. The Qingbaikou and Mesozoic strata are only locally distributed, providing less provenance material, which affected only the conglomerates in the northern area and southern area. In particular, a large part of the mud component in the conglomerate of the southern area came from the clastic rocks of the Mesozoic.

With the deposition of conglomerates in the lower Es$^3$, the strata on the Daxing high were continuously eroded and
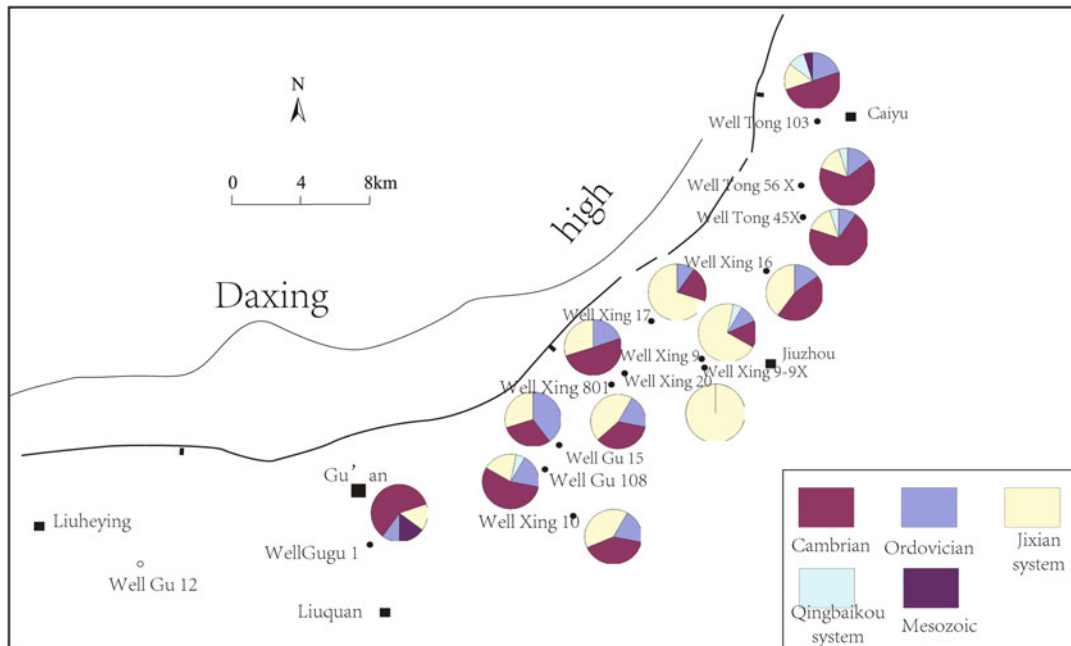
**Fig. 6.33** Distribution of gravel age in the lower Es$^3$ of the Langgu sag
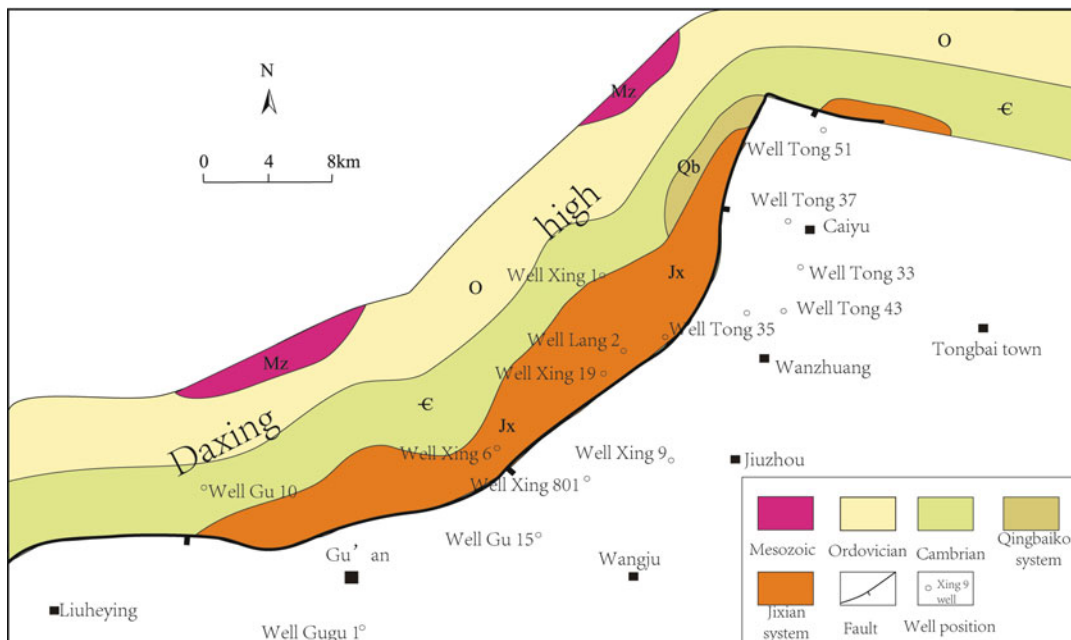


**Fig. 6.34** Strata distribution of the Daxing high before the lower Es$^3$ (modified from Liu et al. 2012a)

the products were carried into the sag. After the deposition of the lower Es$^3$ (before the deposition of the middle Es$^3$), the Mesozoic strata on the Daxing high were basically overall eroded. Therefore, the exposed strata were mainly Middle-Upper Proterozoic Jixian system, Qingbaikou system, the Paleozoic Cambrian and Ordovician (Fig. 6.35).

The distribution of Cambrian and Ordovician strata has been reduced, especially the Ordovician strata were local patchy distribution. At the time, with the overlying strata erosion, the exposed area of underlying Jixian strata has been expanded. In areas where erosion is intense, even the Jixian strata have been completely eroded, revealing the Archean
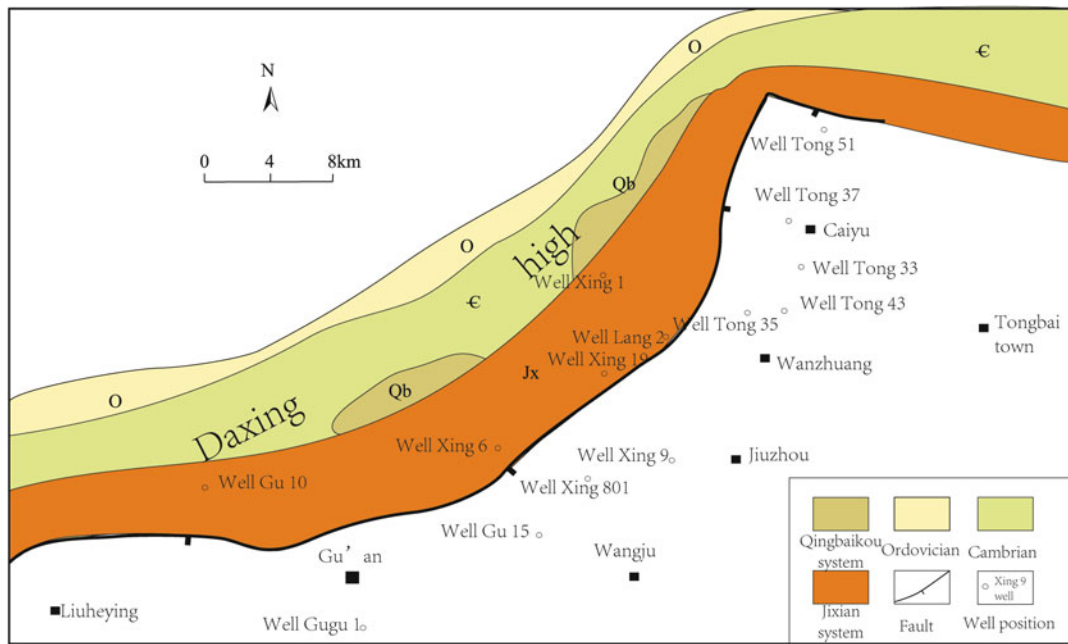
**Fig. 6.35** Strata distribution of the Daxing high after deposition of the lower Es$^3$
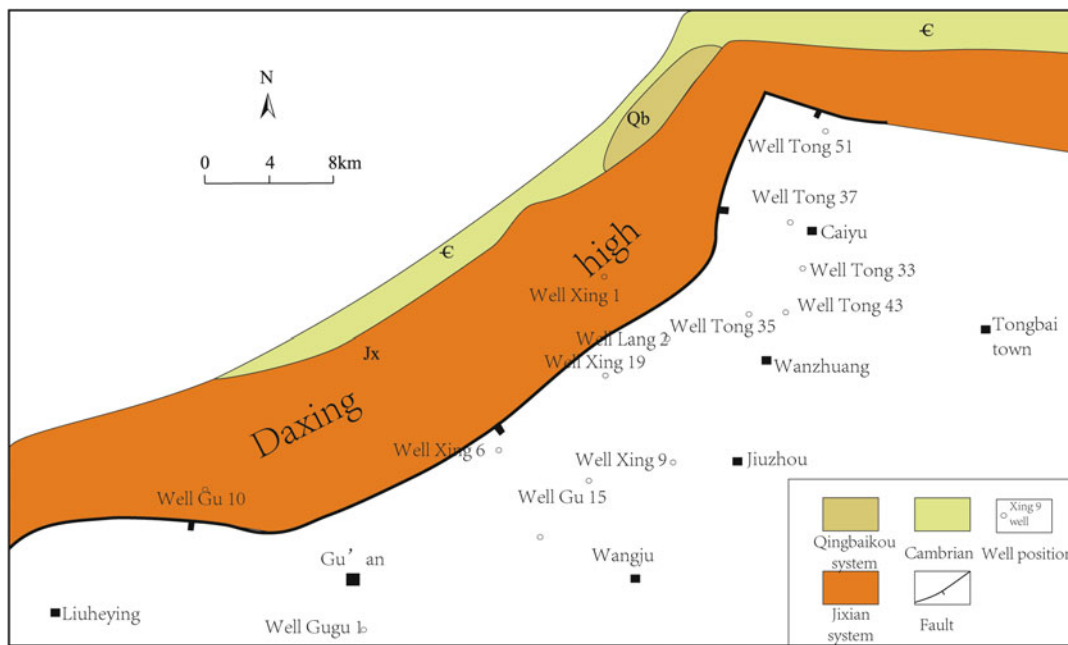


**Fig. 6.36** Strata distribution of the Daxing high after the middle Es$^3$

gneiss strata. During the depositional period of the middle Es$^3$, the Middle-Upper Proterozoic Jixian system and the Paleozoic Cambrian became the main source strata of the Daxing conglomerate, which was locally affected by the Ordovician and Qingbaikou system strata.

With the development of conglomerates in the middle Es$^3$, the strata on the Daxing high are subjected to further weathering and erosion. The exposed strata have undergone great changes after the conglomerates deposits. The main strata were Archean, Middle-Upper Proterozoic Jixian

system, and some Qingbaikou system in the northern areas (Fig. 6.36). Due to continuous weathering and erosion, the height of the Daxing high is obviously reduced. And the paleogeographic environment of the basin is not suitable for development of the coastal conglomerates due to the change of the basin from the intense fault sag period to the return of rift period. Therefore, the Daxing high no more acted as the main source of the sediments of the basin.

## 6.5    Source-Basin and Sedimentary Model

The genesis, shape, size, and lithology of the sand (rock) body in the lake basin are directly controlled by the topography and provenance of the lake basin and the surrounding land (Wu 1986). According to the lithology, sedimentary structure, and vertical sequence of the Daxing conglomerate, simultaneously considering the source composition and paleomorphological features of the conglomerate sediments, the Daxing conglomerate is divided into three types: fault-trough gravity flow, debris flow nearshore subaqueous fan and mudslides nearshore subaqueous fan.

### 6.5.1    Fault-Trough Gravity Flow

The paleogeomorphic background of the Caiyu area in northern Langgu sag is characterized by a fault trough controlled by highs and faults. The fault trough extended to the deep water area of lake basin from Daxing high and via downthrown side of Daxing fault. Therefore, the landform was gentle and the slope was low. The clastic matters from the Cambrian-Ordovician and part of the Jixian System and Mesozoic strata are flowed into the lake basin with currents along the fault-trough, forming the axial fault-trough gravity flow sediments.

The conglomerates in the fault-trough gravity flow mainly include matrix-supported conglomerate and grain-supported conglomerate. Gravels are mainly micrite, granular limestone, dolomicrite and powder crystallinge dolomite, followed by siliceous dolomite. The interstitial matters is mainly limy matters in the grain-supported conglomerate, whereas muddy matters in the matrix-supported conglomerate. The vertical sequence, is mainly manifested as positive rhythm combination composed of main channel and minor channel from bottom to top. The main channel mainly contains grain-supported conglomerate with a few mud content. Single layer thickness of the main channel is big, up to tens of meters or even

hundreds of meters. The minor channel is dominated by matrix-supported conglomerate, and contains many muddy interstitial materials. The single layer thickness of the minor channel is small, usually less than 5 m. And the minor channel is often intermixed with the lake mudstone. The SP and RT curves of the channel facies show high amplitude box shape or toothed box shape. The SP and RT curves of overflowing deposit show toothed bell shape. In vertical, the SP and RT curves of complex of main channel—minor channel—overflowing forms bell shape patterns. In the seismic profile, the fault-trough gravity flow appears as a wedge-like concave filling, with a lateral or nearly horizontal superstructure in the transverse direction, and is manifested as a distinct progradation structure in the longitudinal direction (Fig. 6.37).

### 6.5.2    Debris Flow Nearshore Subaqueous Fan

The paleogeomorphic background of the Jiuzhou area in central Langgu sag is characterized by "high mountain and deep lake" with steep slope. The clastic matters from middle-upper Proterozoic Jixian system and the Paleozoic Cambrian, Ordovician on the high were carried directly into the deep lake area along the ancient canyons and stacked in the downthrown side of the Daxing fault, forming a debris flow nearshore subaqueous fan deposition.

The rock type of debris flow nearshore subaqueous fan is mainly grain-supported conglomerate. Gravels are dominated by dolomicrite and siliceous dolomite, followed by micrite and grain limestone. The interstitial material is mainly limy sediments. This conglomerate body developed successively inner fan, middle fan and outer fan from bottom to top in vertical, presenting upward fining positive rhythm. The inner fan, which faced the valley and was closed to the high, was main channel deposit. The lithology is the grain-supported coarse-boulder conglomerate, with rare sedimentary structure. The thickness of single conglomerate layer of the inner fan is big, up to tens of meters and even several hundreds of meters. The middle fan is braided channel sediments. The lithology is dominated by coarse-middle conglomerate, with massive bedding and scour surface, and represent positive rhythm. The thickness of single conglomerate layer of the middle fan is generally tens of meters. The outer fan is mainly dark gray mudstone interbeded with some thin glutenite beds. The logging curve of debris flow nearshore subaqueous fan represent combination of box shape and toothed box shape, with "high resistivity" characteristics. In the seismic profile, the debris
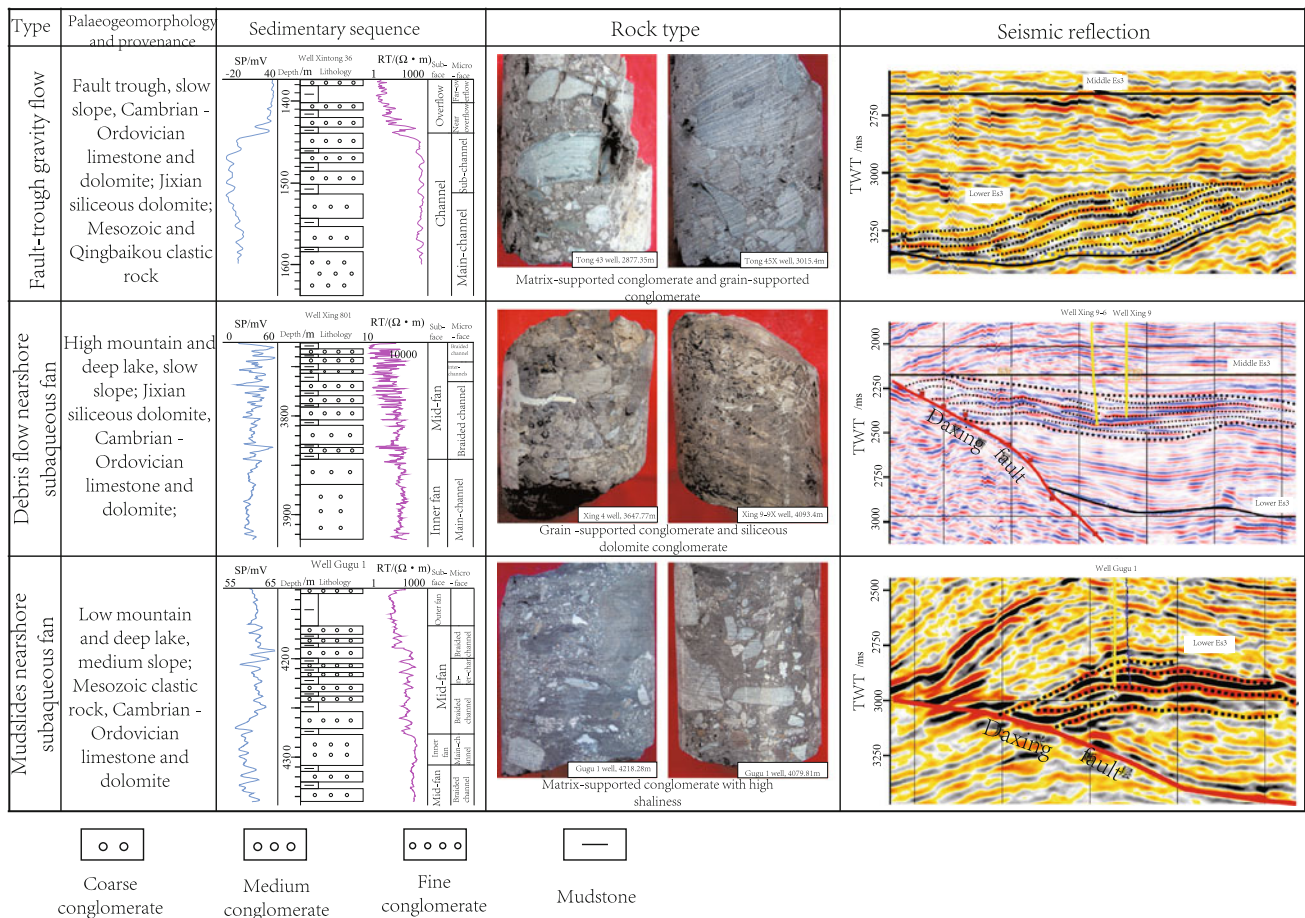
**Fig. 6.37** Genesis types and sedimentary characteristics of the Daxing conglomerate (modified from Liu et al. 2012a)

flow nearshore subaqueous fan represents strong amplitude wedge extending to the lake (Fig. 6.37).

### 6.5.3   Mudslides Nearshore Subaqueous Fan

The terrain slope in the Gu'an area in southern Langgu sag is between the Caiyu area and the Jiuzhou area. The main source strata is the Mesozoic clastic strata and the Cambrian-Ordovician carbonate strata. Thus, mud content is very high in the sediments, forming a mudslides flow nearshore subaqueous fan.

The main rock type is matrix-supported conglomerates. Gravels are mainly micrite, followed by grain limestone, dolomicrite, powder crystalline dolomite and mudstone.

Matrix is dominated by mud and has very high content, abd gravel was "floating" in the matrix. The vertical sequence, like the debris flow type nearshore subaqueous fan, also successively develops the inner fan, middle fan and outer fan from bottom to top. Compared with the debris flow nearshore subaqueous fan, high mud content in each sub-face sediments is its typical feature. The thickness of single conglomerate layer is thin, usually ten meters. The conglomerate and lake mudstone are frequent interbedded with uneven thickness. The SP and RT curves of the mudslides nearshore subaqueous fan are combination of teeth bell shape or box shape. In the seismic profile, the interior of the conglomerate is characterized by the clutter reflection with strong amplitude, and the edge is in finger-like contact with the lake mudstone. The range of the fan which extends to the lake basin is small (Fig. 6.37).

**Fig. 6.38** Sedimentary facies map of the Daxing conglomerate. **a** The middle Es³; **b** the lower Es³ (modified from Liu et al. 2012a)
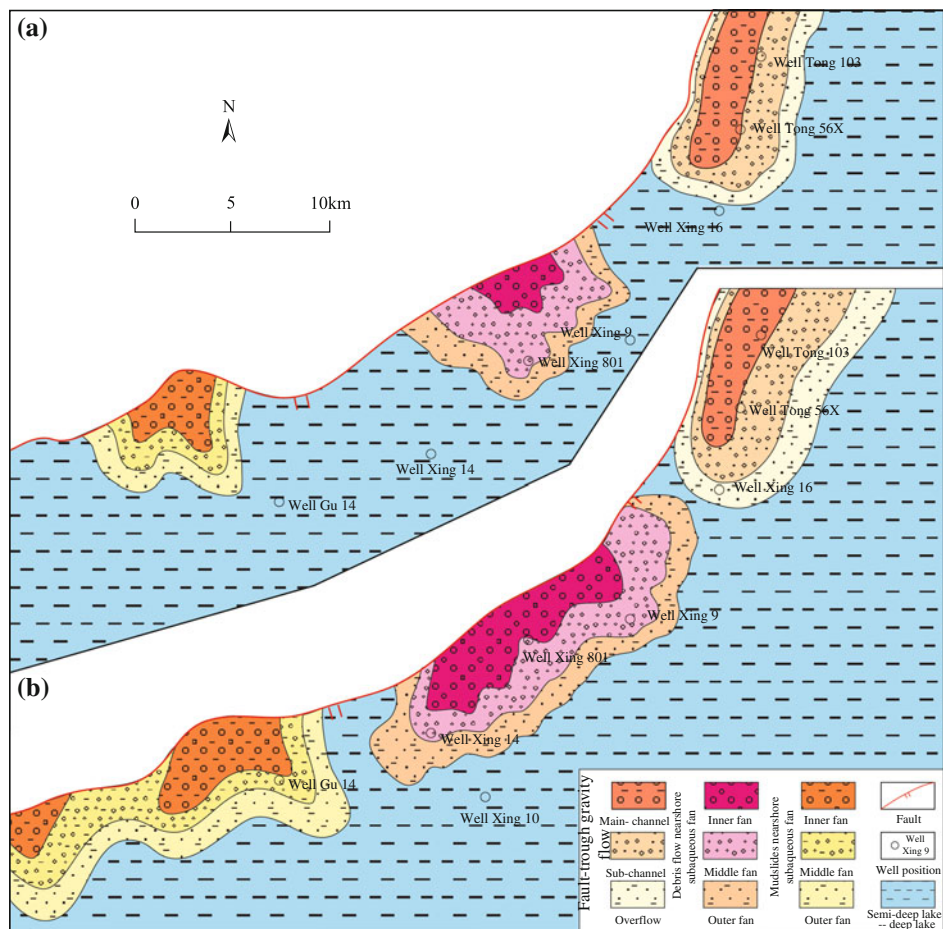


## 6.5.4  Distribution Characteristics of the Conglomerate

In the deposition of lower part of Es³, under intensively movement of the Daxing fault, the sedimentary environment was mainly semi-deep or deep lake and conglomerates developed very well Controlling by the paleogeomorphic and parent rock types on the high, there develop mudslide flow nearshore subaqueous fan, debris flow nearshore subaqueous fan, and fault-trough gravity flow from the south to the north (Fig. 6.38b). The mudslide flow nearshore subaqueous fan in the southern area has large range of development, and the mud content is high. The debris flow nearshore subaqueous fan in the central area was the favorable reservoir in this period, and mainly developed in well Xing 8 and Xing 9 areas. The fault-trough gravity flow in the northern area distribute along the Daxing fault with EN-WS strike. During the sedimentary period of the middle Es³, the conglomerate inherited the characteristics in the lower Es³, but the development range of the conglomerate was reduced (Fig. 6.38a).

## 6.6  Reservoir and Oil-Gas

### 6.6.1  Controls of Gravels on Reservoir

1. Relationship between gravels and conglomerate reservoir

On a microscopic scale, areal porosity in different gravels presents obvious differences, based on petrographic thin-sections analysis. In general, areal porosity in dolomite gravels is higher than that in limestone gravels (Fig. 6.39). The areal porosity of dolomite gravels is generally greater than 10%, and voids in dolomite gravels include solution caves, intergranular pores, intercrystal pores, intergranular dissolved pores, intragranular dissolved pores and intercrystal dissolved pores. The areal porosity of limestone gravels is generally less than 10%, and void spaces in limestone gravels include intergranular pore, intergranular dissolved pores, intragranular dissolved pores and a few solution caves and intercrystal pores.
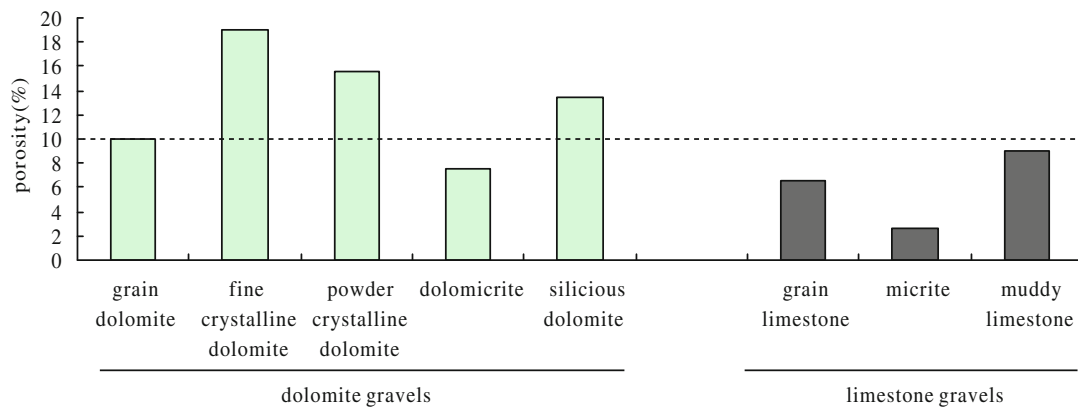
**Fig. 6.39** Histogram of areal porosities of different gravels in the Daxing conglomerate in the Langgu sag (modified from Liu et al. 2012b)

**Fig. 6.40** Histograms of porosity and permeability of dolomite conglomerates and limestone conglomerates in the Daxing conglomerate in the Langgu sag. **a** and **b** Dolomite conglomerates; **c** and **d** Limestone conglomerates (from Liu et al. 2012b)
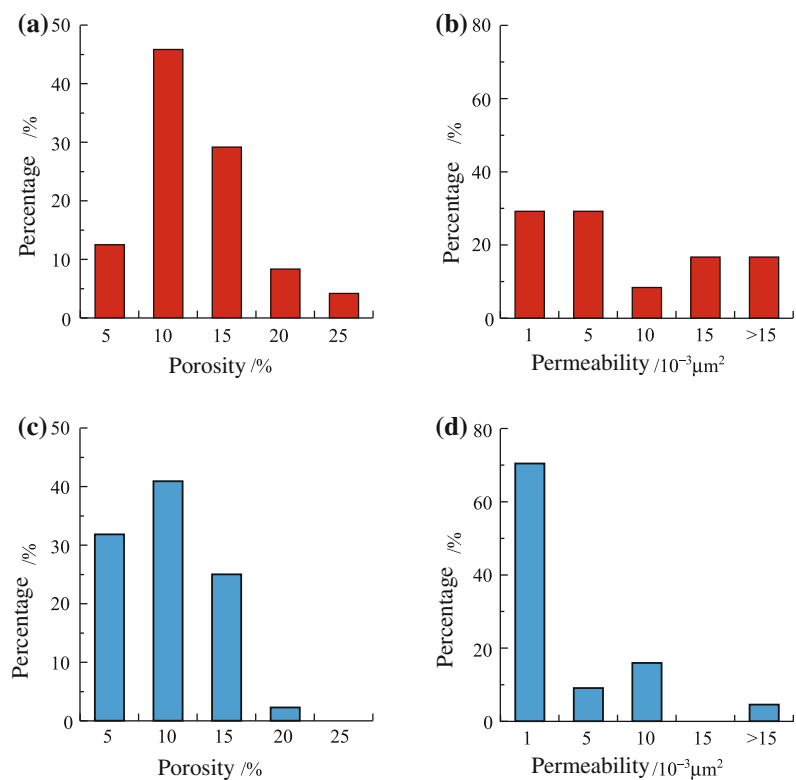


On a macroscopic scale, the differences between gravels result in different poroperm characteristics among the dolomite and limestone conglomerates. The porosity of dolomite conglomerates is usually 5–15%, and the permeability is greater than $1 \times 10^{-3}$ $\mu m^2$. The porosity of limestone conglomerates is usually less than 10%, and the permeability is usually less than $1 \times 10^{-3}$ $\mu m^2$ (Fig. 6.40). Thus, the physical reservoir properties of dolomite conglomerates are obviously better than that of limestone conglomerates.

Gravel composition controls the porosity and permeability of conglomerate reservoirs and consequently controls the HC productivity of conglomerates. Based on the analysis of the relationship between gravel composition and the productivity of oil and gas (data come from well test data, 1000 $m^3$ natural gas ≈ 1 t crude oil), the productivity of oil and gas is positively correlated with the dolomite gravel content and negatively with the limestone gravel content (Fig. 6.41). In other words, the HC productivity of dolomite

**Fig. 6.41** Relationship between gravels and productivity of oil and gas in the Daxing conglomerate (from Liu et al. 2012b)



(a)

(b)
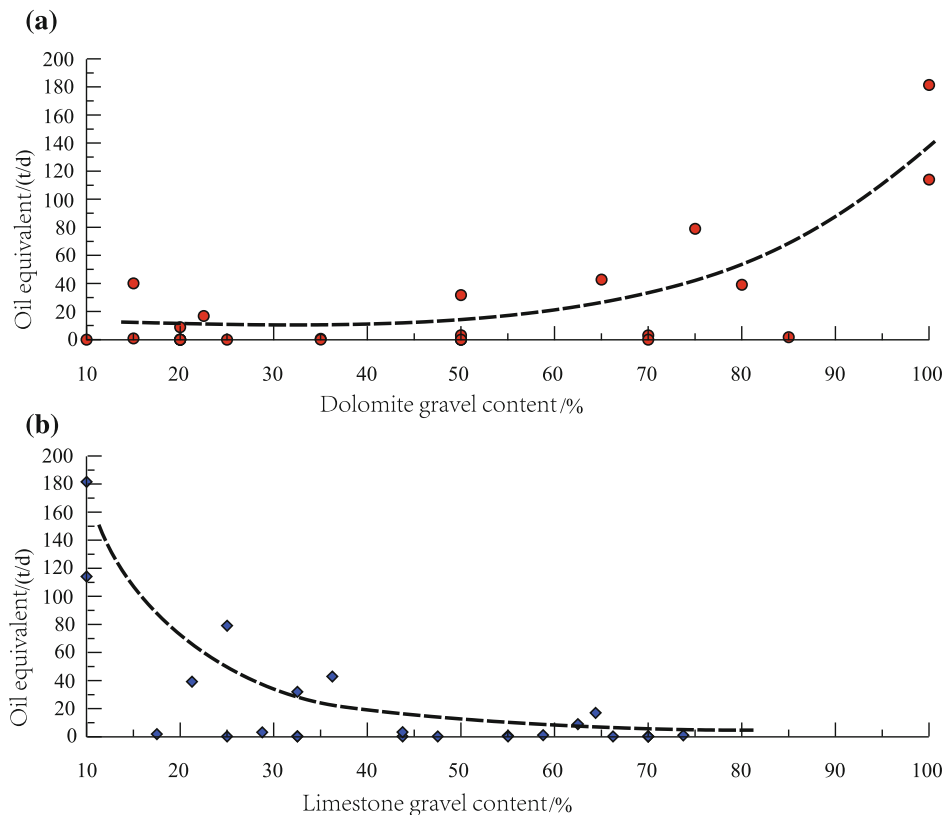
conglomerates is better than those of limestone conglomerates. This observation is strengthened by previous exploration practices.

Through the above analysis, the areal porosity in dolomite gravels is higher than that in limestone gravels on a microscopic scale; moreover, the porosity, permeability and HC productivity of dolomite conglomerates are better than those of limestone conglomerates on a macroscopic scale.
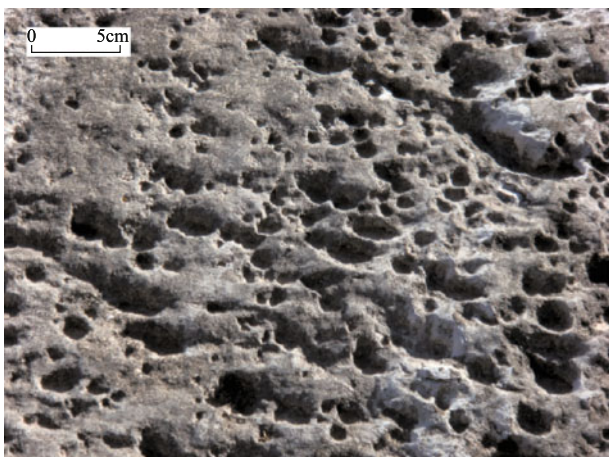


**Fig. 6.42** Dissolved pores in siliceous dolomites of Jixian system (Beijing Yanqing)

Thus, gravel composition plays a key role in determining porosity, permeability and HC productivity of conglomerates.

2. Mechanisms of gravels controlling on reservoir properties

In this section, mechanisms controlling reservoir properties of gravels are checked against two aspects of parent rocks and gravel properties.

Based on the analysis of the gravel compositions of conglomerates as well as lithology and fossil characteristics of basement rocks in the North China platform (Table 6.3), the parent rocks of the Daxing conglomerate mainly originate from lower Paleozoic and middle Proterozoic carbonates. Dolomite gravels are mainly from the middle Proterozoic Changcheng and Jixian Systems (Fig. 6.42), while limestone gravels are usually from lower Paleozoic Cambrian and Ordovician formations.

As with the parent rocks of the Daxing conglomerate, the reservoir properties of lower Paleozoic and middle Proterozoic carbonate rocks are significantly different (Sun 1995; Xiao and Yang 1997). According to measurements, dolomite has higher porosity (Schmoker et al. 1985) and more easily forms high quality reservoirs for oil and gas in Paleozoic and older strata (Ma et al. 2007; Zhu et al. 2009). For example,

oil and gas reserves in dolomite reservoirs account for 80% of recoverable reserves of carbonate reservoirs in North America (Zenger et al. 1980). In China, the porosity of dolomite reservoirs is generally higher than that of limestone reservoirs, especially in the same formation (Liu et al. 2007). Therefore, dolomites have become the main oil and gas reservoirs of carbonate fields in China (such as the Tazhong oil field and Puguang gas field) (Ma et al. 2007; Zheng et al. 2007; Liu et al. 2008; Hu et al. 2009; Zhu et al. 2009). In addition, dolomites in the middle Proterozoic Jixian System developed abundant solution caves (Fig. 6.42) in outcrops in northern Beijing and they exhibit excellent porosity and permeability. This is consistent with the interpretation that dolomite gravels have better reservoir quality than limestone gravels in Paleozoic and older strata.

The gravel size of the Daxing conglomerate is large, ranging from 2 to 20 cm, and some big gravel can reach several dozen centimeters or even a few meters in size. These large gravels were buried rapidly (Zhang et al. 1998; Wang and Liu 2008), which was favorable for preserving the void spaces of the gravels. Combining these conditions with the analysis of reservoir characteristics of parent rocks in the preceding paragraph demonstrates the fact that the porosity and permeability of dolomite conglomerates are superior to those of limestone conglomerates.

In addition, the differences in grain structure, physical nature and dissolution velocity of gravels are significant factors which cause dolomite conglomerates to have a higher porosity and permeability than limestone conglomerates. Different gravel have different resistance to weathering. The siliceous dolomite and dolomite have strong resistant to weathering. Thus, it is easy to form large gravels and preserve lots of inherited porosity. At the same time, under the action of acidic fluid, the dissolution of different gravels at a certain temperature and pressure is also different.

Firstly, dolomites with a crystalline granular texture develop abundant intercrystal micropores in the process of dolomitization and recrystallization. Furthermore, with crystalline grains growing, intercrystal micropores form increasingly. Intercrystal pores, bug holes and fissures associated with dolomites constitute important pore systems of carbonate oil and gas fields in the world (Roehl and Choquette 1985; Liu et al. 2008; Sheng et al. 2009). Moreover, siliceous components in dolomites are also favorable for developing dolomite reservoirs (Liu et al. 2008). Thus, dolomites more easily develop reservoirs than limestone dominated by micritic texture (Huang and Song 1997; Zhang et al. 2009). Dolomite gravels with a crystalline granular texture account for 75% of dolomite gravels in the Daxing conglomerate, and siliceous dolomite gravels
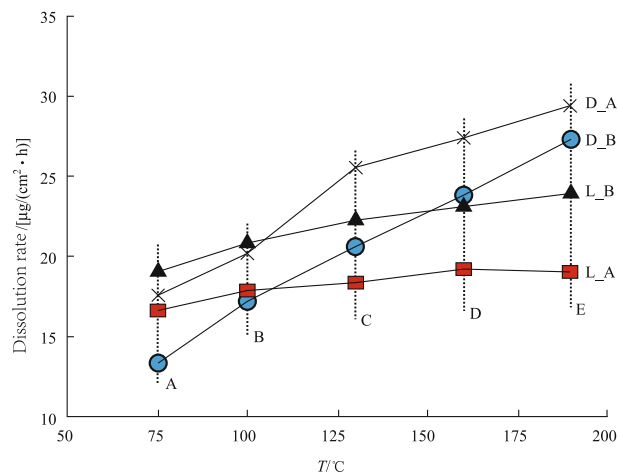


**Fig. 6.43** Dissolution velocities of carbonate samples (modified from Cui et al. 2007). A. 75 °C, 20 MPa, B. 100 °C, 25 MPa, C. 130 °C, 30 MPa, D. 160 °C, 35 MPa, E. 190 °C, 40 MPa; L_A. Dolomitic limestone; L_B. Micrite; D_A. Limy dolomite; D_B. Powder crystalline dolomite

account for 20%. Micrite and muddy limestone gravels account for 70% of limestone gravels. Therefore, reservoirs of dolomite conglomerates have better overall porosity, permeability and HC productivity than limestone conglomerates.

Secondly, laboratory experiments and field observations have demonstrated: (1) dolomite resists better to mechanical and chemical compaction and cementation (Schmoker and Halley 1982). Therefore, the porosity of dolomite does not decrease as rapidly with increasing depth as the porosity of limestone (Sun 1995). (2) Dolomite has a higher ultimate strength and smaller rock compressibility compared with limestone under the same conditions (Handin et al. 1963; Hugman and Friedman 1979; Stearns and Friedman 1972). Therefore, dolomite gravels are much more likely to generate fissures than limestone gravels (Sun 1995; Xiao and Yang 1997). In addition, due to the mechanical strength of dolomite, which keeps fissures open, fissures in dolomite gravels are more likely to be effective permeability channels than those in limestone gravels (Hugman and Friedman 1979). Therefore dolomites have better physical reservoir properties than limestones as depth increases (Schmoker et al. 1985). Furthermore, due to the differences in gravel properties, dolomite conglomerates develop more effective fissures and pores and have a higher porosity and permeability than limestone conglomerates in the Daxing conglomerate.

Finally, in terms of dissolution characteristics (Fig. 6.43), although the initial dissolution velocity of dolomite is only
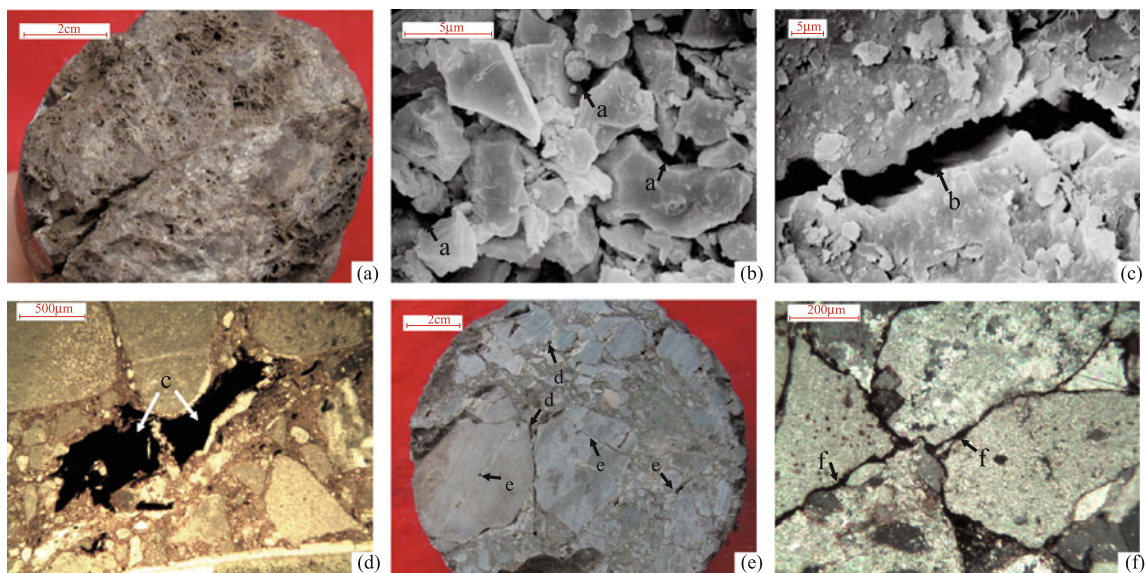
**Fig. 6.44** Reservoir space of the Daxing conglomerate (modified from Liu et al. 2012a). **a** Honeycomb dissolution pores in siliceous dolomite gravel, Wells Xing 9-9X, 4093.4 m; **b** intercrystalline pores in dolomite gravel (a), Well Xing 801, 3410.8 m; **c** open cracks in dolomite gravel (b), Well Xing 4, 3648.02 m; **d** intergranular dissolution pores in edgewise limestone grave (c), Well Tong 35, 2714.75 m; **e** pores (d) and fractures (e) dissolved by limy cements between gravels, Well Tong 43, 2876.35 m; **f** intergranular dissolved fissures in limestone gravels (f), Well Gu 15, 3902.21 m

1/60 up to 1/3 of that of limestone under surface conditions (Liu et al. 2006), the dissolution velocity of dolomite can generally exceed that of limestone under subsurface conditions with increasing temperature and formation pressure (Yang et al. 1995a, b; Xiao 1997; Zhu et al. 2003a; Jiang et al. 2008) (Fig. 6.43). Thus, dissolved secondary pores in dolomites are better developed than those in limestones (Zhu et al. 2003a; Cui et al. 2007; Xu et al. 2008). Moreover, limestone is dominated by differential dissolution, and dolomite is dominated by homogeneous dissolution (Liu et al. 2006). As a result, secondary pores and fissures and HC are distributed more uniformly in dolomites. For the Daxing conglomerate, burial depth is generally more than 3000 m, the subsurface temperatures are usually greater than 110 °C (Zhu et al. 2003a), the formation pressure is between 12 and 18 MPa, and the compaction coefficient is between 1.0 and 1.4 (Wang and Liu 2008). Therefore, under conditions of high temperature and high pressure in the deeply buried conglomerates, dolomite gravels have a higher dissolution velocity than limestone gravels, resulting in higher porosities and permeabilities compared with limestone conglomerates.

### 6.6.2 Controls of Conglomerate Genetic Types on Hydrocarbons

The genetic types of glutenite have obvious control effect on hydrocarbon accumulation, distribution, and production capacity, and the conglomerate reservoir is no exception. The controls of the Daxing conglomerate genesis type on oil and gas manifested as controlling on the storage space and pore permeability characteristics at the micro-level and controlling on oil and gas production capacity at the macro-level.

**Table 6.4** Porosity and permeability characteristics of conglomerate reservoirs in different genetic types

| Genetic types | Porosity (%) | | | | Permeability ($\times 10^{-3}$ μm$^2$) | | | |
|---|---|---|---|---|---|---|---|---|
| | Range | Ordinary | Average | Sample number | Range | Ordinary | Average | Sample number |
| Debris flow nearshore subaqueous fan | 0.8–24.8 | 5–9 | 6.93 | 68 | 0.1–131.7 | 6–14 | 11.16 | 20 |
| Fault-trough gravity flow | 0.6–16.5 | 3–7 | 5.83 | 48 | 0.1–47.2 | 3–6 | 4.99 | 30 |
| Mudslides nearshore subaqueous fan | 0.8–11.95 | 2–6 | 4.99 | 15 | 0.1–9.8 | 1–3 | 2.5 | 8 |

**Fig. 6.45** Daily average oil and gas production of single well in different conglomerate bodies (modified from Liu et al. 2012a)
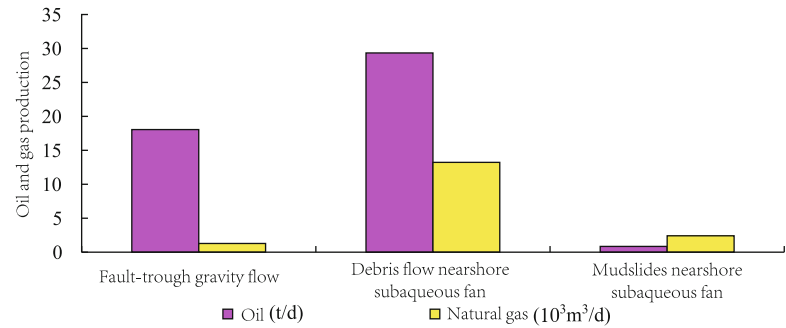


## 1. Reservoir characteristics

The reservoir body of the debris flow nearshore subaqueous fan is mainly braided channels of the middle fan, which are dominated by grain-supported fine conglomerate composed of dolomite and siliceous dolomite gravels. Storage space is made up of dissolution pores in gravels, intercrystal pores and fissure (Fig. 6.44a–c). On the one hand, dolomite gravels inherit abundant dissolved pores from parent rocks (Fig. 6.44a) and are buried immediately after deposition in deep lake, thus the reservoir space in dolomite gravels are preserved. On the other hand, grain-supported and lime-cemented conglomerate dominated by dolomite gravels are favorable for development of secondary pores and fissures in the deep buried diagenetic stage. Therefore, reservoirs of the debris flow type nearshore subaqueous fan develop abundant reservoir spaces, and have better physical properties. Porosity is generally 5–9%, with an average of 6.93%. The permeability is generally from $6 \times 10^{-3}$ to $14 \times 10^{-3}$ $\mu m^2$, with an average of $11.16 \times 10^{-3}$ $\mu m^2$ (Table 6.4).

The reservoir of fault-trough gravity flow conglomerate body is mainly channel conglomerate characterized by medium-fine conglomerates composed of limestone gravels and some dolomite gravels. The rock type has both the grain-supported and lime cemented conglomerates and matrix-supported and muddy interstitial conglomerates. The storage space of this conglomerate is dominated by secondary pores and some dissolved fissures formed by dissolution of components in carbonate gravels and limy cements between gravels (Fig. 6.44d, e). There are also some cracks (Fig. 6.44e). On the one hand, compared with dolomite gravels, limestone gravels are not favorable for preservation of primary pores and development of dissolved pores and fissures in deep buried condition; On the other hand, higher argillaceous sediments result in poor development of pores and fissures. Therefore, the reservoir properties are medium. The porosity is generally 3–7%, with an average of 5.83%. The permeability is generally $3 \times 10^{-3}$ to $6 \times 10^{-3}$ $\mu m^2$, with an average of $4.99 \times 10^{-3}$ $\mu m^2$ (Table 6.4).

The reservoir of mudslides nearshore subaqueous fan conglomerate body is mainly braided channel in middle fan, which is characterized by matrix-supported medium-fine conglomerates composed of limestone, dolomite, some clastic rock gravels, with relatively high content of argillaceous sediments. Storage space is mainly inner-gravel dissolved pores (Fig. 6.44f), with few intercrystal pores developed, whereas inter-gravel pores and fissures do not develop well. Reservoir physical properties are relatively poor. Reservoir porosity is generally 2–6%, with an average of 4.99%. The permeability is generally $1 \times 10^{-3}$ to $3 \times 10^{-3}$ $\mu m^2$, with an average of $2.5 \times 10^{-3}$ $\mu m^2$ (Table 6.4).

## 2. Oil and gas production capacity

The conditions for forming oil and gas reservoirs in the Daxing conglomerate are very favorable. The conglomerate is surrounded by a large set of dark mudstone of $Es^3$. Large sets of dark mudstone can acted as source rocks and also favorable caps. Thick mudstone with a depth of more than 3900 m has entered the wet gas stage. The produced oil and gas gets directly into the conglomerate reservoir, forming oil and gas reservoirs. Therefore, due to the microscopic difference of the conglomerate reservoirs, different conglomerates have different production capacity at the macro level. According to the prospecting oil data of different types of conglomerate in the exploration stage, the oil and gas production capacities of different conglomerate bodies were analyzed. The average daily oil and gas production of single well in the channel reservoir of the fault-trough gravity flow is 18.06 t and $1.27 \times 10^3$ $m^3$ respectively. The average daily oil and gas of single well in the braided channel reservoir of the debris flow nearshore subaqueous fan is 29.34 t and $13.22 \times 10^3$ $m^3$ respectively. The average daily oil and gas of the single well in the braided channel reservoir of the mudslides nearshore subaqueous fan is 0.84 t and $2.41 \times 10^3$ $m^3$ respectively (Fig. 6.45).

It can be seen that the physical properties and oil and gas production capacity of the debris flow nearshore subaqueous fan are obvious better than those of the other two types of conglomerate bodies, and that have been confirmed by exploration practice.

# References

Cui ZA, Bao ZTY, Zhang TF et al (2007) Experimental study on dissolution kinetics of carbonate rocks under burial conditions. J Oil Gas Technol 29(3):204–207

Davies RJ, Posamentier HW, Wood LJ et al (2007) Seismic geomorphology: applications to hydrocarbon exploration and production. The Geological Society, London

Deng HW, Wang HL, Wang DZ (2001) Palaeo-geomorphology: control of sequence filling characteristics of terrestrial rift basin—a case study of lower tertiary in west slope area of Bozhong depression. Pet Nat Gas Geol 22(4):293–296

Dong GC, Sun JM, Zhang SP et al (2002) The characteristics of the Paleogene sequence stratigraphy and the law of oil and gas reservoir in Langgu depression are discussed. Chin Geol 29(4):397–400

Gao HJ (2004) Study on the standard of interpretation of gas reservoirs in Langgu depression. Master's Degree Thesis, Southwest Petroleum Institute, Chengdu, Sichuan

Handin J, Hagar RV, Friedman GM et al (1963) Experimental deformation of sedimentary rocks under confining pressure: pore pressure tests. AAPG Bull 47:717–755

Hu MY, Cai XY, Hu ZG et al (2009) Study on deep burial dissolution of Ordovician carbonate in Tazhong area. J Oil Gas Sci 31(6):49–54

Huang SY, Song HR (1997) Deep karstification of oil and gas reservoirs. China Karst 16(3):189–198

Hugman RHH, Friedman GM (1979) Effects of texture and composition on mechanical behaviour of experimentally deformed carbonate rocks. AAPG Bull 63:1478–1489

Jia DH, Xu CG, Yang B et al (2007) The restoration and evolution of the Paleogene palaeogeomorphology in the central and southern parts of the Liaodong Bay and its control of the sedimentary system. Paleogeography 9(2):155–166

Jiang ZX (2010) Sedimentology, 2nd edn. Petroleum Industry Press, Beijing, pp 112–113

Jiang ZX, Chen DZ, Qiu LW et al (2007) Source-controlled carbonates in a small Eocene half-graben lake basin (Shulu Sag) in central Hebei Province, North China. Sedimentology 54:265–292

Jiang XQ, Wang SY, Fan M et al (2008) Experimental study on dissolution of carbonate rocks in buried diagenetic environment. Oil Exp Geol 30(6):643–646

Jin FM, Fu H, Li ZD et al (2006) The Paleogene sequence stratigraphy and subtle reservoirs exploration in the Ganggu depression, Jizhong depression. Miner Rocks 26(4):75–82

Liu ZH, Dreybrodt W, Li HJ (2006) Limestone and dolomite dissolution rate control mechanism of the Earth Science. J China Univ Geosci 31(3):411–416

Liu RB, Tian JC, Huang Y et al (2007) Characteristics of limestone reservoirs of Sinian Dengying formation and limestone of Silurian Shiniulan formation in southern Sichuan. J Chengdu Univ Technol (Nat Sci Ed) 34(3):245–250

Liu YF, Yin J, Sun XW et al (2008) Cambrian depositional characteristics and high quality dolomite reservoirs in the eastern Tarim basin. Nat Gas Geosci 19(1):126–132

Liu H, Jiang ZX, Zhang RF et al (2012a) The type of Daxing conglomerate in Langgu depression and its control of oil and gas. Oil Explor Dev 39(5):545–551

Liu H, Jiang ZX, Zhang RF et al (2012b) Gravels in the Daxing conglomerate and their effect on reservoirs in the Oligocene Langgu Depression of the Bohai Bay Basin, North China. Mar Pet Geol 29:192–203

Lu HB, Fulthorpe CS, Mann P et al (2005) Miocene-Recent tectonic and climatic controls on sediment supply and sequence stratigraphy: Canterbury basin, New Zealand. Basin Res 17:311–328

Ma YS, Guo TL, Zhao XF et al (2007) The formation mechanism of deep high-quality dolomite reservoirs in Puguang gas field. Chin Sci Ser D 37(Suppl 2):43–52

North China Oilfield geological record preparation group (1988) China petroleum geology records, vol V. Petroleum Industry Press, Beijing, pp 93–96

Perrier R, Quilbier J (1974) Thickness changes in sedimentary layers during compaction history. AAPG Bull 58:507–520

Qi JF, Yang Q (2001) Discussion on the method of decompression correction of clastic rock layer—and discussing the compaction correction method proposed by Li Shaohu, etc. Pet Exp Geol 23 (3):351–356

Roehl PO, Choquette PW (1985) Introduction. In: Roehl PO, Choquette PW (ed) Carbonate petroleum reservoirs. Springer, New York, pp 1–15

Schmoker JW, Halley RB (1982) Carbonate porosity versus depth: a predictable relation for south Florida. AAPG Bull 66:2561–2570

Schmoker JW, Krystinik KB, Halley RB (1985) Selected characteristics of limestone and dolomite reservoirs in the United States. AAPG Bull 69:733–741

Sheng XC, Guo ZF, Liu XM (2009) Characteristics of the Upper Cambrian dolomite reservoir in the Xingshan Area of the Qinling-Dabie Orogenic belt. Pet Geol 31(2):172–176

Song RC, Zhang XN, Dong SY et al (2006) Analysis on controlling factors of paleogene gravel and rock mass in steep slope of Tonggu depression. J Chengdu Univ Technol (Nat Sci Ed) 33(6):587–592

Song RC, Zhang XN, Dong SY et al (2007) The sequence stratigraphy of non-compensated continental rift basins—taking Paleogene in Langgu depression as an example. J Stratigr 31(3):254–260

Stearns DW, Friedman GM (1972) Reservoirs in fractured rock. In: King RE (ed) Stratigraphic oil and gas fields—classification, exploration methods, and case histories, vol 16. AAPG Memoir, pp 82–106

Sun SQ (1995) Dolomite reservoirs: porosity evolution and reservoir characteristics. AAPG Bull 79(2):186–204

Wang ZH, Liu GD (2008) Relationship between abnormal high pressure and hydrocarbon accumulation in Langgu depression. Nat Gas Ind 28(6):69–72

Wang JH, Wang H, Zhao ZX et al (2003) Application of sequence stratigraphy to palaeogeomorphology—taking Tahe oil field as an example. Earth Sci - J China Univ Geol 28(4):421–430

Wu CJ (1986) Lake basin type. J Sediment Sci 4(4):1–27

Xiao LP (1997) The thermodynamics model and the geological exploration direction of the dissolution of carbonate rocks in burial conditions are as follows: the fifth section of the Lower Ordovician Majiagou Formation in the shan-gan-ning basin. Lithofacies Palaeogeography 17(4):57–72

Xiao DM, Yang YF (1997) Dolomite reservoirs: porosity evolution and reservoir characteristics. Foreign Oil Gas Explor 2:139–152

Xu WS, Zhao PR, Nei PF et al (2008) Study on porosity-permeability relationship of limestone and dolomite reservoirs. Oil Gas Geol 29 (6):806–811

Yang JX (2004) Formation mechanism and identification of low resistivity oil and gas reservoir in. Master degree thesis, Northwest University, Xi'an

Yang JJ, Huang SJ, Zhang WZ et al (1995a) The experimental simulation of the different diagenetic processes of carbonate rocks under different temperature and pressure conditions. J Sediment Sci 13(4):49–54

Yang JJ, Huang SJ, Zhang WZ et al (1995b) The experimental simulation of the dissolution process of dolomite under the temperature and pressure conditions of buried diagenesis. J Sediment Sci 13(3):83–88

Zenger DH, Dunham JB, Ethington RL (1980) Concepts and models of dolomitization. SEPM Spec Publ 28:320–328

Zhang ST, Wang F, Huang HH (1998) The formation conditions of Daxing conglomerate oil and gas reservoirs in the west of Langgu depression. J Xi'an Pet Inst 13(4):31–33

Zhang SP, Teng JB, Wang WQ et al (2009) The diagenetic difference and reservoir control factors of the deep sandy conglomerate in Shengli Oilfield. Oil Gas Geol Recov 16(6):12–16

Zhao HG, Liu CY (2003) Detachment and detachment structure. J Northwest Univ (Nat Sci Ed) 33(3):315–319

Zhao JX, Chen HD, Xiang F (2003) Application of high-resolution sequence stratigraphy method in restoration of paleo-topography before deposition. J Chengdu Univ Technol (Nat Sci Ed) 76–81

Zheng JG, Li ZD, Fu H et al (2006) The main controlling factors of strata development in the Paleogene continental fault depression basin in Langgu depression are studied. J Chengdu Univ Technol (Nat Sci Ed) 33(3):240–245

Zheng HR, Wu MB, Wu XW et al (2007) Oil and gas exploration prospect of the Lower Paleozoic dolomite reservoir in Tarim Basin. J Pet Sci 28(2):1–8

Zhu QZ, Li CH, Yang HY (2003a) The relationship between diagenesis and reservoir porosity of the deep conglomerate reservoir in the third member of Shahejie Formation in Langgu depression. Spec Oil Gas Reservoirs 10(3):15–17

Zhu QZ, Li CH, Yang HY (2003b) The formation of Daxing conglomerate in the Langgu depression and hydrocarbon accumulation. Oil Explor Dev 30(4):34–36

Zhu JF, Yu BS, Fan TL et al (2009) Influence of sedimentary diagenetic environment on dolomite reservoirs. Xinjiang Geol 27(1):43–48

# A Source-to-Sink Study of the Paleogene Shulu Sag: Characteristics and Depositional Dynamics of Its Deposits

## 7.1 Geological Background

### 7.1.1 Overview

The Shulu Sag is in the southwestern part of the Jizhong Depression in the Bohai Bay Basin, eastern China (Fig. 7.1a). It is a northeast-southwest trending half-graben basin with the major bounding fault dipping west. The Sag is bounded by the Xinhe fault to the southwest, the Ningjin uplift to the west, and the Hengshui fault to the north, through which it is connected to the Shenxian Sag (Jiang et al. 2007; Liang et al. 2007). Shulu Sag is about 40 km long and 14–18 km wide (Fig. 7.1b), with an exploration area of ca. 700 km$^2$.

The mid-Jurassic to late-Cretaceous Yanshanian Orogeny created three nearly east-trending faults within the Sag, namely, the Hengshui fault, the Taijiazhuang fault, and the Jingqiu fault. The orogeny also formed the Jingqiu and Taijiazhuang paleo-highs, which divide the Sag into three subbasins from north to the south (Jiang et al. 2007; Zhao et al. 2014). Each subbasin further consists of the gentle slope, the slope break, the depression, and the steep slope from west to the east. Altogether, the Shulu Sag is characterized by different subbasins from north to the south, and various topographic zones from west to east (Liang et al. 2007). This paper will focus on the mid- and southern subbasins, both of which lie in proximity to the Che City.

The basement of the Shulu Sag is composed of Archean and Proterozoic metamorphic rocks, Cambrian-Ordovician carbonate rocks, and the Carboniferous-Permian marine carbonaceous siliciclastics from bottom to top, which is directly overlain by Paleogene lacustrine basin fill (Fig. 7.2) (Zhao et al. 2014). The Shulu Sag mainly consist of five depositional successions from bottom to top: the Shahejie Formation, the Dongying Formation, the Guantao Formation, the Minghuazheng Formation and the Pingyuan Formation. The Shahejie Formation here comprises three members: the upper Shahejie Member (Es$_1$), the middle Shahejie Member (Es$_2$), and the lower Shahejie Member

(Es$_3$). The lower member (Es$_3$) can be further divided into upper, middle and lower three submembers based on their lithological characteristics. The lithology of the upper Es$_3$ submember is mainly dark gray mudstones, and sandstone interbeds (Jiang et al. 2007), and the middle Es$_3$ submember consist of calcilutites and shales. The lower Es$_3$ submember, which consists of carbonate conglomerates and calcilutites, is the primary focus of this study. The thickest part of the lower submember is ca. 1200 m. The main sources of the Paleogene deposits are the Paleozoic carbonates, and pre-Cambrian rocks in the eastern, southern and northern parts of the basin. The sediments are transported into the basin in the form of bed loads, suspension loads or dissolved solids (Gierlowski-Kordesch 1998, 2010).

### 7.1.2 Regional Tectonic Features

#### 7.1.2.1 Two Fault Systems

Wang (2014) suggests that the Shulu Sag has undergone two phases of tectonic activity and developed two different types of faults in the early and late phases: basement-involved faults and caprock-detachment faults.

The basement-involved faults started forming simultaneously with the formation of the lake basin and continued until the deposition of the middle Es$_3$ submember. The system is characterized by extensional faults, and the largest throw of the main boundary fault is 200–500 m, exerting an important control on the paleogeography and deposition of the lower Es$_3$ submember.

There are four main basement-involved faults in Shulu Sag: Xinhe fault, Taijiazhuang fault, Jingqiu fault and Xicaogu fault (Fig. 7.3). The northeast-trending boundary fault, the Xinhe fault, lies on the eastern side of the basin and played a major role in the evolution of the basin. The northwest-trending Taijiazhuang fault is in the north of the basin and has a throw of 200–300 m. The Jingqiu fault lies on the southern flank of the basin and comprises two smaller faults. The northern one is trending northeast with a

**Fig. 7.1** Location of the study area within the Bohai Bay Basin (**a**), and structural map of the Shulu Sag (**b**) (modified after Jiang et al. 2007). I. Jizhong Depression; II. Huanghua Depression; III. Jiyang Depression; IV. Bozhong Depression; V. Liaohe Depression; VI. Dongpu Depression

maximum throw of 700 m; the southern fault is oriented northwest with a maximum throw of 500 m. The Xicaogu fault is on the west side of the basin and is oriented northeast. These fault activities resulted in two subsidence centers separated by the southern Jingqiu fault.

The activities of the detachment faults began at the end of the deposition of the third member of Shahejie Formation, and the intensity of the fault activity peaked till the deposition of the first member of Shahejie Formation. Two sets of faults can be recognized based on their trends: the NNE-trending fault located in the Xicaogu area on the slope, and the NW-strike fault located in the Taijiazhuang and

Jingqiu areas. The throws of these faults are typically smaller than 200 m. The faults are characterized by steeper dips in shallow parts, and subordinate faults are well developed.

### 7.1.2.2  Structural Pattern

The Shulu Sag is a half-graben basin with its boundary fault dipping west. The Taijiazhuang and Jingqiu paleo-highs divided the Shulu Sag into three relatively independent depositional centers in the north-south direction, and this study will focus on the middle subbasin. Each subbasin further consists of the gentle slope, the slope break, the depression, and the steep slope from west to the east (Fig. 7.4).
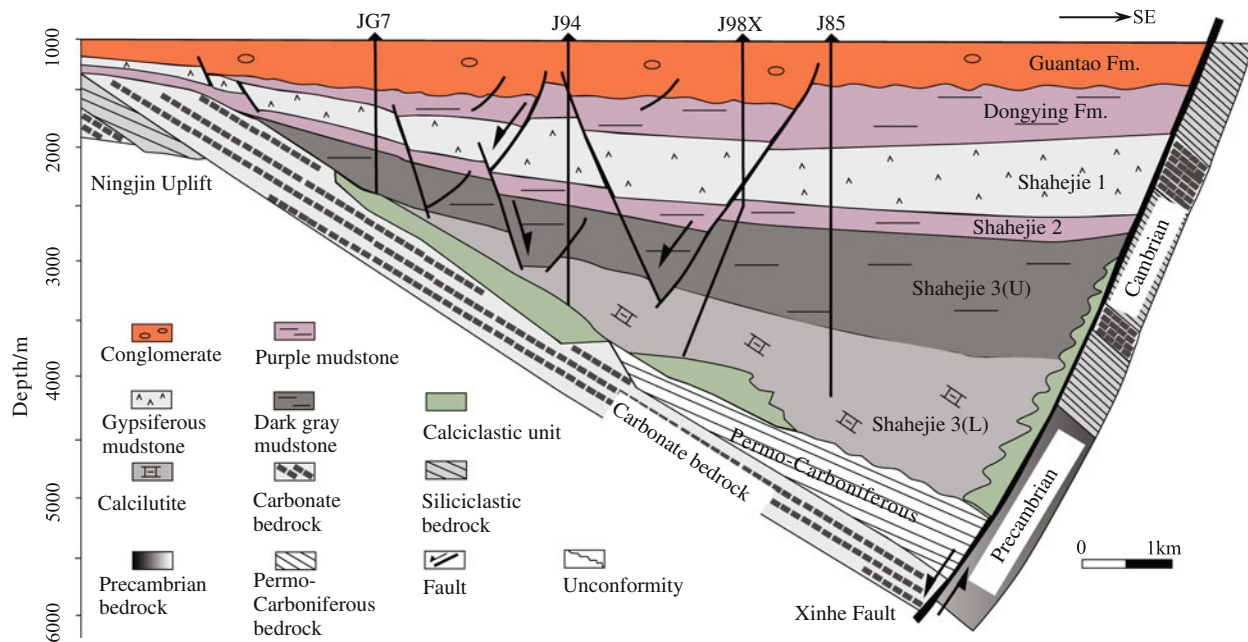
**Fig. 7.2** Schematic diagram of the stratigraphy of Shulu Sag (Modified from Zhao et al. 2014)

### 7.1.3 Basin Evolution

The Shulu Sag was mainly formed in the Eocene, and the basin-forming process continued into Quaternary. The sag has undergone six different stages of evolution since the Indosinian and Yanshanian Orogeny (Yang 2010; Wang 2014; Kong et al. 2005; Li 2015b):

(1) Initial faulting stage (Eocene Kongdian Formation)

Most parts of Bohai Bay basin underwent mantle thermal anomalies in late Cretaceous, which resulted in the uplift of the lithosphere. The Ningjin and the Xinhe uplifts began to raise, and the rock formations were tilted to the east. The primitive pattern of the half-graben formed in early Paleogene and this stage was characterized by intense extensional fault activities and thick conglomerate deposits close to the Ningjin uplift.

(2) The juvenile half-graben stage ($Es_3^x$–$Es_3^z$)

The activities of the NNE-trending Xinhe fault started to intensify in early-middle $Es_3^x$–$Es_3^z$, with a growth index of 1.3–1.9 (Fig. 7.5). The Xinhe fault comprises several NNE-trending growth faults, each of them connecting to the rest with a relatively smaller throw. A series of strike-slip faults formed to adjust the height difference between the footwall and the hanging wall. During this stage, the rapid subsidence facilitated the formation of the lake basin and organic-rich source rocks, resulting in a deep lake basin and different topographic zones from west to east. The weathered products of the adjacent carbonate uplifts were transported by occasional river floods into the basin, forming fan deltas and subaqueous fans in the west and east sides respectively. The fan deltas mainly contain carbonate conglomerates and calcarenites while the subaqueous fans are characterized by carbonate breccia deposits.

(3) The mature half-graben stage ($Es_3^s$–$Es_2$)

From the deposition of the late third member to the second member of Shahejie Formation, the magnitude of tectonic activities gradually decreased, and the lacustrine was slowly uplifted. The fan-delta deposits were quite extensive, and the boundary fault still controlled the depositional thickness.

(4) The late half-graben stage ($Es_1^x$)

The basin has undergone slight uplift and denudation during this time, and a relatively short period of lake transgression followed when the Xinhe fault was active again. The sediments of the lower part of the $Es_1$ member were deposited during the transgression, characterized by sublacustrine facies such as gray shale and oil shale. The salinity of the lake basin also increased during this stage.

**Fig. 7.3** Simplified structural
map of the basement of Shulu
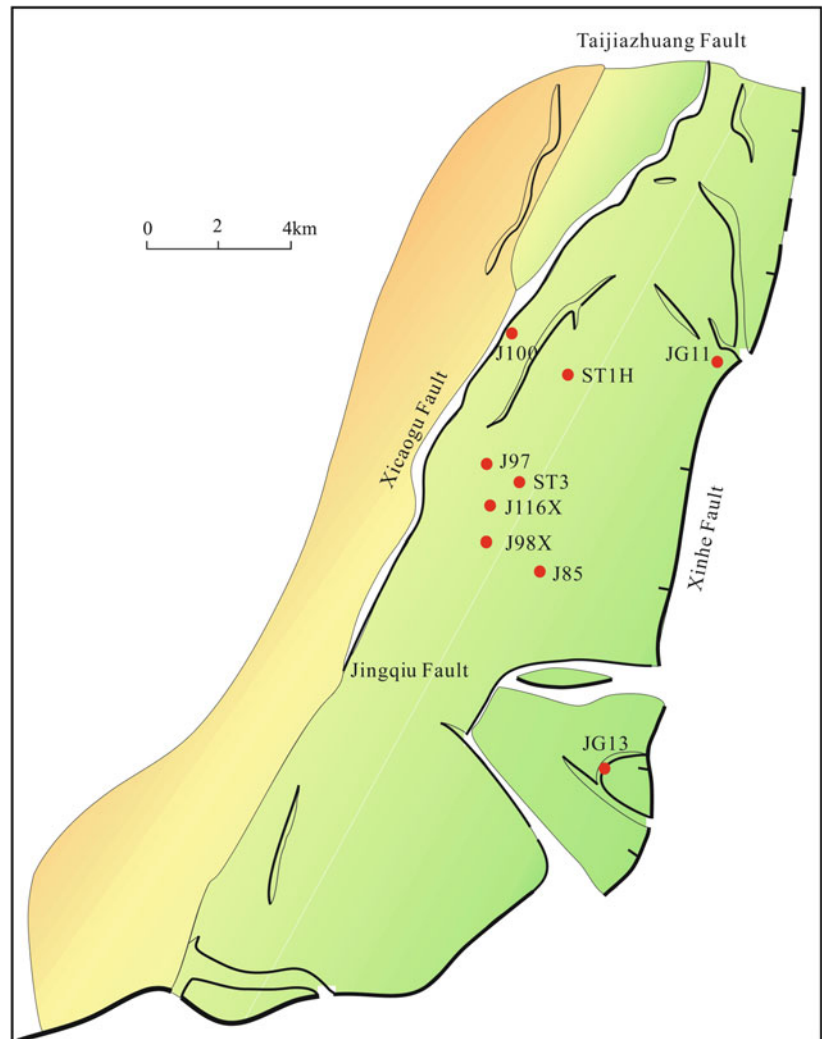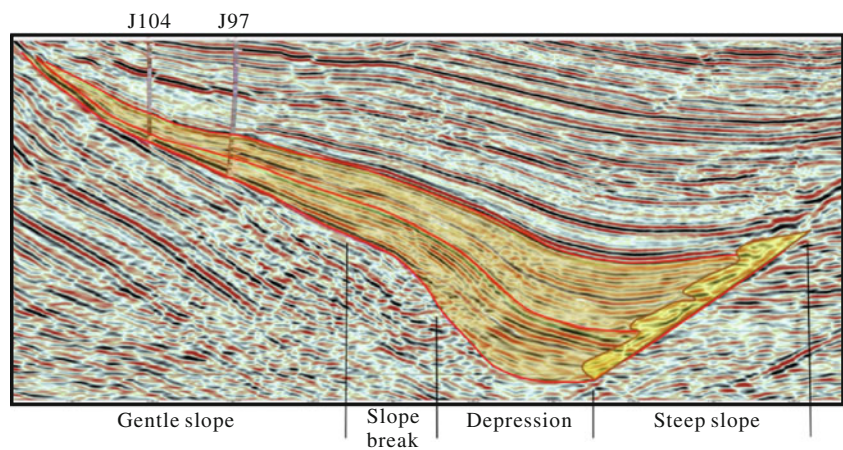Sag. Modified after North China
Oilfield Research Institute



**Fig. 7.4** Dip-oriented seismic
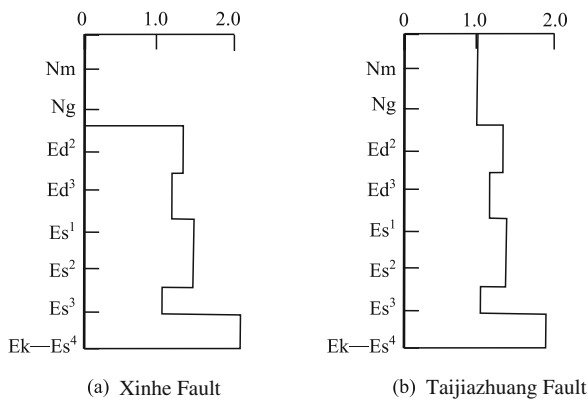profile of the middle subbasin of
Shulu Sag

(a) Xinhe Fault    (b) Taijiazhuang Fault

**Fig. 7.5** Growth index of the main faults in Shulu Sag (Kong et al. 2005). Nm: Minghuazheng formation; Ng: Guantao formation; $Ed_2$: second member of Dongying formation; $Ed_3$: third formation of Dongying formation; $Es_1$: first member of Shahejie formation; $Es_2$: second member of Shahejie formation; $Es_3$: third member of Shahejie formation; Ek—$Es_4$: Kongdian formation-fourth member of Shahejie formation

(5) The end of the half-graben basin ($Es_1{}^s$–$E^d$)

During this stage, the area was uplifting again, and the basin shrank. The Dongying Formation is mainly composed of a set of terrestrial red clastic rocks.

(6) Post-rift stage (Ng–Q)

The Xinhe fault became inactive since the deposition of Guantao Formation, and the rifting process ceased. The basin entered the stage where post-rift subsidence dominates. During this stage, the basin became flat and broad and evolved into fluvial environments, which became the plain landscape today.

### 7.1.4 Stratigraphy

The stratigraphy of the Shulu Sag consists of the basement rock and Paleogene lacustrine deposits. The basement is composed of the Archean and Proterozoic metamorphic rocks, the Cambrian-Ordovician carbonates, and the Carboniferous-Permian coal-bearing marine clastic rocks with the infrequent occurrence of marls. The Paleogene rocks onlapped on the basement, comprising of the Shahejie Formation, the Dongying Formation, the Guantao Formation, the Minghuazhen Formation, and the Pingyuan Formation from bottom to top. The Shahejie Formation can be further divided into three members from bottom to top: the third Shahejie member ($Es_3$), the second member ($Es_2$), and the first Shahejie member ($Es_1$). The $Es_3$ has a thickness range of 0–2200 m. The lower submember of the $Es_3$, which consists of carbonate conglomerates and calcilutites, is the

primary focus of this study. The upper submember of the $Es_3$ consists of black shale with interlayers of fine-grained sandstone. The $Es_2$ has a thickness range of 0–400 m. It is mainly composed of brown-magenta mudstone and light gray fine sandstone. The $Es_1$ lies unconformably above the $Es_2$ with a thickness range of 0–800 m. The $Es_1$ consists of gypsum rock, gypsum-bearing mudstone, brown mudstone and oil shale at the bottom, which passes into light gray fine sandstone, siltstone, and magenta mudstone towards the top.

### 7.1.5 Sequence Stratigraphy of the Lower $E_{s3}$ Submember

Li (2015a) uses the integration of 3D seismic data, well logging, mud logging, cores and geochemical analyses such as total organic carbon (TOC) to build the sequence stratigraphic framework of the lower $E_{s3}$ submember. Five third-order sequences are identified in the lower $E_{s3}$ submember in Shulu Sag from bottom to top, namely, the Sequence I (SQ1), Sequence II (SQ2), Sequence III (SQ3), Sequence IV (SQ4) and Sequence V (SQ5) (Fig. 7.6). This study will adopt the sequence stratigraphic framework.

The bathymetry of the lower $E_{s3}$ submember at the time of deposition shows four distinct zones: the gentle slope, the slope break, the depression, and the steep slope from west to the east (Fig. 7.6). The conglomerates are mainly found in the gentle slope area, the edge of the steep slope area, and the slope break zones of SQ I, II and III. The gentle slope zone is dominated by fan deltas or mass transport deposits resulting from earthquakes; the depression zone has occasional turbidites, and subaqueous fans dominate the steep slope.

## 7.2 Sedimentary Characteristics of the Lower $E_{s3}$ Submember

Based on the core data, thin sections and well logging data, we have: (1) proposed a new rock classification scheme; (2) analyzed the composition of the gravels; and (3) established the well-log criteria for different rock types.

### 7.2.1 Rock Classification Scheme

The main lithology of the lower $E_{s3}$ submember is carbonate. Three groups of rocks have been recognized based on core and thin section observation: calcirudite, calcarenite and calcilutite. The calcirudite can be divided into six categories based on the fabric of the rocks and sources of the clasts (Table 7.1): clast-supported extraformational calcirudite, matrix-supported extraformational calcirudite,
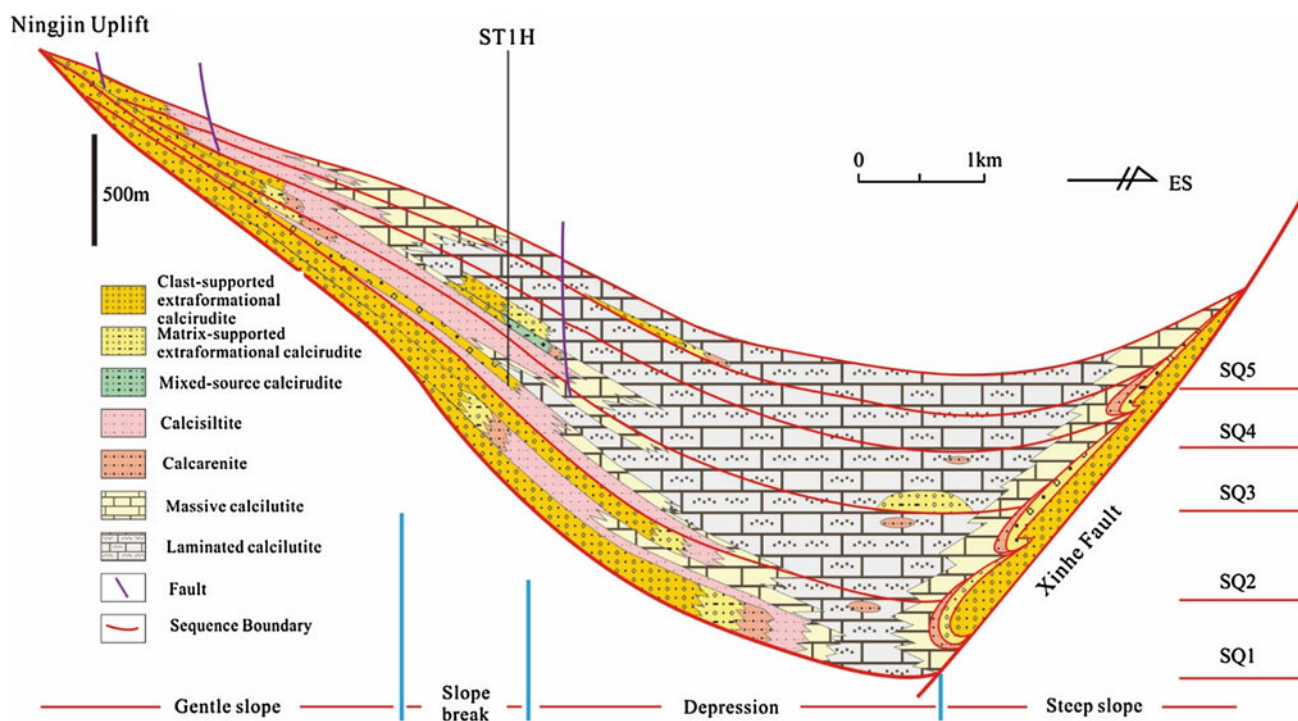
**Fig. 7.6**  Sequence stratigraphic framework of the middle subbasin in the Shulu Sag (modified after Zheng et al. 2015)

**Table 7.1**  Types of calcirudites

| Types | | Extraformational clasts (%) | Intraformational clasts (%) | Matrix |
|---|---|---|---|---|
| Clast-supported | Extraformational type | >75 | <25 | Sparse |
| | Mixed-source type | 50–75 | 25–50 | Sparse |
| | Intraformational type | <50 | >50 | Sparse |
| Matrix-supported | Extraformational type | >75 | <25 | Abundant |
| | Mixed-source type | 50–75 | 25–50 | Abundant |
| | Intraformational type | <50 | >50 | Abundant |

clast-supported mixed-source calcirudite, matrix-supported mixed-source calcirudite, clast-supported intraformational calcirudite, and matrix-supported intraformational calcirudite. The mixed-source intraformational calcirudite is rare in the study area. Calcilutites can be further divided into two types: massive and laminated. There are also interlayers of calcisiltite.

### 7.2.1.1  Clast-Supported Extraformational Calcirudites

In the clast-supported extraformational calcirudites, the percentage of the extraformational gravel-sized clasts is more than 75% of the total gravel content, and the intraformational clasts and matrix are relatively sparse. The cores are dark gray to light gray. The major grain contact types include point and line contacts. The clasts are typically subrounded to subangular, and the grain size of the gravel-sized clasts ranges from 2 mm to 80 cm. The calcirudites are poorly sorted (Fig. 7.7a), with a few showing better sorting (Fig. 7.7b). Most clast-supported extraformational calcirudites are massive or structureless (Fig. 7.7a, c), with some intervals being normally graded (Fig. 7.7b). There are various types of clasts, such as carbonate mudstone (Fig. 7.7d), microcrystalline dolostone, finely crystalline limestone and medium crystalline limestone. There are also a few clasts from previous limestone conglomerate, intraclastic packstone, peloid packstone, and bioclastic limestone. Most of the clasts originate from the carbonate
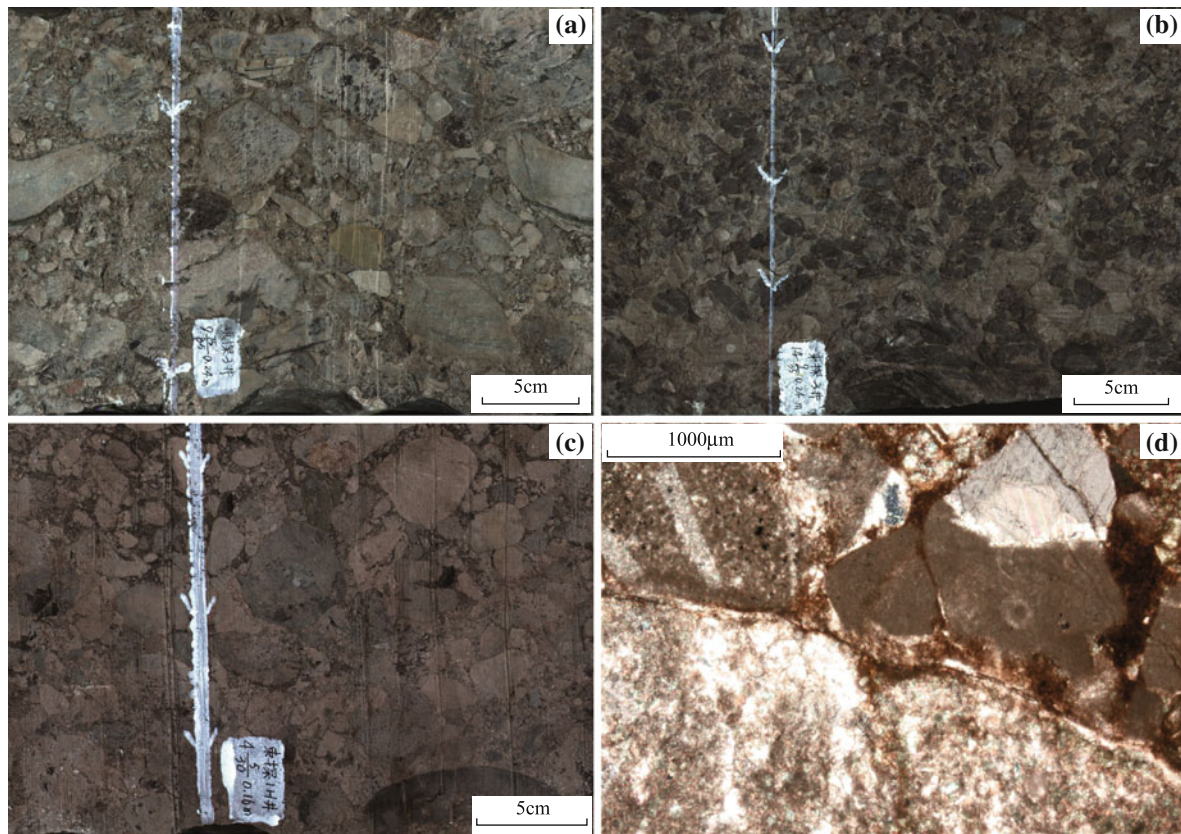
**Fig. 7.7** Clast-supported extraformational calcirudites. **a** Massive clast-supported extraformational calcirudite, Well ST3, core number $9\frac{75}{85}$; **b** normally graded clast-supported extraformational calcirudites; note the close contact between the light gray and dark gravel-sized clasts, Well ST3, core number $14\frac{9}{35}$; **c** massive clast-supported extraformational calcirudite, Well ST3, core number $4\frac{5}{30}$, 3965.25–3969.41 m; **d** note the close contact between different grains, Well ST3, 3969.35 m, cross-polarized light

mudstone and microcrystalline dolostone. The matrix is mainly micritic carbonate, and the cement is primarily calcite, with sparse clay minerals. The thickness of the single-layer matrix-supported extraformational calcirudites ranges from several meters to less than twenty meters.

### 7.2.1.2 Clast-Supported Mixed-Source Calcirudite

There are two types of clasts in clast-supported mixed-source calcirudites: one is terrestrial, extraformational gravels, which make up 50–75% of the total gravel content, and the remaining part is intraformational, making up 25–50%. The content of matrix within clasts is low. The extraformational clasts are smaller than those in clast-supported extraformational calcirudites (Fig. 7.8a), and most of them are light gray to gray. The extraformational clasts originate mainly from lime mudstone and microcrystalline dolostone and show point to line contacts. The grains are subangular to subrounded with relatively poor sorting (Fig. 7.8b–d).

The intraformational clasts result from the erosion and redeposition of the unlithified carbonate sediments and have clear grain boundaries. However, this type of clasts deforms very easily and has irregular shapes such as stripes with deformed tails or irregular circles (Fig. 7.8a). Microscopic observation of intraformational clasts suggests that they come mainly from lime mudstone, containing a small amount of ostracod and mollusk fossils, terrestrial detrital material, pyrite, and organic matter.

### 7.2.1.3 Clast-Supported Intraformational Calcirudites

In the clast-supported intraformational calcirudites, intraformational clasts account for more than 50% of the total gravel content. The color of the intraformational clasts is dominated by dark gray to light gray. The grains are arranged in a slight orientation and irregular in shape. Most of the clasts have been deformed into elongated strips, and some are irregular squares (Fig. 7.9a). The intraformational gravel clasts are much larger than the terrestrial gravels, and their boundaries can be clearly identified in thin sections (Fig. 7.9b), although not as straight as the terrestrial gravels. The composition and structure of the intraformational
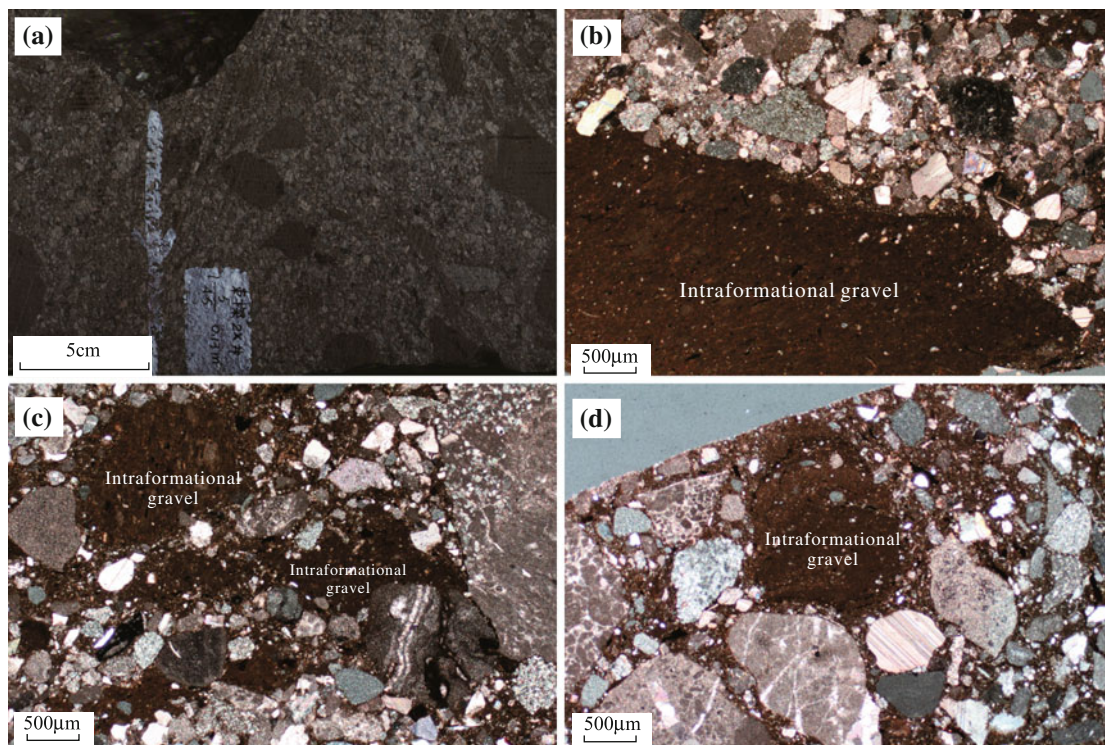
**Fig. 7.8** Clast-supported mixed-source calcirudite. **a** Clast-supported mixed-source calcirudites with dark gray intraformational clasts; the clasts have distinct boundaries and are slightly deformed. The extraformational clasts are gray to light gray and smaller than the intraformational clasts. All the clasts are in close contact, ST2X, core number $1\frac{5}{45}$; **b** clast-supported mixed-source calcirudites. Note the difference between the sizes of extraformational and intraformational clasts, ST2X, core number $1\frac{5}{45}$, cross-polarized light; **c** Note the deformation of intraformational clasts, ST2X, core number $1\frac{5}{45}$, cross-polarized light; **d** Note the variable grain size of the extraformational clasts; the intraformational clast has its distinct boundary, core number $1\frac{5}{45}$, cross-polarized light

gravels are similar to those of fine-grained calcilutites in the basin. They both contain sand-sized terrigenous quartz or feldspar (based on X-ray data), less carbonate rock fragments, organic matter, and ostracod and mollusk bioclasts. A slight difference is that terrigenous grains are less and smaller in the intraformational clast compared to that in the fine-grained calcilutites.

The extraformational clasts are mainly composed of granules and very fine pebbles, filling the space between the intraformational clasts. The extraformational clasts are relatively poorly sorted and mostly subangular to subrounded. The contact types include point and line contacts (Fig. 7.9c, d).

### 7.2.1.4  Matrix-Supported Extraformational Calcirudites

The matrix-supported extraformational calcirudite is similar to its clast-supported counterpart in that the terrigenous gravels account for more than 75% of total gravel content. The thickness of the single matrix-supported extraformational calcirudite bed can reach up to 0.5 m. The color is dominated by dark gray, gray and light gray. The only

difference is that the gravel-sized clasts of the matrix-supported extraformational calcirudites are heterogeneous in size poorly sorted, and instead of being in contact with each other, they are floating in the matrix (Fig. 7.10a–c). The interstitial fillings are mostly sand- or silt-sized carbonate clasts (Fig. 7.10d), being subangular to subrounded and poorly sorted. The interstitial fillings are rich in patchy or strip-shaped organic matter (Fig. 7.10e). The matrix also contains a certain amount of bioclasts such as ostracods (Fig. 7.10f), pyrite, and organic matter (Fig. 7.10 g). Pyrites are mostly spherical under the reflected light (Fig. 7.10h), isolated or as clusters. Due to the difference in composition, the color of the matrix is slightly lighter than that of the intraformational gravel; the fine-grained class of clasts is more abundant in the matrix, and they have larger grain sizes. Both the matrix and the intraformational clasts are relatively rich in organic content.

### 7.2.1.5  Matrix-Supported Mixed-Source Calcirudites

Similar to the clast-supported intraformational calcirudites, the matrix-supported mixed-source calcirudites contain both
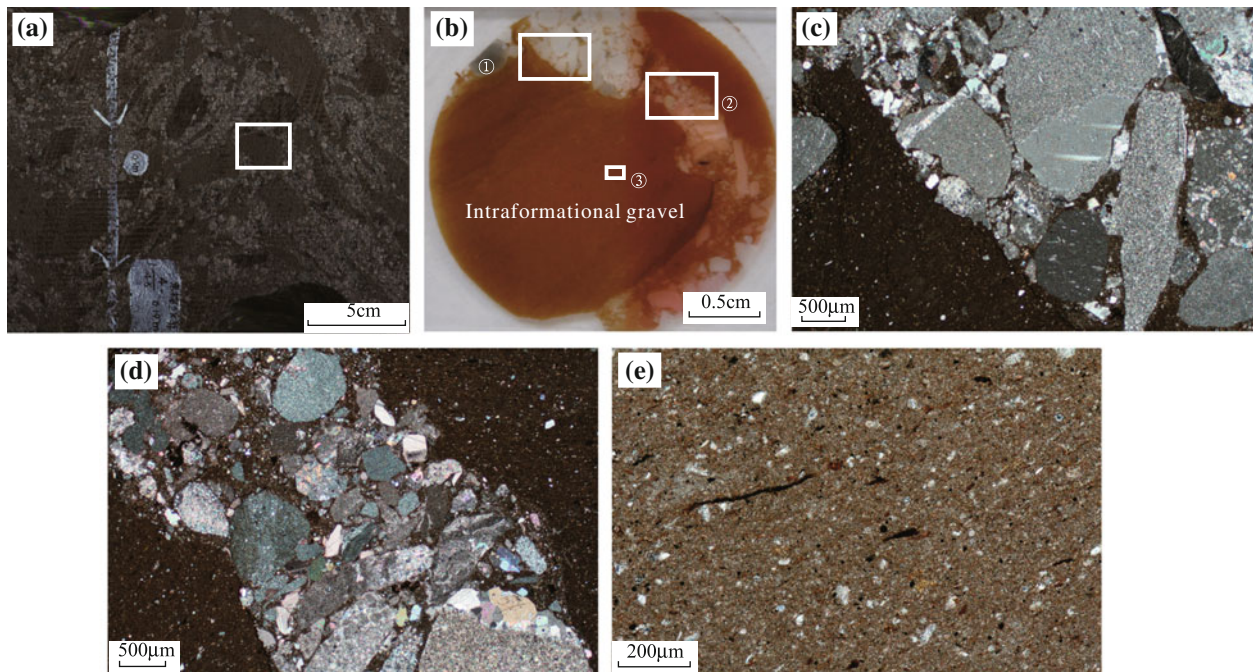
**Fig. 7.9** Clast-supported intraformationalconglomerates. **a** Scanned core interval of clast-supported intraformational calcirudites, Well ST2X, core number $1\frac{4}{45}$; **b** thin section of the white-square covered area in (**a**); intraformational clasts almost occupy the entire section, Well ST2X, core number $1\frac{4}{45}$; **c** a closer look at the area ① in (**b**). Note the distinct boundary between the intraformational and extraformational clasts, Well ST2X, core number $1\frac{4}{45}$, cross-polarized light; **d** a closer look at the area ② in (**b**). Poorly sorted terrigenous clasts filling the space between intraformational clasts, Well ST2X, core number $1\frac{4}{45}$, cross-polarized light; **e** a closer look at the area ③ in (**b**), which is a zoomed-in part of the intraformational clast. It contains strips of organic matter and silt-sized carbonate clasts, Well ST2X, core number $1\frac{4}{45}$, cross-polarized light

terrestrial and intraformational clasts, and the intraformational clasts account for 25–50% of the gravel content (Fig. 7.11a). This type of calcirudite is massive and matrix-supported, with the larger grains floating in the matrix or in point contact with other grains. The terrigenous clasts are light gray in cores, subangular to subrounded, and poorly sorted with variable grain sizes. The composition of these clasts is complex, with the majority resulting from lime mudstone (Fig. 7.11b). The intraformational clasts have relatively clear grain boundaries and are dark gray in cores with round or circle-like shapes. Some of the clasts have undergone deformation and shown irregular shapes. The clasts also contain a small amount of clay- and silt-sized debris, pyrite, organic matter, and few ostracod and mollusk bioclasts (Fig. 7.11c, d).

### 7.2.1.6 Calcarenites and Calcisiltites

The calcarenites are light gray in the cores (Fig. 7.12a), and the calcisiltites interbed with the calcilutites. The calcarenites and calcisiltites consist mainly of sand- or silt-sized carbonate clasts, clay minerals and small amounts of terrestrial grains such as quartz (Table 7.2). The grains of the calcarenites are subrounded to subangular with a grain size between 0.2 and 1 mm. The grains are moderately sorted

with the interstitial space filled with authigenic calcite (Fig. 7.12c). Calcisiltites show normal grading which passes into calcilutites; they also contain small amounts of bioclasts (Fig. 7.12d).

### 7.2.1.7 Laminated Calcilutite

The laminated calcilutite are gray to dark gray in the core with clear lamination and sheet growth (Fig. 7.13a, b). The laminations are couplets of dark/light-colored laminae under the microscope (Fig. 7.13c, d). The thickness of the lamina varies from 100 to 300 μm. The main composition of the laminated calcilutite is calcite, followed by dolomite, clay minerals, quartz, and pyrite, with little feldspar content (Table 7.3).

The laminated calcilutite is composed of three distinct layers under the microscope (Fig. 7.13c, d): (a) light-colored microcrystalline calcite layer, (b) dark lime mud layer, and (c) terrigenous clast layer with clay minerals. The calcite layer is the authigenic calcite formed by biochemical precipitation in the spring and summer seasons, and the clay-bearing terrigenous layer is the product of sedimentation from suspension in the autumn and winter seasons (Valero-Garcés et al. 2014). The terrigenous clastic layer is composed of clay, carbonate minerals, pyrite, quartz, and the
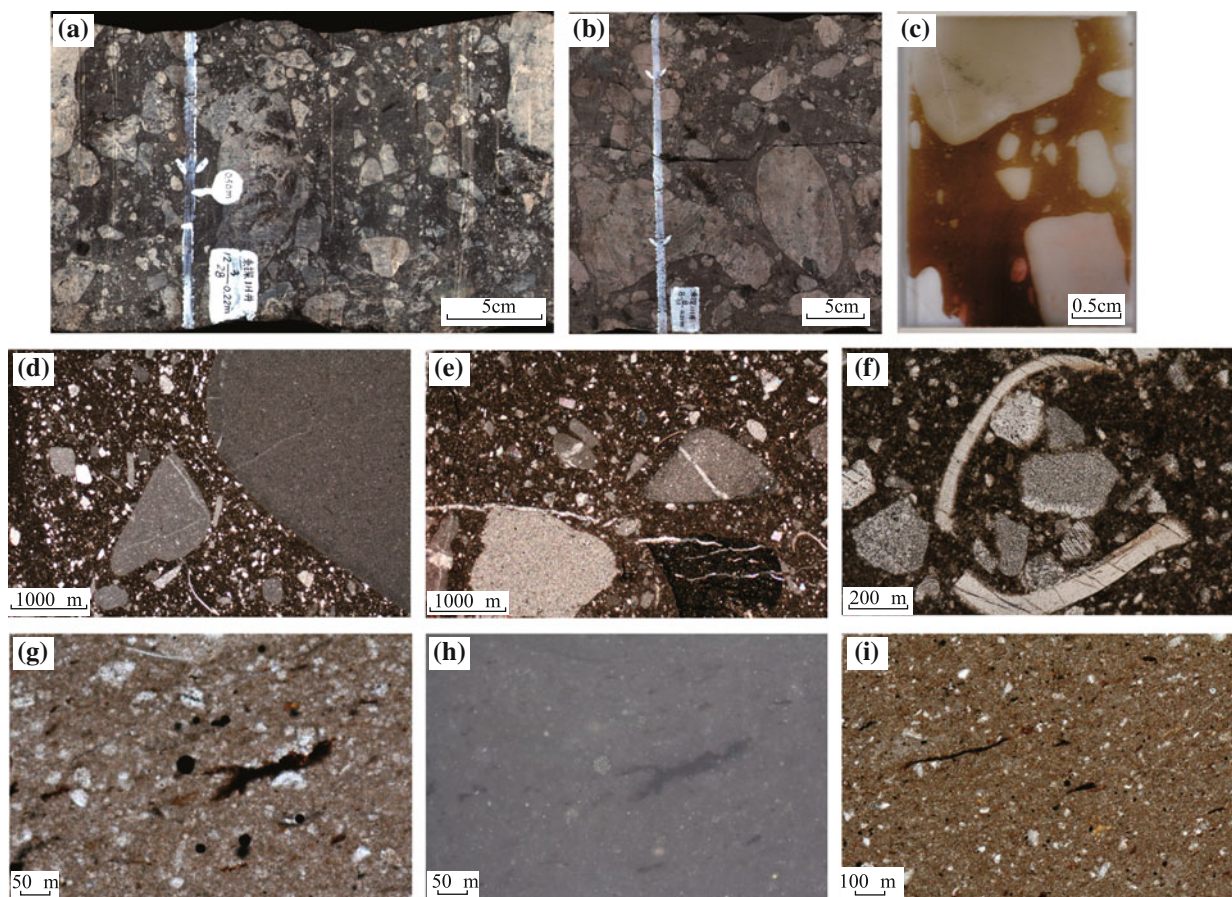
**Fig. 7.10** Matrix-supported extraformational calcirudites. **a** The terrigenous clasts are in the point contact or floating in the matrix, massive structure, Well ST1H, core number $12\frac{3}{28}$; **b** poorly sorted clasts with different sizes, Well ST1H, core number $8\frac{8}{31}$; **c** thin section of the matrix-supported extraformational calcirudite shows the floating terrigenous grains, Well ST1H, core number $7\frac{22}{30}$, polarized light; **d** thin section of the matrix-supported extraformational calcirudite shows the matrix-supported fabric, with sand- or mud-sized carbonate clasts filling the pore space, Well ST1H, core number $11\frac{7}{26}$, polarized light; **e** randomly dispersed organic matter, Well ST1H, core number $11\frac{7}{26}$, cross-polarized light; **f** bioclasts in matrix-supported extraformational-calcirudite, Well ST1H, core number $11\frac{7}{26}$, cross-polarized light; **g** pyrite associated with organic matter, Well ST1H, core number $7\frac{22}{30}$, polarized light; **h** Rounded pyrite cluster shows metallic luster under reflected light, Well ST1H, core number $7\frac{22}{30}$; **i** The intraformational clast contains organic matter and pyrite, well ST2X, core number $1\frac{4}{45}$, polarized light

organic matter. The TOC of the laminated calcilutite is between 0.65 and 5.41%, averaging 1.85%. The recrystallized bladed calcite (d) can develop in the fractures between the laminae, and its formation is associated with the evolution of organic matter.

### 7.2.1.8  Massive Calcilutite

The massive calcilutite is dominantly dark gray or gray-brown in the core (Fig. 7.14a, b) with no clear lamination and occasional thin layers of calcisiltite. The thickest layer of massive calcilutite is 4.05 m (Well ST3, 3986.27–3990.32 m). The massive calcilutite is mainly composed of calcite, followed by dolomite, clay minerals, quartz, pyrite, and little feldspar (Table 7.4). It also contains silt-sized

terrigenous clasts and a few bioclasts (Fig. 7.14c, d). These components were randomly distributed under the microscope. The long axis of the mollusk fossils and some minerals tend to be aligned horizontally. The TOC of massive calcilutite is between 0.77 and 5.54%, averaging 1.68%.

### 7.2.2  Gravel Composition

The gravels of the lower submember of the $Es_3$ third member mainly originate from the carbonate rocks of the Ningjin Uplift on the western flank of the basin, including two broad types: limestone gravel (Fig. 7.15) and dolostone gravel (Fig. 7.16).
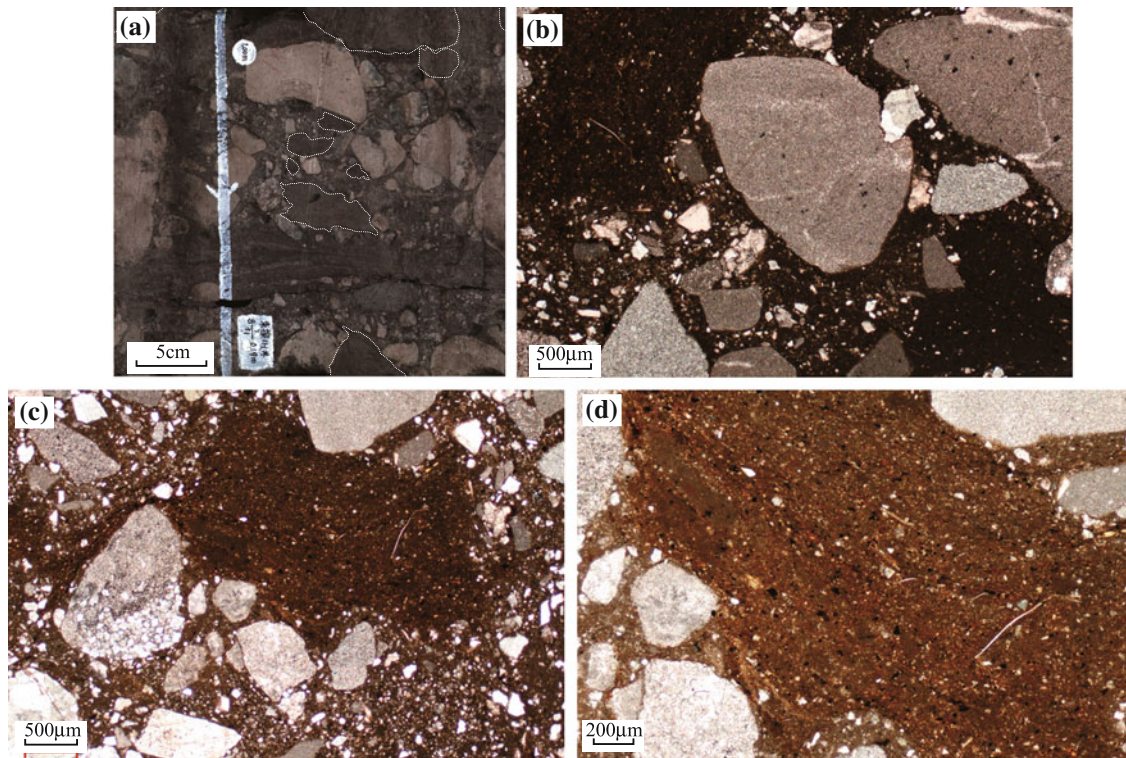
**Fig. 7.11** Matrix-supported mixed-source calcirudites. **a** The gray-white terrestrial clasts deform the gray-black intraformational gravels into various shapes, Well ST1H, core number $8\frac{7}{31}$; **b** the terrigenous clasts are mainly from lime mudstones; the intraformational clasts have the shape of grains, Well ST1H, core number $8\frac{12}{31}$, polarized light; **c** poorly sorted terrigenous clasts, well ST1H, core number $8\frac{12}{31}$, polarized light; **d** the intraformational clast contains mud- and silt-sized debris, pyrite, and few bioclasts, Well ST1H, $8\frac{12}{31}$, polarized light

### 7.2.2.1 Limestone Gravel

The proportion of limestone gravel in the study area is 60% of the total gravel and mainly result from packstone and lime mudstone. Packstone gravels account for about 40% of the total limestone gravel, including oolitic packstone (Fig. 7.15a, b), flat-pebble rudstone (Fig. 7.15c), peloid packstone (Fig. 7.15d–f) and bioclastic limestone (Fig. 7.15g–j). The grain size of the ooids in the oolitic packstone is 0.5–1.0 mm, and the ooids have vaguely radial crystal structures and concentric layers. The cement of the oolitic packstone includes both micrite and sparry calcite. The flat-pebble rudstone contains intraclasts with variable grain sizes and most of the intraclasts have elongated shapes with oxidized coatings. The coarse gravels tend to be arranged in a slightly parallel manner, and the arrangement of small gravels is a little messy. The grain size of the peloids in peloid packstone ranges from 0.05 to 1 mm. Peloid packstones are well sorted, and the cement is mainly sparry calcite. The bioclasts in bioclastic limestone originate from crinoids, gastropods, sponges, and trilobites.

The ratio of the lime mudstone gravels is about 60%. The mudstone is composed mainly of micrite, and it can be seen under the microscope that some of the fractures or vugs are filled recrystallized sparry calcite (Fig. 7.15k–l).

### 7.2.2.2 Dolostone Gravel

The dolostone gravels account for 30% of the total gravel in the study area, and the source rocks include medium crystalline dolostone (Fig. 7.16a–d), finely crystalline dolostone (Fig. 7.16e–f), very finely crystalline dolostone (Fig. 7.16g), and microcrystalline dolomite (Fig. 7.16h–i). The medium crystalline dolostone, finely crystalline dolostone and very finely crystalline dolostone are composed of dolomite crystals of different sizes. The dolomite crystals have euhedral to subhedral forms and are in concavo-convex contact with each other. The crystals are formed because of replacement and recrystallization. The microcrystalline dolostone is mainly composed of microcrystalline dolomite. The crystals are subhedral to anhedral and have small grain sizes and uniform structures.

### 7.2.2.3 Siliciclastic Gravel

In addition to carbonate gravels, there are a few silicate gravels (about 10%), including chert, chalcedony, and quartz. Chert is a cryptocrystalline, microcrystalline or finely crystalline silica aggregate (Fig. 7.17a–c); chalcedony is a type of cryptocrystalline silica (Fig. 7.17b); there are fractures inside the quartz gravels, and some quartz grains have overgrowths (Fig. 7.17d).
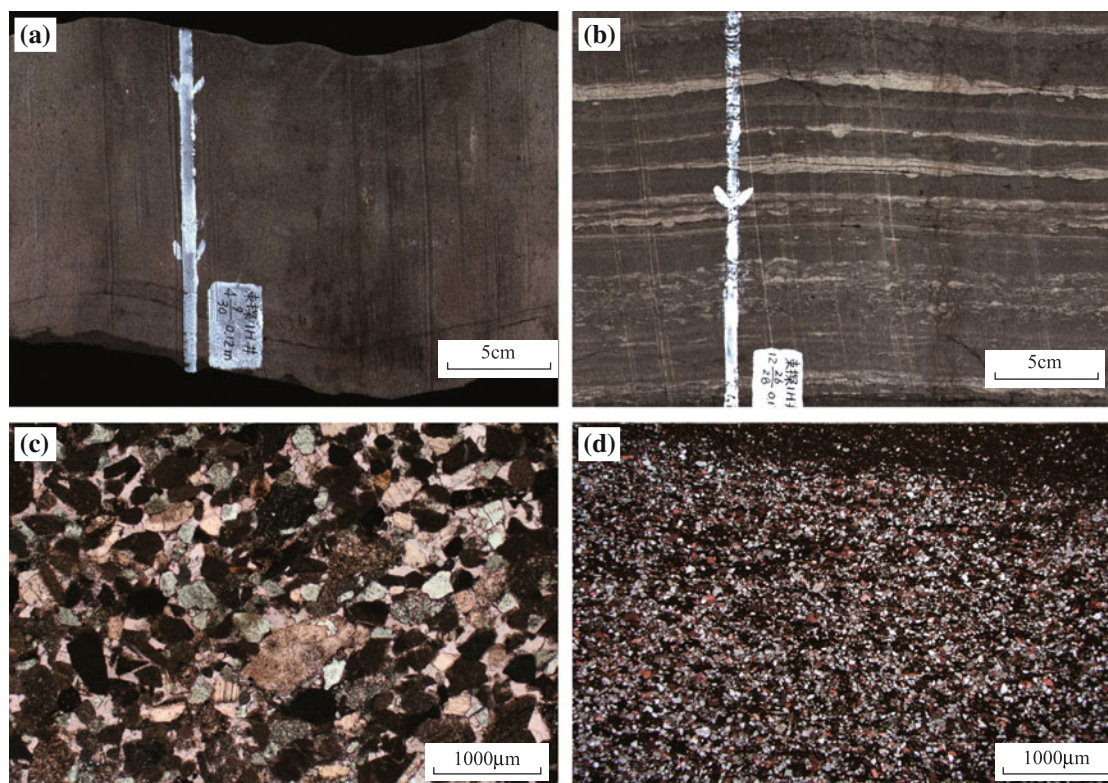
**Fig. 7.12** Calcarenites and calcisiltites. **a** Light gray calcarenites in core, Well ST1H, core number $4\frac{9}{30}$; **b** interlayered calcisiltites and calcilutites, Well ST1H, core number $12\frac{26}{28}$; **c** the grains of the calcarenite are mainly composed of terrigenous carbonate minerals and in close contact with each other, with little or no matrix. The grains are relatively well sorted and vary from subrounded to subangular, Well ST1H, $8\frac{19}{31}$, polarized light; **d** laminated calcisiltites are composed of silt-sized terrigenous carbonate debris and micrite. The grains are in point-line contact and fining upwards into calcilutite. There are occasional bioclasts, Well ST1H, 3973.4 m, polarized light

**Table 7.2** Composition of the calcarenites and calcisiltites in the lower submember of Es$_3$

| Minerals | Average (%) | Number of samples | Min value (%) | Max value (%) |
|---|---|---|---|---|
| Calcite | 38.7 | 42 | 1 | 79 |
| Dolomite | 36.9 | 42 | 3 | 76 |
| Clay minerals | 11.9 | 42 | 1 | 44 |
| Quartz | 10.9 | 42 | 2 | 35 |
| Feldspar | 0.07 | 42 | 0 | 1 |
| Pyrite | 0.17 | 42 | 0 | 2 |
| Siderite | 1.36 | 42 | 0 | 15 |

## 7.2.3  Well Log Identification

### 7.2.3.1  Clast-Supported Extraformational Calcirudites

The main criteria for recognition of clast-supported extraformational calcirudites on well log include the large thickness, low GR value, and high resistivity (Fig. 7.18). Also, the high DEN value, low CNL value, and the crossover of resistivity and acoustic log are also useful features that can help identify this facies. Well log also shows high dolomite content in most intervals of clast-supported extraformational calcirudites and this feature can also be used as an additional criterion for recognition of the facies. Caution must be taken in using the high dolomite content criterion since some intervals also show a high content of calcite.

### 7.2.3.2  Matrix-Supported Extraformational Calcirudites

The thickness of matrix-supported extraformational calcirudites is apparently smaller than that of its clast-supported counterpart. Because of the difference in matrix and composition, the logging curves have serrated features
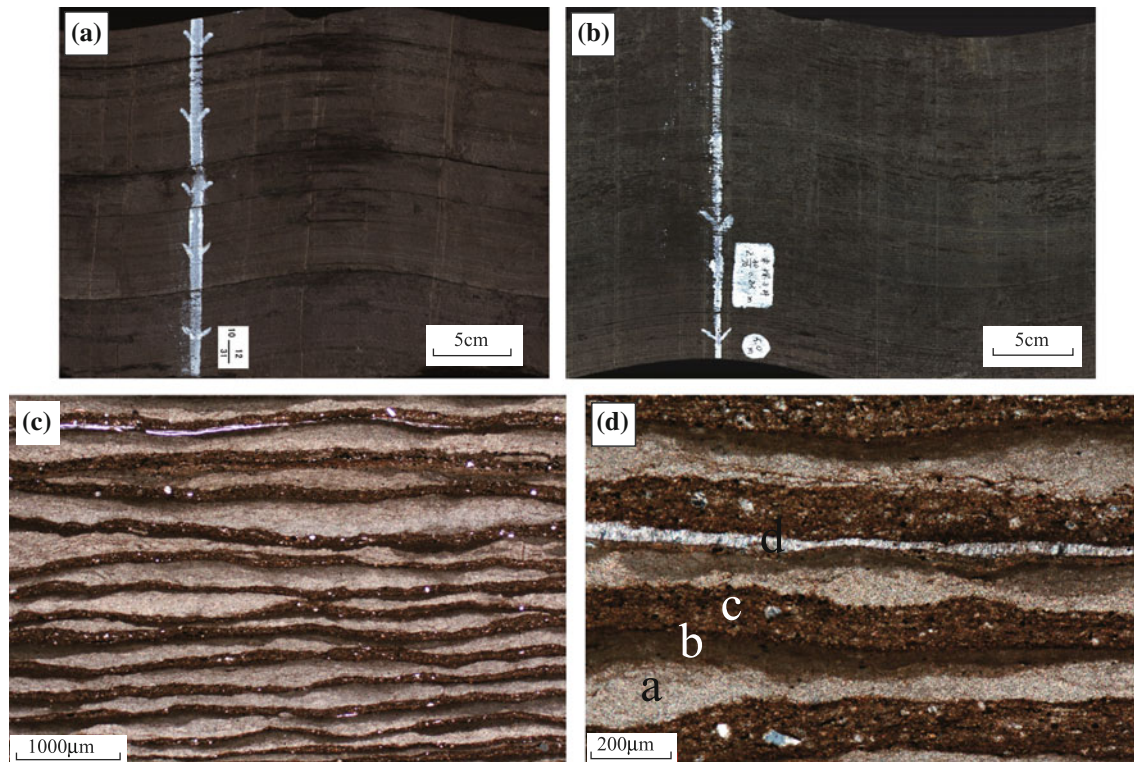
**Fig. 7.13** Laminated calcilutite. **a** Gray-brown laminated calcilutite in core with clear laminations, Well ST1H, core number $10\frac{12}{31}$; **b** dark gray laminated calcilutite, Well ST3, core number $2\frac{30}{76}$; **c** couplets of straight or wavy dark/light-colored laminae, Well ST1H, core number $13\frac{17}{57}$, polarized light; **d** is zoomed-in part of c showing the three-layer texture of the laminated calcilutite, with layer a being sparry microcrystalline calcite, layer b the dark-colored lime mud, and layer c the terrigenous clast layer containing clay minerals; layer d is the recrystallized bladed calcite cement, Well ST1H, core number $13\frac{17}{57}$, cross-polarized light

**Table 7.3** Composition of the laminated calcilutites in the lower submember of Es$_3$ of Shulu Sag

| Minerals | Average (%) | Number of samples | Min value (%) | Max value (%) |
|---|---|---|---|---|
| Calcite | 57.3 | 105 | 22 | 93 |
| Dolomite | 15.9 | 105 | 2 | 57 |
| Clay minerals | 14.5 | 105 | 2 | 40 |
| Quartz | 10.4 | 105 | 2 | 30 |
| Feldspar | 0.4 | 105 | 0 | 2 |
| Pyrite | 1.43 | 105 | 0 | 7 |

(Fig. 7.19), such as GR and resistivity, which is different from the clast-supported calcirudites. In addition, the GR value is slightly higher than that of the clast-supported calcirudites. The crossover of DEN and CNL, as well as the crossover of resistivity and acoustic log, becomes smaller.

### 7.2.3.3 Mixed-Source Calcirudites

Mixed-source calcirudites include clast-supported mixed-source calcirudites, matrix-supported mixed-source calcirudites, and clast-supported intraformational calcirudites. These calcirudites are mainly found in Well ST2X and Well ST3; there is also a small amount in Well ST1H. The mixed-source calcirudites are typically found above the extraformational calcirudites, and the bed thickness is relatively small compared to the extraformational calcirudites. The small bed thickness makes it harder to identify this facies on well log. The GR value of the mixed-source calcirudites is slightly higher than that of the extraformational calcirudites, and the values are in the range of fine-grained carbonate rocks. The acoustic travel time is relatively low, which can aid in differentiating the mixed-source calcirudites from the fine-grained carbonate rocks. In addition, the crossover of DEN and CNL is significantly smaller than that of the extraformational calcirudites (Fig. 7.20).
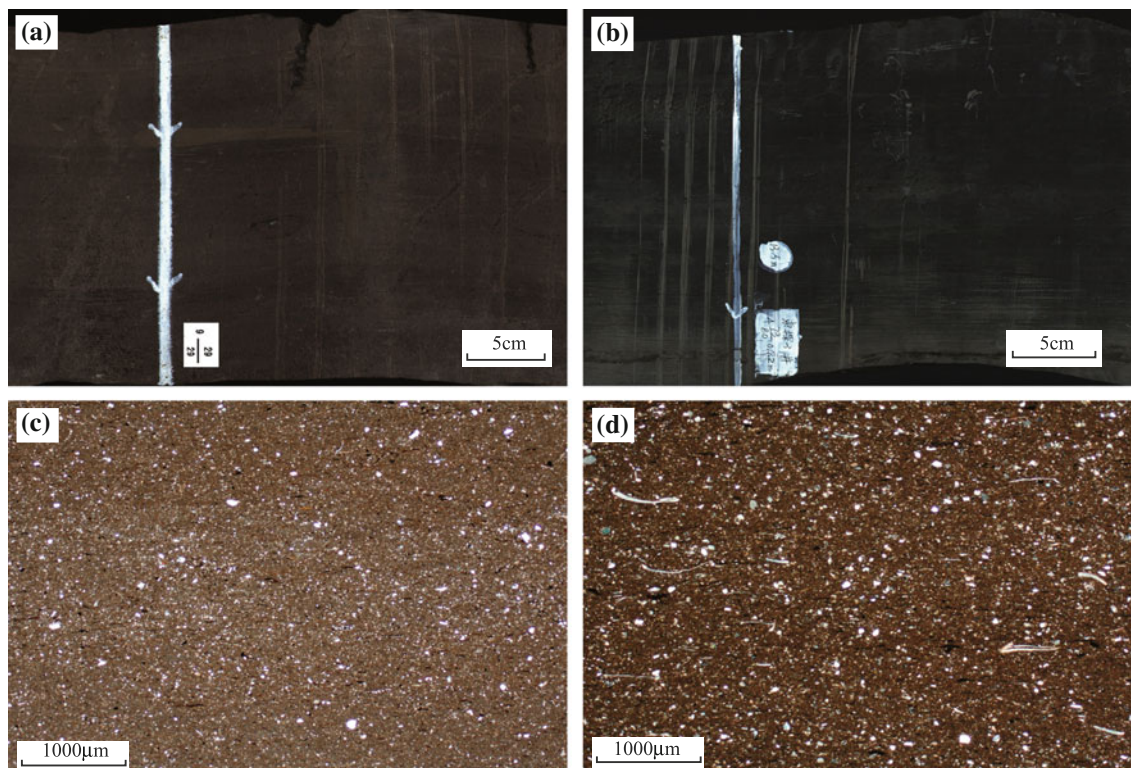
**Fig. 7.14** Massive calcilutite. **a** Gray-brown massive calcilutite with no clear lamination, well ST1H, core number $9\frac{29}{29}$; **b** dark gray, massive calcilutite, Well ST3, core number $4\frac{73}{80}$; **c** massive calcilutite dominated by lime mud, well ST1H, core number $11\frac{21}{26}$, polarized light; **d** massive calcilutite containing silt-sized terrigenous clasts and ostracod and mollusk fossils, well ST1H, core number $9\frac{25}{29}$, cross-polarized light

**Table 7.4** Composition of the massive calcilutites in the lower submember of $Es_3$ of Shulu Sag

| Minerals | Average (%) | Number of samples | Min value (%) | Max value (%) |
|---|---|---|---|---|
| Calcite | 61.2 | 89 | 22 | 92 |
| Dolomite | 13.6 | 89 | 3 | 44 |
| Clay minerals | 13.5 | 89 | 2 | 39 |
| Quartz | 10 | 89 | 2 | 29 |
| Feldspar | 0.3 | 89 | 0 | 2 |
| Pyrite | 1.3 | 89 | 0 | 8 |

#### 7.2.3.4 Calcarenites and Calcisiltites

Calcarenites and calcisiltites are less developed in the study area, and the bed thickness is small. In the core, calcarenites are typically bounded by massive calcilutites above and below, with occasional contact with matrix-supported extraformational calcirudites, which results in an abrupt shift on well logs. The calcarenites and calcisiltites are characterized by low resistivity, large DEN, and high GR variability on well logs. The low content of calcite and high content of dolomite is one of the main features separating the calcarenite and calcisiltite from the calcilutite (Fig. 7.21).

#### 7.2.3.5 Laminated Calcilutite

This type of calcilutite is relatively well developed in the study area, and its GR value is higher than the extraformational calcirudites. The resistivity is greater than that of the calcisiltite and calcisiltite. It is also different from massive calcilutite in that it has a higher content of calcite and lower content of dolomite (Fig. 7.22).

#### 7.2.3.6 Massive Calcilutite

Massive calcilutite is another major facies in the study area, with larger bed thickness. The clay content is relatively high
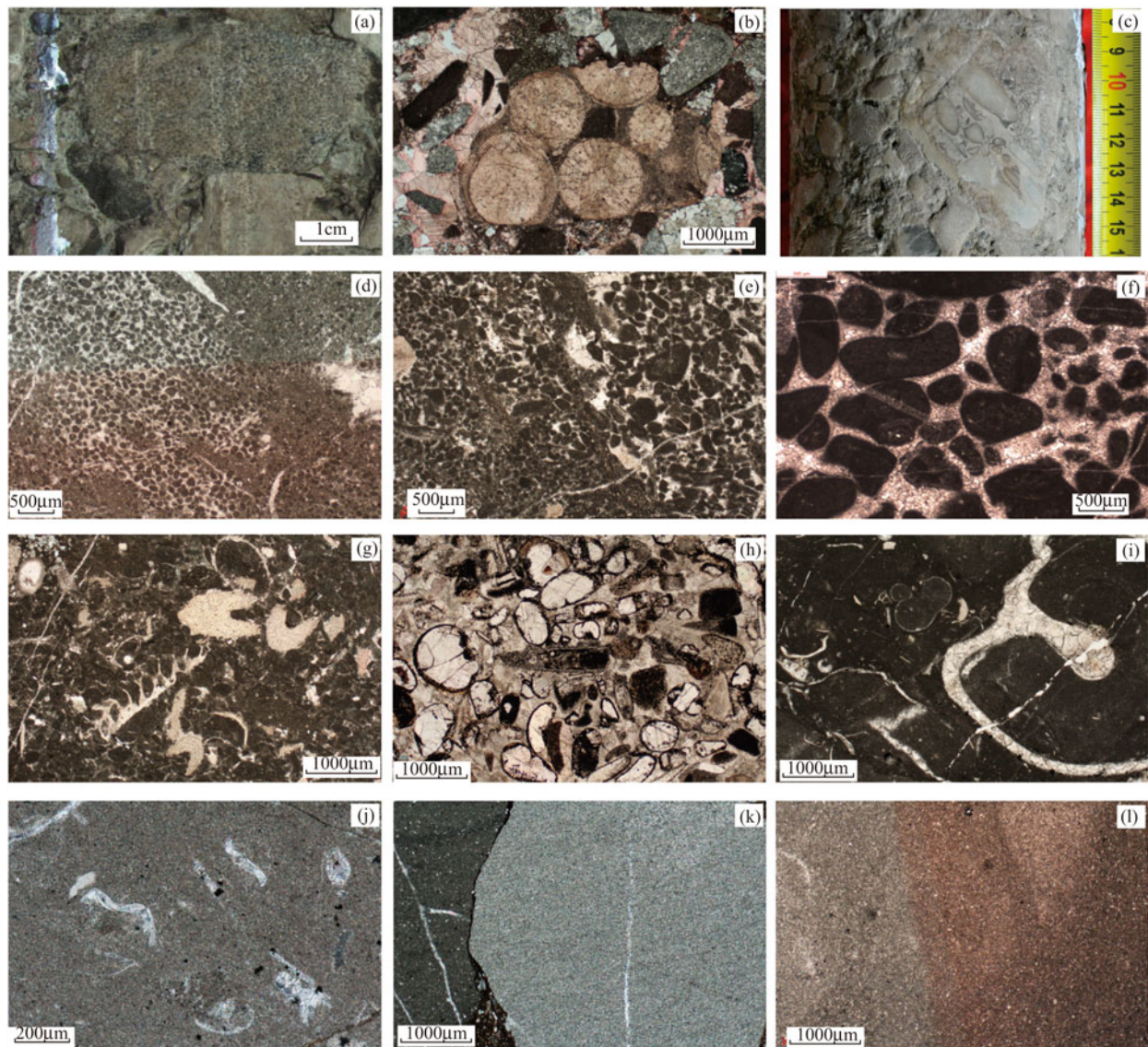
**Fig. 7.15** Limestone gravels of the Shulu conglomerates. **a** The oolitic limestone gravel in the core, Well ST3, core number $9\frac{17}{85}$; **b** the oolitic limestone gravel in thin section, Well Jin404, core number $9\frac{9}{13}$, polarized light; **c** flat-pebble rudstone gravel, Well ST3, core number $9\frac{66}{85}$; **d** peloid limestone gravel, Well ST2X, core number $1\frac{20}{45}$, polarized light; **e** peloid limestone gravel, Well Jin98X, core number $7\frac{8}{20}$, polarized light; **f** peloid limestone gravel, Well ST3, 4254.3 m, polarized light; **g** bioclastic limestone gravel, Well Jin94, core number $5\frac{17}{20}$, polarized light; **h** bioclastic limestone gravel, Well ST1H, $5\frac{29}{32}$, polarized light; **i** bioclastic limestone gravel, Well Jin97, core number $5\frac{10}{13}$, polarized light; **j** bioclastic limestone gravel, Well ST2X, core number $1\frac{27}{45}$, cross-polarized light; **k** micritic limestone gravel, Well ST2X, core number $1\frac{42}{45}$, cross-polarized light; **l** micritic limestone gravel, well ST1H, core number $2\frac{23}{23}$, polarized light

in this facies, resulting in higher GR value on well log. The resistivity is low and acoustic travel time is high, and their crossover is small (Fig. 7.23).

### 7.2.4 Lithology Distribution

Based on the core, sidewall coring and well log data, we have interpreted the lithology of the key wells in the lower submember of Es$_3$ of Shulu Sag. We have chosen the wells Jin100, Jin97, and ST3 to make a cross section showing the facies distribution (Fig. 7.24), and the wells are located on the landward side of the gentle slope, the gentle slope, and the slope break zones, respectively.

In general, the extraformational calcirudites (both clast- and matrix-supported types), the massive and laminated calcilutites are the most abundant lithology in the study area. Sequence I is characterized by widespread, thick bedded
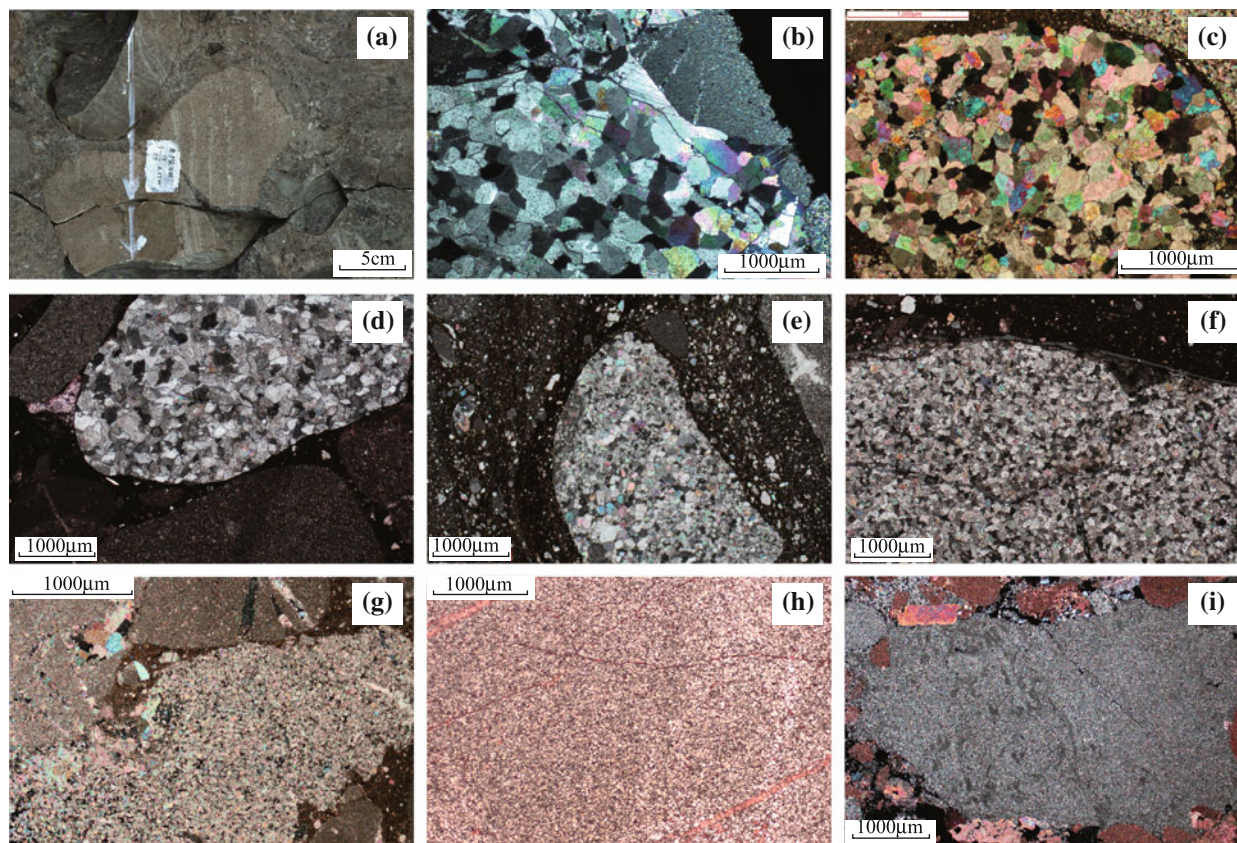
**Fig. 7.16** Dolostone gravels of the Shulu conglomerates. **a** Medium-crystalline dolomite in the core, Well ST3, core number $9\frac{79}{85}$; **b** medium-crystalline dolostone gravel, Well ST1H, 3979.98 m, cross-polarized light; **c** medium-crystalline dolostone gravel, Well ST3, 3871.19 m, cross-polarized light; **d** medium-crystalline dolostone gravel, Well ST1H, core number $2\frac{1}{23}$, cross-polarized light; **e** fine-crystalline dolomite, boring probe ST1H, core number 89/31, orthorhombic; **f** fine-crystalline dolostone gravel, Well ST1H, $5\frac{27}{32}$, crosspolarized light; **g** very finely crystalline dolostone gravel, Well ST2X, 3729.12 m, cross polarized light; **h** microcrystalline dolostone gravel, Well ST3, 4255.6 m, polarized light; **i** microcrystalline dolostone gravel, Well Jin97, 3863.5 m, cross polarized light

extraformational calcirudites, as can be seen in all the wells with straight curves showing low GR, low AC, and high resistivity. During the deposition of Sequence II, the basin is dominated by laminated and massive calcilutites, with the only exception being the clast-supported extraformational calcirudites near the edge of the basin. The deposits of Sequence III consist of thick bedded clast-supported extraformational calcirudites near the edge of the basin, which gradually transit into the calcarenites and laminated calcilutites further into the basin. During this time, the mixed-source calcirudites first appeared in some wells near the slope break zone. Laminated and massive calcilutites dominate Sequence IV and Sequence V with occasional interbeds of the matrix-supported extraformational calcirudites. The calcirudites are mainly distributed in Sequence I and Sequence III, as well as near the edge of the basin in Sequence II. The calcirudites in Sequences I and Sequences II are interpreted to result from fan delta deposition while those in Sequence III are potentially mass transport deposits triggered by earthquakes.

## 7.3 The Impact of Tectonic Activity on Sedimentation

Based on cores, thin sections observation and regional geologic analysis, lacustrine carbonate seismites are identified for the first time in the lowermost part of the third member of the Shahejie Formation in the Shulu Sag. The main characteristics include soft-sediment liquefied and brittle deformation structures. In addition, allogenetic seismoturbidites appear in the in situ seismites, suggesting an earthquake origin.

### 7.3.1 Types and Characteristics of Seismites

#### 7.3.1.1 Sedimentary Dikes

Sedimentary dikes are common in Sequence III. They consist typically of soft-sediment injections that crosscut laminated strata. The infill varies in color from faint yellow to gray, and in grain size from coarse-grained silt to fine gravel. They may
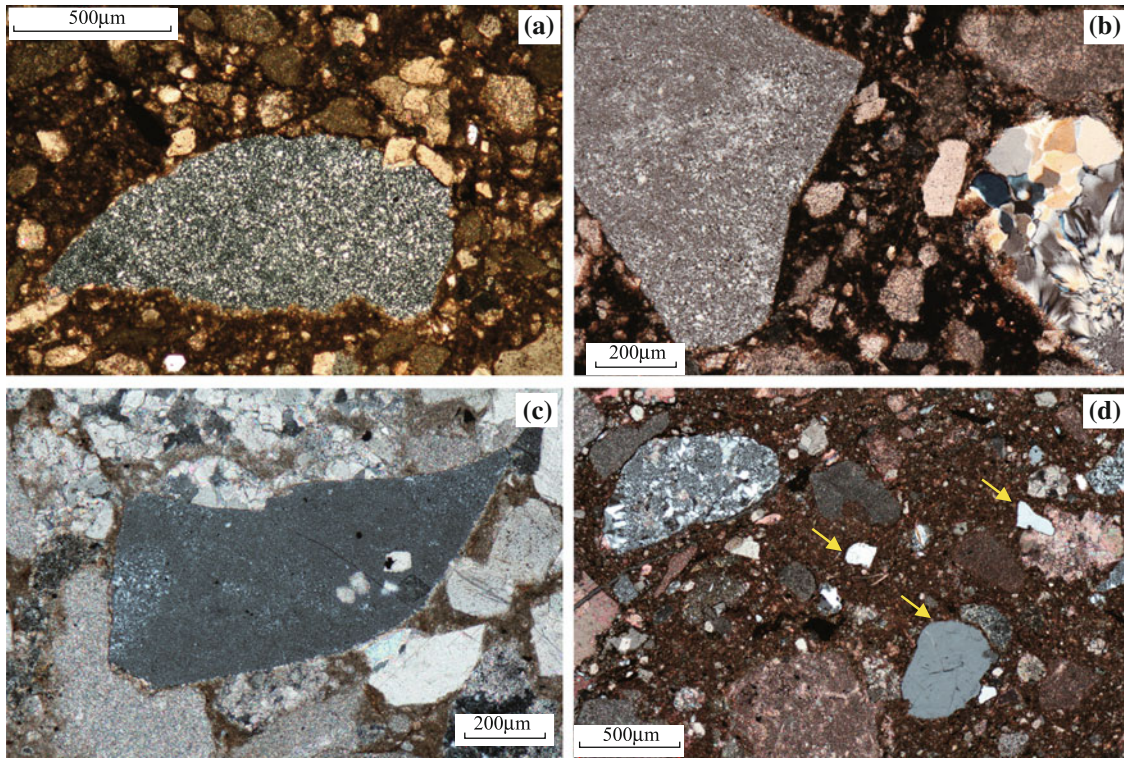
**Fig. 7.17** Siliciclastic gravels and terrigenous quartz of the conglomerates of Shulu Sag. **a** Chert gravel, Well ST3, 3808.57 m, cross polarized light; **b** Chert and chalcedony gravels, Well ST1H, core number $6\frac{4}{6}$, cross polarized light; **c** Chert gravel, Well ST1H, core number $8\frac{2}{31}$, cross polarized light; **d** Quartz gravel, Well Jin404, core number $9\frac{4}{13}$, cross polarized light
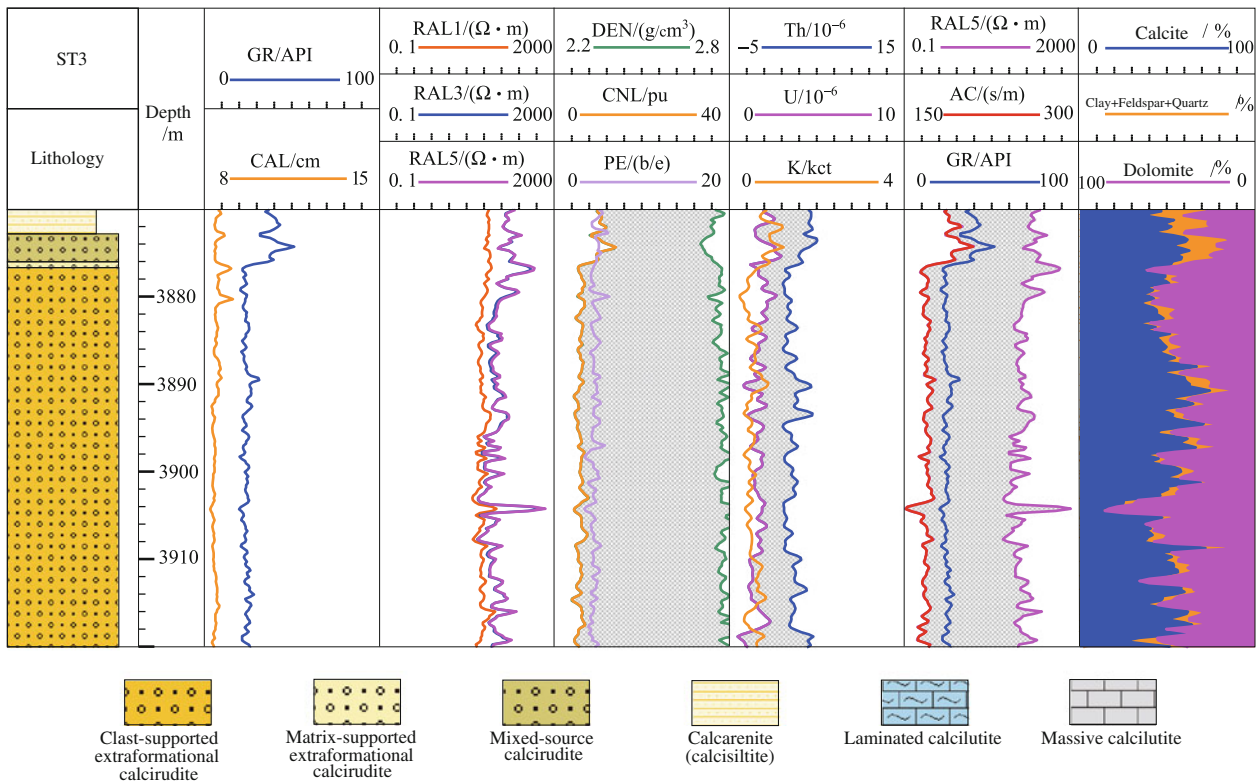


**Fig. 7.18** Well log features of extraformational clastic-supported calcirudite
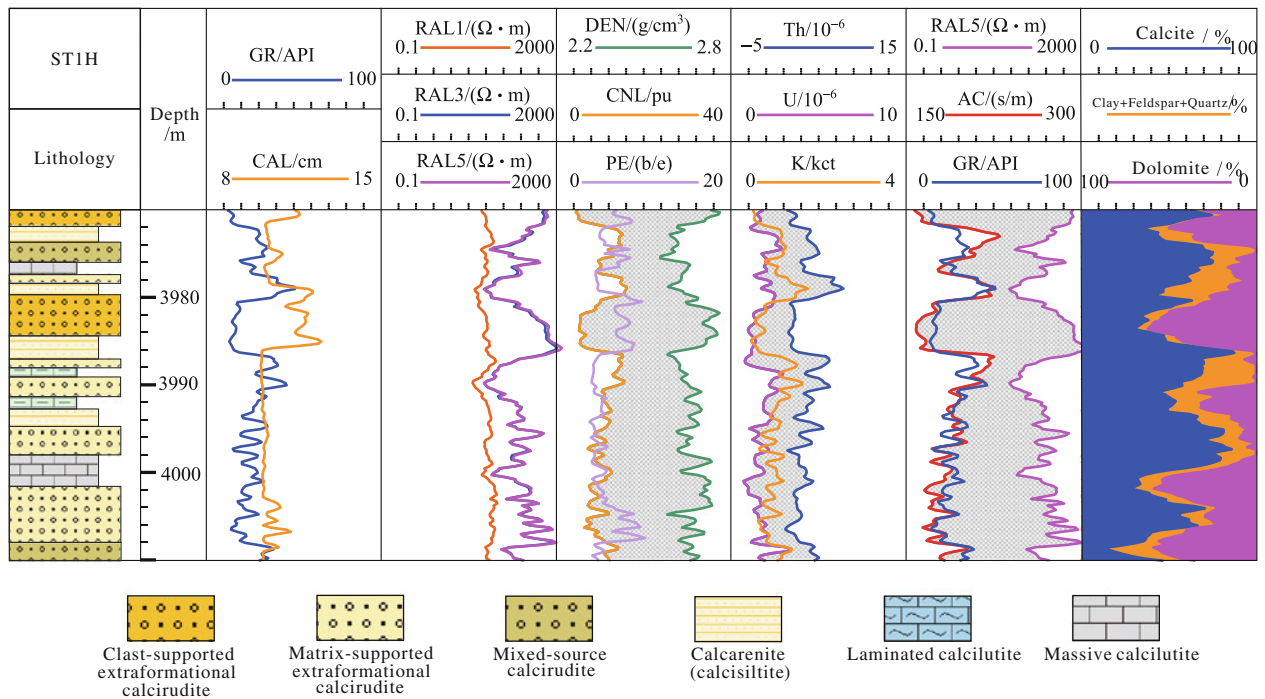
**Fig. 7.19** Well log features of matrix-supported extraformational calcirudite
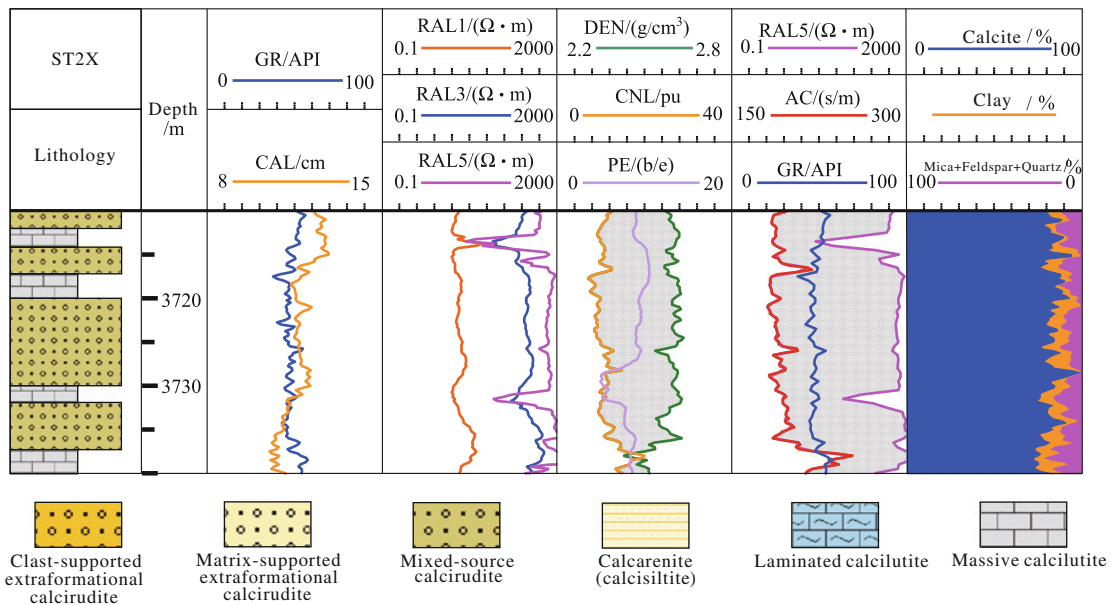


**Fig. 7.20** Well log features of mixed-source calcirudites

be called clay dikes, sand dikes, breccia dikes, or carbonate micrite veins. The clastic dikes exhibit irregular morphologies and terminate downward, straight to sinuous in vertical view. Thickness of dikes constantly changes and the shape of these liquefied bodies can be enteroid, conical, or tabular. Dikes may exceed 10 cm in vertical extent (Fig. 7.25a) and are up to 3 cm wide. At their termination, dikes are thinner

with a detached calcarenite nodule. Two breccia dikes can merge into one and end with a recumbent tail. Gravel-sized clasts associated with these dikes are poorly sorted, subrounded, or subangular (Fig. 7.25b). In well ST2X, calcarenite dikes taper downward, and branch and two of the branches can be cut into three parts by microfaults (Fig. 7.25c–d).
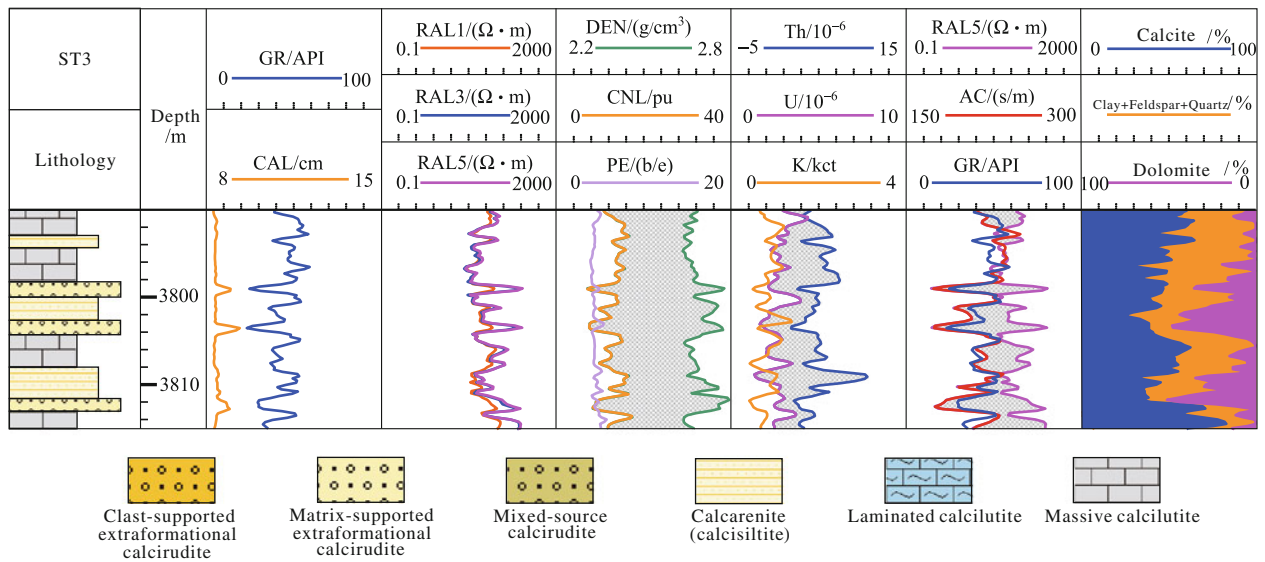
**Fig. 7.21** Well log features of calcarenites and calcisiltites
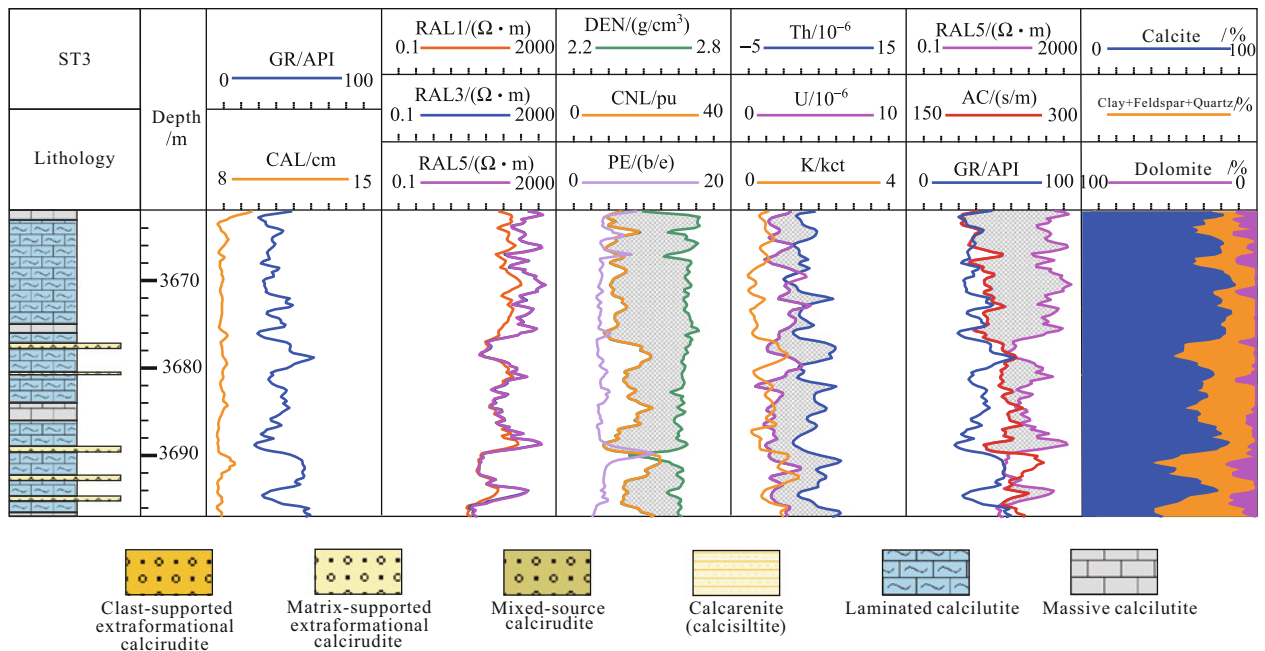


**Fig. 7.22** Well log features of laminated calcilutite

Sedimentary dikes are penecontemporaneous with sedimentation (Martel and Gibling 1993). They are formed by the injection of fluidized sediment from some underlying or overlying source and emplaced upwards or downwards under abnormal pressure (Berra and Felletti 2011). The downward-tapering morphology is the evidence for loss of shear strength and fluidization velocity (Törő and Pratt 2015). Downward emplacement of dikes has been attributed to Neptunian dikes related to the infilling of fissures (Montenat et al. 1991, 2007), dewatering due to compaction (Tanner 1998), or earthquake activity (Pratt 1998). Considering orientation, geometric relationships, and the nature of the infilling (Törő and Pratt 2015), here the sedimentary dikes are interpreted as injection features induced by
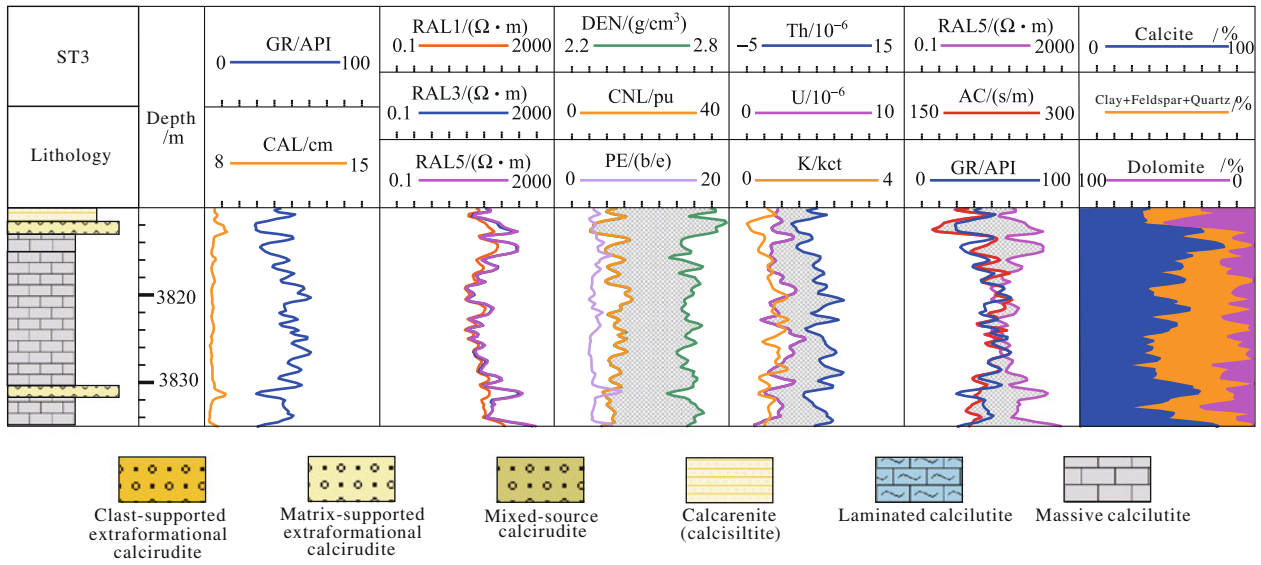
**Fig. 7.23** Well log features of massive calcilutite
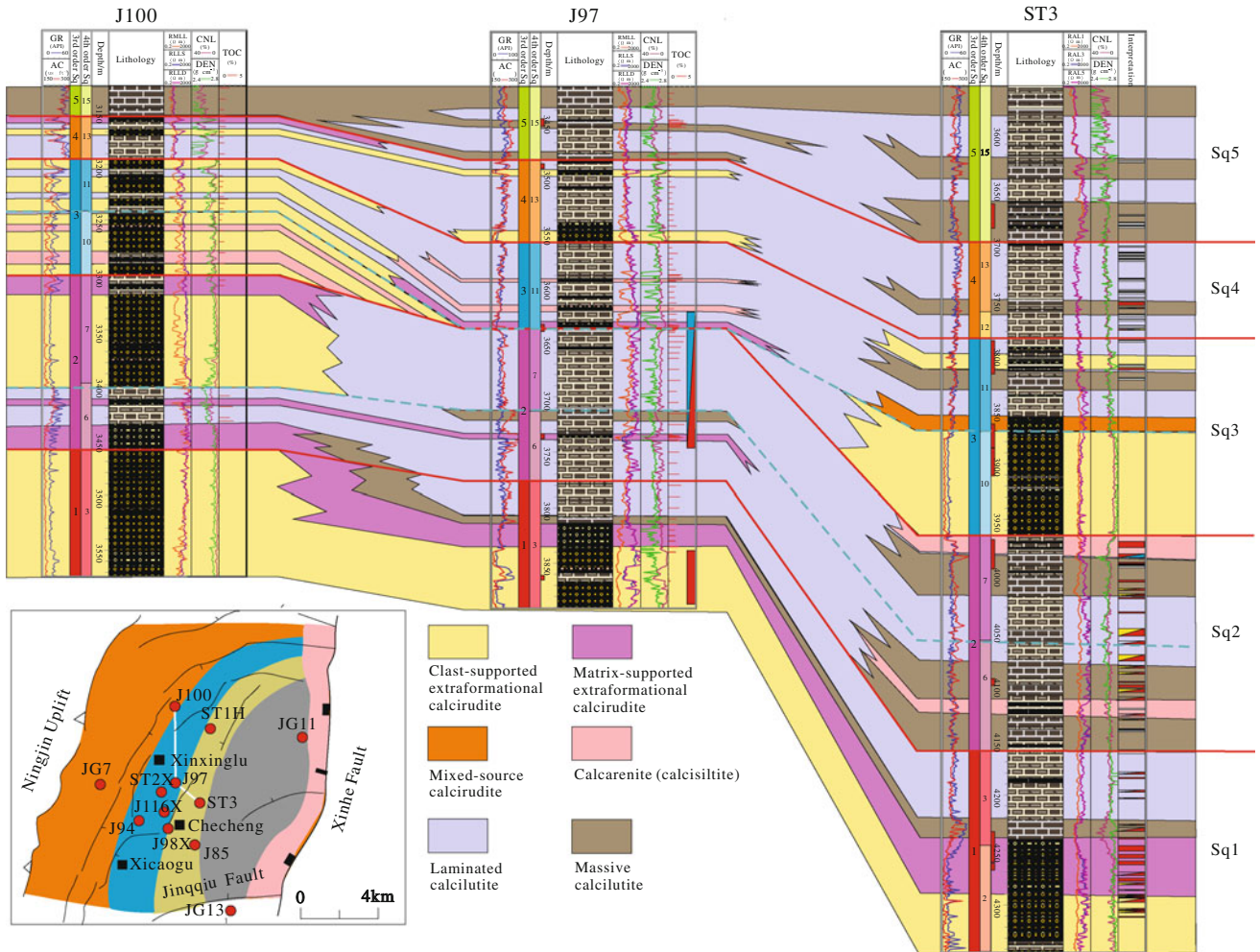


**Fig. 7.24** Cross-section of the Well Jin100-Well Jin97-Well ST3 showing facies distribution
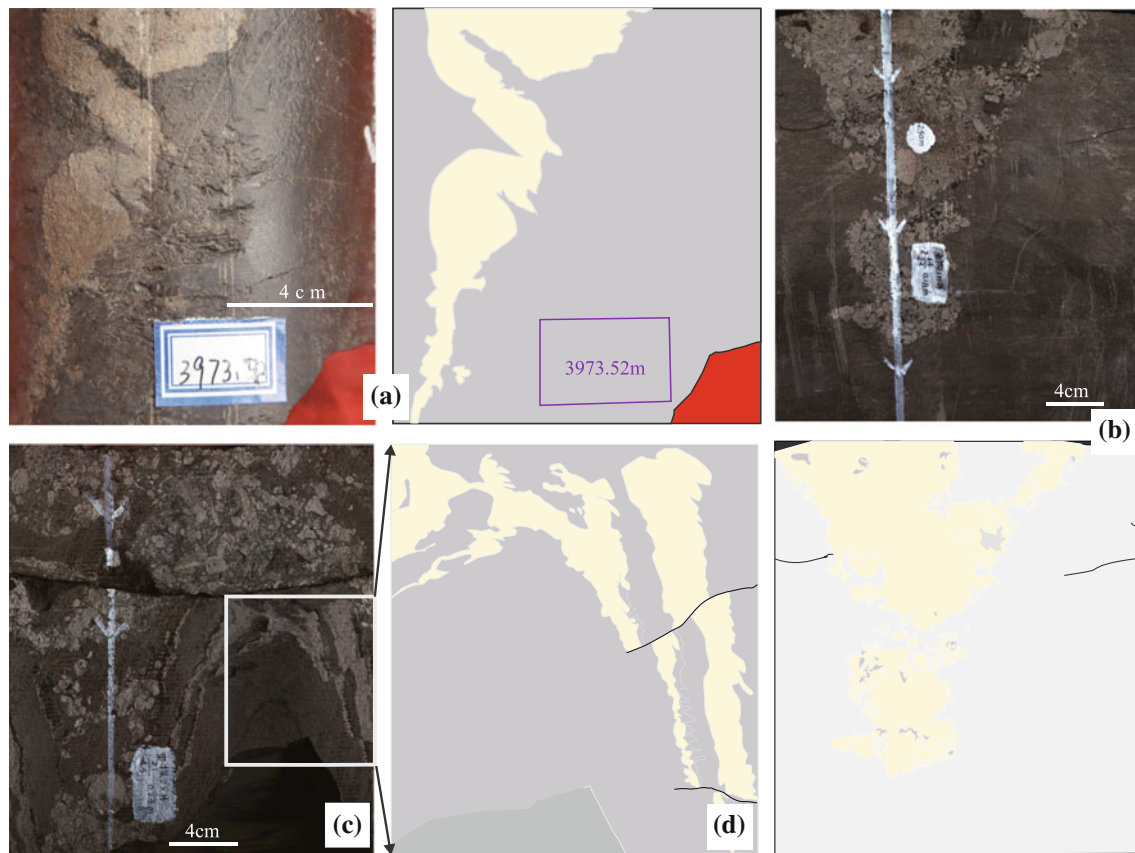
**Fig. 7.25** Core image and tracing of sedimentary dikes in Sequence III (Zheng et al. 2015). **a** Sausage-shaped calcarenite dike. From well ST1H, at 3973.52 m. **b** Breccia dike made up of subangular to subrounded gravel-sized carbonate clasts. From well ST1H, at 3961.6 m. **c** Calcarenite dike associated with micro-faults. From well ST2X, at 3725.17 m. **d** Tracing of the calcarenite dike. Arrows indicate the direction of the bottom of the strata, not the top

earthquakes. Sedimentary dikes cut by microfaults indicate a minor shock after the process of water escape when the layers are more lithified.

### 7.3.1.2 Hydraulic Shattering

In well ST1H in Sequence III, a group of parallel veins of calcarenite are present in the massive calcilutite associated with many horizontal to slightly oblique minor veins or dikes. This structure is characterized by groups of arched calcarenite veins or dikes (Fig. 7.26a), with 4-cm-wide lenses composed of coarse sand between them. A single dike shows an enteroid or tabular shape surrounded by many linear minor dikes. The axial surface of this structure is exactly upright.

As the energy needed is fast growing, hydraulic shattering can occur where strong hydraulic forces cause calcarenite veins or dikes to spread laterally into the surrounding strata (Obermeier 1996; Zhang et al. 2007; Ettensohn et al. 2011). The morphology of the dikes exhibits a clear fluidization with liquefaction, including the addition of minor dikes. There was a sudden upward-directed hydraulic force, believed to be the result of earthquake-induced liquefaction (Obermeier 1996).

### 7.3.1.3 Diapir Structures

In the well of ST1H of the Shulu Sag, mushroom-like diapirs and arched diapirs are made of calcarenites or calcirudites, which intrude and deform overlying laminites in Sequence III. The mushroom-like structures consist of gravel-sized clasts, of which the largest is 6 cm in length. The mushroom head shows a width of about 8 cm and a height of up to 4 cm (Fig. 7.26b). The outside lining of the mushroom cap is calcisiltite. Apart from the presence of the mushroom-like diapirs, domical diapirs have also been observed in the lowermost submember of Es3 of the Shulu Sag. These small domes contain coarse- to medium-grained calcarenite with dimensions of 10 cm in width and 5 cm in height (Fig. 7.26c). The overlying layer has been bent and fractures are generated right above the dome.

Many studies have described diapiric injection by silt-sized sediment or fine-grained sand (Chapman 1983; Hempton and Dewey 1983; Scott and Price 1988; Mohindra
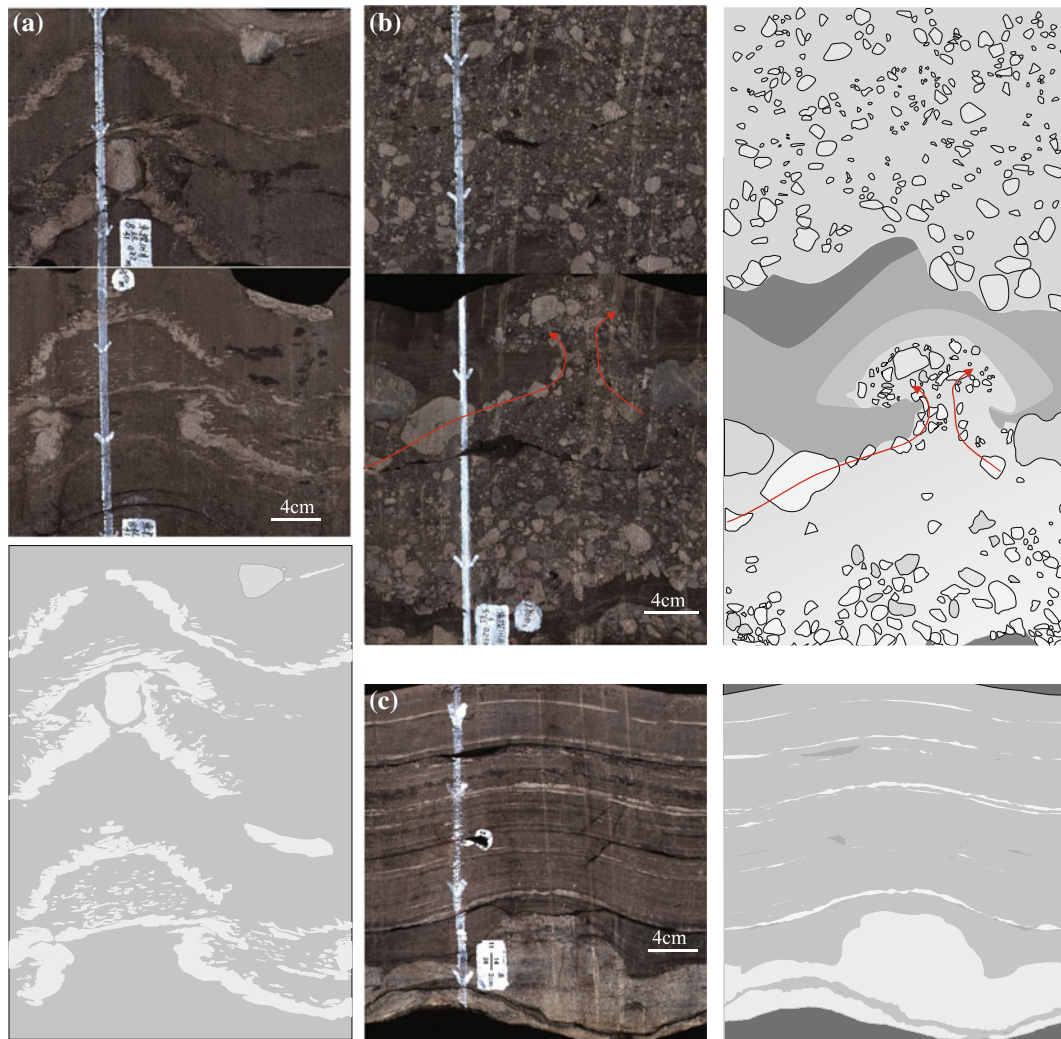
**Fig. 7.26** Vertically scanned core image and tracing of ductile deformation structures in Sequence III (from Zheng et al. 2015). **a** Hydraulic shattering. A group of parallel-liquefied calcarenite dikes with many horizontal to slightly oblique minor dikes at 3993.1 m. **b** Mushroom-like diapir composed of carbonate gravels and silt-sized sediment at 3974.73 m. Note the long axis orientation of the gravels (red arrows). **c** Arched diapir. Water-saturated calcarenites intrude and deform overlying bed at 4080.1 m. Arrows indicate the direction of the bottom of the strata, not the top

and Bagati 1996; Moretti 2000; Rodríguez-Pascua et al. 2000, 2010; McLaughlin and Brett 2004; Berra and Felletti 2011). They are small diapir-like morphologies intruding upward, which are similar to "sand volcanoes" but do not reach the surface (Montenat et al. 2007). The formation of the diapir-like structures may result from liquefaction and fluidization due to seismic shock or load-induced deformation (Berra and Felletti 2011). Rapid loading of sediments is an interpretation discarded here based on the morphologic characteristics of these diapirs. The long axis orientation of the gravel-sized clasts in the mushroom-like structures demonstrates the upward flow of poor-sorted clasts as a quasi-fluid or viscous solid pushing into the overlying laminites. The bent overlying layer and the fractures above

the dome indicate the forces of upward intrusion. Therefore, this structure can be confidently ascribed to a seismic activity rather than the load effects.

### 7.3.1.4  Convolute Lamination

The thickness of the disturbed laminae ranges from 1 to 20 cm. The morphology is irregular but laterally deformed synclines and anticlines with individual fold reaching up to 5–10 cm in height and averaging 5–10 cm in width (Fig. 7.27a–b) in Sequence III. These folded layers consist of interbeds of thin calcisiltite–calcilutite. The anticlinal flanks are gentle, and there are no clear sliding structures nor injection veins. The orientation of fold axes is almost upright (Fig. 7.27a–b) which contrasts with randomly oriented axes
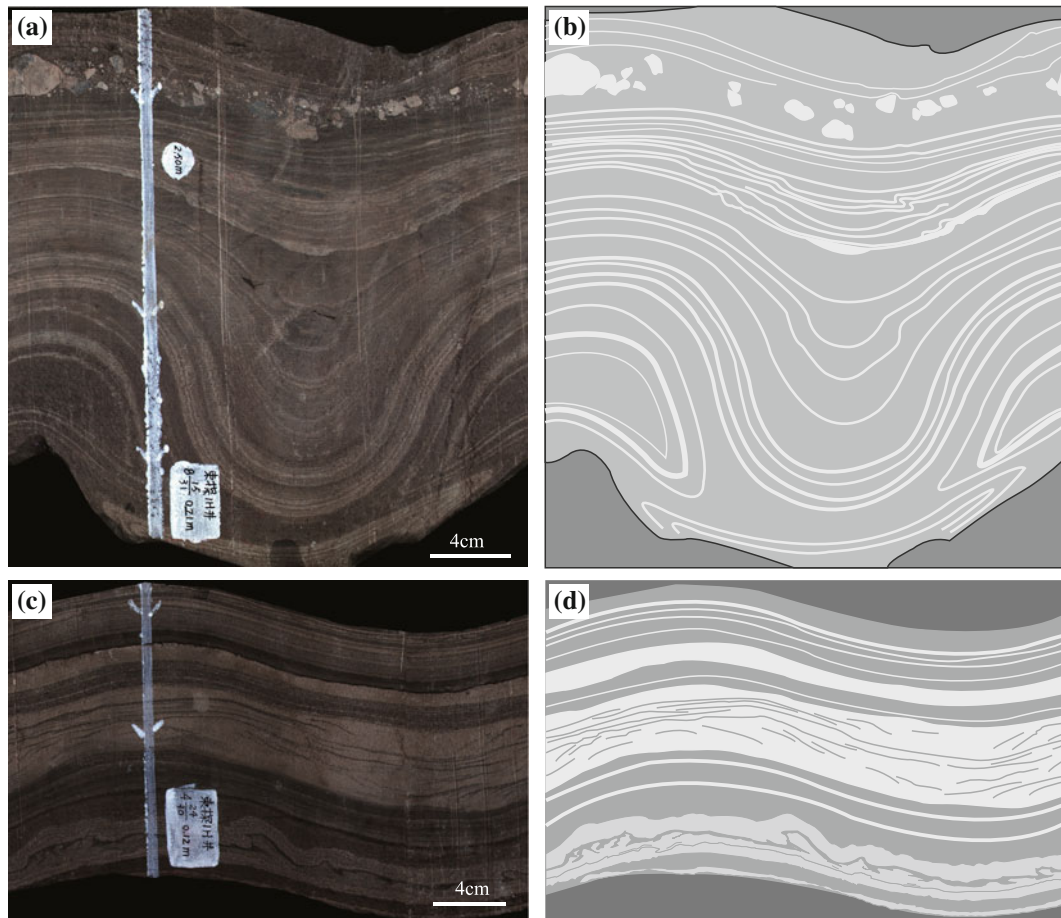
**Fig. 7.27** Vertically scanned core image and tracing of convolute lamination in Sequence III (from Zheng et al. 2015). **a–b** Deformation is showing laterally alternating synclines and anticlines. From well ST1H, at 3992.07 m. **c–d** Folded layers with irregular fold axes did not affect underlying and overlying strata. From well ST1H, at 3972.55 m. Arrows indicate the direction of the bottom of the strata, not the top

in Fig. 7.27b. The orientation of fold axes varies from inclined to nearly horizontal, and the fold amplitudes are about 2 cm (Fig. 7.27c–d).

Convolute lamination is a kind of small-scale deformational structure within a calcarenite bed or thin calcisiltite–calcilutite layers where the overlying and underlying layers are undisturbed. It is formed when sediments are still unconsolidated. The origin of similar deformational structures has been attributed to loading pressures (Dzulynski and Smith 1963), downslope slumping (Strachan 2002; Alsop and Marco 2011), and an elastic–plastic response of sediment to shear stress (Dzulynski and Smith 1963; Hibsch et al. 1997; Rodríguez-Pascua et al. 2000; Rodríguez-López et al. 2007; Rana et al. 2013) by currents on the sediment surface, or an earthquake. Based on lithology similarity of convolute lamination and overlying beds and the fold morphology lacking uniform axial planes, sediment loading and slumping can be ruled out. Shearing by currents can be discarded due to lack of erosional disconformities between convolute lamination and superjacent deposits. Consequently, the structure

is probably related to a hydroplastic deformation caused by earthquakes.

### 7.3.1.5 Load Structures, Flame Structures, and Ball-and-Pillow Structures

Load-flame structures, found in Sequence III, show several centimeters wide asymmetric concave profiles of light-gray calcarenite over dark-gray undulating calcilutite (Fig. 7.28). Flame-like calcilutite protrudes upward into coarser calcarenite (Fig. 7.28a–b). Scattered gravel-sized clasts of carbonate rock are mixed with medium- to coarse-grained calcarenite within the underlying laminae (Fig. 7.28a–b). The overlying beds are thin interbeds of calcisiltite and calcilutite that are undisturbed. Load and ball-and-pillow structures are present below a small synsedimentary fault in one example (Fig. 7.28c–d). Small-scale ball-and-pillow structures are nodules or elongated lenses made of fine-grained calcarenite about 0.1 cm in width (Fig. 7.28c–d).

These SSDSs show denser sediment sinking into less dense sediment (Suter et al. 2011). Flame structures always
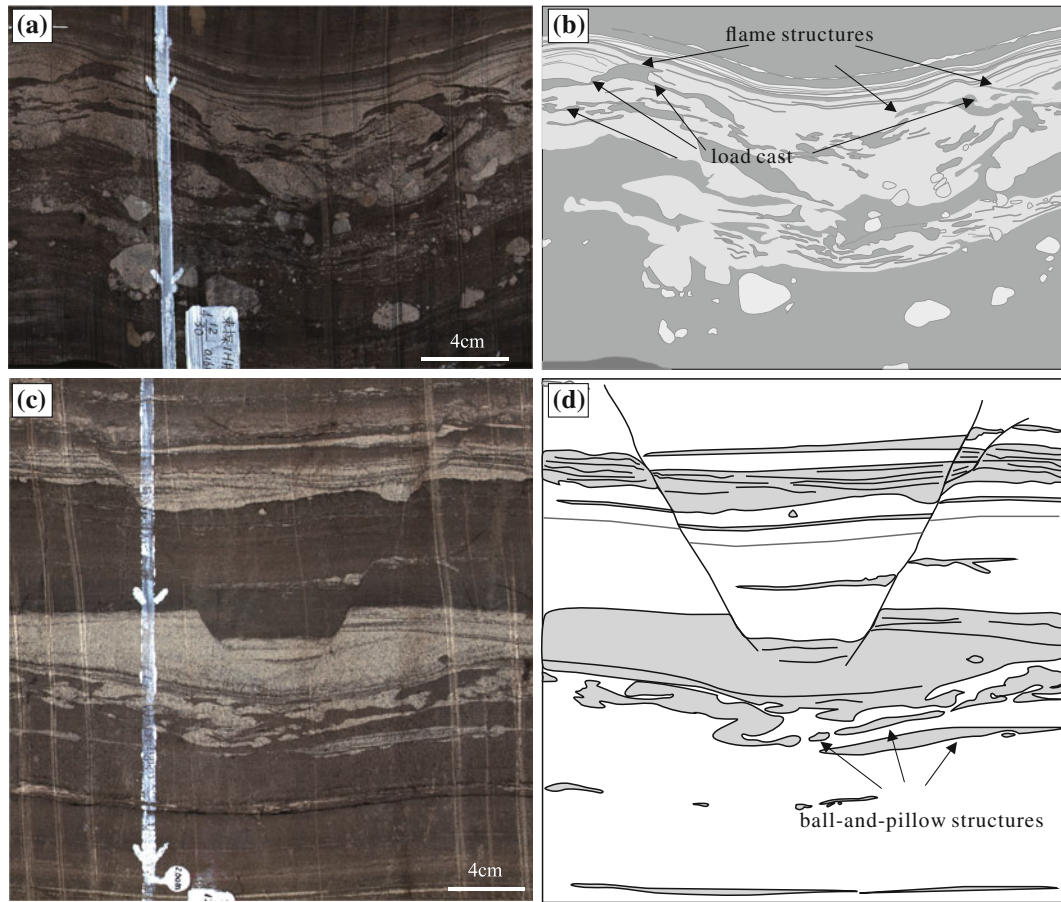
**Fig. 7.28** Vertically scanned core image and tracing of load, flame, and ball-and-pillow structures in Sequence III from the lowermost sub-member of Es₃ (from Zheng et al. 2015). **a–b** Load and flame structures. From well ST1H, at 3970.41 m. **c–d** Ball-and-pillow structure under a small synsedimentary fault. From well ST1H, at 4084.2 m. Arrows indicate the direction of the bottom of the strata, not the top

appear in association with load structures. Moreover, ball-and-pillow structures represent an advanced stage of load structures detached from the overlying parent bed (Ghosh et al. 2012). They may form as a result of gravitational instabilities related to density differences or uneven loading (Lowe 1975; Moretti et al. 1999; Neuwerth et al. 2006; Moretti and Sabato 2007). Alternatively, load structures may also form due to earthquakes (Du et al. 2008; Fortuin and Dabrio 2008; Rana et al. 2013), as simulated by Owen (1996). Large-scale load structures (>0.5 m) can be interpreted as seismites (Moretti and Sabato 2007), which nevertheless cannot be observed in the core.

### 7.3.1.6 Loop Bedding

Loop bedding, which is well developed in wells J97 and ST3, occurs alone or in chains in Sequence III and Sequence V. It is made of interlaminated calcisiltite–calcilutite, giving morphologies of loops or links of concentric rings. In most cases, the loop is 10 cm in width, and the height ranges typically from 3 to 10 cm (Fig. 7.29a–f). This structure can be associated with laterally extensive folding

and convolute lamination (Fig. 7.29a–b). A lump of irregularly shaped calcarenite is present in the lower part of the biggest loop in Fig. 7.29b. Deformation in Fig. 7.29c can be described as a simple loop-like deformation at first glance. However, closer inspection shows that some or all the individual layers are convoluted laminae interpenetratively deformed and there is a microfault filled with calcite across two sets of "loops."

These SSDSs are interpreted as loop beddings consisting of multiple-ringed concentric lamellas that are connected laterally. They are different from the chain-like loop beddings described by Calvo et al. (1998) and Rodríguez-Pascua et al. (2000) in appearance. The loop beddings here have convolute laminae and normal microfaulting displaying a ductile–brittle behavior of unlithified to progressively more lithified laminated sediments (Fig. 7.29e–f). This structure is interpreted as a result of the tensile stress of successive minor seismic shocks (Calvo et al. 1998; Rodríguez-Pascua et al. 2000; Yuan et al. 2006). The development of loop bedding is thought to reflect the low magnitude of earthquakes.
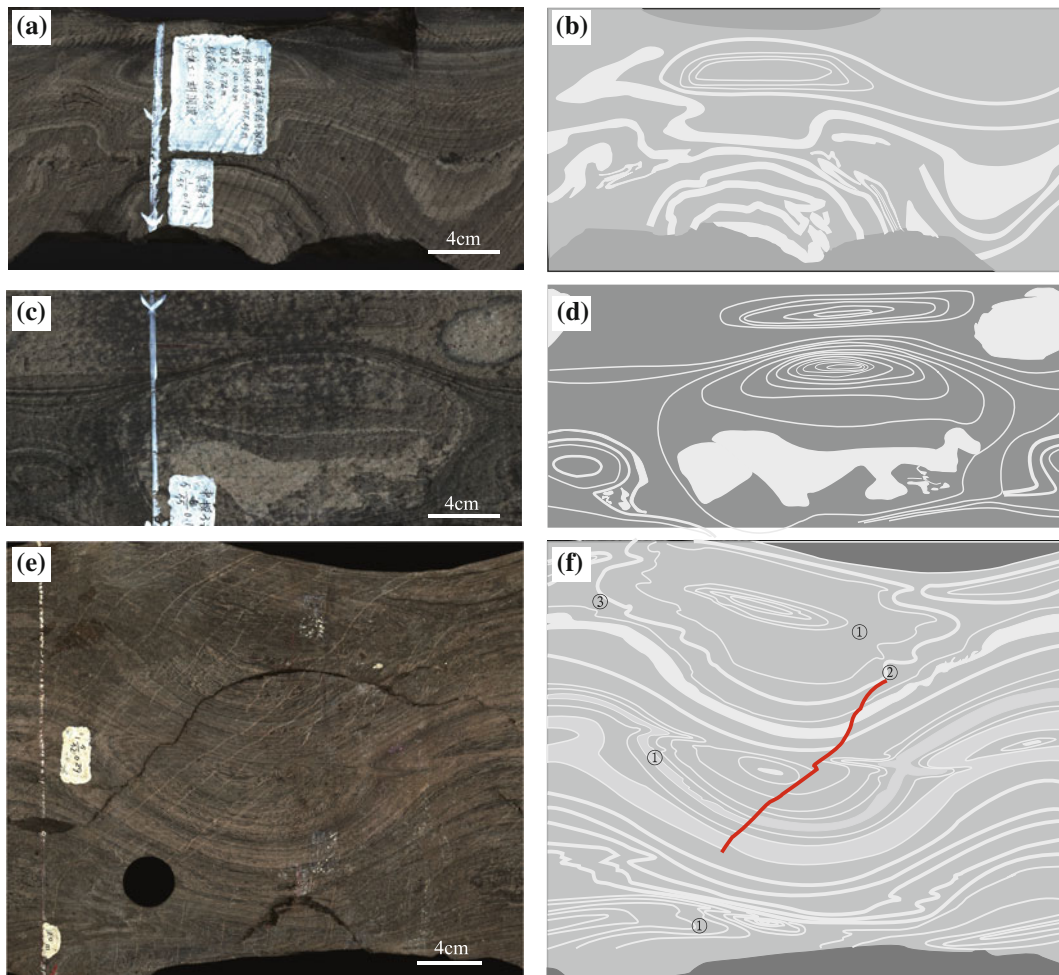
**Fig. 7.29** Vertically scanned core image and tracing of loop bedding in Sequences III and V (from Zheng et al. 2015). **a–b** Concentric loops with convolute lamination. From well ST3, at 3865.56 m. **c–d** Loop bedding. Note the complex deformation of calcarenite. From well ST3, at 3866.29 m. **e–f** ① Loop bedding, ② microfault, and ③ convolute lamination. From well J97, at 3449.24 m. Arrows indicate the direction of the bottom of the strata, not the top

### 7.3.1.7 Subsidence Structure

The laminae of calcilutite are bent downward with minor disruption by large gravel-sized clasts of weathered carbonate rock (Fig. 7.30) in this structure found in Sequence III and V. The size of these clasts varies from 0.5 to 5 cm, and the direction of long axes varies from upright to inclined to recumbent. The laminae exactly under the gravel-sized clasts have been significantly distorted.

Bent laminae appear to result from an interstitial overpressure and a drastic decrease in shear strength within the calcilutite. The most significant driving force might be an unstable density gradient. This overloading process is related to liquefaction induced by the rapid input of sediment on a soft substratum (Moretti et al. 2001). Deformation occurred when the underlying laminated calcilutite was poorly consolidated and water-saturated. It is assumed that weathered rock from the nearby Ningjin uplift fell into soft sediment

from a great height to form the dispersed gravel-sized clasts. The trigger mechanism may be earthquake activity.

### 7.3.1.8 Synsedimentary Faults

Various types of synsedimentary faults clearly moved consolidated to less consolidated strata vertically or at an angle are present in Sequence III and Sequence V of many wells, including small graben structures in wells ST3, ST1H, and J85 (Fig. 7.31a–e), microfaults in well ST1H (Fig. 7.31f–i), and a series of microfaults in well J97 (Fig. 7.31j–k). A vast majority of synsedimentary faults are normal faults between the unaffected upper and lower layers. The lithologies of the disturbed sediment consist of fine- to medium-grained calcarenite and locally calcilutite; however, there are exceptions, including pebble-sized carbonate gravel appearing in a synsedimentary fault (Fig. 7.31b–c). Some of the fault planes that are filled with sediments are flat (Fig. 7.31d–e),
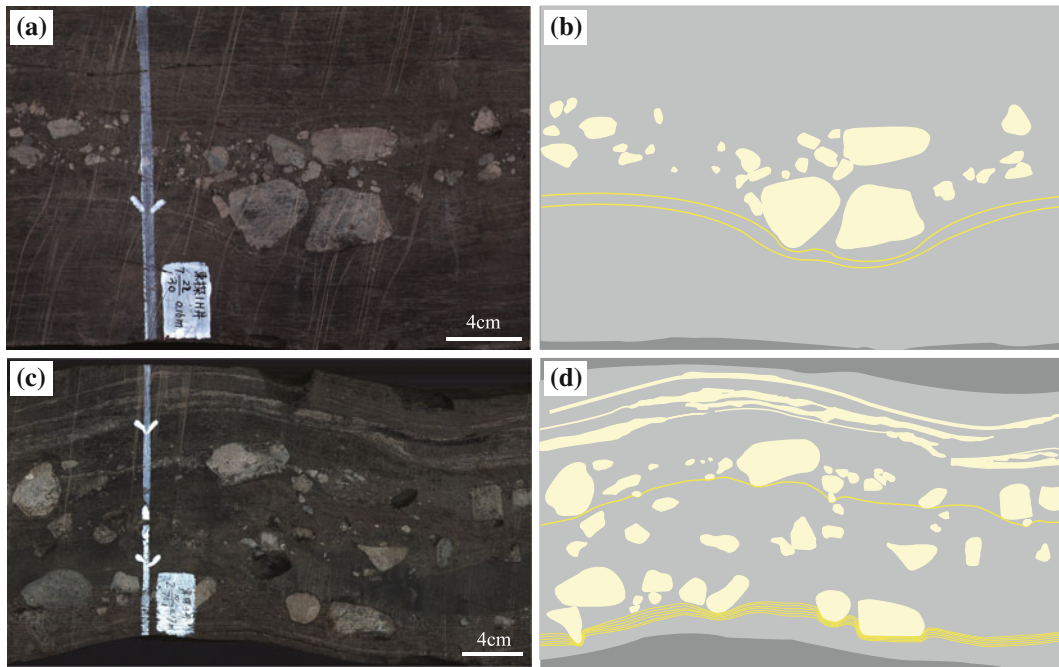
**Fig. 7.30** Vertically scanned core image and tracing of subsidence structures in Sequences III and V (from Zheng et al. 2015). **a–b** Bent laminae of calcilutite from well ST1H, at 3988.05 m. **c–d** Deformed bedding from well ST3, at 3676.84 m. Arrows indicate the direction of the bottom of the strata, not the top
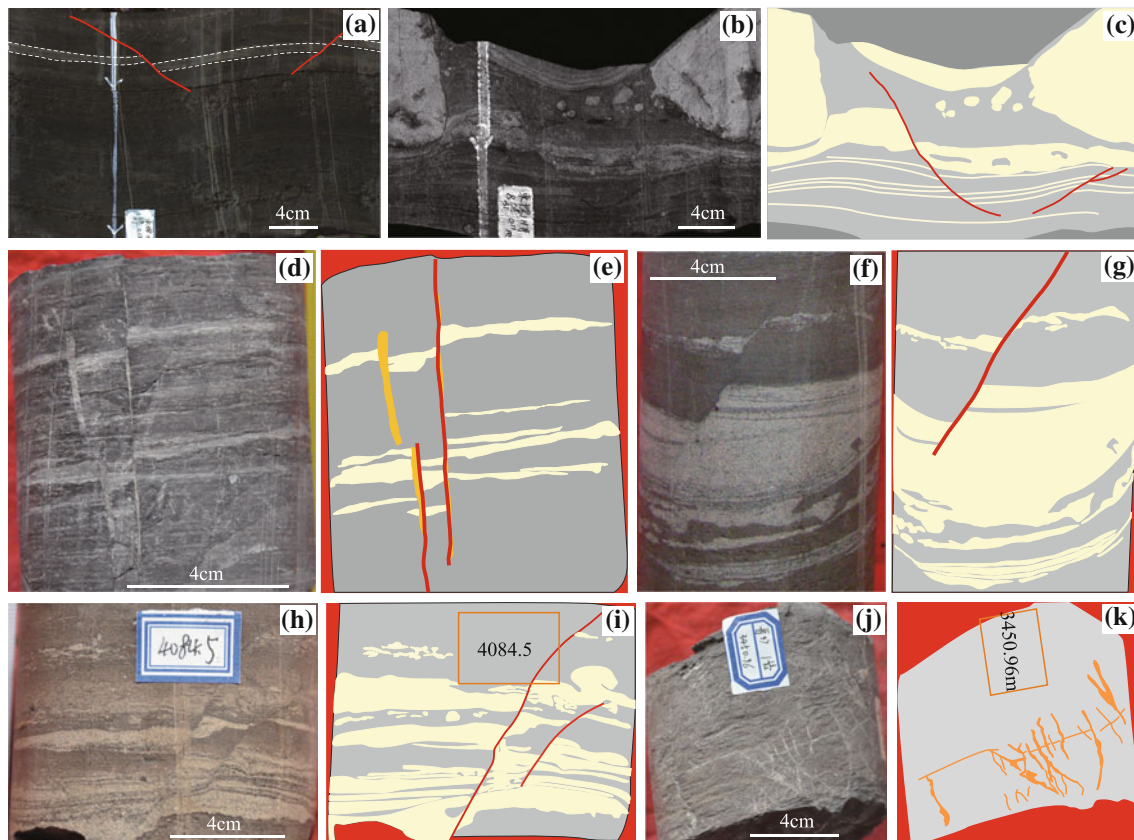


**Fig. 7.31** Various types of synsedimentary faults in Sequences III and V (from Zheng et al. 2015). **a** Small-scale graben. From well ST3, at 3800.94 m. **b–c** Pebble-sized clasts appear in a synsedimentary fault. The faults disappear downwards and do not affect the underlying laminated deposits. From well ST1H, at 3992.18 m. **d–e** Small-scale graben. From well J85, at 3770.95 m. **f–g** Normal faults. From well ST1H, at 4084.43 m. **h–i** Normal faults. From well ST1H, at 4084.5 m. **j–k** A series of microfaults. From well J97, at 3450.96 m. Arrows indicate the direction of the bottom of the strata, not the top

and some are irregular (Fig. 7.31b–c, f–i). The dip angle of the faults is large, about 50°–80° with offsets varying between 0.2 and 2 cm. Also, the thickness across the fault is incongruent in Fig. 7.31b–c, f–i.

Some synsedimentary fault planes were not planar originally because the sediments were not well consolidated and responded with a ductile behavior (Mohindra and Bagati 1996; Rossetti and Góes 2000; Neuwerth et al. 2006). Straight fault surfaces indicate brittle failure of the relatively consolidated material. Most of the synsedimentary faults are interpreted as a result of seismic activities (Pratt 1994; Mohindra and Bagati 1996; Bhattacharya and Bandyopadhyay 1998; Kahle 2002; Fortuin and Dabrio 2008; Taşgin et al. 2011; El Taki and Pratt 2012; Törő and Pratt 2015). Differential compaction may cause small-scale faults as well (Fortuin and Dabrio 2008; Törő and Pratt 2015), whereas such a mechanism is not possible here as the overlying bed is mainly laminated calcilutite or massive calcilutite, same as the faulted bed. A seismic origin is more probable.

### 7.3.1.9 Seismoturbidites

A large calcirudite bed of Paleozoic carbonate clasts from the Ningjin uplift with poor sorting appears in well ST3 over a total thickness of 100 m within Sequence III. The calcirudite is generally clast-supported with normal grading or structureless. The gravel-sized clasts (few millimeters to 1 m in length) range from angular, subangular, to subrounded with a matrix composed of calcilutite. The direction of major axes of the clasts is random, recumbent, inclined, or upright (Fig. 7.32a, b). Lithology of the clasts includes crystalline dolomite, micrite, oolitic limestone, bioclastic limestone, and flat-pebble rudstone.

By contrast, in well ST1H there is matrix-supported mixed-sourcecalcirudite containing significant soft-sediment deformation. The clasts are 0.5–10 cm in diameter, subangular to subrounded. The matrix is calcilutite, calcarenite, and pebbly calcirudites, mixed with organic matter and pyrite. Poorly sorted gravel-sized carbonate clasts in Fig. 7.32c constitute a loop that is roughly 10 cm wide and 8 cm high. Vortex-like structures composed of calcisiltite–calcilutite or calcarenite are distributed in the matrix of the calcirudites in Fig. 7.32d, e. Matrix-supported calcirudite with subangular clasts floating in the dark-gray matrix is intermingled with soft-sediment deformation, such as recumbent sedimentary dikes (Fig. 7.32d) and hydraulic shattering (Fig. 7.32f). Furthermore, syndepositional faults with 2 cm offsets were discovered in the matrix-supported calcirudite of well ST1H (Fig. 7.32f) at 3992.18 m.

Gravity flow deposits triggered by an earthquake and those triggered by changes in climate or sedimentation rates are difficult to distinguish (Gorsline et al. 2000; Shiki et al. 2000; Bertrand et al. 2008; Carrillo et al. 2008; Fanetti et al. 2008; Wagner et al. 2008; Van Daele et al. 2014) since they

all contain massive bedding and graded beds (Nakajima and Kanai 2000). Lithology, geochemistry, chronology, and physical properties can be used in the assessment of paleoearthquake activity (Gorsline et al. 2000; Wagner et al. 2008; Leroy et al. 2010; Faridfathi and Ergin 2012) in finer-grained sediments, but difficult in sediments composed of gravel-sized clasts. Seismoturbidites are the products of gravity-flow deposits as a response to seismic activity (Mutti et al. 1984), including debris-flow deposits and turbidites. Megaturbidites have been generally regarded as the result of an earthquake (Mutti et al. 1984; Séguret et al. 1984). The thickness of the clast-supported calcirudite in Sequence III of well ST3 (Fig. 7.32a, b) is up to 100 m. They can be considered as megaturbidites. There is no steep-slope paleotopography in the ST1H well area to form gravity-flow deposits along the slope of the Shulu Sag, as noted in the geometries of these beds (Fig. 7.6). Such continuous and thick calcirudite could not be the result of wave action or flood deposition because the large clasts are poorly sorted and most of them are angular. In addition, there is no sedimentologic evidence for storm activity within these successions. Due to the lack of other feasible mechanisms, these calcirudites are interpreted as slumps caused by earthquakes.

Turbidites were probably triggered by an earthquake if the sediments have a close relationship with autochthonous seismites. Syndepositional faults, which were discovered in the turbidites of well ST1H (see Fig. 7.32f) at 3992.18 m of Sequence III, suggest synchronicity of the seismites and turbidites. Also, many SSDSs are present with matrix-supported calcirudite in this Sequence of well ST1H (Fig. 7.32d–f). These characteristics provide strong evidence for an interpretation that the trigger mechanism of these debris-flow deposits or turbidites was indeed the earthquake activities.

### 7.3.1.10 Mixed-Source Calcirudite

Mixed-source calcirudite is relatively common in Sequence III of the Shulu Sag. This lithofacies contains two kinds of clasts. One is Ordovician and Cambrian carbonate rocks transported from the Ningjin uplift, and the other is Paleogene intrabasinal gravel-sized micritic intraclasts. The color of Paleozoic carbonate clasts is light gray or gray, and the size is smaller than the Paleogene intraclasts (Fig. 7.33a). The Paleozoic clasts are mainly angular to subangular micritic limestone and dolomite clasts with poor sorting from Ningjin uplift. The Paleogene intraclasts also have distinct boundaries but are deformed. These intraclasts show deformational characteristics of soft sediment such as elongation or squashed textures (Fig. 7.33b, c), giving lacerated or subrounded morphology (Fig. 7.33a–c). The long axes direction of intraclasts with burrs on the edge varies from upright to recumbent. The composition of the Paleogene intraclasts is dark-gray, massive calcilutite with shelly
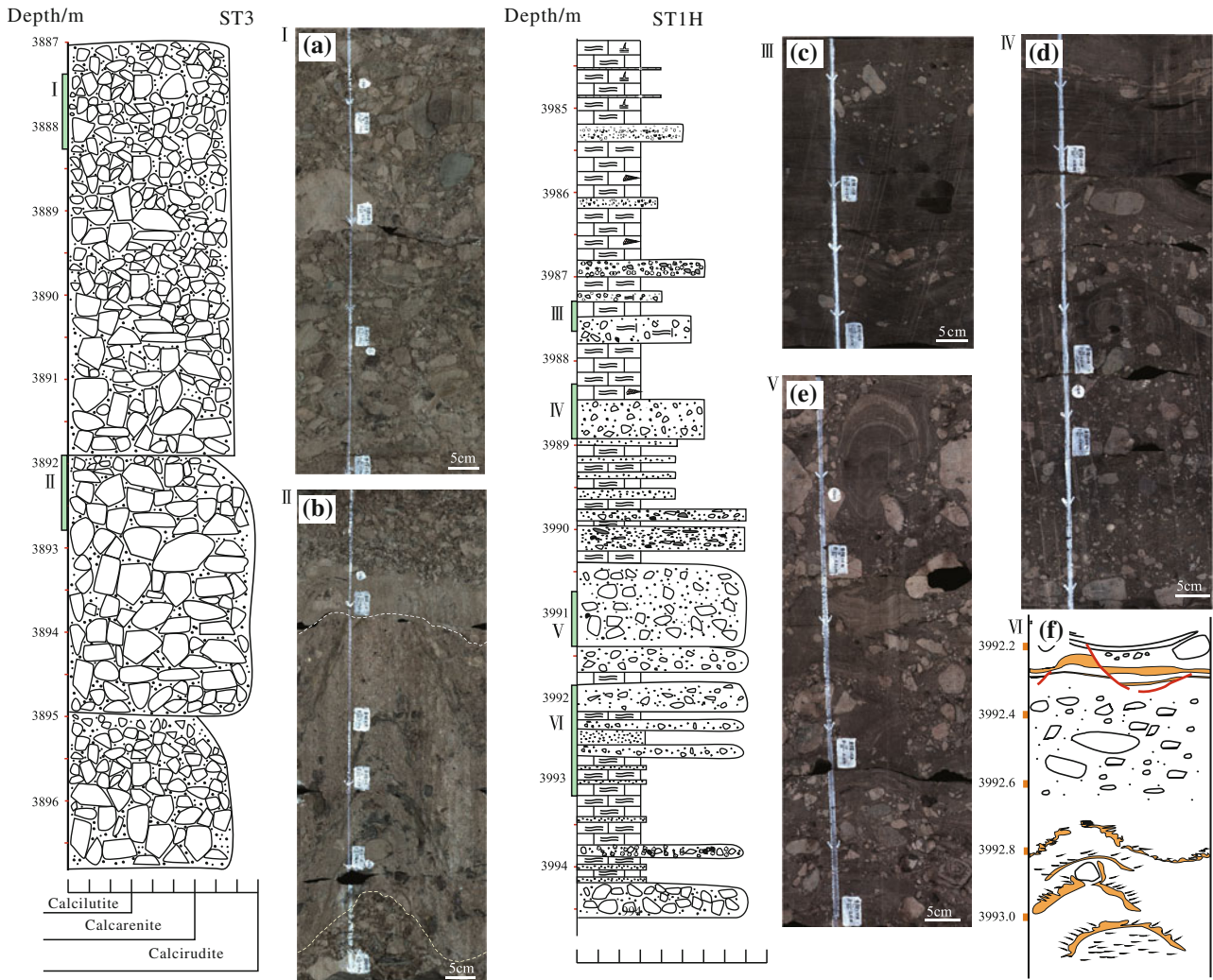
**Fig. 7.32** Seismoturbidites of Sequence III in the lowermost sub-member of Es3 in wells ST3 and ST1H of the Shulu Sag (modified from Zheng et al. 2015). The clast-supported calcirudite in well ST3 consists of angular–subangular coarse clasts poorly sorted, with random directions of the major axes of the clasts. Abundant soft-sediment deformation structures are in the matrix-supported calcirudite of well ST1H, such as calcarenite dikes and hydraulic shattering. Arrows indicate the direction of the bottom of the strata, not the top

fossils, small quartz grains, pyrite, and organic matter. Transport occurred while the rock clasts were unconsolidated. Twenty centimeters length of calcarenite dikes and microfaults with 0.5 cm offsets are present in the mixed-source calcirudite in Sequence III of well ST2X (Fig. 7.25c, d).

Mixed-source calcirudite is interpreted to be a particular manifestation of debris-flow deposits generated by earthquake activity. Gravel-sized micritic intraclasts transported while unconsolidated are like rip-up intraclasts of the eastern Alboran Basin (Braga and Comas 1999). They may be derived from erosion by the gravity flow on the underlying calcilutite substratum. Calcarenite dikes and microfaults are usually considered to be induced by seismic movements (Pratt 1998; Fortuin and Dabrio 2008; Taşgin et al. 2011; Törő and Pratt 2015), and their presence in association with the calcirudite demonstrates a direct link between the mixed-source calcirudite and seismicity.

### 7.3.1.11  Other Structures

Morphology of these deformation structures is similar to load structures induced by liquefaction. One-centimeter-wide symmetric but elliptical shape composed of fine-grained calcarenite occurs in the calcilutite below the overlying strata of calcarenite in Sequence III (Fig. 7.34a, b). On its right, long or thick pores are present in an approximately horizontal direction, and they are filled with sediments from an overlying layer. The structures can be interpreted as calcarenite-filled burrows. Many small-scale nodules or balls consisting of fine-grained calcisiltite and calcarenite (Fig. 7.34c, d) occur in the massive calcilutite under calcarenite beds. Most of them are about 0.1 cm in
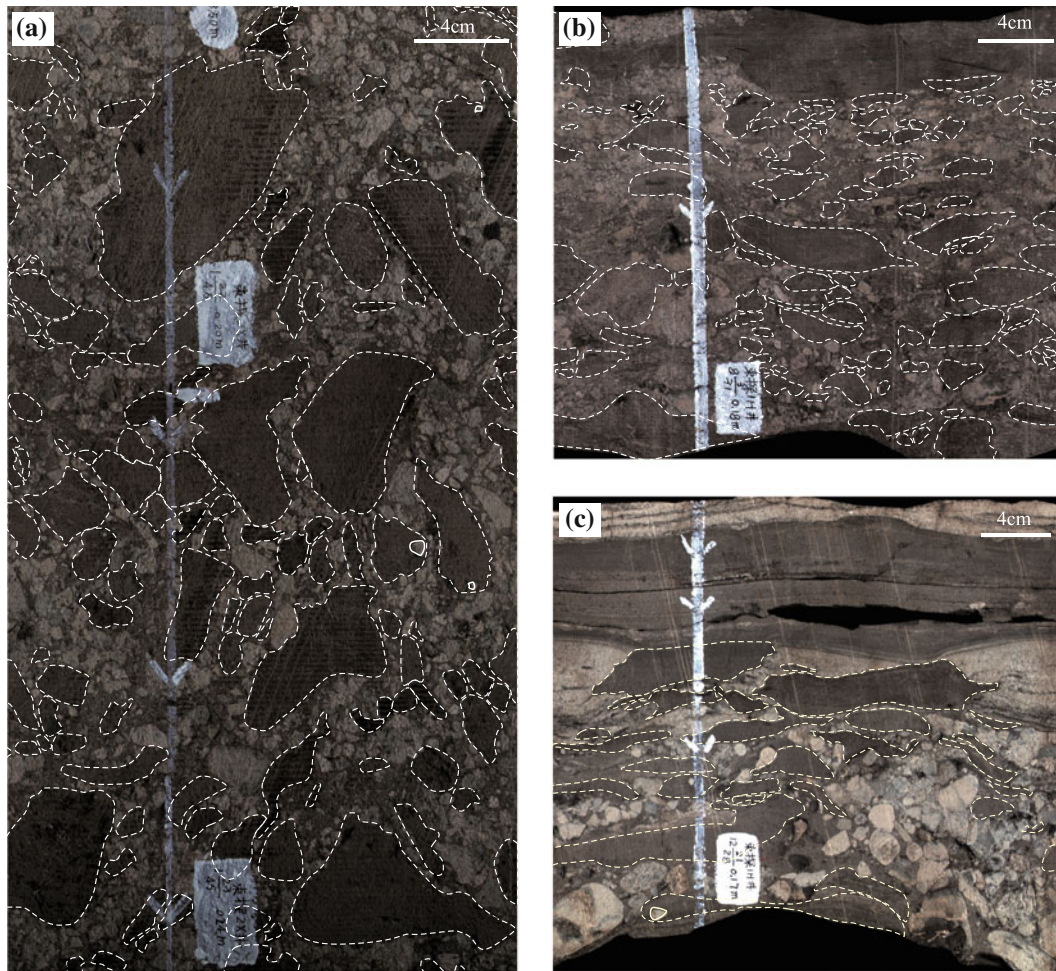
**Fig. 7.33** Mixed-source calcirudite in Sequence III from the lower-most submember of Es3 of the Shulu Sag (modified after Zheng et al. 2015). The dark-gray parts are Paleogene micritic intraclasts mixed in with the Paleozoic light-gray carbonate clasts. The matrix is calcisiltite. The micritic intraclasts are elongated or squashed as well as lacerated or subrounded. **a** From well ST2X, at 3725.2–3725.61 m. **b** From well ST1H, at 3989.89 m. **c** From well ST1H, at 4086.34 m. Arrows indicate the direction of the bottom of the strata, not the top

width and generally show irregular shapes. The millimeter-thick nodules or balls can be attributed to bioturbation by animals moving through the layers of alternating lithology (Moretti and Sabato 2007).

### 7.3.2 Seismites Sequence

The most sensitive sediments to the earthquake activity are fine-grained materials (Moretti et al. 1999; Owen and Moretti 2011). For this reason, seismites develop more readily in deltaic plains and lacustrine environments, where such silty deposits, including a large volume of water for saturation of sediments, are common.

A complete vertical sequence of about 2.4 m thick found through core observation in well ST1H in Sequence III shows, from the base to the top: (A) underlying undeformed layers, (B) synsedimentary faults, (C) liquefied carbonate rocks, (D) allogenic seismoturbidites, and (E) overlying undeformed layers (Fig. 7.35).

Before an earthquake, the consolidation strata were undisturbed, that are, the underlying undeformed layers (A), composed of calcilutite with thin-bedded calcisiltite. When a quake was initiated, the consolidation strata were unaffected while ductile strata tended to flow or brittle deformation occurred under stress for existing unconsolidated and semisolid sediment. Next, a layer containing synsedimentary faults (B) formed a small graben associated mainly with some small load and ball-and-pillow structures (Fig. 7.35). As the seismic activity reached a climax, liquefaction started. The main lithology of Unit C (liquefied carbonate rocks) was calcilutite and minor calcisiltite, and the structures comprised flute casts, ball-and-pillow structures, and some deformation. In the upper part of this unit, microfaults were observed through the microscope. Then, energy started to decay and allogenic seismoturbidites (D) which are from
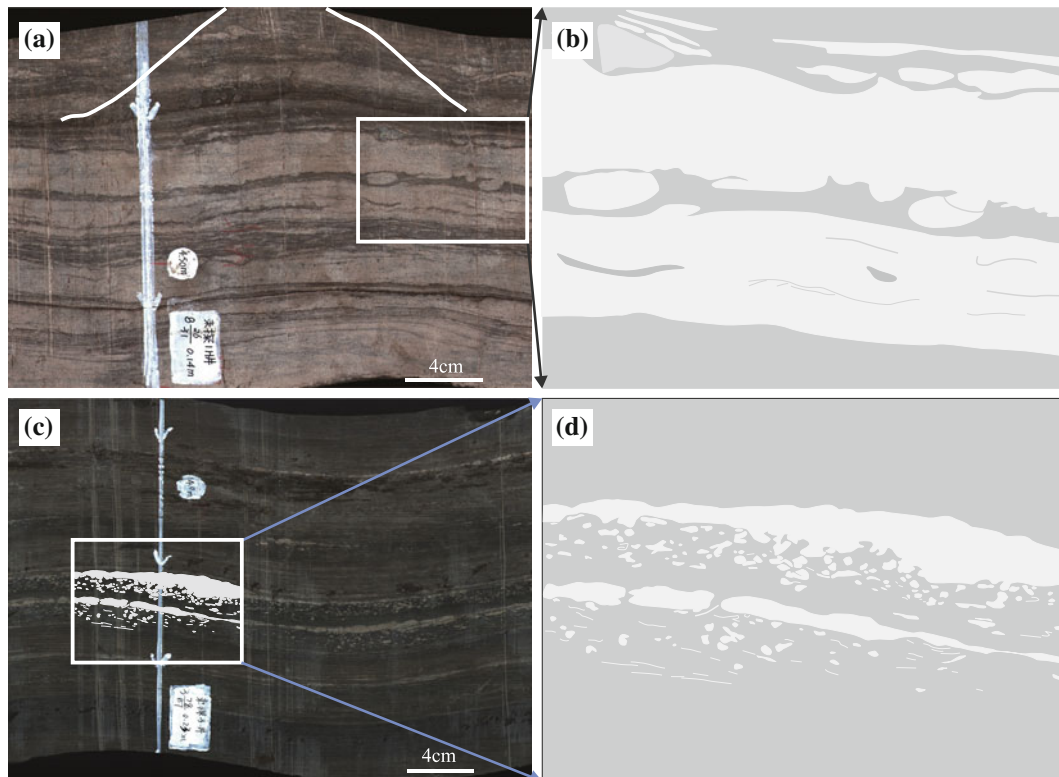
**Fig. 7.34** Other structures in Sequences III from the lowermost submember of Es$_3$ of the Shulu Sag (Zheng et al. 2015). **a–b** Bioturbation traces. From well ST1H, at 3993.97 m. **c–d** Small-scale nodules or balls. From well ST3, at 3802.78 m. Arrows indicate the direction of the bottom of the strata, not the top

Ningjin uplift and composed of "matrix-supported calcirudite" with Paleozoic clasts of varying sizes, were deposited. Breccia dikes were present in this layer as well. After the earthquake, undeformed sediments continued to be deposited, showing an abrupt contact with the underlying turbidite segment. The overlying undeformed layer (E) was calcilutite with thin-bedded calcisiltite, about 2 m thick (part of it is shown in Fig. 7.35). This seismites sequence reflects the seismic process of increasing then decreasing energy levels.

Sedimentary sequence patterns reflect the depositional process of an earthquake. The composition of a seismites sequence may be not the same in all cases (Mutti et al. 1984; Song 1988; Qiao et al. 1994). Sequences of seismic events were first described as (from the base) consisting of undisturbed beds, fault-grading beds, a rubble zone, a homogenized zone, and undisturbed beds (Seilacher 1969, 1984). A complete sequence of a calcareous megaturbidite induced by earthquakes can be up to 5–30 m (Mutti et al. 1984; Séguret et al. 1984), which has similar components and reflects the same change in energy. A seismite–tsunamite sequence with hummocky bedding represents an earthquake event with a related tsunami event (Song 1988; Qiao et al. 1994; Du et al. 2001). Sequence A–B–C–D–E reflects the whole process of a strong seismic event from initiation to

culmination, then decline and cessation (Fig. 7.35). Like in any other sedimentary sequence (e.g., Bouma sequences), some unit or units may be absent in the section (Qiao et al. 1994). Incomplete combinations, such as C–D–E and D–E, are prevalent. The full pattern of a seismites sequence is controlled by the magnitude of the earthquake, lithology, and the structural position where an earthquake occurred (Yuan 2004).

### 7.3.3　Criterion of Seismites

#### 7.3.3.1　Origin of Deformation

Morphologic characteristics of deformed structures are controlled by the initial rheologic properties of the sediment and the driving force system, not by the trigger (Owen 1987; Ezquerro et al. 2015). Consequently, it is hard to distinguish between seismically and non-seismically induced SSDSs (Owen and Moretti 2011). However, analysis of morphology and the sedimentary and tectonic context will aid in determining the mechanism promoting sediment deformation (Törő et al. 2015; Törő and Pratt 2015).

Several SSDSs can be attributed to endogenic processes, such as bioturbation (Fig. 7.34a–d). Lack of evidence for

| Sequence | Unit | Depth/m | Sequence features | Structure and lithology | Photos of cores |
|---|---|---|---|---|---|
| overlying undeformed layer | E | 4082.2 | | calcilutite with thin-bedded calcisiltite | |
| allogenetic seismoturbidite | D | 4082.4 – 4082.6 | | Matrix-supported extraformational calcirudite | |
| | | | | breccia dike | |
| | | 4082.8 – 4083 – 4083.2 | | Matrix-supported extraformational calcirudite | |
| liquefied carbonate rocks | C | 4083.4 | | calcilutite with thin-bedded calcisiltite | |
| | | 4083.6 | | deformation structures | |
| | | 4083.8 | | ball-pillow structures | |
| | | 4084 | | flute cast | |
| synsedimentary faults | B | 4084.2 | | syndepositional faulting ball-pillow structures | |
| underlying undeformed layer | A | 4084.4 – 4084.6 | | calcilutite with thin-bedded calcisiltite | |

**Fig. 7.35** Seismites sequence in well ST1H from Sequence III in the lowermost submember of Es$_3$ of the Shulu Sag (after Zheng et al. 2015). From the base to the top: underlying undeformed layer, synsedimentary faults, liquefied carbonate rocks, allogenic seismoturbidite, and overlying undeformed layer. The pattern of deformation in this sequence reflects the changing energy levels during an earthquake. Arrows indicate the direction of the bottom of the strata, not the top

subaerial exposure precludes a desiccation origin. No ripple cross-lamination or hummocky cross-stratification indicating storm deposits (Molina et al. 1998; Alfaro et al. 2002) is present in the lowermost submember of the Shahejie 3 of the Shulu Sag.

Given the tectonic setting, the best explanation for the trigger mechanism for these SSDSs is syndepositional to post-depositional earthquakes. The following factors point to

a seismic triggering agent within the sediments of the lacustrine Shahejie Formation: (i) Seismites are widely distributed in the Shulu Sag, such as in wells ST1H, ST3, J85, J97, and J116X. (ii) There are multiple sets of stacked "seismites" separated by undeformed beds. (iii) Seismites of Paleogene age have also been found in the nearby Paleocene Jinxian Sag of the Jizhong Depression that is similar in structure to the Shulu Sag (Yang et al. 2014). Those

interpreted seismically induced structures include water-escape channels, load casts, flame structures, ball-and-pillow structures, and micro-synsedimentary faults. (iv) Structural association of synsedimentary faults with sedimentary dikes, load structures, and loop bedding has been interpreted as concurrently seismically deformed (e.g., Kahle 2002; El Taki and Pratt 2012; Wallace and Eyles 2015). (v) Similar SSDSs have been reproduced in the laboratory through the modeling of earthquake effects in water-saturated soft sediments (Owen 1996; Moretti et al. 1999). (vi) Growth indices of the nearby NW-trending Taijiazhuang fault and the NNE-trending Xinhe fault during the third member of the Shahejie Formation (Kong et al. 2005) indicate that these faults could have controlled the topographic relief within the basin and exerted a significant influence on the distribution of sediment and its deformation.

### 7.3.3.2  Episodic Activities

Like modern earthquakes, paleoearthquakes may be episodic (Qiao and Li 2009; Feng 2013). An active seismic period normally has some activity events in succession. An ancient earthquake record comprises some deformation of sediment layers (Feng 2013). Several seismite layers separated by undeformed sediments can be considered as an earthquake episode. Some episodes compose an active period when the time interval between two episodes is longer than the time between its separate earthquake sedimentary records. The long-time interval is manifested by a thick succession of undeformed sediments between two episodes in stratigraphic sections. In the observation of outcrop or core, if there are multiple soft-sediment deformation and brittle deformation layers in a succession, it is most probable that the deformation was caused by ancient earthquakes, not by other factors (Qiao and Li 2009).

In the core from well ST1H located in the hanging wall of the Xinhe fault, about 20 activity events (in blue) are recorded based on soft-sediment deformation patterns. They can be interpreted as nine seismic episodes and two active phases. One is colored pink from 3959 to 3994.4 m and the other is light green from 4072 to 4087 m (Fig. 7.36). More than 10 layers of soft-sediment deformation within a 10-m length of core are present (e.g., 3985–3994.4 m and 4077.6–4087 m). Soft-sediment deformation recurring intensively within strata over several meters may be explained best as the seismic origin.

### 7.3.3.3  Relationship of Seismites, Seismicity, and Sequences

Seismites can provide information about the magnitude and occurrence of ancient earthquakes. Soft-sediment deformation is mainly distributed in Sequence III from the lowermost submember of Es3 in the Shulu Sag (Fig. 7.37). Allochthonous seismoturbidites and mixed-source calcirudite are well developed here. In comparison, fewer seismites exist in other sequences, but this may be due to the distribution of the drilled cores. However, considering the impact of the earthquakes on underlying consolidated strata, the fractures in Sequence III are rarer than in Sequence I and Sequence II, which points to earthquake activity in Sequence III that is perhaps more substantial than that in Sequence IV and Sequence V. Earthquakes may have occurred during the deposition of Sequence IV and Sequence V, but much weaker in intensity.

Loop bedding and subsidence structures are the main types of seismites in Sequence V (Fig. 7.37). As described, loop bedding was interpreted as a result of the tensile stress of successive minor seismic shocks. The core located in Sequence IV of well J97 is less than 5 m thick, composed of calcisiltite, and is undisturbed, so minimal seismic activity in IV is inferred. In Sequence II, there are almost no soft-sediment liquefied and compressional structures and just one or two small-scale faults. In Sequence I, no seismites are present. Earthquakes appear to have been most active in Sequence III during the deposition of the lowermost submember of Es3 in the Shahejie Formation of the Shulu Sag, east China (Fig. 7.38).

## 7.4  Provenance and Depositional Processes of the Calcirudites

The calcirudites in Shulu Sag can be divided into two major types based on (1) the integration of the regional geology, drilling, well log and seismic data, (2) detailed analysis of the cores from wells ST1H, ST3, Jin116X, and Jin100, and (3) sedimentary structures and facies distribution.

The first type of calcirudites is interpreted to be deposited by braided channels on fan delta plains and subaqueous channels in fan delta front. The second type of calcirudites is mass transport deposits and seismites triggered by earthquakes with distinguishable sort deformation structures (such as liquefaction structures, flame structures, and ball-and-pillow structures). Sequences I and II include fan delta, semi-deep lake, and deep lake deposits. Sequence III consists of mass transport deposits and seismites triggered by earthquakes. The areal extent of the calcirudites became limited during the deposition of Sequences IV and V. Therefore, we focus primarily on Sequences I and III for more detailed discussion of the provenances and depositional processes of the two types of calcirudites.
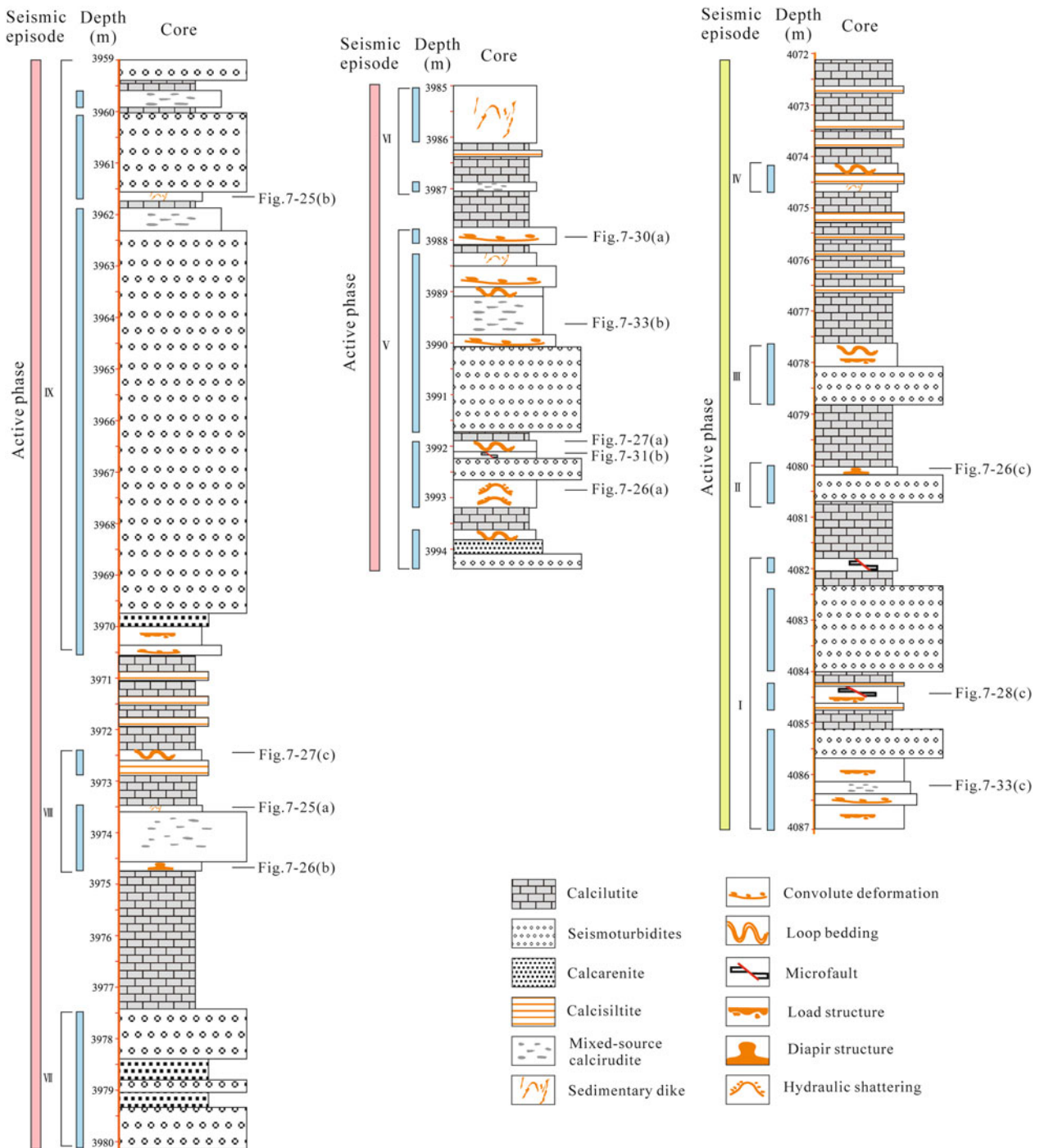
**Fig. 7.36** Soft sediment deformation in well ST1H in Sequence III from the lowermost submember of Es₃ of Shulu Sag (modified after Zheng et al. 2015). An ancient earthquake record comprises SSDSs, seismoturbidites, or mixed-source calcirudites. Each section can be considered as an activity event (in blue). They are separated by thin undeformed layer. Several seismite layers separated by thick undeformed sediments can be regarded as an earthquake episode. Some episodes compose an active period. About 20 activity events (blue) are present, which can be interpreted as nine seismic episodes and two active phases. One is colored pink from 3959 to 3994.4 m, and the other is light green from 4072 to 4087 m
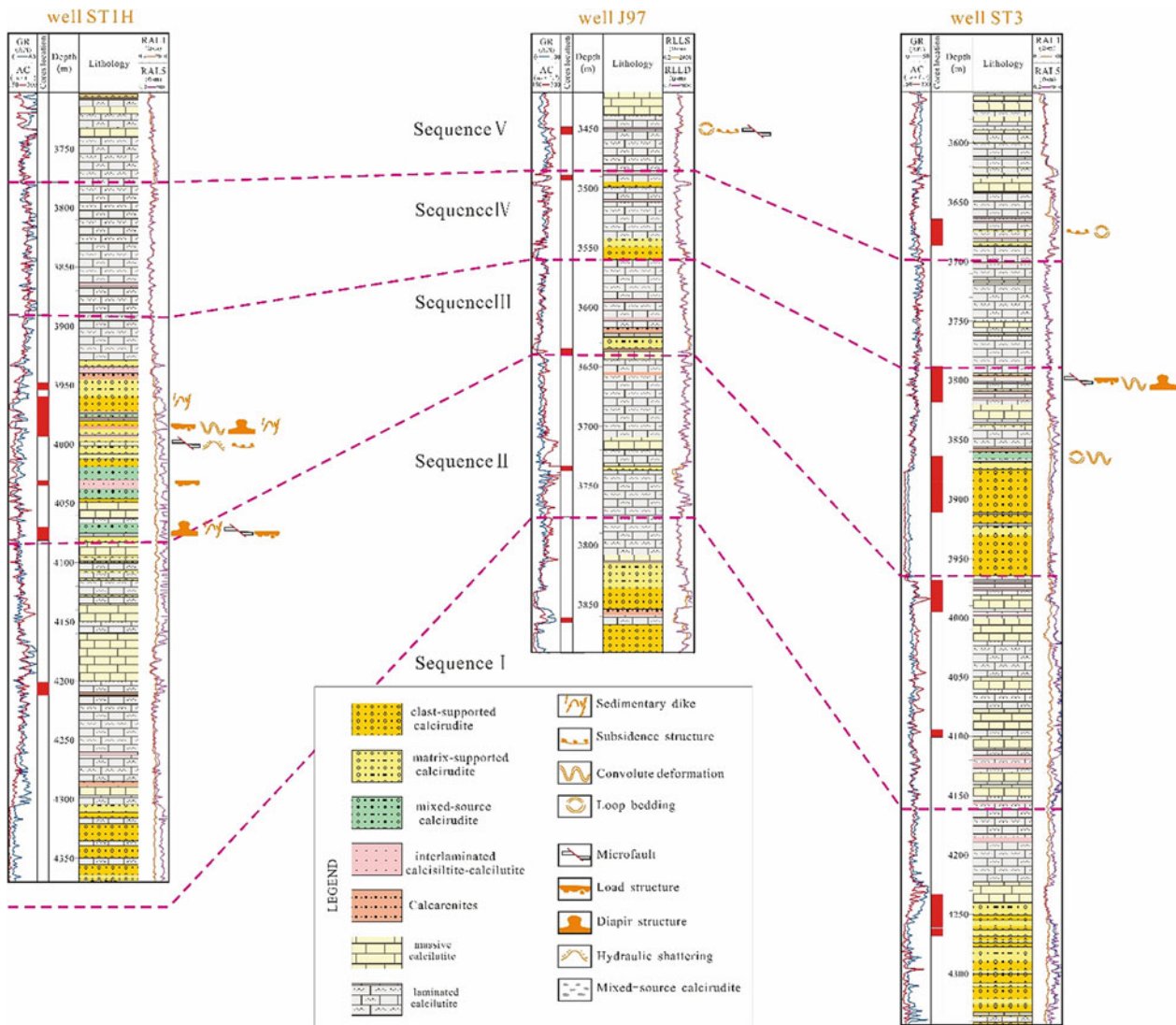
**Fig. 7.37** Distribution of seismites in the cores from the lowermost submember of Es3 of the Shulu Sag (Zheng et al. 2015). Soft-sediment deformation is mainly present in Sequence III and fewer seismites exist in other sequences. It can be inferred then that the earthquakes are most active in Sequence III and weaker to absent in the other sequences. The red pillars in the second column show the location of the drilling core

### 7.4.1  Depositional Environments and Facies Models of the Calcirudites

1. Fan delta

(1)  Sedimentary characteristics

The calcirudites were widely distributed during the deposition of Sequence I and had been found in wells such as ST2X, ST3, Jin94, Jin97, and Jin116X. Based on the sedimentary characteristics of these calcirudites, they have been interpreted as fan delta deposits. The fan deltas are characterized by the alternation of the relatively low base flows and catastrophic flood events. The flood events are far more efficient in transporting and depositing sediments (Zhang et al. 2000), which often results in nearly instantaneous and catastrophic sedimentary records (Xue and Galloway 1991; Zhu and Xin 1994). Due to the proximity to the source area, the deposits of fan deltas are mainly controlled by the provenance and are typically sand-gravel mixtures with poor sorting and high clay content. The textural maturity of sediments is also low. In general, a fan delta can be divided into delta plain, delta front, and pro delta subenvironments.

Fan-delta plain is the subaerial part of the fan delta and is characterized by debris flow and braided gravel-bed river sedimentation (Jiang 2010). The braided river deposits are dominated by the clast-supported extraformational calcirudites (Fig. 7.39a, b), which have light gray to gray colors.
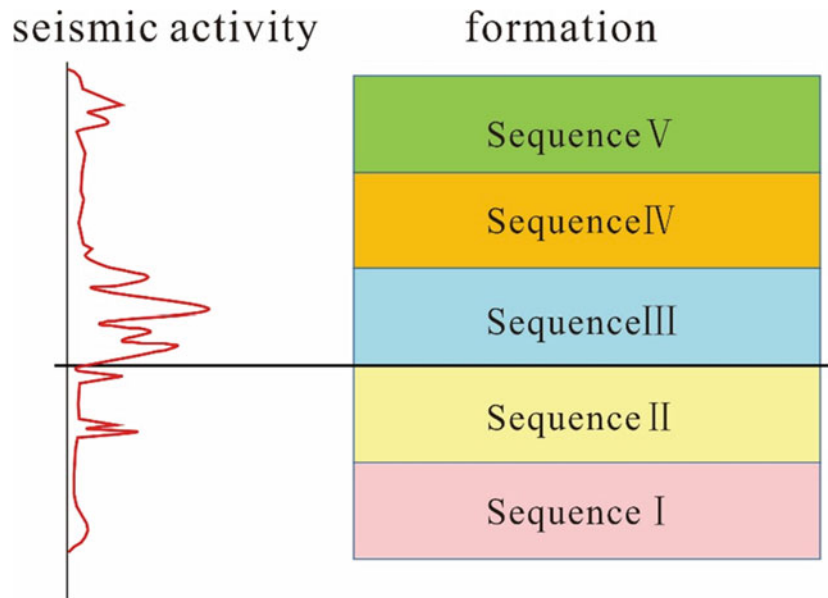
The gravels are poorly sorted and in close contact with each other (Fig. 7.39c), with the largest grain size being ca. a dozen-odd centimeters. The majority of the gravels are subrounded and they mainly originate from lime mudstone and pellet packstone, with few from dolostone. The intergranular spaces are filled with clay- to sand-sized terrigenous carbonate rock debris. Most calcirudites beds have normal grading and erosional bases.

The fan delta front is dominated by the clast- or matrix-supported extraformational calcirudites (Fig. 7.39d–g) with thin layers of calcilutites. Braided channel deposition includes both clast- and matrix supported extraformational calcirudites. The calcirudite beds are mostly massive with single bed thickness of ca. 1 m. Typical features of subaqueous channel deposits are uncommon, with the only occurrence in the 14th coring of well ST3. The calcirudite bed is composed of clast-supported terrigenous gravels and shows imbrication and normal grading (Fig. 7.39d). The gravels at the bottom have grain sizes of 4–5 cm and gradually fine into gravels with the size of ca. 1 cm. The gravels are gray to dark gray, medium to well sorted and subrounded. The main source rocks for the gravels are lime mudstones (Fig. 7.39f), with few pellet packstones and microcrystalline dolostone.

The interfluvial deposits are mainly composed of calcisiltite and laminated calcilutite, with some containing plant stem fossils and coal fragments. The mouth bar deposits have been found in the lower part of the 16th coring of Well ST3. The mouth bar deposits coarsen upwards from the matrix-supported calcirudites at the bottom to clast-supported calcirudites at the top (Fig. 7.39e). The gravels of the matrix-supported calcirudites are subrounded

and well sorted. The source rocks of the gravels include lime mudstone (Fig. 7.39g), microcrystalline dolostone and bioclastic limestone.

The prodelta marks the transition from the delta and the semi-deep lake and contains dark-colored laminated calcilutite alternating with thin layers of calcisiltite or calcarenite (Fig. 7.39h–k). The deposits of the prodelta were not stable and may form sediment gravity flows under the influence of external triggering mechanisms. The gravity flows can form calcarenites or calcisiltites. The calcisiltites lack the A and B intervals of Bouma sequence, and only show intervals DE or CDE. The massive calcilutite is also one of the principal facies of the prodelta, which usually contains quartz, carbonate rock fragments, and organic matter.

(2) Facies model

The majority of previous work on fan deltas focused on marine basins (Wescott and Ethridge 1980; Dutton 1982; Vos 1981; Tamura and Masuda 2003; McConnico and Bassett 2007), and only a few studied fan deltas entering lakes (Sneh 1979; Pollard et al. 1982; Pondrelli et al. 2008). Researchers in China have worked mainly on lacustrine fan deltas (Zhu and Xin 1994; Sheng 1993; Luo et al. 2009; Hu et al. 2005; Li 1982; Zhang 2006). The key difference between the two types of fan deltas is that the deposits in lacustrine basins have undergone much less reworking by waves and tides compared to that in the ocean. In addition, the lake level fluctuations are often more frequent than sea level changes, leading to more rapid and abrupt facies changes.

The fan delta system can develop in the gentle slope belt during the rifting of half-graben lake basins (Wang 1993).

| Facies | Sub-facies | Facies succession | core photos | slice photos |
|---|---|---|---|---|

Fan delta — fan delta plain

**Well J100**

Depth/m   Lithology   Microfacies

braid-river channel

A — Well J100 3495.79m  Clast-supported extraformational calcirudite
B — Well J100 3495.38m  Clast-supported extraformational calcirudite
C — Well J100 3495.38m（-）  Clast-supported extraformational calcirudite

Fan delta — fan delta front

**Well ST3**

Depth/m   Lithology   Microfacies

distributary channel
mouth bar
mouth bar
mouth bar

D — Well ST3 4251.5-4251.74m  inbricate structures with normal graded bed sequence
E — Well ST3 4265.1-4265.5m  reverse graded bedding
F — Well ST3 4252.76m（-）  gravel of micrite limestones
G — Well ST3 4265.36m（-）  Clast-supported extraformational calcirudite

Fan delta — pre-fan delta

**Well ST1H**

Depth/m   lithology

H, I — Well ST1H 4074.53-4074.73m / Well ST1H 4075.88-4076.1m  calcilutite interbedded with calcarenite
J — Well ST1H 4209.24m（-）  Laminated calcilutite
K — Well ST1H 4211.14m（-）  Laminated calcilutite

**LEGEND**

- Clast-supported extra-formational calcirudite
- Matrix-supported extra-formational calcirudite
- Mixed-source calcirudite
- Calcarenite or calcisiltite
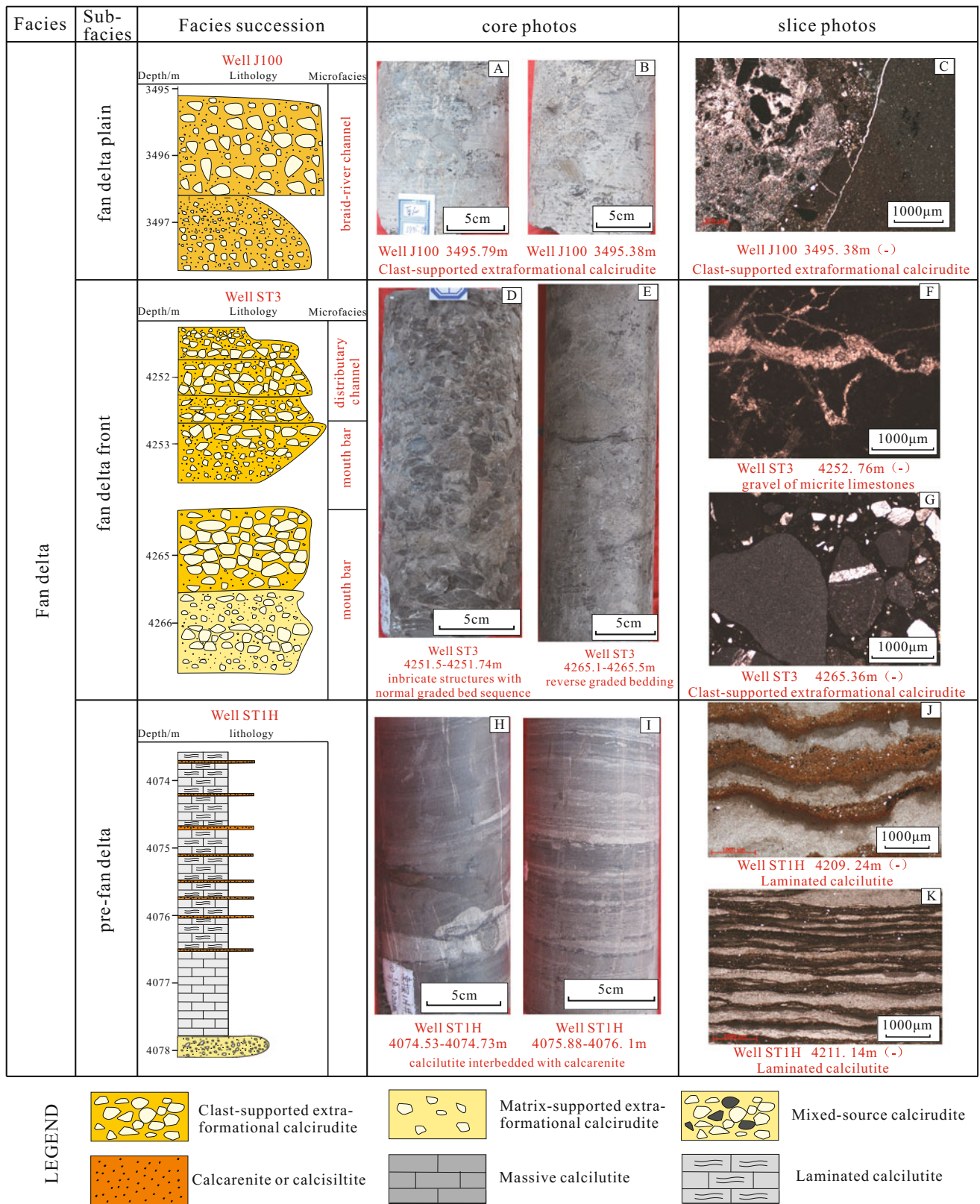- Massive calcilutite
- Laminated calcilutite

**Fig. 7.39** Sedimentary characteristics of fan deltas (modified after Liu et al. 2017)

During the early stage of Es$_3$, the Shulu Sag had undergone extensive rifting, and the Ningjin uplift formed the west slope of the basin (Kong et al. 2005). During this period, the basin was characterized by steep and narrow slope (Cui et al. 2003), abundant sediment supply, and arid climate. Under the influence of catastrophic flood events, the sediments from the Ningjin uplift were transported and deposited near the lake shore and formed the fan delta plain. The dominant facies is the clast-supported extraformational calcirudites. When the braided rivers entered the lake, they became the subaqueous channels of the delta front. The main facies include both clast- and matrix-supported extraformational calcirudites. The lateral stability of the channels is low, leading to poorly developed or missing mouth bars (Xue and Galloway 1991; Li 1982). As the sediments rapidly accumulated in the front, they were unstable and transported under the external triggering mechanism to form gravity flow deposits (Zou et al. 2009). Fine-grained terrestrial material was in suspension and deposited in semi-deep lake and deep lake. The sediments and planktonic algae together formed the organic-rich calcilutite (Fig. 7.40). The flood events control the distribution of the calcarenites and calcirudites, and the vertical facies change reflects the relative changes of lake level and the rate of sediment supply.

#### 7.4.1.1  Mass Transport Deposits and Seismites

(1)  Sedimentary characteristics

The mass transport deposits are triggered by seismic or other events, with many sediments being transported under the influence of gravity. During the deposition of Sequence III, the distribution of the calcirudites are limited. Except the Well Jin94 near the edge of the basin, the calcirudites have only been found in Wells Jin100, ST1H, and ST3. The calcirudites in Well ST3 is ca. 100 m, while there are almost no calcirudites in Wells Jin98X, ST2X, and Jin116X, which lie between the edge of the basin and the Well ST3. The calcirudites in Well ST3 are associated with soft sediment deformation structures, such as sedimentary dikes, liquefaction structures, diapir structures, convolute lamination,
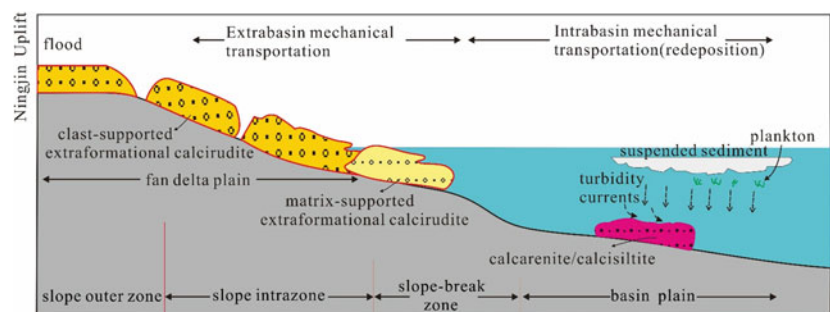
loop bedding, flame structures, ball and pillow structures as well as some syndepositional faults.

The rocks with the deformational structures (refer to Sect. 7.3 for a detailed discussion) are interpreted as seismites and have been found in Wells ST1 and ST3. The seismites are mainly found in 3959–3994.4 m and 4072–4087 m in Well ST1. The hundred-meter-thick clast-supported calcirudites in Well ST3 can be called "seismoturbidites." Sequence III has been interpreted as mass transport deposits and seismites triggered by seismic events.

The hundred-meter-thick calcirudites of Well ST3 have been interpreted as the main channel deposits of the upper seismoturbidites fan system. The clast-supported calcirudites are mostly massive (Fig. 7.41a, b). The gravels are mainly light gray to gray and are poorly sorted, with grain size ranging from 3 mm to 80 cm. The matrix is primarily carbonate, and the content is low in these calcirudites. Some intervals show normal grading with the majority being massive. The structures indicate rapid transport and deposition. The source rocks of the gravels include lime mudstone, microcrystalline dolostone, finely crystalline dolostone, pellet limestone, flat-pebble rudstone with red oxidized rings, and occasionally ooid limestones. The age of the source rocks is from Cambrian or Ordovician.

The braided streams of the middle fan in seismoturbidites fan consists of all five types of calcirudites in the study area. The mixed-source calcirudites were formed by mixing the terrigenous gravels with intraformational rip-up clasts (Fig. 7.41c–f). The rip-ups are in situ or may have undergone a short distance of transport. The textures of the rip-ups can be used to distinguish between the two types: the in situ rip-ups are angular with signs of tearing or burrs around the edges, while those that were transported are subangular to subrounded. The terrigenous gravels are relatively small with the maximum grain size being ca. 2 cm. The intraformational gravels are relatively large, the grain size ranging from 5 to 15 cm. The terrigenous gravels fill the intergranular pore space of the intraformational gravels. The mixed-source calcirudite is one unique facies of the seismoturbidite fan system.

Fig. 7.40  Facies model of the fan delta in Shulu Sag (modified after Liu et al. 2017)
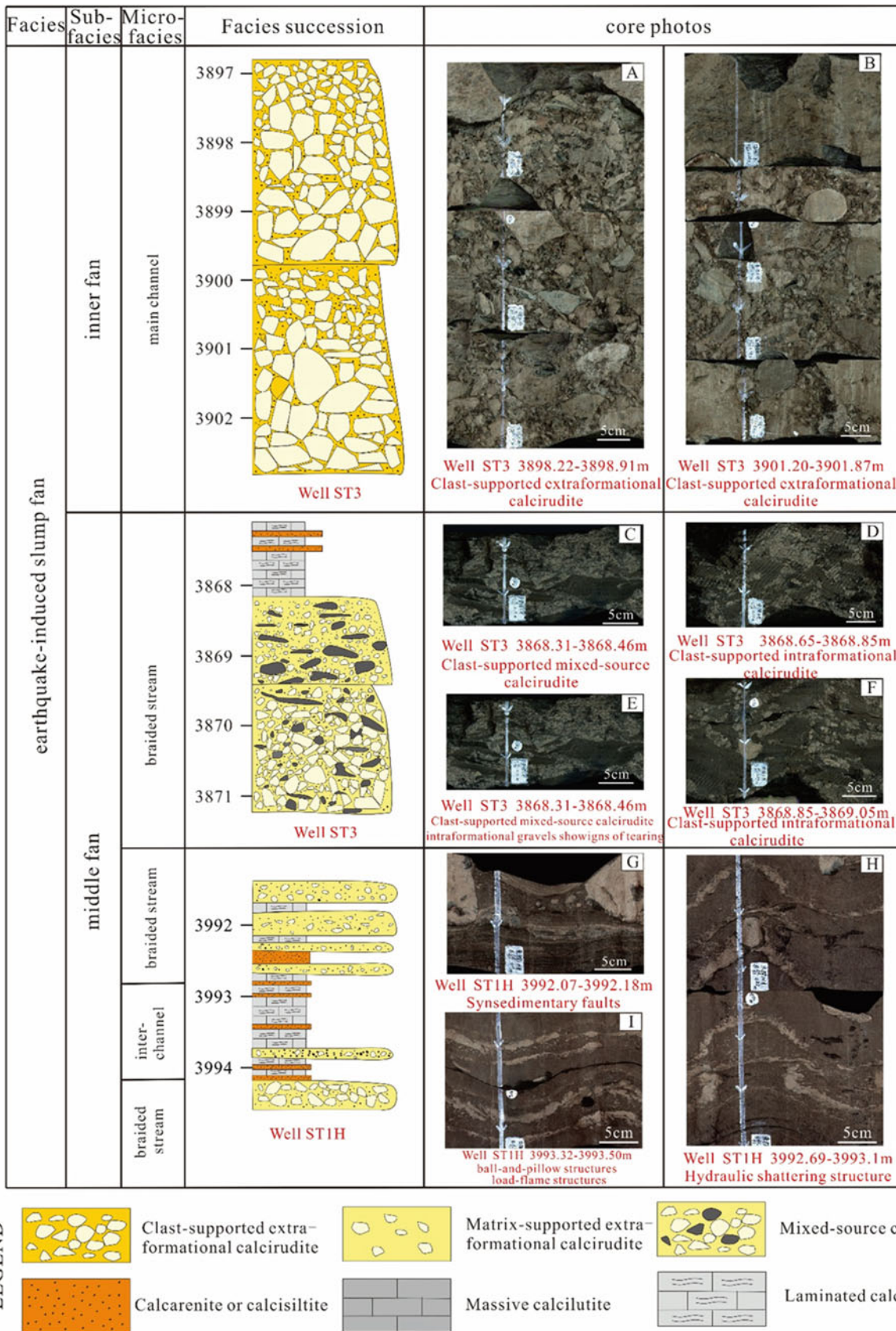
| Facies | Sub-facies | Micro-facies | Facies succession | core photos | |
|---|---|---|---|---|---|
| earthquake-induced slump fan | inner fan | main channel | Well ST3 | A — Well ST3 3898.22–3898.91m Clast-supported extraformational calcirudite | B — Well ST3 3901.20–3901.87m Clast-supported extraformational calcirudite |
| | middle fan | braided stream | Well ST3 | C — Well ST3 3868.31–3868.46m Clast-supported mixed-source calcirudite / E — Well ST3 3868.31–3868.46m Clast-supported mixed-source calcirudite intraformational gravels showigns of tearing | D — Well ST3 3868.65–3868.85m Clast-supported intraformational calcirudite / F — Well ST3 3868.85–3869.05m Clast-supported intraformational calcirudite |
| | | braided stream / inter-channel / braided stream | Well ST1H | G — Well ST1H 3992.07–3992.18m Synsedimentary faults / I — Well ST1H 3993.32–3993.50m ball-and-pillow structures load-flame structures | H — Well ST1H 3992.69–3993.1m Hydraulic shattering structure |

LEGEND

- Clast-supported extra-formational calcirudite
- Matrix-supported extra-formational calcirudite
- Mixed-source calcirudite
- Calcarenite or calcisiltite
- Massive calcilutite
- Laminated calcilutite

**Fig. 7.41** Sedimentary characteristics of seismoturbidites (modified after Liu et al. 2017)

In the case of earthquakes, the pre-existing sediments are first modified, resulting in brittle deformation, compressional deformation, and liquefaction deformation. Some small faults (Fig. 7.41g), liquefaction structures (Fig. 7.41h), load casts, small ball-and-pillow structures (Fig. 7.41i), and liquefied sandstone dikes, namely in situ seismites. These in situ seismites and thin-bedded continuous or discontinuous calcisiltites and calcarenites are the deposits of the interchannel or the outer fan of the seismoturbidite fan.

(2)   Facies model

Unlike the fan delta which has relatively well-established theories to guide the exploration, most of the works on seismites focused on their formation conditions and recognition criteria and the facies model of the seismoturbidite fan is rarely described in literature (Owen 1996; Obermeier 1996; Pope et al. 1997; Bhattacharya and Bandyopadhyay 1998; Fortuin and Dabrio 2008; Owen et al. 2011; Owen and Moretti 2011; Mugnier et al. 2011). There are some papers on the analysis of the formational process and features of the Xiejiadian seismites in Longmen Mt. (Wang 2010; Tian 2010). In general, the morphology of the seismites is affected by the geomorphology and magnitude of the earthquake at the time of deposition. The NW-trending Taijiazhuang fault has a growth index of 1.1–1.8 during Es$_3$ and the NNE-trending Xinhe fault has a growth index of 1.3–1.9. There are some NE-trending syndepositional normal faults on the western slope of the basin. These faults that were active during Sequence III were probably responsible for the earthquakes that triggered the seismites.

During the deposition of Sequence III, the slope of the hanging wall side of the half-graben is gentle, and the entire slope can be divided into the outer slope, the inner slope, the slope break and the depression. In the early stage of the earthquakes, the sediments were first reworked to form seismites such as diapirs and liquefaction structures, calcarenites, and calcisiltites (Fig. 7.42). Earthquakes shattered the carbonate outcrops into smaller clasts and induced debris flows. During the transport, turbidity currents induced by the earthquake erode the underlying soft sediments and entrain them into the currents. When the currents flow to the slope break zone, they come to a stop and deposit the gravels here. The resultant deposits include all the five types of calcirudites (Fig. 7.42), and they are in sharp contact with the underlying sediments. There are also some debris flow lag deposits in the low-lying areas of the inner slope (Fig. 7.42), but the areal extent and thickness are much smaller than the sediments near the slope break. There is an equilibrium position between the inner slope and the slope break zone, where sediments cannot be preserved. The equilibrium may explain why the dominant facies of Wells Jin98X and Jin116X are calcilutites yet Well ST3 has hundred-meter thick calcirudites.

## 7.4.2   Distribution of the Calcirudites

### 7.4.2.1   Vertical Distribution

We choose the dip-oriented Wells Jin104-Jin97-ST3 (Fig. 7.43) and strike-oriented Wells ST1H-ST3-Jin116X-Jin98X (Fig. 7.44) as two key sections to delineate the vertical distribution of the calcirudites.

(1)   Jin104-Jin97-ST3

During the deposition of SequenceI, the fan deltas mainly developed on the edge of the basin. Both the Wells Jin97 and ST3 have penetrated the deposits of delta plain and the channels of delta front. The lithofacies include mainly clast- and matrix-supported extraformational calcirudite. When it came to Sequence II, the sequence was dominated by lacustrine facies, and the only fan delta deposits were found in Well Jin104. Sequence III was characterized by the seismoturbidite fan near the slope break. The main channel deposits of the fan were found in Well ST3, which then

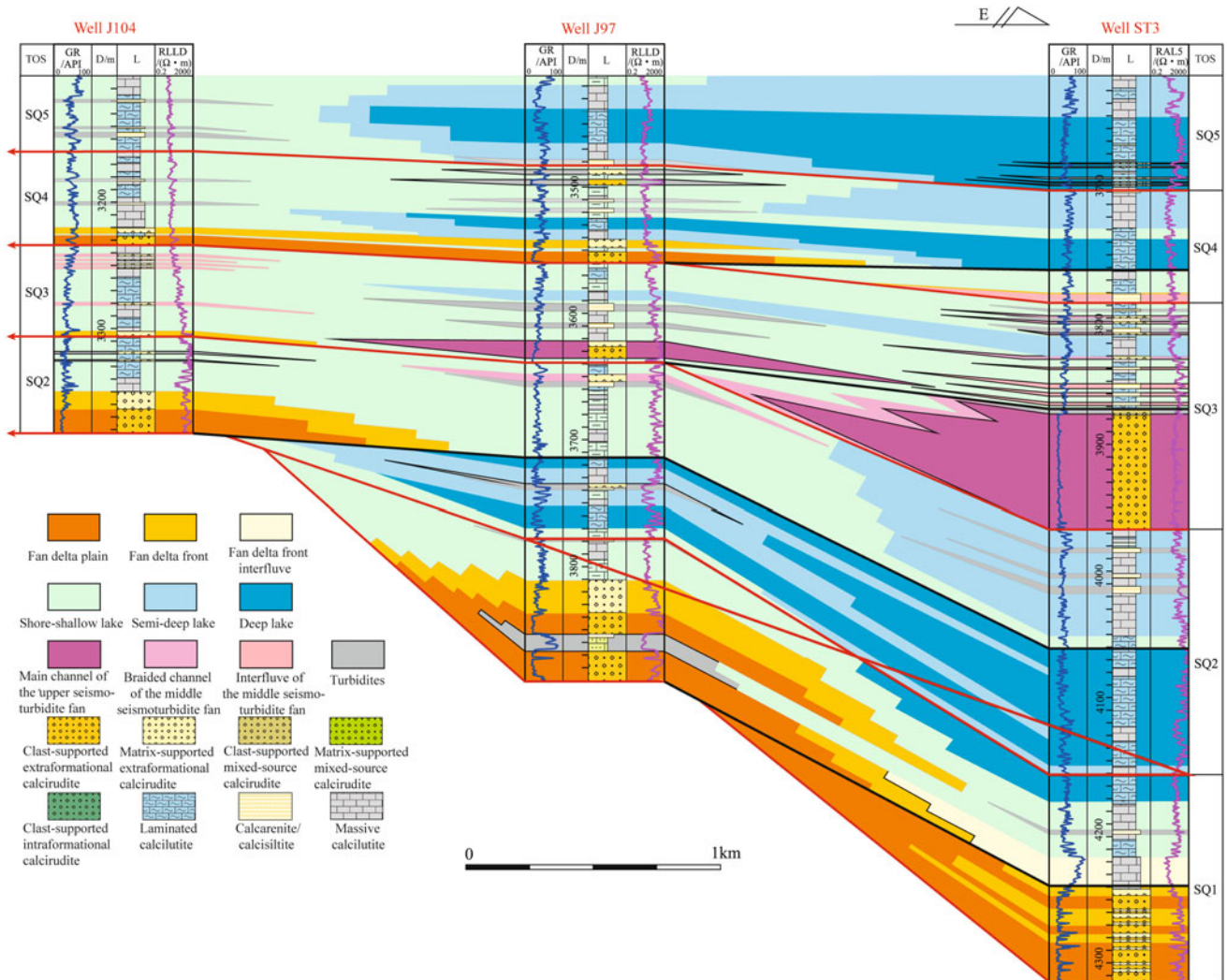**Fig. 7.42** Facies model of the seismoturbidites (modified after Liu et al. 2017)
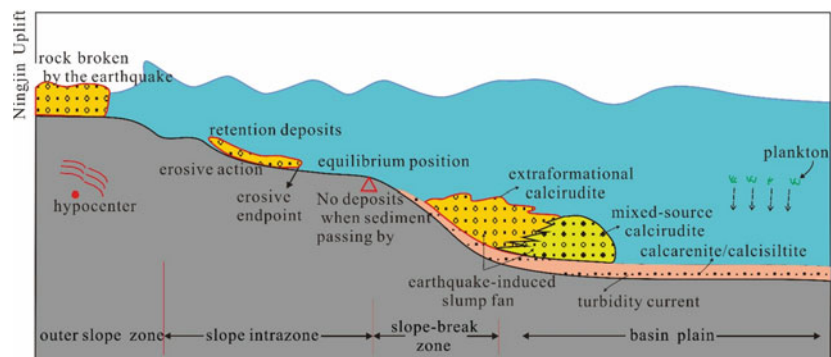
**Fig. 7.43** The cross-section of wells Jin104-Jin97-ST3, TOS—third order sequence, D—Depth, L—Lithology

passed into the braided channel and lacustrine deposition upwards, the dominant lithofacies including clast-supported intraformational and mixed-source calcirudites, as well as calcilutites. There are seismites found in Well Jin97 and almost none in Well Jin104. Sequence IV and Sequence V were dominated by lacustrine laminated and massive calcilutites.

(2)   ST1H-ST3-Jin116X-Jin98X

In the strike-oriented section (Fig. 7.44), the extent of the fan delta was extensive during the deposition of Sequence I. The fan delta deposits have been found in Wells ST3 and Jin116X. They should also exist in Wells Jin98X and ST1H based on the prediction. The extent of fan deltas was smaller in Sequence II, and the characteristic deposits have only been found in Wells ST1 and Jin98X. Lacustrine deposition

dominates the remaining two wells. Sequence III was characterized by the seismoturbidite fan near the slope break. The main channel deposits, the clast-supported calcirudites, were found in Well ST3; the middle fan braided channel deposits, including clast- or matrix-supported extraformational calcirudites as well as a few clast-supported mixed-source calcirudites, matrix-supported mixed-source calcirudites, and clast-supported intraformational calcirudites. The remaining two wells are mainly lacustrine deposition. Sequences IV and V consist mainly of fine-grained lacustrine deposition, such as in Wells ST3, Jin116X, and Jin98X.

### 7.4.2.2   Planform Distribution

Based on the facies analysis using core data, wells logs, well correlation, the planform facies distribution is constrained. Using the 3D seismic data, lithology inversion data, core and
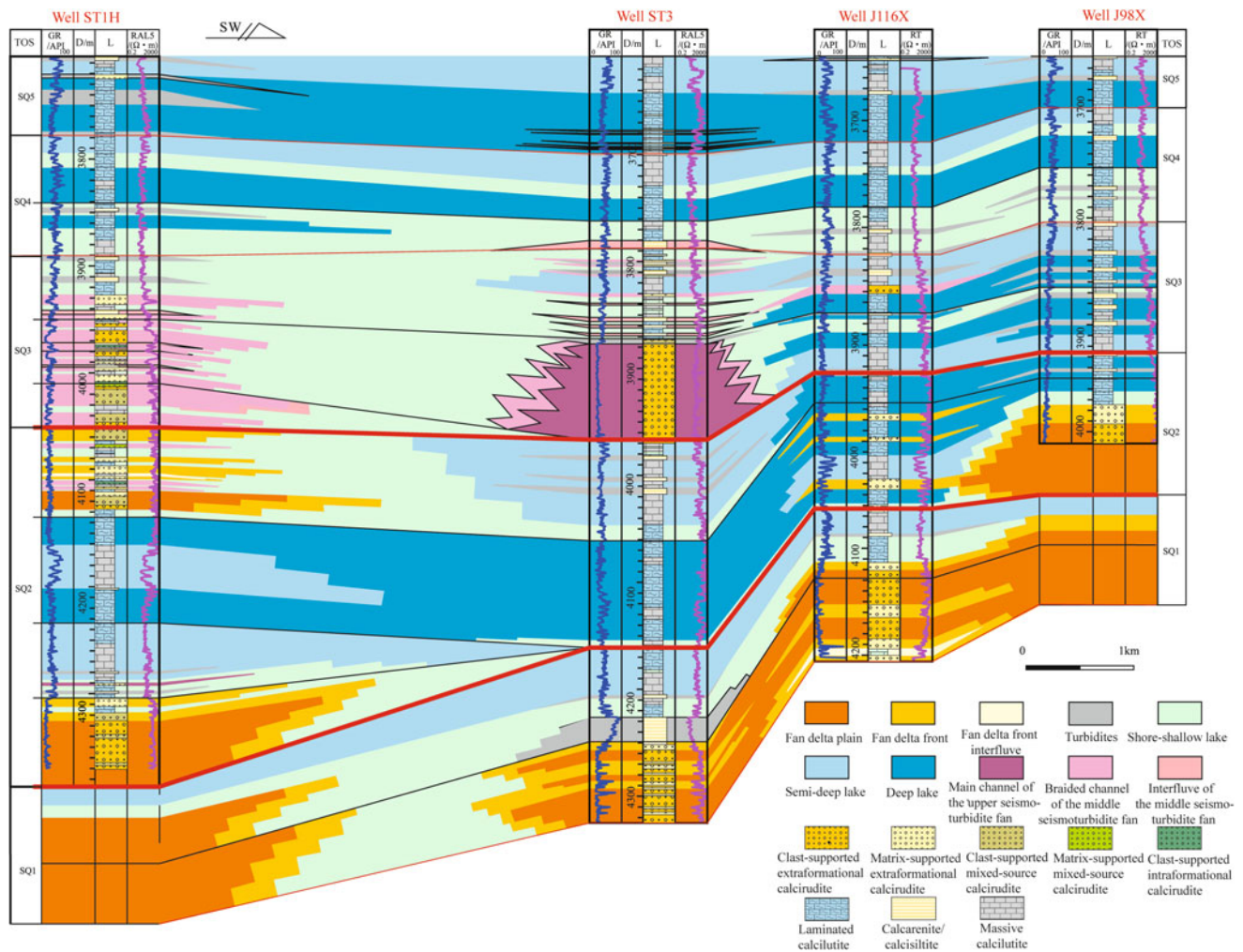
**Fig. 7.44** The cross-section of the wells ST1H-ST3-Jin116X-Jin98X, TOS—third order sequence, D—Depth, L—Lithology

well log data, the following contour maps of Sequences I and III were made by Landmark, Jason, Surfer, Petrol and other geological software: (1) the stratigraphic thickness, (2) the calcirudite thickness, and (3) the volumetric percentage of the calcirudites. The planform distribution of the calcirudite facies was established based on the contour maps and RMS amplitude of the seismic data. The focus of this study is on the western slope of the Shulu Sag, and the facies distribution of the eastern steep slope zone is based on existing data and previous research results, which will not be described in detail.

(1) Planform distribution of calcirudites in Sequence I

The formation of fan deltas is controlled by the structural type of the basin, the distance between the source and the sink, and paleoclimate (Li 1998). The western part of the study area is broad gentle slope, and the east part is the Xinhe fault. The main source of sediments comes from the Ningjin uplift on the west side, and the depositional center of the basin is located near the Xinhe fault. Based on the pollen data, the vegetation consisted mainly of angiosperms and gymnosperms during the deposition of Sequence I, with little evidence of ferns which require hot and humid climate. The vegetation pattern suggests the paleoclimate during Sequence I was like the current subtropical climate, with an annual mean temperature of 16–17 °C (Ren 1986). Under such climatic conditions, heavy rainfall events tend to result in catastrophic floods, carrying significant amounts of coarse sediments out of the mountain and accumulating in the piedmont, forming the main body of fan delta deposition.

During the deposition of Sequence I, the delta fan deposition was well developed in the gentle slope belt, and some fans were connected to each other, for example, near the Wells Jin53 and Jin116X. The fan delta plain consists mainly of clast-supported extraformational calcirudites, and

**Fig. 7.45** Facies distribution of Sequence I in the lower submember of Es$_3$
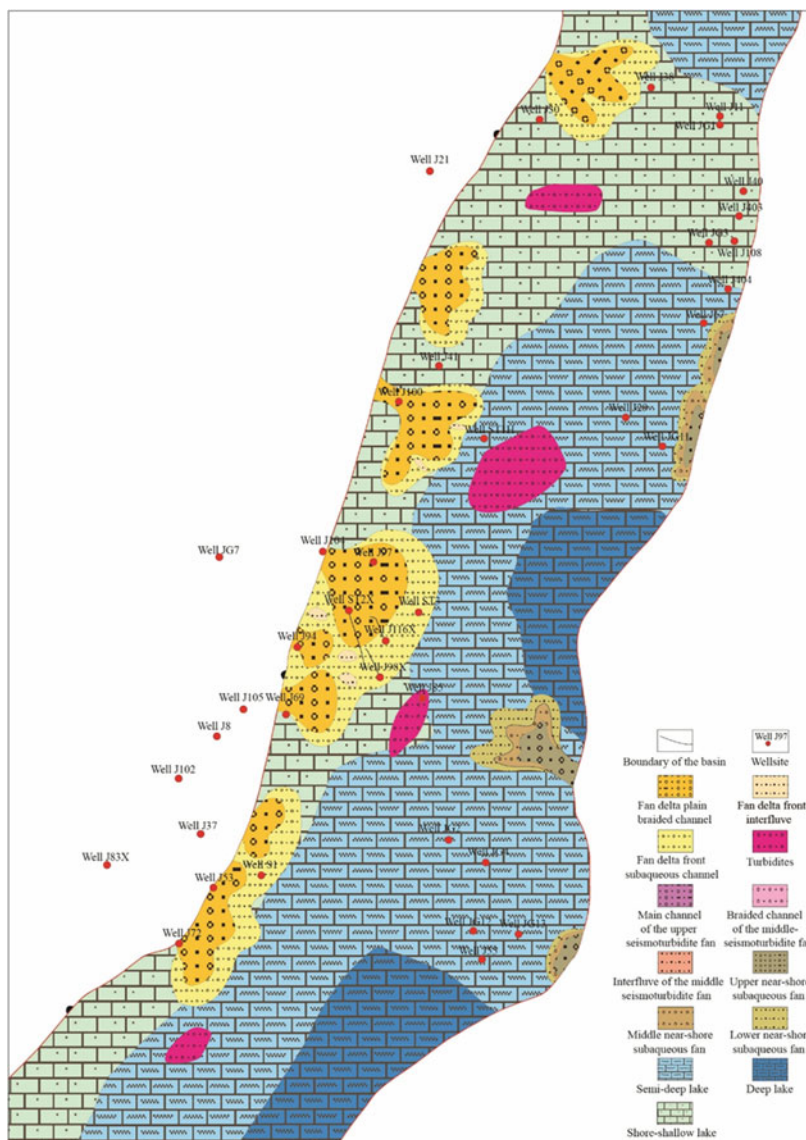
the fan delta front includes braided channel and interfluve. The facies of the braided channel include both clast- and matrix-supported calcirudites while the interfluve is characterized by calcarenites. In the prodelta, turbidity currents deposit some calcarenites with few structures associated with deformation or slump. Semi-deep lake and deep lake mainly consist of organic-rich laminated and massive calcilutites (Fig. 7.45). Next to the Xinhe fault in the east, there are three small subaqueous fan systems.

(2) Planform distribution of calcirudites in Sequence III

The slope gradient of the western slope became smaller during Sequence III, and the areal extent of the fan delta was relatively limited. The main lithofacies near the Wells Jin100, Jin94 and Jin37 (Fig. 7.46) is clast-supported extraformational calcirudites. The vegetation was still dominated by angiosperms and gymnosperms, with the percentage of gymnosperms higher than that of Sequence I. The ferns were still rare to see. It is estimated that about 20 earthquakes occurred during Sequence III based on the core data of Well ST1H (Zheng et al. 2015). The earthquake-induced in situ seismites are widely spread in the lake basin. The seismites have a variety of soft-sediment deformation structures, such as diapirs and convolute lamination, which are the results of compression, extension, and shearing. The fine-grained sediments of semi-deep and deep lake (water-saturated calcarenites) are more sensitive to liquefaction, and the semi-deep and deep lakes are the major environments for preserving seismites (Li et al. 2008).

The main and the braided channels of the seismic-induced seismoturbidite fan are mainly distributed near the slope

**Fig. 7.46** Facies distribution of Sequence III in the lower submember of Es$_3$
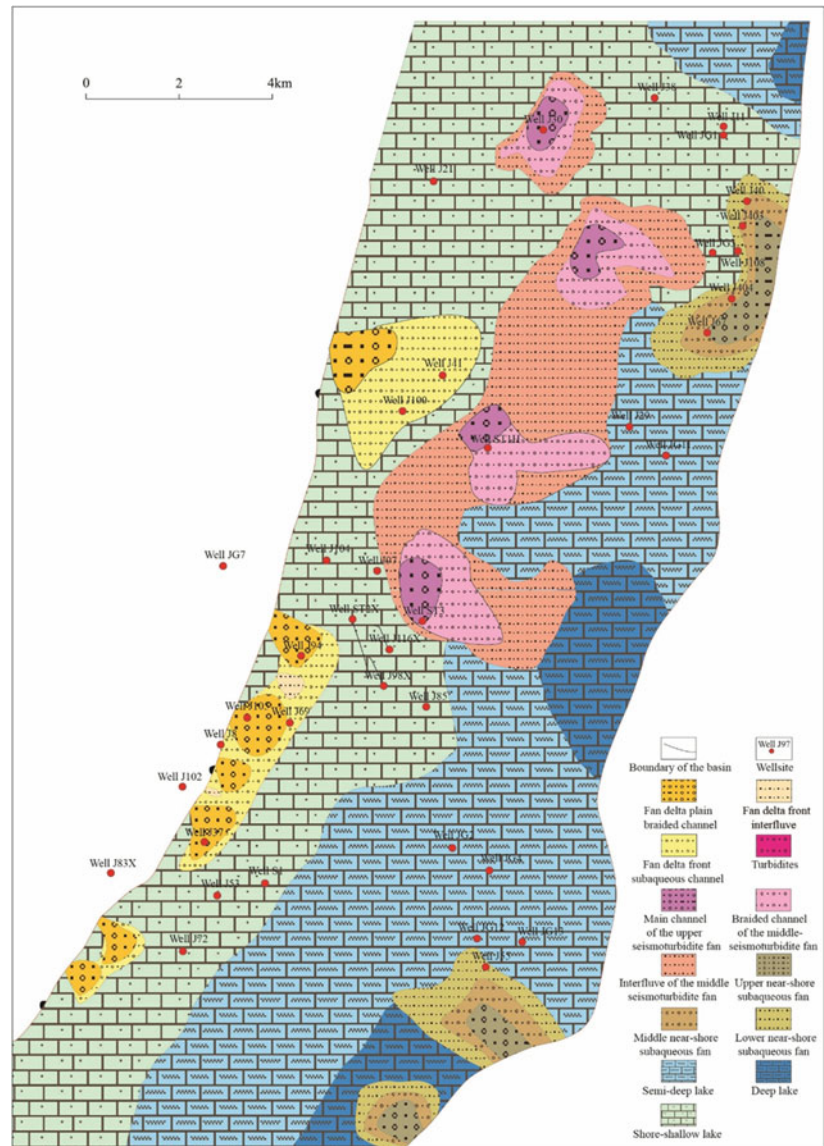


break belt (Fig. 7.44), such as in the position of the Wells ST3 and ST1H. The dominant lithofacies of the main channel is the clast-supported extraformational calcirudites, while the braided channels include all types of calcirudites (Fig. 7.44). The scale of nearshore subaqueous fan next to the steep slope zone is much larger than that in Sequence I, and the deposits have been found in Wells Jin403 and Jin404 as well as near the deep lake area in the south of the basin. The lithofacies include clast- and matrix-supported extraformational calcirudites. The semi-deep and deep lake deposits mainly consist of organic-rich laminated and massive calcilutites.

### 7.4.3 Relationship Between Two Types of Calcirudites

The depositional environment of Well Jin100 in Sequence III was interpreted to be fan delta. The main lithofacies is clast-supported extraformational calcirudites with medium sorting and subangular to subrounded grains (Fig. 7.47a). ST1H was dominated by the seismoturbidite fan deposition, which contains clast- or matrix-supported extraformational calcirudites. The rocks have subrounded grains and relatively good sorting (Fig. 7.47b). The source rocks for the gravels in Wells Jin100 and ST1H are similar,
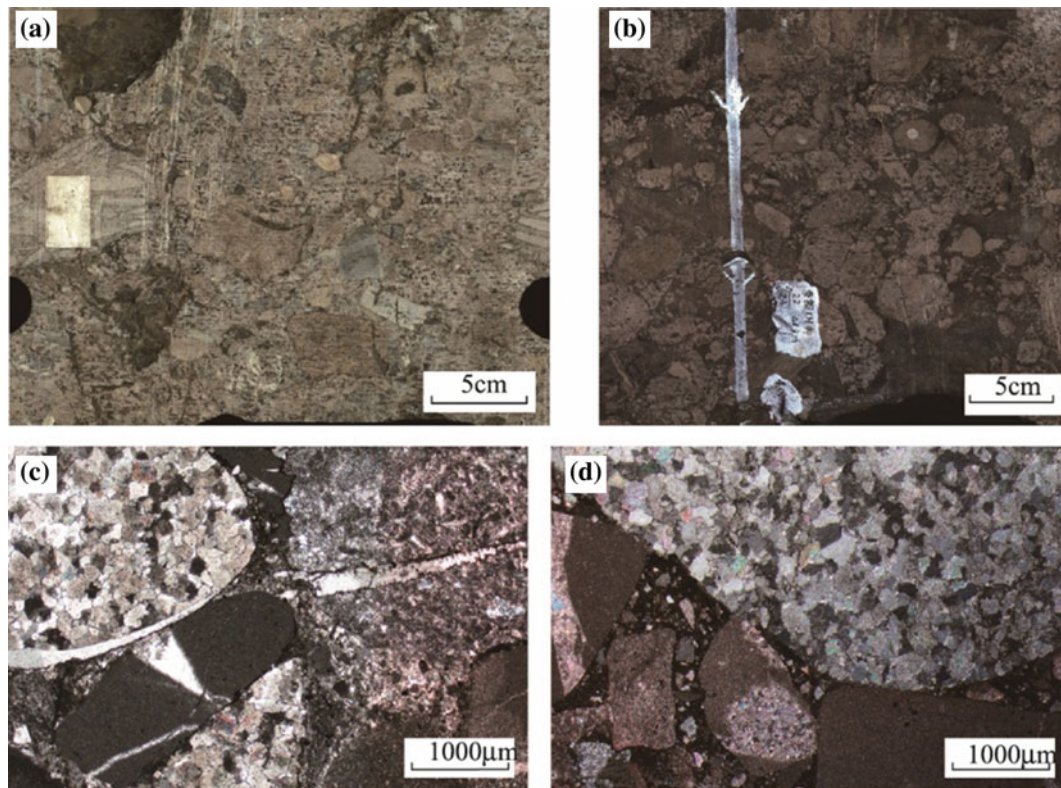
**Fig. 7.47** Sedimentary characteristics of Wells Jin100 and ST1H in Sequence III. **a** The gravels are in close contact, and the core is massive, Well Jin100, core number $4\frac{18}{32}$; **b** the terrigenous grains are in point or line contact, Well ST1H, core number $2\frac{22}{23}$; **c** thin section of the core in (**a**). The gravels come from medium crystalline dolostone and lime mudstone, Well Jin100, core number $4\frac{18}{32}$; **d** the gravels are in point or line contact, and the source rocks include medium crystalline dolostone and lime mudstone, Well ST1H, core number $2\frac{20}{23}$

mainly medium crystalline dolostone and lime mudstone (Fig. 7.47c, d). The size of the gravels in both wells is close to each other, and the sorting and roundness of the sediments are also similar. It is hypothesized that the sediments of the Well ST1H may be derived from fan delta deposition of Well Jin100.

The total thickness of the calcirudites in Well ST3 is close to 100 m, and the size of the gravels range from several millimeters to around ninety centimeters. The rocks are poorly sorted, and the long axes of the gravels are mostly upright (Fig. 7.48). In addition, there are no calcirudites between Well ST3 and the edge of the basin (ca. 3 km long) based on the inversion data provided by the Qianneng Hengxin Energy Technology Co., Ltd. Therefore, it is inferred that the deposits of Well ST3 come directly from the Ningjin uplift.
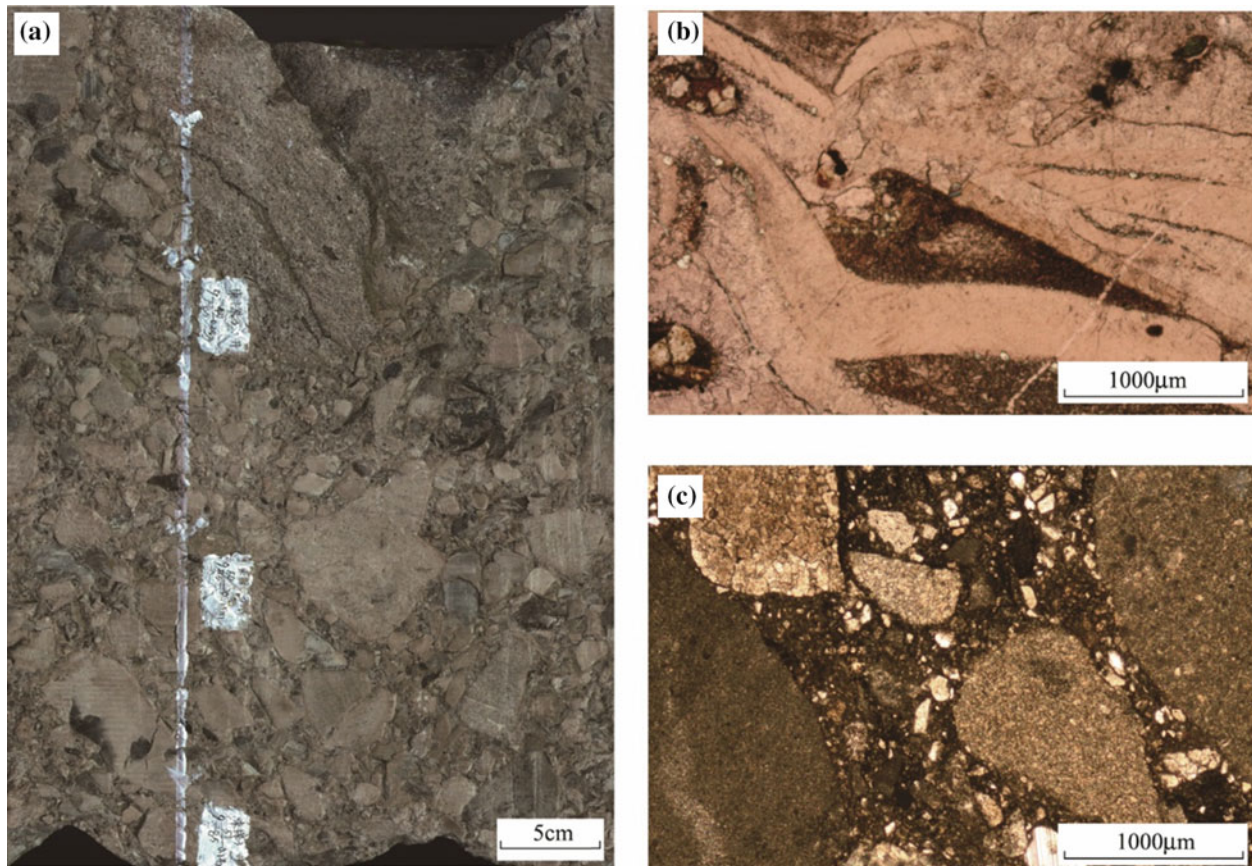
**Fig. 7.48** Sedimentary characteristics of Well ST3 in Sequence III. **a** The clast-supported extraformational calcirudite is massive and poorly sorted, Well ST3, core number $9\frac{49-51}{85}$; **b** bioclastic limestone gravel, Well ST3, 3893.68 m; **c** lime mudstone and dolostone gravels, Well ST3, 3907.21 m

# References

Alfaro P, Delgado J, Estévez A, Molina JM, Moretti M, Soria JM (2002) Liquefaction and fluidization structures in Messinian storm deposits (Bajo Segura Basin, Betic Cordillera, southern Spain). Int J Earth Sci 91(3):505–513

Alsop GI, Marco S (2011) Soft-sediment deformation within seismogenic slumps of the Dead Sea Basin. J Struct Geol 33(4):433–457

Berra F, Felletti F (2011) Syndepositional tectonics recorded by soft-sediment deformation and liquefaction structures (continental Lower Permian sediments, Southern Alps, Northern Italy): stratigraphic significance. Sed Geol 235(3):249–263

Bertrand S, Charlet F, Chapron E et al (2008) Reconstruction of the Holocene seismotectonic activity of the Southern Andes from seismites recorded in Lago Icalma, Chile, 39°S. Palaeogeogr Palaeoclimatol Palaeoecol 259(2):301–322

Bhattacharya HN, Bandyopadhyay S (1998) Seismites in a Proterozoic tidal succession, Singhbhum, Bihar, India. Sed Geol 119(3):239–252

Braga JC, Comas MC (1999) Environmental significance of an uppermost Pliocene carbonate debris flow at site 978. In: Zahn R, Comas MC, Klaus A (eds) Proceedings of the ocean drilling program, scientific results, vol 161, pp 77–81

Calvo JP, Rodriguez-Pascua M, Martin-Velazquez S et al (1998) Microdeformation of lacustrine laminite sequences from Late Miocene formations of SE Spain: an interpretation of loop bedding. Sedimentology 45(2):279–292

Carrillo E, Beck C, Audemard FA, Moreno E et al (2008) Disentangling late quaternary climatic and seismo-tectonic controls on Lake Mucubají sedimentation (Mérida andes, Venezuela). Palaeogeogr Palaeoclimatol Palaeoecol 259(2):284–300

Chapman RE (1983) Petroleum geology. Elsevier, Amsterdam, 415 p

Cui Z, Wu J, Li L et al (2003) The fan delta depositional characteristics and oil-bearing properties of the 3rd Member of the Shahejie Formations in the slope zone of Shulu Sag. J Northwest Univ (Nat Sci Ed) 33(3):320–324

Du Y, Zhang C, Han X (2001) Ancient earthquake events of Kunyang group in Central Yunnan and its geological significance in deposition. Sci China (Series D) 31(4):283–289

Du YS, Xu YJ, Yang JH (2008) Soft-sediment deformation structures related to earthquake from the Devonian of the Eastern North Qilian Mts. and its tectonic significance. Acta Geologica Sinica-English Ed 82(6):1185–1193

Dutton SP (1982) Pennsylvanian fan-delta and carbonate deposition, Mobeetie Field, Texas Panhandle. AAPG Bulletin 66(4):389–407

Dzulynski S, Smith AJ (1963) Convolute lamination, its origin, preservation, and directional significance. J Sediment Res 33(3):616–627

El Taki H, Pratt BR (2012) Syndepositional tectonic activity in an epicontinental basin revealed by deformation of subaqueous carbonate laminites and evaporites: seismites in Red River strata

(Upper Ordovician) of southern Saskatchewan, Canada. Bull Can Pet Geol 60(1):37–58

Ettensohn FR, Zhang CH, Gao LZ et al (2011) Soft-sediment deformation in epicontinental carbonates as evidence of paleoseismicity with evidence for a possible new seismogenic indicator: accordion folds. Sed Geol 235(3):222–233

Ezquerro L, Moretti M, Liesa CL et al (2015) Seismites from a well core of palustrine deposits as a tool for reconstructing the palaeoseismic history of a fault. Tectonophysics. Tectonophysics 655:191–205

Fanetti D, Anselmetti FS, Chapron E et al (2008) Megaturbidite deposits in the Holocene basin fill of Lake Como (southern Alps, Italy). Palaeogeogr Palaeoclimatol Palaeoecol 259(2):323–340

Faridfathi FY, Ergin M (2012) Holocene sedimentation in the tectonically active Tekirdağ Basin, western Marmara Sea, Turkey. Quatern Int 261:75–90

Feng Z (2013) Sedimentology in China (Second Edition). Petroleum Industry Press, Beijing, pp 507–615

Fortuin AR, Dabrio CJ (2008) Evidence for Late Messinian seismites, Nijar Basin, south-east Spain. Sedimentology 55(6):1595–1622

Ghosh SK, Pandey AK, Pandey P, Ray Y, Sinha S (2012) Soft-sediment deformation structures from the Paleoproterozoic Damtha Group of Garhwal Lesser Himalaya, India. Sed Geol 261–262:76–89

Gierlowski-Kordesch EH (1998) Carbonate deposition in an ephemeral siliciclastic alluvial system: Jurassic Shuttle Meadow Formation, Newark Supergroup, Hartford Basin, USA. Palaeogeogr Palaeoclimatol Palaeoecol 140:161–184

Gierlowski-Kordesch EH (2010) Lacustrine carbonates, in carbonates in continental settings, vol 1: facies, environments, and processes. In: Alonso-Zarza AM, Tanner LH (eds) Developments in sedimentology, vol 61, Elsevier, Amsterdam, pp 1–101

Gorsline DS, De Diego T, Nava-Sanchez EH (2000) Seismically triggered turbidites in small margin basins: Alfonso Basin, western Gulf of California and Santa Monica Basin, California borderland. Sed Geol 135(1):21–35

Hempton MR, Dewey JF (1983) Earthquake-induced deformational structures in young lacustrine sediments, East Anatolian Fault, southeast Turkey. Tectonophysics 98(3):T7–T14

Hibsch C, Alvarado A, Yepes H et al (1997) Holocene liquefaction and soft-sediment deformation in Quito (Ecuador): a paleoseismic history recorded in lacustrine sediments. J Geodyn 24(1):259–280

Hu X, Chen H, Ji X et al (2005) The Jurassic delta deposit system tract and sedimentation model in the western Sichuan foreland basin, China. Petrol Geol Exp 27(3):226–231

Jiang Z (2010) Sedimentology (second edition). Petroleum Industry Press, Beijing

Jiang Z, Chen D, Qiu L et al (2007) Source-controlled carbonates in a small Eocene half-graben lake basin (Shulu Sag) in central Hebei Province, North China. Sedimentology 54(2):265–292

Kahle CF (2002) Seismogenic deformation structures in microbialites and mudstones, Silurian Lockport Dolomite, northwestern Ohio, U. S.A. J Sediment Res 72(1):201–216

Kong DY, Shen H, Liu JY, Yin W (2005) Origin of the transverse accommodation zone of the Shulu subbasin in the Jizhong depression. Geology in China 32:166–171 (in Chinese with English abstract)

Leroy SAG, Schwab MJ, Costa PJM (2010) Seismic influence on the last 1500-year infill history of Lake Sapanca (North Anatolian Fault, NW Turkey). Tectonophysics 486(1):15–27

Li Y (1982) Early Oligocene fan-deltas in Liaohe Rift. Pet Expoloration Dev 9(4):17–23

Li W (1998) Fan delta deposits in Jurassic in the depression of the SW Tarim Basin. Acta Sedimentologica Sinica 16(2):150–154

Li H (2015a) Sequence stratigraphy and characteristics of the tight reservoirs in the 3rd member of the Eocene Shahejie Formation, Shulu Sag: [master degree thesis]. China University of Geosciences (Beijing), Beijing

Li Q (2015b) Evaluation of rudstone and marlstone tight reservoir in lower part of the Shahejie 3 formation of the Shulu Sag, Jizhong depression. Doctoral degree thesis. China University of Geosciences (Beijing), Beijing

Li Y, Liu C, Wang X (2008) Discovery and significance of seismites in Late Tertiary Yanchang formation of Ordos Basin. Acta Sedimentol Sin 26(5):772–779

Li Y, Gong L, Zeng L et al (2012) Characteristics of features and their contribution to the deliverability of tight conglomerate reservoirs in the Jiulongshan Structure. Nat Gas Ind 32(1):22–26

Liang H, Kuang H, Liu J et al (2007) Discussion on origin for marls of the member 3 of Shahejie formation of Paleogene in Shulu Sag of Central Hebei Depression. J Palaeogeoraphy 9(2):167–174

Liu X, Zheng L, Jiang Z, Kong X (2017) Formation mechanisms of rudstones and their effects on reservoir quality in the Shulu Sag, Bohai Bay Basin, eastern China. J Earth Sci 28(6):1097–1108

Lowe DR (1975) Water escape structures in coarse-grained sediments. Sedimentology 22(2):157–204

Luo S, Lin C, Zhai Q et al (2009) Reservoir sedimentation characteristics and sedimentation model of lower Es_3 of Bijia block in Binnan Oilfield. J China Univ Petrol (Ed Nat Sci), 33(2):12–17

Martel AT, Gibling MR (1993) Clastic dykes of the Devono-Carboniferous Horton Bluff Formation, Nova Scotia: storm-related structures in shallow lakes. Sed Geol 87(1):103–119

Mcconnico TS, Bassett KN (2007) Gravelly Gilbert-type fan delta on the Conway Coast, New Zealand: foreset depositional processes and clast imbrications. Sed Geol 198(3):147–166

McKee ED, Goldberg M (1969) Experiments on formation of contorted structures in mud. Geol Soc Am Bull 80(2):231–244

McLaughlin PI, Brett CE (2004) Eustatic and tectonic control on the distribution of marine seismites: examples from the Upper Ordovician of Kentucky, USA. Sed Geol 168(3):165–192

Mohindra R, Bagati TN (1996) Seismically induced soft-sediment deformation structures (seismites) around Sumdo in the lower Spiti valley (Tethys Himalaya). Sed Geol 101(1):69–83

Molina JM, Alfaro P, Moretti M, Soria JM (1998) Soft-sediment deformation structures induced by cyclic stress of storm waves in tempestites (Miocene, Guadalquivir Basin, Spain). Terra Nova 10:145–150

Montenat C, Barrier P, d'Estevou PO (1991) Some aspects of the recent tectonics in the strait of Messina, Italy. Tectonophysics 194(3):203–215

Montenat C, Barrier P, d'Estevou PO et al (2007) Seismites: an attempt at critical analysis and classification. Sed Geol 196(1):5–30

Moretti M (2000) Soft-sediment deformation structures interpreted as seismites in middle-late Pleistocene aeolian deposits (Apulian foreland, southern Italy). Sed Geol 135(1):167–179

Moretti M, Sabato L (2007) Recognition of trigger mechanisms for soft-sediment deformation in the Pleistocene lacustrine deposits of the Sant'Arcangelo Basin (Southern Italy): Seismic shock vs. overloading. Sed Geol 196(1):31–45

Moretti M, Alfaro P, Caselles O et al (1999) Modelling seismites with a digital shaking table. Tectonophysics 304(4):369–383

Moretti M, Soria JM, Alfaro P, Walsh N (2001) Asymmetrical soft-sediment deformation structures triggered by rapid sedimentation in turbiditic deposits (Late Miocene, Guadix Basin, Southern Spain). Facies 44(1):283–294

Mugnier JL, Huyghe P, Gajurel AP et al (2011) Seismites in the Kathmandu basin and seismic hazard in central Himalaya. Tectonophysics 509(1):33–49

Mutti E, Lucchi FR, Séguret M et al (1984) Seismoturbidites: a new group of resedimented deposits. Mar Geol 55(1):103–116

Nakajima T, Kanai Y (2000) Sedimentary features of seismoturbidites triggered by the 1983 and older historical earthquakes in the eastern margin of the Japan Sea. Sed Geol 135(1):1–19

Neuwerth R, Suter F, Guzman CA et al (2006) Soft-sediment deformation in a tectonically active area: the Plio-Pleistocene Zarzal formation in the Cauca Valley (Western Colombia). Sed Geol 186(1):67–88

Nichols RJ, Sparks RSJ, Wilson CJN (1994) Experimental studies of the fluidization of layered sediments and the formation of fluid escape structures. Sedimentology 41(2):233–253

Obermeier SF (1996) Use of liquefaction-induced features for paleo-seismic analysis-an overview of how seismic liquefaction features can be distinguished from other features and how their regional distribution and properties of source sediment can be used to infer the location and strength of Holocene paleo-earthquakes. Eng Geol 44(1):1–76

Owen G (1987) Deformation processes in unconsolidated sands. In: Jones ME, Preston RMF (eds) Deformation of sediments and sedimentary rocks. Geological Society special publication 29, pp 11–24

Owen G (1996) Experimental soft-sediment deformation: structures formed by the liquefaction of unconsolidated sands and some ancient examples. Sedimentology 43(2):279–293

Owen G, Moretti M (2011) Identifying triggers for liquefaction-induced soft-sediment deformation in sands. Sed Geol 235(3):141–147

Owen G, Moretti M, Alfaro P (2011) Recognising triggers for soft-sediment deformation: current understanding and future directions. Sed Geol 235(3):133–140

Pollard J, Steel R, Undersrud E (1982) Facies sequences and trace fossils in lacustrine/fan delta deposits, Hornelen Basin (M. Devonian), western Norway. Sed Geol 32(1):63–87

Pondrelli M, Rossi AP, Marinangeli L et al (2008) Evolution and depositional environments of the Eberswalde fan delta, Mars. Icarus 197(2):429–451

Pope MC, Read JF, Bambach R et al (1997) Late Middle to Late Ordovician seismites of Kentucky, southwest Ohio and Virginia: sedimentary recorders of earthquakes in the Appalachian basin. Geol Soc Am Bull 109(4):489–503

Pratt BR (1994) Seismites in the Mesoproterozoic Altyn Formation (Belt Supergroup), Montana: a test for tectonic control of peritidal carbonate cyclicity. Geology 22(12):1091–1094

Pratt BR (1998) Syneresis cracks: subaqueous shrinkage in argillaceous sediments caused by earthquake-induced dewatering. Sed Geol 117(1):1–10

Qiao X, Li H (2009) Effect of earthquake and ancient earthquake on sediments. J Palaeogeoraphy 11(6):593–610

Qiao X, Song T, Gao L et al (1994) Seismic sequences of carbonate rock vibration liquefaction. Acta Geologica Sninca 68(1):16–34

Rana N, Bhattacharya F, Basavaiah N et al (2013) Soft sediment deformation structures and their implications for Late Quaternary seismicity on the South Tibetan Detachment System, Central Himalaya (Uttarakhand), India. Tectonophysics 592:165–174

Ren Y (1986) Depositional environments of Shulu depression-viewed from the point of micropaleotanic florae. Acta Sedimentol Sin 4(4):101–107

Rodríguez-López JP, Meléndez N, Soria AR, Liesa CL, Van Loon AJ (2007) Lateral variability of ancient seismites related to differences in sedimentary facies (the synrift Escucha Formation, mid-Cretaceous, eastern Spain). Sed Geol 201(3):461–484

Rodríguez-Pascua MA, Calvo JP, De Vicente G et al (2000) Soft-sediment deformation structures interpreted as seismites in lacustrine sediments of the Prebetic Zone, SE Spain, and their potential use as indicators of earthquake magnitudes during the Late Miocene. Sed Geol 135(1):117–135

Rodríguez-Pascua MA, Garduño-Monroy VH, Israde-Alcántara I et al (2010) Estimation of the paleoepicentral area from the spatial gradient of deformation in lacustrine seismites (Tierras Blancas Basin, Mexico). Quatern Int 219(1):66–78

Rossetti DF, Góes AM (2000) Deciphering the sedimentological imprint of paleoseismic events: an example from the Aptian Codó formation, northern Brazil. Sediment Geol l 135(1):137–156

Scott B, Price S (1988) Earthquake-induced structures in young sediments. Tectonophysics 147(1):165–170

Séguret M, Labaume P, Madariaga R (1984) Eocene seismicity in the Pyrenees from megaturbidites of the South Pyrenean Basin (Spain). Mar Geol 55(1):117–131

Seilacher A (1969) Fault-graded beds interpreted as seismites. Sedimentology 13(1–2):155–159

Seilacher A (1984) Sedimentary structures tentatively attributed to seismic events. Mar Geol 55(1):1–12

Sheng H (1993) The fan delta sediments in Liaohe Faulted Basin. Petrol Expoloration Dev 20(3):60–66

Shiki T, Kumon F, Inouchi Y et al (2000) Sedimentary features of the seismo-turbidites, Lake Biwa, Japan. Sed Geol 135(1):37–50

Sneh A (1979) Late Pleistocene fan-deltas along the Dead Sea rift. J Sediment Res 49(2):541–552

Song TR (1988) A probable earthquake-tsunami sequence in Precambrian carbonate strata of Ming Tombs District, Beijing. Chin Sci Bull 33(13):1121–1124

Strachan LJ (2002) Slump-initiated and controlled syndepositional sandstone remobilization: an example from the Namurian of County Clare, Ireland. Sedimentology 49(1):25–41

Sun D, Shen H, Liu J et al (2005) Origin of the transverse accommodation zone of the Shulu subbasin in the Jizhong depression. Chin Geol 32(04):166–171

Suter F, Martínez JI, Vélez MI (2011) Holocene soft-sediment deformation of the Santa Fe–Sopetrán Basin, northern Colombian Andes: evidence for pre-Hispanic seismic activity? Sed Geol 235(3–4):188–199

Tamura T, Masuda F (2003) Shallow-marine fan delta slope deposits with large-scale cross-stratification: the Plio-Pleistocene Zaimoku-zawa formation in the Ishikari Hills, northern Japan. Sed Geol 158(3):195–207

Tanner PWG (1998) Interstratal dewatering origin for polygonal patterns of sand-filled cracks: a case study from late Proterozoic metasediments of Islay, Scotland. Sedimentology 45:71–89

Taşgin KC, Orhan H, Türkmen I et al (2011) Soft-sediment deformation structures in the late Miocene Şelmo Formation around Adiyaman area, Southeastern Turkey. Sed Geol 235(3):277–291

Tian M (2010) Formation model of seismic geologic body in Wenchuan earthquake. Master degree thesis. Southwest Petroleum University, Chengdu

Törő B, Pratt BR (2015) Eocene paleoseismic record of the Green River formation, Fossil Basin, Wyoming-implications of synsedimentary deformation structures in lacustrine carbonate mudstones. J Sediment Res 2015(85):855–884

Törő B, Pratt BR, Renaut RW (2015) Tectonically induced change in lake evolution recorded by seismites in the Eocene Green River Formation, Wyoming. Terra Nova 27:218–224

Valero-Garcés B, Morellón M, Moreno A et al (2014) Lacustrine carbonates of Iberian Karst Lakes: sources, processes and depositional environments. Sed Geol 299(15):1–29

Van Daele M, Cnudde V, Duyck P et al (2014) Multidirectional, synchronously-triggered seismo-turbidites and debrites revealed by X-ray computed tomography (CT). Sedimentology 61(4):861–880

Vos RG (1981) Sedimentology of an Ordovician fan delta complex, western Libya. Sed Geol 29(2):153–170

Wagner B, Reicherter K, Daut G et al (2008) The potential of Lake Ohrid for long-term palaeoenvironmental reconstructions. Palaeogeogr Palaeoclimatol Palaeoecol 259(2):341–356

Wallace K, Eyles N (2015) Seismites within Ordovician-Silurian carbonates and clastics of Southern Ontario, Canada and implications for intraplate seismicity. Sed Geol 316:80–95

Wang Q (1993) Fan delta model. Petroleum Industry Press, Beijing

Wang W (2010) Characteristics and control factors of earthquake accumulation in Xie Shan family of Longmen Mountain. Master degree thesis. Southwest Petroleum University, Chengdu

Wang S (2014) Lacustrine Marl reservoir formation and distribution of Shulu Sag. Doctoral degree thesis. China University of Mining and Technology (Beijing), Beijing

Wescott WA, Ethridge FG (1980) Fan-delta sedimentology and tectonic setting—Yallahs fan delta, southeast Jamaica. AAPG Bull 64(3):374–399

Xue L, Galloway WE (1991) Classification of fan delta, braided-river delta and delta system. Acta Geologica Sninca 65(2):141–153

Yang J (2010) The study on the sedimentary microfacies and diagenesis of Shahejie formation of West Slope of Shulu Depression. China University of Petroleum, Dongying

Yang J, Wang H, Nie L et al (2014) Discovery and geological significance of seismites of Paleogene in Jinxian Sag, Jizhong depression. Acta Sedimentol Sin 32(4):634–642

Yuan J (2004) The property and geological significance of seismites of Paleogene in Huimin Sag, Shandong Province. Acta Sedimentol Sin 22(1):41–46

Yuan J, Chen X, Tian H (2006) Formation of loop bedding in Jiyang Sub-basin, Paleogene. Acta Sedimentol Sin 24(5):666–671

Zhang F (2006) Fan delta and braided delta sediments in Baiyinchagan depression. Acta Geoscientica Sninca 26(6):553–556

Zhang C, Liu Z, Shi D et al (2000) Formed proceesing and evaluation disciplinarian of dan delta. Acta Sedimentol Sin 18(4):521–526

Zhang C, Wu Z, Gao L et al (2007) Earthquake-induced soft-sediment deformation structures in the Mesoproterozoic Wumishan Formation, North China, and their geologic implications. Sci China, Ser D Earth Sci 50(3):350–358

Zhao X, Li Q, Jiang Z et al (2014) Organic geochemistry and reservoir characterization of the organic matter-rich calcilutite in the Shulu Sag, Bohai Bay Basin, North China. Mar Pet Geol 51:239–255

Zheng L, Jiang Z, Liu H et al (2015) Core evidence of paleoseismic events in Paleogene deposits of the Shulu Sag in the Bohai Bay Basin, east China, and their petroleum geologic significance. Sed Geol 328:33–54

Zhu X, Xin Q (1994) Important features of Lacustrine Fan. J Univ Petrol, China (Ed Nat Sci) 18(3):6–11

Zou C, Zhao Z, Yang H et al (2009) Genetic mechanism and distribution of sandy debris flows in terrestrial lacustrine basin. Acta Sedimentol Sin 27(6):1065–1075